ACHIEVING A LONG-LIVED CHARGE-SEPARATED FE(II) CHROMOPHORE: INSIGHTS INTO THE ROLE OF REORGANIZATION ENERGY ON THE ULTRAFAST PHOTOPHYSICAL PROCESSES OF D^6 POLYPYRIDYL COMPLEXES

By

Monica Catherine Carey

A DISSERTATION

Submitted to
Michigan State University
in partial fulfillment of the requirements
for the degree of

Chemistry—Doctor of Philosophy

2018

ABSTRACT

ACHIEVING A LONG-LIVED CHARGE-SEPARATED FE(II) CHROMOPHORE: INSIGHTS INTO THE ROLE OF REORGANIZATION ENERGY ON THE ULTRAFAST PHOTOPHYSICAL PROCESSES OF D^6 POLYPYRIDYL COMPLEXES

By

Monica Catherine Carey

Photoredox catalysis reactions are ubiquitous in nature. These processes require a long-lived charge-separated state that is ideally suited for redox-based chemistry and photovoltaic applications. Many common chromophores used in these systems are ruthenium(II)-based, but the low earth abundance of this metal makes it non-viable for large-scale applications in the long-term. The first row congener of Ru(II) is iron(II), but its decreased ligand field strength relative to the second row transition metal causes the metal-to-ligand charge transfer (MLCT) excited state to be depopulated on an ultrafast timescale, deactivating into metal-centered ligand field (LF) excited states that are inefficient for photovoltaic applications. The aim of this work is to understand the fundamental differences in the photophysical processes of Ru(II) and Fe(II) analogues.

Three strategies can be envisioned for prolonging the MLCT lifetime in Fe(II) complexes: (1) prohibiting the vibrational modes associated with the MLCT→LF transition with synthetic modifications to the ligand, (2) increasing the ligand field strength to tune the LF and MLCT states such that the potential energy surface diagram for Fe(II) resembles that of Ru(II), or (3) extending conjugation within the ligand away from the metal center, thereby decoupling the MLCT and LF excited states. Any one of these approaches will inherently affect the reorganization energy, or the amount of energy required for the reactants to undergo vibrational and nuclear motions in order to achieve the geometry of the products without any electron transfer or electronic state crossing occurring. Variable-temperature transient absorption (VT-TA) spectroscopy is a methodology that

has been developed to initially study the ground state recovery (GSR) processes of some low-spin Fe(II) polypyridyl complexes. Arrhenius parameters for this class of compounds are found experimentally for the first time and from these data, semi-classical Marcus theory analysis is performed, allowing for inner-sphere (i.e., complex-only) reorganization energies to be found for each. The H_{ab}^4/λ ratio is determined to be different between bis-tridentate and tris-bidentate species, which is postulated to imply a difference in nuclear coordinate for the relaxation process. The VT-TA methodology is also applied to a bis-tridentate compound for which GSR is both nearly barrierless and nearly at the crossing-point of the $^5T_2/^3T_1$ as the lowest-energy excited state. The outer-sphere reorganization energy is adjusted through the use of counteranions and solvents in an attempt to tune the barrierless nature of the complex. The identity of the solvent did appear to affect the reorganization energy and the inverted region may have been accessed.

The solvation dynamics of the vibrational cooling process in a Ru(II) chromophore were studied as a function of excitation wavelength in a series of alcohol and nitrile solvents. A dual solvation mechanism was observed depending on the amount of excess energy given to the system. Through the use of a sterically-encumbered analogue, the large aryl rotation in the MLCT excited state was determined to be the relevant nuclear coordinate in the vibrational cooling process as it related to the solvation. The Fe(II) analogue of this complex has also been prepared and studied in order to draw direct comparisons of the photophysical processes of these two related systems. These analogues are based on ligands with extended conjugation. In order to study the effects of delocalization on the excited state lifetime, other compounds of this type have been prepared and preliminary measurements of the MLCT lifetimes indicate that increasing delocalization away from the Fe(II) center lengthens the charge-separated lifetime, which is an important first step in achieving long-lived charge transfer states for this class of compounds

This work is dedicated to the girls and women who are told that they can’t do something.
Prove them wrong.

ACKNOWLEDGMENTS

Although I am the one receiving the degree and honorific, this dissertation was the work of so many: I could never have achieved this on my own, and I owe so much to those who shared their experience and knowledge, as well as to those who stood by my side during this process. To Jim, for believing in me and my work, for guiding and supporting me, and for your eternal interest and enthusiasm in my research and career. To my family, for listening to me and being nothing but supportive over these six years. To Bob Rasico, Glenn Wesley, Richard Staples, and Dan Holmes, for being so generous with your time and help. To my committee for their continued guidance and support. To my friends, for being wonderful people I knew I could count on. To the McCusker group, for all the help you provided with my science. And finally, to Mr. Spahr, Mr. Sharp, and Dr. Marsh, for inspiring my interests and believing in my abilities.

TABLE OF CONTENTS

LIST OF TABLES

LIST OF FIGURES

LIST OF SCHEMES

KEY TO ABBREVIATIONS

1-BuOH: 1-butanol

1-HexOH: 1-hexanol

1-OctOH: 1-octanol

A: absorbance

A: amplitude

A: frequency factor

A: initial two-dimensional array of data

a: state a

A_{std}: absorbance of standard solution

A_{unk}: absorbance of unknown solution

acac: acetylacetonate

ACS: American Chemical Society

AM 1.5 G: air mass 1.5 global

AN: acceptor number

AP: analyzing polarizer

AU: arbitrary units

b: state b

BAr^{F-}: tetrakis[(3,5-trifluoromethyl)phenyl]borate

bpy: 2,2'-bipyridine

bpy': 4,4'-disubstituted-2,2'-bipyridine

BT-CCD: back-thinned charge-coupled device

BuCN: butyronitrile

C: autocorrelation matrix for U and V

c: deviation of Gaussian distribution

c: speed of light

caab: 4,4'-cyanoacrylic acid-2,2'-bipyridine

CASSCF: complete active space self-consistent field

CD: circular dichroism

CFC: chlorofluorocarbon

CN-Me-bpy: 4,4'-dicyano-5,5'-dimethyl-2,2'-bipyridine

d: degree of freedom

DCM: dichloromethane

dcpp: 2,6-bis(2-carboxypyridyl)pyridine

DFT: density functional theory

δ: error associated with a value

Δ: change in

ΔG or ΔG^{o}: free energy

Δν: spectral bandwidth

ΔS: change in spin

dmb: 4,4'-dimethyl-2,2'-bipyridine

dmesb: 4,4'-dimesityl-2,2'-bipyridine

dmib: 4,4'-(di-2,5-dimethylisoxazolyl)-2,2'-bipyridine

DMSO: dimethyl sulfoxide

dpb: 4,4’-diphenyl-2,2’-bipyridine

dqp: 8’-diquinolinyl-2,6-pyridine

DSSC: dye-sensitized solar cell

dtbb: 4,4’-di-*tert*-butyl-2,2’-bipyridine

dvpp: 2,6-bis(2-divinylpyridyl)pyridine

e: charge of the donor or acceptor

E: energy

E_a: activation energy

E_{em}: emission energy

E^{ox}: oxidation potential

E_{pulse}: energy per pulse

ϵ_0: static dielectric constant

ϵ_{op}: optical dielectric constant

ESA: excited state absorption

ESI-MS: electrospray-ionization mass-spectrometry

ESIPT: excited state intramolecular proton transfer

Et_2O: diethyl ether

η: viscosity

EtOAc: ethyl acetate

EtOH: ethanol

EXAFS: extended X-ray absorption fine structure

f: force constant

f: repetition rate

F: slope of potential energy surface

$f_{Between\ Groups}$: variance between two data sets

$f_{Within\ Groups}$: error from one data set

FC: Franck-Condon factor

Fc/Fc^+: ferrocene/ferrocenium couple

FWHM: full-width at half-maximum

GA: global analysis

GDD: group delay dispersion

GSB: ground state bleach

GSR: ground state recovery

GVD: group velocity delay

H: enthalpy of reaction

H_{ab}: electronic coupling matrix element

H_{str}: structural enthalpy of reaction

H_{SO}: spin-orbit Hamiltonian operator

$h\nu$: energy of a photon

$\hbar$: reduced Planck’s constant

$\hbar\omega$: oscillation frequency

HexCN: hexanenitrile

HPLC: high performance liquid chromatography

I: intermediate

I_0: transmitted light of probe without excitation

I_{em}: emission intensity

I_{std}: intensity of standard solution

I_{unk}: intensity of unknown solution

IPCC: Intergovernmental Panel on Climate Change

IRF: instrumental response function

ISC: intersystem crossing

IVR: intramolecular vibrational energy redistribution

k: rate constant

k_{ab}: rate of transition from state a to state b

k_B: Boltzmann constant

k_d: diffusion rate constant

k_{ET}: electron transfer rate constant

k_{GSR}: ground state recovery rate constant

k_{nr}: nonradiative rate constant

k_r: radiative rate constant

L: ligand

λ: reorganization energy

λ: wavelength

λ_{calc}: calculated reorganization energy

λ_{exc}: excitation wavelength

λ_{exp}: experimental reorganization energy

λ_{is}: inner-sphere reorganization energy

λ_{max}: wavelength of the maximum of the feature

λ_{os}: outer-sphere reorganization energy

λ_{probe}: probe wavelength

LCOE: levelized cost of electricity

LF: ligand field

LIOAS: light-induced optoacoustic spectroscopy

LMCT: ligand-to-metal charge transfer

ln: natural logarithm

m: mass

M: metal

m: methylene linker

MC: monochromator

Me: methyl substituent

MeCN: acetonitrile

MeOH: methanol

MLCT: metal-to-ligand charge transfer

mol equiv.: molar equivalents

N: Avogadro's number

n: index of refraction

n: number of elements within one group

N: overall sample size

N3: *cis*-bis(isothiocyanato)bis(2,2'-bipyridyl-4,4'-dicarboxylato)ruthenium(II)

N719: di-tetrabutylammonium *cis*-bis(isothiocyanato)bis(2,2'-bipyridyl-4,4'-dicarboxylato)ruthenium(II)

N_{ax}: axial nitrogen

N_{eq}: equatorial nitrogen

n_{std}: refractive index of standard solution

n_{unk}: refractive index of unknown solution

N/A: not applicable

ND: neutral density

NHC: *N*-heterocyclic carbene

NMR: nuclear magnetic resonance

$[O_2]$: concentration of oxygen

OD: optical density

OKE: optical Kerr effect

ω: angular frequency

OPA: optical parametric amplifier

p: phenylene linker

P: product

p: reduced energy gap

P_{ab}: probability of transition from a to b

P_{ave}: average power

P_{peak}: peak power

P(ϵ): solvent polarity

PAC: photoacoustic calorimetry

paniterpy: 5,5”-bis(4-methoxy-2,6-di-*iso*-propylphenyl)-2,2’:6’,2”-terpyridine

PAS: photoacoustic spectroscopy

PC: propylene carbonate

PDA: photodiode array

PES: potential energy surface

Ph: phenyl

Φ: quantum yield

ϕ_2: group delay dispersion

Φ_{std}: quantum yield of standard solution

Φ_{unk}: quantum yield of unknown solution

PMT: photomultiplier tube

PrCN: propionitrile

PTFE: polytetrafluoroethylene

py: pyridine

Q: nuclear coordinate

Q_0: equilibrium coordinate

Q_B: barrier coordinate

$Q^{\ddagger}$: displacement between minimum of reactant surface and barrier

qphen: 8’-quinolinyl-2-phenanthroline

R: distance between donor and acceptor species

R: reactant

r_0: radius of species in its ground state

r_A: radius of acceptor species

r_D: radius of donor species

R(*n*): solvent polarizability

r^*: radius of species in its excited state

ref.: reference

regen: regenerative amplifier

ρ: density of states-weighted Franck-Condon factor

s: confidence interval

S: entropy of reaction

S: Huang-Rhys factor

S: weighting factors of U and V

S/N: signal-to-noise ratio

SCO: spin-crossover

SSCE: saturated sodium calomel electrode

S_{str}: structural entropy of reaction

SVD: singular value decomposition

T: temperature

t: terpyridine moiety

^{t}bu or ^{t}butyl: *tert*-butyl

t: time

TA: transient absorption

τ: lifetime

⟨τ⟩: average solvation time

τ_{abs}: transient absorption lifetime

τ_{conv}: convolved full-width at half-maximum of two Gaussians

τ_{em}: emission lifetime

τ_{exc}: excitation pulse duration

t_{in}: input pulse duration

t_{out}: output pulse duration

τ_{MLCT}: metal-to-ligand charge transfer lifetime

τ_{probe}: probe pulse duration

τ_{pulse}: pulse duration

τ_{VC}: vibrational cooling time constant

TBA: tetrabutylammonium

TD-DFT: time-dependent density functional theory

terpy: 2,2':6',2"-terpyridine

THF: tetrahydrofuran

TICT: twisted intramolecular charge transfer

tpvpvp: 4'-phenylene-*trans*-vinylene-phenylene-*trans*-vinylene-phenylene-2,2':6',2"-terpyridine

tren(py)$_3$: tris(*N*-(2-pyridylmethyl)-2-iminoethyl)amine

U: spectral component of two-dimensional data decomposed by singular value decomposition

UN: United Nations

UNFCCC: United Nations Framework Convention on Climate Change

USD: United States dollar

UV-Vis: ultraviolet-to-visible region spectrophotometry

V: kinetic component of two-dimensional data decomposed by singular value decomposition

V: potential energy

v: velocity

v: vinylene linker

V: volume

V_{solv}: solvent-induced volume

V_{str}: structural volume

v/v: volume-to-volume ratio

VC: vibrational cooling

VT: variable-temperature

X: displacement amplitude

x_P: equilibrium coordinate of product

x_R: equilibrium coordinate of reactant

ζ: spin-orbit coupling constant

CHAPTER 1. ENDEAVORING TO ACHIEVE EFFICIENT IRON(II) DYES FOR SOLAR ENERGY CONVERSION APPLICATIONS

1. The Global Energy Crisis

There are few subjects on which one could find that greater than 97% of scientists agree. Climate change is one of those topics.[1-3] If, however, you were to poll the United States on this very question, only 49% believe that scientists think global warming is happening,[4] and only 12% could accurately guess the near consensus among scientists.[3,5] This is only one, albeit revelatory, example of the paradoxical nature of climate change. In many respects, the discussion of climate change is heavily focused on the future, but many of the effects are being observed right now: an unusually warm summer in the northern hemisphere, a three-year drought in South Africa, powerfully damaging hurricanes like Harvey and Maria, destructive wildfires in Greece, California, and, incredibly, *the Arctic Circle* – and these are only a few of the most relevant examples from 2017-2018. And while approximately two-thirds of these extreme natural disasters have been attributed to or made more severe by climate change,[6] this phenomenon is perceived by non-scientists as an abstract occurrence with a high degree of uncertainty.[7,8]

In a nearly unanimous way, however, scientists not only agree that climate change is occurring, but that the cause is human-made.[1,6,9] This is also a point of accord by many of the leading scientific organizations, such as the American Association for the Advancement of Science, the American Chemical Society, the U.S. National Academy of Sciences, and the U.S. National Aeronautics and Space Administration,[1] a veritable alphabet soup of agreement. This list would be remiss if the United Nations (UN) were not included. The UN Framework Convention on Climate Change (UNFCCC) sponsored the Kyoto Protocol in 1997, a major multilateral

agreement with the intention of reducing greenhouse gas emissions globally. By this time, a hole in the ozone layer in Antarctica had been observed and determined to be caused by chlorofluorocarbons (CFCs), leading to the Montréal Protocol. This treaty effectively banned CFCs worldwide, allowing the ozone to recover, and showing the effectiveness of international cooperation.[10,11] The Kyoto Protocol likewise identified six main greenhouse gases that were deleterious to the earth's atmosphere: carbon dioxide, methane, nitrous oxide, hydrofluorocarbons, perfluorocarbons, and sulfur hexafluoride. Relative to the Montréal Protocol, this treaty was only modestly successful – largely due to the lack of participation by the United States and China, the two global leaders in harmful emissions, as well as the global financial crisis.[10,11] In an attempt to form a worldwide coalition to reduce greenhouse gas emissions, the UNFCCC adopted the Paris Agreement in 2015. Here, 175 parties were signatory to the treaty of 196 nations worldwide.[12] This agreement was unusual not only in the overwhelming number of member nations to participate, but in the specificity of its goals and the flexibility of achieving said goals. The global temperature was set to rise no more than 2 ºC "above pre-industrial levels" by the reduction of greenhouse gas emissions by the middle of the 21st century.[8] It should now be evident that not only do 97% of scientists agree on the occurrence and cause of climate change, but so do more than 89% of global leaders.

Also under the auspices of the UN, the Intergovernmental Panel on Climate Change (IPCC) regularly releases a report fully detailing the causation and impacts of climate change, as well as models that are used to guide policymaking decisions. These data have shown that while some climate abnormalities may be caused by natural forces, climate change follows one particular trend and are clearly anthropogenic (or human-made) in cause.[9] The simultaneity of the Industrial Revolution and the increased concentration of CO_2 and other greenhouse gases hints at climate

change's true origins: the burning of fossil fuels. Gas, oil, and coal are known carbon-emitters. As the concentrations of CO_2, CH_4, and N_2O have increased, the global temperature has followed suit. Since the beginning of the Industrial Age (i.e., ca. 1760-1840 CE), the atmospheric concentration of CO_2 has risen by 40%; since 1880 CE, the average global temperature likewise increased by ~0.85 ºC.[9] The current concentration of CO_2 is 406.48 ppm as reported from the Mauna Loa Observatory in Hawai'i for late-August 2018.[13] This level is at an unprecedented high for not only the past two centuries, but likely the past 20 million years.[9,12] Furthermore, the rate of growth of CO_2 concentrations has more than doubled in the past two decades relative to the 1990s,[12] revealing the impetus for the Paris Climate Agreement. Herein lies another paradox of climate change: despite knowing the correlation of greenhouse gas concentration and average global temperature, it is as yet unknown what CO_2 level will yield what specific temperature.[12] However, it is widely accepted that a temperature increase of much more than 2 ºC relative to pre-Industrial times will have wide-ranging, long-term effects on the planet that cannot be reversed.[9,14]

Many of these consequences are ecological. The average global temperature is continuously climbing, which has reduced the mass of the glaciers in Greenland and Antarctica.[9] The result, then, is rise in the sea level by 0.19 m over the last century, as well as a decrease in the pH of the oceans. The highly interrelated nature of the ecosystem is such that a drastic change in the earth's bodies of water induces both droughts and heavy rainfalls, depending on the geographic location. Overall, this has the effect of changing the salinity of bodies of water: increasing where evaporation occurs due to droughts and decreasing where rainfall is heaviest.[9] Additionally, snow cover is generally lessening, and coral reefs are observed to be undergoing a bleaching process, effectively dying.

It is no wonder, then, that animal populations are dwindling and species are shifting their

migration patterns. Likewise, humans are beginning to see real-world consequences of global climate change, not just in shifting weather patterns, but also in changes in food and water supply, an increase in heat-related mortalities, disruption of infrastructure, as well as the routine flooding of coastal cities which causes displacement.[9] These effects are all consequences of the increased concentration of CO_2 and other greenhouse gases in the earth's atmosphere. A disproportionate fraction of these emissions come directly from the energy sector and will only continue to increase over the coming decades.[9,12] And while reducing these emissions over the next few years is crucial, it is also only a first step. The lifetime of CO_2 in the ecosystem ($CO_{2,atmosphere} \rightleftharpoons CO_{2,ocean}$) is on the order of 500-1000 years;[9,12] therefore a permanent alternative strategy to burning fossil fuels must be developed and implemented in order to limit the effects of climate change.

Should the climate change-based reasoning not suffice, a purely economic argument can be made for renewables. By the middle of the 21st century, the global population is expected to be 10 billion. The three fossil fuels (i.e., oil, natural gas, and coal) are the biggest suppliers of energy globally, and ~20% of that energy is used to generate electricity.[15] This percentage is likely to grow as personal electronic devices grow in popularity. The amount of these energy sources in the earth is finite, limiting their usability beyond a certain time period. Additionally, because fossil fuels are naturally occurring, not every country will have equal access to them; many nations will desire energetic independence as the geopolitics surrounding natural resources is incredibly fraught. This is in large part due to many of the world's oil reserves being held by the Russian Federation, Saudi Arabia, Iran, Iraq, Kuwait, Venezuela, and other war-torn nations.[16] In this way, developed and developing countries can respond to the demand for a higher living standard even as their population increases.

Clearly, there is a real financial incentive for non-fossil fuels, in addition to an ecological

one. Renewable energy sources offer a path towards greater stores of energy, increased energy independence, and a reduced carbon footprint. These methods offer a low-carbon or wholly carbon-neutral alternative to traditional fossil fuels. It is fortuitous, then, that in 2017, the usage of renewables grew more relative to any other energy source, producing ~25% of energy worldwide.[17] Together, China and the United State represented 50% of the increase in renewable-based electricity. While the demand for coal and gas-generated electricity did increase their use by 284 and 94 terawatt hours (TWh), oil was reduced by 9 TWh, while renewables increased by 383 TWh, which is greater than the combined increase in both coal and gas.[17]

There are many alternatives when choosing renewable energy sources, each with its own set of advantages and disadvantages. Though not a renewable, nuclear energy is a source of low carbon emissions. This technology is mature, and many reactors are currently operable, predominantly in Europe, North America, and Asia. Many disadvantages keep old reactors from being updated and new reactors from being built, including but not limited to proliferation of nuclear weapons, public opinion, safety, and waste management.[9] Biomass is not carbon-neutral, but is one of the most important renewables due to its relative abundancy and low cost. This category may be as simple as burning wood for fuel (thus its popularity in low-income regions) but has also been updated to include biofuels for transportation uses. Important innovations are being made in this area in which waste can be converted into an energy supply.[15] The final four most popular renewable energy sources are hydroelectric, geothermal, wind, and solar powers. Hydroelectric is the most developed of these, followed closely by on-shore wind technology while off-shore technology is still in process. Solar and wind are the most used renewables as of 2017, and with good reason: combined, these two processes have the capability of providing 80% of the annual U.S. electricity demand based on recent years.[18]

On its own, the amount of incident solar irradiation on the earth in about one hour is more than the entire year's worth of energy demanded, based on values from 2001.[19] Photovoltaic devices are those that capture sunlight and convert it into electrical power. China produces and houses these devices more than any other country, as evidenced by the fact that in 2016, 26% of the photovoltaics installed globally were in China.[20] The United States began joining this market recently as well, and now makes up more than 10% of the market share. The traditional photovoltaic for commercial use is made of crystalline silicon, representing the first generation of these materials. Efficiencies for silicon-based devices have been reported as high as 24%, but average 18-24%.[20] A second generation of photovoltaics are beginning to come on-line, utilizing thin-film technologies. The two most recognizable materials are cadmium telluride (CdTe) and copper indium gallium selenium, or CIGS. Modules employing these films have demonstrated average efficiencies of 12-16% as of 2012.[20]

The obvious disadvantage to natural phenomena-based renewable energy sources is that they require those natural events to be occurring in order to generate electricity. Just as it is not always a sunny, clear day, the wind is not always blowing. Much work is being done to improve energy storage for these renewables, such that solar power collected during the day can still be utilized at night or even a full season later.[18] This will also require access for these renewable energy sources to the electrical grids for disbursement of power far away from the collection source. Renewables are likely to compete with traditional fossil fuels for this access while they are being developed and increasingly implemented. They are being employed more and more frequently, though, due in no small part to the plummeting costs of these technologies. Over the last decade, photovoltaic devices saw a price decrease of more than 80%, with the cost of electricity generated by those modules likewise dropping nearly 75%.[20] Wind turbines have seen a similar

price reduction in both the devices and the power costs. These trends are driven both by technological advances and by economies of scale, meaning the price of producing these materials in bulk has decreased substantially. The average levelized cost of electricity (LCOE) of fossil fuels per kWh is USD 0.05-0.17 in 2017.[20] New estimates show that the LCOE for renewables by 2020 will be within this same range, if not lower. Specifically, the global weighted average LCOE for solar energy is expected to be USD 0.03/kWh as soon as this year.[20] These estimates point to a future in which renewables are invariably cheaper alternatives to fossil fuels, only serving to enhance their attractiveness.

Renewable technology, as well as methods such as carbon capture and storage, provide a path toward reduced carbon emissions, as well as sufficient energy supply for the ever-growing demand. Technological advancements are increasingly allowing renewables to be more universally accessible. It is through these advancements and aggressive policy changes that alternative energy sources can overshadow the stranglehold on the market that fossil fuels have. These policies must be on the local and national levels, in industries as well as by individual consumers. And thus we come to the final paradox of climate change: although humans and their technology invariably caused it, humans and their technology can also begin to reverse climate change and mitigate its effects.

2. Dye-Sensitized Photovoltaic Devices

Charge separation is an increasingly important process that can be utilized for a wide variety of applications. Notably, photo-induced charge separation results in the generation of a potential gradient, which can be employed as usable energy. This conversion of light into chemical energy has humble origins in the form of photosynthesis, but it also has significant implications

for the field of photovoltaics in which electricity is generated.[21-23] In order to fully understand and eventually improve the generation of photocurrent, the elementary steps after excitation and the subsequent redistribution of charge must first be characterized and understood. Coordination compounds represent one class of molecules that have demonstrated both photophysical and redox properties that are desirable for charge separation applications, such as their use in dye-sensitized solar cells (DSSCs)[24,25] and photoredox catalysis.[26] With their ability to absorb light in the visible region, transition metal-based complexes are appealing for use as chromophores, or light absorbers, to potentially produce electrical current. For example, ruthenium(II) polypyridyl complexes have become the cornerstone of photovoltaic devices over the past 40 years due to their desirable photophysical properties.[27] These complexes tend to exhibit long-lived (nanosecond to microsecond) excited states in which the molecule is redox-active as a result of the charge separation. The metal-to-ligand charge transfer, or MLCT, excited state is responsible for that redox activity. This state is characterized by a simultaneously oxidized metal (M) center and reduced ligand (L), as described in eqn. (1.1).

$$[M^{II}(L)_3]^{2+} \xrightarrow{h\nu} [M^{III}(L)_2(L^{-})]^{2+} \quad (1.1)$$

Here, an electron initially in a d orbital on the metal is excited into a ligand-based π^* orbital, thereby producing a charge-separated state. The position and long-lived nature of the excited electron on the periphery of the molecule allows for efficient charge transfer, making chromophores of this type ideal candidates for photovoltaic-type applications.

The prototypical Ru(II) polypyridyl complex is $[Ru(bpy)_3]^{2+}$ for which bpy is the 2,2'-bipyridine ligand. This complex has been studied extensively as a model of d^6 photophysics (represented in Scheme 1.1) and high-efficiency photochemistry. Upon visible excitation, $[Ru(bpy)_3]^{2+}$ has been found to form a ^{1}MLCT Franck-Condon state, which then decays to the

^{3}MLCT excited state on an approximately 30 fs timescale, as determined by femtosecond fluorescence upconversion[28,29] and femtosecond stimulated Raman spectroscopy[30] When coupled with the near degeneracy of the ^{1}MLCT and ^{3}MLCT in the manifold, intersystem crossing (ISC) proceeds in a rapid and efficient manner,[30] allowing for the process to occur with a near unity quantum yield.[28,30-32] The ultrafast (i.e., sub-nanosecond) ISC observed is often cited as being due to the increased spin-orbit coupling afforded by the heavy Ru(II) center, increasing the mixing of the spin terms of the MLCT excited states.[33,34] McCusker and coworkers found that the transient absorption spectrum of $[Ru(bpy)_3]^{2+}$ is unchanged after 300 fs, at which point it is also superimposable with the same data on the nanosecond timescale. This implies that by ~300 fs, the fully thermalized ^{3}MLCT excited state has been accessed, which is the lowest-energy excited state in $[Ru(bpy)_3]^{2+}$.[32] Alternatively, Okada et al. observed a probe-wavelength dependent kinetic component on the order of 0.6-1.3 ps (dependent on the solvent used) and attributed this to a vibrational cooling (VC) process along the ^{3}MLCT surface.[29] This process allows the ~1 eV of excess energy from the excitation and subsequent ISC events to be anharmonically redistributed from the chromophore into the surrounding medium. While studying aqueous $[Ru(bpy)_3]^{2+}$ by fluorescence upconversion, however, Chergui and coworkers observed no such vibrational process.[28] They subsequently concluded that the dynamics found by Okada were likely due to intramolecular vibrational energy redistribution, or IVR, in which the excess thermal energy stored in the chromophore upon excitation is redistributed into lower-energy vibrational modes of the complex.[35] Analogously, solvent-dependent dynamics have been previously observed on the ultrafast timescale in $[Ru(bpy)_3]^{2+}$, in somewhat controversial data published by McCusker et al.[31] Femtosecond transient absorption anisotropy measurements in a series of three nitrile solvents (i.e., acetonitrile, propionitrile, and butyronitrile) displayed solvent-dependent relaxation kinetics

in which the measured time constants increased monotonically with increasing alkyl chain length of the nitrile and were found to be consistent with the inertial response of the individual solvents. It was therefore postulated that the solvation response was in fact coupled to the charge delocalization in the chromophore, with reorientation of the solvent concluding as the charge came to be localized on a single bipyridine (Scheme 1.2). An ultrafast delocalized excited state in $[Ru(bpy)_3]^{2+}$ has been described previously,[36] but its existence is still contested in the Ru(II) community.[37]

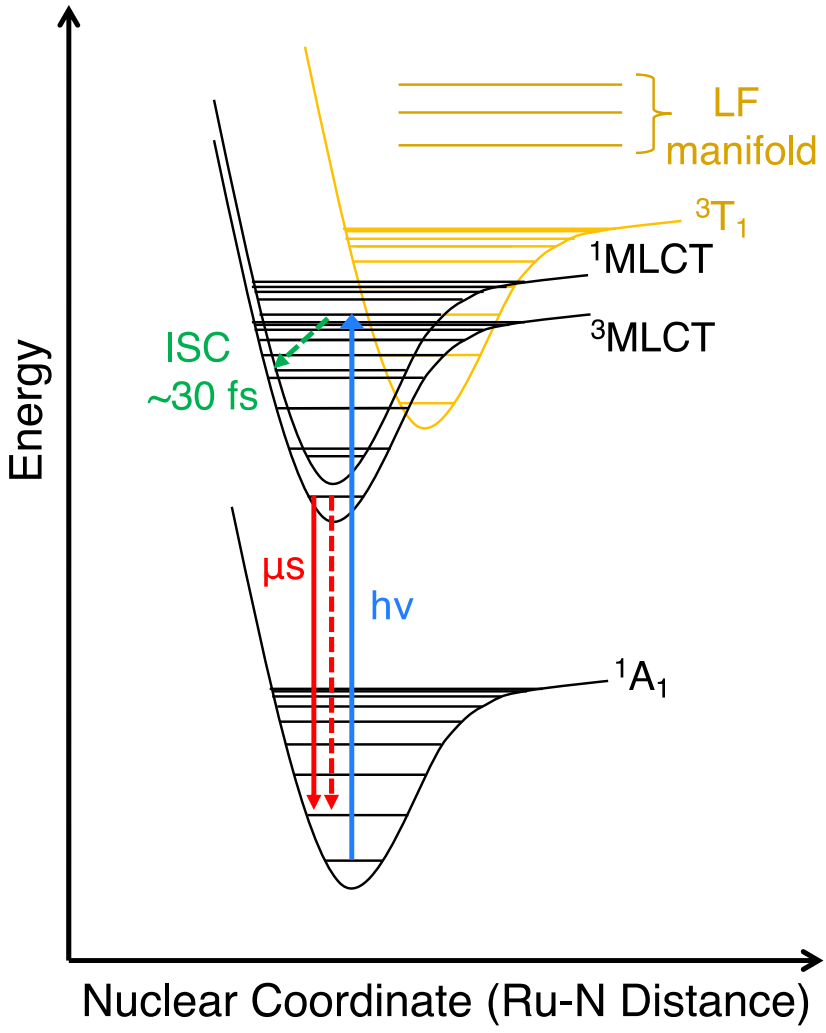

Scheme 1.1. Potential energy surface diagram for $[Ru(bpy)_3]^{2+}$ along the Ru-N coordinate. Excitation in the visible region forms the ^{1}MLCT excited state, which intersystem crosses to the ^{3}MLCT state in ~30 fs. There are contradicting reports as to whether vibrational energy redistribution occurs in the ^{3}MLCT excited state. Ground state recovery then occurs either radiatively (solid arrow) or nonradiatively (dashed arrow) to the $^1A_1$ ground state on the order of 1 μs, depending on the solvent. The lowest-lying ligand field (LF) state lies energetically above the MLCT manifold with other LF excited states and does not participate in the photophysical processes except when thermally accessed.

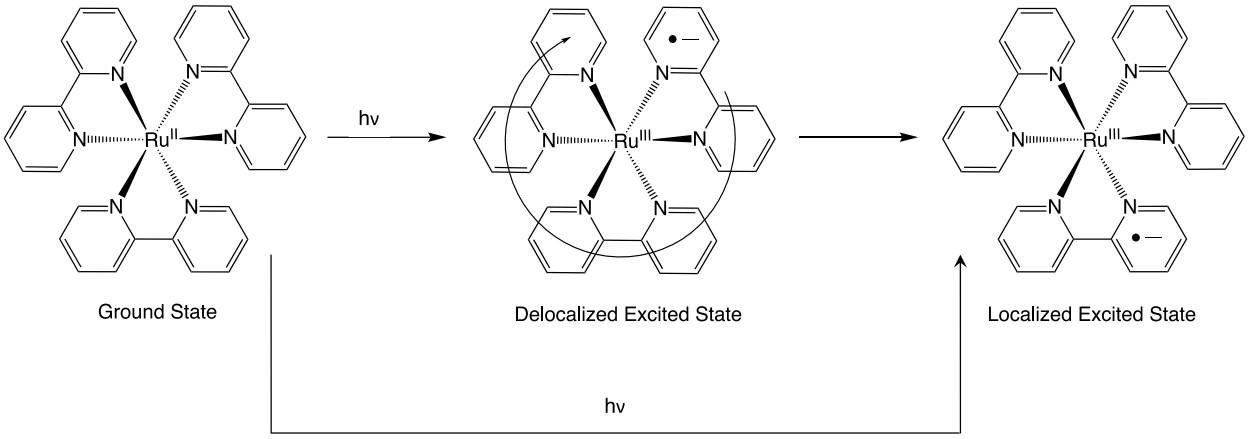

Scheme 1.2. Proposed electronic delocalization/localization in the excited state dynamics of $[Ru(bpy)_3]^{2+}$. In the delocalized picture (top arrows), excitation forms an excited state in which the electron transfers between ligands on the timescale of the solvent inertial response, until it comes to rest on a single ligand. Alternatively, excitation may directly produce the localized excited state (bottom arrow).

In addition to femtosecond fluorescence from the ^{1}MLCT state, $[Ru(bpy)_3]^{2+}$ is more commonly studied for the phosphorescence displayed from its ^{3}MLCT excited state.[30,38] Meyer and coworkers have found that k_r, the radiative rate constant, associated with the ^{3}MLCT excited state to $^1A_1$ ground state conversion via the emission of light is relatively insensitive to solvent, as is the emission energy (E_{em}) for the most part.[38] On the other hand, the nonradiative rate constant, k_{nr} (a measure of the dissipation of energy by heat), showed a dependence on both solvent and temperature. Charge transfer states are highly susceptible to solvation effects, particularly by polar solvents which are capable of stabilizing the separated charges. This describes the solvent-dependent lifetimes of $[Ru(bpy)_3]^{2+}$ for $k_{nr} > k_r$. Indeed, Meyer found that $\ln(k_{nr})$ vs. E_{em} yielded a linear correlation in alcoholic solvents; interestingly, water was found to deviate substantially from the line.[38] The temperature dependence observed in k_{nr} can be explained by the ligand field strength

of Ru(II) polypyridyls. In this class of compounds, the ligand field strength is great enough that only low-spin complexes are observed, and the $^3T_1$ is invariably the lowest energy ligand field excited state,[27] as indicated by the d^6 Tanabe-Sugano diagram.[39] The ligand field (LF) states, however, are nearly degenerate with the MLCT manifold (Scheme 1.1), and in some cases are actually energetically below that manifold as is observed with $[Ru(terpy)_2]^{2+}$, in which terpy is the 2,2':6',2"-terpyridine ligand.[26,27,40,41] In some instances, then, thermal energy may allow population of the $^3T_1$ ligand field state, which thus reduces k_r as well as the quantum yield (Φ) of the ^{3}MLCT state formation. Higher-lying LF states are often associated with ligand dissociation and may therefore also reduce k_{nr} by inadvertently undergoing photochemistry. Caspar and Meyer theorized that the solvent effects observed in $[Ru(bpy)_3]^{2+}$ were likely linked to photodissociation of the ligand, with subsequent solvent coordination occurring, thereby affecting the observed rates of ground state recovery.[38]

The photophysics and photochemistry of Ru(II) polypyridyls have long dominated photovoltaic research,[24,25,42] and have recently come to define the field of photoredox catalysis.[43-45] This is in large part due to the long-lived charge transfer excited state present in $[Ru(bpy)_3]^{2+}$ and its analogues. The appendage of an anchoring group such as a carboxylic acid allows for chemisorption to a semiconductor. In fact, the two most commonly referenced and studied dyes are N3 and N719, $[Ru^{II}$(4,4'-dicarboxy-2,2'-bipyridine)$_2$(isothiocyanate)$_2]$ in which the carboxylic acid is protonated for N3 but tetrabutylammonium ions replace protons in N719.[42] Upon excitation, the electron promoted from the Ru(II) center to the bipyridyl ligand may be transferred to the semiconductor surface, then diffuse through the semiconductor nanoparticles to the back electrode in order to produce a current. Interfacial electron transfer from the chromophore to the semiconductor, also known as injection, is a multiexponential process that typically occurs on the

order of femtoseconds to picoseconds. It is critical, then, that the excited state lifetime of the dye outlast the injection rate for a moderately efficient cell. As of August 2018, the highest efficiency certified dye-sensitized solar cell utilizes a Ru(II) sensitizer to achieve 11.9% power conversion efficiency under one sun illumination (AM 1.5 G, 1000 Wm^{-2}).[46,47] When used as a photocatalyst for redox-based reactions, the excited electron of the Ru(II) complex may oxidatively or reductively react with a second species to initiate the catalytic cycle. These reactions are typically bimolecular and therefore the MLCT excited state of the ruthenium-based catalyst must live longer than the rate of diffusion, which occurs on the order of nanoseconds and is solvent-dependent.[43] For these, and many analogous photovoltaic processes, the limiting step is the lifetime of the charge-separated excited state. When the MLCT is the lowest-lying excited electronic state, it frequently relaxes on the order of hundreds of nanoseconds to microseconds. It is easy to understand, then, why Ru(II) polypyridyl-based chromophores with their long-lived charge-separated excited states, visible absorption profile with relatively high extinction coefficients, and synthetic tunability are so highly studied in the areas requiring photo-initiated reactions.

3. Adapting Iron For Redox Applications

The case for ruthenium chromophores is strong but falls apart when dissecting long-term and scaled viability. While the catalyst is not the greatest material cost of a DSSC, the price of ruthenium is of some concern. The current cost of ruthenium is nearly 8200 USD/kg,[48] which will obviously translate to starting material costs for cell fabrication. More importantly, however, is the driving force for the cost: elemental abundance. It is currently estimated that ruthenium is the sixth least abundant naturally occurring element in the earth's crust.[49] If Ru-based photovoltaics were to be scaled for global use, all of the ruthenium would be entirely used up within years. Because

the goal of applications such as DSSCs is to alleviate strain on the earth's natural resources and to find more efficient methods of harvesting solar energy, it would be all too counterproductive then to work solely on ruthenium-based devices. Analogous compounds must be found and developed to have competing, if not improved, efficiencies. Coupled to their increased abundance, these materials would also be more cost-effective, allowing for large-scale manufacturing and greater access for people of all income levels, and thus a reduced dependence on carbon-emitting and other limited natural resources.

Many groups have already begun to tackle this problem. Indeed, work done on zinc(II) phthalocyanines[50] and sterically rigid Cu(I) dyes[51] show enormous promise. Alternatively, organic dyes have also been studied, removing the concern for metal choice, but having the disadvantageous side effect of reduced synthetic tunability.[52] Ideally, the wealth of knowledge that has been gained from the work done on Ru(II) dyes could be incorporated into new chromophores prepared from more abundant materials. This would keep the chemistry and photophysical processes from being so unrecognizable as to essentially be resetting the entire field of photovoltaics back to zero. The metal of choice, then, is iron. Iron is the first-row transition metal congener of ruthenium, maintaining the d^6 electronic configuration provided both are in the 2+ oxidation state. It is not uncommon for Fe(II) polypyridyls to be studied, including $[Fe(bpy)_3]^{2+}$, as direct analogues of the Ru(II) compounds. Most relevant, though, is the abundance of iron in the earth's crust. Where ruthenium is the sixth least abundant, iron is estimated to be the fourth *most* abundant element, drastically improving the cost efficiency and scalability of iron-based solar cells.

3.1 Fundamental Disadvantages to Using Low-Spin Fe(II)

Despite the incredible salesmanship above, it should be apparent that there are inherent

pitfalls to using Fe(II) polypyridyl chromophores for photon-to-current conversion processes. The use of an iron sensitizer has been reported previously in a DSSC setup.[53] The N3 analogue [Fe(4,4'-di-H_2carboxy-2,2'-bipyridine)$_2$(CN)$_2$] prepared by Ferrere and Gregg was found to perform with only 0.10% efficiency. While the conditions for the device were not optimized in this study, low-spin Fe(II) polypyridyl dyes are, typically, approximately 1-2 orders of magnitude less efficient than their Ru(II) counterparts.[54]

Ultimately, the poor performance of iron dyes is owed to the smaller ionic radius of Fe(II) relative to Ru(II). As a first row transition metal, the orbital overlap achieved between the metal and ligand is much less than in analogous second row elements. This greatly reduces the ligand field strength of iron dyes. When the photophysics of this class of compounds was first being intensely studied in the 1970s and 1980s, the nature of the lowest energy excited state was not immediately apparent. The ground state absorption spectra for Fe(II) polypyridyls are generally red-shifted relative to their Ru(II) analogues, but still display MLCT transitions in the visible region. Low-spin Fe(II) complexes, as a rule, though, do not emit.[33,55] Electronic excited state spectra were collected to compare these two metal-centered systems, and where Ru(II) displayed a positive ΔA feature (excited state absorption) associated with a lowest energy MLCT excited state, no such positive band was observed in Fe(II) chromophores.[34,56,57] This was the very first evidence of the attenuated ligand field strength in iron-based dyes relative to the ruthenium analogues, such that the lowest energy excited state was actually LF and not MLCT in nature. Furthermore, due to the extremely short (i.e., sub-nanosecond) lifetime of Fe(II) chromophores, it was further concluded that the ground and lowest energy excited states in the iron-based complexes were likely to be coupled. The energetic difference between the ground state and the ^{3}MLCT state in Ru(II) dyes is large, and the molecular geometries are very similar, such that these potential

energy surfaces are nested, lengthening the lifetimes to be on the order of microseconds.[55] Over the course of nearly 25 years, researchers slowly transitioned from claiming the lowest energy excited state was ^{1}LF or ^{3}LF to citing either a ^{3}LF or ^{5}LF state.[56,58-62] The exact spin could not be distinguished for these Fe(II) compounds, until nearly simultaneously, work by Hauser,[63] and McCusker et al.[57] finally identified the $^5T_2$ as the lowest energy excited state.

By the early 1990s, iron had been found to be fundamentally different from ruthenium in terms of its photophysics. While the complexes themselves may appear similar, following excitation, $[Ru(bpy)_3]^{2+}$ forms a MLCT excited state with a microsecond lifetime, whereas $[Fe(bpy)_3]^{2+}$ displays a ligand field excited state that is three orders of magnitude shorter in lifetime. Not only is a LF state metal-centered, making it a worse candidate for charge-transfer processes than MLCT states, but it is also lower in energy than the charge separated states, thus reducing the driving force for electron transfer and – specifically with regards to DSSCs – resulting in weaker overlap with the conduction band of titanium dioxide, TiO_2.[53,54] That being said, the ground state absorption spectrum of $[Fe(bpy)_3]^{2+}$ does display a signature MLCT band in the visible region, and the iron-based Ferrere dye was capable of producing an amount of photocurrent, albeit one-tenth that of an average Ru-based DSSC device.[53] As the photophysics are not so altered in moving from ruthenium to iron that the MLCT excited states are entirely lost, the question then is why do the MLCT excited states only minimally participate in electron injection?

This question could only begin to be answered with the advent of femtosecond laser spectroscopy. The first report of a sub-nanosecond MLCT deactivation timescale came when the formation of the $^5T_2$ was found to be complete within ~700 fs.[57] Nearly a decade later, this rate was narrowed down even further in an Fe(II) hexadentate complex, for which depopulation of the MLCT manifold was described as occurring in a sub-100 fs manner by transient absorption

spectroscopy.[64] This lifetime has now been generally verified in a variety of Fe(II) polypyridyl complexes, though is more frequently reported as a ~130 fs specifically in $[Fe(bpy)_3]^{2+}$.[65-68] This ultrafast deactivation from the charge-separated excited explains the poor performance of Fe(II) polypyridyl-based dyes in DSSCs.

Over time, much of the photophysical cycle of $[Fe(bpy)_3]^{2+}$ has been determined through a wide variety of spectroscopic techniques (Scheme 1.3). Visible excitation of $[Fe(bpy)_3]^{2+}$ prepares a ^{1}MLCT excited state that undergoes sub-30 fs ISC into the ^{3}MLCT.[65,69] The MLCT manifold is depopulated in ~130 fs and ultimately results in the formation of the $^5T_2$ lowest energy excited state with unity quantum yield.[61] The $^5T_2$ electronic configuration is $(t_{2g})^4(e_g^*)^2$ and therefore produces a 0.2 Å (or 10%) bond elongation in the excited state relative to the $^1A_1$ ground state, which is $(t_{2g})^6(e_g^*)^0$.[70] While this quintet excited state is known, the pathway from the ^{3}MLCT is hotly contested in the Fe(II) community. Ultrafast X-ray absorption near edge structure[65] and X-ray fluorescence[66] spectroscopies were performed and yielded similar results but vastly different interpretations. For the latter set of data, spectral and kinetic modeling confirmed that a ^{3}T intermediate needed to be included to fit the data.[66] The relaxation pathway was found to be ^{1}MLCT→^{3}MLCT→^{3}T→$^5T_2$. The intermediate was determined to only be transiently populated. In the case of the X-ray absorption study, the data were observed to plateau around 250 fs.[65] The authors note that these kinetics could be fit with a sub-60 fs component if a singlet or triplet intermediate were introduced, but they deemed this lifetime to be unreasonable considering the high frequency nature of the vibrational modes at these positions on the potential energy surfaces; the relaxation pathway in this case was ^{1}MLCT→^{3}MLCT→$^5T_2$.[65] Some ab initio computational work has been done in an attempt to address this question, and found that the $^5T_2$ state crosses to the MLCT manifold near the lowest energy vibrational mode of the charge transfer

states.[71] These results, while not definitive, appear to at least provide a pathway in which direct MLCT→$^5T_2$ interconversion might occur.

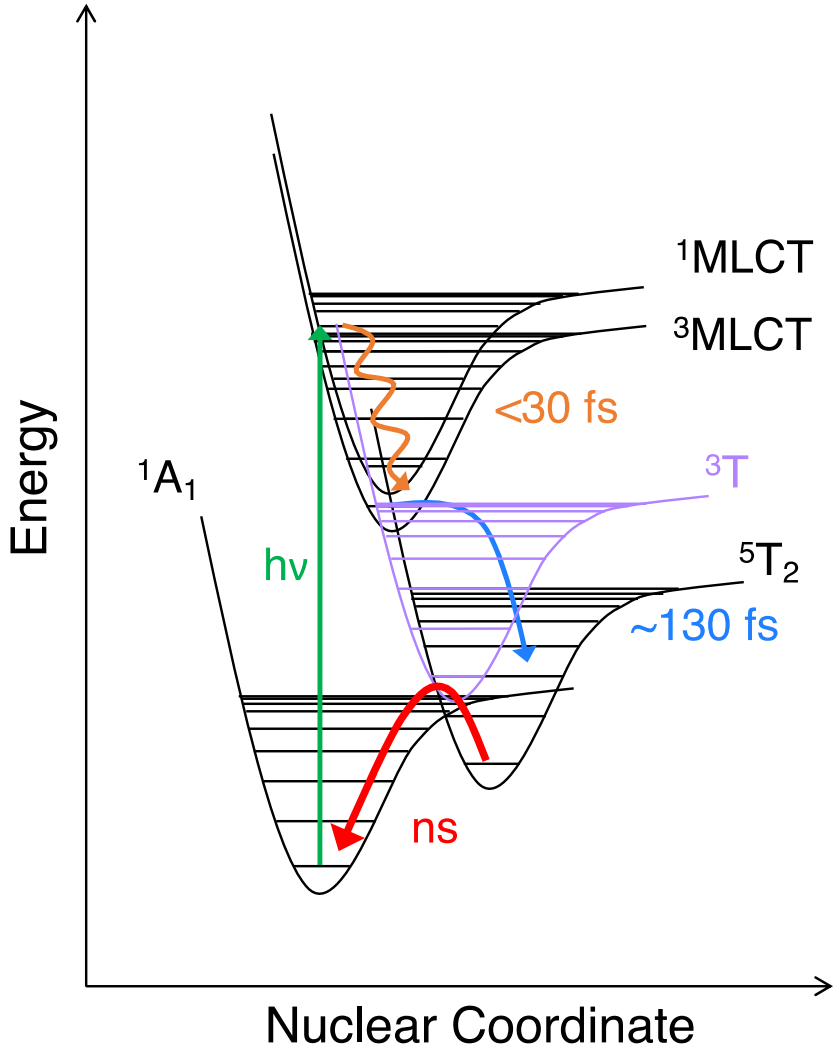

Scheme 1.3. Potential energy surfaces for $[Fe(bpy)_3]^{2+}$ along the Fe-N bond distance nuclear coordinate. Visible excitation prepares the ^{1}MLCT excited state, followed by sub-30 fs intersystem crossing to the ^{3}MLCT. The MLCT manifold is depopulated in approximately 130 fs and may transiently populate the ^{3}T ligand field state during deactivation to the lowest energy excited state, the $^5T_2$. Ground state recovery occurs to the $^1A_1$ on the order of 1 ns, depending on solvent.

From the $^5T_2$, ground state recovery to the $^1A_1$ occurs on the hundreds of picosecond to nanosecond timescale. This lifetime is found to be highly dependent on both the ligand and solvent environment.[72,73] Although MLCT excited states are inherently influenced by the nature of the solvent, as described for Ru(II) complexes above, the sub-150 fs lifetime is not long enough to fully allow solvent reorientation to the instantaneous dipole moment of the chromophore. Any solvent effects, then, must be a result of the LF states. It is not intuitive that metal-centered excited states would display lifetimes with as strong a dependence on solvent as the charge-transfer excited states in Ru(II)-based chromophores. Just as is true for $[Ru(bpy)_3]^{2+}$, water is especially noted to be an outlier.[72,73] These effects have generally been postulated as being related to the volume expansion for the $^1A_1 \rightarrow {}^5T_2$ transition, as well as the excited state being more prone to solvent-aided stabilization relative to the ground state.[73]

3.2 Strategies to Lengthen the MLCT Lifetime in Fe(II) Chromophores

It is clear that the photophysical processes of analogous Fe(II) and Ru(II) polypyridyl complexes are comparable in many ways. They have MLCT transitions that absorb light in the visible region. The ^{1}MLCT$\rightarrow{}^3$MLCT intersystem crossing occurs in ~30 fs due to the heavy metal centers. The lowest-energy excited state in each complex is formed with near unity quantum yield, and ground state recovery from that state is highly solvent-dependent. But despite all their similarities, Fe(II)-based dyes convert photons to electricity with $^1/_{10} - {}^1/_{100}$ the efficiency of their Ru(II) congeners. Based on Schemes 1.1 and 1.3, then, three possible strategies can be envisioned in which to increase the MLCT lifetime for these Fe(II) complexes.

3.2.1 Inverting the MLCT and Ligand Field Excited State Energetics

The most simplistic method for lengthening the charge transfer lifetime in Fe(II) polypyridyls is by increasing the ligand field strength of the chromophores; in principle, this will

raise the LF states to lie energetically above the MLCT manifold and effectively make the excited electronic picture for Fe(II) dyes the same as the Ru(II) analogues. On paper, this should be relatively straightforward. However, pushing the LF manifold above the MLCT states would require much greater ligand field strength, particularly for a first row transition metal complex. From the Tanabe-Sugano d^6 diagram of a generic octahedral complex with a d^6 electron configuration,[39] the ligand field strength would need to increase not just to the $^5T_2/^3T_1$ crossing point such that the lowest energy ligand field excited state is the $^3T_1$, but likely well beyond that point. For many decades, the only first row transition metal compound with a lowest energy $^3T_1$ excited state was $[Co(CN)_6]^{3-}$, as reported by Miskowski and coworkers.[74] Cyano-ligands are commonly employed in the endeavor to increase ligand field strength due to their standing in the spectrochemical series. Very recently, $[Fe(bpy)(CN)_4]^{2-}$ was studied by combined ultrafast X-ray fluorescence and absorption spectroscopies.[75] The effect of solvatochromism due to the cyano ligands played a critical role in the ultrafast dynamics of the chromophore. In water, the same sub-100 fs MLCT deactivation is observed, but relaxation proceeds to the $^3T_1$ ligand field state, rather than the typical $^5T_2$. When the complex is dissolved in weaker Lewis acids such as acetonitrile or dimethyl sulfoxide, however, the MLCT excited state is observed to be the lowest energy excited state with a single picosecond lifetime, meaning the ligand field manifold has been energetically promoted so deactivation is unfeasible. This compound, then, has achieved the desired goal of a lowest-energy MLCT excited state, although the dynamics are highly sensitive to the nature of the solvent.

The addition of electron-withdrawing substituents in the 4,4'-positions of the bpy ligand, for example, might be expected to reduce electron density in the Fe-N bond, thereby increasing the ligand field strength. Computational work by Ashley and Jakubikova on this very premise

seems to indicate this strategy will not be effective.[76] For a series of 4,4'-disubstituted $[Fe(bpy')_3]^{2+}$ complexes, the Fe(II/III) oxidation potential (which gives a measure of the energetics of the t_{2g} set of orbitals) spanned 2.07 V, whereas the free energy between the $^1A_1$ and $^5T_2$ ligand field states varied no more than 0.29 V. These results imply that while the t_{2g} orbitals may be greatly stabilized or destabilized upon the addition of π-donor or -withdrawing agent, respectively, the e_g* orbitals are likewise being affected such that the overall driving force for the compounds are unchanged. However, this picture changes when studying the bis(tridentate) $[Fe(terpy)_2]^{2+}$ complex.[77] For this work, the position of substitution on the peripheral pyridyl rings was varied with different conjugated moieties. The addition of these heterocyclic, π-donating groups is estimated to red-shifts the absorption profile while increasing the MLCT character of the lowest energy excited state. One compound specifically, $[Fe(4'\text{-carboxylic acid-}4,4''\text{-di(2,3,4-triaminothiophene)})_2]^{2+}$ is predicted to increase the ligand field manifold to lie energetically above the charge transfer states. It is therefore difficult to say with any certainty whether an inversion of LF and MLCT manifolds is possible in Fe(II) polypyridyls.

Due to the ease of synthetic modification, terpy-based Fe(II) complexes are also highly studied. Work done by Jamula et al. showed that by increasing the octahedral symmetry about the metal center for a terpy-type ligand system through the appending of carbonyl linkers, a greater ligand field strength could be achieved.[78] Although the $^3T_1$ state was not achieved, $[Fe(dcpp)_2]^{2+}$ (dcpp = 2,6-di(2-carboxypyridyl)pyridine) is one polypyridyl that came incredibly close. The ligand structure proved to significantly stabilize the t_{2g} orbitals of Fe(II), as evidenced by its electrochemical properties, resulting in a very red-shifted absorption spectrum. Unfortunately, the ground state recovery lifetime has been reduced by nearly a factor of four relative to $[Fe(bpy)_3]^{2+}$ to 280 ± 10 ps, that has subsequently been assigned as coming from the $^5T_2$ excited state via

ultrafast X-ray spectroscopy.[79]

In a slightly different vein, Fe(II) carbene chemistry has seen a resurgence as of late due to the promising results yielded initially by Liu and coworkers.[80] Here, complexes with the *N*-heterocyclic carbene (NHC) ligands are afforded a 9 ps lifetime out of the ^{3}MLCT excited state despite having a ligand field-based lowest energy excited state – a remarkable result owed to the significant σ-donating ability of these C-donor ligands. This effect is further observed in the relatively short Fe-C bond distance (~0.13 Å). Calculations on injection from this complex with an appended carboxylic acid linker into a semiconductor improved the efficiency of injection, particularly from the lower-lying ^{3}MLCT excited state.[81] Despite this marked improvement in MLCT lifetime in an Fe(II) chromophore and computational results, application of these NHCs with a carboxylate anchoring group displayed very poor performance in a DSSC device.[82] While the efficiency for the Ferrere cell (using a dye with a sub-200 fs MLCT state lifetime) was 0.10%, a two-order of magnitude decrease in the MLCT deactivation rate (i.e., 16 ps MLCT lifetime) only improved the efficiency to 0.13%. Since the initial report by Liu et al., newer Fe(II) carbene complexes have continued to be designed and prepared,[83,84] with one in particular having since yielded a 528 ps lifetime believed to be from the MLCT manifold.[85] This field is yet in its infancy but appears to show the most potential for achieving Ru(II)-like photophysics. The question at hand, however, is whether the strategy to increase ligand field strength in order to elongate the MLCT lifetime is viable for Fe(II) polypyridyl complexes.

3.2.2 Disrupting the MLCT Manifold Deactivation Nuclear Coordinate

The first strategy described above is a question of electronics; an alternative approach aims instead at disrupting the relaxation pathway of interest along the nuclear coordinate. This method would require precise knowledge of the vibrational modes responsible and/or participating in the

ultrafast deactivation from the MLCT manifold into the $^5T_2$ state. With this information in hand, targeted synthetic modifications may be made to the ligand scaffolding to inhibit these motions,[86] thereby increasing the barrier to LF relaxation and extending the MLCT lifetime. This method has been performed previously within the McCusker research group[87,88] on another first row transition metal complex, $Cr^{III}(acac)_3$, for which acac is the acetylacetonate ligand. Ultrafast transient absorption spectroscopy found intersystem crossing from the Franck-Condon to the lowest-energy excited state to occur in a sub-100 fs fashion. From combinatorial vibrational coherence and computational data, a vibrational mode corresponding to the Cr-O bond lengthening and large amplitude acac backbone motion was identified as the major nuclear motion occurring during ISC. In an attempt to elongate the ISC process, prohibition of this ligand stretching mode was targeted and *t*-butyl substituents were added to the outermost carbon atoms on the acac ligand. This addition sterically hindered the large amplitude motions, which resulted in a reduced rate of intersystem crossing by more than an order of magnitude, proving the viability of this strategy.

Theoretical work has also been performed on $[Fe(bpy)_3]^{2+}$ in an attempt to identify the major coordinate for MLCT→LF relaxation.[89] Ray-Dutt, classic Bailar, and a distorted or "dancing" Bailar torsions were investigated, in which the Ray-Dutt and dancing Bailar twists were found to be lower in energy, thus likely linked to intersystem crossing. This has been experimentally observed by Stock et al., who studied an Fe(II) spin-crossover (SCO) complex with a tripod-like geometry.[90] Through ultrafast X-ray and magnetic measurements in conjunction with calculations, trigonal twisting was identified as the nuclear coordinate associated with the quintet-to-singlet conversion. A dual Bailar twisting and breathing mode was found to be hindered by the stereochemistry of the ligand, providing a ~33 kJ/mol barrier to the reaction, which is consistent with the results from Jakubikova.[89]

It is difficult at this juncture, however, to know how interconnected the vibrational coordinates for the MLCT→LF and $^5T_2 \rightarrow {}^1A_1$ relaxation processes are. Some clues are provided by the low-spin $[Fe(tren(py)_3)]^{2+}$ complex, for which $tren(py)_3$ = tris(*N*-(2-pyridylmethyl)-2-iminoethyl)amine. Methyl groups may be substituted systematically onto the 6-position of the pyridyl ring, affording SCO complexes upon the addition of either one or two methyl groups, and a high-spin complex for the fully methylated version.[91,92] Not only are these methyls electron-donating so as to reduce the ligand field strength of the complex, but they also serve to sterically prohibit good orbital overlap between the metal and ligands.[93] Even the fully protonated compound has a relatively long $^5T_2$ state lifetime for a low-spin Fe(II) polypyridyl complex: approximately 60 ns in acetonitrile.[92] It is evident that the cage-like structure surrounding the metal center hinders the torsional motions that facilitate ground state recovery. That being said, the MLCT→LF conversion has been measured by femtosecond transient absorption,[65] picosecond soft X-ray,[93] and femtosecond stimulated Raman scattering spectroscopies;[94] all three were consistent with each other, in which they found time constants of sub-100 fs, 85 ± 75 fs, and 190 ± 50 fs, respectively. It is clear that the steric encumbrance hindering torsion along the $^5T_2 \rightarrow {}^1A_1$ coordinate does not significantly lengthen the MLCT lifetime in $[Fe(tren(py)_3)]^{2+}$ relative to $[Fe(bpy)_3]^{2+}$. It is probable that this process does not access the same vibrational modes as the MLCT deactivation, reinforcing the need for intimate knowledge of these specific reaction coordinates.

3.2.3 Extending the Delocalization in the MLCT Excited States

Like the previous two strategies, the final method that is envisioned to increase the lifetime of the MLCT states in Fe(II) polypyridyls has been somewhat explored in the literature, but not to nearly the same extent. Recall that upon excitation, the MLCT state is formed and typically lasts for less than 130 fs. Despite being a charge-separated state, the distance between the oxidized

Fe(III) center and the reduced bipyridine ligand is not overly large. The addition of conjugated substituents could serve to increase the distance between the excited electron and the metal; if the distance grows large enough, the electron may lose memory of its starting position and remain on the ligand for a longer period of time, thereby extending the lifetime of the MLCT state. And indeed, many phenyl-substituted Fe(II) complexes have been synthesized with bpy, terpy, and phenanthroline backbones,[95-98] in which these compounds displayed a red-shifted MLCT excited state by ground state absorption spectroscopy relative to the parent complex. By increasing the delocalization of the MLCT excited state, the phenyl moieties actually reduce the distortion of the excited state relative to the ground state, such that these potential energy surfaces are nested.[99] This serves to increase the observed lifetime while increasing the quantum yield of emission as vibronic coupling between the lowest energy excited state and the $^1A_1$ ground state is reduced and thereby decreases k_{nr}. This has been observed in $[Ru(4,4'\text{-diphenyl-}2,2'\text{-bipyridine})_3]^{2+}$ by Damrauer and coworkers,[99] as well as in 4'-*para*-tolyl-terpy complexes of ruthenium and osmium.[40]

In a series of complexes with systematically increasing units of delocalization, the lifetimes of Ru(II) terpy-like compounds were studied.[100] As previously mentioned, the bis-tridentate nature of terpyridine reduces the ligand field strength of $[Ru(terpy)_2]^{2+}$ such that its lowest energy excited state is actually the $^3T_1$ state and has a lifetime on the order of 250 ps.[41] In this work, phenylene and vinylene linkers were appended to $[Ru(terpy)_2]^{2+}$-based trimers. The excited state lifetime increased to 10 ns when a phenylene-vinylene-phenylene linker between terpyridines on adjacent Ru(II) atoms were placed at the 4'-position of the terpy backbone and increased again to 320 ns with an additional phenylene-vinylene linkage in the ligand before the terpyridine backbone. That is a more than 1000-fold increase in excited state lifetime through the simple addition of

conjugated substituents. The authors went on to synthesize a Ru/Fe/Ru linear trimer in which each metal was coordinated to two terpyridine ligands with the Ru atoms flanking Fe. The terpy units were bridged via a vinylene linker such that the overall structure (from left to right) would be: terpy-Ru-terpy-phenylene-vinylene-phenylene-terpy-Fe-terpy-phenylene-vinylenephenylene-terpy-Ru-terpy. The MLCT absorptions specific to the Fe(II) metal center were able to be spectroscopically identified, and excitation into this band yielded a 275 ns lifetime with no observable ultrafast deactivation to a lower-lying LF state. Without further characterization by methods such as spectroelectrochemistry, however, it is difficult to know if the extended delocalization alone increased the Fe(II) MLCT lifetime, or if the Ru(II) atoms played a role. Analogous work done on a strictly Fe(II) monomer or trimer could be more compelling.

While not exactly the same, a cyclic Fe(II) terpy-based trimer complex was prepared with a series of conjugated linkages.[101] The linkers of interest that were used were acetylene, phenylene, and a 1,4-di-acetylene-2,5-di-dodecamethoxy-phenylene. Again, they were placed at the 4'-position of the terpyridine backbone. In every complex, an ultrafast component was observed with a time constant on the order of ~100 fs, which is consistent with the MLCT deactivation lifetime of the monomeric $[Fe(terpy)_2]^{2+}$ complex.[102] However, upon excitation into the terpy-based π-π^* absorption at 330 nm and probing on the red side of the $^1MLCT \leftarrow {}^1A_1$ absorption at 675 nm, a long-lived (ps) excited state absorption feature is observed. At this pump-probe combination, it is highly likely that the single picosecond lifetime is indicative of the MLCT manifold. Again, these results are difficult to fully interpret considering the trimeric nature of the complex, but all these data together appear to indicate that extended delocalization may serve increase the MLCT lifetime in Fe(II) chromophores.

4. The Critical Role of Reorganization Energy

Any one of the proposed methods outlined above for lengthening the MLCT lifetime will impart substantial geometric distortions in the resultant Fe(II) chromophore relative to the more commonly studied complexes. These distortions are likely to translate to the excited states of the compounds as well, especially when one considers the ~0.2 Å Fe-N bond elongation that occurs concomitantly with $^1A_1 \rightarrow {}^5T_2$ interconversion.[70] It is not only imperative then to understand the energetic effects that these alterations will have on the photophysical dynamics, but also the nuclear coordinates being accessed at each step along the relaxation pathway. While synthetic modifications may lengthen the MLCT lifetime along one coordinate, a new excited state crossing could then arise along a separate mode that had been previously unimportant. It is therefore critical that the energetics and vibrational modes of these complexes are constantly assessed and reassessed with each subsequent ligand alteration.

Fortunately, the nonradiative kinetics associated with Fe(II) chromophores can be described by semi-classical Marcus theory,[103] eqn. (1.2):

$$k_{nr} = \frac{2\pi}{\hbar}|H_{ab}|^2 \frac{1}{\sqrt{4\pi\lambda k_B T}} e^{-\frac{(\lambda+\Delta G^\circ)^2}{4\lambda k_B T}} \quad (1.2)$$

Here, k_{nr} is the nonradiative rate constant, ħ is the reduced Planck's constant, and T is temperature. The coupling between electronic states is given by H_{ab}, and the driving force between the states of interest is represented by ΔG°. Finally, λ gives the reorganization energy. This term defines the energy required for the reactants to transform into the products without undergoing any electron transfer process.[22] This transformation requires vibrational motion of the complex and is therefore a measure of both the vibrational modes and energy of the excited state dynamics. λ gives a measure of the relationship between the rate of the reaction and ΔG°, as determined by the squared function in the exponential product of eqn. (1.2). Under conditions for which $\lambda > |\Delta G^\circ|$, this is

defined as the Marcus normal region in which an increase in driving force will result in an increase in k_{nr}. When $\lambda \cong |\Delta G^{o}|$, the barrierless region has been reached for which the fastest nonradiative rate is achieved. Any further increase in the free energy, such that $\lambda < |\Delta G^{o}|$, will then translate to a decrease in the observed rate, which is known as the Marcus inverted region.[22,103,104] These three regions are displayed in Scheme 1.4. Finally, the reorganization energy is comprised of two components: inner-sphere (λ_{is}) and outer-sphere (λ_{os}). λ_{is} is specific to the vibrational modes and nuclear motion of the chromophore, whereas λ_{os} is dependent on the environment surrounding the complex of interest. The outer-sphere component, then, can provide insight into the specific solute-solvent interactions that accompany excited state processes. The application of this form of Marcus theory to nonradiative decay will be further described (vide infra), but for the time being, it is apparent that a substantial amount of information can be derived from this equation. When combined with vibrational and structural experimental data and computational analysis, a much more thorough understanding of the molecular-level relaxation process in these Fe(II) complexes may be garnered.

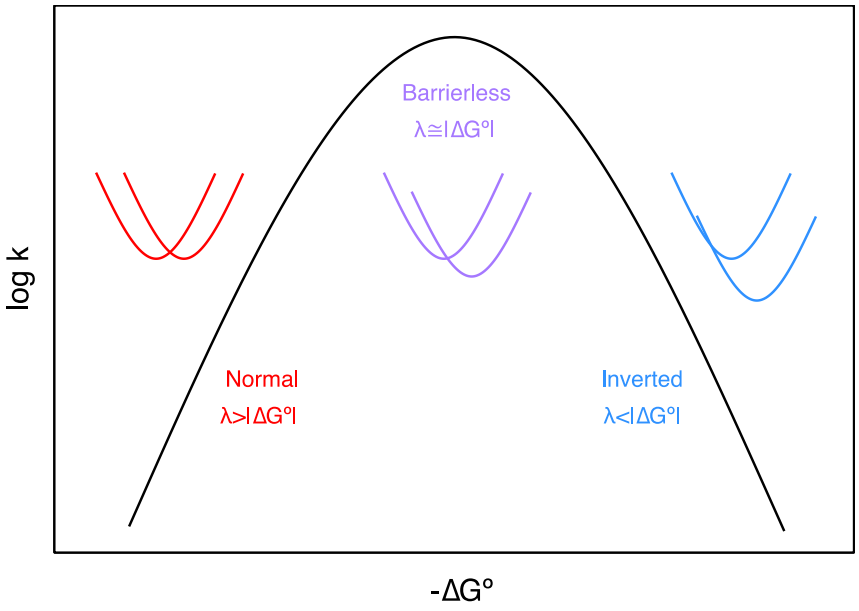

Scheme 1.4. The generalized "Marcus curve" for the logarithm of the rate of reaction versus the free energy between the reactant and product potential energy surfaces. The normal region (red) is described by $\lambda > |\Delta G^{o}|$. As the driving force increases, a maximum rate of reaction is achieved for $\lambda \cong |\Delta G^{o}|$, which is known as the barrierless region (purple). With any further increase in ΔG^{o}, however, the rate decreases in the inverted region (blue), as $\lambda < |\Delta G^{o}|$.

4.1 Methods for Determining Energetic Parameters

The most straightforward method for determining Marcus parameters and their relationship to one another is through the use of variable-temperature (VT) time-resolved measurements. In this way, k_{nr} may be determined as a function of T. Another simpler way of expressing eqn. (1.2) is by the Arrhenius equation, from which Marcus theory was based on:

$$k_{nr} = Ae^{-\frac{E_a}{k_B T}} \tag{1.3}$$

in which A is the frequency factor, E_a is the activation energy, and k_B is Boltzmann's constant. The frequency factor encompasses the preexponential term in eqn. (1.2) and describes the rate of

the reaction in the absence of a barrier. Linearizing eqn. (1.3) allows for explicit values of A and E_a to be found for a set of relaxation rates over some temperature range. These terms will be specific to the complex of interest, the relaxation process being investigated, and the experimental conditions under which the system is analyzed.

The question therefore becomes one of how to go about measuring k_{nr}. Traditionally this is done either by time-resolved emission[105] or transient absorption (TA) spectroscopy.[21] In the case of Fe(II) chromophores, emission does not occur and the processes of interest are on the sub-nanosecond timescale in the Fe(II) polypyridyl complexes we are proposing to study. And although ultrafast VT-TA setups have been described previously, they have largely been used in the realms of photosynthesis[106] and physics.[107] Previously, picosecond VT-TA anisotropy spectroscopy has been employed to study the temperature dependence of interligand electron transfer in $[Ru(bpy)_3]^{2+}$ by Malone and Kelley.[108] However, for various technical reasons, ultrafast VT-TA has not been applied to transition metal complexes in solution before.

TA spectroscopy represents a pump-probe technique in which the pump pulse is used to create an initial excited state, and then the probe pulse creates a second absorption event which will monitor the subsequent kinetics.[109] These two pulses are delayed with respect to one another, thereby generating a time-resolved profile of the excited dynamics of the complex being studied. If the probe pulse reaches the sample before the pump, no signal will be observed. It is only upon excitation by the pump pulse that the temporal evolution may be monitored by the probe pulse. As the laser systems used to collect the data in this dissertation have been described extensively by others previously,[110,111] a lengthy review of them will not be provided here. Additionally, a complete description of TA setups in general is given in an excellent review by Megerle and coworkers that inspired much of the experimental design used within this work.[112]

This experiment may be performed in one of two regimes that reflect how the sample is probed: as a full spectrum or at a single wavelength (Fig. 1.1). Full spectral data are the excited state equivalent of a UV-Vis, or ground state absorption spectrum, at selected time delays in which a white light continuum is used and the data are depicted as the change in absorbance (ΔA) versus wavelength. They provide a complete picture of the excited state dynamics over the probe window. To fully understand which processes are being monitored, it is necessary to collect both ground state absorption and full spectra data. The former allows for identification of the state that is initially prepared by the pump pulse; the latter is used to determine the excited state process being measured. Unfortunately, what a full spectral measurement provides in spectral resolution it loses in temporal resolution; it is therefore common to select a probe wavelength of interest in order to monitor the kinetics more accurately. These traces show ΔA as a function of time delay between the pump and probe pulse and allow for precise characterization of the kinetic profile. The addition of an optical cryostat in the sample position allows for temperature-dependent nonradiative lifetimes of Fe(II) chromophores to be measured, providing a method for both Arrhenius and Marcus analyses to be performed on the photophysical processes of this class of compounds.

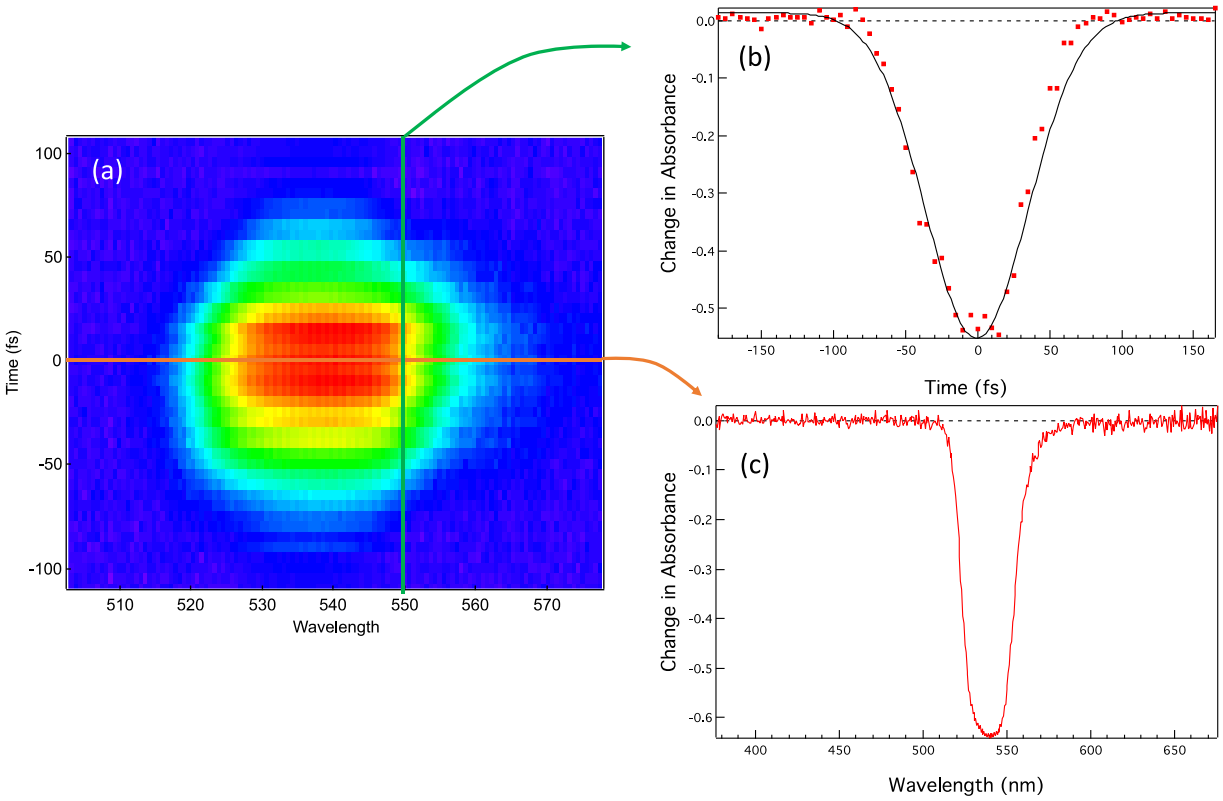

Figure 1.1. (a) Two-dimensional full spectral data of the optical Kerr effect induced between the pump and probe pulses when both are 550 nm. (b) If the data are plotted for one specific probe wavelength versus the time delay, a kinetic trace can be collected. (c) The data can also be plotted against the probe wavelength, providing a one-dimensional full spectral trace.

Due to the nonemissive, metal-centered nature of the ligand field states that dominate Fe(II) photophysics, accurate thermodynamic information on these excited states is hard to come by. Some of the best and only estimates of the $^5T_2/^1A_1$ driving force associated with the relaxation from the $^5T_2$ state to the $^1A_1$ come from the SCO community. These are compounds in which the two ligand field states are nearly degenerate ($|\Delta G^o| < k_BT$) such that the excited state can be accessed by changes in temperature, pressure, or via light absorption.[57,92] VT lifetimes may yield thermodynamic parameters that allow for ΔG^o to be calculated from Gibbs' equation. Although

the specific driving force is greatly reduced relative to prototypical Fe(II) polypyridyl complexes, it is believed that many of the same vibrational modes will be accessed for a low-spin and SCO compound of similar ligand scaffolding. Calculations can then be performed on a series of analogous compounds to estimate $\Delta\Delta G^{o}$, and therefore $\Delta\lambda$,[113] providing an initial understanding of the crucial nuclear coordinates involved in the relaxation of Fe(II) compounds.

A final tool to be used in the development of methodologies for studying Fe(II) polypyridyl photophysics is, surprisingly, Ru(II) compounds. As already described, the excited state processes undergone in this class of complexes is much simpler due to the higher energy ligand field manifold relative to the MLCT states. In attempting to diagnose the ultrafast MLCT→LF conversion, information regarding the charge transfer excited states is critical, and more easily garnered from Ru(II) analogues. Experimental methodologies may be developed on these simpler compounds, and then used more rigorously to study the Fe(II) compounds of interest. Moreover, Ru(II) polypyridyls are not restricted to analysis by TA studies only. The presence of luminescent states also allows for steady state and time-resolved emission spectroscopies to be performed, as well as quantum yield determination. All of these data together tell a more complete story of the MLCT manifold in these d^6 compounds.

Ultimately, the MLCT→LF deactivation in Fe(II) polypyridyl chromophores is the nuclear coordinate of interest. For various technical and computation reasons, this coordinate cannot be measured directly. Unfortunately, the data presented in this dissertation do not directly measure the MLCT deactivation coordinate by VT-TA. When variable-temperature measurements are being discussed with respect to Fe(II) complexes, unless otherwise noted, the ground state recovery process is being investigated. Eventually, these data can be used in conjunction Ru(II) analogues, which help to identify the MLCT→$^1A_1$ nuclear coordinate. It is through the combined usage of all

of these methods and computation work that the fundamental photophysics of Fe(II) polypyridyls can be better understood.

5. Nonradiative Decay Theory

As mentioned above, semi-classical Marcus theory is adept at describing the nonradiative ground state recovery dynamics in Fe(II) complexes and has been successfully applied previously.[104,114] This may seem counterintuitive, particularly to those who associate Marcus theory solely with electron transfer. True, this model was developed to describe bimolecular self-exchange electron transfer reactions in solution,[115-117] however, this theory has evolved over time and can be used to describe other phenomena,[22] such as intramolecular nonradiative decay. In some regards, this may not be surprising. Metal-to-ligand charge transfer, for example, may be a nonradiative process that accompanies electron transfer between two species that are physically separated from one another (albeit linked covalently) in a unimolecular fashion. The theory applies just as well to a ligand field state interconversion, as is observed in SCO complexes, or the ground state recovery of low-spin Fe(II) polypyridyls. Marcus theory is simply a classical treatment of a reaction rate describing electronic states and need not be applied to electron transfer from one physical location to another, be it inter- or intra-molecularly.

Marcus theory, like the Arrhenius equation, was ultimately derived from Fermi's Golden Rule which describes the nonradiative rate of a transition between two states with two different electronic configurations.[117] It is defined as:

$$k_{ab} = \frac{2\pi}{\hbar}|H_{ab}|^2\rho \tag{1.4}$$

Here, the rate of the transition (k) from the initial state (a) to the final state (b) is a function of the Hamiltonian matrix element describing the electronic communication between the two states (H_{ab}),

and the density of states-weighted Franck-Condon factor (ρ). Nonradiative decay theory evolved from Fermi's golden rule, predominantly through the work of Jortner[118] in an attempt to more accurately define the temperature dependence of reaction rates. At warmer temperatures, a linear dependence exists between ln(k) and T^{-1}. Upon reaching low temperatures however, experimental reaction rates are observed to level off, that is, they become temperature-independent. This has been identified as electron tunneling, in which vibrational wavefunction overlap between the two electronic states allows for vertical energy transfer beneath the barrier. In this way, a reaction may occur even without the thermal energy typically required to surmount the free energy of activation. Classical intramolecular electron transfer treatments only predict the trend seen for warmer temperatures as tunneling is not allowed by this theory. The derivation of the semi-classical and quantum mechanical theories has been described in great detail elsewhere.[117] Since all of the kinetics depicted in this dissertation occur in the high-temperature region, at which these models converge to one temperature-dependent picture, only the details for the classical Marcus theory and its expressions will be examined here.

Fermi's Golden Rule is not only an excellent starting point for discussing nonradiative decay theory, it also takes the form that broadly describes each of the theories that will be elaborated on hereafter. Namely, a reaction rate is comprised of the product of a nuclear factor and an electronic one. In eqn. (1.4), the electronic component is H_{ab}, the electronic coupling matrix element. The Franck-Condon factor incorporates the nuclear part of the equation. This separation of electronic and nuclear factors is a consequence of the Born-Oppenheimer approximation, in which electronic motion is instantaneous with respect to nuclear motion due to the size of the respective particles.

We take first the electronic factor, which Marcus derived from transition state or activated

complex theory. Much of the subsequent discussion is taken from Barbara, Meyer, and Ratner.[22] This model follows reactants (R) transforming into products (P) via an intermediate (I), or transition state (Scheme 1.5). The reaction is assumed to occur solely along one nuclear coordinate, and the potential energy surfaces used to describe the reactants and products are harmonic oscillators, such that the potential energy surfaces may be described by:

$$V_R = \frac{1}{2} f(Q + Q_0)^2 \tag{1.5a}$$

$$V_P = \frac{1}{2} f(Q - Q_0)^2 \tag{1.5b}$$

for which the potential energy (V) of the reactants and products are found using Hooke's law, with f being the force constant, Q being the distance along some nuclear coordinate, and Q_0 being the position of the minimum of the well. Transition state theory also makes use of adiabatic potential energy surfaces. Adiabaticity refers to the degree to which electronic states are coupled. If the oscillator frequency can be represented as $\hbar\omega \ll k_BT$, then very weak communication occurs between the two states, and they are referred to as nonadiabatic: the potential energy surfaces are only weakly interacting and population transfer is unlikely. If $H_{ab} = 0$, then the surfaces are diabatic and no transition between these states may occur. If, however, $\hbar\omega \gg k_BT$, the states are referred to as adiabatic, or highly coupled. This results in an avoided crossing of the two states (Scheme 1.5), which dramatically increases the transition probability. Adiabaticity also requires that if a transition proceeds from one surface to the next, the reverse reaction may not occur. The reaction barrier can be described in many ways, including the Eyring equation or collision theory, but is often expressed as the Arrhenius equation, eqn. (1.3). Again, the frequency factor, A, envelops the electronic piece of the function, whereas the exponential describes the nuclear motion. In fact, Arrhenius's equation became the basis for Marcus's theory. Arrhenius defines the energy required for the reactants to reach the transition state as the free energy of activation, or E_a (Scheme 1.5).

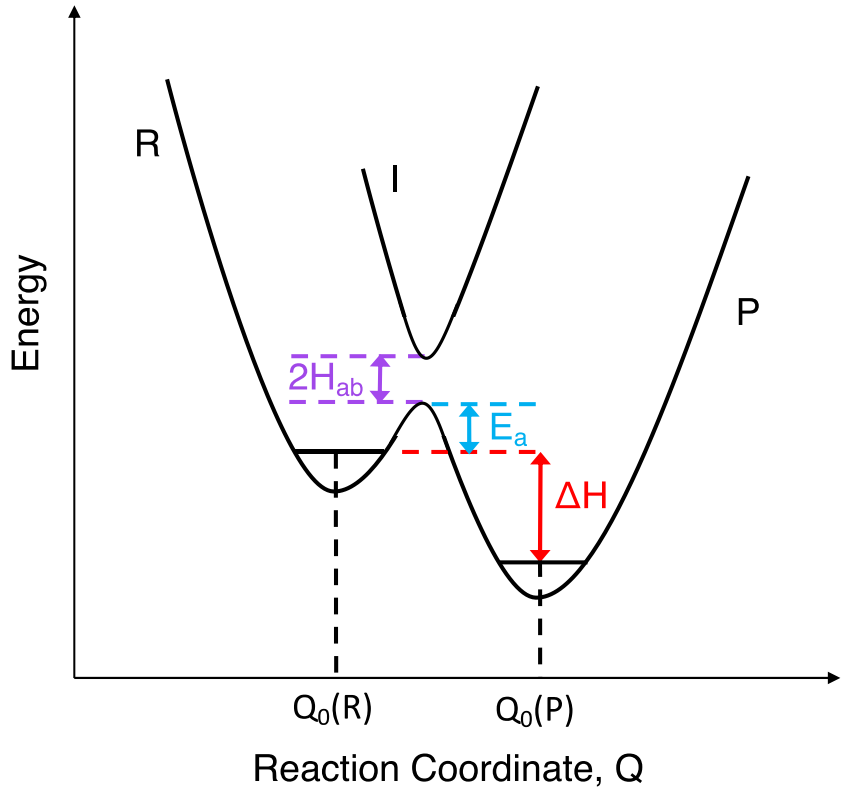

Scheme 1.5. Reaction coordinate depicting the components of transition state theory. The potential energy surfaces are assumed to be harmonic oscillators, and the reaction proceeds from the reactant (R) centered around Q_0(R) to the product (P) parabola at Q_0(P) with no back reaction being possible due to the adiabaticity of the states. This adiabatic nature also presents as an avoided crossing, in which H_{ab} is sufficiently large that the two states are highly coupled and form an intermediate (V_I) transition state. The enthalpy of the reaction is given by ΔH, while E_a shows the energy requirement for surmounting the barrier from the reactant state.

The transition state drawn in Scheme 1.5 in the case of ground state recovery for Fe(II) polypyridyls actually represents a higher-lying ^{3}LF excited state. The $^5T_2 \rightarrow {}^1A_1$ transition is doubly spin-forbidden as ΔS=2, such that there can be no first-order interaction between these two states.

A second-order spin-orbit coupling interaction must be invoked, whereby the $^5T_2$ and $^3T_1$ states interact, as do the $^3T_1$ and $^1A_1$ states with some spin-orbit coupling constant, ζ.[114] This may be shown as:

$$\langle {}^1A_1|H_{SO}|{}^3T_1\rangle = -\sqrt{6}\zeta \quad (1.6a)$$

$$\langle {}^3T_1|H_{SO}|{}^5T_2\rangle = \sqrt{3}\zeta \quad (1.6a)$$

The second-order spin-orbit coupling allows the reaction to proceed despite the first-order coupling between the reactant and product states being nearly diabatic.

Despite having many degrees of freedom, transition state theory relies on the assumption that the active nuclear coordinate is isolatable from all others, simplifying the picture to one vibrational mode. Ultimately, this has the result of taking multidimensional potential energy surfaces and reducing them to nothing more than parabolas. The reaction above can be redrawn (as in Scheme 1.6) to allow the exothermicity of the reaction (ΔH) to be expressed from potential energy surfaces. This is possible if the entropic contributions for the reaction are assumed to be zero (which is unlikely for $^5T_2 \rightarrow {}^1A_1$ transitions with ΔFe-N being on the order of 0.2 Å but will be allowed for the purposes of this discussion). The free energy, ΔG^o is then equal to the energetic difference between V_R and V_P at their equilibrium positions:

$$\Delta G^0 = \frac{1}{2}f[Q_B - Q_0(R)]^2 - \frac{1}{2}f[Q_B - Q_0(P)]^2 \quad (1.7)$$

in which Q_B is the nuclear position of the barrier. From its definition, the reorganization energy can be mathematically expressed as

$$\lambda = \frac{1}{2}f[Q_0(R) - Q_0(P)]^2 \quad (1.8)$$

which shows the parabolic nature of this constant. Similarly, the free energy of activation can be translated into potential energy surfaces by the relationship $E_a = V_R[Q_B]-V_R[Q_0(R)]$. This quantity is a measure of the energy difference of the barrier at Q_B and the reactants at $Q_0(R)$:

$$E_a = \frac{1}{2} f[Q_B - Q_0(R)]^2 \tag{1.9}$$

From eqn. (1.7), Q_B may be found algebraically in terms of $Q_0(R)$ and $Q_0(P)$ based on the fact that $V_R[Q_B(R)] = V_P[Q_B(P)]$, such that

$$Q_B = \frac{\Delta G^0}{f}\left(\frac{1}{Q_P - Q_R}\right) + \left(\frac{Q_P + Q_R}{2}\right) \tag{1.10}$$

Substitution of this expression for Q_B and λ from eqn. (1.8) into eqn. (1.9) yields

$$E_a = \frac{(\lambda + \Delta G^0)^2}{4\lambda} \tag{1.11}$$

in which the activation energy is expressed in terms of reorganization energy and driving force. In this way, these thermodynamic and electronic parameters may be accurately used to describe the potential energy surfaces involved in an electronic transition (Scheme 1.6). Furthermore, eqn. (1.11) directly equates the Arrhenius and Marcus theories. Eqn. (1.3) may then be understood as:

$$k_{nr} = A exp\left\{\frac{-(\lambda + \Delta G^0)^2}{4\lambda k_B T}\right\} \tag{1.12}$$

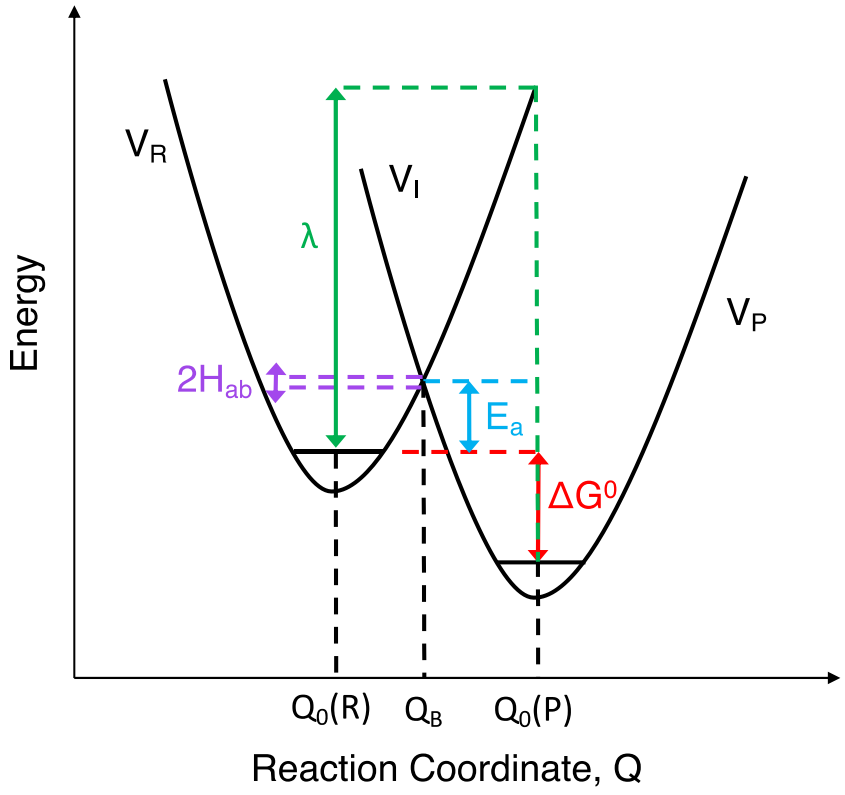

Scheme 1.6. Potential energy surfaces for an electronic transition from the reactants (V_R) to the products (V_P) along some reaction coordinate, Q. The position of the barrier is given by Q_B. For simplicity, diabatic curves are shown, and as such H_{ab}, or the coupling between electronic states, would be approximately 0 cm^{-1}. The activation energy (E_a) is given by the energy difference between the crossing point and the lowest vibrational state of the reactant surface. ΔG^o, the free energy, shows the exothermicity of the reaction. The reorganization energy (λ) represents the energy required for the atoms in the reactants to rearrange to resemble the atoms in the products, without any surface crossing occurring.

The electronic term may now be taken into consideration and will be guided by a discussion from DeVault.[117] By Arrhenius theory, the frequency factor is the rate of the reaction in the limit

$E_a = 0$. This term can be treated as a probability of the passage from reactants to products via Q_B using the Landau-Zener Quantum Mechanical formulation. The probability, P_{ab}, is described as

$$P_{ab} = \frac{2\pi}{\hbar}|H_{ab}|^2 \frac{1}{v\Delta F} \tag{1.13}$$

for which v is the velocity of the system as it passes along the nuclear coordinate through the transition state, and ΔF is the change in slope between the reactant and product potential energy surfaces at Q_B. The displacement amplitude, X, of the oscillation in the reactant state may be expressed by

$$X = \sqrt{\frac{2E}{m\omega^2}} \tag{1.14}$$

Taken from the classical expression for an oscillating system, E represents the total energy of the oscillating state, m is the mass, and ω is the angular frequency. It is convenient here to denote the displacement between the minimum of the reactant surface $Q_0(R)$ and the barrier Q_B as $Q^{\ddagger}$. The velocity, v, of the system as it passes through $Q^{\ddagger}$ is thus

$$v = \omega\sqrt{X^2 - Q^{\ddagger 2}} \tag{1.15}$$

Likewise, ΔF may be found based on the geometry of the intersecting parabolas at Q_B from Scheme 1.5:

$$\Delta F = \frac{d}{dX}(v_a - v_b) \tag{1.16a}$$

such that

$$\Delta F = f[Q_0(R) - Q_0(P)] \tag{1.16b}$$

From Hooke's law and the expression for reorganization energy from eqn. (1.8), this may be rewritten as

$$\Delta F = \omega\sqrt{2\lambda m} \tag{1.16c}$$

The expressions for the velocity and change in slope for the reactants and products are then substituted into eqn. (1.13), giving the rate of the reaction, eqn. (1.17).

$$k_{ab} = \frac{\omega}{\pi} P_{ab} \tag{1.17a}$$

$$k_{ab} = \frac{2\pi}{\hbar} |H_{ab}|^2 \frac{1}{\omega\sqrt{2\lambda m\left(X^2 - Q^{\ddagger 2}\right)}} \tag{1.17b}$$

It is clear from eqn. (1.17) that the rate of the transition is given by the frequency at which the transition state is passed through, as governed by the probability of the transition populating the product surface. The average rate of passage from the reactant surface to that of the products may be found over a Boltzmann distribution of energies such that

$$k_{ab} = \frac{\int_E^\infty k(E) exp\left\{\frac{-E}{k_B T}\right\} dE}{\int_0^\infty exp\left\{\frac{-E}{k_B T}\right\} dE} \tag{1.18a}$$

$$k_{ab} = \frac{2\pi}{\hbar} |H_{ab}|^2 \left(\frac{\omega\sqrt{2m}}{\sqrt{k_B T}}\right)\left(\frac{1}{\omega\sqrt{2\lambda m}}\right) exp\left\{\frac{-E_a}{k_B T}\right\} \tag{1.18b}$$

From here, terms may be reduced and the preexponential factor from eqn. (1.18b) is used in combination with the exponential term determined from eqn. (1.11) to result in the semi-classical Marcus expression for nonradiative decay, as originally introduced in eqn. (1.2). This derivation may be performed via alternate methods,[119] but the result will ultimately be the same. The application of quantum mechanics to Marcus theory allows for the vibrational overlap that participates in electronic transitions to be accounted for, while still taking advantage of the Marcus relationship between the activation energy, driving force, and reorganization energy.

Finally, a further note on the Marcus reorganization energy is required. As discussed previously, λ is the sum of the total contributions of both inner-sphere and outer-sphere components, relating to the intramolecular vibrations and the surrounding medium of the chromophore respectively. For systems that participate in energy transfer, λ may be estimated from the Stokes shift, as one-half of the energy difference between corresponding absorption and emission maxima. Alternatively, in the self-exchange reactions that came to define Marcus

electron transfer theory, the reorganization energy is defined as four times the activation energy.[22] Because λ appears in both the preexponential and exponential factors in the nonradiative decay expression, it encompasses both nuclear and electronic components. In some ways, it is the best determinant of microscopic motions of the chromophore. λ_{is} can be related to the degree of nuclear distortion between the reactant and product states:

$$\lambda_{is} = S\hbar\omega \tag{1.19a}$$

for

$$S = \frac{f}{2\hbar\omega}[Q_0(R) - Q_0(P)]^2 \tag{1.19b}$$

In eqn. (1.19), S is known as the Huang-Rhys factor. The calculation of S is limited to a single nuclear coordinate. To a first approximation, however, S may be a powerful indicator of how two potential energy surfaces are nested along the horizontal axis. Furthermore, λ_i represents the structural changes undergone as the reaction proceeds from reactants through the transition state to the products. As for λ_{os}, this parameter may depict specific solvent-solute interactions. Classically, Marcus defined this term according to a dielectric continuum model:[116]

$$\lambda_{os} = (\Delta e)^2 \left(\frac{1}{2r_D} + \frac{1}{2r_A} - \frac{1}{R}\right)\left(\frac{1}{\epsilon_\infty} - \frac{1}{\epsilon_0}\right) \tag{1.20}$$

This model is based on two spherical species, the donor and acceptor, surrounded by a medium defined as a dielectric continuum. The total charge transferred is given by Δe, and the radii of the donor and acceptor are r_D and r_A, respectively. R represents the distance between the centers of the two species. The final term is for the modeling of the solvent, for which ϵ_∞ and ϵ_0 are the optical and static dielectric constants, respectively. Unfortunately, eqn. (1.20) is not applicable to the systems that will be studied here due to the assumptions it is built on: namely, that electron transfer is occurring, that it be between two particles, that those particles are spherical, and that solvent medium is well-described by a bulk function.

The semi-classical Marcus expression for nonradiative decay has been derived and shown

to be applicable to the ligand field transitions that will be studied in this work. From this equation in conjunction with VT-TA measurements, the critical thermodynamic parameter ΔG^{o} for the energetic difference between the $^{5}T_{2}$ and $^{1}A_{1}$ states may begin to be estimated. The electronic coupling constant, H_{ab}, for these two states is likely to be very near to 0 cm^{-1} due to the doubly spin-forbidden nature of the transition. That being said, H_{ab} has previously been estimated to be on the order of 170 cm^{-1}.[104,114] These measurements may provide some insight into the true magnitude of the coupling between these states. And most importantly, inner- and outer-sphere reorganization energy contributions may be determined, providing crucial insight into the vibrational modes that participate in the MLCT deactivation process into lower-lying ligand field states. Based on the information provided by VT-TA and Marcus theory, significant progress may be made in extending the charge transfer lifetime in Fe(II) polypyridyls, thereby improving the outlook for these chromophores in the realm of photovoltaic applications.

6. Concluding Comments

This dissertation is a compilation of the work performed over six years in an attempt to better understand the fundamental photophysical processes of low-spin Fe(II) polypyridyl complexes. It serves to expand the wealth of knowledge available on this class of compounds and attempts to provoke ideas for future studies. The ultimate goal of this research is to extend the MLCT lifetime of Fe(II) complexes in a knowable and reproducible manner. In some regards, this was achieved. Perhaps more importantly, this work sought to understand on a molecular level the effect that the metal, ligand backbone, substituents, counteranions, solvent, and excitation energy have on complexes of this type in an effort to truly define the multicomponent parameter that is Marcus reorganization energy.

Chapter 2 describes the ultrafast VT-TA methodology that was designed and implemented so as to perform Arrhenius and Marcus analyses on Fe(II) chromophores. A family of $[Fe(bpy)_3]^{2+}$-type compounds are studied and compared to $[Fe(terpy)_2]^{2+}$, resulting in reaction barriers being reported for these complexes for the first time. In Chapter 3 is a second variable-temperature study, in this case of $[Fe(dcpp)_2]^{2+}$. The ground state recovery process in this compound is found to be nearly barrierless, the first to be reported. The nature of these dynamics allow for the fine-tuning of that barrier by external perturbations, such as via a change in counteranion and solvent. Chapter 4 takes a departure from iron-based chromophores but continues the work begun in Chapter 3 with a thorough study of the effects of solvent and excitation energy on the excited state evolution of a Ru(II) polypyridyl system. These outer-sphere components drive the photophysics observed for this complex and provide insight into MLCT-based dynamics. Finally, Chapter 5 draws a direct comparison between Fe(II) and Ru(II) photophysical processes with the iron analogue of the compound studied in Chapter 4 being prepared and analyzed. These results also serve as a conduit to the research of the effects of extended delocalization on the MLCT lifetime in Fe(II) chromophores.

The data and interpretations provided in this dissertation offer a more thorough understanding of some prototypical Fe(II) complexes, as well as a few that are relatively under-studied. Three strategies are provided and explored in an attempt to increase the charge transfer lifetime of this class of compounds. As is true with the implementation of renewable energy sources to solve the global energy crisis, it will not be one approach that solves the problem, but an amalgamation of all these methods. In this way, the MLCT lifetime may actually be lengthened such that these chromophores are comparable with their second row congeners, thereby providing a path to a high-efficiency, Fe(II)-based photovoltaic device and greatly improving the global

energy outlook.

REFERENCES

REFERENCES

1. Cook, J. Oreskes, N.; Doran, P. T.; Anderegg, W. R. L.; Verheggen, B.; Maibach, E. W.; Carlton, J. S.; Lewandowsky, S.; Skuce, A. G.; Green, S. A.; Nuccitelli, D.; Jacobs, P.; Richardson, M.; Winkler, B.; Panting, R.; Rice, K. Consensus on Consensus: A Synthesis of Consensus Estimates on Human-Caused Global Warming. *Environ. Res. Lett.* **2016**, *11*, 048002; DOI: 10.1088/1748-9326/11/4/048002.

2. van der Linden, S. L.; Leiserowitz, A. A.; Feinberg, G. D.; Maibach, E. I. The Scientific Consensus on Climate Change as a Gateway Belief: Experimental Evidence. *PLoS ONE* **2015**, *10*, e0118489; DOI: 10.1371/journal.pone.0118489.

3. Maibach, E.; Myers, T.; Leiserowitz, A. Climate Scientists Need to Set the Record Straight: There is a Scientific Consensus That Human-Caused Climate Change is Happening. *Earth's Future* **2014**, *2*, 295–298; DOI: 10.1002/2013EF000226.

4. Howe, P. D.; Mildenberger, M.; Marlon, J. R.; Leiserowitz, A. Geographic Variation in Opinions on Climate Change at State and Local Scales in the USA. *Nature Climate Change* **2015**, *5*, 596-603; DOI: 10.1038/nclimate2583.

5. Leiserowitz, A.; Maibach, E.; Roser-Renouf, C.; Feinberg, G.; Rosenthal, S. Climate Change in the American Mind: American's Global Warming Beliefs and Attitudes in April 2014. Yale University and George Mason University. Yale Project on Climate Change Communication: New Haven, CT, 2014

6. Schiermeier, Q. Droughts, Heatwaves and Floods: How to Tell When Climate Change is to Blame. *Nature* **2018**, *560*, 20-22; DOI: 10.1038/d41586-018-05849-9.

7. Weber, E. U. What Shapes Perceptions of Climate Change? New Research Since 2010. *WIREs Clim. Change* **2016**, *7*, 125-134; DOI: 10.1002/wcc.377.

8. Adoption of the Paris Agreement. Proposal by the President, Paris Climate Change Conference – November 2015, COP 21. Paris, France, 2015.

9. Climate Change 2014: Synthesis Report. Contribution of Working Groups I, II and III to the Fifth Assessment Report of the Intergovernmental Panel on Climate Change. Intergovernmental Panel on Climate Change (IPCC): Geneva, Switzerland, 2014.

10. Hansen, J.; Sato, M.; Ruedy, R.; Lacis, A.; Oinas, V. Global Warming in the Twenty-First Century: An Alternative Scenario. *Proc. Natl. Acad. Sci.* **2000**, *97*, 9875-9880; DOI: 10.1073/pnas.170278997.

11. Shishlov, I.; Morel, R.; Bellassen, V. Compliance of the Parties to the Kyoto Protocol in the Commitment Period. *Climate Policy* **2016**, *16*, 768-782; 10.1080/14693062.2016.1164658.

12. Lewis, N. S. Aspects of Science and Technology in Support of Legal and Policy Frameworks

Associated with a Global Carbon Emissions-Control Regime. *Energy Environ. Sci.* **2016**, *9* 2172-2176, and references therein; DOI: 10.1039/c6ee00272b.

13. Earth System Research Laboratory: Global Monitoring Division. Trends in Atmospheric Carbon Dioxide. https://www.esrl.noaa.gov/gmd/ccgg/trends/monthly.html (accessed Aug 24, 2018).

14. United Nations, Framework Convention on Climate Change. UN Climate Change Annual Report 2017. Bonn, Germany, 2018.

15. Royal Dutch Shell plc. Sustainability Report 2017. https://reports.shell.com/sustainability-report/2017/ (accessed Aug 26, 2018).

16. Organization of the Petroleum Exporting Countries. Member Countries. https://www.opec.org/opec_web/en/about_us/25.htm (accessed Aug 26, 2018).

17. International Energy Agency. Global Energy & CO_2 Status Report: The Latest Trends in Energy and Emissions in 2017. https://www.iea.org/geco/renewables/ (accessed Aug 24, 2016).

18. Shaner, M. R.; Davis, S. J.; Lewis, N. S.; Caldeira, K. Geophysical Constraints on the Reliability of Solar and Wind Power in the United States. *Energy Environ. Sci.* **2018**, *11*, 914-925; DOI: https://doi.org/10.1039/c7ee03029k.

19. Tsao, J.; Lewis, N.; Crabtree, G. Solar FAQs. https://www.sandia.gov/~jytsao/Solar%20FAQs.pdf (accessed Aug 26, 2018), and references therein.

20. International Renewable Energy Agency. Renewable Power Generation Costs in 2017. Abu Dhabi, 2018.

21. McCusker, J. K. Femtosecond Absorption Spectroscopy of Transition Metal Charge-Transfer Complexes. *Acc. Chem. Res.* **2003**, *36*, 876-887; DOI: 10.1021/ar030111d.

22. Barbara, P. F.; Meyer, T. J.; Ratner, M. A. Contemporary Issues in Electron Transfer Research. *J. Phys. Chem.* **1996**, *100*, 13148-13168, and references therein; DOI: 10.1021/jp9605663.

23. Monat, J. E.; Rodriguez, J. H.; McCusker, J. K. Ground- and Excited State Electronic Structures of the Solar Cell Sensitizer Bis(4,4'-dicarboxylato-2,2'-bipyridine)bis(isothiocyanato)ruthenium(II). *J. Phys. Chem. A* **2002**, *106*, 7399-7406; DOI: 10.1021/jp020927g.

24. Hagfeldt, A.; Boschloo, G.; Sun, L.; Kloo, L.; Pettersson, H. Dye-Sensitized Solar Cells. *Chem. Rev.* **2010**, *110*, 6595-6663; DOI: 10.1021/cr900356p.

25. Armaroli, N.; Balzani, V. Solar Electricity and Solar Fuels: Status and Perspectives in the Context of the Energy Transition. *Chem. Eur. J.* **2016**, *22*, 32-57; DOI:

10.1002/chem.201503580.

26. Abrahamsson, M.; Becker, H.-C.; Hammarström, L. Microsecond ^{3}MLCT Excited State Lifetimes in Bis-Tridentate Ru(II)-Complexes: Significant Reductions of Non-Radiative Rate Constants. *Dalton Trans.* **2017**, *46*, 13314-13323; DOI: 10.1039/c7dt02437a.

27. Juris, A.; Balzani, V.; Barigelletti, F.; Campagna, S.; Belser, p.; von Zelewsky, A. Ru(II) Polypyridine Complexes: Photophysics, Photochemistry, Electrochemistry, and Chemiluminescence. *Coord. Chem. Rev.* **1988**, *84*, 85-277, and references therein; DOI: 10.1016/0010-8545(88)80032-8.

28. Cannizzo, A.; van Mourik, F.; Gawelda, W.; Zgrablic, G.; Bressler, Ch.; Chergui, M. Broadband Femtosecond Fluorescence Spectroscopy of $[Ru(bpy)_3]^{2+}$. *Angew. Chem. Int. Ed.* **2006**, *45*, 3174-3176; DOI: 10.1002/anie.200600125.

29. Bhasikuttan, A. C.; Suzuki, M.; Nakashima, S.; Okada, T. Ultrafast Fluorescence Detection in Tris(2,2'-bipyridine)ruthenium(II) Complex in Solution: Relaxation Dynamics Involving Higher Excited States. *J. Am. Chem. Soc.* **2002**, *124*, 8398-8405; DOI: 10.1021/ja026135h.

30. Yoon, S.; Kukura, P.; Stuart, C. M.; Mathies, R. A. Direct Observation of the Ultrafast Intersystem Crossing in Tris(2,2'-bipyridine)ruthenium(II) Using Femtosecond Stimulated Raman Spectroscopy. *Molec. Phys.* **2006**, *104*, 1275-1282; DOI: 10.1080/00268970500525846.

31. Yeh, A. T.; Shank, C. V.; McCusker, J. K. Ultrafast Electron Localization Dynamics Following Photo-Induced Charge Transfer. *Science*, **2000**, *290*, 307-313; DOI: 10.1126/science.289.5481.935.

32. Damrauer, N. H.; Cerullo, G.; Yeh, A.; Boussie, T. R.; Shank, C. V.; McCusker, J. K. Femtosecond Dynamics of Excited-State Evolution in $[Ru(bpy)_3]^{2+}$. *Science* **1997**, *275*, 54-57; DOI: 10.1126/science.275.5296.54.

33. Kober, E. M.; Meyer, T. J. Concerning the Absorption Spectra of the Ions $M(bpy)_3^{2+}$ (M = Fe, Ru, Os; bpy = 2,2'-Bipyridine). *Inorg. Chem.* **1982**, *21*, 3967-3977; DOI: 10.1021/ic00141a021.

34. Palmer, R. A.; Piper, T. S. 2,2'-Bipyridine Complexes. I. Polarized Crystal Spectra of Tris(2,2'-bipyridine)copper(II), -nickel(II), -cobalt(II), -iron(II), and -ruthenium(II). *Inorg. Chem.* **1966**, *5*, 864-878; DOI: 10.1021/ic50039a034.

35. Brown, A. M.; McCusker, C. E.; Carey, M. C.; Blanco-Rodriguez, A. M.; Towrie, M.; Clark, I. P.; Vlček, A.; McCusker, J. K. Vibrational Relaxation and Redistribution Dynamics in Ruthenium(II) Polypyridyl-Based Charge-Transfer Excited States: A Combined Ultrafast Electronic and Infrared Absorption Study. *J. Phys. Chem. A*; DOI: 10.1021/acs.jpca.8b06197.

36. Braun, D.; Huber, P.; Wudy, J.; Schmidt, J.; Yersin, H. Electron Delocalization and Localization in Mixed-Ligand $[Ru(LL)_n(LL')_{3-n}]^{2+}$ Complexes. *J. Phys. Chem.* **1994**, *98*,

8044-8049; DOI: 10.1021/j100084a021.

37. Dongare, P.; Myron, B. D. B.; Wang, L.; Thompson, D. W.; Meyer, T. J. $[Ru(bpy)_3]^{2+*}$ Revisited. Is It Localized or Delocalized? How Does It Decay? *Coord. Chem. Rev.* **2017**, *345*, 86-107; DOI: 10.1016/j.ccr.2017.03.009.

38. Caspar, J. V.; Meyer, T. J. Photochemistry of $Ru(bpy)_3^{2+}$. Solvent Effects. *J. Am. Chem. Soc.* **1983**, *105*, 5583-5590; DOI: 10.1021/ja00355a009.

39. Tanabe, Y.; Sugano, S. On the Absorption Spectra of Complex Ions II. J. Phys. Soc. Jpn. 1954, 9, 766-779; DOI: 10.1143/JPSJ.9.766.

40. Amouyal, E.; Mouallem-Bahout, M. Photophysical Study of Tolylterpyridine Complexes. Intramolecular Electron Transfer in an Osmium(II) Dyad. *J. Chem. Soc. Dalton Trans.* **1992**, 509-513; DOI: 10.1039/dt9920000509.

41. Sun, Q.; Mosquera-Vazquez, S.; Suffren, Y.; Hankache, J.; Amstutz, N.; Lawson Daku, L. M.; Vauthey, E.; Hauser, A. On the Role of Ligand-Field States for the Photophysical Properties of Ruthenium(II) Polypyridyl Complexes. *Coord. Chem. Rev.* **2015**, *282-283*, 87-99; DOI: 10.1016/j.ccr.2014.07.004.

42. Nazeeruddin, M. K.; Kay, A.; Rodicio, I.; Humphry-Baker, R.; Müller, E.; Liska, P.; Vlachopoulos, N.; Grätzel, M. Conversion of Light to Electricity by *cis*-X_2Bis(2,2'-bipyridyl-4,4'-dicarboxylate)ruthenium(II) Charge-Transfer Sensitizers (X = Cl^-, Br^-, I^-, CN^-, and SCN^-) on Nanocrystalline TiO_2 Electrodes. *J. Am. Chem. Soc.* **1993**, *115*, 6382-6390; DOI: 10.1021/ja00067a063.

43. Arias-Rotondo, D. M.; McCusker, J. K. The Photophysics of Photoredox Catalysis: A Roadmap for Catalyst Design. *Chem. Soc. Rev.* **2016**, *45*, 5803-5821, and references therein; DOI: 10.1039/c6cs00526h.

44. Nicewicz, D. A.; MacMillan, D. W. C. Merging Photoredox Catalysis with Organocatalysis: The Direct Asymmetric Alkylation of Aldehydes. *Science*, **2008**, *322*, 77-80; DOI: 10.1126/science.1161976.

45. Ischay, M. A.; Anzovino, M. E.; Du, J.; Yoon, T. P. Efficient Visible Light Photocatalysis of [2+2] Enone Cycloadditions. *J. Am. Chem. Soc.* **2008**, *130*, 12886-12887; DOI: 10.1021/ja805387f.

46. Komiya, R.; Fukui, A.; Murofushi, N.; Koide, N.; Yamanaka, R.; Katayama, H. Improvement of the Conversion Efficiency of a Monolithic Type Dye-Sensitized Solar Cell Module. *Tech. Digest, 21st International Photovoltaic Science and Engineering Conference*, Fukuoka, Nov 2011; p. 2C-5O-08.

47. Green, M. A.; Emery, K.; Hishikawa, Y.; Warta, W.; Dunlop, E. D.; Levi, D. H.; Ho-Baillie, A. W. Y. Solar Cell Efficiency Tables (Version 49). *Prog. Photovoltaics, Res. Appl.* **2017**, *25*, 3-13; DOI: 10.1002/pip.2855.

48. Ruthenium Prices and Ruthenium Charts, http://www.infomine.com/investment/metal-prices/ruthenium/, (accessed August 2018).

49. Abundance of Elements in Earth's Crust – Periodic Table and List, https://sciencenotes.org/abundance-of-elements-in-earths-crust-periodic-table-and-list/, (accessed August 2018).

50. Ragoussi, M.-E.; Ince, M.; Torres, T. Recent Advances in Phthalocyanine-Based Sensitizers for Dye-Sensitized Solar Cells. *Eur. J. Org. Chem.* **2013**, 6475-6489, and references therein; DOI: 10.1002/ejoc.201301009.

51. Chen, L. X.; Shaw, G. B.; Novozhilova, I.; Liu, T.; Jennings, G.; Attenkofer, K.; Meyer, G. J.; Coppens, P. MLCT State Structure and Dynamics of a Copper(I) Diimine Complex Characterized by Pump-Probe X-ray and Laser Spectroscopies and DFT Calculations. *J. Am. Chem. Soc.* **2003**, *125*, 7022-7034; DOI: 10.1021/ja0294663.

52. Lin, L.-Y.; Tsai, C.-H.; Wong, K.-T.; Huang, T.-W.; Hsieh, L.; Liu, S.-H.; Lin, H.-W.; Wu, C.-C.; Chou, S.-H.; Chen, S.-H.; Tsai, A.-I. Organic Dyes Containing Coplanar Diphenyl-Substituted Dithienosilole Core for Efficient Dye-Sensitized Solar Cells. *J. Org. Chem.* **2010**, *75*, 4778-4785; DOI: 10.1021/jo100762t.

53. Ferrere, S.; Gregg, B. A. Photosensitization of TiO_2 by [Fe^{II}(2,2'-bipyridine-4,4'-dicarboxylic acid)$_2$(CN)$_2$]: Band Selective Electron Injection from Ultra-Short-Lived Excited States. *J. Am. Chem. Soc.* **1998**, *120*, 843-844; DOI: 10.1021/ja973504e.

54. Tichnell, C. R. Unpublished results.

55. Creutz, C.; Chou, M.; Netzel, T. L.; Okumura, M.; Sutin, N. Lifetimes, Spectra, and Quenching of the Excited States of Polypyridine Complexes of Iron(II), Ruthenium(II), and Osmium(II). *J. Am. Chem. Soc.* **1980**, *102*, 1309-1319; DOI: 10.1021/ja00534a014.

56. Kirk, A. D.; Hoggard, P. E.; Porter, G. B.; Rockley, M. G.; Windsor, M. W. Picosecond Flash Photolysis and Spectroscopy: Transition Metal Coordination Compounds. *Chem. Phys. Lett.* **1976**, *37*, 199-203; DOI: 10.1016/0009-2614(76)80198-4.

57. McCusker, J. K.; Walda, K. N.; Dunn, R. C.; Simon, J. D.; Magde, D.; Hendrickson, D. N. Subpicosecond ^{1}MLCT $\rightarrow$ $^5T_2$ Intersystem Crossing of Low-Spin Polypyridyl Ferrous Complexes. *J. Am. Chem. Soc.* **1993**, *115*, 298-307; DOI: 10.1021/ja00054a043.

58. Fink, D. W.; Ohnesorge, W. E. Temperature Effects on Charge-Transfer Luminescence Intensity of Some Transition Metal Ion Chelates. *J. Am. Chem. Soc.* **1969**, *91*, 4995-4998; DOI: 10.1021/ja01046a009.

59. Street, A. J.; Goodall, D. M.; Greenhow, R. C. Transient Bleaching of Tris(1,10-phenanthroline) Iron(II). *Chem. Phys. Lett.* **1978**, *56*, 326-329; DOI: 10.1016/0009-2614(78)80251-6.

60. Winkler, J. R.; Creutz, C.; Sutin, N. Solvent Tuning of the Excited-State Properties of (2,2'-

Bipyridine)tetracyanoferrate(II): Direct Observation of a Metal-to-Ligand Charge-Transfer Excited State of Iron(II). *J. Am. Chem. Soc.* **1987**, *109*, 3470-3471; DOI: 10.1021/ja00245a053.

61. Bergkamp, M. A.; Chang, C.-K.; Netzel, T. L. Quantum Yield Determinations for Sub-Nanosecond-Lived Excited States and Photoproducts. Application to Inorganic Complexes and Photosynthetic Models. *J. Phys. Chem.* **1983**, *87*, 4441-4446; DOI: 10.1021/j100245a024.

62. Bergkamp, M. A.; Brunschwig, B. S.; Gütlich, P.; Netzel, T. L.; Sutin, N. Temperature Dependence of the Lifetimes of the Ligand-Field States of Tris(1,10-phenanthroline)iron(II). *Chem. Phys. Lett.* **1981**, *81*, 147-150; DOI: 10.1016/0009-2614(81)85346-8.

63. Hauser, A. Excited-State Lifetimes of $[Fe(bipy)_3]^{2+}$ and $[Fe(phen)_3]^{2+}$. *Chem. Phys. Lett.* **1990**, *173*, 507-512; DOI: 10.1016/0009-2614(90)87244-L.

64. Monat, J. E.; McCusker, J. K. Femtosecond Excited-State Dynamics of an Iron(II) Polypyridyl Solar Cell Sensitizer Model. *J. Am. Chem. Soc.* **2000**, *122*, 4092-4097; DOI: 10.1021/ja992436o.

65. Bressler, Ch.; Milne, C.; Pham, V.-T.; ElNahhas, A.; van der Veen, R. M.; Gawelda, W.; Johnson, S.; Beaud, P.; Grolimund, D.; Kaiser, M.; Borca, C. N.; Ingold, G.; Abela, R.; Chergui, M. Femtosecond XANES Study of the Light-Induced Spin Crossover Dynamics in an Iron(II) Complex. *Science* **2009**, *323*, 489-392; DOI: 10.1126/science.1165733.

66. Zhang, W.; Alonso-Mori, R.; Bergmann, U.; Bressler, Ch.; Chollet, M.; Galler, A.; Gawełda, W.; Hadt, R. G.; Hartsock, R. W.; Kroll, T.; Kjær, K. S.; Kubiček, K.; Lemke, H. T.; Liang, H. W.; Meyer, D. A.; Nielsen, M. M.; Purser, C.; Robinson, J. S.; Solomon, E. I.; Sun, Z.; Sokaras, D.; van Driel, T. B.; Vankó, G.; Weng, T.-C.; Zhu, D.; Gaffney, K. J. Tracking Excited-State Charge and Spin-Dynamics in Iron Coordination Complexes. *Nature* **2014**, *509*, 345-348; DOI: 10.1038/nature13252.

67. Consani, C.; Prémont-Schwarz, M.; ElNahhas, A.; Bressler, Ch.; van Mourik, F.; Cannizzo, A.; Chergui, M. Vibrational Coherences and Relaxation in the High-Spin State of Aqueous $[Fe(bpy)_3]^{2+}$. *Angew. Chem. Int. Ed.* **2009**, *48*, 7184-7187; DOI: 10.1002/anie.200902728.

68. Cannizzo, A.; Milne, C. J.; Consani, C.; Gawelda, W.; Bressler, Ch.; van Mourik, F.; Chergui, M. Light-Induced Spin Crossover in Fe(II)-Based Complexes: The Full Photocycle Unraveled by Ultrafast Optical and X-Ray Spectroscopies. *Coord. Chem. Rev.* **2010**, *254*, 2677-2686; DOI: 10.1016/j.ccr.2009.12.007.

69. Gawelda, W.; Cannizzo, A.; Pham, V.-T.; van Mourik, F.; Bressler, Ch.; Chergui, M. Ultrafast Nonadiabatic Dynamics of $[Fe^{II}(bpy)_3]^{2+}$ in Solution. *J. Am. Chem. Soc.* **2007**, *129*, 8199-8206; DOI: 10.1021/ja070454x.

70. Gawelda, W.; Pham, V.-T.; Benfatto, M.; Zaushitsyn, Y.; Kaiser, M.; Grolimund, D.; Johnson, S. L.; Abela, R.; Hauser, A.; Bressler, Ch.; Chergui, M. Structural Determination

of a Short-Lived Excited Iron(II) Complex by Picosecond X-Ray Absorption Spectroscopy. *Phys. Rev. Lett.* **2007**, *98*, 057401; DOI; 10.1103/PhysRevLett.98.057401.

71. de Graaf, C.; Sousa, C. Study of the Light-Induced Spin Crossover Process of the $[Fe^{II}(bpy)_3]^{2+}$ Complex. *Chem. Eur. J.* **2010**, *16*, 4550-4556; DOI: 10.1002/chem.200903423.

72. Bressler, Ch.; Gawelda, W.; Galler, A.; Nielsen, M. M.; Sundström, V.; Doumy, G.; March, A. M.; Southworth, S. H.; Young, L.; Vankó, G. Solvation Dynamics Monitored by Combined X-Ray Spectroscopies and Scattering: Photoinduced Spin Transition in Aqueous $[Fe(bpy)_3]^{2+}$. *Faraday Discuss.* **2014**, *171*, 169-178; DOI: 10.1039/c4fd00097h.

73. Miller, J. N.; McCusker, J. K. Outer-Sphere Effects on the Excited State Dynamics of Ligand Field States in Fe(II) Polypyridyl Complexes. *Manuscript in preparation.*

74. Miskowski, V. M.; Gray, H. B.; Wilson, R. B.; Solomon, E. I. Position of the $^3T_{1g} \leftarrow {}^1A_{1g}$ Transition in Hexacyanocobaltate(III). Analysis of Absorption and Emission Results. *Inorg. Chem.* **1979**, *18*, 1410-1412; DOI: 10.1021/ic50195a057.

75. Kjær, K. S.; Kunnus, K.; Harlang, T.; van Driel, T. B.; Ledbetter, K.; Hartsock, R. W.; Reinhard, M. E.; Koroidov, S.; Li, L.; Laursen, M. G.; Biasin, E.; Hansen, F. B.; Vester, P.; Christensen, M.; Haldrup, K.; Nielsen, M. M.; Chabera, P.; Liu, Y.; Tatsuno, H.; Timm, C.; Uhlig, J.; Sundström, V.; Németh, Z.; Szemes, D. S.; Bajnóczi, É.; Vankó, G.; Alonso-Mori, R.; Glownia, J. M.; Nelson, S.; Sikorski, M.; Sokaras, D.; Lemke, H. T.; Canton, S. E.; Wärnmark, K.; Persson, P.; Cordones, A. A.; Gaffney, K. J. Solvent Control of Charge Transfer Excited State Relaxation Pathways in $[Fe(2,2'\text{-bipyridine})(CN)_4]^{2-}$. *Phys. Chem. Chem. Phys.* **2018**, *20*, 4238-4249, and references therein; DOI: 10.1039/c7cp07838b.

76. Ashley, D. C.; Jakubikova, E. Tuning the Redox Potentials and Ligand Field Strength of Fe(II) Polypyridines: The Dual π-Donor and π-Acceptor Character of Bipyridine. *Inorg. Chem.*; DOI: 10.1021/acs.inorgchem.8b01002.

77. Mukherjee, S.; Torres, D. E.; Jakubikova, E. HOMO Inversion as a Strategy for Improving the Light-Absorption Properties of Fe(II) Chromophores. *Chem. Sci.* **2017**, *8*, 8115-8126; DOI: 10.1039/c7sc02926h.

78. Jamula, L. L.; Brown, A. M.; Guo, D.; McCusker, J. K. Synthesis and Characterization of a High-Symmetry Ferrous Polypyridyl Complex: Approaching the $^5T_2/^3T_1$ Crossing Point for Fe^{II}. *Inorg. Chem.* **2014**, *53*, 15-17; DOI: 10.1021/ic402407k.

79. Britz, A.; Assefa, T.; Galler, A.; Gawełda, W.; Khakhulin, D.; Doumy, G.; March, A. M.; Németh, Z.; Pápai, M.; Roszályi, E.; Cho, H.; Kim, T. K.; Yarranton, J. T.; Mukherjee, S.; Schoenlein, R. W.; Jakubikova, E.; Huse, N.; McCusker, J. K.; Southworth, S. H.; Young, L.; Vankó, G.; Bressler, Ch. $[Fe(dcpp)_2]^{2+}$ Ligand-Field Excited State Geometry and Spin Characterized with Combined Ultrafast X-ray Spectroscopies. *Submitted.*

80. Liu, Y.; Harlang, T.; Canton, S. E.; Chábera, P.; Suárez-Alcántara, K.; Fleckhaus, A.; Vithanage, D. A.; Göransson, E.; Corani, A.; Lomoth, R.; Sundström, V.; Wärnmark, K.

Towards Longer-Lived Metal-to-Ligand Charge Transfer States of Iron(II) Complexes: An *N*-Heterocyclic Carbene Approach. *Chem. Commun.* **2013**, *49*, 6412-6414; DOI: 10.1039/c3cc43833c.

81. Mukherjee, S.; Liu, C.; Jakubikova, E. Comparison to Interfacial Electron Transfer Efficiency in $[Fe(ctpy)_2]^{2+}$-TiO_2 and $[Fe(cCNC)_2]^{2+}$-TiO_2 Assemblies: Importance of Conformational Sampling. *J. Phys. Chem. A* **2018**, *122*, 1821-1830; DOI: 10.1021/acs.jpca.7b10932.

82. Duchanois, T.; Etienne, T.; Cebrián, C.; Liu, L.; Monari, A.; Beley, M.; Assfeld, X.; Haacke, S.; Gros, P. C. An Iron-Based Photosensitizer with Extended Excited-State Lifetime: Photophysical and Photovoltaic Properties. *Eur. J. Inorg. Chem.* **2015**, 2469-2477; DOI: 10.1002/ejic.201500142.

83. Liu, Y.; Kjær, K. S.; Fredin, L. A.; Chábera, P.; Harlang, T.; Canton, S. E.; Lidin, S.; Zhang, J.; Lomoth, R.; Bergquist, K.-E.; Persson, P.; Wärnmark, K.; Sundström, V. A Heteroleptic Ferrous Complex with Mesoionic Bis(1,2,3-triazol-5-ylidene) Ligands: Taming the MLCT Excited State of Iron(II). *Chem. Eur. J.* **2014**, *21*, 3628-3639; DOI: 10.1002/chem.201405184.

84. Duchanois, T.; Etienne, T.; Beley, M.; Assfeld, X.; Perpète, E. A.; Monari, A.; Gros, P. C. Heteroleptic Pyridyl-Carbene Iron Complexes with Tuneable Electronic Properties. *Eur. J. Inorg. Chem.* **2014**, 3747-3753; DOI: 10.1002/ejic.201402356.

85. Chabera, P.; Kjær, K. S.; Prakash, O.; Honarfar, A.; Liu, Y.; Fredin, L. A.; Harlang, T. B.; Lidin, S.; Uhlig, J.; Sundström, V.; Lomoth, R.; Persson, P.; Wärnmark, K. A Fe Hexa-N-Heterocyclic Carbene Complex with a 528 ps Metal-to-Ligand Charge-Transfer Excited-State Lifetime. *J. Phys. Chem.* **2018**, *9*, 459-463; DOI: 10.1021/acs.jpclett.7b02962.

86. Adelman, S. L.; Paulus, B. C.; Jakubikova, E.; McCusker, J. K. Disrupting the Nuclear Coordinate in a Low-Spin Iron(II) Polypyridyl Complex to Extend its MLCT Excited-State Lifetime. *Manuscript in preparation.*

87. Paulus, B. C.; Foszcz, E. D.; Proshlyakov, D. A.; McCusker, J. K. Probing Excited State Deactivation Mechanisms of Transition Metal Complexes Through Observation of Vibrational Coherence. *Manuscript in preparation*

88. Schrauben, J. N.; Dillman, K. L.; Beck, W. F.; McCusker, J. K. Vibrational Coherence in the Excited State Dynamics of $Cr(acac)_3$: Probing the Reaction Coordinate for Ultrafast Intersystem Crossing. *Chem. Sci.* **2010**, *1*, 405-410; DOI: 10.1039/c0sc00262c.

89. Ashley D. C.; Jakubikova, E. Ray-Dutt and Bailar Twists in Fe(II)-tris(2,2'-bipyridine): Spin States, Sterics, and Fe−N Bond Strengths. *Inorg. Chem.* **2018**, *57*, 5585-5596; DOI: 10.1021/acs.inorgchem.8b00560.

90. Stock, P.; Deck, E.; Hohnstein, S.; Korzekwa, J.; Meyer, K.; Heinemann, F. W.; Breher, F.; Hörner, G. Molecular Spin Crossover in Slow Motion: Light-Induced Spin-State transitions in Trigonal Prismatic Iron(II) Complexes. *Inorg. Chem.* **2016**, *55*, 5254-5265; DOI:

10.1021/acs.inorgchem.6b00238.

91. Khalil, M.; Marcus, M. A.; Smeigh, A. L.; McCusker, J. K.; Chong, H. H. W.; Schoenlein, R. W. Picosecond X-Ray Absorption Spectroscopy of a Photoinduced Iron(II) Spin Crossover Reaction in Solution. *J. Phys. Chem. A* **2006**, *110*, 38-44; DOI: 10.1021/jp055002q.

92. Hoselton, M. A.; Drago, R. S.; Wilson, L. J.; Sutin, N. Direct Measurement of Spin-State Lifetimes in Solution for Some Iron(II) Spin Equilibrium Complexes Derived from Hexadentate Ligands. *J. Am. Chem. Soc.* **1976**, *98*, 6967-6969; DOI: 10.1021/ja00438a036.

93. Huse, N.; Kim, T. K.; Jamula, L. L.; McCusker, J. K.; de Groot, F. M. F.; Schoenlein, R. W. Photo-Induced Spin-State Conversion in Solvated Transition Metal Complexes Probed via Time-Resolved Soft X-Ray Spectroscopy. *J. Am. Chem. Soc.* **2010**, *132*, 6809-6816; DOI: 10.1021/ja101381a.

94. Smeigh, A. L.; Creelman, M.; Mathies, R. A.; McCusker, J. K. Femtosecond Time-Resolved Optical and Raman Spectroscopy of Photoinduced Spin Crossover: Temporal Resolution of Low-to-High Spin Optical Switching. *J. Am. Chem. Soc.* **2008**, *130*, 14105-14107; DOI: 10.1021/ja805949s.

95. Braga, T. G.; Wahl, A. C. Rates of Electron Transfer from Osmium(II) to Iron(III) Complex ions Containing 2,2'-Bipyridine or Its Derivatives as Ligands. Effects of Electrolytes at Low Concentrations and Reactant-Separation Distance. *J. Phys. Chem.* **1985**, *89*, 5822-5828; DOI: 10.1021/j100272a049.

96. Leidner, C. R.; Murray, R. W. Electron-Transfer Reactions of Iron, Ruthenium, and Osmium Bipyridine and Phenanthroline Complexes at Polymer/Solution Interfaces. *J. Am. Chem. Soc.* **1984**, *106*, 1606-1614; DOI: 10.1021/ja00318a010.

97. Munzert, S. M.; Schwarz, G.; Kurth, D. G. Kinetic Studies of the Coordination of Mono- and Ditopic Ligands with First Row Transition Metal Ions. *Inorg. Chem.* **2016**, *55*, 2565-2573; DOI: 10.1021/acs.inorgchem.5b02931.

98. Rao, J. M.; Macero, D. J.; Hughes, M. C. Dual Role of *Para*-Phenyl Substituents in Aromatic Imine Ligand Complexes of Cobalt and Iron. *Inorg. Chim. Acta* **1980**, *41*, 221-226; DOI: 10.1016/S0020-1693(00)88458-3.

99. Damrauer, N. H.; Boussie, T. R.; Devenney, M.; McCusker, J. K. Effects of Intraligand Electron Delocalization, Steric Tuning, and Excited-State Vibronic Coupling on the Photophysics of Aryl-Substituted Bipyridyl Complexes of Ru(II). J. Am. Chem. Soc. 1997, 119, 8253-8268; DOI: 10.1021/ja971321m.

100. Baitalik, S.; Wang, X.-Y.; Schmehl, R. H. A Trimetallic Mixed Ru(II)/Fe(II) Terpyridyl Complex with a Long-Lived Excited State in Solution at Room Temperature. *J. Am. Chem. Soc.* **2004**, *126*, 16304-16305; DOI: 10.1021/ja044561s.

101. Yoon, Z. S.; Chuan, Y.-T.; Li, S.; Newkome, G. R.; Goodson, T. Ultrafast Time-Resolved Spectroscopy of Self-Assembled Cyclic Fe(II)-Bisterpyridine Complexes. *J. Phys. Chem. B*

2010, *114*, 11731-11736; DOI: 10.1021/jp104836k.

102. Brown, A. M. Excited-State Dynamics of Iron(II)-Based Charge-Transfer Chromophores. Ph.D. Thesis, Michigan State University, East Lansing, MI, 2011.

103. Marcus, R. A.; Sutin, N. Electron Transfers in Chemistry and Biology. *Biochim. Biophys. Acta* **1985**, *811*, 265-322; DOI: 10.1016/0304-4173(85)90014-X.

104. Sutin, N. Nuclear, Electronic, and Frequency Factors in Electron-Transfer Reactions. *Acc. Chem. Res.* **1982**, *15*, 275-282; DOI: 10.1021/ar00081a002.

105. Claude, J. P.; Meyer, T. J. Temperature Dependence of Nonradiative Decay. *J. Phys. Chem.* **1995**, *99*, 51-54; DOI: 10.1021/j100001a010.

106. Huber, H.; Meyer, M.; Scheer, H.; Zinth, W.; Wachtveitl, J. Temperature Dependence of the Primary Electron Transfer Reaction in Pigment-Modified Bacterial Reaction Centers. *Photosynth. Res.* **1998**, *55*, 153-162; DOI: 10.1023/A:1006013613075.

107. Farr, E. P.; Zho, C.-C.; Challa, J. R.; Schwartz, B. J. Temperature Dependence of the Hydrated Electron's Excited-State Relaxation. II. Elucidating the Relaxation Mechanism Through Ultrafast Transient Absorption and Stimulated Emission Spectroscopy. *J. Chem. Phys.* **2017**, *147*, 074504; DOI: 10.1063/1.4985906.

108. Malone R. A.; Kelley, D. F. Interligand Electron Transfer and Transition State Dynamics in Ru(II) Trisbipyridine. *J. Chem. Phys.* **1991**, *95*, 8970-8976; DOI: 10.1063/1.461228.

109. Berera, R.; van Grondelle, R.; Kennis, J. T. M. Ultrafast Transient Absorption Spectroscopy: Principles and Application to Photosynthetic Systems. *Photosynth. Res.* **2009**, *101*, 105-118; DOI: 10.1007/s11120-009-9454-y.

110. Foszcz, E. D. Understanding the Interplay Between Geometry and Ultrafast Dynamics in Ligand Field Excited States of Inorganic Chromophores. Ph.D. Thesis, Michigan State University, East Lansing, MI, 2015.

111. Miller, J. N. Ultrafast Dynamics of Iron(II)-Based Complexes in Solution and Semiconductor-Chromophore Assemblies. Ph.D. Thesis, Michigan State University, East Lansing, MI, 2018.

112. Megerle, U.; Pugliesi, L.; Schriever, C.; Sailer, C.F.; Riedle, E. Sub-50 fs Broadband Absorption Spectroscopy with Tunable Excitation: Putting the Analysis of Ultrafast Molecular Dynamics on Solid Ground. *Appl. Phys. B* **2009**, *96*, 215-231; DOI: 10.1007/s00340-009-3610-0.

113. Adelman, S. L.; Jakubikova, E. Unpublished results.

114. Buhks, E.; Navon, G.; Bixon, M.; Jortner, J. Spin Conversion Processes in Solutions. *J. Am. Chem. Soc.* **1980**, *102*, 2918-2923; DOI: 10.1021/ja00529a009.

115. Marcus, R. A. On the Theory of Oxidation-Reduction Reactions Involving Electron Transfer. I. *J. Chem. Phys.* **1956**, *24*, 966-978; DOI: 10.1063/1.1742723.

116. Marcus, R. A. On the Theory of Electron Transfer Reactions. VI. Unified Treatment for Homogeneous and Electrode Reactions. *J. Chem. Phys.* **1965**, *43*, 679-701; DOI: 10.1063/1.1696792.

117. DeVault, D. *Quantum-Mechanical Tunnelling in Biological Systems*, 2nd ed.; Cambridge University Press: New York, 1984, and references therein.

118. Jortner, J. Temperature Dependent Activation Energy for Electron Transfer Between Biological Molecules. *J. Chem. Phys.* **1976**, *64*, 4860- ; DOI: 10.1063/1.432142.

119. Schrauben, J. N. Electronic Structure and Excited State Dynamics of Chromium(III) Complexes. Ph.D. Thesis, Michigan State University, East Lansing, MI, 2010.

CHAPTER 2. VARIABLE-TEMPERATURE ULTRAFAST SPECTROSCOPY YIELDS INSIGHT INTO RELAXATION PATHWAYS OF FE(II) POLYPYRIDYL COMPLEXES

1. Introduction

For over half a century, $[Fe(bpy)_3]^{2+}$ (bpy = 2,2'-bipyridine) has been the benchmark for an array of iron(II) complexes.[1-16] Among its attributes, $[Fe(bpy)_3]^{2+}$ is one of the most well-studied and well-understood of the first-row transition metal complexes and provides a good fundamental handle for d^6 photophysics. For this chromophore, and for nearly all Fe(II) polypyridyls, absorption of visible light excites the low-spin $^1A_1$ ground state into the singlet metal-to-ligand charge transfer (MLCT) state, whereupon ultrafast intersystem crossing to the ^{3}MLCT occurs in ~20 fs.[1] Deactivation out of the MLCT manifold occurs in <100 fs[2] with unit efficiency[3] via a ligand field manifold, sampling a ^{3}T state,[4] into the lowest energy excited state, the $^5T_2$.[5] Ground state recovery from this ligand field state occurs on the order of 1 ns[6] and is dependent on the nature of the solvent.[7]

Despite our knowledge of these photophysical processes, there remain a number of unanswered fundamental questions about this model complex. For instance, although attempts have been made to estimate the zero-point energy difference (ΔG^o) between the ground state and lowest energy excited state ($^1A_1/^5T_2$), a range of values spanning nearly one eV (i.e. 2000-9000 cm^{-1}) exists in the literature.[8-10,17,18] The challenge intrinsic to the question of ΔG^o for these complexes is that the $^5T_2 \rightarrow {}^1A_1$ transition is doubly spin-forbidden with $\Delta S=2$, is a multi-electron process, and does not emit; therefore there is no immediately apparent way to experimentally determine this energy. Consequently, other fundamental energetic parameters are unknown with regard to the ground state recovery of $[Fe(bpy)_3]^{2+}$. Values for the Marcus reorganization energy associated with the relaxation (λ) and the coupling of the two electronic states (H_{ab}) for Fe(II)

polypyridyl complexes have been estimated, but not directly measured. For example, Sutin uses the lifetime of $[Fe(bpy)_3]^{2+}$ along with modified electron-transfer theory to posit ΔG^o = -7300 cm^{-1}, λ = 4800, and H_{ab} = 20-200 cm^{-1}.[8] Likewise, using energy gap theory, Jortner approximated the electronic coupling constant from the Fe(II) free ion and found it to be 170 cm^{-1}.[17,18] Hauser et al. studied $[Fe(bpy)_3]^{2+}$ doped into a Zn(II) lattice by variable-temperature time-resolved absorption spectroscopy.[10] Using Jortner's H_{ab} value, they determined the activation energy (E_a) of ground state recovery to be 364 cm^{-1} for a zero-point energy difference of -2000 cm^{-1}. These values are some of the best, and only, indicators for energetic parameters of the electronic states available in the literature, yet they are merely estimates and lack experimental verification.

To gain a better grasp on these energetic parameters, many have taken advantage of Fe(II) spin-crossover complexes,[9,19-21] in which the excited state is in a thermal equilibrium with the ground state. For this type of system, variable-temperature magnetic susceptibility measurements can be used to find ΔG^o. From the driving force, reorganization energy can be found. A wide array of values exist in the literature for a whole host of complexes with varying degrees of similarity to the Fe(II) polypyridyl complexes of interest here.[19,20] As part of a study on a series of spin-crossover complexes, Conti et al. studied a low-spin Fe(II) complex with a relatively long-lived excited state by variable-temperature nanosecond transient absorption spectroscopy.[21] Unlike other reports at the time, their data produced an electronic coupling constant on the order of single wavenumbers. That being said, $[Fe(bpy)_3]^{2+}$, with a zero-point energy difference substantially greater than k_BT, is not spin-crossover rendering these methods inaccessible.

Although there are clearly inherent challenges to experimentally determining ΔG^o, other energetic parameters are technically within reach, namely the activation energy and the frequency factor, or the rate in the absence of the barrier. The most direct method of determining activation

energy is through the use of Arrhenius behavior, where measuring the rate of reaction as a function of temperature yields both E_a and the frequency factor. Although it is a very obvious solution, variable-temperature transient absorption spectroscopy is not a widely employed technique; when performed on the ultrafast timescale, it is even less commonly employed.[22] One substantive reason for this is broadening of ultrafast pulses caused by the glass introduced from the optical cryostat necessary to control the temperature in these experiments. Advantageously, the lifetimes of the four Fe(II) complexes studied here are on the order of nanoseconds, allowing for the utilization of relatively longer pulses (~150 fs), minimizing the effects of broadening. For the first time, variable-temperature ultrafast transient absorption spectroscopy is performed on $[Fe(bpy)_3]^{2+}$ is studied as a model complex, along with two 4,4'-di-substituted bipyridine compounds (Scheme 2.1). Comparisons between this family and a terpyridyl iron(II) system allows for deeper understanding of intrinsic differences between the complexes. Through this method, Arrhenius parameters are determined for each complex, and essential electronic values can begin to be found and interpreted. We believe that with our specific experimental setup, this technique becomes an incredibly powerful tool in the study of fundamental energetic parameters of Fe(II) complexes.

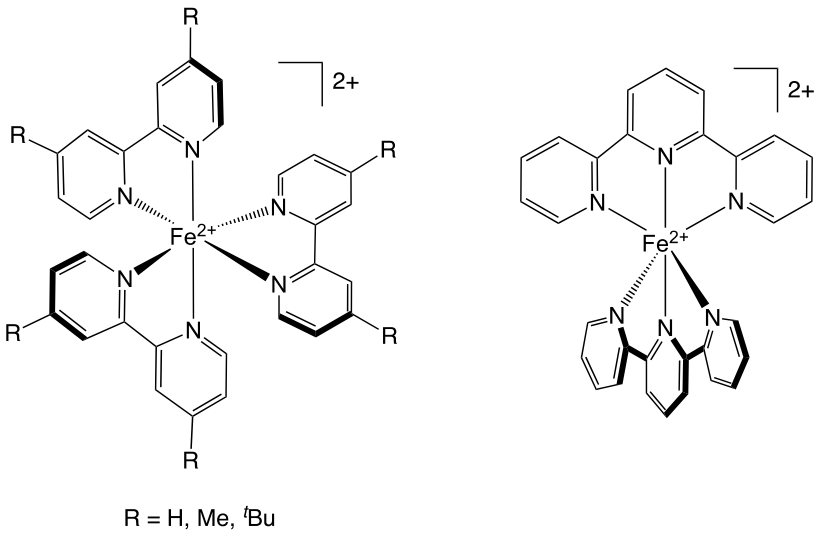

Scheme 2.1. The four complexes used in these studies. Left: $[Fe(bpy')_3]^{2+}$ family, in which R = H is $[Fe(bpy)_3]^{2+}$, R = Me is $[Fe(dmb)_3]^{2+}$, and R = ^{t}Bu is $[Fe(dtbb)_3]^{2+}$. Right: $[Fe(terpy)_2]^{2+}$.

2. Experimental

2.1 Materials and Synthesis

2.1.1 General

The four complexes studied herein are: tris(2,2'-bipyridine) iron(II) hexafluorophosphate, $[Fe(bpy)_3](PF_6)_2$; tris(4,4'-dimethyl-2,2'-bipyridine) iron(II) hexafluorophosphate, $[Fe(dmb)_3](PF_6)_2$; tris(4,4'-di-*tert*-butyl-2,2'-bipyridine) iron(II) hexafluorophosphate, $[Fe(dtbb)_3](PF_6)_2$; and bis(2,2':6',2"-terpyridine) iron(II) hexafluorophosphate, $[Fe(terpy)_2](PF_6)_2$. They were prepared according to previously reported procedures.[11-13] ^{1}H NMR spectra were collected on a Bruker 500 MHz NMR spectrometer. Electrospray-ionization mass-spectrometry (ESI-MS) was performed on a Waters Xevo G2-XS Quadrupole Time-of-Flight spectrometer in positive mode. NMR and mass spectra were collected and analyzed by S. L. Adelman. HPLC grade acetonitrile was purchased from Sigma-Aldrich and used as received. Ground state absorption

spectra were collected with a Varian (now Agilent) Cary 50 UV-Vis spectrophotometer.

Electrochemical data were collected by S. L. Adelman using a CH Instruments Model CHI620D electrochemical workstation under inert atmosphere in an argon-filled glove box. A standard three-electrode setup was used to obtain Fe(II/III) potentials with differential pulse voltammetry and cyclic voltammetry in acetonitrile with 0.1 M $TBAPF_6$ using a Pt working electrode and a Ag reference electrode. $TBAPF_6$ was purchased from Oakwood Chemical Company and recrystallized from ethanol twice before use. All potentials are referenced internally to Fc/Fc^+.

$[Fe(dmb)_3](PF_6)_2$ was recrystallized by vapor diffusion of diethyl ether into methanol, while $[Fe(terpy)_2](PF_6)_2$ was recrystallized by vapor diffusion of diethyl ether into acetonitrile. In both cases, the single crystals were mounted in paratone oil and transferred to the cold nitrogen gas stream of the diffractometer for data collection. Single crystal X-ray diffraction was collected on suitable crystals mounted on a Bruker APEX-II CCD diffractometer with CuK_α radiation at the Center for Crystallographic Research at Michigan State University. The crystal structures were solved by S. L. Adelman.

2.1.2 Characterization of Free Ligands and Complexes

2,2'-bipyridine (bpy) ^{1}H NMR (500 MHz, [d_6-acetone], δ) [8.67 (ddd, 1 H, J = 0.82, 2.73, 4.65 Hz), 8.48 (dt, 1 H, J = 1.08, 7.96 Hz), 7.92 (ddd, 1 H, J = 1.8, 7.64 Hz), 7.41 (ddd, 1 H, 1.23, 2.72, 6.1 Hz)].

4,4'-dimethyl-2,2'-bipyridine (dmb) ^{1}H NMR (500 MHz, [d_6-acetone], δ) [8.51 (d, 1 H, J = 4.72 Hz), 8.30 (m, 1 H), 7.23 (m, 1 H), 2.44 (s, 3 H)].

4,4'-di-*tert*-butyl-2,2'-bipyridine (dtbb) ^{1}H NMR (500 MHz, [d_6-acetone], δ) [8.58 (dd, 1 H, J = 0.77, 5.23 Hz), 8.54 (dd, 1 H, J = 0.75, 2.0 Hz), 7.44 (dd, 1 H, J = 2.03, 5.14 Hz)].

Tris(2,2'-bipyridine) iron(II) hexafluorophosphate $[Fe(bpy)_3](PF_6)_2$ ^1H NMR (500 MHz, [d_6-acetone], δ) [8.85 (d, 1 H, J = 8.09 Hz), 8.27 (t, 1 H, J = 7.84 Hz), 7.74 (d, 1 H, J = 5.61 Hz), 7.59 (t, 1 H, J = 6.79 Hz)]. ESI-MS (m/z): $[C_{30}H_{24}N_6Fe]^{2+}$ calcd. 262.07; found 262.06.

Tris(4,4'-dimethyl-2,2'-bipyridine) iron(II) hexafluorophosphate $[Fe(dmb)_3](PF_6)_2$ ^1H NMR (500 MHz, [d_6-acetone], δ) [8.70 (s, 1 H), 7.51 (d, 1 H, J = 5.79), 7.40 (dd, 1 H, J = 1.23, 5.82), 2.58 (s, 3 H)]. ESI-MS (m/z): $[C_{36}H_{36}N_6Fe]^{2+}$ calcd. 304.12; found 304.10.

Tris(4,4'-di-*tert*-butyl-2,2'-bipyridine) iron(II) hexafluorophosphate $[Fe(dtbb)_3](PF_6)_2$ ^1H NMR (500 MHz, [d_6-acetone], δ) [8.94 (d, 1 H, J = 1.75 Hz), 7.57 (d, 1 H, J = 5.69 Hz), 7.52 (d, 1 H, J = 5.93 Hz), 1.40 (s, 9 H). ESI-MS (m/z): $[C_{36}H_{36}N_6Fe]^{2+}$ calcd. 430.26; found 430.28.

Bis(2,2':6',2"-terpyridine) iron(II) hexafluorophosphate $[Fe(terpy)_2](PF_6)_2$ ^1H NMR (500 MHz, [d_6-acetone], δ) [9.25 (d, 2 H, J = 8.06 Hz), 8.88 (t, 1 H, J = 7.99 Hz), 8.80 (ddd, 2 H, J = 0.6, 2.11, 8.07 Hz), 8.05 (td, 2 H, J = 1.48, 7.72 Hz), 7.44 (ddd, 2 H, J = 0.6, 2.3, 5.74 Hz), 7.25 (ddd, 2 H, J = 0.6, 1.32, 6.54 Hz). ESI-MS (m/z): $[C_{30}H_{22}N_6Fe]^{2+}$ calcd. 261.06; found 261.04.

2.1.3 Crystal Structure Determination

$[Fe(dmb)_3](PF_6)_2$ crystal data: $C_{40}H_{45}F_{12}FeN_6OP_2$, M_r = 971.61, triclinic, a = 8.6648(2) Å, b = 14.3856(3) Å, c = 17.4683(4) Å, T= 173 K, space group P-1 (No. 2), Z = 2, 25863 reflections measured, 7808 unique (Rint = 0.1207), which were used in all calculations. The final wR(F2) was 0.0625 (all data). CCDC 1810752.

$[Fe(terpy)_2](PF_6)_2$ crystal data: $C_{34}H_{28}F_{12}FeN_8P_2$, M_r = 894.43, tetragonal, a = 12.3462(2) Å, b = 12.3462(2) Å, c = 48.9067(9) Å, T = 173 K, space group $P4_1$ (no. 76), Z = 8, 26729 reflections measured, 11934 unique (Rint = 0.0446), which were used in all calculations. The final wR(F2) was 0.1140 (all data). CCDC 1810753.

2.2 Ultrafast Transient Absorption Spectroscopy

Ultrafast transient absorption (TA) spectroscopy measurements were carried out as previously described,[23] with the following modifications: The Ti:sapphire oscillator (Coherent Mira 900) is now pumped by a diode-pumped solid state laser (Coherent Verdi V6) operating at 5.0 W. The output from the regenerative amplifier (Positive Light Spitfire) is split 70:30 to the pump and probe lines, respectively. The pump wavelength is tunable in the visible region by use of an optical parametric amplifier (Light Conversion TOPAS), the output of which is double-passed by retroreflectors mounted on a 1.2 m delay stage (Aerotech) controlled by Soloist CP software. This set-up affords 13 ns of delay between the pump and probe pulses, a necessity when collecting ground state recovery dynamics of Fe(II) polypyridyl complexes. The detection scheme utilizes ~10 nm UV/Vis bandpass notch filters (Thorlabs) to select the probe wavelength of 530 nm that was desired from the white light continuum, which is then focused onto a Si amplified photodiode (Thorlabs).

For the data displayed here, the typical excitation energy was ~5 μJ, such that all data was collected in the linear regime. The ground state absorbance for each of the samples was approximately 0.7 in a 1-cm sample cryogenic cuvette (FireFlySci) at 490 nm, the excitation wavelength, and no spectral changes were observed after the variable-temperature experiments were complete. Pulse characterization is performed within the cryostat by optical Kerr effect (OKE) measurements made in acetonitrile, yielding approximately 160 fs pulses. Cross-correlation performed in acetonitrile gives an instrument response function better than 300 fs. The spectra shown here are an average of approximately 10 scans, with no single scan giving a fit that is a statistical outlier. Monoexponential and Arrhenius fits to the data were performed with Igor Pro (v. 6.37) software. All error reported was propagated across multiple data sets.

2.3 Variable-Temperature Measurements

In order to obtain spectra at a continuum of temperatures, an optical Dewar (Janis Research SuperTran-VP 100) was implemented, with capabilities of maintaining temperatures <2-325 K. Initially, a turbomolecular pumping station (Pfeiffer Vacuum HiCube 80 Eco) brings the pressure of the outer jacket of the cryostat to 10^{-6} mbar, thereby producing an insulating atmosphere. A liquid nitrogen storage Dewar (International Cryogenics, Inc.) is connected to the cryostat with a transfer line (Janis Research) that remains in place throughout data collection for minimal cryogen loss. The continuous-flow setup also allows for the cryostat to remain stationary throughout data collection, thereby minimizing changes in the pump/probe overlap within the sample. The temperature of the sample within the cryostat is monitored (Lake Shore Cryotronics) by two sensors placed above and below the sample mount. The average of these two temperatures is assumed to be the sample temperature, affording better than ±2 K certainty. A schematic of the variable-temperature ultrafast set-up can be seen in Scheme 2.2. No stabilization time was necessary as data collection is on the order of one hour, more than sufficient for the sample temperature to equilibrate.

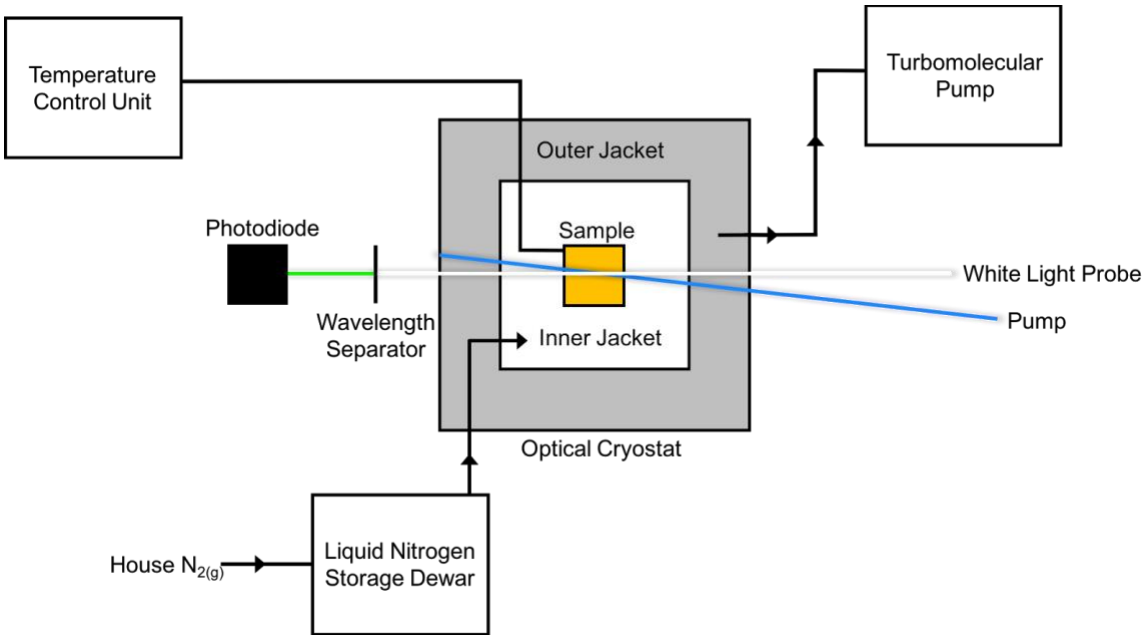

Scheme 2.2. Schematic overview of the variable-temperature apparatus used within the standard ultrafast transient absorption setup. Arrows demonstrate the direction of the air flow; for example, the turbomolecular pump pulls vacuum on the outer jacket, whereas the cooled nitrogen flows into the inner jacket of the cryostat.

3. Results and Discussion

3.1 Characterization

3.1.1 Ground State Absorption Spectra

The same pump probe cross-section was used to study each of the complexes. Specifically, all four compounds were excited at 490 nm and probing at 530 nm. An overlay of the ground state absorption spectra for the four complexes can be seen in Fig. 2.1. The spectra have been normalized to the excitation energy for an absorbance of 0.7, as is used for these experiments. All three of the $[Fe(bpy')_3]^{2+}$ complexes have very similar spectra, with the typical MLCT band shape centered around ca. 500 nm. In the case of $[Fe(bpy)_3]^{2+}$, the manifold is narrower, with the red edge being blue-shifted relative to the other two complexes. At the probe wavelength, the

absorbance for $[Fe(bpy)_3]^{2+}$ is 0.74 AU and is 0.8 for $[Fe(dmb)_3]^{2+}$ and $[Fe(dtbb)_3]^{2+}$. $[Fe(terpy)_2]^{2+}$, however, is another case, entirely. The entire MLCT manifold is red-shifted compared to the bpy-based family. It also displays much sharper features. Because of these factors, the absorbance at the probe wavelength is 1.0 AU. For all of these complexes, the rather high absorption at the probe energy serves to decrease the detected signal by way of reducing the amount of light transmitted through the sample. All kinetics were checked for linearity, however, and signal was optimized by focusing the pump and probe as tightly as possible within the sample.

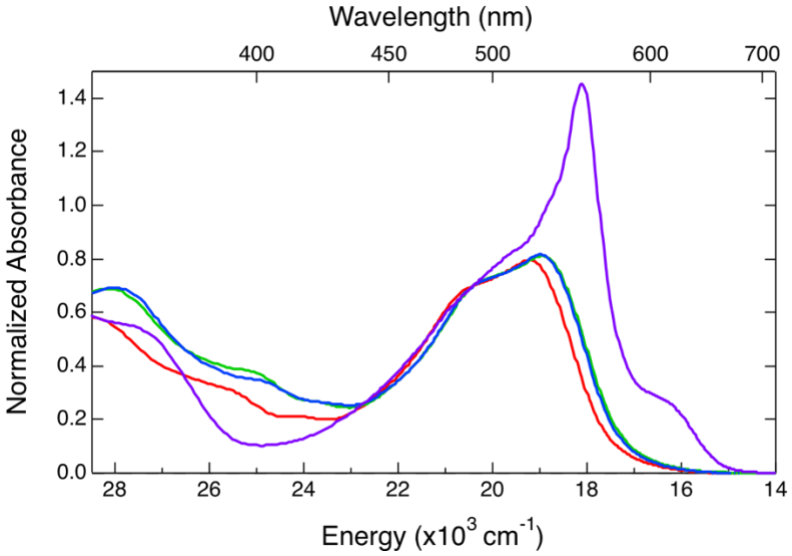

Figure 2.1. Ground state absorption spectra of the four Fe(II) polypyridyl complexes: $[Fe(bpy)_3](PF_6)_2$ in red, $[Fe(dmb)_3](PF_6)_2$ in green, $[Fe(dtbb)_3](PF_6)_2$ in blue, and $[Fe(terpy)_2](PF_6)_2$ in purple. All spectra are normalized to 0.7 AU at 490 nm (~20400 cm^{-1}). See text for details.

3.2 Crystal Structures

Single-crystal X-ray structures have not been previously reported for either

$[Fe(dmb)_3](PF_6)_2$ or $[Fe(terpy)_2](PF_6)_2$. The structure of $[Fe(dmb)_3](PF_6)_2$ can be found in Fig. 2.2, and $[Fe(terpy)_2](PF_6)_2$ in Fig. 2.3. The Fe-N bond distances given in Table 2.1 are typical for low-spin Fe(II) complexes, as expected. $[Fe(terpy)_2](PF_6)_2$ deviates the most from octahedral symmetry of all four complexes, with *cis* N-Fe-N angles spanning 80.82-99.97º. Significant distortion is also observed in the Fe-N bond distances, in which the axial bonds are ~1.88 Å whereas approximately 1.97 Å bond lengths are seen for the equatorial N-Fe bonds. Compared to the *trans* N-Fe-N angles of ca. 175º in the $[Fe(bpy')_3](PF_6)_2$ family, those for $[Fe(terpy)_2](PF_6)_2$ are 167.75 ± 9.60º, supporting the descent in symmetry from octahedral. This is to be expected, however, due to the tridentate nature of the ligand, which more strained than its bidentate analogues.

Relative to the other members of the $[Fe(bpy')_3](PF_6)_2$ family, $[Fe(dmb)_3](PF_6)_2$ is the lowest in symmetry, with $[Fe(bpy)_3](PF_6)_2$ being the highest. This is evidenced by the greater variance in *cis* N-Fe-N angles for the methylated complex. To gauge the electron-donating ability of the R groups in the substituted bpy family, two parameters are closely examined: 1) the Fe-N distances, and 2) the C-C bond distance connecting the R group to the bipyridine backbone. In the first case, the Fe-N bond increases for the complexes as dtbb < dmb < bpy; secondly, the C-C bond is longer in the case of $[Fe(dtbb)_3](PF_6)_2$. These two pieces of data indicate that the ^{t}butyl group is less electron-donating than the methyl group. Although the structures reported herein are of the ground state geometries, knowledge of the effects of the ligands on the iron center inform the understanding of the ligand field strength and is therefore relevant to discussion of the photophysics of the complexes.

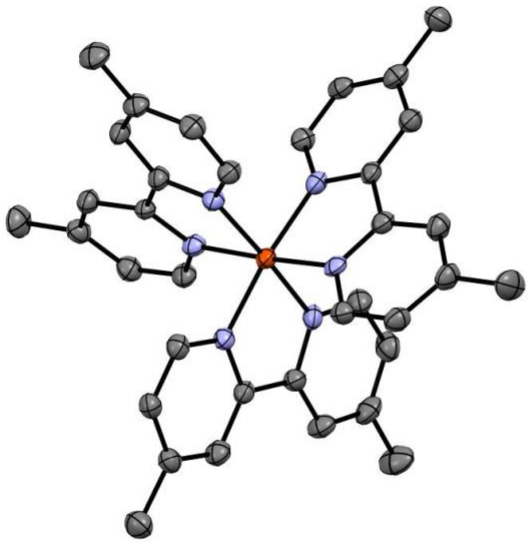

Figure 2.2. X-ray crystal structure of $[Fe(dmb)_3](PF_6)_2$, with solvent molecules and counteranions omitted for clarity. Crystals grown and solved by S. L. Adelman.

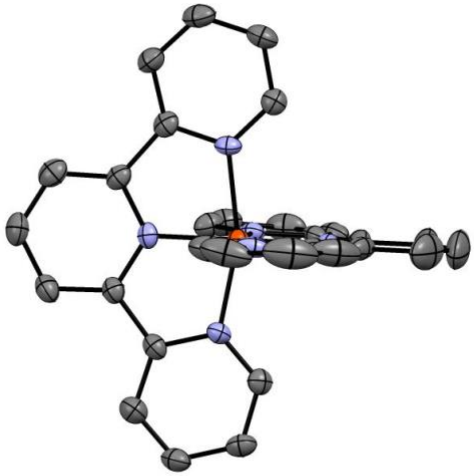

Figure 2.3. X-ray structure of $[Fe(terpy)_2](PF_6)_2$, with solvent molecules and counteranions omitted for clarity. Crystals grown and solved by S. L. Adelman.

Table 2.1. Bond distances and angles from X-ray crystallographic data for all four complexes.

Complex	Fe-N Distance (Å)	*Cis* N-Fe-N Angle (°)	*Trans* N-Fe-N Angle (°)	Ref.
$[Fe(bpy)_3](PF_6)_2$	1.967	81.86-94.31	174.61	[14]
$[Fe(dmb)_3](PF_6)_2$	1.967 ± 0.006	80.92-97.52	175.10 ± 1.19	This work
$[Fe(dtbb)_3](PF_6)_2$	1.957 ± 0.001	81.06-95.84	174.54 ± 1.66	[13]
$[Fe(terpy)_2](PF_6)_2$	1.944 ± 0.049	80.82-99.97	167.75 ± 9.60	This work

3.3 Challenges of Variable-Temperature Ultrafast Spectroscopy

It is well-established that ultrashort (sub-ns) laser pulses will temporally broaden when propagating through media.[24,25] This phenomenon, known as chirp, artificially increases the instrument response function. In cases in which the kinetics are <100 fs, this is severely detrimental to the data collection. In fact, the only previous report that was found in which variable-temperature ultrafast transient absorption spectroscopy was being performed on a transition metal complex in solution used 30 ps pulses.[22] A pulse duration on this order should experience minimal to no effects due to dispersion. The exact amount of chirp introduced to an ultrafast pulse can be calculated (see Chapter 2 Section 3.3.1), as well as the extent to which the pulse will be broadened. The pump and probe pulses used in this experiment were characterized by OKE spectroscopy in a 1 mm path length cuvette without the cryostat and found to be on the order of 150 fs. In this regime, the amount of dispersion introduced by the windows of the cryostat and 1-cm path length cuvette is predicted to be negligible, a result observed in the OKE spectrum collected for the sample within the Dewar. We would also expect no meaningful effect of chirp on the kinetics measured here as the lifetimes of the complexes in this report are on the order of single nanoseconds, four orders of

magnitude larger than the predicted dispersion effect.

To further verify the lack of effect the optical Dewar plays on the kinetics, ground state recovery dynamics of the four complexes were collected with the sample in the cryostat at room temperature. The lifetimes of $[Fe(bpy)_3]^{2+}$ and $[Fe(terpy)_2]^{2+}$ reported here are consistent with what has been observed previously.[6,15] Creutz et al. reported a ground state recovery rate for $[Fe(dmb)_3]^{2+}$ in water, which has intrinsically different dynamics than in acetonitrile.[7,12] To the best of our knowledge, a ground state recovery rate has not been reported for $[Fe(dtbb)_3]^{2+}$. It should be noted that the lifetime of $[Fe(terpy)_2]^{2+}$ under these conditions is such that the ground state does not fully recover within the dynamic range possible here. Typically, data collection out to approximately 4-5 times the ground state recovery lifetime is required for the signal to completely return to zero (i.e. confidence in the lifetime from the fit). In this case, there will always be greater inherent error in the lifetime, and therefore all values calculated from the lifetime reported for $[Fe(terpy)_2]^{2+}$ than for the other complexes studied here.

While the glass from the cryostat imposes a static form of error into the results, the change in temperature provides a dynamic one. Many different factors display a dependence on temperature that can present challenges to reproducible data collection. The first, and perhaps most obvious, difficulty comes in the form of solvent purity, specifically, the presence of water. Water here acts to raise the freezing point of the solvent, thereby facilitating a higher temperature fluid-to-glass transition. This transition is notorious for altering observable rates due to the disordered nature of the semi-solid solution.[26] The choice of HPLC grade acetonitrile here for use as the solvent helps to minimize this issue since this grade is intrinsically very pure. By ^{1}H NMR, the water content in the acetonitrile used in these studies is <0.4% (see Chapter 2 Section 3.3.2). Related to this concept is the overall decrease in solubility of the solute as temperature decreases.

This is observed as a reduced I_0 of the sample, and therefore a smaller ΔA. The error from this does not alter the overall time constants measured for the sample.

Finally, the effect of temperature on the index of refraction has been the most significant, and the most difficult to avoid or correct for. The temperature dependence of some common solvents[27,28] including acetonitrile[29,30] has been studied previously. Specifically, as temperature decreases, the refractive index increases; this means that relative to the path of the laser beam at room temperature, the beam will refract more at lower temperatures. The result of this is two-fold. In the first case, the beams' overlap within the center of the 1-cm cuvette will actually deviate with changing temperature. A greater effect will be seen for the pump rather than the probe as the pump enters the sample at a less collinear angle (5-10º relative to the probe). The best solution found for this problem is to optimize overlap on the side of the cuvette away from the detector (i.e. where the beams first enter the sample). In this configuration, the probe beam should traverse a relatively straight path to the detector, and any beam refraction in the pump due to solvent should occur after the beams have overlapped, thus minimizing adverse effects. If a glass is not to be formed, a shorter pathlength cuvette could also be used to aid in these efforts. The second way in which the change in index of refraction as a function of temperature is observed is the amount of pump scatter that reaches the detector. In terms of ΔA, scatter appears as a negative signal superimposed on the solute's kinetics. What is generally observed in these experiments is a greater amount of scatter at colder temperatures. A negative ΔA on top of the ground state bleach with an exponential decay results in an artificially shortened observed time constant. Here, as with the case when water was present in the solvent, bimodal Arrhenius behavior is seen. The most straightforward approach to solve this problem would be the use of a monochromator as part of a two-color setup to attenuate the effects of the scatter. In these results, however, we were limited to the use of a white light

continuum probe and 10 nm bandpass filter, and therefore chose to probe at wavelengths spectrally far (> 50 nm) from the scatter so as to not distort the data.

3.3.1 Pulse Broadening Calculations

Based on the optical material, the exact amount of dispersion introduced to a pulse as it propagates through that material.[31] These calculations are defined by variables such as group velocity delay (GVD) and group delay dispersion (GDD), which is in turn determined by properties that are specific to the type of glass or material through which the pulse is traveling. For our purposes, the calculations were made for fused silica, the glass of the optical windows of the cryostat. There are four windows (two in the outer jacket, two in the inner jacket) plus the two glass faces of the sample cuvette, summing to approximately 12 mm of fused silica. Based on the material properties and this distance, the GVD can be found as a function of wavelength:

$$GVD = \frac{\lambda^3}{2\pi c^2}\left(\frac{d^2n}{d\lambda^2}\right) \tag{2.1}$$

in which λ is wavelength, c is the speed of light, and $(d^2n/d\lambda^2)$ is the second derivative of the index of refraction for the material. The GDD (φ_2) of the material is then the product of the GVD and the distance of material through which the pulse is propagating. Here, that distance is 12 mm. To determine the temporal effect that dispersion will have on a pulse of a certain input duration (Δt_{in}), Δt_{out} can be calculated from the GDD at a specific wavelength:

$$\Delta t_{out} = \frac{\sqrt{\Delta t_{in}^4 + 16(ln2)^2\varphi_2^2}}{\Delta t_{in}} \tag{2.2}$$

The results of this calculation can be found in Fig. 2.4 comparing a pulse that travels through no media, and a pulse traveling through 12 mm of fused silica (i.e. the setup reported here). In general, as the amount of glass increases, the output pulse is lengthened more relative to the input pulse. This effect is especially dominant in pulses <40 fs. In the case of a 20 fs pulse, the output is

broadened to 119 fs, six times the original pulse duration. For the setup used in this work, however, the pulses were on the order of 150 fs, for which almost no broadening is calculated – or experimentally observed. These calculations serve to reinforce the idea that variable-temperature measurements are experimentally challenging on the ultrafast timescale for reasons such as pulse broadening.

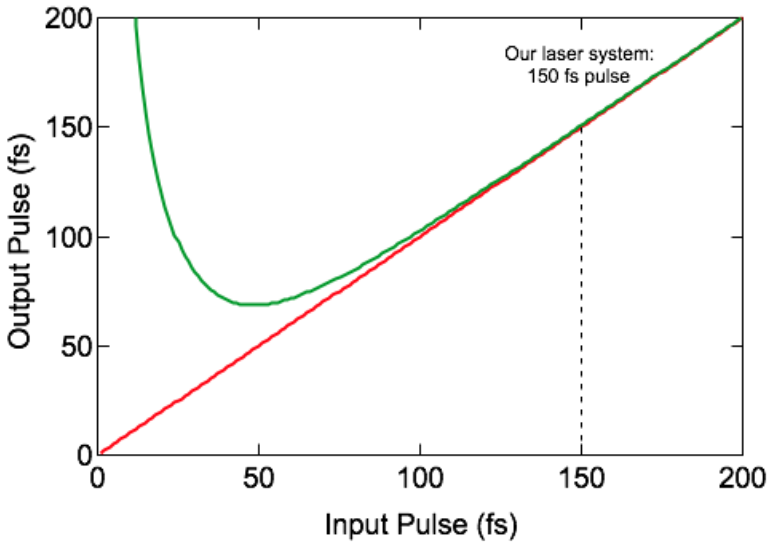

Figure 2.4. Calculated effects of group velocity delay (GVD) or dispersion on an ultrafast laser pulse. The red trace shows an input pulse that does not traverse through media and is therefore equivalent to its output pulse. In green is the calculated duration of a pulse at 490 nm propagating through 12 mm of fused silica. The dashed line denotes 150 fs, which is the pulse duration used in the work reported here.

3.3.2 Water Content of Acetonitrile

Fe(II) polypyridyl complexes are known to show a solvent dependence on ground state recovery rate.[7] Additionally, relative to acetonitrile (228 K), the solvent used in these studies, water

has a significantly higher freezing point at 273 K. The presence of water, then, in the solvent in large enough quantities could serve to affect the observed rates, and therefore all subsequently calculated parameters. To prevent against this, HPLC grade acetonitrile was chosen, and the water content was measured by ^{1}H NMR (Fig. 2.5 and 2.6). For both spectra, acetonitrile is the quintet at 1.96 ppm, and water is the singlet at 2.13 ppm. ^{13}C satellites are observable for the acetonitrile. In the blank spectrum (Fig. 2.5), residual acetone from cleaning the NMR tubes is seen at 2.11 ppm. For the blank, the amount of water by integration is 18% (i.e. the integrated value of water divided by the sum of integrated values). To determine the water content in the HPLC grade acetonitrile, the water peak integration was set to equal 0.24, which is seen in the blank. The amount of water in the solvent, then is <0.4%. This purity is sufficient for the variable-temperature experiments performed, and no adverse effects (e.g. bimodal Arrhenius behavior, unexpected room temperature lifetimes) are observed.

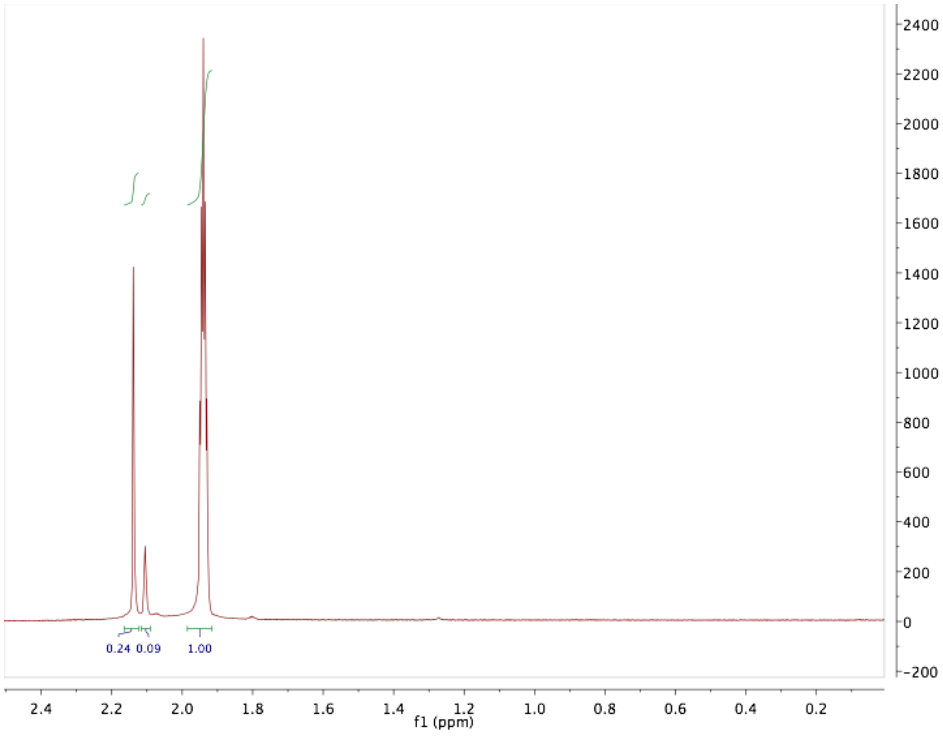

Figure 2.5. ^{1}H NMR of CD_3CN blank. Assignments can be found in the text.

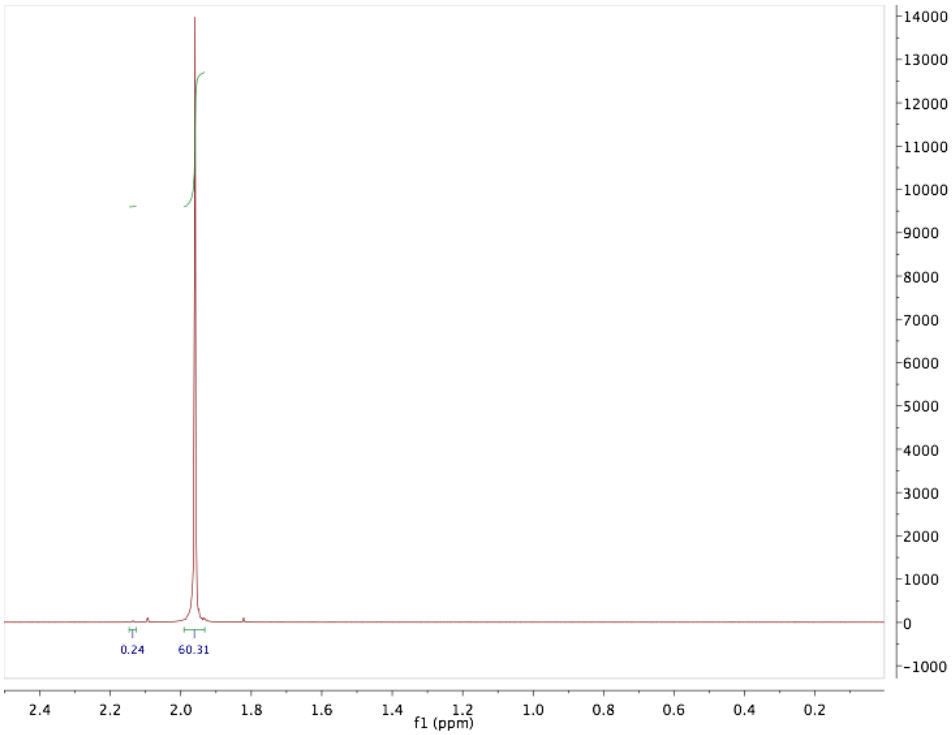

Figure 2.6. ^{1}H NMR spectrum of HPLC-grade acetonitrile in CD_3CN. Assignments can be found in the text.

3.4 Arrhenius and Marcus Parameters of $[Fe(bpy')_3]^{2+}$ Series

The activation energy in the $^5T_2 \rightarrow {}^1A_1$ conversion was measured first in the prototypical $[Fe(bpy)_3]^{2+}$ complex. To do this, the ground state recovery time constant, k_{nr}, was found as a function of temperature (T), as given by the Arrhenius relationship

$$k_{nr} = Ae^{-\frac{E_a}{k_B T}} \tag{2.3}$$

in which A is the preexponential factor, E_a is the activation energy, and k_B is Boltzmann's constant. Only the solution phase lifetimes were of interest, and thus the glass-to-fluid transition was avoided. For all of the complexes reported herein, care was taken to ensure that the same anion (PF_6^-), solvent (acetonitrile), and excitation and probe wavelengths (490 and 530 nm, respectively) were used for each complex. This should minimize any outer-sphere effects and allow for direct

comparison of complex-only, or inner-sphere, dynamics. The freezing point of acetonitrile is 228 K, so 235 K was chosen as the lowest temperature point, and data were collected every 5 K. The data for $[Fe(bpy)_3]^{2+}$ in MeCN are shown in Fig. 2.7 and summarized in Table 2.2. At room temperature, the lifetime of the complex is 1.05 ± 0.02 ns; when cooled to 235 K, the lifetime is 1.52 ± 0.03 ns; a 50% increase that is rather large considering that $[Fe(bpy)_3]^{2+}$ has long been believed to be near barrierless, but within the Marcus normal region.[8] The Arrhenius plot of the VT data (Fig. 2.8) yields an activation energy of 310 ± 15 cm^{-1} and a frequency factor with a value of 230 ± 20 ps^{-1}. For context, this 1.5k_BT barrier causes a 4.5-fold increase in k_{nr}. The activation energy reported here is surprisingly similar to that reported by Hauser et al. considering these measurements are solution-phase, whereas the sample in their measurements was a solid.[10] All of these data place $[Fe(bpy)_3]^{2+}$ firmly in the normal region, but further from barrierless than previously believed.

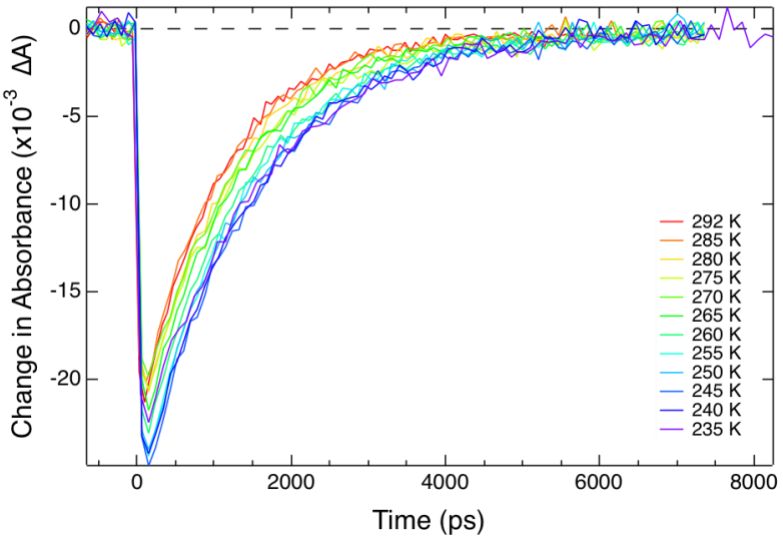

Figure 2.7. Variable-temperature lifetimes of $[Fe(bpy)_3]^{2+}$ upon excitation at 490 nm and probing at 530 nm. At room temperature (red), the lifetime of the complex is 1.05 ± 0.02 ns. This lengthens with decreasing temperature to 235 K (purple), at which point the lifetime is 1.52 ± 0.03 ns.

Table 2.2. Summary of the lifetime of the complexes at room temperature and 235 K, and the Arrhenius values found from the variable-temperature experiments.

Complex	Lifetime at 292 K (ns)	Lifetime at 235 K (ns)	A (ps^{-1})	E_a (cm^{-1})
$[Fe(bpy)_3](PF_6)_2$	1.05 ± 0.02	1.52 ± 0.03	230 ± 20	310 ± 15
$[Fe(dmb)_3](PF_6)_2$	1.32 ± 0.02	2.01 ± 0.04	240 ± 20	345 ± 10
$[Fe(dtbb)_3](PF_6)_2$	1.07 ± 0.01	1.56 ± 0.02	230 ± 15	315 ± 15
$[Fe(terpy)_3](PF_6)_2$	5.2 ± 0.1	12.6 ± 1.7	150 ± 55	755 ± 70

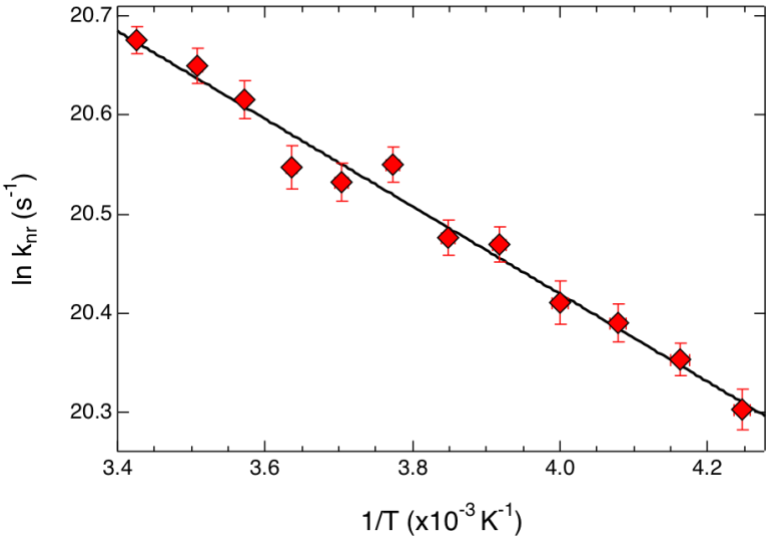

Figure 2.8. Arrhenius plot for $[Fe(bpy)_3]^{2+}$ showing average $\ln(k_{nr})$ as a function of inverse temperature from variable-temperature lifetimes. The data fit very well ($R^2 = 0.98$) to a single mode, for which the barrierless rate is 230 ± 20 ps^{-1}, and the activation energy is 310 ± 15 cm^{-1}.

Two other 4,4'-di-substituted complexes in the $[Fe(bpy')_3]^{2+}$ family were studied, the dimethyl- (dmb) and di-*tert*-butyl- (dtbb) derivatives. The methyl group is slightly more electron donating into the bipyridine backbone, with the ^{t}butyl being the much more sterically bulky

substituent. These electronic and steric effects may change the activation energy for these complexes with respect to the parent compound, $[Fe(bpy)_3]^{2+}$. In the case of $[Fe(dmb)_3]^{2+}$, the room temperature ground state recovery lifetime is lengthened to 1.32 ± 0.02 ns in acetonitrile. Interestingly, the lifetime of $[Fe(dtbb)_3]^{2+}$ in acetonitrile is much more analogous to $[Fe(bpy)_3]^{2+}$, being 1.07 ± 0.01 ns at room temperature. It is not unexpected for the lifetime of $[Fe(dtbb)_3]^{2+}$ to be so similar to that of $[Fe(bpy)_3]^{2+}$ due to the fact that the ^{t}butyl group is not an especially good electron donor. The effect of the substituent is negligible on the lifetime with respect to both electronic and steric factors. In contrast, however, the methyl group is a very good electron donor, and as such, the lifetime of $[Fe(dmb)_3]^{2+}$ is longer by 300 ps. By electron donating ability alone, ligand field strength should decrease across the series $[Fe(bpy)_3]^{2+} > [Fe(dtbb)_3]^{2+} > [Fe(dmb)_3]^{2+}$. Decreased driving force coinciding with a decrease in k_{nr}, as is seen for $[Fe(dmb)_3]^{2+}$, confirms that the transition is occurring in the Marcus normal region.

In the variable temperature data for the substituted-bpy complexes (Fig. 2.9 and 2.10), the lifetime at 235 K for $[Fe(dmb)_3]^{2+}$ is 2.01 ± 0.04 ns, the same 1.5-fold increase from room temperature. Analogous results are seen in $[Fe(dtbb)_3]^{2+}$, for which ground state recovery is 1.56 ± 0.02 ns at 235 K. In each of these cases, the Arrhenius parameters were solved for, and activation energies for $[Fe(dmb)_3]^{2+}$ and $[Fe(dtbb)_3]^{2+}$ were found (Fig. 2.11 and 2.12). More importantly, the preexponential factors for the complexes are identical for the whole family of Fe(II) bpy-based complexes. The frequency factor corresponds to the nonradiative rate in the absence of a barrier. The fact that this value is constant for the entire family, despite changes in E_a for different complexes, is highly intriguing and will be explored further.

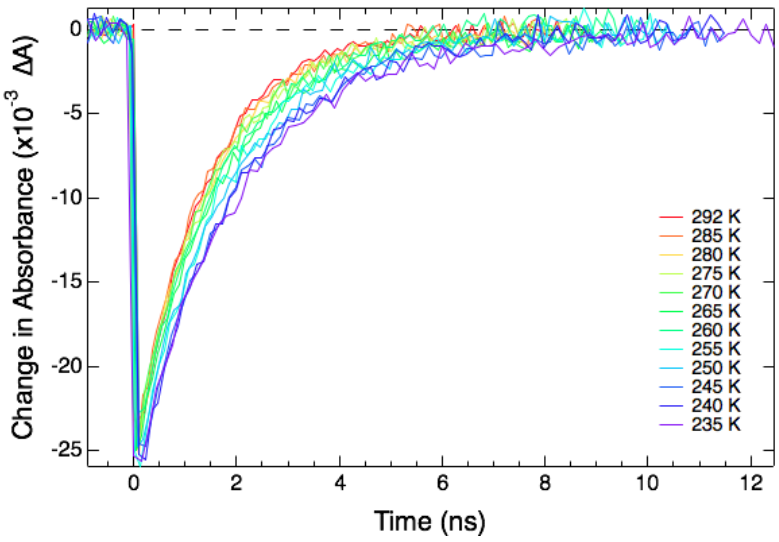

Figure 2.9. Ground state recovery lifetimes of $[Fe(dmb)_3]^{2+}$ as a function of temperature. Excitation was performed at 490 nm, and the probe was 530 nm.

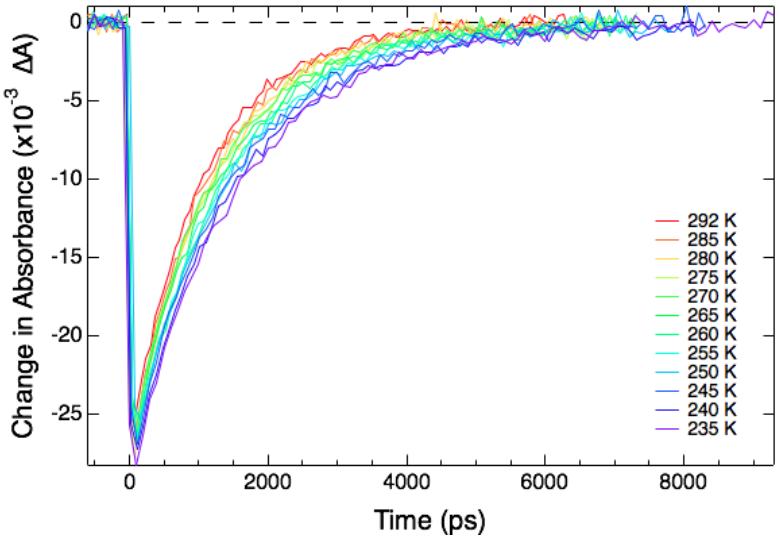

Figure 2.10. Ground state recovery lifetimes of $[Fe(dtbb)_3]^{2+}$ as a function of temperature. Excitation was performed at 490 nm, and the probe was 530 nm.

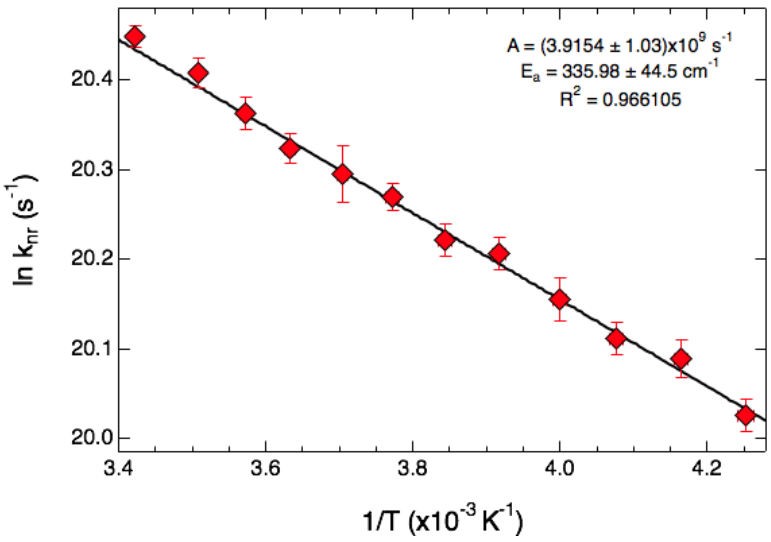

Figure 2.11. Arrhenius plot of the averaged $[Fe(dmb)_3]^{2+}$ variable-temperature data. The preexponential factor, A, was found to be 240 ± 20 ps^{-1}, with the activation energy being 345 ± 10 cm^{-1}. The data fit well (R^2 = 0.97) to a single mode.

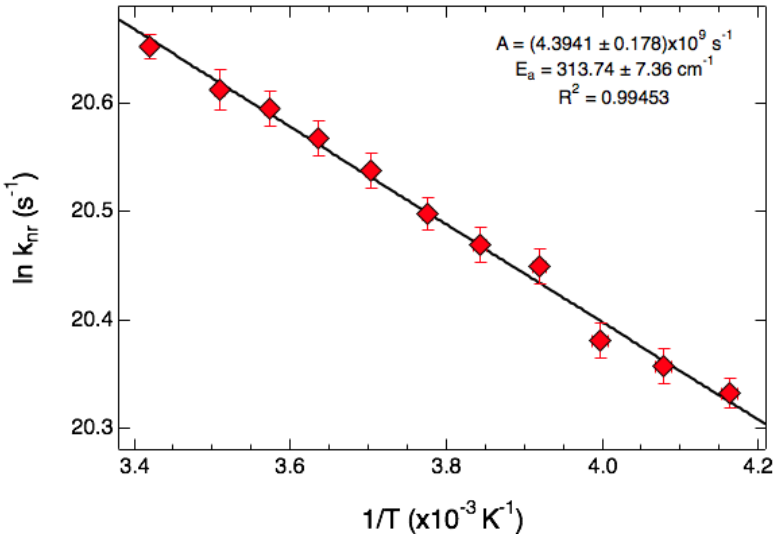

Figure 2.12. Arrhenius plot of the averaged $[Fe(dtbb)_3]^{2+}$ variable-temperature data. The preexponential factor, A, was found to be 230 ± 15 ps^{-1}, with the activation energy being 315 ± 15 cm^{-1}. The data fit well (R^2 = 0.99) to a single mode.

The goal of this work was to determine the reorganization energy associated with the ground state recovery process of these Fe(II) complexes. To this end, a relationship can be derived between the Arrhenius activation energy (E_a) and the Marcus reorganization energy (λ), in which $\Delta G°$ is the driving force:

$$E_a = \frac{(\lambda+\Delta G°)^2}{4\lambda} \tag{2.4}$$

This is possible because the semi-classical Marcus equation[32,33] was derived from the Arrhenius relationship, such that

$$k_{nr} = \frac{2\pi}{\hbar}|H_{ab}|^2 \frac{1}{\sqrt{4\pi\lambda k_B T}} e^{-\frac{(\lambda+\Delta G°)^2}{4\lambda k_B T}} \tag{2.5}$$

Here, there is the additional variable of H_{ab}, the electronic coupling constant, or the extent to which two electronic states communicate with each other. Previously, Sutin estimated values of $\Delta G°$, λ, and H_{ab} for the $^5T_2 \rightarrow {}^1A_1$ transition in $[Fe(bpy)_3]^{2+}$.[8] The problem arises in attempting to unambiguously solve for these three unknowns given only two pieces of data (i.e. k_{nr} and T). To approximate one of these unknowns, the driving force of the other complexes will be calculated from the electrochemical data:

$$\Delta G°_{complex} = \Delta G°_{[Fe(bpy)_3]^{2+}} + \left(E^{ox}_{complex} - E^{ox}_{[Fe(bpy)_3]^{2+}}\right) \tag{2.6}$$

Here, we are assuming an initial driving force ($\Delta G°_{[Fe(bpy)_3]^{2+}}$) and using the Fe(II/III) oxidation couple for $[Fe(bpy)_3]^{2+}$ as a reference. The difference between $E^{ox}_{[Fe(bpy)_3]^{2+}}$ and $E^{ox}_{complex}$ is then taken from the assumed $\Delta G°$ value, giving an approximate zero-point energy difference for the complex of interest.

The value of $\Delta G°$ remains a critical, yet elusive, component in analyzing these data. Although we are able to glean relative comparisons between the complexes, the use of eqn. (2.6) is likely not a good indicator of the actual value of $\Delta G°$. The oxidation potential for the Fe(II/III)

couple speaks to the energy required to remove an electron from the t_{2g} set of orbitals on the metal center. It does not, however, give any indication of the energy of the e_g* orbitals relative to the t_{2g}, and therefore contains only half of the information required to estimate the zero-point energy difference between the $^1A_1$ and $^5T_2$ electronic states. Furthermore, electrochemical potentials are one-electron processes, which is very much not the situation in the $^1A_1 \rightleftharpoons {}^5T_2$ transition, formally $(t_{2g})^6(e_g^*)^0 \rightleftharpoons (t_{2g})^4(e_g^*)^2$. That being said, the initial assumption of a value of -7300 cm^{-1} (as originally cited by Sutin[8]) for $[Fe(bpy)_3]^{2+}$ is necessary to determine values for the other unknown parameters, H_{ab} and λ. It also falls well within the range of values postulated over the years, which then inform the error bars for these calculations. Specifically, a range of approximately 2000-9000 cm^{-1} has been theorized,[8,10,17,18] so H_{ab} and λ are found for a ΔG^o of ± 10%, the error of which is arbitrary but is approximately one standard deviation over the range of values. The error we assume here reflects the degree of uncertainty surrounding ΔG^o but is not so large as to artificially broaden the error bars on all values solved for and thus falsely equating the different complexes.

The first set of Marcus parameters determined are those of $[Fe(bpy)_3]^{2+}$. From eqn. (2.4), E_a = 310 ± 15 cm^{-1}, and the assumption of ΔG^o = -7300 ± 730 cm^{-1}, λ is then found to be 11000 ± 1000 cm^{-1}. This reorganization energy value is nearly twice what Sutin originally estimated, which was approximately 4800 cm^{-1}.[8] Due to the parabolic nature of the Marcus curve, two values for reorganization energy can be obtained. If, however, $[Fe(bpy)_3]^{2+}$ is in the normal region as Sutin postulates, then $\Delta G^o > -\lambda$,[32,33] and the λ reported here is reasonable. It should be noted that although Sutin cites a 4800 cm^{-1} value for reorganization energy, this could only be true if the ground state recovery process occurred in the inverted region. From ΔG^o and the parabolas Sutin is solving for, the other λ value must be for the normal part of the Marcus curve, and corresponds to a value of ~11000 cm^{-1}, which is in excellent agreement with our experimentally determined reorganization

energy. Furthermore, in using the Sutin values for λ and ΔG°, one obtains an activation energy of 325 cm^{-1}. For these reasons, we have very high confidence in the specific ΔG° for $[Fe(bpy)_3]^{2+}$ that we cite here. Using a further relationship between the Arrhenius and Marcus equations in eqn. (2.7), H_{ab} is found to be 4.4 ± 0.3 cm^{-1}.

$$A = \frac{2\pi}{\hbar}|H_{ab}|^2 \frac{1}{\sqrt{4\pi\lambda k_B T}} \tag{2.7}$$

The electronic coupling constant found is consistent with what is to be expected of the highly nonadiabatic coupling between two states with ΔS = 2. It is, however, 1-2 orders of magnitude smaller than the commonly reported values in the literature.[8,10,17,18] The precision on the value is also tightly constrained due to the fact that it has negative quartic power dependence on the reorganization energy. For example, a change of H_{ab} from 4 to 5 cm^{-1} while holding A constant will cause λ to decrease from 1000 to 20 cm^{-1}. To be clear, we do not believe that we know the value of H_{ab} to the tenth of one wavenumber: experimentally determining the difference even between a 4 versus 5 cm^{-1} electron coupling constant is unrealistic. The fact that the Arrhenius preexponential tracks to the Marcus H_{ab} and λ terms as H_{ab}^4/λ necessarily dictates that in these complexes, small perturbations on H_{ab} will have huge consequences for the values of both A and λ. For the purposes of this analysis, it is critical that this ratio can be found from an experimentally determined parameter, A, and not from the assumed value of ΔG°. The H_{ab}^4/λ ratio, then, is not only incredibly sensitive, but it has a very high degree of confidence. As a consequence of A, it may also be highly indicative of the nature of the excited states and the relaxation pathway of the complex at hand. In the case of $[Fe(bpy)_3]^{2+}$, this ratio is 1/(30 ± 5).

In order to determine the significance of all these Marcus parameters of $[Fe(bpy)_3]^{2+}$, the same analysis is performed on the family of complexes. A summary of these values can be found in Table 2.3. For $[Fe(dmb)_3]^{2+}$, these values are clearly very similar to those of $[Fe(bpy)_3]^{2+}$. In

moving to $[Fe(dtbb)_3]^{2+}$, however, the parameters are slightly modified, but still within error of the other bpy-based complexes. Unsurprisingly then, the H_{ab}^4/λ ratio is relatively constant across this family; specifically, ratios of $1/(33 \pm 4)$ and $1/(29 \pm 4)$ are found for $[Fe(dmb)_3]^{2+}$ and $[Fe(dtbb)_3]^{2+}$, respectively.

Table 2.3. Electrochemical potentials for the Fe(II/III) oxidation and the corresponding Marcus parameters of the four complexes.

Complex	ΔE^{ox} (V)[a]	ΔG^o (cm^{-1})	λ (cm^{-1})	H_{ab} (cm^{-1})	H_{ab}^4/λ
$[Fe(bpy)_3](PF_6)_2$	0.68	-7300 ± 730	11000 ± 1000	4.4 ± 0.2	$1/(30 \pm 5)$
$[Fe(dmb)_3](PF_6)_2$	0.52	-6000 ± 600	9700 ± 900	4.2 ± 0.1	$1/(33 \pm 4)$
$[Fe(dtbb)_3](PF_6)_2$	0.53	-6100 ± 610	9500 ± 900	4.3 ± 0.2	$1/(29 \pm 4)$
$[Fe(terpy)_3](PF_6)_2$	0.72	-7600 ± 760	14100 ± 1200	6.2 ± 1.2	$1/(14 \pm 9)$

a Oxidation potentials vs. Fc/Fc^+ in 0.1 M $TBAPF_6$ in MeCN with a Ag reference electrode.

Despite the differences in activation energies and driving forces between these three complexes, A is unchanged between them. The consequently nearly constant H_{ab}^4/λ ratio derived from A lead to the postulation that this ratio is in fact a measure of the relaxation pathway for the $^5T_2 \rightarrow {}^1A_1$ transition. The reorganization energy of the transition can be related to the nuclear coordinate of interest, and the electronic coupling constant describes the nature of the transition (e.g., nonradiative), so a ratio of these two parameters as a function of the barrierless rate could be construed to form a mathematical representation of the major vibrational mode(s) active for the electronic transition. Though these Fe(II) complexes have various electronic and steric differences, the major mode of relaxation is believed to be along the Fe-N bond lengthening coordinate. This largely stems from ultrafast X-ray data showing the 10% increase in bond length from 1.96 Å to

2.16 Å from the singlet to quintet state, respectively.[34] Recently, however, Ashley and Jakubikova have performed DFT and complete active space self-consistent field (CASSCF) calculations on $[Fe(bpy)_3]^{2+}$ and suggested that torsional motion could play a critical role in all intersystem crossing events, but particularly in the ligand field states which are longer-lived relative to the MLCT excited states.[35] They observe that the spin state of the complex is highly correlated to the symmetry of the transition state, which is attributed to the bond-lengthening that occurs concomitantly with twisting into a trigonal prismatic geometry. The Ray-Dutt twist (with C_{2v} geometry) is found to be significantly lower in energy than the classic Bailar (D_{3h} symmetry), as well as a new intermediate geometry termed the "dancing Bailar," which shifts the ligands slightly away from the Fe(II) center and is D_{3h} symmetry. It is therefore presumed that $^5T_2 \rightarrow {}^3T \rightarrow {}^1A_1$ ground state recovery is facilitated by a Ray-Dutt twist due to this being the only intermediate energetically viable. The researchers conclude by saying that full multidimensional potential energy surfaces must be calculated in order to know the transition state with any certainty; this work will have the added benefit of helping to determine the structural changes (and therefore spin states) accessed by $[Fe(bpy)_3]^{2+}$ upon MLCT deactivation. Ashley and Jakubikova implied that the 6,6'-positions were the most likely to influence the transition state by steric hindrance. Thus, these trigonal prismatic torsions are expected to be available to all members of the $[Fe(bpy')_3]^{2+}$ series of complexes as they are all substituted at the 4,4'-positions and neither sterics nor electronics should greatly affect the active nuclear motion for ground state recovery. Likewise, if H_{ab}^4/λ is unchanged in this family, then it is reasonable that the relaxation pathway is also consistent.

3.4.1 Effect of Diethyl Ether in Lattice on Lifetime of Complexes.

As previously mentioned, solvent can play a huge role in the lifetimes of Fe(II) polypyridyl complexes. The authors were concerned with the presence of diethyl ether in the ^1H NMR spectrum

of $[Fe(dmb)_3]^{2+}$. On its face, this is hardly unusual as recrystallizations of these complexes are performed by diethyl ether diffusions into acetonitrile solutions.[13,15] Diethyl ether has also been observed in the crystal structures of some of the compounds, indicating its presence in the lattice.[13] However, by ^1H NMR, diethyl ether existed in a 1:2 mol ratio to $[Fe(dmb)_3]^{2+}$. As a solvent, its bulk properties are incredibly different from acetonitrile, which could be cause for concern. For example, the dielectric constant of acetonitrile is 36.64, but is 4.27 in the case of diethyl ether.[36] Because the nature of the outer-sphere reorganization energy is unknown, the effect that the presence of ether will have on $^5T_2 \rightarrow {}^1A_1$ transition is also uncertain. To ensure that the variable-temperature results for $[Fe(dmb)_3]^{2+}$ were unchanged by the diethyl ether, a sample of $[Fe(bpy)_3](PF_6)_2$ was doped with excess diethyl ether (125 mol equiv.). The lifetime at room temperature was found to be 1030 ± 20 ps, which is identical to the undoped sample. However, there was the possibility that the ether could somehow affect the energetics of one electronic state more than the other, thereby changing the activation energy (E_a). Variable-temperature measurements were then made, and E_a was found to be 310 ± 15 cm^{-1} (Fig. 2.13 and 2.14). Due to the similarity in nature of $[Fe(bpy)_3]^{2+}$ and $[Fe(dmb)_3]^{2+}$, it can definitively be concluded that at this concentration, the diethyl ether does not significantly affect either the room temperature lifetime, or the Arrhenius parameters for these Fe(II) complexes.

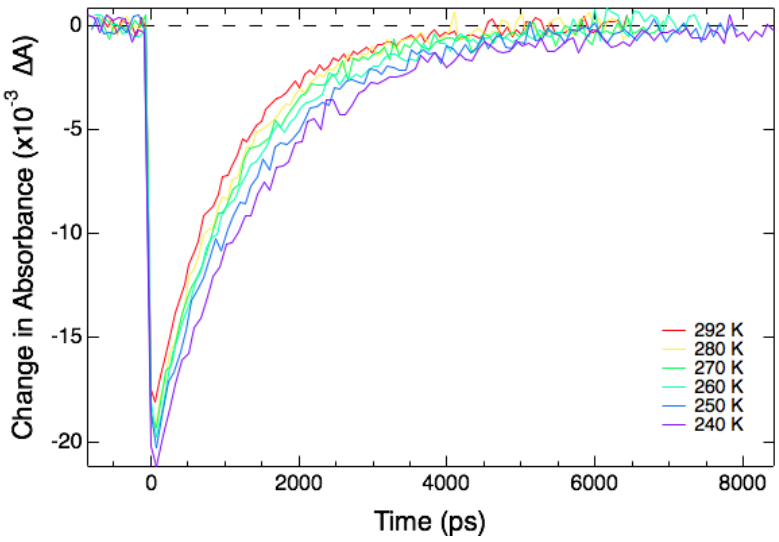

Figure 2.13. Ground state recovery lifetimes of $[Fe(bpy)_3]^{2+}$ doped with 125 mol equiv. of diethyl ether, as a function of temperature. Excitation was performed at 490 nm, and the probe was 530 nm. Lifetimes at the various temperatures are within error of those reported for the sample without diethyl ether.

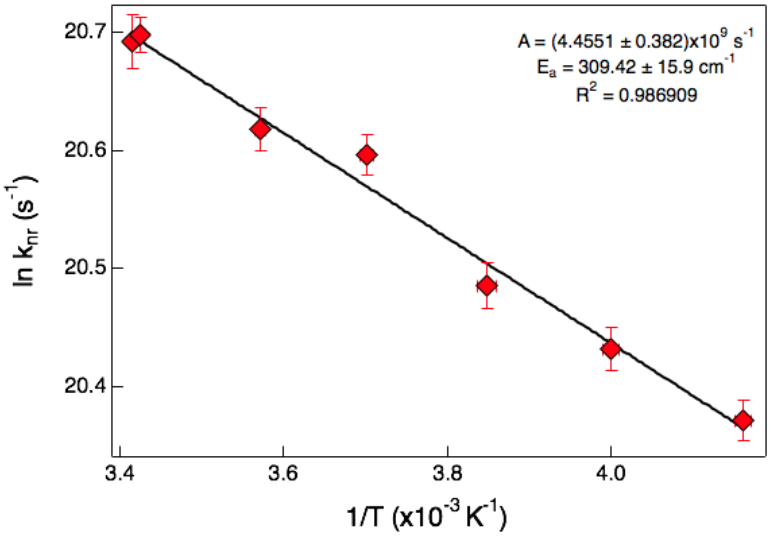

Figure 2.14. Arrhenius plot of the averaged variable-temperature data of $[Fe(bpy)_3]^{2+}$ doped with 125 mol equiv. of diethyl ether. The preexponential factor, A, was found to be 225 ± 20 ps^{-1}, with the activation energy being 310 ± 15 cm^{-1}. These values are in excellent agreement with the Arrhenius factors found for the undoped $[Fe(bpy)_3]^{2+}$ sample. The data fit well (R^2 = 0.99) to a single mode.

3.5 Arrhenius and Marcus Parameters of $[Fe(terpy)_2]^{2+}$

To test this hypothesis, the same analysis is performed for $[Fe(terpy)_2]^{2+}$, which has been postulated to be in the normal region, and further from barrierless than $[Fe(bpy)_3]^{2+}$ due to its longer ground state recovery lifetime. Moreover, although $[Fe(terpy)_2]^{2+}$ sees an analogous bond lengthening from the $^1A_1$ to the $^5T_2$ state, it has been demonstrated by combined time-resolved X-ray techniques and theoretical work that the ground state relaxation of $[Fe(terpy)_2]^{2+}$ is not well-described by a single nuclear coordinate.[37] Additionally, recent calculations from Nance et al. identify the terpy rocking motion to be an important vibrational mode in this relaxation pathway.[38] To remain consistent in our study between the complexes, the same pump (490 nm) and probe (530 nm) wavelengths were used, despite the red-shifted MLCT maximum for $[Fe(terpy)_2]^{2+}$

relative to the bpy' series (Fig. 2.1). For comparison, ground state recovery lifetimes as a function of temperature were collected with redder wavelengths and all results were consistent with those at the pump-probe energies used here, as is expected for ground state recovery. In looking at the variable temperature measurements, a much more noticeable change in rate of ground state recovery is observed in the TA data as the temperature changes (Fig. 2.15). As seen in Table 2.2, the lifetime of $[Fe(terpy)_2]^{2+}$ in MeCN at 235 K is 12.6 ± 1.7 ns, a nearly than 2.5-fold lengthening from the 5.2 ± 0.1 ns lifetime at room temperature. This dramatic increase in room temperature lifetime and lengthening at colder temperatures lends credence to the belief that $[Fe(terpy)_2]^{2+}$ is further normal of the barrierless region than $[Fe(bpy)_3]^{2+}$. The Arrhenius plot (Fig. 2.16) confirms this, showing the E_a for $[Fe(terpy)_2]^{2+}$ is 755 ± 70 cm^{-1}, more than twice that of $[Fe(bpy)_3]^{2+}$ (Fig. 2.17 and 2.18). Likewise, the preexponential factor is approximately 150 ± 55 ps^{-1}. The disparity between the barrierless rate and k_{nr} is greater than a factor of 30. Two points of interest arise here: the faster barrierless rate and greater absolute value of ΔG^o for $[Fe(terpy)_2]^{2+}$ relative to any member of the $[Fe(bpy')_3]^{2+}$ family. These data tend to imply that terpy in fact has a stronger ligand field strength than bpy'. The implications of this are discussed further in Chapter 2 Section 3.5.1.

With the Arrhenius parameters in hand, and ΔG^o = -7700 ± 770 cm^{-1},[15] it can then be determined that the reorganization energy is 14300 ± 1200 cm^{-1}. This is significantly more energy required in the ground state recovery process than with the bpy' family of complexes. Likewise, H_{ab} is increased to 6.2 ± 1.2 cm^{-1}, indicating a greater extent of coupling between the ground and excited electronic states, but still very clearly nonadiabatic as the magnitude remains less than 10 cm^{-1}.

As mentioned before, care was taken to measure as nearly as possible only the inner-sphere components. That may not be entirely true, and efforts to parse out the outer-sphere parameters for

these complexes are expanded on in Chapter 3 of this work.[7] To a first approximation, however, we take all values here as being intrinsic to the Fe(II) complex at hand. That being said, the H_{ab}^4/λ ratio for $[Fe(terpy)_2]^{2+}$ is greatly reduced relative to the $[Fe(bpy')_3]^{2+}$ series and is $1/(14 \pm 9)$. Any change in this ratio we believe implies a change in the nature of the relaxation pathway from the $^5T_2$ to the $^1A_1$ state. The values found in this study then serve to reinforce the experimental[37] and theoretical[38] findings that imply that the major modes of the $^5T_2 \rightarrow {}^1A_1$ transition in $[Fe(bpy')_3]^{2+}$-based complexes and $[Fe(terpy)_2]^{2+}$ lie along very separate coordinates. Future studies should include variable-temperature measurements of other Fe(II) polypyridyl families in order to begin to determine how generalizable these results are. For example, will $[Fe(phen)_3]^{2+}$-type complexes relax along the Fe-N bond lengthening coordinate, or another coordinate altogether? To this end, collaboration with theory helps to give a physical origin to the otherwise inconclusive H_{ab}^4/λ ratio for these complexes.

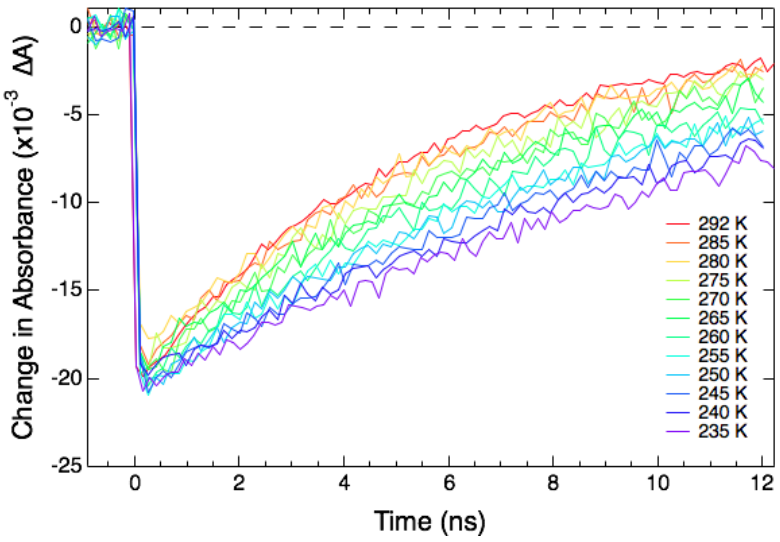

Figure 2.15. Ground state recovery lifetimes of $[Fe(terpy)_3]^{2+}$ as a function of temperature. Excitation was performed at 490 nm, and the probe was 530 nm. Because of the delay stage used in this experiment, at no temperature does the molecule recover the ground state fully (i.e. the signal returns to zero). This effect is only worsened at cold temperatures, to such an extent that the signal appears to be linear. These issues give rise to the increase in uncertainty on the lifetimes and subsequently calculated values.

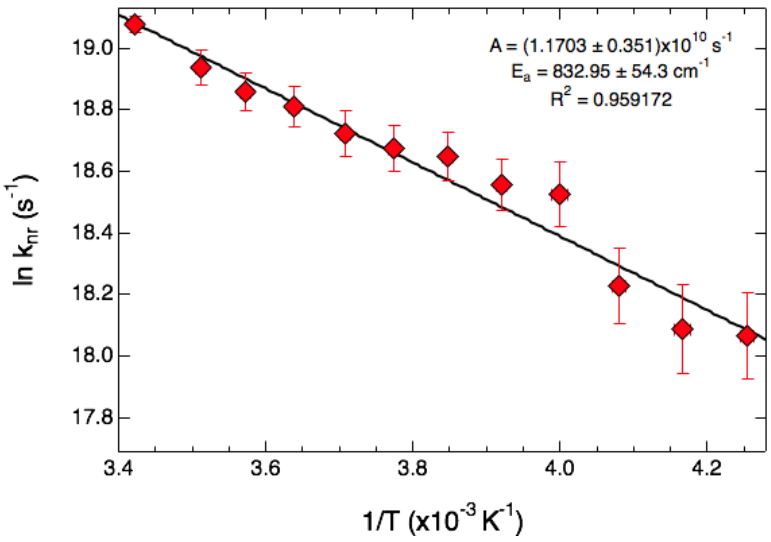

Figure 2.16. Arrhenius plot of the averaged $[Fe(terpy)_2]^{2+}$ variable-temperature data. The preexponential factor, A, was found to be 150 ± 55 ps^{-1}, with the activation energy being 755 ± 70 cm^{-1}. The data fit well (R^2 = 0.96) to a single mode.

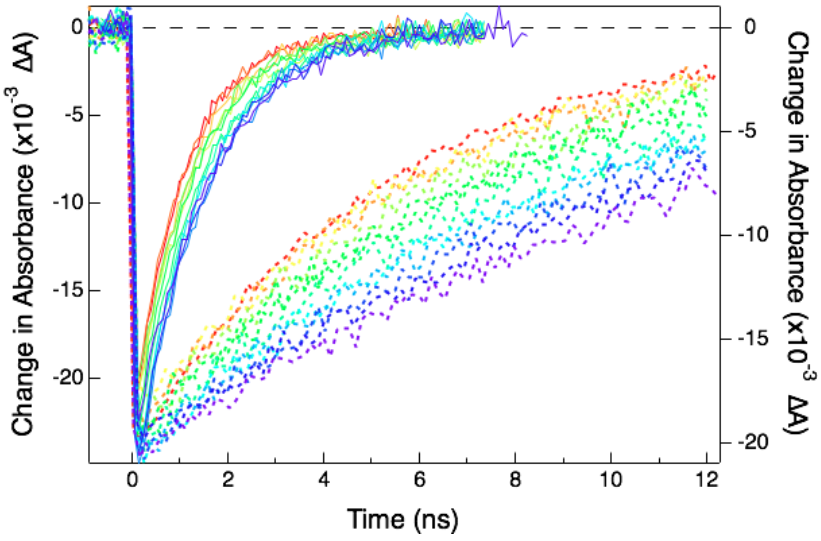

Figure 2.17. Overlay of the variable-temperature ultrafast transient absorption spectra for $[Fe(bpy)_3]^{2+}$ (—) and $[Fe(terpy)_2]^{2+}$ (--). The traces indicate the temperature of the sample, red being 292 K to purple being 235 K. The left axis shows the scale for the $[Fe(bpy)_3]^{2+}$, whereas $[Fe(terpy)_2]^{2+}$ is plotted against the right axis.

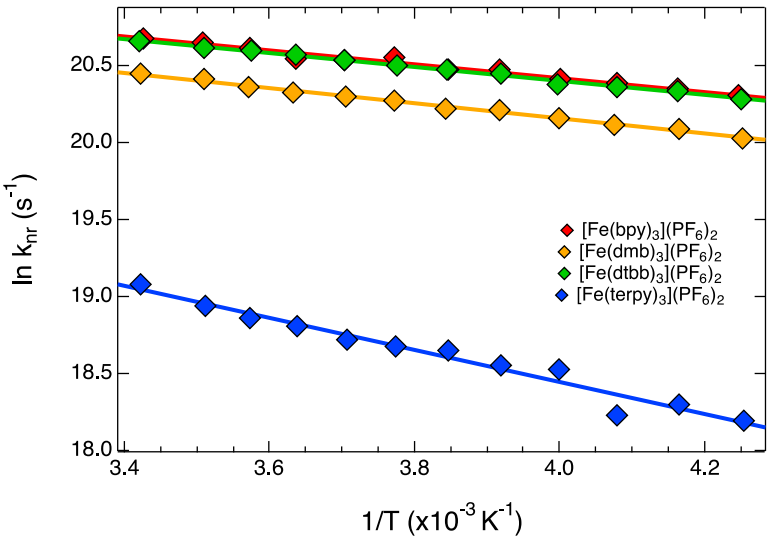

Figure 2.18. Comparison of the Arrhenius plots for the four complexes. The data are displayed as diamonds, and the straight line is the fit of the data: $[Fe(bpy)_3]^{2+}$ in red, $[Fe(dmb)_3]^{2+}$ in orange, $[Fe(dtbb)_3]^{2+}$ in green, and $[Fe(terpy)_2]^{2+}$ in blue.

3.5.1 The Ligand Field Strength of $[Fe(terpy)_2]^{2+}$

The common wisdom among chemists who study polypyridyl complexes has long been that terpy has a lower ligand field strength than bpy. This is supported, in part, by the increased lifetime of $[Fe(terpy)_2]^{2+}$ relative to $[Fe(bpy)_3]^{2+}$. With decreased ΔG^o, the $^1A_1$ and $^5T_2$ potential energy surfaces become more degenerate, thereby increasing the activation barrier between them. This increase in k_{nr} is most commonly studied in spin-crossover complexes, which can live for tens to hundreds of nanoseconds due to ΔG^o values on the order of 200 cm^{-1}. Further evidence for the reduced ligand field strength of terpy compared to bpy comes in the form of the Ru(II) analogues. $[Ru(terpy)_2]^{2+}$ has been shown to have a drastically reduced lifetime (~250 ps),[39] relative to the μs lifetime of $[Ru(bpy)_3]^{2+}$.[40,41] Although the trend is opposite what is observed in the Fe(II) complexes, the phenomenon is described by the same origin. The supposed lower ligand field strength of terpy brings the ligand field states to be isoenergetic with the MLCT manifold in

$[Ru(terpy)_2]^{2+}$, thereby providing an alternate route for ground state recovery.

In direct contrast to this hypothesis, however, is the electrochemical and absorption data. A series of Co(III) analogues were prepared by J. T. Yarranton.[42] The benefit of Co(III) is that the MLCT excited states are much higher in energy, making LF transitions more readily observable. For example, the $^1A_1 \rightarrow {}^3T_1$ in $[Co(bpy)_3](PF_6)_2$ is found at ca. 13800 cm^{-1}. In the case of $[Fe(terpy)_2]^{2+}$, it is found to be 15500 cm^{-1}, thus demonstrating that, in the case of Co(III), terpy has a stronger ligand field than bpy. This is not unexpected given that terpy contains three basic N-donors to the two on bpy. The inherent limitations in the use of electrochemical data to determine ligand field strength has already been expanded on (see Chapter 2 Section 3.4). That being said, the oxidation potentials of $[Fe(bpy)_3]^{2+}$ and $[Fe(terpy)_2]^{2+}$ appear to give corroborating evidence to this trend, although it is possible and even likely that those potentials only reflect a 300 cm^{-1} shift in the t_{2g} set of orbitals in $[Fe(terpy)_2]^{2+}$ relative to $[Fe(bpy)_3]^{2+}$.

Based on Marcus theory, then, if the ΔG^o for $[Fe(terpy)_2]^{2+}$ > $[Fe(bpy)_3]^{2+}$ and ground state recovery for $[Fe(bpy)_3]^{2+}$ occurs in the Marcus normal region, the only way the lifetime of $[Fe(terpy)_2]^{2+}$ can be longer than that of $[Fe(bpy)_3]^{2+}$ is if the $^5T_2 \rightarrow {}^1A_1$ conversion is an inverted process. Unless, that is, ground state recovery in these two complexes are on two separate Marcus curves. This would be determined by a change in reorganization energy, which the data herein reflect. A marked difference in the H_{ab}^4/λ ratio we believe denotes relaxation along a different nuclear coordinate in $[Fe(terpy)_2]^{2+}$ than in $[Fe(bpy)_3]^{2+}$ (or any member of its family of complexes). It is probable, then, that the ligand field states in $[Fe(terpy)_2]^{2+}$ are further along one nuclear coordinate than they are in $[Fe(bpy)_3]^{2+}$, a fact which would appear in S, the Huang-Rhys factor, the electronic coupling between states, and could thus manifest as a greater activation barrier despite also having a greater ΔG^o. This hypothesis is supported by the crystal structure of

$[Fe(terpy)_2]^{2+}$, wherein the average Fe-N_{ax} bond distance is 1.884(5) Å but is elongated for the Fe-N_{eq} distance to 1.978(5) Å. This nearly 5% increase in bond length shows the asymmetry of the complex, leading to weaker orbital overlap in the equatorial positions. Interestingly, $[Ru(terpy)_2]^{2+}$ shows a similar 4% elongation from the axial to equatorial Fe-N bond distances, 1.985(11) to 2.067(5) Å, respectively.[43] Considering the much greater size and radial distance of the orbitals of Ru(II) compared to Fe(II), the fact that $[Ru(terpy)_2]^{2+}$ experiences just as much asymmetry as $[Fe(terpy)_2]^{2+}$ suggests this is a result of the ligand itself. Decreased orbital overlap with two-thirds of the donor atoms could easily explain the shift in nuclear coordinate, ΔQ.

Force constant analysis was performed on harmonic potential energy surfaces of $[Fe(bpy)_3]^{2+}$ and $[Fe(terpy)_2]^{2+}$ in order to determine the effects, if any, on S. This value is the degree of separation between the minima of potential energy surfaces with respect to a single nuclear coordinate. While more routinely found through spectral analysis of emission profiles,[44] Hauser has previously estimated S in $[Fe(bpy)_3](PF_6)_2$ doped into a $[Zn(bpy)_3](PF_6)_2$ matrix through the use of variable-temperature nanosecond transient absorption spectroscopy.[10] The force constants found here are an order of magnitude greater than those reported (Table 2.4). Using eqn. (2.8), S can be determined as a function of the force constant:

$$S = \frac{1}{2}\left(\frac{f\Delta Q^2}{\hbar\omega}\right) \tag{2.8}$$

in which f is the force constant in dyn/cm, ħω is the vibrational frequency (here taken to be 200-300 cm^{-1}), and $\Delta Q \cong 2.45\Delta r$ (Δr being the change in Fe-N bond distance between the ground and excited states).[10] As Table 2.4 shows, S increases from the solid-state to solution-phase sample of $[Fe(bpy)_3](PF_6)_2$, which may reflect the enhanced freedom allowed in solution versus in a matrix. More importantly, S likewise increases from $[Fe(bpy)_3]^{2+}$ to $[Fe(terpy)_2]^{2+}$. These are very preliminary results that lend credence to the hypothesis that terpy is both a stronger field ligand

than bpy, and forms more distorted complexes, thereby displacing the $^5T_2$ potential energy surface farther along a nuclear coordinate from the $^1A_1$ ground state relative to bpy-based complexes.

Table 2.4. Force constant analysis of $[Fe(bpy)_3]^{2+}$ and $[Fe(terpy)_2]^{2+}$.

Complex	Δr (Å)	ΔQ (Å)	f (10^6 dyn/cm)	S	λ_{exp} (cm^{-1})	λ_{calc} (cm^{-1})
$[Zn_{1-x}Fe_x(bpy)_3](PF_6)_2$[a]	0.204	0.5	0.2	45 ± 5	-	-
$[Fe(bpy)_3](PF_6)_2$	0.197[b]	0.482	1.12	280 ± 55	4800 11000	5500 18400
$[Fe(terpy)_3](PF_6)_2$	0.222[c]	0.544	1.14	355 ± 70	4100 14100	6900 21900

a From ref. 10, for comparison.

b From the crystal structure from ref. 14. The excited state was approximated as a 10% increase in Fe-N distance.

c From ref. 37. The bond distances were taken as an average of two Fe-N_{eq} and one Fe-N_{ax}.

While these results do at first glance appear promising, further inspection shows that with these force constants, the reorganization energy from the $^5T_2$ to the $^1A_1$ surface is not what has been experimentally determined (see Table 2.4 and Fig. 2.19 and 2.20). For this analysis, the force constant was taken to be the same for the both electronic states, and the potential energy surfaces were assumed to be harmonic oscillators. Both of these assumptions were made simply for ease of calculation. Higher level calculations are needed to more precisely discuss the displacement between the LF manifold and the ground state in $[Fe(terpy)_2]^{2+}$ and $[Fe(bpy)_3]^{2+}$. This may yield further insight into the nuclear coordinate(s) responsible for ground state recovery in these complexes.

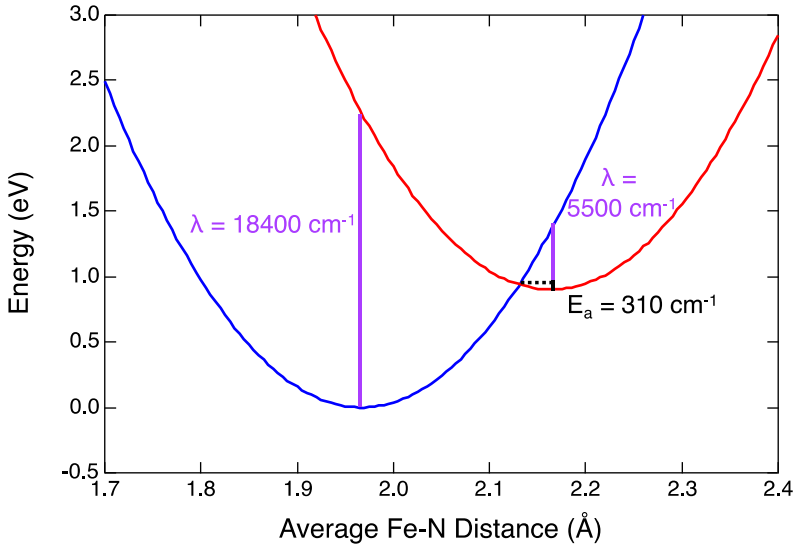

Figure 2.19. Potential energy surfaces calculated from harmonic oscillators for $[Fe(bpy)_3](PF_6)_2$ in MeCN. The blue traces represent the $^1A_1$ ground state, whereas the red curves are the $^5T_2$ excited states. The activation and reorganization energies are given (see text and Table 2.4 for more details).

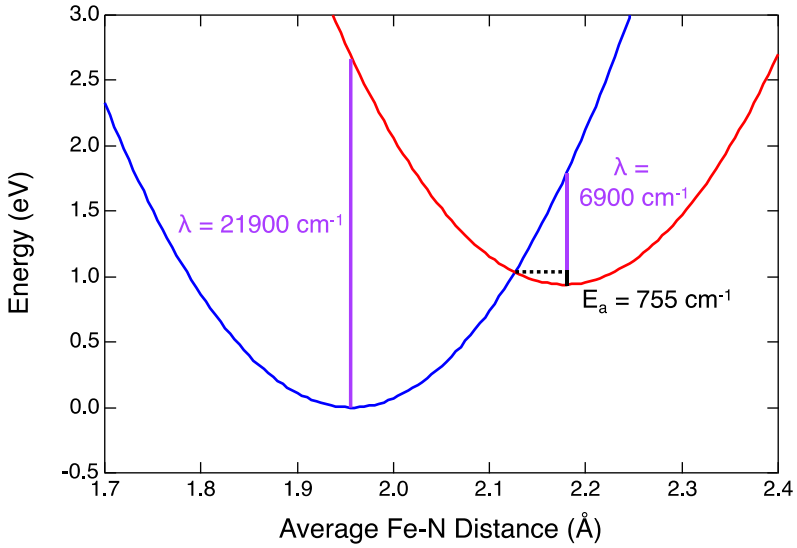

Figure 2.20. Potential energy surfaces calculated from harmonic oscillators for $[Fe(terpy)_2](PF_6)_2$ in MeCN. The blue traces represent the $^1A_1$ ground state, whereas the red curves are the $^5T_2$ excited states. The activation and reorganization energies are given (see text and Table 2.4 for more details).

4. Future Works and Conclusions

In this study, we provide the first direct measurements of Arrhenius parameters of non-spin-crossover Fe(II) polypyridyl complexes. Variable-temperature ultrafast transient absorption spectroscopy was used to study the ground state recovery rates for three $[Fe(bpy')_3]^{2+}$-type complexes and $[Fe(terpy)_2]^{2+}$. Each of the four complexes was found to lie in the Marcus normal region, confirming previous suspicions. From the Arrhenius values, a relationship to semi-classical Marcus theory was drawn in order to determine energetic parameters that have long been unknown. These findings revealed a nearly constant H_{ab}^4/λ ratio for the $[Fe(bpy')_3]^{2+}$ family of approximately 1/30, a value that changed drastically to 1/14 in the case of $[Fe(terpy)_2]^{2+}$. Based on the unchanging nature of this ratio for the bpy-based series, we postulate this ratio to in fact be a mathematical

representation of the major nuclear coordinate accessed for the relaxation in these different types of complexes. In the case of $[Fe(bpy)_3]^{2+}$, it is likely this mode is the Fe-N bond elongation, whereas the terpy ligand rocking mode is more likely to be the predominant relaxation pathway for $[Fe(terpy)_2]^{2+}$.

The single greatest caveat to this work is the estimation of ΔG^o. We attempted to be as forthright as possible as to the potential errors that may arise from the method we used. However, a starting value of the driving force was required such that relative ratios of the Marcus parameters could be determined. In these ratios there is a much greater degree of certainty than in the absolute values of λ and H_{ab}. Unfortunately, the problem of ΔG^o remains prohibitive to unambiguously determining λ and H_{ab}. The $^5T_2 \rightarrow {}^1A_1$ transition is doubly-spin forbidden, non-emissive, ligand field in nature, and a multi-electron event. All of these factors make measuring ΔG^o for this process incredibly elusive. It is possible, then, that an absolute zero-point energy difference for Fe(II) polypyridyl complexes will not be found experimentally.

4.1 $^5T_2$ Excited State Energetics Determined by Photoredox Methods

One method can be proposed at this time to experimentally narrow down the magnitude of ΔG^o for this family of complexes, a summary for which is found in Scheme 2.3. Analogous routes have been previously reported in the photoredox catalysis literature by Meyer[45,46] and others.[47-49] This involves the use of an Fe(II) complex of interest with a lifetime long enough to beat the diffusion limit,[46] such as $[Fe(terpy)_2]^{2+}$, and a series of oxidants of increasing oxidizing strength. Considering the electron configuration of the $^5T_2$ and $^1A_1$ states, the former will be more easily oxidized than the singlet due its doubly occupied e_g^* non-bonding orbitals. Solutions of the iron dye with the various oxidants will be studied time-resolved transient absorption spectroscopy such that $[Fe(terpy)_2]^{2+}$ will be photoexcited then relax to the $^5T_2$ state, allowing for the oxidizing agent

to generate $[Fe^{III}(terpy)_2]^{3+}$. The mild-to-strong oxidant will need to have an oxidation potential less than the Fe(II/III) couple, 0.72 V vs. Fc, leaving many options available.[50] Ideally, it would also be spectroscopically silent in the visible region such that only the dynamics of the chromophore are observed. Spectroelectrochemical data of the complex as both the Fe(II) and the Fe(III) chromophore would aid in the spectral assignments associated with MLCT in the $[Fe^{II}(terpy)_2]^{2+}$ as compared to the ligand-to-metal charge transfer (LMCT) states and any other spectral features corresponding to the $[Fe^{III}(terpy)_2]^{2+}$ compound. Any bands specific to $[Fe^{III}(terpy)_2]^{3+}$ when studying the 2+ species by time-resolved transient absorption spectroscopy will thus be assignable and will make known the fact that the oxidizing agent was capable of removing an electron from the e_g* orbitals in the $^5T_2$ state of the Fe complex. Electrochemistry would give the oxidation potential of the Fe(II/III) couple and the reduction potential of the oxidizing agent. The Fe(II/III) couple, as discussed already, gives a measure of the energy of the t_{2g} orbitals in the $^1A_1$ state. The reduction potential of the oxidant capable of generating Fe(III) from the compound's lowest energy excited state should, likewise, gives an upper limit of the energy of the e_g* orbitals of the $^5T_2$.

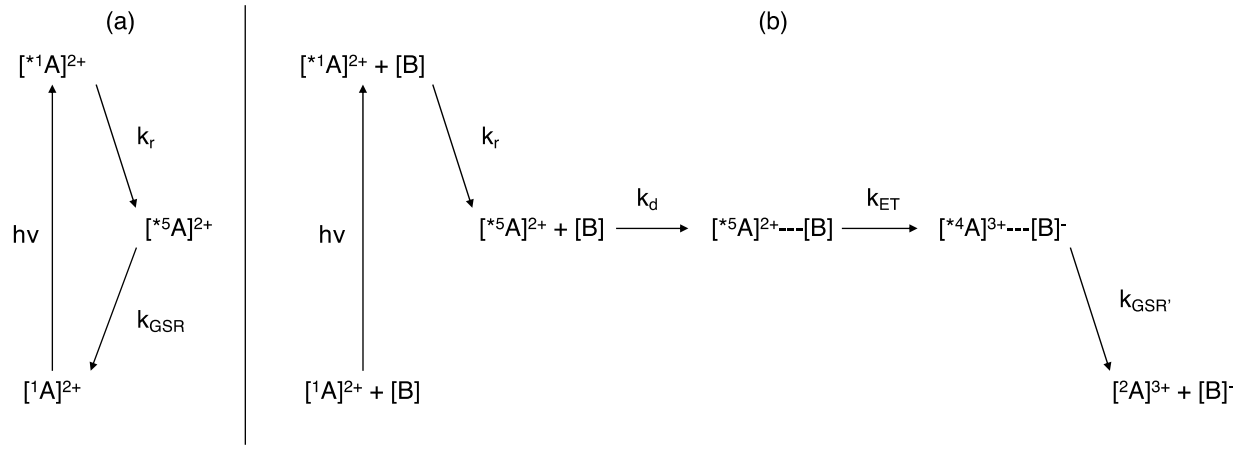

Scheme 2.3. Kinetic scheme for method proposed to determine ΔG^{o} range in Fe(II) complexes. (a) Abridged photophysical cycle for typical Fe(II) polypyridyl, [A]. (b) Expected photochemical reaction for Fe(II) complex excited in the presence of a strong oxidant, [B], thereby undergoing oxidation in the quintet state. In both cases, the $[^{1}A]^{2+}$ state represents the singlet ground state of the Fe(II) complex; k_r is the sum of the relaxation processes from the ^{1}MLCT (here $[*^{1}A]^{2+}$) to the lowest energy excited state, $[*^{5}A]^{2+}$ or $^{5}T_2$; and k_{GSR} is the recovery of the ground state. Diffusion (k_d) brings the product to within such a distance (here $[*^{5}A]^{2+}$---[B]) that electron transfer (k_{ET}) can occur to form the $[*^{4}A]^{3+}$---$[B]^{-}$ product which then relaxes with $k_{GSR'}$ to the respective ground states.

This photochemical process is likely what is occurring in studies of photoredox catalysis systems with Fe(II) compounds.[51] For example, in the α-alkylation of aldehydes, $[Fe(bpy)_3]Br_2$ was used as a photocatalyst with comparable yields to those obtained with $[Ru(bpy)_3]^{2+}$. In the case of the ruthenium catalyst, electron transfer occurs from the MLCT excited state, which is very long-lived. With its metal-centered lowest-energy excited state, though, reduction from $[Fe(bpy)_3]Br_2$ must be occurring from the $^{5}T_2$. In addition to the novel nature of the use of Fe(II) to photocatalyze a reaction, this work serves to provide a smaller range of oxidation potential for

the brominated aldehydes used. Although the method outlined here is yet another estimation of ΔG^{o}, and can only provide a range of values, it is likely to be much more accurate than the use of only Fe(II/III) potentials that has been employed in this work. It will also serve to potentially provide error bars smaller than the 10% that were used here, which will ultimately propagate into the error calculations and reduce uncertainty for all the Marcus parameters of these Fe(II) dyes.

4.2 Direct Quantification of Driving Force by Photoacoustic Spectroscopy

Another promising method for the determination of thermodynamic parameters of Fe(II) polypyridyl complexes is photoacoustic spectroscopy (PAS), though more recently referred to as LIOAS, or laser-induced optoacoustic spectroscopy. This method is an incredibly sensitive probe for nonradiative kinetics and thermodynamics.[52,53] The general concept of LIOAS is simple: a sample is irradiated, some or all of that excess energy is dissipated via heat, the increase in temperature of the sample results in an increase in local pressure that radiates as a wave if the irradiation is pulsed, at which point it is detected by an acoustic sensor, such as a microphone or piezoelectric device. While most notably used with mid-IR lasers on gaseous samples,[53] this technique has been successfully applied to solution-phase transition metal-based chromophores. Fe(II/III) porphyrins,[54,55] hexacyanoferrates,[56] and organoiron(II) carbonyl complexes[60] specifically have been studied by LIOAS and photoacoustic calorimetry (PAC), which monitors sound waves as a function of temperature. From gas law, volume is inversely proportional to the pressure of the system, therefore LIOAS and PAC are uniquely situated to measure any volume change of the complex in solution. Miller and McCusker have identified through DFT and Solid-G calculations that the relatively large volume expansion from the $^{1}A_{1}$ ground state to the $^{5}T_{2}$ excited state in low-spin Fe(II) polypyridyls to be inextricably tied to the solvation energy of the ground state recovery process.[7] Being able to confirm that postulation experimentally, and as a

function of solvent, would be a huge boon to this field.

Previously, PAC has been performed on $[Ru(bpy)_3]^{2+}$ and used $[Fe(bpy)_3]^{2+}$ as a reference.[58] The Ru(II) sample was measured over a range of 5-25 ºC and was found to have two volume changes associated with it: the first being for MLCT←$^1A_1$ excitation, and the second being the MLCT→$^1A_1$ relaxation. These two volumes were found to be equal and opposite, and calculated using eqns. (2.9) and (2.10):

$$\Delta V = \Delta V_{str} + \Delta V_{solv} \tag{2.9}$$

$$\Delta V_{str} = \frac{4}{3}\pi N[(r^*)^3 - (r_0)^3] \tag{2.10}$$

Here, ΔV is the reaction volume and it consists primarily of two components, the inner-sphere or structural volume changes (ΔV_{str}) and the volume change caused by solvent (ΔV_{solv}).[58] In the case of $[Ru(bpy)_3]^{2+}$, solvent effects were assumed to play a negligible role and thus $\Delta V \sim \Delta V_{str}$. The volume change was approximated by a sphere with ground state radius r_0 and excited state radius r^*. N is Avogadro's number. From this work, the complex was observed to contract by ca. 0.01 Å upon excitation, then expand 0.01 Å upon relaxation to the ground state. The enthalpy of reaction for $[Ru(bpy)_3]^{2+}$ was found to be 43.7 kcal·mol^{-1} for the absorption process, and -40.0 kcal·mol^{-1} for relaxation, or an average of approximately 14500 cm^{-1} for each transition. From this same work, the $[Fe(bpy)_3]Cl_2$ compound in water was found to expand by 15.5 cm^3·mol^{-1} at 23 ºC. Using this value and Hupp and Weaver's approximation of 6.8 Å for the radius of the complex,[59] $[Fe(bpy)_3]^{2+}$ the radial expansion is ~0.04 Å. This is a factor of two larger than the Fe-N bond elongation observed from ultrafast X-ray spectroscopy,[34] implying that ΔV_{solv} is not negligible for this class of compounds, thus solvent-dependent PAC measurements are critical and expected to give more insight into the low-spin to high-spin interconversion in Fe(II) polypyridyls.

As to the original question of determining ΔGº through a more direct route, LIOAS and

PAC have an intrinsic downside. While the enthalpic contributions are easily monitored by these methods, the Gibbs free energy equation (i.e., $\Delta G = \Delta H - T\Delta S$) requires the entropy of the system, ΔS, to be known if the free energy is the unknown quantity. Borsarelli and Braslavsky, however, have been able to quantify both the driving force and entropy associated with $[Ru(bpy)_3]^{2+}$ upon photoexcitation.[60] LIOAS measurements were performed of the chloride salt in water, and reaction enthalpy-structural volume change correlations were plotted, giving a line with the form:

$$\Delta H_{str} = \Delta G + X\Delta V_{str} \tag{2.11}$$

The slope here is clearly $T\Delta S_{str}/\Delta V_{str}$ where $T\Delta S$ is found to be 99 ± 30 kJ·mol^{-1}; this would make $\Delta S(293\ K) = 338 \pm 102$ J·K^{-1}. Considering the fact that the structural reorganization for $[Ru(bpy)_3]^{2+}$, in principle, is very small based on the -0.01 Å contraction upon photoexcitation, this 0.3% entropic contribution to the system makes sense in context. It is possible that the charge-separated nature of the MLCT excited state is giving rise to enhanced solute-solvent interactions, thus increasing ΔS for $[Ru(bpy)_3]^{2+}$. Although, ground state recovery in $[Fe(bpy)_3]^{2+}$ is notably solvent-dependent,[7] so it would be interesting to see how the entropy for the iron systems compare relative to their Ru(II) counterparts. It is clear that PAC and LIOAS are potentially very powerful tools in the arsenals of low-spin Fe(II) chemists.

Despite the obstacles imposed by the ambiguity of ΔG^o, the work performed here determined relative ratios of Marcus parameters, which should be able to be used in conjunction with theoretical methods to determine likely modes of relaxation - and the effects of substituents on these modes - in low-spin Fe(II) polypyridyls. The type of experiment described in this study may be equally powerful in studying other transition metal systems, such as Cu(I) photosensitizers, which have shown to have incredibly large reorganization energies due to structural changes upon excitation.[61] Although much work remains to better understand this class of compounds, variable-

temperature ultrafast transient absorption has proven to be an extremely useful tool in the understanding of fundamental photophysical properties of these specific Fe(II) complexes, and promises to provide increasingly important information on future systems.

REFERENCES

REFERENCES

1. Gawelda, S.; Cannizzo, A.; Pham, V.-T.; van Mourik, F.; Bressler, Ch.; Chergui, M. Ultrafast Nonadiabatic Dynamics of $[Fe^{II}(bpy)_3]^{2+}$ in Solution. *J. Am. Chem. Soc.* **2007**, *129*, 8199-8206; DOI: 10.1021.ja070454x.

2. Monat, J. E.; McCusker, J. K. Femtosecond Excited-State Dynamics of an Iron(II) Polypyridyl Solar Cell Sensitizer Model. *J. Am. Chem. Soc.* **2000**, *122*, 4092-4097; DOI: 10.1021.ja992436o.

3. Bergkamp, M. A.; Chang, C.-K.; Netzel, T. L. Quantum Yield Determinations for Sub-Nanosecond-Lived Excited States and Photoproducts. Applications to Inorganic Complexes and Photosynthetic Models. *J. Phys. Chem.* **1983**, *87*, 4441-4446; DOI: 10.1021/j100245a024.

4. Zhang, W.; Alonso-Mori, R.; Bergmann, U.; Bressler, Ch.; Chollet, M.; Galler, A.; Gawełda, W.; Hadt, R. G.; Hartsock, R. W.; Kroll, T.; Kjær, K. S.; Kubiček, K.; Lemke, H. T.; Liang, H. W.; Meyer, D. A.; Nielsen, M. M.; Purser, C.; Robinson, J. S.; Solomon, E. I.; Sun, Z.; Sokaras, D.; van Driel, T. B.; Vankó, G.; Weng, T.-C.; Zhu, D.; Gaffney, K. J. Tracking Excited-State Charge and Spin Dynamics in Iron Coordination Complexes. *Nature* **2014**, *509*, 345-348; DOI: 10.1038/nature13252.

5. Sutin N.; Creutz, C. Light Induced Electron Transfer Reactions of Metal Complexes. *Pure & Appl. Chem.* **1980**, *52*, 2717-2738; DOI: 10.1351/pac198052122717.

6. Kirk, A. D.; Hoggard, P. E.; Porter, G. B.; Rockley, M. G.; Windsor, M. W. Picosecond Flash Photolysis and Spectroscopy: Transition Metal Coordination Compounds. *Chem. Phys. Lett.* **1976**, *37*, 199-203; DOI: 10.1016/0009-2614(76)80198-4.

7. Miller, J. N.; McCusker, J. K. Outer-Sphere Effects on the Excited State Dynamics of Ligand Field States in Fe(II) Polypyridyl Complexes. *Manuscript in preparation.*

8. Sutin, N. Nuclear, Electronic, and Frequency Factors in Electron-Transfer Reactions. *Acc. Chem. Res.* **1982**, *15*, 275-282; DOI: 10.1021/ar00081a002.

9. Hauser, A. Light-Induced Spin Crossover and the High-Spin→Low-Spin Relaxation. *Top. Curr. Chem.* **2004**, *234*, 155-198; DOI: 10.1007/b95416.

10. Hauser, A.; Vef, A.; Adler, P. Intersystem Crossing Dynamics in Fe(II) Coordination Compounds. *J. Chem. Phys.* **1991**, *95*, 8710-8717; DOI: 10.1063/1.461255.

11. Fink, D. W.; Ohnesorge, W. E. Temperature Effects on Charge-Transfer Luminescence Intensity of Some Transition Metal Ion Chelates. *J. Am. Chem. Soc.* **1969**, *91*, 4995-4998; DOI: 10.1021/ja01046a009.

12. Creutz, C.; Chou, M.; Netzel, T. L.; Okumura, M.; Sutin, N. Lifetimes, Spectra, and

Quenching of the Excited States of Polypyridine Complexes of Iron(II), Ruthenium(II) and Osmium(II). *J. Am. Chem. Soc.* **1980**, *102*, 1309-1319; DOI: 10.1021/ja00524a014.

13. England, J.; Scarborough, C. C.; Weyhermüller, T.; Sproules, S.; Wieghardt, K. Electronic Structures of the Electron Transfer Series $[M(bpy)_3]^n$, $[M(tpy)_2]^n$, and $[Fe(^tbpy)_3]^n$ (M = Fe, Ru; *n* = 3+, 2+, 1+, 0, 1-): A Mössbauer Spectroscopic and DFT Study. *Eur. J. Inorg. Chem.* **2012**, 4605-4621; DOI: 10.1002/ejic.201200232.

14. Dick, S. Crystal Structure of Tris(2,2'-bipyridine)iron(II) Bis(hexafluorophosphate), $(C_{10}H_8N_2)_3Fe(PF_6)_2$. *Z. Kristallogr. - New Cryst. Struct.* **1998**, *213*, 356; DOI: 10.1524/ncrs.1998.213.14.355.

15. Jamula, L. L.; Brown, A. M.; Guo, D.; McCusker, J. K. Synthesis and Characterization of a High-Symmetry Ferrous Polypyridyl Complex: Approaching the $^5T_2/^3T_1$ Crossing Point for Fe^{II}. *Inorg. Chem.* **2014**, *53*, 15-17; DOI: 10.1021/ic402407k.

16. Fereira, H.; von Eschwege, K. G.; Conradie, J. Electronic Properties of Fe Charge Transfer Complexes – A Combined Experimental and Theoretical Approach. *Electrochim. Acta* **2016**, *216*, 339-346; DOI: 10.1016/j.electacta.2016.09.034.

17. Buhks, E.; Navon, G.; Bixon, M.; Jortner, J. Spin Conversion Processes in Solution. *J. Am. Chem. Soc.* **1980**, *102*, 2918-2923; DOI: 10.1021/ja00529a009.

18. Hauser, A. Excited-State Lifetimes of $[Fe(bipy)_3]^{2+}$ and $[Fe(phen)_3]^{2+}$. *Chem. Phys. Lett.* **1990**, *173*, 507-512; DOI: 10.1016/0009-2614(90)87244-L.

19. Goodwin, H. A. Spin Transitions in 6-Coordinate Iron(II) Complexes. *Coord. Chem. Rev.* **1976**, *18*, 293-325; DOI: 10.1016/S0010-8545(00)80430-0.

20. Kumar, K. S.; Ruben, M. Emerging Trends in Spin Crossover (SCO) Based Functional Materials and Devices. *Coord. Chem. Rev.* **2017**, *346*, 176-205; DOI: 10.1016/j.ccr.2017.03.024.

21. Conti, A. J.; Xie, C. L.; Hendrickson, D. N. Tunneling in Spin-State Interconversion of Ferrous Spin-Crossover Complexes – Concentration-Dependence of Apparent Activation-Energy Determined in Solution by Laser-Flash Photolysis. *J. Am. Chem. Soc.* **1989**, *111*, 1171-1180; DOI: 10.1021/ja00186a002.

22. Malone R. A.; Kelley, D. F. Interligand Electron Transfer and Transition State Dynamics in Ru(II) Trisbipyridine. *J. Chem. Phys.* **1991**, *95*, 8970-8976; DOI: 10.1063/1.461228.

23. Juban, E. A.; McCusker, J. K. Ultrafast Dynamics of ^2E State Formation in $Cr(acac)_3$. *J. Am. Chem. Soc.* **2005**, *127*, 6857-6865; DOI: 10.1021/ja042153i.

24. Megerle, U.; Pugliesi, L.; Schriever, C.; Sailer, C.F.; Riedle, E. Sub-50 fs Broadband Absorption Spectroscopy with Tunable Excitation: Putting the Analysis of Ultrafast Molecular Dynamics on Solid Ground. *Appl. Phys. B* **2009**, *96*, 215-231; DOI: 10.1007/s00340-009-3610-0.

25. Berera, R.; van Grondelle, R.; Kennis, J. T. M. Ultrafast Transient Absorption Spectroscopy: Principles and Application to Photosynthetic Systems. *Photosynth. Res.* **2009**, *101*, 105-118; DOI: 10.1007/s11120-009-9454-y.

26. Lumpkin, R. S.; Meyer, T. J. Effect of the Glass-to-Fluid Transition on Excited-State Decay. Application of the Energy Gap Law. *J. Phys. Chem.* **1986**, *90*, 5307-5312; DOI: 10.1021/j100412a080.

27. El-Kashef, H. Optical and Electrical-Properties of Materials. *Rev. Sci. Instrum.* **1994**, *65*, 2056-2061; DOI: 10.1063/1.1144812.

28. Aminabhavi T. M.; Patil, V. B. Density, Viscosity, Refractive Index, and Speed of Sound in Binary Mixtures of Ethenylbenzene with N,N-Dimethylacetamide, Tetrahydrofuran, N,N'-Dimethylformamide, 1,4-Dioxane, Dimethyl Sulfoxide, Chloroform, Bromoform, and 1-Chloronaphthalene in the Temperature Interval (298.15-308.15) K. *J. Chem. Eng. Data* **1998**, *43*, 497-503; DOI: 10.1021/je980031y.

29. Aralaguppi, M. I.; Jadar C. V.; Aminabhavi, T. M. Density, Refractive Index, Viscosity, and Speed of Sound in binary Mixtures of 2-Ethoxyethanol with Dioxane, Acetonitrile, and Tetrahydrofuran at (298.15, 303.15, and 308.15) K. *J. Chem. Eng. Data* **1996**, *41*, 1307-1310; DOI: 10.1021/je960133t.

30. Shukla, R. K.; Kumar, A.; Awasthi, N.; Srivastava, U.; Gangwar, V. S. Density, Viscosity and Refractive Index of Binary Liquid Mixtures at 293.15, 298.15, 303.15, 308.15, and 313.15 K. *Exp. Therm. Fluid Sci.* **2012**, *37*, 1-11; DOI: 10.1016/j.expthermflusci.2011.08.005.

31. Newport Application Note 29, http://assets.newport.com/webDocuments-EN/images/12243.PDF, (accessed November 2017).

32. Marcus, R. A.; Sutin, N. Electron Transfers in Chemistry and Biology. *Biochim. Biophys. Acta* **1985**, *811*, 265-322; DOI: 10.1016/0304-4173(85)90014-X.

33. Barbara, P. F.; Meyer, T. J.; Ratner, M. A. Contemporary Issues in Electron Transfer Research. *J. Phys. Chem.* **1996**, *100*, 13148-13168; DOI: 10.1021/jp9605663.

34. Khalil, M.; Marcus, M. A.; Smeigh, A. L.; McCusker, J. K.; Chong H. H. W.; Schoenlein, R. W. Picosecond X-ray Absorption Spectroscopy of a Photoinduced Iron(II) Spin Crossover Reaction in Solution. *J. Phys. Chem. A* **2006**, *110*, 38-44; DOI: 10.1021/jp055002q.

35. Ashley, D. C.; Jakubikova, E. Ray-Dutt and Bailar Twists in Fe(II)-Tris(2,2'-bipyridine): Spin States, Sterics, and Fe-N Bond Strengths. *Inorg. Chem.* **2018**, *57*, 5585-5596; DOI: 10.1021/acs.inorgchem.8b00560.

36. CRC Handbook of Chemistry and Physics, 98th ed., http://hbcponline.com/faces/documents/06_33/06_33_0001.xhtml, (accessed September 2017).

37. Vankó, G.; Bordage, A.; Pápai, M.; Haldrup, K.; Glatzel, P.; March, A. M.; Doumy, G.; Britz, A.; Galler, A.; Assefa, T.; Cabaret, D.; Juhin, A.; van Driel, T. B.; Kjær, K. S.; Dohn, A.; Møller, K. B.; Lemke, H. T.; Gallo, E.; Rovezzi, M.; Németh, Z.; Rozsályi, E.; Rozgonyi, T.; Uhlig, J.; Sundström, V.; Nielsen, M. M.; Young, L.; Southworth, S. H.; Bressler, Ch.; Gawełda, W. Detailed Characterization of a Nanosecond-Lived Excited State: X-ray and Theoretical Investigation of the Quintet State in Photoexcited $[Fe(terpy)_2]^{2+}$. *J. Phys. Chem. C* **2015**, *119*, 5888-5902; DOI: 10.1021/jacs.jpcc.5b00557.

38. Nance, J.; Bowman, D. N.; Mukherjee, S.; Kelley, C. T.; Jakubikova, E. Insights into the Spin-State Transitions in $[Fe(tpy)_2]^{2+}$: Importance of the Terpyridine Rocking Motion. *Inorg. Chem.* **2015**, *54*, 11259-11268; DOI: 10.1021/acs.inorgchem.5b01747.

39. Balzani, V.; Juris, A.; Barigelletti, F.; Belser, P.; von Zelewsky, A. Photophysical Properties of Ruthenium(II) Polypyridine Complexes. *Riken Q.* **1984**, *78*, 78-85.

40. Juris, A.; Balzani, V.; Belser, P.; von Zelewsky, A. Characterization of the Excited-State Properties of Some New Photosensitizers of the Ruthenium (Polypyridine) Family. *Helv. Chim. Acta* **1981**, *64*, 2175-2182; DOI: 10.1002/hlca.19810640723.

41. Juris, A.; Balzani, V.; Barigelletti, F.; Campagna, S.; Belser, P.; von Zelewsky, A. Ru(II) Polypyridine Complexes: Photophysics, Photochemistry, Electrochemistry, and Chemiluminescence. *Coord. Chem. Rev.* **1988**, *84*, 85-277; DOI: 10.1016/0010-8545(88)80032-8.

42. Yarranton, J. T. Unpublished results.

43. Lashgari, K.; Kritikos, M.; Norrestam, R.; Norrby, T. Bis(terpyridine)ruthenium(II) Bis(hexafluorophosphate) Diacetonitrile Solvate. *Acta Cryst., Sect. C: Cryst. Struct. Commun.* **1999**, *C55*, 64-67; DOI: 10.1107/S0108270198011378.

44. Damrauer, N. H.; Boussie, T. R.; Devenney, M.; McCusker, J. K. Effects of Intraligand Electron Delocalization, Steric Tuning, and Excited-State Vibronic Coupling on the Photophysics of Aryl-Substituted Bipyridyl Complexes of Ru(II). *J. Am. Chem. Soc.* **1997**, *119*, 8253-8268; DOI: 10.1021/ja971321m.

45. Bock, C. R.; Whitten, D. G.; Meyer, T. J. Photochemistry of Transition Metal Complexes. Mechanism and Efficiency of Energy Conversion by Electron-Transfer Quenching. *J. Am. Chem. Soc.* **1975**, *97*, 2909-2911; DOI: 10.1021/ja00843a055.

46. Bock, C. R.; Connor, J. A.; Gutierrez, A. R.; Meyer, T. J.; Whitten, D. G.; Sullivan, B. P.; Nagle, J. K. Estimation of Excited-State Redox Potentials by Electron-Transfer Quenching. Application of Electron-Transfer Theory to Excited-State Redox Processes. *J. Am. Chem. Soc.* **1979**, *101*, 4815-4824, and references therein; DOI: 10.1021/ja00511a007.

47. Ceroni, P; Balzani, V. Photoinduced Energy and Electron Transfer Processes. In *The Exploration of Supramolecular Systems and Nanostructures by Photochemical Techniques*; Ceroni, P., Ed.; Springer: Netherlands, 2012; pp 21-38; DOI: 10.1002/chem.201102260.

48. Prier, C. K.; Rankic, D. A.; MacMillan, D. W. C. Visible Light Photoredox Catalysis with Transition Metal Complexes: Applications in Organic Synthesis. *Chem. Rev.* **2013**, *113*, 5322-5363, and references therein; DOI: 10.1021/cr300503r.

49. Eberson, L. Electron-Transfer Reactions in Organic-Chemistry. *Adv. Phys. Org. Chem.* **1982**, *18*, 79-185, and references therein; DOI: 10.1016/S0065-3160(08)60139-2.

50. Connelly, N. G.; Geiger, W. E. Chemical Redox Agents for Organometallic Chemistry. *Chem. Rev.* **1996**, *96*, 877-910; DOI: 10.1021/cr940053x.

51. Gualandi, A.; Marchini, M.; Mengozzi, L.; Natali, M.; Lucarini, M.; Ceroni, P.; Cozzi, P. G. Organocatalytic Enantioselective Alkylation of Aldehydes with $[Fe(bpy)_3]Br_2$ Catalyst and Visible Light. *ACS Catal.* **2015**, *5*, 5927-5931; DOI: 10.1021/acscatal.5b01573.

52. West, G. A.; Barrett, J. J.; Siebert, D. R.; Reddy, K. V. Photoacoustic Spectroscopy. *Rev. Sci. Instrum.* **1983**, *54*, 797-817; DOI: 10.1063/1.1137483.

53. Braslavsky, S. E.; Heibel, G. E. Time-Resolved Photothermal and Photoacoustic Methods Applied to Photoinduced Processes in Solution. *Chem. Rev.* **1992**, *92*, 1381-1410, and references therein; DOI: 10.1021/cr00014a007.

54. Barker, B. D.; Larsen, R. W. Volume and Enthalpy Profiles of CO Binding to Fe(II) Tetrakis-(4-sulfonatophenyl)porphyrin. *J. Inorg. Biochem.* **2001**, *85*, 107-116; DOI: 10.1016/S0162-0134(01)00190-8.

55. Skrzypek, D.; Madejska, I.; Habdas, J.; Dudkowiak, A. The Spectroscopic Characterisation of Proline Derivatives of Tolyl-Porphyrins and Their Iron and Cobalt Complexes. *J. Mol. Struct.* **2008**, *876*, 177-185; DOI: 10.1016/j.molstruc.2007.06.016.

56. Reguera, E.; Marín, E.; Calderón, A.; Rodríguez-Hernández, J. Photo-Induced Charge Transfer in Prussian Blue Analogues as Detected by Photoacoustic Spectroscopy. *Spectrochim. Acta, Part A* **2007**, *68*, 191-197; DOI: 10.1016/j.saa.2006.11.013.

57. Butler, I. S.; Li, H.; Gao, J. P. Comparison of Photoacoustic, Attenuated Total Reflection, and Transmission Infrared Spectra of Crystalline Organoiron(II) Carbonyl Complexes. *Appl. Spectrosc.* **1991**, *45*, 223-226; DOI: 10.1366/0003702914337425.

58. Goodman, J. L.; Herman, M. S. Reaction Volumes of Excited State Photoprocesses. *Chem. Phys. Lett.* **1989**, *163*, 417-420; DOI: 10.1016/0009-2614(89)85160-7.

59. Hupp, J. T.; Weaver, M. J. Solvent, Ligand, and Ionic Charge Effects on Reaction Entropies for Simple Transition-Metal Redox Couples. *Inorg. Chem.* **1984**, *23*, 3639-3644; DOI: 10.1021/ic00190a042.

60. Borsarelli, C. D.; Braslavsky, S. E. Volume Changes Correlate with Enthalpy Changes During the Photoinduced Formation of the ^{3}MLCT State of Ruthenium(II) Bipyridine Cyano Complexes in the Presence of Salts. A Case of the Entropy-Enthalpy Compensation Effect. *J. Phys. Chem. B* **1998**, *102*, 6231-6238; DOI: 10.1021/jp981235o.

61. Chen, L. X.; Shaw, G. B.; Novozhilova, I.; Liu, T.; Jennings, G.; Attenkofer, K.; Meyer, G. J.; Coppens, P. MLCT State Structure and Dynamics of a Copper(I) Diimine Complex Characterized by Pump-Probe X-ray and Laser Spectroscopies and DFT Calculations. *J. Am. Chem. Soc.* **2003**, *125*, 7022-7034; DOI: 10.1021/ja0294663.

CHAPTER 3. THE INFLUENCE OF OUTER-SPHERE REORGANIZATION ENERGY ON A BARRIERLESS REACTION IN THE EXCITED STATE DYNAMICS OF AN OCTAHEDRAL IRON(II) POLYPYRIDYL COMPLEX

1. Introduction

In the ongoing quest to lengthen the lifetime of the charge-separated metal-to-ligand charge transfer (MLCT) excited states in low-spin Fe(II) complexes, the most apparent and seemingly straightforward is through the manipulation of excited state ordering. A scenario can be imagined in which the ligand field (LF) strength of the Fe(II) complex is so increased that the metal-centered electronic excited states are significantly destabilized such that they lie energetically above the MLCT states. In this case, the excited state ordering of the Fe(II)-based compound would very closely represent that of typical Ru(II) chromophores with long-lived MLCT lifetimes. In order to achieve such a goal, the ligands of the complex would have to be manipulated so as to drastically increase the ligand field strength. This would likely place the complex on the Tanabe-Sugano diagram for d^6 electronic configurations in which the lowest-lying excited state is the $^3T_1$ state.[1]

Until very recently, there were no known Fe(II) complexes with this electronic state ordering; this is in large part due to the inherent difficulties of distinguishing the spin of the excited state, particularly in short-lived complexes. Simultaneous optical absorption and X-ray emission spectroscopies, however, have the advantageous of observing molecular structure as excited state dynamics evolve, proving to be an incredibly useful tool. Gaffney et al. have recently used this technique to study $[Fe(bpy)(CN)_4]^{2-}$ in a series of solvents.[2,3] Cyano ligands have long shown a propensity towards solvatochromism,[4] and this complex was no exception. In the aprotic solvents acetonitrile, dimethylsulfoxide, and tetrahydrofuran, the low energy MLCT absorption band was

very red-shifted and typically centered at ~700 nm.[2] For these solvents, it was observed that the lowest-energy excited state was actually MLCT in nature, and it decayed to the ground state on the order of 20 ps. This is still the only known example of an Fe(II) complex with this electronic state ordering. If the same complex is dissolved in a protic solvent like methanol or water, though, that MLCT absorption band blue shifts to λ_{max} ~550 and 490 nm, respectively.[3] Due to MLCT states being energetically destabilized, the lowest energy excited state reverts back to being LF in nature, though it is the $^3T_1$ excited state as opposed to the $^5T_2$. These studies represent an important benchmark in the field of low-spin Fe(II) photophysics, as they show the same complex being able to achieve either a MLCT or $^3T_1$ lowest energy excited state, with the determining factor being the solvent. Although the case study provided above is a very unique example due to the highly solvatochromic nature of the -CN moieties, this method of outer-sphere reorganization energy impacting excited state energetics is well worth pursuing, albeit in moderately more representative Fe(II) polypyridyl complexes.

Another avenue pursued in the name of lengthened MLCT lifetimes was the synthesis of a more perfectly octahedral Fe(II) complex, namely 2,6-bis(2-carboxypyridyl)pyridine iron(II), $[Fe(dcpp)_2]^{2+}$ (Scheme 3.1).[5] With its high symmetry, the ligand field strength was greatly increased. Unfortunately, the lowest energy excited state was still a metal-centered ligand field state; ground state recovery from this excited state, however, was unique in its rate. The lifetime of $[Fe(dcpp)_2]^{2+}$ in acetonitrile was observed to be 280 ± 10 ps, which is 3 times faster than that of $[Fe(bpy)_3]^{2+}$. It was postulated that either the ligand field strength was so much greater that the $^3T_1$ lowest lying excited state was accessed, or that the reorganization energy of $[Fe(dcpp)_2]^{2+}$ was drastically increased relative to $[Fe(bpy)_3]^{2+}$. With respect to the former, recent ultrafast X-ray studies[6] have determined that ground state recovery occurs from a quintet excited state along with

a Jahn-Teller distortion in this state. This leaves reorganization energy as the most probable influencer of the excited state dynamics in this compound.

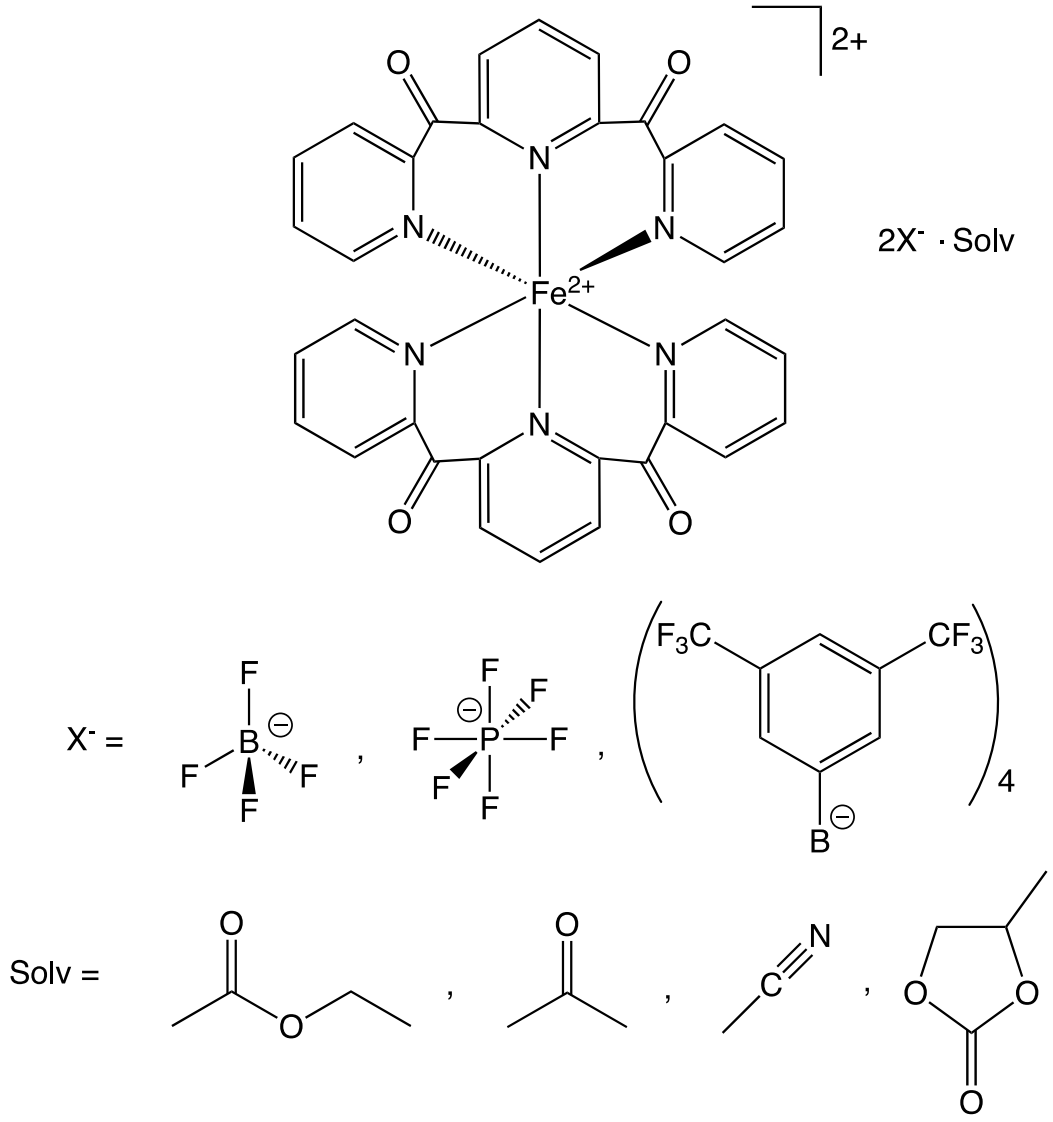

Scheme 3.1. Molecular structure of $[Fe(dcpp)_2]^{2+}$; the series of counteranions (X) for use in this work: tetrafluoroborate (BF_4^-), hexafluorophosphate (PF_6^-), and tetrakis[(3,5-trifluoromethyl)phenyl]borate (BAr^{F-}); and the solvents (Solv) of choice: ethyl acetate (EtOAc), acetone, acetonitrile (MeCN), and propylene carbonate (PC).

A large volume of work has previously been done on the solvation effects on ground state recovery in $[Fe(bpy)_3]^{2+}$.[7-12] though the results were largely qualitative. Preliminary work has been performed in the way of ultrafast variable-temperature transient absorption (VT-TA) measurements on $[Fe(bpy)_3]Cl_2$ in a series of solvents in order to determine the effects of solvent on ground state recovery in this complex (Appendix A). Historically, outer-sphere reorganization energy in this class of compounds has been believed to be quite large, nearly 0.5 eV for both $[Fe(bpy)_3]^{2+}$ and $[Fe(terpy)_2]^{2+}$ by some accounts.[13] During the course of the VT work on $[Fe(bpy)_3]^{2+}$, it became apparent that this estimation is over an order of magnitude too large. It then became highly desirable to expand this type of study to $[Fe(dcpp)_2]^{2+}$, a complex whose reorganization energy is under question. The methodology outlined in Chapter 2 of this work was used to study the ground state recovery of this complex under a variety of conditions in order to parse out the outer-sphere contributions to the $^5T_2 \rightarrow {}^1A_1$ transition.[14] We believe this is the first instance of quantitative outer-sphere reorganization energies being determined for various solvents and counteranions of any low-spin Fe(II) polypyridyl complexes. It is also the first time the Arrhenius parameters are being found for $[Fe(dcpp)_2]^{2+}$. As was the case with Chapter 2, Marcus nonradiative decay theory is applied and estimations are made for these values as well.

2. Experimental

2.1 Materials and Synthesis

2.1.1 General

All salts of $[Fe(dcpp)_2]^{2+}$ were prepared by J. T. Yarranton. The synthetic route to prepare $[Fe(dcpp)_2](PF_6)_2$ has been previously reported.[5] The solvents used were: propylene carbonate (Acros Organics, 99.5%), ethyl acetate (Macron Fine Chemicals, ACS grade), dichloromethane

(Jade Scientific, spectrograde), acetonitrile (Sigma-Aldrich, HPLC grade), tetrahydrofuran (Fisher Scientific, ACS grade), and acetone (Jade Scientific, spectrograde). All samples were prepared in air.

2.1.2 Characterization

Characterization by ^{1}H NMR and mass spectrometry of the different salts of $[Fe(dcpp)_2]^{2+}$ was performed by J. T. Yarranton. Timed ^{1}H NMR studies were carried out by M. C. Carey and were collected with a Bruker 500 MHz NMR spectrometer. Ground state absorption spectra were collected on a Cary 50 spectrophotometer (Varian, now Agilent) at a fast collection rate with background subtraction.

Single crystals of $[Fe(dcpp)_2](BF_4)_2$ were grown and mounted in paratone oil and transferred to the cold nitrogen gas stream of the diffractometer for data collection. Single crystal X-ray diffraction was collected on suitable crystals mounted on a Bruker APEX-II CCD diffractometer with CuK_α radiation at the Center for Crystallographic Research at Michigan State University. The crystal structures were solved by J. T. Yarranton.

2,6-Bis(2-carboxypyridyl)pyridine iron(II) tetrakis[(3,5-trifluoromethyl)phenyl]borate $[Fe(dcpp)_2](BAr^F)_2$ ^{1} H NMR (500 MHz, [d_6-acetone], δ) [8.79 (t, 1 H, J = 7.82Hz), 8.54 (dd, 2 H, J = 2.10, 5.77 Hz), 8.37 (t, 2 H, J = 7.78 Hz), 8.23 (d, 2 H, J = 7.78 Hz), 8.11 (d, 2 H, J = 5.35 Hz), 7.78 (m, 8 H), 7.67 (s, 4 H), 7.52 (t, 2 H, J = 6.74 Hz)].

2,6-Bis(2-carboxypyridyl)pyridine iron(II) tetrakis[(3,5-trifluoromethyl)phenyl]borate $[Fe(dcpp)_2](BAr^F)_2$ in dichloromethane ^{1}H NMR (500 MHz, [d_6-acetone], δ) [8.73 (t, 1 H, J = 7.76Hz), 8.48 (d, 2 H, J = 7.69 Hz), 8.32 (t, 2 H, J = 7.60 Hz), 8.18 (d, 2 H, J = 7.76 Hz), 8.01 (d, 2 H, J = 5.37 Hz), 7.75 (m, 8 H), 7.60 (d, 4 H, J = 2.08 Hz), 7.45 (m, 2 H)].

2.2 Ultrafast Transient Absorption Spectroscopy

2.2.1 Variable-Temperature Measurements

The ultrafast laser system used to measure ground state recovery lifetimes of the series of $[Fe(dcpp)_2]^{2+}$ salts has been previously described[7,14-16] and is fully detailed in Chapter 2. The variable-temperature setup has likewise been expanded on.[14]

The samples prepared for these measurements had an absorbance of 0.3-0.5 AU at the excitation wavelength in a 1-cm pathlength cryogen-safe quartz cuvette (FireFlySci) and were typically excited with ~5 μJ, with all data being collected within the linear regime. Pump wavelengths used in this study were 490 and 610 nm and are specified for the data collected. Only a 540 nm probe was used. Pulse characterization is performed with the cryostat in place by optical Kerr effect (OKE) measurements made in acetonitrile. The pulses are nominally 160 fs, giving an instrument response function of approximately 300 fs. Any spectra displayed are an average of at least 10 scans, with no single scan being a statistical outlier. The Arrhenius plots and values given are for the combined total data of that type collected. Monoexponential and Arrhenius fits were performed using Igor Pro (v. 6.37) software, and unless otherwise noted, all error reported is propagated across multiple data sets.

2.2.2 MLCT Lifetime Measurements

The MLCT lifetimes of Fe(II) complexes are well-known to be very short (<200 fs),[17] so a laser setup with a shorter IRF was desired to have the most accurate measure of this kinetic process. A shorter pulse system was used to collect MLCT lifetime data on $[Fe(dcpp)_2]^{2+}$. In this setup, which has been previously described,[18] a Mantis oscillator (Coherent) is pumped by a 5 W optically pumped semiconductor laser, the output of which seeds a Legend Elite regenerative amplifier (Coherent) that is pumped by an Evolution pumping laser (Coherent) at a1 kHz repetition rate. The

output pulses are nominally 35 fs in duration and is split 80/20 to pump and probe OPerA Solo optical parametric amplifiers (Coherent), respectively. These are tunable across 240-20000 nm but were used in this instance in the visible region. Specifically, pump wavelengths of 490 and 610 nm and a probe wavelength of 540 nm were of interest. Both the pump and probe lines propagate through a folded Brewster prism pair (Thorlabs) to preemptively compensate for dispersion. The probe is translated on a linear actuator stage (Soloist) relative to the probe in order to collect transients as a function of time delay. The pump line is optically chopped at approximately 480 Hz which is connected to a lock-in amplifier. A small portion of the probe line is picked off to act as a reference for fluctuations in the laser power over the course of data collection. The polarization of the beams is set magic angle to each other in order to collect only population dynamics, and not polarization effects. Both the pump and probe are focused collinearly at <5º into the sample, at which point the pump is blocked and the probe is detected by a Si photodiode (Thorlabs) after traversing a monochromator with a ~1 nm bandwidth for wavelength selection.

The samples prepared for these measurements were studied in 1-mm pathlength quartz cuvettes (FireFlySci) with absorbances of 0.3-0.5 AU at the excitation wavelength. Due to the high peak power of the temporally short pulses used in this experiment, the average power was kept lower than what was used for the VT measurements. Specifically, the pump power was 2 μJ relative to the 0.5 μJ of the probe. The pump pulse duration when λ_{exc} = 490 nm was 60 fs and was <50 fs when λ_{exc} = 610 nm. The probe pulse duration remained constant at 96 fs throughout the measurements. These pulse duration measurements were made by OKE in methanol, and the IRF was determined by cross-correlation in acetonitrile. For more information on pulse and system characterization, please see Appendix B. The data displayed are an average of more than 10 scans, each collected between 1-3 times. Mono- and bi-exponential fits were performed in Igor Pro

software.

3. Results and Discussion

The purpose of this work is to study the outer-sphere effects on the ground state recovery of $[Fe(dcpp)_2]^{2+}$. To that end, the complex was prepared with three different counteranions: tetrafluoroborate (BF_4^-), hexafluorophosphate (PF_6^-), and tetrakis[(3,5-trifluoromethyl)phenyl]-borate (BAr^{F-}), as can be seen in Scheme 3.1. The role of solvent was also investigated. In $[Fe(dcpp)_2]^{2+}$, the carbonyl is highly susceptible to attack by proton sources, which results in the deterioration of the ligand. Protic solvents, therefore, were precluded from use. Four solvents were chosen to span a wide range of bulk solvent properties (e.g., dielectric constant, viscosity); namely, ethyl acetate (EtOAc), acetone, acetonitrile (MeCN), and propylene carbonate (PC) were used.

3.1 Characterization

3.1.1 X-Ray Crystallography

High quality single crystals of $[Fe(dcpp)_2](BF_4)_2$ were able to be grown and studied by single-crystal X-ray diffraction. The geometric measurements from this complex were then compared to the same measurements of $[Fe(dcpp)_2](PF_6)_2$.[5] The results of this comparison can be found in Table 3.1. The crystals with the BF_4^- counteranion were observed to be birefringent, as indicated by the clear change in crystal color under polarized light upon a 90º reorientation.

Table 3.1. Single crystal X-ray data comparison between the PF_6^- and BF_4^- salts of $[Fe(dcpp)_2]^{2+}$.

	$[Fe(dcpp)_2](PF_6)_2$ [a]	$[Fe(dcpp)_2](BF_4)_2$ [b]
Fe-N_{ax} (Å)	1.9738	1.964
Fe-N_{eq} (Å)	1.986(3)	1.982(2)
C-O (Å)	1.212(1)	1.212(2)
Cis N-Fe-N (º)	88.8 ± 0.1	88.8 ± 0.2
Trans N-Fe-N (º)	178.3 ± 0.7	177.8 ± 0.3
O-N (Å)	3.4800-3.5402	3.457-3.530
CO1-Py torsion (º)	26.5	26.5
CO2-Py torsion (º)	41.5	44.5

a Taken from ref. 5.

b Data collected by J. T. Yarranton.

Interestingly, changes in the structure of the cation were observed with a simple metathesis of the counteranion. Both structures were of the same space group (Pbcn), and many of their geometric components are the same. All bond ligand-Fe bond angles are within error of each other, for instance. One of the hallmarks of a tridentate ligand is a shorter axial bond relative to the equatorial bond distances. This is present in both salts of $[Fe(dcpp)_2]^{2+}$. However, in the case of the BF_4^- salt, the Fe-N_{ax} distance is significantly shorter even than the same Fe-N_{ax} distance in the PF_6^- salt. This was confirmed by statistical analysis and error propagation of the single crystal data. Likewise, the distance between the O of the carbonyl and the N atoms of the pyridine rings was measured and a range is given for each complex. For each of those O-N distances, the BF_4^- salt displays bonds that are on average 0.02 Å shorter than the same bonds in the PF_6^- salt. Shorter bond distances in $[Fe(dcpp)_2](BF_4)_2$ would tend to imply a greater degree of stabilization in that salt over the PF_6^-. Notably, though, there is more torsion in the angle of the carbonyl relative to the plane of the pyridine. These data taken together would seem to suggest that the central pyridyl

moieties of the dcpp ligand are bound more tightly to the Fe(II) center, inducing greater distortion in the wrapping of the peripheral pyridyls around the metal. The net effect, however, is that the $[Fe(dcpp)_2](BF_4)_2$ is lower in energy than $[Fe(dcpp)_2](PF_6)_2$. This is a surprising result considering the BF_4^- and PF_6^- anions are typically regarded as being very similar. PF_6^- may be slightly more polarizable due to its larger size relative to BF_4^-. But in that respect, BF_4^- is a smaller, harder anion, and may in fact be able to fit closer to the metal center and provide a greater extent of stabilization.

These results are very interesting, in large part due to the surprising nature of them. It should be remembered, though, that these structures are for the crystals as solids while also in their ground states. It may be tempting to extrapolate these results to the photophysical processes that will be described (vide infra), but the solution-phase nature of the measurements will necessarily change the geometry of the complex, to say nothing of the photoexcitation into excited states. That being said, work is ongoing to grow quality crystals of $[Fe(dcpp)_2](BAr^F)_2$ to have knowledge of the ground state geometry of all three complexes as well as the stabilizing role of the counteranions for this study.

3.1.2 Ground State Absorption Spectra

To further characterize the ground state properties of the $[Fe(dcpp)_2]^{2+}$ complexes, UV-Vis spectra were collected for each of the three salts in MeCN. As Jamula et al. originally described,[5] the visible spectrum shows a very broad progression of bands of increasing intensity (Fig. 3.1). The absorption maximum for the BF_4^-, PF_6^-, and BAr^{F-} salts are 607, 605, and 606 nm, respectively, and show very little change across the entire absorption profile. Albeit a minor spectral shift, this is our first indicator that the anion has an effect on the energy of the ^{1}MLCT excited state. Relative to the PF_6^- salt, the BF_4^- analogue is stabilized by 54 cm^{-1}, and the BAr^{F-} salt is stabilized by 27 cm^{-1}. To a first approximation, it would appear that the UV-Vis spectra and X-ray data are in

agreement when comparing the PF_6^- and BF_4^- analogues of $[Fe(dcpp)_2]^{2+}$, suggesting that the latter is lower in energy.

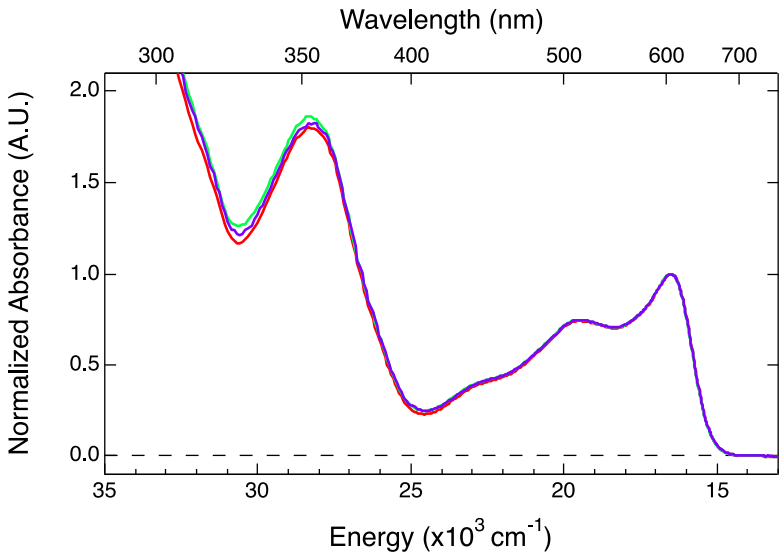

Figure 3.1. Ground state absorption spectra of $[Fe(dcpp)_2]^{2+}$ salts, normalized to the MLCT maximum: BF_4^- at 607 nm (purple), PF_6^- at 605 nm (red), and BAr^{F-} at 606 nm (green).

As discussed in the introduction, solvatochromism is not uncommon in these types of chromophores.[19] One might expect the high activity of the carbonyl to mimic the effects of the cyano ligand in the case of $[Fe(bpy)(CN)_4]^{2-}$.[3] The obvious difference being that the cyano was bound directly to the Fe(II) center, amplifying its effects as compared to the carbonyl which is cross-conjugated into the pyridyl backbone of the dcpp ligand. Any interaction of the carbonyl with the solvent would have an attenuated effect on the Fe(II) itself. Thus, it is unsurprising that solvatochromism is displayed in $[Fe(dcpp)_2]^{2+}$, though only to a small degree. For the sake of comparison, only the BAr^{F-} counteranion was used with all four of these solvents; this was also a necessity due to the increased solubility of the BAr^{F-} salt. Often, this property is correlated with the Gutmann acceptor number (AN),[20-22] of which a moderate range is available from EtOAc

(9.3),[23] acetone (12.5), MeCN (18.9), and PC (18.3).[24] For comparison purposes, the dielectric constant was also used as a parameter of interest: EtOAc (ϵ_0 = 6.08), acetone (ϵ_0 = 21.01), MeCN (ϵ_0 = 36.64), and PC (ϵ_0 = 66.14).[25] Despite this span of an order of magnitude, the difference between the absorption maximum in the different solvents is only 4 nm (109 cm^{-1}), between EtOAc (λ_{max} = 605 nm) and PC (λ_{max} = 609 nm), as can be seen in Fig. 3.2. These results are somewhat unexpected as the most stabilized MLCT band corresponds to the solvent with the lowest dielectric constant, which is counter to what was seen with $[Fe(dcpp)(CN)_4]^{2-}$. The correlation is no better when using AN as the parameter of interest, as one would expect the higher AN to correlate to higher MLCT energy, clearly the reverse of what is observed here.

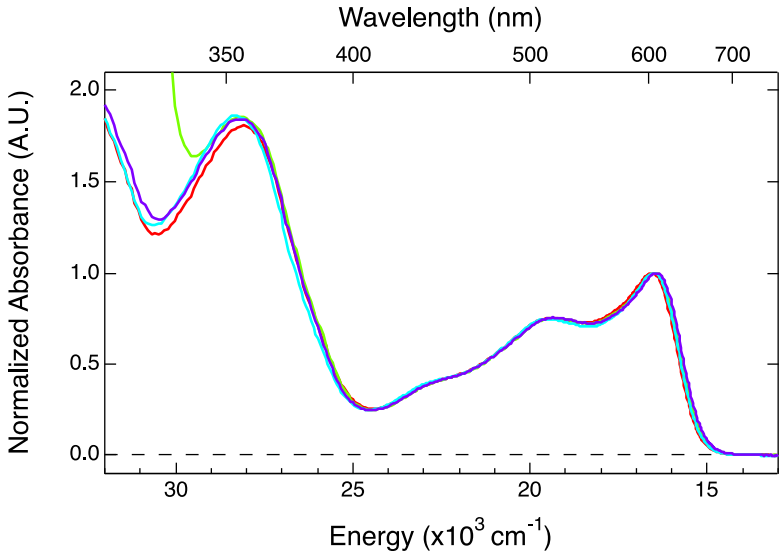

Figure 3.2. Ground state absorption spectra of $[Fe(dcpp)_2](BAr^F)_2$ in EtOAc (red), acetone (green), MeCN (blue), and PC (purple). The spectra are normalized to the MLCT maximum.

3.2 Measuring Outer-Sphere Reorganization Energy

3.2.1 $[Fe(dcpp)_2](PF_6)_2$

With the structural and ground state absorbance data in hand, the ultrafast variable-

temperature methodology that has been previously designed[14] was used to study this unique complex. The PF_6^- salt was originally studied in MeCN by Jamula et al. and was found to have a ground state recovery lifetime of 280 ± 10 ps at room temperature.[5] With such a short lifetime, it was postulated that the reorganization energy of this complex must be extraordinarily high with respect to other more typical Fe(II) polypyridyl complexes, such as $[Fe(bpy)_3]^{2+}$ and $[Fe(terpy)_2]^{2+}$. The VT measurements found that at 235 K, the lifetime has increased to 340 ± 10 ps (Fig. 3.3). Based on the Arrhenius equation, eqn. (3.1), the natural log of the rate of ground state recovery, k_{nr}, can be plotted against the inverse temperature, T, thereby linearizing the data and allowing for the activation energy E_a and preexponential factor A to be determined, according to eqn. (3.2).

$$k_{nr} = Ae^{\frac{-E_a}{k_B T}} \tag{3.1}$$

$$\ln k_{nr} = \ln A - \frac{E_a}{k_B}\left(\frac{1}{T}\right) \tag{3.2}$$

In these equations, k_B is the Boltzmann constant. From this Arrhenius plot (Fig. 3.4), an activation energy of 115 ± 15 cm^{-1} is found, which is nearly three times smaller than that of $[Fe(bpy)_3]^{2+}$. The barrierless rate, A, is found to be 165 ± 15 ps^{-1}. What is immediately apparent is the magnitude of E_a for this complex, and the fact that $E_a < k_BT$. The $^5T_2 \rightarrow {}^1A_1$ transition, then, must necessarily be in the Marcus barrierless region, an extraordinary finding for this transition in an Fe(II) polypyridyl complex.[26-28] This result is also confirmed by the DFT analysis performed on the ultrafast X-ray spectroscopies of $[Fe(dcpp)_2]^{2+}$ that found the only barrier possible to explain the data was that of ~30 meV, which is in very good agreement with the results presented here.[6]

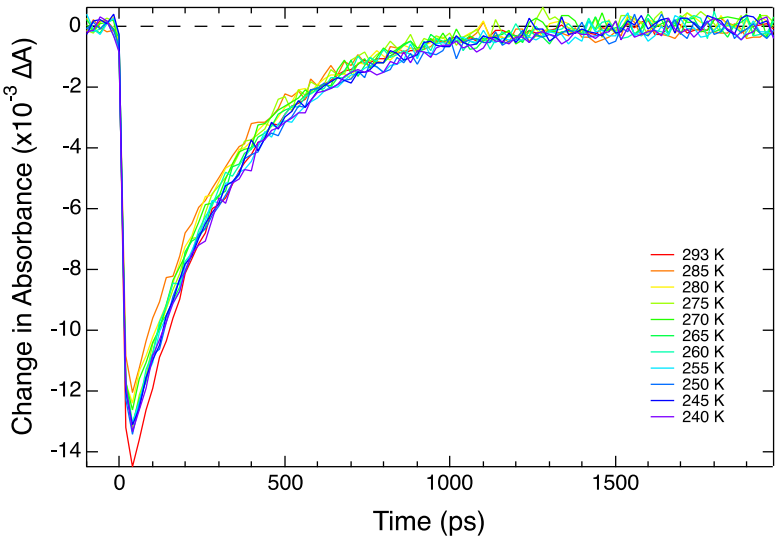

Figure 3.3. Representative variable-temperature lifetimes of $[Fe(dcpp)_2](PF_6)_2$ in MeCN. Excitation occurred at 490 nm, and a 540 nm probe was used. At room temperature (red) the lifetime of the complex is 290 ± 5 ps, and at 235 K (not shown) the average lifetime is 340 ± 10 ps.

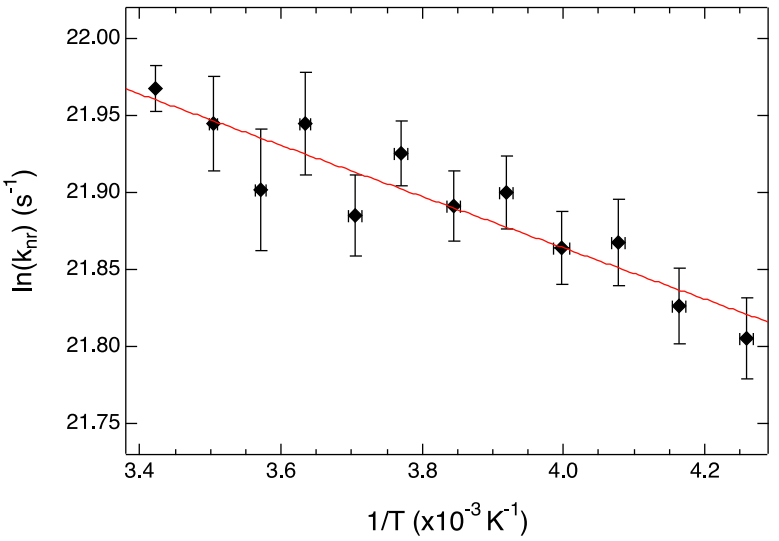

Figure 3.4. Arrhenius plot for average variable-temperature data of $[Fe(dcpp)_2](PF_6)_2$ in MeCN. From these data, the barrierless rate is 165 ± 15 ps^{-1}, and the activation energy is 115 ± 15 cm^{-1}. The correlation was modest, with $R^2 = 0.738$.

To the best of our knowledge, this is the first time a barrierless photophysical process has been definitively identified in a transition metal complex. Barrierless electron transfer has been previously reported in compounds of this type, especially as intramolecular electron transfer in Ru(II) polypyridyls,[29,30] However, most other excited state reactions that proceed with $E_a \sim 0$ cm^{-1} occur in organic fluorophores,[31,32] with respect to some isomerization coordinate,[33-35] or concomitantly with proton transfer (known as excited state intramolecular proton transfer, or ESIPT).[36,37] It has previously been supposed that the MLCT$\rightarrow{}^5T_2$ conversion is likely to occur in a barrierless fashion simply due to the ultrafast timescale of the intersystem crossing,[38] which is observed to be ~130 fs.[39,40] The charge transfer deactivation process is expected to be adiabatic; for the $\Delta S = 2$ ${}^5T_2 \rightarrow {}^1A_1$ transition, which is highly nonadiabatic (i.e., $H_{ab} \sim 6$ cm^{-1}), to be barrierless appears to be unprecedented.

The barrierless nature of $[Fe(dcpp)_2](PF_6)_2$ can on its own explain the very short lifetime of the complex relative to more prototypical Fe(II) chromophores. In Chapter 2, it was determined that the barriers of $[Fe(bpy)_3]^{2+}$ and $[Fe(terpy)_2]^{2+}$ are 310 ± 15 cm^{-1} and 755 ± 70 cm^{-1}, respectively. Knowing that $[Fe(dcpp)_2]^{2+}$ is on a separate Marcus curve from either of these complexes, it still follows that in order for this compound to be in the barrierless region, it must have a greater driving force (ΔG^o) than either of the other two complexes. We have previously described[14] the inherent difficulties in determining an accurate ΔG^o for the ground state recovery process of Fe(II) polypyridyl complexes. To attempt to estimate the reorganization energy (λ) of $[Fe(dcpp)_2]^{2+}$, however, nonradiative decay theory must be used:

$$k_{nr} = \frac{2\pi}{\hbar}|H_{ab}|^2 \frac{1}{\sqrt{4\pi\lambda k_B T}} e^{\frac{-(\lambda+\Delta G^o)^2}{4\lambda k_B T}} \quad (3.3)$$

in which H_{ab} is the electronic coupling element.[27,28] The VT-TA experiment measures k_{nr} as a function of T, leaving ΔG^o, λ, and H_{ab} as unknowns. It is possible to obtain a ratio of H_{ab}^4/λ by

relating the Arrhenius and Marcus equations such that

$$A = \frac{2\pi}{\hbar}|H_{ab}|^2 \frac{1}{\sqrt{4\pi\lambda k_B T}} \quad (3.4)$$

Similarly, ratios of λ and ΔGº may be found from another relationship between these equations:

$$E_a = \frac{(\lambda+\Delta G^o)^2}{4\lambda} \quad (3.5)$$

These are only ratios, though, and no unique values for these three parameters may found without the absolute determination of one of them. Although we have not identified the exact value of ΔGº for any of these complexes, work is ongoing in this realm. We have, however, found a method of approximating ΔGº for the time being in order to better understand the relationship of these parameters in the ground state recovery process. ΔGº is the energetic difference between the ground and excited states in the process of interest. The energies of these electronic states are determined by the ligand field strength of the complex, and thus the Δ_O between the t_{2g} and e_g* set of orbitals.[1] In other six-coordinate compounds such as $[Fe(bpy)_3]^{2+}$ or $[Fe(terpy)_2]^{2+}$, the geometric distortions induced by the ligands make it so that it is inappropriate to discuss the orbitals (and therefore the electronic states) in terms of octahedral symmetry. It is very commonly done, but not the most accurate. In the case of $[Fe(dcpp)_2]^{2+}$, however, the molecule is of higher symmetry and so the octahedral label may be more suitable. Electrochemistry has been used previously[14] to estimate Δ_O, which was extrapolated to discuss ΔGº for ground state recovery in these Fe(II) polypyridyls. The premise being that the (II/III) oxidation potential for iron center should effectively give a measure of the energy of the t_{2g} orbitals. Assuming the e_g* orbitals are unaffected, a stabilization would correspond to a greater ligand field strength, and therefore a greater displacement between the $^5T_2$ and $^1A_1$. This assumption has inherent faults but is the best approximation available to us at this time. For the determination of ΔGº of $[Fe(dcpp)_2]^{2+}$, the oxidation potential is taken relative to that of $[Fe(bpy)_3]^{2+}$, for which we have a high level of

confidence in its driving force. Specifically, eqn. (3.6) is used:

$$\Delta G^{\circ}_{[Fe(dcpp)_2]^{2+}} = \Delta G^{\circ}_{[Fe(bpy)_3]^{2+}} + \left(E^{ox}_{[Fe(dcpp)_2]^{2+}} - E^{ox}_{[Fe(bpy)_3]^{2+}}\right) \quad (3.6)$$

in which E^{ox} is the Fe(II/III) couple for the complex of interest, and ΔG^{o} of $[Fe(bpy)_3]^{2+}$ is taken as -7300 cm^{-1}.[14,26]

One of the intriguing aspects of $[Fe(dcpp)_2]^{2+}$ is the fact that its oxidation potential is so positively shifted compared to either $[Fe(bpy)_3]^{2+}$ or $[Fe(terpy)_2]^{2+}$. Whereas the latter two complexes have Fe(II/III) potentials on the order of 0.66 and 0.71 V vs. $Ag/AgNO_3$ (respectively), the same potential for $[Fe(dcpp)_2]^{2+}$ is 1.29 V. A greater amount of energy, therefore, is required to remove an electron from the metal center for this complex than for the more traditional Fe(II) polypyridyls. Supposing that the energy of the e_g* orbitals has remained constant across all three complexes, the driving force for $[Fe(dcpp)_2]^{2+}$ is -12220 cm^{-1}, nearly double that of the other two complexes. This is in keeping with the barrierless nature of $[Fe(dcpp)_2]^{2+}$, which would require increased driving force to speed up the rate of reaction relative to transitions occurring in the Marcus normal region.

With an estimate of ΔG^{o} in hand, the other two Marcus parameters, λ and H_{ab}, can be found (Table 3.2). Error bars of ±10% are placed on ΔG^{o} to represent the uncertainty of that value, and error is propagated through the calculations (see Appendix C). Using eqn. (3.5), λ is found to be 14800 ± 1600 cm^{-1}. Likewise, H_{ab} can be determined from eqn. (3.4) to be 5.6 ± 0.2 cm^{-1}, reflecting the highly nonadiabatic nature of the $\Delta S = 2$ spin transition from the $^5T_2$ to the $^1A_1$ state. This value of reorganization energy is already significantly higher than that of $[Fe(bpy)_3]^{2+}$ (11000 ± 1000 cm^{-1}) but is in keeping with the λ of $[Fe(terpy)_2]^{2+}$ (14100 ± 1200 cm^{-1}). Similarly, the H_{ab}^4/λ ratio which is postulated to represent the nuclear motion of the ground state recovery transition is 1/(15 ± 2), which is the same as that of $[Fe(terpy)_2]^{2+}$. Considering the tridentate nature of the dcpp and

terpy ligands, it seems reasonable that the two complexes might relax via similar pathways. In the case of $[Fe(terpy)_2]^{2+}$, ultrafast X-ray experiments[41] and theoretical considerations[42] have suggested that the complex relaxes along a ligand rocking motion coordinate. Unlike the terpy ligand which remains relatively planar when bound to Fe(II), the dcpp ligand with its extended distance between pyridyl rings from the carbonyl moieties has the capability of wrapping around the metal center. With this geometry, a rocking motion for dcpp as ground state recovery occurs seems less likely. However, the work by Britz et al. used extended X-ray absorption fine structure (EXAFS) spectroscopy to study the geometry of $[Fe(dcpp)_2]^{2+}$ as it relaxed through its excited state pathway upon photoexcitation.[6] EXAFS showed that while the Fe-N_{ax} bond distance only increased from 1.96 ± 0.01 to 2.05 ± 0.02 Å between the $^1A_1$ to $^5T_2$ states, respectively, the equatorial bond distances changed much more drastically from 1.98 ± 0.01 to 2.21 ± 0.02 Å. These data seem to imply that a rocking motion could be possible, as could a scissoring-type motion. As was the case with the VT-TA results of $[Fe(bpy)_3]^{2+}$ and $[Fe(terpy)_2]^{2+}$, these VT results of $[Fe(dcpp)_2]^{2+}$ (particularly the H_{ab}^4/λ ratio) appear to confirm ultrafast X-ray spectroscopy results, thereby confirming the importance and relevance of this methodology.

Table 3.2. Arrhenius and Marcus parameter values of $[Fe(dcpp)_2]^{2+}$ relative to $[Fe(bpy)_3]^{2+}$ and $[Fe(terpy)_2]^{2+}$.

Complex	A (ps^{-1})	E_a(cm^{-1})	$-\Delta G^o$ (cm^{-1})[a]	λ (cm^{-1})	H_{ab} (cm^{-1})	H_{ab}^4/λ
$[Fe(dcpp)_2]^{2+}$	165 ± 15	115 ± 15	12220 ± 1220	14800 ± 1600	5.6 ± 0.2	1/(15 ± 2)
$[Fe(bpy)_3]^{2+}$	230 ± 20	310 ± 15	7300 ± 730	11000 ± 1000	4.4 ± 0.2	1/(30 ± 5)
$[Fe(terpy)_2]^{2+}$	150 ± 55	755 ± 70	7600 ± 760	14100 ± 1200	6.2 ± 1.2	1/(14 ± 9)

a Values calculated from electrochemical data from ref. 5 and eqn. (3.6) of this work.

3.2.2 The Role of the Counteranion

Although ultrafast X-ray studies have concluded that the lowest energy excited state of $[Fe(dcpp)_2]^{2+}$ is the $^5T_2$, those same studies showed a Jahn-Teller distortion, implying an amount of participation from a triplet ligand field state.[6] It is safe to say that the ligand field strength of dcpp is much greater than that of either bpy or terpy, as evidenced by the barrierless ground state recovery transition. Thus, the original proposition of Jamula et al. that $[Fe(dcpp)_2]^{2+}$ appears to be near the $^5T_2/^3T_1$ crossing point on the Tanabe-Sugano diagram is reasonable.[5] The goal of this work is to determine the role of outer-sphere effects on the barrierless transition. Reactions occurring in the Marcus barrierless region are by necessity energetically very delicate: $E_a \lesssim k_BT$, so in principle, very little outside influence would be required to tip the reaction from barrierless to either the normal or inverted region. Exactly how much energy would be required to push the ligand field strength such that the $^3T_1$ is the lowest energy excited state is as yet unknown, though work is ongoing in that respect, and will be discussed further (vide infra).

The fine energetic balance between two ligand field states described here is very reminiscent of spin-crossover (SCO) complexes, which are predicated on that very concept.[43] The difference being that the two ligand field states for $[Fe(dcpp)_2]^{2+}$ are the lowest and second-lowest excited states, whereas with SCO complexes, it is the ordering of the ground and lowest energy excited state in question. While external forces such as pressure, temperature, and light are capable of driving the electronic configuration change necessary to switch the electronic states, it is also possible for subtler perturbations on energy to induce the same effects as $\Delta G^o \sim k_BT$. Historically, non-coordinating solvent and counterion have been used extensively.[44-47] We, therefore, will study these outer-sphere influences on the ground state recovery of $[Fe(dcpp)_2]^{2+}$ to determine how parallel this reaction is to SCO complexes.

In solution-phase studies, the role of the counterion is to stabilize the charge of the chromophore as well as to (ideally) improve the complex's solubility in the solvent of choice. It is apparent, then, that the counterion will play a role in the thermodynamics of the compound. Many systematic studies of the influence of counterion on an Fe(II) SCO complex observed magnetic properties of the solid-state material. These will be inherently different interactions (i.e., packing forces) than when the molecules are in solution (i.e., solvation energy). That being said, a clear trend has emerged from this literature.[45-47] To illustrate this point, tris{4-[(6-methanol)-2-pyridyl]-3-aza-3-butenyl}amine iron(II) emerges as a strong case study, in which the counterion was varied to study the effect of anion size.[46] These data, as well as analogous studies by Lemercier et al. suggest that smaller counterions are better able to stabilize the e_g* orbitals, decreasing the ligand field strength, and forming the high-spin complex, whereas larger counterions allow for the complex to exist in its low-spin configuration.[47] The analysis of these results is predicated on the ability of the larger anions to disrupt the crystal lattice, which only presents as the sample is in the solid phase.

In this work, the size of the counterion was increased from BF_4^- to PF_6^- to BAr^{F-}. These three complexes were studied in MeCN so as to isolate any effects from the anion. The VT measurements of the ground state recovery lifetimes of $[Fe(dcpp)_2](BF_4)_2$ and $[Fe(dcpp)_2](BAr^F)_2$ are shown in Fig. 3.5 and 3.6, respectively. That of $[Fe(dcpp)_2](PF_6)_2$ can be found in Fig. 3.3, and the corresponding overlay of the Arrhenius plots is in Fig. 3.7. The data is summarized in Table 3.3. Considering the size and charge density differential between BF_4^- and BAr^{F-}, it is surprising that so little difference was seen in any of the Arrhenius or Marcus parameters between these three salts. All values found are within error of each other.

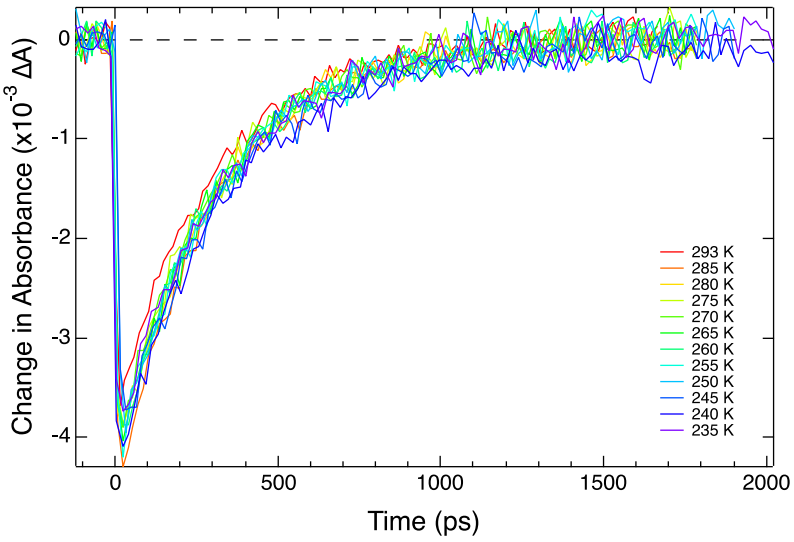

Figure 3.5. Representative variable-temperature lifetimes of $[Fe(dcpp)_2](BF_4)_2$ in MeCN. Excitation occurred at 490 nm, and a 540 nm probe was used. At room temperature (red) the lifetime of the complex is 295 ± 5 ps, and at 235 K (purple) the average lifetime is 325 ± 10 ps.

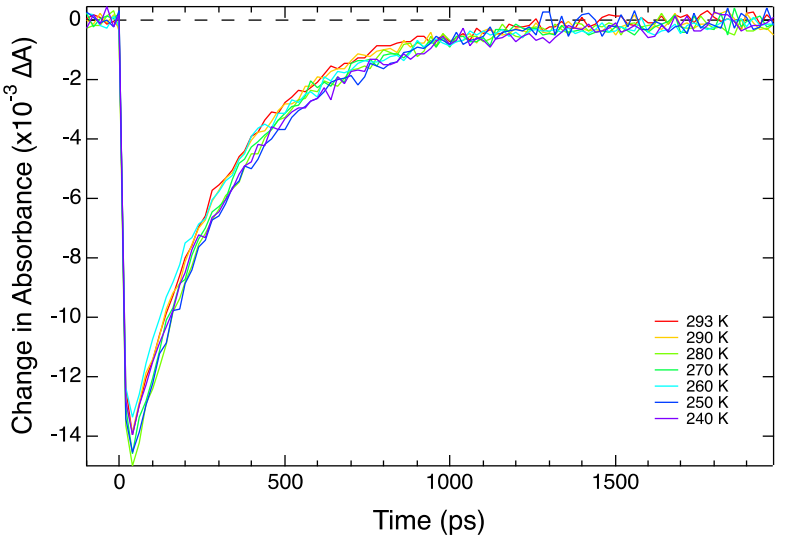

Figure 3.6. Representative variable-temperature lifetimes of $[Fe(dcpp)_2](BAr^F)_2$ in MeCN. Excitation occurred at 490 nm, and a 540 nm probe was used. At room temperature (red) the lifetime of the complex is 285 ± 5 ps, and at 235 K (not shown) the average lifetime is 315 ± 5 ps.

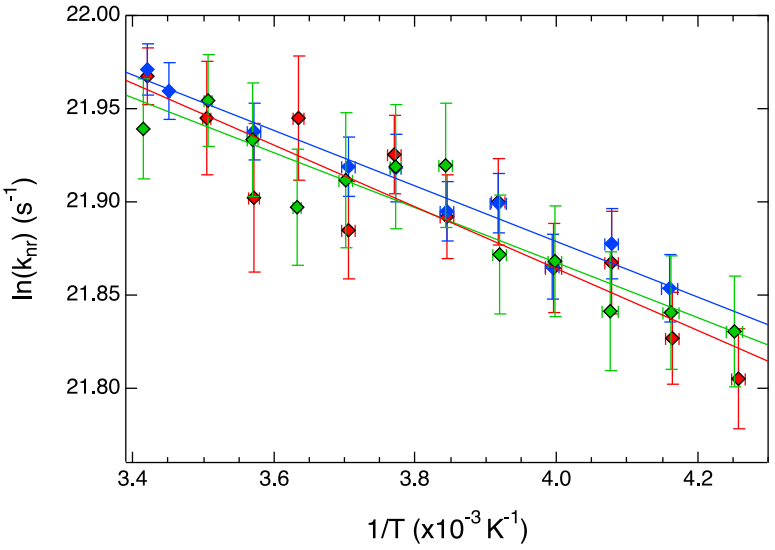

Figure 3.7. Overlaid Arrhenius plot for average variable-temperature data of $[Fe(dcpp)_2](PF_6)_2$ (red), $[Fe(dcpp)_2](BF_4)_2$ (green), and $[Fe(dcpp)_2](BAr^F)_2$ (blue) in MeCN. The Arrhenius values from these plots can be found in Table 3.3. The correlations were modest, with R^2 for the PF_6^- salt being 0.738, 0.580 for the BF_4^- salt, and 0.884 for the BAr^{F-} compound.

Table 3.3. Arrhenius and Marcus parameters of $[Fe(dcpp)_2]^{2+}$ with varying counteranions.

Anion	A (ps^{-1})	E_a(cm^{-1})	$-\Delta G°$ (cm^{-1})	λ (cm^{-1})	H_{ab} (cm^{-1})	H_{ab}^4/λ
BAr^{F-}	170 ± 15	110 ± 20	12220 ± 1220	14800 ± 1600	5.6 ± 0.2	1/(16 ± 3)
PF_6^-	165 ± 15	115 ± 15	12220 ± 1220	14800 ± 1600	5.6 ± 0.2	1/(15 ± 2)
BF_4^-	175 ± 10	105 ± 10	12220 ± 1220	14700 ± 1600	5.5 ± 0.2	1/(17 ± 2)

There are a few possible explanations for this apparent lack of dependence on the counteranion. Firstly, when a halide salt series was studied by Lemercier et al., only the F^- salt was high-spin, whereas the all of the other three halide complexes were SCO, implying that the perturbation imposed from the counterion is very subtle.[47] It is possible that the changes observed

in the Arrhenius average values are real, but so small as to be obscured by the error on the measurements. The specific anions chosen could also be an issue, as there could not be enough size differential between the three. BF_4^- and PF_6^- are very similar in size relative to BF_4^-, so a smaller anion could be desirable. Chloride was considered, but the synthesis of this complex proved to be incredibly cumbersome due to chloride's tendency to preferentially coordinate to the Fe(II) center over the dcpp ligand. Another option might be fluoride, but that would, on its face, appear to present the same challenges as chloride.

Alternatively, it is highly probable that size is not the true parameter of the anion that should be analyzed. While polarizability of the anion may seem like an attractive choice, it cannot tell the whole story. For example, BAr^{F-} is undoubtedly more polarizable than BF_4^-. However, the sheer volume and bulk of BAr^{F-} inhibits its ability to get spatially close to the cation, thereby reducing its ability to stabilize the charged species. A far better parameter is coordinating ability. To be clear, none of the anions being discussed within this work are forming any type of bond with the cation in any way. In fact, all three are typically deemed weakly- or non-coordinating. But the term "coordinating ability" encompasses both the size of the anion, and its polarizability. It describes how close any atom from the anion can get to the metal center of the Fe(II) complex. To get at this, density functional theory calculations have been performed previously, studying many factors of cation-anion pairs.[48] In this work, the coordinating ability of various anions was assessed by the partial charge of the most peripheral atoms. The logic, here, being that the stronger the Lewis base, the more stability afforded to the cation. However, the most basic atom may be at the center of the anion and therefore shielded by larger ligands. The smaller the partial charge, the less coordinating ability of that counteranion. An interesting trend emerged when comparing the three ions of interest for this work. BAr^{F-} showed the weakest coordinating ability (as expected) with a

partial charge on the fluorine of -0.22, and also unsurprisingly, PF_6^- had a strong coordinating ability with a fluorine partial charge of -0.44. What was unexpected was that in the case of BF_4^-, the partial charge on the fluorine was -0.25, indicating that the negative charge was equally distributed amongst the four fluorine atoms, and making its coordinating ability much more similar to that of BAr^{F-} than to PF_6^-.

Regardless of the calculated values, BAr^{F-} and PF_6^- should have distinctly different sizes, polarizabilities, and coordinating abilities. And yet, the VT data show that there is no significant difference in ground state recovery between the two salts. The most obvious conclusion to draw is that the counterion does not effectively alter the ligand field energy in the specific case of $[Fe(dcpp)_2]^{2+}$, at least insofar as to cause the $^3T_1$ to be the lowest energy excited state. This could be due to the lifetime of the complex not being long-lived enough for sufficient stabilization, or it could be that the dcpp ligand effectively shields the Fe(II) center from the counterion. If either of these is a contributing factor, solvation will not have the same limitations, and may provide more insight into the outer-sphere reorganization contributions of $[Fe(dcpp)_2]^{2+}$.

3.2.3 Solvent Effects

In a polar solvation mechanism, the solvent acts to reorient itself to the dipole moment of the solute (see Chapter 4).[15] It follows that a solvent with greater dielectric constant should be better able to lower the energy of a solute with a large dipole moment. Such a phenomenon gives rise to solvatochromism particularly in charge transfer species,[49] though in this work we are more interested in the solvatochromism of the $^5T_2$ excited state. This state is metal-centered, so it would seem unlikely that solvent would play much of a role in its thermodynamics; however, recent work[7] has shown that the ground state recovery of $[Fe(bpy)_3]^{2+}$ is in fact highly dependent on solvent identity. The goal, then, will be to determine if such a solvent exists that is capable of

destabilizing the $^5T_2$ to such an extent that the $^3T_1$ might actually be the lowest energy excited state. A quintet ligand field state should, in principle, be more susceptible to solvation effects due to the greater volume expansion with the doubly occupied e_g* orbitals relative to the triplet state.

With these goals in mind, the effect of solvent on ground state recovery for $[Fe(dcpp)_2]^{2+}$ was studied by VT-TA spectroscopy. The BAr^{F-} salt was utilized so as to make for a clean comparison across the series. The results for MeCN can be seen in Figs. 3.6 and 3.7 (above), while those of EtOAc, acetone, and PC are in Figs. 3.8-3.11. A summary of the solvent data can be found in Tables 3.4 and 3.5. It is immediately apparent that, unlike the counteranions, the solvent does in fact affect the Arrhenius values. As was the case with $[Fe(bpy)_3]^{2+}$, the ground state recovery lifetime at room temperature changes with solvent. The longest lifetime is observed in MeCN, whereas the shortest lifetimes are in PC and acetone, which are within error of each other. This is immediately noteworthy as MeCN and acetone are much closer in dielectric constant than acetone and PC, a first indication that the dielectric constant is not the parameter of interest in these systems. The AN of the solvent also does a poor job of predicting either the lifetime or the barrier of the rate of reaction. As it so happens, the activation energy does initially follow a trend in which it increases with increasing dielectric constant from EtOAc to MeCN. PC, however, does not follow that trend, with an activation energy much closer to 0 cm^{-1}. A note on the average E_a reported for $[Fe(dcpp)_2](BAr^F)_2$ in PC: two data sets were collected in which the activation energy was 60 ± 60 cm^{-1} and 20 ± 35 cm^{-1}. When all the data were collectively fit with the Arrhenius equation, the E_a found was 50 ± 35 cm^{-1} with an R^2 value of 0.115. We believe this value to essentially be 0 cm^{-1} based on the individual plots and find it more likely that in combining the data, a correlation was found by the curve fitting software that does not truly exist.

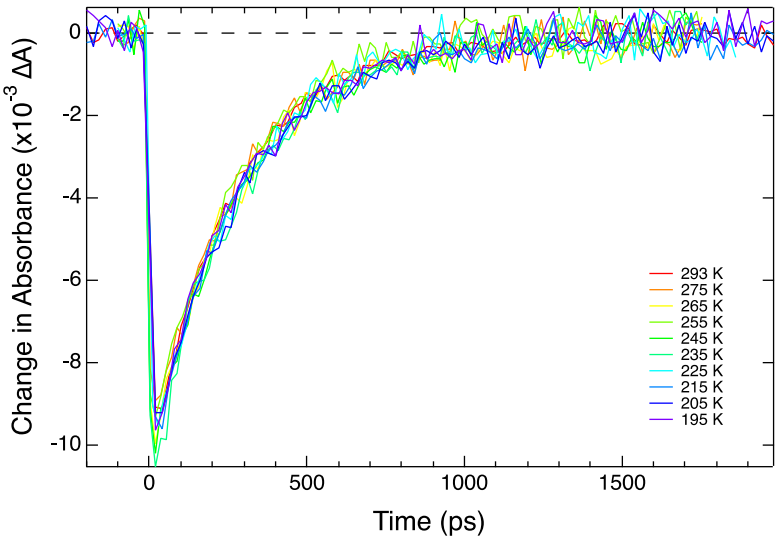

Figure 3.8. Representative variable-temperature lifetimes of $[Fe(dcpp)_2](BAr^F)_2$ in EtOAc. Excitation occurred at 490 nm, and a 540 nm probe was used. At room temperature (red) the lifetime of the complex is 265 ± 5 ps, and at 235 K (cyan) the average lifetime is 275 ± 10 ps.

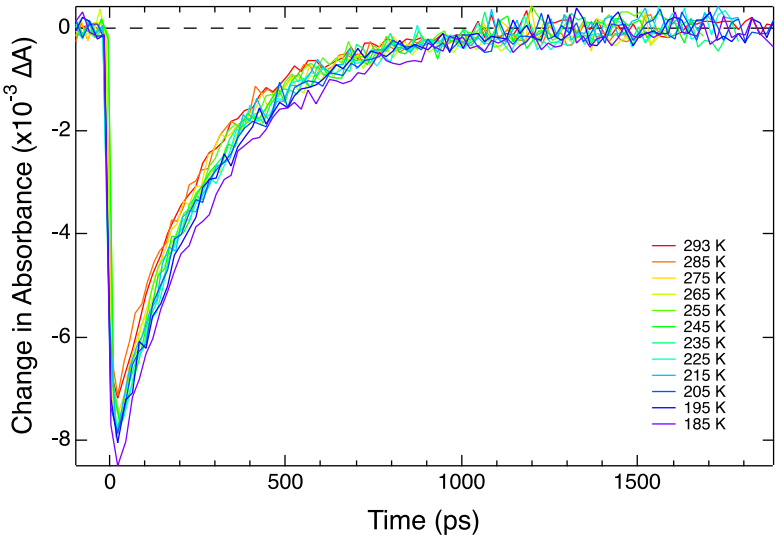

Figure 3.9. Representative variable-temperature lifetimes of $[Fe(dcpp)_2](BAr^F)_2$ in acetone. Excitation occurred at 490 nm, and a 540 nm probe was used. At room temperature (red) the lifetime of the complex is 240 ± 5 ps, and at 235 K (cyan) the average lifetime is 255 ± 10 ps.

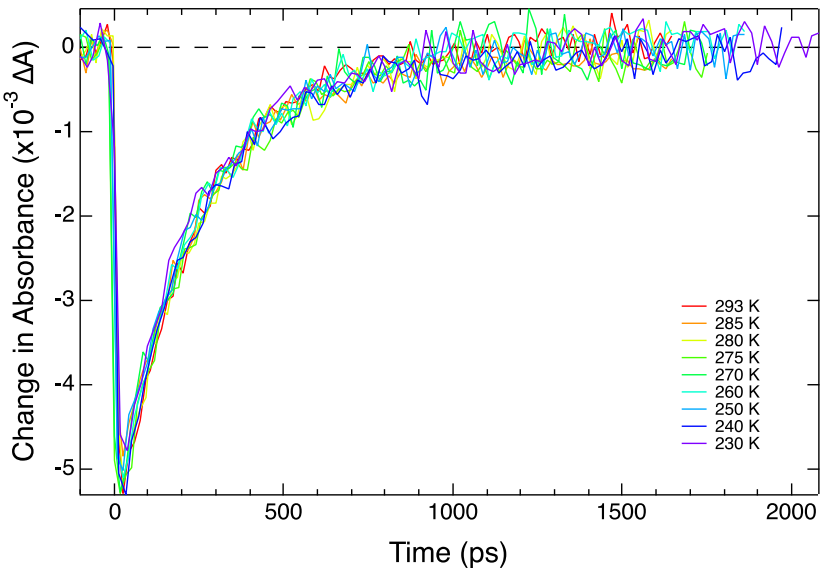

Figure 3.10. Representative variable-temperature lifetimes of $[Fe(dcpp)_2](BAr^F)_2$ in PC. Excitation occurred at 490 nm, and a 540 nm probe was used. At room temperature (red) the lifetime of the complex is 245 ± 5 ps, and at 235 K (not shown) the average lifetime is 255 ± 10 ps.

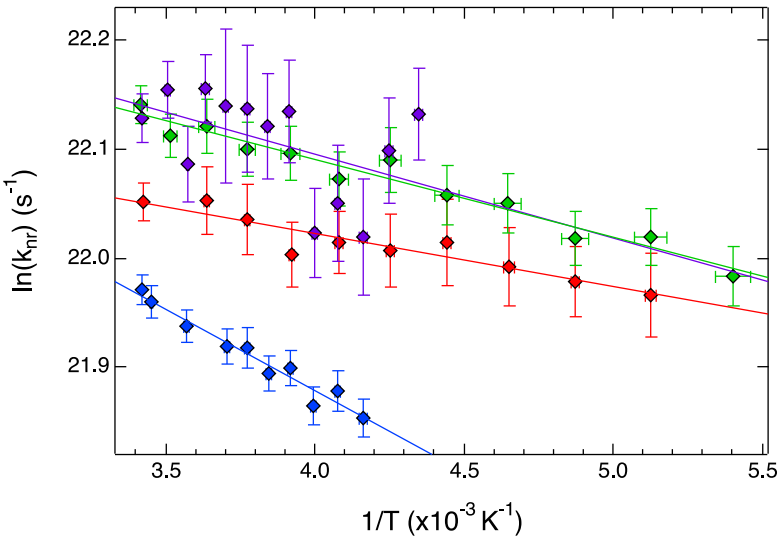

Figure 3.11. Overlaid Arrhenius plot for average variable-temperature data of $[Fe(dcpp)_2](BAr^F)_2$ in EtOAc (red), acetone (green), MeCN (blue), and PC (purple). The Arrhenius values from these plots can be found in Table 3.4. The correlations were modest to poor, with R^2 for the EtOAc data being 0.737, 0.821 for acetone, 0.884 for MeCN, and 0.077 for the PC data.

Table 3.4. Summary of VT-TA data and Arrhenius parameters of $[Fe(dcpp)_2](BAr^F)_2$ in the four different solvents.

Solvent	Lifetime at 293 K (ps)	Lifetime at 235 K (ps)	A (ps^{-1})	E_a(cm^{-1})
PC	245 ± 5	255 ± 10	195 ± 35	50 ± 35
MeCN	285 ± 5	315 ± 5	170 ± 15	110 ± 20
Acetone	240 ± 5	255 ± 10	185 ± 15	55 ± 15
EtOAc	265 ± 5	275 ± 10	225 ± 5	35 ± 5

Table 3.5. Comparison of Marcus parameters of $[Fe(dcpp)_2](BAr^F)_2$ in the four solvents.

Solvent	$-\Delta G^o$ (cm^{-1})	λ (cm^{-1})	H_{ab} (cm^{-1})	H_{ab}^4/λ
PC	12220 ± 1220	13800 ± 1700	5.1 ± 0.5	1/(22 ± 8)
MeCN	12220 ± 1220	14800 ± 1600	5.6 ± 0.2	1/(16 ± 3)
Acetone	12220 ± 1220	14000 ± 1500	5.2 ± 0.2	1/(19 ± 4)
EtOAc	12220 ± 1220	13600 ± 1500	4.7 ± 0.1	1/(28 ± 2)

Based on traditional solvatochromism models around charge transfer-type excited states, it would be expected that the solvents with the greater dielectric constants or ANs would better stabilize the excited states. This was generally observed in the UV-Vis spectra of $[Fe(dcpp)_2](BAr^F)_2$ in these solvents (Fig. 3.2), in which λ_{max} of the ^{1}MLCT in PC (ϵ_0 = 66.14, AN = 18.3) was the lowest energy (609 nm), whereas λ_{max} in EtOAc (ϵ_0 = 6.08, AN = 9.3) was the highest energy (605 nm).[22-25] This clearly did not track to the ligand field excited state. One would expect that if ground state recovery is occurring on the normal side of the Marcus barrierless region, that by increasing one of these parameters of the solvent, the energy of the excited state should be stabilized, thereby resulting in an increased activation energy. The outlier is clearly PC with its barrier of nearly 0 cm^{-1} despite having the largest dielectric constant. The correlation is no better when using AN. It is probable that neither of these solvent properties affects the ligand field states in the same way it affects the ^{1}MLCT, and perhaps a different solvent parameter should be correlated to this trend. However, it may also be that a specific solute-solvent interaction is at work in PC that is not present with any of the other solvents.

What can be said, however, is that the outer-sphere reorganization energy does appear to change with different solvents, more so than with counteranion. By using $[Fe(dcpp)_2](BAr^F)_2$ in

MeCN as a reference (arbitrary), the Δλ should correlate to only outer-sphere contributions as the salt is not changing (Table 3.6). These values of Δλ, it should be noted, are additive to whatever outer-sphere reorganization energy is present in the BAr^{F-} anion in MeCN. All of the changes in λ are smaller than the error bars on any one value of reorganization energy, but a few comments can be made on the trends in the data. First, as has been noted already, the difference induced by counterion is very small, especially relative to that of the solvents. Secondly, the supposed outer-sphere reorganization energy from the solvents is consistently much less than what has been previously reported in the literature (e.g. nearly 0.5 eV) for the $^5T_2 \rightarrow {}^1A_1$ interconversion.[13] Precluding the idea that the BAr^{F-}/MeCN conditions impose 5000 cm^{-1} of outer-sphere reorganization energy, which seems unreasonable considering the non-coordinating nature of BAr^{F-} and the small size of MeCN, it seems safe to say that the outer-sphere contributions are significantly less in this Fe(II) system than has long been estimated.

Table 3.6. Difference in reorganization energy of $[Fe(dcpp)_2]^{2+}$ in different counteranions and solvents relative to BAr^{F-} in MeCN.

Counteranion	Solvent	λ (cm^{-1})	Δλ (cm^{-1})
BF_4^-	MeCN	14700 ± 1600	-100
PF_6^-	MeCN	14800 ± 1600	0
BAr^{F-}	MeCN	14800 ± 1600	-
BAr^{F-}	PC	13800 ± 1700	-1000
BAr^{F-}	Acetone	14000 ± 1500	-800
BAr^{F-}	EtOAc	13600 ± 1500	-1200

On the other hand, $\Delta\lambda$ measured here is an order of magnitude greater than has been cited by Blackbourn and Hupp.[50] In their study of a mixed-valent Ru(II/III) dimer, the outer-sphere reorganization energy was found to be 125-150 cm^{-1} in the first solvation shell. It is difficult to compare their data to the systems studied herein due to the relative inner-sphere reorganizational component. The Ru dimer was found to have $\lambda < 4800$ cm^{-1} due to contributions from spin-orbit coupling and ligand field asymmetry. The inner- to outer-sphere ratio for that system is on the order of 32:1, whereas the incredibly large inner-sphere reorganization energy in $[Fe(dcpp)_2]^{2+}$ gives a ratio closer to 140:1. Drawing a direct parallel to this complex is unwise but provides another point of comparison when analyzing these unique data for $[Fe(dcpp)_2]^{2+}$.

3.2.4 Calculations of Marcus Parameters

Thus far, all of the Marcus values reported have been calculated from the Arrhenius plots with the assumption that ΔG^o is held constant. This is in keeping with the method used here to estimate ΔG^o (with eqn. (3.6) and electrochemical data). Based on chemical intuition, however, this scenario is unlikely. As already mentioned, the purpose of counteranions and solvent is to effectively change the thermodynamics of the electronic states of the complex. ΔG^o then should be modified upon the addition of any of these variable. It has also been previously mentioned, though, that the precise determination of ΔG^o is incredibly challenging for the transitions of interest in this class of complexes. Furthermore, if the driving force for ground state recovery is changing, as we believe it is, the magnitude of $\Delta\Delta G^o$ is likely very small relative to the absolute value of ΔG^o. True, we are discussing barrierless kinetics in which $E_a < k_BT$, but there is no indication that a 1% change in the driving force should have outsized influence over the activation energy.

In an attempt to more fairly, if not accurately, portray the relative changes of the Marcus parameters, these calculations were performed instead holding either λ or H_{ab} constant, the results

of which can be seen in Tables 3.7 and 3.8, respectively. With this method, no single value was changed significantly; the only real difference amongst the results is the size of the error bars. A perfect case is in the comparison of ΔG^o for $[Fe(dcpp)_2](BAr^F)_2$ in acetone. The average value between the three methods changes from -12220 to -13100 cm^{-1}, a 7% difference. The error bars increase from 1200 to 2600 to 5200 when holding ΔG^o, λ, and H_{ab} constant respectively. This serves to illustrate the very tight restraints on the value of H_{ab}. Importantly, the ratio of H_{ab}^4/λ is wholly unaffected based on the method of calculation of the Marcus parameters because this ratio is determined only by A, an experimentally-derived Arrhenius value. The degree of confidence in this ratio is very high, then.

Table 3.7. Marcus values calculated from a constant reorganization energy.

Counteranion	Solvent	$-\Delta G^o$ (cm^{-1})	λ (cm^{-1})	H_{ab} (cm^{-1})	H_{ab}^4/λ
BF_4^-	MeCN	12400 ± 1400	14900 ± 1490	5.4 ± 0.3	1/(17 ± 2)
PF_6^-	MeCN	14700 ± 1700	14900 ± 1490	5.6 ± 0.3	1/(15 ± 2)
BAr^{F-}	MeCN	12300 ± 1700	14900 ± 1490	5.6 ± 0.4	1/(16 ± 3)
BAr^{F-}	PC	13200 ± 5100	14900 ± 1490	5.2 ± 0.6	1/(22 ± 8)
BAr^{F-}	Acetone	13100 ± 2600	14900 ± 1490	5.3 ± 0.3	1/(19 ± 4)
BAr^{F-}	EtOAc	13500 ± 1600	14900 ± 1490	4.8 ± 0.2	1/(28 ± 2)

Table 3.8. Marcus values calculated from a constant electronic coupling matrix element.

Counteranion	Solvent	$-\Delta G^{o}$ (cm^{-1})	λ (cm^{-1})	H_{ab} (cm^{-1})	H_{ab}^4/λ
BF_4^-	MeCN	10900 ± 3200	12900 ± 6100	5.2 ± 0.5	1/(17 ± 2)
PF_6^-	MeCN	28400 ± 8700	11300 ± 5400	5.2 ± 0.5	1/(15 ± 2)
BAr^{F-}	MeCN	9900 ± 3400	11800 ± 6000	5.2 ± 0.5	1/(16 ± 3)
BAr^{F-}	PC	15200 ± 10000	17100 ± 10500	5.2 ± 0.5	1/(22 ± 8)
BAr^{F-}	Acetone	13100 ± 5200	14300 ± 7100	5.2 ± 0.5	1/(19 ± 4)
BAr^{F-}	EtOAc	19700 ± 5800	20700 ± 9300	5.2 ± 0.5	1/(28 ± 2)

In all likelihood, ΔG^{o} has modest changes depending on the solvent and counteranion. It seems reasonable to expect that with a change in driving force, both the reorganization energy and electronic coupling constant will also be affected. Given the nature of these measurements, we are unable to parse out differences in one parameter over the other two. Additionally, given the scale of H_{ab}, it seems highly unlikely for any experimental technique to be capable of determining this parameter to the tenth of a wavenumber. As can be seen in Tables 3.7 and 3.8, however, is that an increase in H_{ab} for $[Fe(dcpp)_2](BAr^F)_2$ in EtOAc from 4.8 to 5.2 cm^{-1} increases reorganization energy to 2.5 eV, a truly unrealistic value.

3.3 The Effect of Excitation Energy

3.3.1 Ground State Recovery

Over the course of the study of $[Fe(dcpp)_2]^{2+}$, the excitation wavelength has been a matter of interest. In work by Brown, it was observed that the ground state recovery process occurs independently of the pump wavelength (as expected), but that the MLCT lifetime does not.[51] It was an open question, then, as to whether or not excitation wavelength would alter the activation

energy or frequency factor. Gaussian deconvolution was performed on the spectra of all three complexes in MeCN, and very little difference was observed between them. As a rule, Gaussian deconvolution of absorption spectra is simply a mathematical way of picturing underlying band structure to a UV-Vis spectrum and is in no way a certainty. Band shape and position is arbitrary based on the fitting software and best initial guess, but it is a method used to approximate electronic potential energy surfaces. The deconvolved spectrum of $[Fe(dcpp)_2](PF_6)_2$ can be found in Fig. 3.12. For the bands predominantly present in the visible region, five Gaussians were required. The band centered around ca. 360 nm has a poor fit owing to the fact that there is a high intensity UV band from the π-π* transition on the ligand should overlap with the blue edge of this MLCT band. The features in the visible region have been previously assigned as being MLCT in nature; visible bands in Fe(II) polypyridyls with extinction coefficients on the order of 10^4 M^{-1} cm^{-1} are commonly accepted as MLCT.[5,51,52] Based on the spectrum in Fig. 3.12, excitation at 490 nm should be preferentially exciting only the band centered at ~500 nm. By pumping at 610 nm, though, that same band may be accessed in addition to the two other lower energy states. The true nature of these MLCT states is unknown: the physical location of the excited electron on the ligand may be crucial information when attempting to analyze the excitation wavelength-dependent MLCT lifetimes, for example. Pump wavelength dependence studies on the VT-TA spectroscopy of $[Fe(dcpp)_2]^{2+}$ attempts to probe this question.

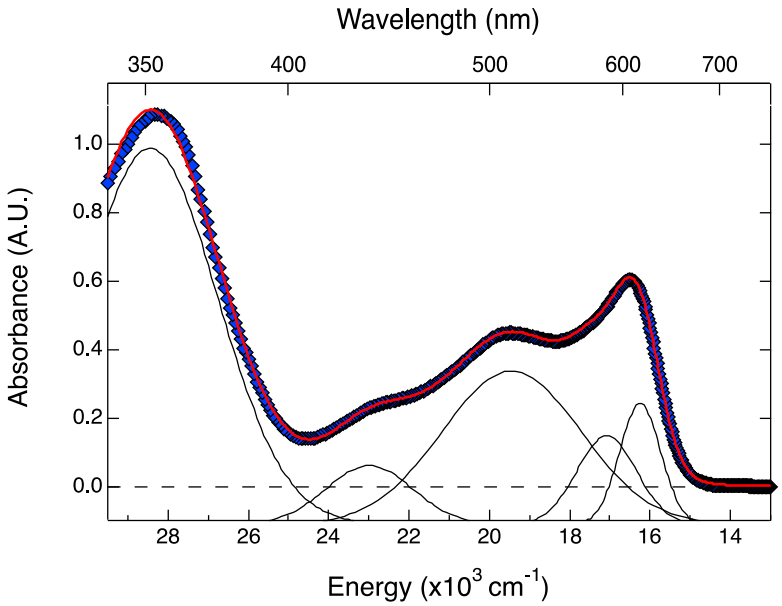

Figure 3.12. Gaussian deconvolution of the ground state absorption spectrum of $[Fe(dcpp)_2](PF_6)_2$ in MeCN. The experimental data are the blue diamonds, the calculated Gaussian bands are the black lines (offset for clarity), and the convolved fit is the red trace.

The ground state recovery lifetime of $[Fe(dcpp)_2]^{2+}$ was studied by VT-TA as a function of pump wavelength with a variety of salts and solvents. A summary of these data can be found in Table 3.9. In comparing the data, no changes are observed based on excitation wavelength. A and E_a in all cases are within error of each other, which propagates into the Marcus parameter calculations. What is noticeably different between the data sets, however, is the goodness of the Arrhenius fit, as represented by R^2. In each case, this value was greater when the pump wavelength was 610 nm, even if the difference was relatively small, as was the case with the PF_6^-/MeCN conditions.

Table 3.9. Summary of parameters measured and calculated from VT-TA of $[Fe(dcpp)_2]^{2+}$ as a function of excitation wavelength.

Counteranion	Solvent	λ_{exc} (nm)	A (ps^{-1})	E_a (cm^{-1})	H_{ab}^4/λ	R^2
BAr^{F-}	MeCN	490	170 ± 15	110 ± 20	1/(16 ± 3)	0.884
BAr^{F-}	MeCN	610	160 ± 5	120 ± 10	1/(14 ± 1)	0.976
PF_6^-	MeCN	490	165 ± 15	115 ± 15	1/(15 ± 2)	0.760
PF_6^-	MeCN	610	185 ± 15	95 ± 15	1/(19 ± 3)	0.776
PF_6^-	Acetone	490	190 ± 10	50 ± 10	1/(20 ± 2)	0.819
PF_6^-	Acetone	610	195 ± 10	50 ± 5	1/(21 ± 2)	0.900
BF_4^-	MeCN	490	175 ± 10	105 ± 10	1/(17 ± 2)	0.580
BF_4^-	MeCN	610	165 ± 20	135 ± 20	1/(15 ± 4)	0.797

In more than one set of data there was the suggestion of bimodal Arrhenius behavior. In these cases, the barrier was essentially 0 cm^{-1} at warmer temperatures (T > 245 K), and 50-100 cm^{-1} at colder temperatures. Where MeCN is the solvent, this phenomenon would not be observable as the freezing point of MeCN is 228 K, limiting the number of lower temperature points able to be collected. As was discussed in Chapter 1, the Arrhenius equation is well-suited to describe reactions in the warm temperature limit. Under this condition, the classical, semi-classical, and quantum mechanical representations of reaction kinetics converge to the same description, which is represented by Arrhenius behavior. At colder temperatures, however, only the lowest vibrational modes will be accessible within an electronic state, and the reaction cannot proceed by surmounting the barrier. A reaction may occur, though, if the wavefunctions of the vibrational modes for both the reactant and product surfaces are coupled.[28] In this case, quantum mechanical

tunneling may occur, in which the electronic conversion transpires via a horizontal process (i.e., energy is conserved).[53] Because thermal energy is not required to facilitate the reaction, these dynamics are temperature-independent. It is possible that any bimodal behavior seen in the Arrhenius plot may be caused by tunneling, as it is observed at colder temperatures. This has been seen in the $^5T_2 \rightarrow {}^1A_1$ transition in an Fe(II) polypyridyl complex previously.[54] The application of VT-TA on the ground state recovery process of $[Fe(dcpp)_2]^{2+}$ at significantly colder temperatures will allow for identification or rejection of the tunneling hypothesis. Tunneling is temperature-independent, and thus the rate of ground state recovery should be unchanged.

These data led to an interesting alternative proposition: if $E_a < k_BT$, does it necessarily follow that the Arrhenius plot will be linear? In acetone, for example, the coldest temperature attainable is 180 K, at which $k_BT = 125\ cm^{-1}$. This value is larger than any measured E_a for $[Fe(dcpp)_2]^{2+}$. It may be entirely possible that for barrierless reactions, the Arrhenius plot should not be linear.

3.3.2 MLCT Lifetimes

One other possibility insinuated by the excitation wavelength dependence results is that upon exciting into the different ^{1}MLCT electronic states, there is a different deactivation pathway into the LF manifold, such that the $^3T_1$ state is more populated via one route than the other (Scheme 3.2). Excitation at 490 nm should create a vibrationally hot ^{1}MLCT state that is highly coupled to lower-lying electronic states due to an increased density of states at higher energies. If the decay pathway is even slightly different from that followed by λ_{exc} = 610 nm, then it may more fully populate the $^3T_1$ relative to the $^5T_2$ considering how coupled and degenerate these two states are postulated to be in this system. Ground state recovery from the $^5T_2$ must occur via a triplet intermediate state due to the $^5T_2 \rightarrow {}^1A_1$ transition being $\Delta S = 2$. If, however, that triplet state is

already partially formed, which may be especially true at warmer temperatures, then the barrier associated with ground state recovery will be lower, if not nearly 0 cm^{-1}. At colder temperatures, the $^3T_1$ may still be populated, though to a lesser degree as there will not be as much thermal energy. In this case, ground state recovery will occur in a more traditional way, i.e., from the $^5T_2$ excited state, and will thus have a larger barrier.

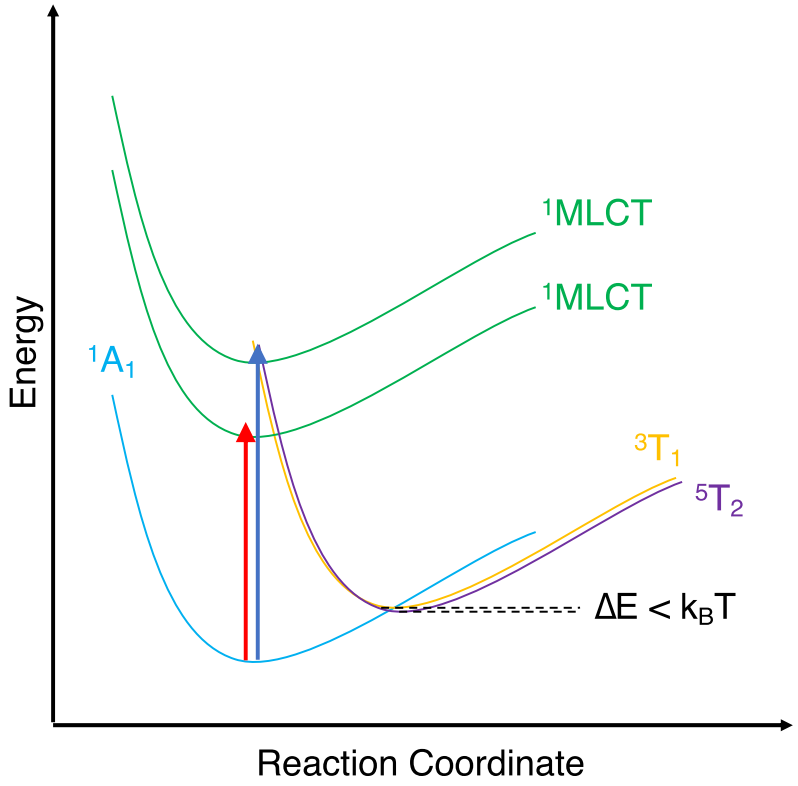

Scheme 3.2. Proposed potential energy surfaces versus some nuclear coordinate (not the Fe-N bond distance) for $[Fe(dcpp)_2]^{2+}$ illustrating the possible relaxation pathways upon excitation at 490 nm (blue arrow) or 610 nm (red arrow) when the $^5T_2$ and $^3T_1$ excited states are nearly degenerate. See text for more details.

Evidence of this proposed mechanism may be given by pump-dependence MLCT lifetime

measurements of $[Fe(dcpp)_2](PF_6)_2$ in MeCN. For these data, the shorter pulse laser system was used. To draw as close a comparison as possible to the VT-TA data, a 540 nm probe was used. At this wavelength, there is a ground state bleach that masks any excited state absorbance features that would be from the MLCT states. The kinetics are of the MLCT deactivation into the lower-lying $^5T_2$ state, as evidenced by a decay from a positive feature (MLCT excited state absorption) into a negative signal (loss of the ground state) that is long-lived. Upon excitation at 490 nm, the MLCT is deactivated with a lifetime of 35 ± 5 fs (Fig. 3.13). This is shorter than the IRF of this system and is corroborated by data previously collected which found a deactivation complete within the 75 fs IRF.[51] Unfortunately, the exact pump-probe combination used in that experiment is unknown. In moving to the 610 nm pump wavelength, the MLCT lifetime is increased by nearly a factor of four to 120 ± 20 fs (Fig. 3.14).

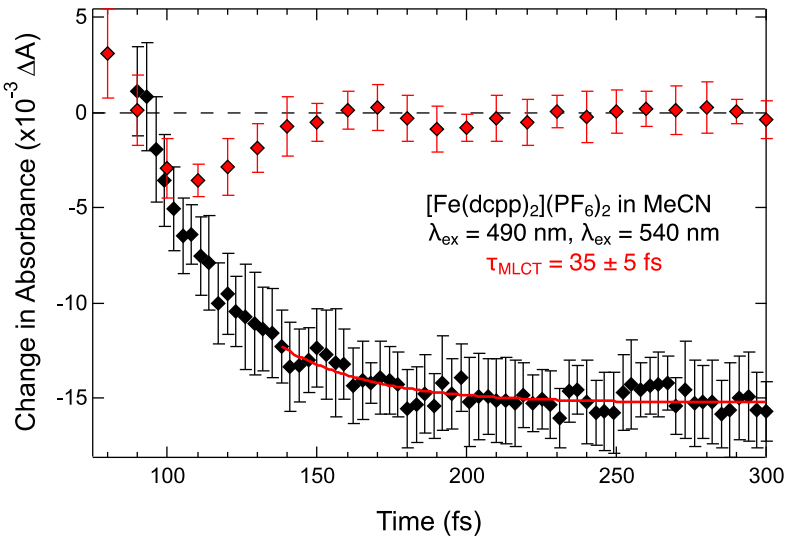

Figure 3.13. Single-wavelength kinetics of $[Fe(dcpp)_2](PF_6)_2$ in MeCN, pumped at 490 nm and probed at 540 nm. The kinetics measured (black diamonds) are those of the deactivation out of the MLCT manifold into the LF manifold and correspond to a MLCT lifetime (red trace) of 35 ± 5 fs. The solvent (red diamonds) data are shown for reference.

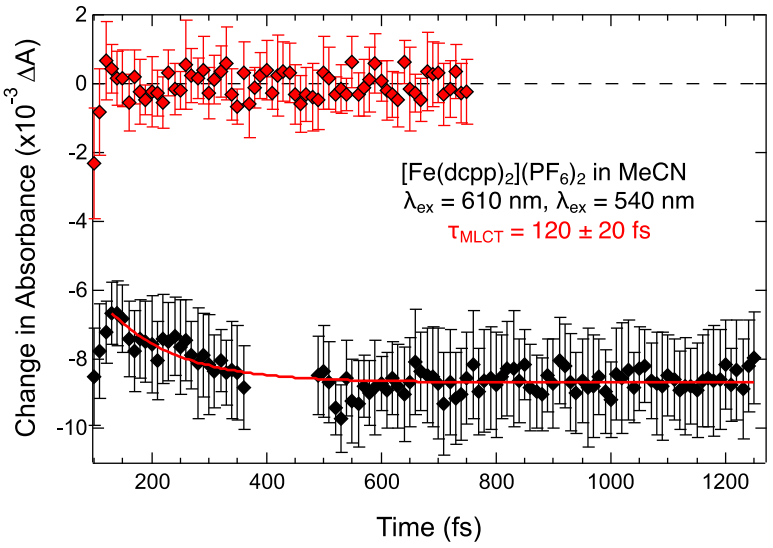

Figure 3.14. Single-wavelength kinetics of $[Fe(dcpp)_2](PF_6)_2$ in MeCN, pumped at 610 nm and probed at 540 nm. The kinetics measured (black diamonds) are those of the deactivation out of the MLCT manifold into the LF manifold and correspond to a MLCT lifetime (red trace) of 120 ± 20 fs. A portion of the data at 375-475 fs is omitted for clarity due to oscillations of unknown origin. The solvent (red diamonds) data are shown for reference.

The decreased rate of deactivation out of the MLCT manifold upon lower energy excitation is unexpected, as pump wavelength-dependent MLCT lifetimes have not – to the best of our knowledge – been previously reported. It does appear to corroborate the notion that at higher energies, there is a greater density of excited states leading to increased electronic coupling to facilitate relaxation into the LF manifold. Based on these results, a further characterization of MLCT lifetimes as a function of pump wavelength is highly desirable so as to gain further understanding of the charge transfer states. If the ultimate goal of work on Fe(II) polypyridyls is to extend the lifetime of the charge-transfer species, a complete characterization of mechanisms by which deactivation occurs is necessary. To further this understanding of the fundamental

photophysical processes in Fe(II) complexes, VT-TA may be performed while monitoring the MLCT lifetime. This will be an incredibly technically challenging experiment owing to the use of the cryostat with ultrashort (<50 fs) laser pulses. But this experiment may give insight into potential energy surface crossings between the MLCT and LF manifolds, information that may otherwise be restricted to theoretical work. This deactivation is ultrafast, it is also highly non-adiabatic, and therefore cannot be represented by semi-classical Marcus theory. But if the vibrational modes associated with the relaxation process can be determined, synthetic modifications may be able to specifically target and hinder those modes, thereby decreasing the rate of deactivation.

As to why a change in MLCT lifetime might affect the R^2 value on an Arrhenius plot of the ground state recovery, the postulation of a metastable $^3T_1$ state degenerate with the $^5T_2$ surface has been put forth. To verify this hypothesis, variable temperature full spectral transient absorption data are desirable. If, as supposed, ground state recovery occurs from both the $^5T_2$ and thermally populated $^3T_1$, then the TA spectrum should inherently have a different appearance than at colder temperatures when only the $^5T_2$ is populated. TA involves the excitation from the ground state, upon which the molecule undergoes its typical relaxation pathway to the lowest energy excited state. The probe then excites from that lowest energy excited state into spin-allowed excited states. When probe absorption occurs from a quintet state, only quintet-quintet transitions are allowed. If, however, both the $^5T_2$ and $^3T_1$ are acting as lowest energy excited state, then absorption into triplet states will also be allowed. The ^{3}MLCT band is present in the UV-Vis spectrum of these Fe(II) complexes (often visualized as a tail on the red edge of the ^{1}MLCT bands), though it is very low intensity, broad, and typically lies underneath the ^{1}MLCT transitions which have much higher extinction coefficients. In that way, VT-ground state absorption spectroscopy may also be

informative about the exact excited states being populated in $[Fe(dcpp)_2]^{2+}$.

3.4 Additional Peculiarities: $[Fe(dcpp)_2]^{2+}$ in Dichloromethane

Through the course of these studies, a wide selection of solvents has been considered and discarded for various reasons. As previously mentioned, protonated solvents react with the carbonyl of the dcpp ligand, and ultimately destroy the complex. In the case of tetrahydrofuran (THF), this solvent was desired for its low dielectric constant (ϵ_0 = 7.58)[25] and AN (8.0).[22] VT data were in fact collected on $[Fe(dcpp)_2](BAr^F)_2$ in THF, but after ca. 16 h, the solution had lost all color. A timed UV-Vis study (Fig. 3.15) shows the disintegration of the complex over time in THF. Over the course of the first four hours, no visible change is observed to the structure of the bands, apart from a systematic decrease in absorbance. Between hours four and five, however, all evidence of the MLCT band has disappeared, indicating the dissociation of the Fe(II) complex. Based on these results, the VT data collected in THF were considered null.

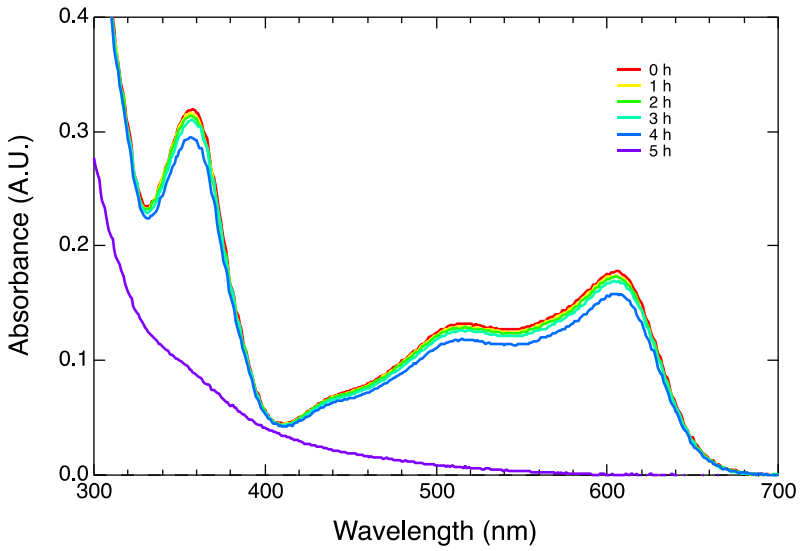

Figure 3.15. Timed ground state absorption study of $[Fe(dcpp)_2](BAr^F)_2$ in THF.

Another alternative with a low dielectric constant was considered: dichloromethane

(DCM), for which ϵ_0 = 8.93;[25] however, this solvent is slightly more complicated by the fact that it has the highest AN, 20.4.[22] It was immediately apparent from the ground state absorption spectrum (Fig. 3.16) that DCM was acting differently upon $[Fe(dcpp)_2]^{2+}$ than any other solvent. The MLCT band centered at 350 nm was of much greater intensity when the complex was dissolved in DCM as opposed to any other solvent. Furthermore, the MLCT maximum is bluer (λ_{max} = 604 nm) than in any other solvent. No VT measurements were made of $[Fe(dcpp)_2](BAr^F)_2$ in DCM, but lifetimes were collected. As was true with $[Fe(bpy)_3]^{2+}$,[7] the lifetime of $[Fe(dcpp)_2]^{2+}$ in DCM is greatly elongated – from 280 ± 10 ps in MeCN to 470 ± 10 ps (Fig. 3.17). That is more than a 50% increase in ground state recovery lifetime. The MLCT lifetime was also lengthened, though modestly, to 180 ± 55 fs when λ_{exc} = 610 nm (Fig. 3.18). This remains one of the longest MLCT lifetimes for a simple Fe(II) polypyridyl complex. It also shows that the solvent is capable of affecting the rate of deactivation from the MLCT into the LF manifold. This has long been understood to be true in Ru(II) polypyridyl complexes, the MLCT in these types of complexes is the lowest energy excited state and survives for nano- to microseconds.[55] Solvent interference in charge transfer excited states with these lifetimes is wholly expected. On the order of a few hundred femtoseconds, however, and as an intermediate to a lower lying excited state, as is the case with Fe(II) complexes, solvation dynamics surrounding the MLCT is not obvious. It is yet another effect that must be further characterized to better understand what influence we have over the lifetime of this charge transfer state. These specific results of $[Fe(dcpp)_2](BAr^F)_2$ in DCM should, though, be taken with a grain of salt. The increased absorbance of the band at λ_{max} = 350 nm may actually indicate a higher concentration of free ligand. ^{1}H NMR studies were performed (Fig. 3.19) in order to determine whether the solvent was having an adverse effect on the compound (e.g., destroying the ligand, dissociating the complex). In this experiment, $[Fe(dcpp)_2](BAr^F)_2$ was

dissolved in $(CD_3)_2CO$, and then compared to the same solution with a drop of undeuterated DCM. Upon addition of the DCM, it was necessary to baseline correct the spectrum through the use of a fifth order polynomial. The reason for this needed correction is unclear. After this is performed, the integrations are unchanged with or without DCM. However, with DCM present, every aromatic signal is shifted upfield, indicating a greater degree of shielding. Furthermore, the signals are not shifted by one constant offset. For example, the triplet centered at 8.79 ppm in $(CD_3)_2CO$ shifts by -0.06 ppm when DCM is added. However, the doublet at 8.11 ppm is shifted by -0.10 ppm upon the addition of DCM. No sign of a paramagnetic species is observed, but these spectra were only collected out to 14.0 ppm. In future studies, this window should be expanded to preclude the presence of any heteroleptic or paramagnetic sample present. Work is currently ongoing to determine the origin of these unusual NMR signals, with the ultimate goal of validating or rejecting the ultrafast measurements that were collected on this compound.

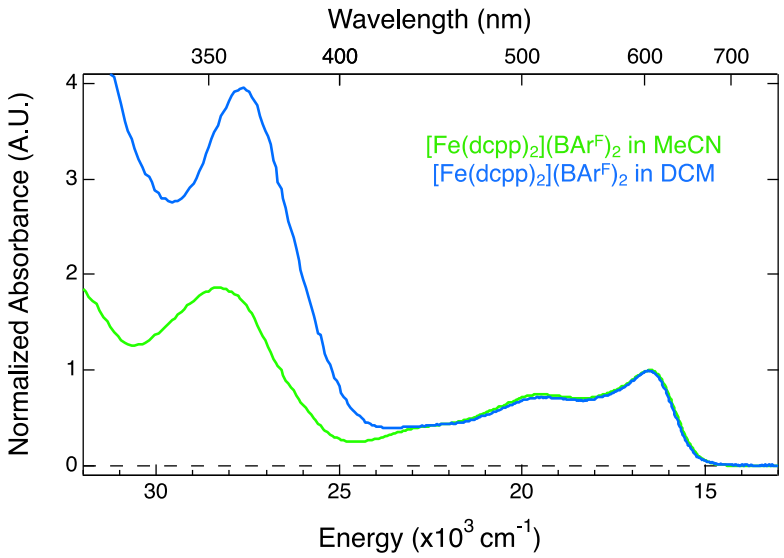

Figure 3.16. Ground state absorption spectra of $[Fe(dcpp)_2](BAr^F)_2$ in MeCN (green) and DCM (blue).

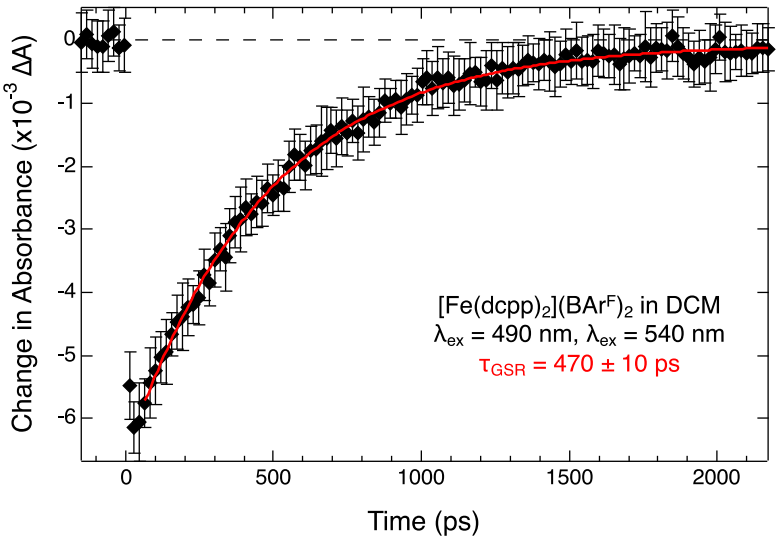

Figure 3.17. Ground state recovery lifetime of [Fe(dcpp)$_2$](BAr^F)$_2$ in DCM (black diamonds) upon excitation at 490 nm and probing at 540 nm. The fit (red trace) showed a lifetime of 470 ± 10 ps.

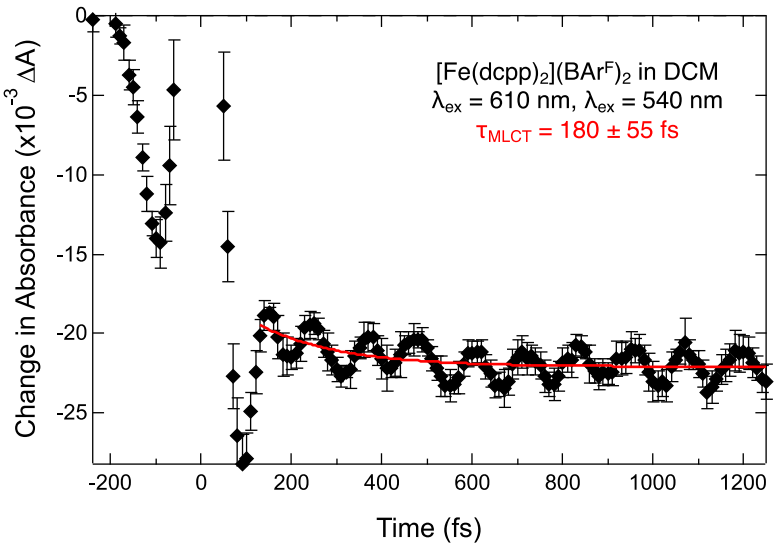

Figure 3.18. MLCT kinetics of [Fe(dcpp)$_2$](BAr^F)$_2$ in DCM measured at 540 nm upon excitation at 620 nm. The data (black diamonds) displayed vibrational coherence caused by the solvent interacting with a very temporally short pump pulse. The fit (red trace) gave a MLCT lifetime of 180 ± 55 fs.

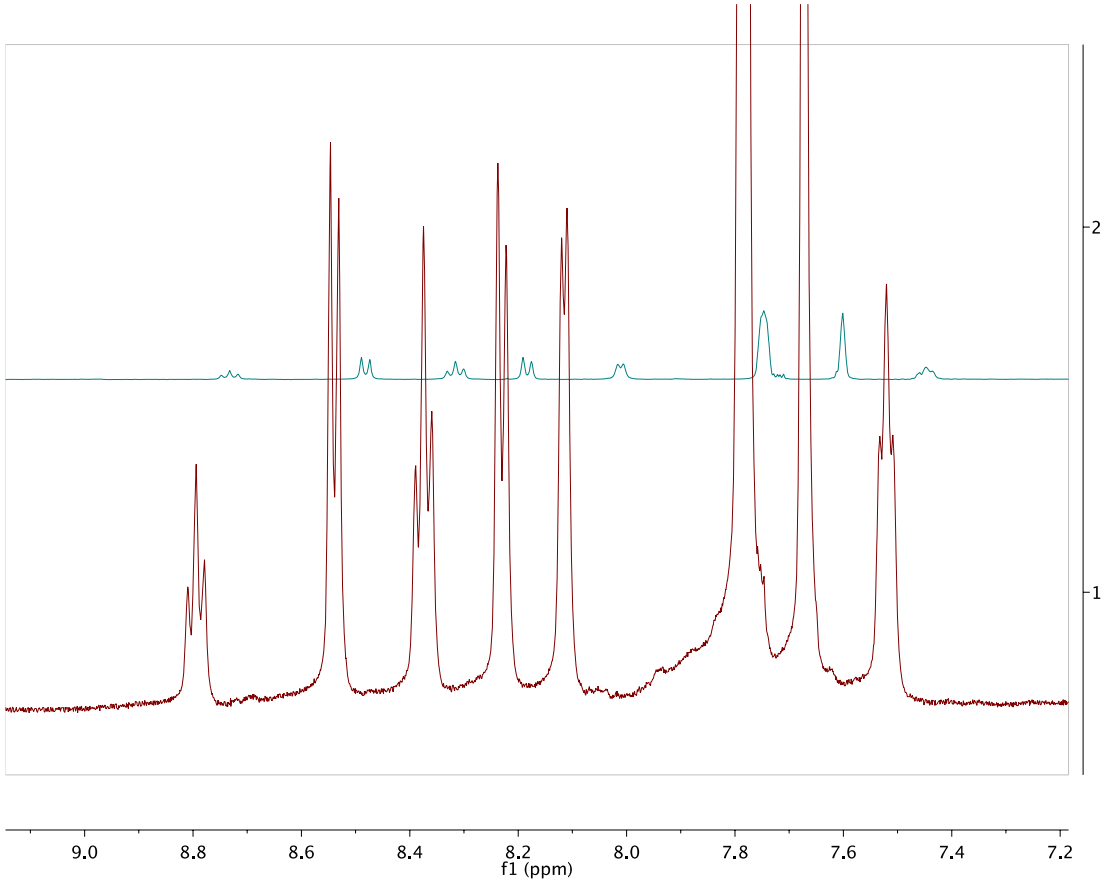

Figure 3.19. ^{1}H NMR of $[Fe(dcpp)_2](BAr^F)_2$ in $(CD_3)_2CO$ (bottom, red) and doped with a small amount of undeuterated DCM (top, green). Assignments can be found in the text.

4. Future Works and Conclusions

Through the use of ultrafast variable-temperature transient absorption spectroscopy, the ground state recovery process in $[Fe(dcpp)_2]^{2+}$ has been studied and found to be nearly barrierless with an activation energy less than k_BT. From the VT-TA data, Arrhenius plots were prepared which allowed for the determination of Marcus parameters through relationships between these two theories. The outer-sphere reorganization energy was estimated by a method inspired by spin-crossover literature, in which the counteranion and solvent was systematically changed to alter the

ligand field strength of the complex. This allowed for $\Delta\lambda$ to be found in reference to $[Fe(dcpp)_2](BAr^F)_2$ in MeCN. It was found that changing the counteranion led to very small differences in reorganization energy (0-100 cm^{-1}), whereas the solvent played a much more important role, inducing $\Delta\lambda$ values of 800-1200 cm^{-1}. It was the BAr^{F-} salt of the complex in propylene carbonate that displayed the most barrierless behavior. No set of conditions affected the ligand field strength so much that the $^3T_1$ became the lowest-lying excited state. However, ultrafast X-ray[6] and pump wavelength dependence studies imply presence of the triplet state during the ground state recovery process. To complete the studies begun here, the best course of action would be for analogous work to be done using the simultaneous ultrafast X-ray absorption and emission spectroscopies described by Britz et al.[6] This method will give much more information on the structure of the complex as a function of counteranion, solvent, and excitation wavelength than can be obtained with visible transient absorption spectroscopy. Only then will real inferences regarding the outer-sphere reorganization energy be able to be made.

The barrierless nature of this complex likely due to it being nearly perfectly octahedral. A secondary consequence of the higher symmetry is the unique absorption profile. These MLCT bands have been assigned, but the exact nature of them is unknown. It would be useful to have a more thorough understanding of these states in order to better design complexes with long-lived MLCT states. Spectroelectrochemistry is a method used to assign an absorption band as MLCT, but it is not capable of giving the physical origin of the charge transfer (e.g., metal-to-carbonyl, metal-to-central pyridyl ring). One technique that could begin to address this question is circular dichroism (CD) spectroscopy. This method uses circularly-polarized light to essentially collect a UV-Vis of a chiral molecule, such as $[Fe(dcpp)_2]^{2+}$.[56,57] CD spectroscopy has been previously performed on $[Fe(bpy)_3]^{2+}$, a D_3 molecule in its crystal form, and displayed bisignate features

centered around the MLCT bands.[58] In layman's terms, the MLCT of $[Fe(bpy)_2]^{2+}$ can, to a first approximation, be deconvolved into two Gaussians. In the CD spectrum, a positive feature corresponded to the red Gaussian, and then flipped its sign such that a negative feature occurred in the position of the blue Gaussian. This has been postulated to be caused by $L\pi^* \leftarrow M\pi$ along two separate axes,[58] though the exact assignment has been a source of debate for over 50 years.[56] Knowing the axes along which MLCT excitation is occurring can bring molecular-level insight into the analysis of the photophysical properties of $[Fe(dcpp)_2]^{2+}$. Additionally, time-dependent density functional theory calculations on $[Fe(dcpp)_2]^{2+}$ may be able to provide a deeper understanding of the location of the wavefunctions at different excitation energies. Work is ongoing in that respect with our collaborators, the Jakubikova group at North Carolina State University.

Finally, the outer-sphere reorganization energy can be studied in a slightly modified way: via the solvation effects on iron(II) cyanides and cyano-substituted Fe(II) chromophores. This phenomenon[4] has already been looked at to a certain extent with the $[Fe(bpy)(CN)_4]^{2-}$ complex,[2,3,19] but further work may help derive new understanding of solvent-solute and solvent-solvent interactions. In fact, Yang et al. used solvatochromism to estimate the reorganization energy of a series of $[Fe(bpy')(CN)_4]^{2-}$ complexes.[19] The polar N-end of the cyano ligand interacts strongly with solvent molecules, particularly very polar molecules, and those capable of forming hydrogen bonds.[4] When bound directly to the metal center, as is the case with $[Fe(bpy)(CN)_4]^{2-}$, the influence of the solvent on the cyanide will be directly relayed to the iron center. Whereas when the -CN moiety is a substituent on the bpy ligand, as with tris(4,4'-dicyano-2,2'-bipyridine) iron(II), $[Fe(4,4'\text{-}CN\text{-}bpy)_3]^{2+}$, CN-solvent interaction will be not affect the metal as strongly due to shielding from the bipyridine. An Arrhenius and Marcus analysis on compounds such as

$[Fe(4,4'\text{-}CN\text{-}bpy)_3]^{2+}$, $[Fe(bpy)_2(CN)_2]$, and $[Fe(bpy)(CN)_4]^{2-}$ will be able to get a measure of the outer-sphere reorganization energy with solvents that interact with various degrees of strength to the cyano group. Additionally, inner-sphere contributions may be able to be estimated from these measurements as well, and the influence of the solvent directly through the CN group to the iron versus solvent effects on the CN mediated by the bipyridine linkage to the metal center. The ultrafast variable-temperature methodology is still very young but holds limitless promise in its ability to educate us further on the fundamental properties of these iron chromophores.

REFERENCES

REFERENCES

1. Figgis, B. N.; Hitchman, M. A. *Ligand Field Theory and Its Applications*; Wiley-VCH: New York, 2000.

2. Zhang, W.; Kjær, K. S.; Alonso-Mori, R.; Bergmann, U.; Chollet, M.; Fredin, L. A.; Hadt, R. G.; Hartsock, R. W.; Harlang, T.; Kroll, T.; Kubiček, K.; Lemke, H. T.; Liang, H. W.; Liu, Y.; Nielsen, M. M.; Persson, P.; Robinson, J. S.; Solomon, E. I.; Sun, Z.; Sokaras, D.; van Driel, T. B.; Weng, T.-C.; Zhu, D.; Wärnmark, K.; Sundström, V.; Gaffney, K. J. Manipulating Charge Transfer Excited State relaxation and Spin Crossover in Iron Coordination Complexes With Ligand Substitution. *Chem. Sci.* **2017**, *8*, 515-523; DOI: 10.1039/C6SC03070J.

3. Kjær, K. S.; Kunnus, K.; Harlang, T. C. B.; van Driel, T. B.; Ledbetter, K.; Hartsock, R. W.; Reinhard, M. E.; Koroidov, S.; Li, L.; Laursen, M. G.; Biasin, E.; Hansen, F. B.; Vester, P.; Christensen, M.; Haldrup, K.; Nielsen, M. M.; Chabera, P.; Liu, Y.; Tatsuno, H.; Timm, C.; Uhlig, J.; Sundström, V.; Németh, Z.; Szemes, D. S.; Bajnóczi, É.; Vankó, G.; Alonso-Mori, R.; Glownia, J. M.; Nelson, S.; Sikorski, M.; Sokaras, D.; Lemke, H. T.; Canton, S. E.; Wärnmark, K.; Persson, P.; Cordones, A. A.; Gaffney, K. J. Solvent Control of Charge Transfer Excited State Relaxation Pathways in $[Fe(2,2'\text{-bipyridine})(CN)_4]^{2-}$. *Phys. Chem. Chem. Phys.* **2018**, *20*, 4238-4249; DOI: 10.1039/c7cp07838b.

4. Schilt, A. A. Mixed Ligand Complexes of Iron(II) and (III) with Cyanide and Aromatic Di-imines. *J. Am. Chem. Soc.* **1960**, *82*, 3000-3005; DOI: 10.1021/ja01497a007.

5. Jamula, L. L.; Brown, A. M.; Guo, D.; McCusker, J. K. Synthesis and Characterization of a High-Symmetry Ferrous Polypyridyl Complex: Approaching the $^5T_2/^3T_1$ Crossing Point for Fe^{II}. *Inorg. Chem.* **2014**, *53*, 15-17; DOI: 10.1021/ic402407k.

6. Britz, A.; Assefa, T.; Galler, A.; Gawełda, W.; Khakhulin, D.; Doumy, G.; March, A. M.; Németh, Z.; Pápai, M.; Roszályi, E.; Cho, H.; Kim, T. K.; Yarranton, J. T.; Mukherjee, S.; Schoenlein, R. W.; Jakubikova, E.; Huse, N.; McCusker, J. K.; Southworth, S. H.; Young, L.; Vankó, G.; Bressler, Ch. $[Fe(dcpp)_2]^{2+}$ Ligand-Field Excited State Geometry and Spin Characterized with Combined Ultrafast X-ray Spectroscopies. *Submitted.*

7. Miller, J. N.; McCusker, J. K. Outer-Sphere Effects on the Excited State Dynamics of Ligand Field States in Fe(II) Polypyridyl Complexes. *Manuscript in preparation.*

8. Haldrup, K.; Vankó, G.; Gawełda, W.; Galler, A.; Doumy, G.; March, A. M.; Kanter, E. P.; Bordage, A.; Dohn, A.; van Driel, T. B.; Kjær, K. S.; Lemke, H. T.; Canton, S. E.; Uhlig, J.; Sundström, V.; Young, L.; Southworth, S. H.; Nielsen, M. M.; Bressler, Ch. Guest-Host Interactions Investigated by Time-Resolved X-ray Spectroscopies and Scattering at MHz Rates: Solvation Dynamics and Photoinduced Spin transition in Aqueous $Fe(bipy)_3^{2+}$. *J. Phys. Chem. A* **2012**, *116*, 9878-9887; DOI: 10.1021/jp306917x.

9. Lawson, Daku, L. M. Spin-State Dependence of the Structural and Vibrational Properties of

Solvated Iron(II) Polypyridyl Complexes from AIMD Simulations: Aqueous $[Fe(bpy)_3]Cl_2$, a Case Study. *Phys. Chem. Chem. Phys.* **2018**, *20*, 6236-6253; DOI: 10.1039/c7cp07862e.

10. Lawson Daku, L. M.; Hauser, A. Ab Initio Molecular Dynamics Study of an Aqueous Solution of $[Fe(bpy)_3](Cl)_2$ in the Low-Spin and in the High-Spin States. *J. Phys. Chem. Lett.* **2010**, *1*, 1830-1835; 10.1021/jz100548m.

11. Bressler, Ch.; Gawełda, W.; Galler, A.; Nielsen, M. M.; Sundström, V.; Doumy, G.; March, A. M.; Southworth, S. J.; Young, L.; Vankó, G. Solvation Dynamics Monitored by Combined X-ray Spectroscopies and Scattering: Photoinduced Spin Transition in Aqueous $[Fe(bpy)_3]^{2+}$. *Faraday Discuss.* **2014**, *171*, 169-178; 10.1039/c4fd00097h.

12. Haldrup, K.; Gawełda, W.; Abela, R.; Alonso-Mori, R.; Bergmann, U.; Bordage, A.; Cammarata, M.; Canton, S. E.; Dohn, A. O.; van Driel, T. B.; Fritz, D. M.; Galler, A.; Glatzel, P.; Harlang, T.; Kjær, K. S.; Lemke, H. T.; Møller, K. B.; Németh, Z.; Pápai, M.; Sas, N.; Uhlig, J.; Zhu, D.; Vankó, G.; Sundström, V.; Nielsen, M. M.; Bressler, Ch. Observing Solvation Dynamics with Simultaneous Femtosecond X-ray Emission Spectroscopy and X-ray Scattering. *J. Phys. Chem. B* **2016**, *120*, 1158-1168; 10.1021/acs.jpcb.5b12471.

13. Watanabe, I.; Ono, K.; Ikeda, S. Photoelectron Emission Study of Iron(II) and Cobalt(II) Complexes in Aqueous Solution. Reorganization Energies. *Bull. Chem. Soc. Jpn.* **1991**, *64*, 352-357; 10.1246/bcsj.64.352.

14. Carey, M. C.; Adelman, S. L.; McCusker, J. K. Insights Into the Excited State Dynamics of Fe(II) Polypyridyl Complexes from Variable-Temperature Ultrafast Spectroscopy. *Submitted.*

15. Carey, M. C.; Li, S.; Damrauer, N. H.; McCusker, J. K. Excitation Energy-Induced Dual Solvation Mechanism in Ru(II) Polypyridyl Revealed by Ultrafast Spectroscopy. *Manuscript in preparation.*

16. Juban, E. A.; McCusker, J. K. Ultrafast Dynamics of ^2E State Formation in $Cr(acac)_3$. *J. Am. Chem. Soc.* **2005**, *127*, 6857-6865; DOI: 10.1021/ja042153i.

17. Monat, J. E.; McCusker, J. K. Femtosecond Excited-State Dynamics of an Iron(II) Polypyridyl Solar Cell Sensitizer Model. *J. Am. Chem. Soc.* **2000**, *122*, 4092-4097; DOI: 10.1021.ja992436o.

18. Brown, A. M.; McCusker, C. E.; Carey, M. C.; Blanco-Rodriguez, A. M.; Towrie, M.; Clark, I. P.; Vlček, A.; McCusker, J. K. Vibrational Relaxation and Redistribution Dynamics in Ruthenium(II) Polypyridyl-Based Charge-Transfer Excited States: A Combined Ultrafast Electronic and Infrared Absorption Study. *J. Phys. Chem. A*; DOI: 10.1021/acs.jpca.8b06197.

19. Yang, M.; Thompson, D. W.; Meyer, G. J. Charge-Transfer Studies of Iron Cyano Compounds Bound to Nanocrystalline TiO_2 Surfaces. *Inorg. Chem.* **2000**, *41*, 1254-1262; DOI: 10.1021/ic011069q.

20. Timpson, C. J.; Bignozzi, C. A.; Sullivan, B. P.; Kober, E. M.; Meyer, T. J. Influence of Solvent on the Spectroscopic Properties of Cyano Complexes of Ruthenium(II). *J. Phys. Chem.* **1996**, *100*, 2915-2925; DOI: 10.1021/jp953179m.

21. Posse, M. E. G.; Katz, N. E.; Baraldo, L. M.; Polonuer, D. D.; Colombano, C. G.; Olabe, J. A. Comparative Bonding and Photophysical Properties of 2,2'-Bipyridine and 2,2'-Bipyrazine in Tetracyano Complexes Containing Ruthenium and Osmium. *Inorg. Chem.* **1995**, *34*, 1830-1835; DOI: 10.1021/ic00111a034.

22. Gutmann, V. *The Donor-Acceptor Approach to Molecular Interactions*; Plenum: New York, USA, 1978.

23. Chastrette, M.; Carretto, J. Statistical Study of Solvent Effects-II Analysis of Some Empirical Parameters of Solvent Polarity. *Tetrahedron* **1982**, *38*, 1615-1618; DOI: 10.1016/0040-4020(82)80137-3.

24. Marcus, Y. *Solvent Mixtures: Properties and Selective Solvation*; CRC Press: Taylor & Francis Group: New York, 2002.

25. CRC Handbook of Chemistry and Physics, 98th ed., http://hbcponline.com-/faces/documents/06_33/06_33_0001.xhtml, (accessed June 2018).

26. Sutin, N. Nuclear, Electronic, and Frequency Factors in Electron-Transfer Reactions. *Acc. Chem. Res.* **1982**, *15*, 275-282; DOI: 10.1021/ar00081a002.

27. Marcus, R. A.; Sutin, N. Electron Transfers in Chemistry and Biology. *Biochim. Biophys. Acta* **1985**, *811*, 265-322; DOI: 10.1016/0304-4173(85)90014-X.

28. Barbara, P. F.; Meyer, T. J.; Ratner, M. A. Contemporary Issues in Electron Transfer Research. *J. Phys. Chem.* **1996**, *100*, 13148-13168; DOI: 10.1021/jp9605663.

29. Gaal, D. A.; Hupp, J. T. Thermally Activated, Inverted Interfacial Electron Transfer Kinetics: High Driving Force Reactions Between Tin Oxide Nanoparticles and Electrostatically-Bound Molecular Reactants. *J. Am. Chem. Soc.* **2000**, *122*, 10956-10963; DOI: 10.1021/ja0024744.

30. Meylemans, H. A.; Lei, C. F.; Damrauer, N. H. Ligand Structure, Conformational Dynamics, and Excited-State Electron Delocalization for Control of Photoinduced Electron transfer Rates in Synthetic Donor-Bridge-Acceptor Systems. *Inorg. Chem.* **2008**, *47*, 4060-4076; DOI: 10.1021/ic701776k.

31. Ovejas, V.; Fernández-Fernández, M.; Montero, R.; Longarte, A. On the Ultrashort Lifetime of Electronically Excited Thiophenol. *Chem. Phys. Lett.* **2016**, *661*, 206-209; DOI: 10.1016/j.cplett.2016.08.082.

32. Du, M.; Fleming, G. R. Femtosecond Time-Resolved Fluorescence Spectroscopy of Bacteriorhodopsin: Direct Observation of Excited State Dynamics in the Primary Step of the Proton Pump Cycle. *Biophys. Chem.* **1993**, *48*, 101-111; DOI: 10.1016/0301-

4622(93)85002-Y.

33. Ghosh, R.; Nandi, A.; Palit, D. K. Solvent Sensitive Intramolecular Charge Transfer Dynamics in the Excited States of 4-*N*,*N*-dimethylamino-4'-nitrobiphenyl. *Phys. Chem. Chem. Phys.* **206**, *18*, 7661-7671; DOI: 10.1039/C5CP07778H.

34. Dobryakov, A. L.; Quick, M.; Richter, C.; Knie, C.; Ioffe, I. N.; Granovsky, A. A.; Mahrwald, R.; Ernsting, N. P.; Kovalenko, S. A. Photoisomerization Pathways and Raman Activity of 1,1'-difluorostilbene. *J. Chem. Phys.* 2017, 146, 044501; DOI: 10.1063/1.4974357.

35. Ma, F.; Yartsev, A. Ultrafast Photoisomerization of Pinacyanol: Watching an Excited State Reaction Transiting From Barrier to Barrierless Forms. *RSC Adv.* **2016**, *6*, 45210-45218; DOI: 10.1039/C6RA03299K.

36. Chou, P.-T.; Chen, Y.-C.; Yu, W.-S.; Chou, Y.-H.; Wei, C.-Y.; Cheng, Y.-M. Excited-State Intramolecular Proton Transfer in 10-Hydroxybenzo[h]quinoline. *J. Phys. Chem. A* **2001**, *105*, 1731-1740; DOI: 10.1021/jp002942w.

37. Che, M.; Gao, Y.-J.; Zhang, Y.; Xia, S.-H.; Cui, G. Electronic Structure Calculations and Nonadiabatic Dynamics Simulations of Excited-State Relaxation of Pigment Yellow 101. *Phys. Chem. Chem. Phys.* **2018**, *20*, 6524-6532; DOI: 10.1039/C7CP07692D.

38. Chergui, M. Ultrafast Photophysics of Transition Metal Complexes. *Acc. Chem. Res.* **2015**, *48*, 801-808; DOI: 10.1021/ar500358q.

39. Zhang, W.; Alonso-Mori, R.; Bergmann, U.; Bressler, Ch.; Chollet, M.; Galler, A.; Gawełda, W.; Hadt, R. G.; Hartsock, R. W.; Kroll, T.; Kjær, K. S.; Kubiček, K.; Lemke, H. T.; Liang, H. W.; Meyer, D. A.; Nielsen, M. M.; Purser, C.; Robinson, J. S.; Solomon, E. I.; Sun, Z.; Sokaras, D.; van Driel, T. B.; Vankó, G.; Weng, T.-C.; Zhu, D.; Gaffney, K. J. Tracking Excited-State Charge and Spin-Dynamics in Iron Coordination Complexes. *Nature* **2014**, *509*, 345-348; DOI: 10.1038/nature13252.

40. Consani, C.; Prémont-Schwarz, M.; ElNahhas, A.; Bressler, Ch.; van Mourik, F.; Cannizzo, A.; Chergui, M. Vibrational Coherences and Relaxation in the High-Spin State of Aqueous $[Fe(bpy)_3]^{2+}$. *Angew. Chem. Int. Ed.* **2009**, *48*, 7184-7187; DOI: 10.1002/anie.200902728.

41. Vankó, G.; Bordage, A.; Pápai, M.; Haldrup, K.; Glatzel, P.; March, A. M.; Doumy, G.; Britz, A.; Galler, A.; Assefa, T.; Cabaret, D.; Juhin, A.; van Driel, T. B.; Kjær, K. S.; Dohn, A.; Møller, K. B.; Lemke, H. T.; Gallo, E.; Rovezzi, M.; Németh, Z.; Rozsályi, E.; Rozgonyi, T.; Uhlig, J.; Sundström, V.; Nielsen, M. M.; Young, L.; Southworth, S. H.; Bressler, Ch.; Gawełda, W. Detailed Characterization of a Nanosecond-Lived Excited State: X-ray and Theoretical Investigation of the Quintet State in Photoexcited $[Fe(terpy)_2]^{2+}$. *J. Phys. Chem. C* **2015**, *119*, 5888-5902; DOI: 10.1021/jacs.jpcc.5b00557.

42. Nance, J.; Bowman, D. N.; Mukherjee, S.; Kelley, C. T.; Jakubikova, E. Insights into the Spin-State Transitions in $[Fe(tpy)_2]^{2+}$: Importance of the Terpyridine Rocking Motion. *Inorg. Chem.* **2015**, *54*, 11259-11268; DOI: 10.1021/acs.inorgchem.5b01747.

43. Goodwin, H. A. Spin Transitions in Six-Coordinate Iron(II) Complexes. *Coord. Chem. Rev.* **1976**, *18*, 293-325; DOI: 10.1016/S0010-8545(00)80430-0.

44. Real, J. A.; Gaspar, A. B.; Muñoz, M. C. Thermal, Pressure, and Light Switchable Spin-Crossover Materials. *Dalton Trans.* **2005**, 2062-2079; 10.1039/B501491C.

45. Gütlich, P.; Hauser, A.; Spiering, H. Thermal and Optical Switching of Iron(II) Complexes. *Angew. Chem. Int. Ed.* **1994**, *33*, 2024-2054; DOI: 10.1002/anie.199420241.

46. Klug, C. M.; McDaniel, A. M.; Fiedler, S. R.; Schulte, K. A.; Newell, B. S.; Shores, M. P. Anion Dependence in the Spin-Crossover Properties of a Fe(II) Podand Complex. *Dalton Trans.* **2012**, *41*, 12577-12585; 10.1039/C2DT31213A.

47. Lemercier, G.; Verelst, M.; Bousseksou, A.; Varret, F.; Tuchagues, J.-P. Towards Control of the Intrinsic Characteristics of Spin-Crossover in Ferrous Materials. In *Magnetism: A Supramolecular Function*; Kahn, O., Ed.; Springer: Dordrecht, 1996; Vol. 484; pp 335-356.

48. Krossing, I.; Raabe, I. Relative Stabilities of Weakly Coordinating Anions: A Computational Study. *Chem. Eur. J.* **2004**, *10*, 5017-1030; DOI: 10.1002/chem.200400087.

49. Curtis, J. C.; Sullivan, B. P.; Meyer, T. J. Hydrogen-Bonding-Induced Solvatochromism in the Charge-Transfer Transitions of Ruthenium(II) and Ruthenium(III) Ammine Complexes. *Inorg. Chem.* **1983**, *22*, 224-236, and references therein; DOI: 10.1021/ic00144a009.

50. Blackbourn, R. L.; Hupp, J. T. Probing the Molecular Basis of Solvent Reorganization in Electron-Transfer Reactions. *J. Phys. Chem.* **1988**, *92*, 2817-2820; DOI: 10.1021/j100321a024.

51. Brown, A. M. Excited-State Dynamics of Iron(II)-Based Charge-Transfer Chromophores. Ph.D. Thesis, Michigan State University, East Lansing, MI, 2011.

52. Creutz, C.; Chou, M.; Netzel, T. L.; Okumura, M.; Sutin, N. Lifetimes, Spectra, and Quenching of the Excited States of Polypyridine Complexes of Iron(II), Ruthenium(II) and Osmium(II). *J. Am. Chem. Soc.* **1980**, *102*, 1309-1319; DOI: 10.1021/ja00524a014.

53. DeVault, D. *Quantum-Mechanical Tunnelling in Biological Systems*, 2nd ed.; Cambridge University Press: New York, 1984, and references therein.

54. Conti, A. J.; Xie, C.-L.; Hendrickson, D. N. Tunneling in Spin-State Interconversion of Ferrous Spin-Crossover Complexes: Concentration Dependence of Apparent Activation Energy Determined in Solution by Laser-Flash Photolysis. *J. Am. Chem. Soc.* **1989**, *111*, 1171-1180; DOI: 10.1021/ja00186a002.

55. Juris, A.; Balzani, V.; Barigelletti, F.; Campagna, S.; Belser, P.; von Zelewsky, A. Ru(II) Polypyridine Complexes: Photophysics, Photochemistry, Electrochemistry, and Chemiluminescence. *Coord. Chem. Rev.* **1988**, *84*, 85-277, and references therein; DOI: 10.1016/0010-8545(88)80032-8.

56. Bosnich, B. Application of Exciton Theory to the Determination of the Absolute Configurations of Inorganic Complexes. *Acc. Chem. Res.* **1969**, *2*, 266-273; 10.1021/ar50021a002.

57. Braterman, P. S.; Noble, B. C.; Peacock, R. D. Circular Dichroism Spectra of Δ-$[Ru(bpy)_3]^{2+/+/0/-}$. *J. Phys. Chem.* **1986**, *90*, 4913-4915; 10.1021/j100412a006.

58. Dragna, J.; Pescitelli, G.; Tran, L.; Lynch, V. M.; Anslyn, E. V.; Di Bari, L. *In Situ* Assembly of Octahedral Fe(II) Complexes for the Enantiomeric Excess Determination of Chiral Amines Using Circular Dichroism Spectroscopy. *J. Am. Chem. Soc.* **2012**, *134*, 4398-4407; 10.1021/ja211768v.

CHAPTER 4. DUAL SOLVATION MECHANISM IN RU(II) POLYPYRIDYL COMPLEX DRIVEN BY EXCITATION ENERGY

1. Introduction

In the realm of photovoltaic devices, Ru(II)-based polypyridyl complexes remain some of the most highly studied chromophores.[1-3] These compounds tick many of the most important boxes. They have long-lived charge-separated excited states that are primarily metal-to-ligand charge transfer (MLCT), formally $\{Ru^{II}(L)_6\} \overset{h\nu}{\rightarrow} \{Ru^{III}(L^{-})(L)_5\}$, with lifetimes on the order of hundreds of nanoseconds to microseconds. The MLCT excited state not only takes a metal-centered electron and promotes it onto the periphery of the compound, thereby making it useful for electron collection, but these types of excited states also absorb visible photons well which is critical for solar energy applications. If the goal is to use these complexes for light-to-energy conversion, it is critical to understand the various radiative and nonradiative ways through which energy is diverted and lost, as these processes will ultimately limit the efficiency of the chromophores.

The prototypical Ru(II) polypyridyl is $[Ru(bpy)_3]^{2+}$, with bpy being 2,2'-bipyridine. This complex has been studied extensively, particularly as a point of comparison for some of its decorated analogues. One such complex is $[Ru(dpb)_3]^{2+}$ (dpb = 4,4'-diphenyl-2,2'-bipyridine, Scheme 4.1), which has displayed an anomalously high quantum yield (Φ) for the formation of the ^{3}MLCT, by some estimates a factor of six greater than that of $[Ru(bpy)_3]^{2+}$.[4,5] Damrauer and coworkers studied the photophysical properties of $[Ru(dpb)_3]^{2+}$ and found the specific nature of the substituent must play a critical role based on the observation that Φ for the 4,4'-dimethyl-substituted $[Ru(dmb)_3]^{2+}$ complex is only twice that of $[Ru(bpy)_3]^{2+}$.[6] Therefore it was postulated

that the delocalization afforded by the phenyl substituent was the main determinant of the increased the radiative rate (k_r) in $[Ru(dpb)_3]^{2+}$ relative to its analogues. In fact, *ab initio* results found that while the ring was canted ~44º in the ground state, as a radical (mimicking the MLCT excitation) the phenyl rotated such that the entire system was coplanar. While these calculations were performed on 4-phenylpyridine for simplicity, the results were suggestive of a delocalized excited state.[6,7] Electrochemical data supported this conclusion by showing that the $^3MLCT/^1A_1$ energy gap in $[Ru(dpb)_3]^{2+}$ was nearly identical to that of $[Ru(dmb)_3]^{2+}$; the measured difference actually indicated the gap was 200-300 cm^{-1} less in the phenyl version of the complex, which would imply a reduced k_r. The alternative was that extended conjugation of the dpb ligand would decrease the nuclear coordinate between the ground and excited states, thereby increasing reducing vibrational overlap and thus decreasing k_{nr}. This hypothesis was tested by time-resolved resonance Raman spectroscopy of $[Ru(dpb)_3]^{2+}$, and its mesitylated analogue, $[Ru(dmesb)_3]^{2+}$ (Scheme 4.1). The mesityl substituent nominally extends delocalization just as is the case with the phenyl ring, however the *ortho*-methyl groups sterically hinder coplanarity from being achieved in the MLCT excited state. The results from the Raman spectroscopy appeared to corroborate the hypothesis: upon excitation, the C=C ring stretch at 1615 cm^{-1} in the ground state shifted to significantly lower energy (1548 cm^{-1}) in $[Ru(dmesb)_3]^{2+}$ than in $[Ru(dpb)_3]^{2+}$ (1599 cm^{-1}). These data were interpreted as the phenyl ring with its ability to rotate to coplanarity with the bipyridine backbone was less distorted in the excited state than the mesityl.[6]

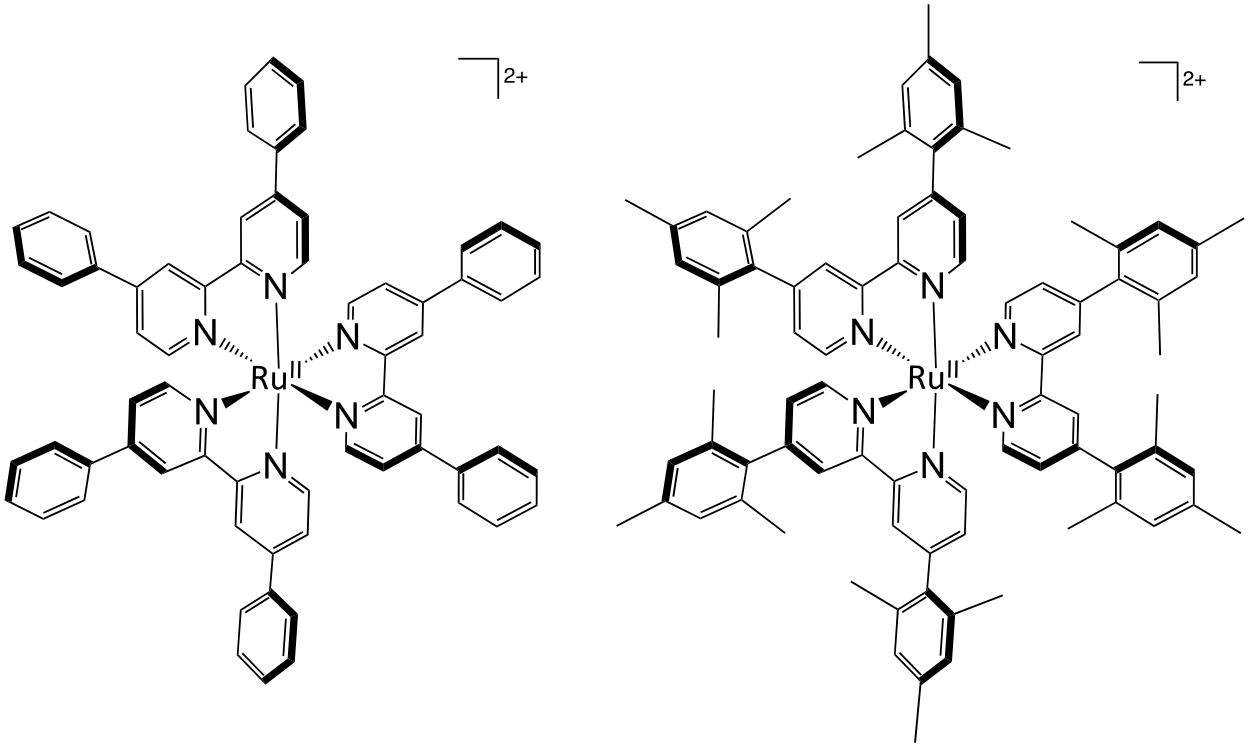

Scheme 4.1. Perspective drawings of the two complexes that are featured most prominently in this work, inspired by Damrauer and coworkers[6]: (Left) $[Ru(dpb)_3]^{2+}$ and (Right) $[Ru(dmesb)_3]^{2+}$.

To further investigate the photophysical properties of $[Ru(dpb)_3]^{2+}$, Damrauer and McCusker used ultrafast transient absorption (TA) spectroscopy.[8] Using spectroelectrochemistry, the excited state absorption feature centered around 532 nm was determined to be an indicator of the reduced intraligand excited state dynamics. Upon excitation at 400 nm into the ^{1}MLCT, two ultrafast components were observed at 532 nm: $\tau_1 = 200 \pm 50$ fs and $\tau_2 = 2.0 \pm 0.5$ ps. The shorter kinetic component was also observed in $[Ru(dmb)_3]^{2+}$ on the order of 120 fs, and was attributed, in part, to ^{1}MLCT→^{3}MLCT intersystem crossing. However, τ_2 in $[Ru(dmb)_3]^{2+}$ was 5.0 ± 0.5 ps. From these results, it was concluded that at this pump-probe combination and in acetonitrile, vibrational cooling on the ^{3}MLCT surface was being observed with the faster rate in $[Ru(dpb)_3]^{2+}$ indicating that the ring rotation facilitated the vibrational relaxation process.[8] Not only did these

data serve as further confirmation of a delocalized excited state, they also indicated the timescale on which the phenyl rotation and consequent ^{3}MLCT excited state thermalization occurs.

Polar solvation is the response of solvent molecules to the charge redistribution of a solute.[9,10] Intramolecular charge transfer, as occurs in MLCT transitions, are commonly studied in the solute as these drive large solvent reorganization. There are primary two types of solvent effects, static and dynamic. Where static solvation raises or lowers the energy of activation of a reaction, the dynamic response affects the rate of reaction. This dynamic process is actually a combination of solvent reorientation modes and proceeds on a multitude of timescales. The shortest (<500 fs) is modeled well by a Gaussian distribution and is often referred to as the "inertial" response of a solvent to the solute.[11] A single to tens of picoseconds process also occurs that is the relaxation of the bulk solvent; this may be known as dielectric friction if the solvent is dipolar (i.e., having a permanent dipole moment) or viscoelastic when nonpolar.

The inertial component is typically more solute-solvent interactions, whereas the solvent relaxation involves solvent-solvent dynamics.[12,13] Thus, concentration of the solute can affect the time scale of the solvation response.[10] In a complex undergoing a MLCT transition, for example, the positive dipole of the solvent will reorient toward the ligand with the excited electron so as to stabilize the energy of this state. As the electron relaxes back to the metal center, the solvent molecules will have been forced to position their dipoles in the same direction; without a charged species to orient to, the electrostatic repulsion will force the solvent molecules to reorganize into lower energy, random directions. In low solute concentrations, then, the loss of the CT excited state affords an increased solvent reorientation rate as the solvent concentration is high. Likewise, the more polar the solvent, the faster the rate of solvent relaxation.[9]

The shorter time component in solvation dynamics typically dominates the amplitude of

the response, but the slower kinetic process is critical, particularly in larger solute molecules. Collisions between the solute and solvent may occur in these types of chromophores. More commonly, dielectric friction may be present in polar solvents which is made up of the dipole-dipole interactions between solute and solvent molecules. Upon charge redistribution in the former, the solvent mechanically reorients, often via rotation, to the newly formed dipole moment in the solute.[10] Translation of the solvent may also occur but is less energetically efficient than rotation and librational motion.[11]

$[Ru(dpb)_3]^{2+}$ provides a unique opportunity to study the effect of multiple driving forces for vibrational relaxation occurring simultaneously. Immediately upon excitation, the ^{1}MLCT excited state decays rapidly (<100 fs)[14,15] to a vibrationally hot ^{3}MLCT state. In the charge-separated excited state, a large instantaneous dipole moment exists which should induce a strong response from a polar solvent. Furthermore, the process being studied on the picosecond timescale is ascribed to vibrational cooling, in which excess energy from the excitation event is dissipated by the solute into the solvent bath. Polar solvation dynamics are likely to be the dominant mechanism coupled to MLCT excitation and vibrational cooling in $[Ru(dpb)_3]^{2+}$. However, these dynamics are likely to be complicated by the large-amplitude motion of the phenyl. Rotation of a large aromatic on its own is a predominantly frictional force, and is therefore likely to induce bulk solvent translation, or even a nonpolar solvation response.[11,16] In this type of solvation mechanism, the viscosity of the solvent plays a much larger role, dictating the rate of solvent translation away from the solute.[17]

No near transition metal analogue for the dichotomy of large instantaneous dipole versus bulky reorganization that is displayed in $[Ru(dpb)_3]^{2+}$ was able to be found in the literature. Large-amplitude motion dynamics have been studied previously in intramolecular electron transfer

reactions primarily in organic chromophores such as 9,9'-bianthryl and 4-(9-anthryl)-N,N-dimethylaniline.[10,18] Some of the closest examples of what may be observed come in the form of organic complexes that display what is known as a twisted intramolecular charge transfer (TICT) excited state. Complexes such as 9,9'-bianthryl exist in a certain nonpolar conformation in the ground state, and upon excitation, produce a charge-separated species that forces a geometric rotation. In this compound, the rate of the electron transfer reaction was found to be much shorter than was predicted by the solvent longitudinal (i.e., translational) relaxation time constant.[18] This time constant is a measure of the bulk solvent response in the absence of a solute molecule, and as such neglects any specific solute-solvent interactions that dictate particularly the short-time kinetics of solvation.[1] The results for 9,9'-bianthryl were reported for a series of n-alkane nitrile solvents; specific solvation dynamics become increasingly more important in H-bonding species, such as n-alcohols. Studies were performed on a fluorescent probe molecule, 4-N,N-dimethylaminobenzonitrile in a series of linear alcohols.[19,20] In shorter-chain alcohols like methanol and ethanol, the solvation dynamics were well-described by a single exponential function, whereas longer-chain solvents displayed multiexponential behavior. Again, the solvation relaxation time was found to be far shorter than the longitudinal relaxation time. Together, these data served to show that the solvent molecules were more intimately to the excited state of the chromophore than is implied by the bulk solvent parameters. It is apparent then that the specific intermolecular interactions must be accounted for within a polar solvation model.

The original work by Damrauer and McCusker provided insight into the photophysical behavior of $[Ru(dpb)_3]^{2+}$, but ultimately left more questions to be answered. The exact nature of the solvation mechanism of this complex, as indicated above, may be guessed at but is yet unknown. Likewise, the physical origins of τ_1 were unable to be determined due to the ~250

instrument response function of the laser system being used. One method that will be used in attempt to address these questions is variable-excitation wavelength studies; these may have the added benefit of shedding further light on the vibrational cooling and phenyl rotation dynamics of $[Ru(dpb)_3]^{2+}$. The goal of this work is to expand on the previously acquired data of the excited state evolution of $[Ru(dpb)_3]^{2+}$. The vibrational cooling time constant is measured in a series of 1-alcohols and 1-nitriles of increasing chain lengths. A competition between the frictional forces of the alkyl chain and the dielectric response of the polar functional will be under investigation. Ultimately this will provide a more complete understanding of the mechanism of excited state evolution in $[Ru(dpb)_3]^{2+}$.

2. Experimental

2.1 Materials and Synthesis

2.1.1 General

All reagents and solvents were used as received, unless otherwise noted. Sodium tetrakis[(3,5-trifluoromethyl)phenyl]borate ($NaBAr^F$, >98%) was generously donated by Thomas Boussie of Rennovia. For synthesis and purification, ethanol (EtOH, Decon Labs, 100%), HCl (Macron Fine Chemicals, ACS grade), acetonitrile (MeCN, Sigma-Aldrich, ACS grade), methanol (MeOH, Sigma-Aldrich, ACS grade), diethyl ether (Et_2O, Sigma-Aldrich, ACS grade), SiO_2 gel (Sorbtech, 40-75 μm), and dichloromethane (DCM, Sigma-Aldrich, ACS grade) were used without further purification. Proton nuclear magnetic resonance (^1H NMR) spectroscopy was performed on a Bruker 500 MHz NMR spectrometer. Electrospray-ionization mass-spectrometry (ESI-MS) data was collected on a Waters Xevo G2-XS Quadrupole Time-of-Flight spectrometer in positive mode.

Tris(4,4'-diphenyl-2,2'-bipyridine) ruthenium(II) dichloride, $[Ru(dpb)_3]Cl_2$. This synthetic route is based on what was reported by Damrauer et al. with modifications.[6,21] The 4,4'-diphenyl-2,2'-bipyridine (dpb) ligand was synthesized by D. M. Arias-Rotondo according to a previously published procedure,[6] and $Ru(DMSO)_4Cl_2$ was prepared by C. R. Tichnell based on a reported route.[22] Free dpb ligand (0.32 mmol, 0.102 g) and $Ru(DMSO)_4Cl_2$ (0.1 mmol, 0.049 g) were added to 10 mL bubble-degassed EtOH. This suspension was heated to reflux on a Schlenk line. As the dpb dissolved, the solution turned a dark orange-brown. The solution was allowed to stir under N_2 with heating for 72 h. To drive precipitation of the chloride salt of the complex, 6 M HCl was added dropwise with stirring under positive N_2 pressure.[21] Immediate precipitation was observed to occur as the suspension became a lighter, brighter orange color that was much more opaque than the solution. The product was filtered and washed with deionized water multiple times. ^{1}H NMR (500 MHz, [D_2O], δ) [9.26 (d, 6 H, J = 2.0 Hz), 8.02 (m, 18 H), 7.86 (dd, 6 H, J = 1.9, 6.1 Hz), 7.58 (m, 18 H)]. CHN analysis of $RuC_{66}H_{48}N_6Cl_2 \cdot 4H_2O$: calculated C 67.80, H 4.83, N 7.19; found C 67.91, H 5.05, N 6.54.

A portion of the $[Ru(dpb)_3]Cl_2$ synthesized above was metathesized to the hexafluorophosphate salt (PF_6^-) with the intention of using this salt to grow single crystals for X-ray diffraction studies. This was previously performed by A. L. Smeigh.

Tris(4,4'-diphenyl-2,2'-bipyridine) ruthenium(II) [(3,5-trifluoromethyl)phenyl]borate, $[Ru(dpb)_3](BAr^F)_2$. Metathesis to the BAr^F salt was performed according to a previously published route.[6] Briefly, the $[Ru(dpb)_3]Cl_2$ product (0.091 mmol, 0.100 g) from above was dissolved in minimal MeOH (1.5 mL). $NaBAr^F$ (1.826 mmol, 1.618 g) was added to DI H_2O (~17 mL) to form a suspension. The BAr^{F-} salt was added slowly to $[Ru(dpb)_3]Cl_2$, and the suspension was allowed to stir for 1 h under N_2. Unlike the chloride salt, $[Ru(dpb)_3](BAr^F)_2$ did not crash out of the water

system, and the solution remained an orange-brown color. The solvent was removed by rotary evaporation and the $[Ru(dpb)_3](BAr^F)_2$ product was dissolved in pure DCM for column chromatography. A silica gel column was prepared in DCM and used for separation of $[Ru(dpb)_3](BAr^F)_2$ from the impurities in the crude reaction mixture. The desired product ran first and was a yellow-orange color. The next band was colorless and was the excess $NaBAr^F$. Unreacted $Ru(DMSO)_4Cl_2$, heteroleptic $[Ru(dpb)_2]$, and free dpb ligand remain at the top of the column. ^{1}H NMR (500 MHz, [d_4-MeOH], δ) [9.00 (d, 6 H, J = 2.0 Hz), 7.98 (m, 18 H), 7.74 (m, 30 H), 7.63 (m, 18 H)]. ESI-MS (m/z): $[C_{66}H_{48}N_6Ru]^{2+}$ calculated 513.15, found 513.16. CHN analysis: calculated C 56.72%, H 2.64%, N 3.05%; found C 57.25%, H 2.30%, N 2.94%.

Tris(4,4'-dimesityl-2,2'-bipyridine) ruthenium(II) [(3,5-trifluoromethyl)phenyl]borate, $[Ru(dmesb)_3](BAr^F)_2$. The chloride salt, $[Ru(dmesb)_3]Cl_2$ was generated *in situ* via the previously published procedure.[6] The dmesb ligand was prepared by M. D. Woodhouse. Metathesis to the BAr^{F-} salt was performed by the addition of 2.5 mol equiv. of $NaBAr^F$ (0.057 mmol, 0.050 g) in minimal MeCN (~0.5 mL) to $[Ru(dmesb)_3]Cl_2$ (0.023 mmol) in minimal MeCN under N_2. The solution was a dark red-brown. Water was added and a light orange suspension formed, which was allowed to stir under N_2 for 3 h. The water was removed by rotary evaporation and the sample was pumped while in a vacuum desiccator for 4 d. Yield 20 %. ^{1}H NMR (500 MHz, [d_3-MeCN], δ) [8.39 (d, 6 H, J = 1.9 Hz), 7.97 (d, 6 H, J = 5.9 Hz), 7.68 (m, 22 H), 7.28 (m, 6 H), 7.02 (s, 16 H), 6.98 (s, 6 H), 2.30 (s, 18 H)]. ESI-MS (m/z): $[C_{84}H_{84}N_6Ru]^{2+}$ calculated 639.29, found 639.29.

2.1.2 X-Ray Crystallography

Single-crystal X-ray diffraction was collected on suitable crystals of $[Ru(dpb)_3](PF_6)_2$. Crystals were grown by very slow diethyl ether diffusion into an acetonitrile solution of $[Ru(dpb)_3](PF_6)_2$ with two drops of toluene. The crystals were mounted in paratone oil and

transferred to the cold nitrogen gas stream of the diffractometer for data collection. The data were collected on suitable crystals mounted on a Bruker APEX-II CCD diffractometer with MoK_{α} radiation at the Center for Crystallographic Research at Michigan State University. The crystal structure was solved by S. Li and R. J. Staples.

$[Ru(dpb)_3](PF_6)_2$ crystallographic data: $C_{66}H_{48}F_{12}N_6P_2Ru$, M_r = 1316.11, monoclinic, a = 35.263(4) Å, b = 17.6678(19) Å, c = 24.080(3) Å, T = 173 K, space group = C2/c, Z = 8, 53123 reflections measured, 12027 unique (Rint = 0.0980), which were used in all calculations. The final wR(F2) was 0.1461 (all data). Solvent molecules in the structure were heavily disordered and the program BYPASS implemented in Olex2 showed the following void and electrons: 1263.5, 227.6. Possible solvents include Et_2O, EtOH, and MeCN.

2.2 Density Functional Theory Calculations

Density functional theory (DFT) calculations were performed on $[Ru(dpb)_3](PF_6)_2$ and $[Ru(dmesb)_3](PF_6)_2$ using the Gaussian 09 software package.[23] Geometry optimization was done on the ground and excited states of these complexes (Appendix D) with a spin-unrestricted formalism at the B3LYP/LANL2DZ level of theory; this basis set has been shown to perform well for Ru(II) complexes.[24,25] Frequency calculations showed that no imaginary frequencies were obtained, indicating that the calculation was at a global, and not a local, minimum. Time-dependent (TD) calculations were performed on the optimized ground state structures, for which a conductor-like polarizable continuum model (CPCM) with the properties of acetonitrile was used to account for the contributions of the bulk solvent. The first 250 electronic transitions were found for the optimized geometry, corresponding to both singlet and triplet transitions. The orbital pictures for the transitions were prepared in GaussView.

2.3 Steady State and Time-Resolved Spectroscopy

2.3.1 Steady-State Absorption and Emission Spectroscopy

Steady state absorption spectra were collected with a Varian (now Agilent) Cary 50 UV-Vis spectrophotometer. Solvents used for ground state absorption spectra were used as received, without further purification. These include: MeOH (Sigma-Aldrich, HPLC grade), EtOH (Decon Labs, 100%), 1-butanol (1-BuOH, Jade Scientific, ACS grade), 1-hexanol (1-HexOH, Spectrum Chemical, 98%), 1-octanol (1-OctOH, Jade Scientific, reagent grade), MeCN (Sigma-Aldrich, HPLC grade), propionitrile (PrCN, Alfa Aesar, 99%), Butyronitrile (BuCN, Alfa Aesar, 99%), and hexanenitrile (HexCN, Sigma-Aldrich, 98%).

Steady state emission spectra were collected with two separate instruments. A Fluorolog 2 (Horiba Jobin-Yvon) fluorimeter was used to measure the steady state emission and the excitation spectra. A photomultiplier tube detector is implemented in this set-up, and the temperature was not measured directly but assumed to be 293 K. For quantum yield determination, a Quantaurus-QY Absolute PL quantum yield spectrometer (Hamamatsu) with a cooled, back-thinned charge-coupled device (BT-CCD) detector was used. With this setup, an integrating sphere allows for absolute quantum yields to be found, whereas with the Fluorolog, a sample of $[Ru(bpy)_3](PF_6)_2$ (prepared by D. M. Arias-Rotondo) is used as a reference.[26,27] Samples used for emission were prepared in an air-free glove box, such that the absorbance at the pump wavelength was 0.1-0.2 AU. Solvents used for steady state and time-resolved emission spectroscopies were: MeOH (Alfa Aesar, anhydrous, 99%), 1-BuOH (Alfa Aesar, 99%, as received), 1-OctOH, MeCN, and BuCN (as received). Unless otherwise specified, these solvents were also used in the absorption measurements and were freeze-pump-thaw degassed.

2.3.2 Nanosecond Transient Absorption and Emission Spectroscopy

Nanosecond time-resolved measurements were carried out with the same pump source, a Vibrant 355 II Nd:YAG-pumped optical parametric oscillator (OPO, Opotek) which has tunable output from 300-2400 nm at a 10 kHz repetition rate. The IRF of this system is approximately 10 ns. For the emission spectroscopy, a portion of the pump was directed onto a photodiode (ThorLabs) to act as a reference and trigger. The pump is then focused into the sample, which is in a 1-cm pathlength matched cell, and scatter is collected at a 90º angle to the pump. This scatter enters a MacPherson Model 272 f/2 monochromator, and is then detected by a R928 PMT. The signal is monitored and the data collected by a LeCroy Model 9360 300 MHz digitizing oscilloscope. Finally, the data are worked up by a home-built LabVIEW program. The samples for emission are prepared in the same way regardless of whether the experiment is steady state or time-resolved.

In the case of the nanosecond transient absorption (TA) spectroscopy, the pump is immediately directed into a LP980 spectrometer (Edinburgh Systems). In this setup, the laser propagates through the sample, which is prepared such that the absorbance at the excitation wavelength is 0.3-0.7 A.U. This sample is again in a 1-cm pathlength matched cell. White light generated within the LP980 spectrometer enters the sample at 90º to the pump, after which it is focused into the detector. This instrument was run in single-wavelength mode. The pump wavelengths in these two time-resolved experiments were 400, 480, and 550 nm; the pump power was also kept low enough that the kinetics measured were in the linear regime. The probe wavelength was kept at 530 nm unless otherwise specified. All of the nanosecond data were fit with LabVIEW to single-exponential kinetics.

2.3.3 Ultrafast Transient Absorption Spectroscopy

In the ultrafast transient absorption data collected by Damrauer and McCusker, experimental considerations limited the pump wavelength to 400 nm.[8] To draw comparisons, excitation at 400 nm was desirable; however, vibrational dynamics have been demonstrated on occasion to be dependent on excitation energy,[28,29] so other pump wavelengths (i.e., 480 and 550 nm) were additionally used. The highest energy excitation was only possible with the l30 fs pulse system, whereas the lower energy excitation wavelengths were performed with both the 130 and the sub-60 fs pulse laser setups. Another important consideration for these experiments was the instrument response function (IRF). In the original set of data collected, the early-time kinetic component was on the order of the IRF of the laser system used. Through the use of a shorter pulse setup with a shorter IRF, we will be able to more accurately and definitively pinpoint the timescale of that ultrafast lifetime.

Ultrafast transient absorption (TA) spectroscopy measurements were carried out on two separate laser systems. The longer pulse setup has been previously described,[30] and can be found in Chapter 2. The shorter pulse system has also been reported previously.[24] Briefly, a Mantis oscillator (Coherent) seeds a Legend Elite regenerative amplifier (Coherent) that is pumped by Evolution diodes (Coherent). The output of the regen is a 1.2 W of 1 kHz repetition rate 800 nm laser with approximately 35 fs pulses that is split 80:20 to two identical OPerA Solo optical parametric amplifiers (OPAs, Coherent) that serve to tune within the visible region, affording pump and probe lines, respectively. Both the pump and probe traverse a folded Brewster prism pair in order to preemptively compensate for the dispersion introduced by optics along the laser paths. The pump pulse is delayed with respect to the probe pulse by a translating linear actuator (Soloist), affording ~1.3 ns delays. The pump beam passes through a chopper set to a frequency

of ~440 Hz which is coupled to a lock-in amplifier. A small portion of the probe beam is picked off then attenuated and directed into a Si photodiode (ThorLabs) to act as a reference. The pump and probe are focused into the sample at an angle of less than 3º relative to each other. After entering the sample, the pump is blocked whereas the probe is focused into a monochromator with 1 mm entrance and exit slits and then sent onto a Si photodiode (ThorLabs).

For the data displayed here, the typical excitation energy was 2-5 μJ, such that all data was collected in the linear regime. The ground state absorbance for each of the samples was approximately 0.3-0.7 in a 1-mm sample cuvette (FireFlySci) at 400, 480 and 550 nm, the excitation wavelengths, and no spectral changes were observed after the variable-temperature experiments were complete. The probe wavelength could be tuned to exactly 532 nm on the shorter pulse system through the use of the second OPA and the monochromator with ~2 nm spectral bandwidth in the detection setup. In the case of the longer pulse system, however, the pulse is composed of white light is generated by the 800 nm regen output through a translating CaF_2 window. Additionally, a 10 nm bandpass filter centered at 530 nm is used in the detection on this system. Care was taken to ensure that the measurements on both systems were comparable regardless of detection scheme. Pulse characterization is performed within the cryostat by optical Kerr effect (OKE) measurements made in acetonitrile, yielding approximately 160 and sub-60 fs pulses on the longer and shorter systems, respectively. Cross-correlation performed in acetonitrile gives an IRF better than 300 fs on the long pulse system and shorter than 150 fs on the short pulse system. The spectra shown here are an average of more than 10 scans, with no single scan giving a fit that is a statistical outlier. Biexponential fits to the data were performed with Igor Pro software (v. 6.37). All error reported was propagated across multiple data sets.

3. Results

3.1 Synthesis

3.1.1 [Ru(dpb)$_3$](BAr^F)$_2$

In preparing the Ru(II) complexes for measurements of solvation dynamics, it was immediately apparent that a counteranion that allowed for the compound to dissolve in a wide array of solvents was required. The counterion of choice was tetrakis[(3,5-trifluoromethyl)phenyl]borate, a very bulky, non-coordinating ion that allows $[Ru(dpb)_3]^{2+}$ to be dissolved in solvents like 1-OctOH and HexCN, as well as the more traditional solvents of MeOH and MeCN. While there was a synthetic route already outlined for the preparation of $[Ru(dpb)_3](BAr^F)_2$,[31] it was soon determined that purification of any BAr^{F-} salt is complicated by its solubility properties. Thus, the Cl^- salt was first isolated and purified, then the metathesis was performed. Precipitating $[Ru(dpb)_3]Cl_2$ through the use of 6 M HCl requires a word of caution, however.[21] Good results were obtained in this instance, with the salt immediately crashing out as observed by the increased opacity and bright orange solid upon addition of the HCl. It should be noted, though, that acid in the presence of a bipyridine can produce a protonated bipyridine, which would compete with the Ru-bpy coordination, thereby resulting in a heteroleptic complex. This was not observed in the formation of $[Ru(dpb)_3]Cl_2$, but for other bpy-based ligands that may not coordinate to Ru(II) as readily (e.g., those with electron withdrawing substituents), this route may not be appropriate.

3.1.2 [Ru(dmesb)$_3$](BAr^F)$_2$

The mesitylated complex, $[Ru(dmesb)_3]^{2+}$, was desired for these studies so as to begin to understand the nuclear coordinate accessed in the vibrational cooling process (vide infra). Surprisingly, the preparation of $[Ru(dmesb)_3]^{2+}$ was much more challenging than the $[Ru(dpb)_3]^{2+}$

product. The free dmesb ligand as synthesized by M. D. Woodhouse was observed to go from a white to a pink powder in ~24 h. This is attributed to the iron-philic nature of the dmesb, which is apparently much greater in this ligand than in dpb. Although the dpb ligand could be recrystallized out of hot EtOH, this process was only done when the ligand was more than six months old to ensure good product formation. In the case of the dmesb reactions, though, dmesb was recrystallized out of hot EtOH as a matter of standard procedure.

Despite the extra caution taken to ensure recrystallized starting materials (i.e., both the dmesb and $Ru(DMSO)_4Cl_2$), oxidized $\{Ru^{III}(dmesb)_x\}$ product has been observed in some reaction mixtures, in which both homo- (x = 3) and heteroleptic (x = 2) complexes were seen by ^1H NMR (Fig. 4.1). While the steric bulk of the mesitylated ligand was originally believed to be responsible for this oxidation, previous reports have demonstrated that the presence of Cl^- may have the effect of replacing bpy-type ligands, thereby greatly reducing the oxidation potential of the Ru(II/III) couple.[32] This allows for ready oxidation to the Ru(III) heteroleptic complex. The studies of Pearson et al. report that during the growth of single crystals, $[Ru^{II}(bpy)_3]Cl_2$ was observed to form $[Ru^{III}(bpy)_2Cl_2]Cl$. The oxidation potentials for these two complexes are 893 and -84 mV vs. Fc/Fc^+, respectively.[32] If this has been observed in $[Ru(bpy)_3]^{2+}$, it seems reasonable to expect that the steric effects of the dmesb ligand only exacerbate this problem. In fact, while perhaps this complex dissociation and oxidation is expected in solution, the oxidation was actually observed in solid, powdered $[Ru(dmesb)_3](PF_6)_2$, which only had Cl^- present for the initial complexation step of the reaction, as the metathesis to the PF_6^- salt was performed immediately after. This seems to illustrate how easily incorporated and how detrimental chloride ions can be to these complexes.

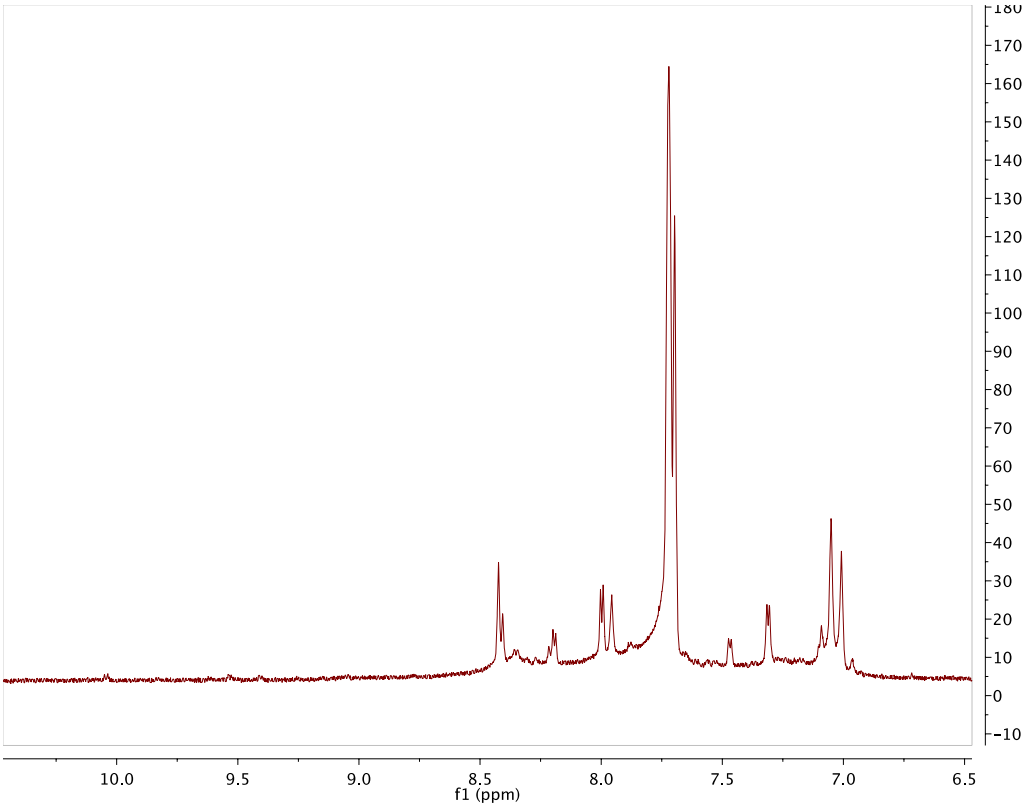

Figure 4.1. ^{1}H NMR spectrum of [Ru(dmesb)$_3$]Cl$_2$ reaction mixture in CD$_3$CN. While many of the main features can be assigned to the desired homoleptic complex (see text for assignments), some features clearly belong to an oxidized and/or heteroleptic complex, as evidenced by the shifts ~10.1 ppm.

Although the route outlined above did produce [Ru(dmesb)$_3$](BAr^F)$_2$, a modified synthesis is proposed here to alleviate the problems that were observed, thereby improving the overall yield and purity. The original report by Damrauer et al. cites a 24 h reaction time for the complexation.[6] Increased reaction time will likely improve the amount of homoleptic complex formed, though reacting for too long may allow for displacement of a dmesb ligand with Cl^- ions. The reaction mixture should remain air-free at all times, and ideally be performed in a glove box under inert atmosphere. If possible, a Ru(II) starting material free of chloride would be ideal. Metathesis to

the BAr^{F-} salt should be performed with deficient equivalents of $NaBAr^{F}$ so that excess counterion is not present. If the product is indeed a mixed salt, it has already been shown that the counteranion does not play a role in the vibrational cooling dynamics being studied here, and are unlikely to affect any of the photophysical processes of these Ru(II) polpyridyls.[4,8,27,31] Additionally, based on the ^{1}H NMR and CHN analysis of the $[Ru(dmesb)_3](BAr^{F})_2$ product, over 20 mol equiv. of water were present in the complex despite being pumped on in a desiccator for 4 d. Drying over P_2O_5 may reduce the amount of water, but it is known that BAr^{F-} is hygroscopic, despite not being soluble in H_2O.[33] This would appear to recommend that this complex be stored either in a vacuum desiccator or in a glove box under inert atmosphere. It should be noted that $[Ru(dpb)_3](BAr^{F})_2$ does not display hygroscopicity to nearly the same degree and has been observed to not decompose when stored in air for years at a time.

Column chromatography was attempted to purify $[Ru(dmesb)_3](BAr^{F})_2$. It was later determined that using nearly any other counteranion would make purification much simpler. That being said, the conditions used for $[Ru(dpb)_3](BAr^{F})_2$ appeared to be viable by thin-layer chromatography (TLC): pure DCM on SiO_2.[31] Unfortunately, these conditions only worked once to purify the product. It was determined by ^{1}H NMR that the major impurity was free ligand, so a sequential solvent system was used on SiO_2 in which the ligand was driven off first by a 25% ethyl acetate (EtOAc) in hexanes solution, and then the complex was moved down the column by either pure EtOAc or pure DCM. Both second solvent systems were found to work, but EtOAc required more solvent and ended up smearing the product more, whereas DCM drove the product more cleanly off as one band. As with the pure DCM on SiO_2, these conditions only purified the complex one time each. Subsequent performance of these exact conditions yielded large amounts of free ligand impurity. This was later attributed to the ease with which the dmesb ligand must dissociate

from the Ru(II) center. These column attempts and complex dissociation led to the rather low yield of the compound. It is therefore recommended that column chromatography not be used as a purification option for $[Ru(dmesb)_3](BAr^F)_2$.

One additional note on the characterization of the mesityl complex. In the mass spectrum of the compound (Fig. 4.2), a repeating feature at m/z 890 is observed. The isotope pattern with the greatest intensity (centered at m/z 890) is assigned to $[Ru(dmesb)_3]^{2+}$. The observed increase of m/z ratios are not typical for Ru(II) polypyridyls. The apparent centers of these isotope patterns are all separated by 14 mass units. It was determined that this corresponds to the oxidation of the methyl groups on the mesityl to aldehydes. Furthermore, some of the sample used for ESI-MS was reserved for ^{1}H NMR, and no evidence of the aldehyde peak was observed (Fig. 4.3), which would be expected to appear around 10 ppm. This indicates that it was impurity on the MS column that was doing chemistry with the sample. Previously, Ru(II) has been observed to catalyze the reaction of methylarenes to the corresponding aromatic aldehyde.[34] That being said, it is critical to thoroughly characterize solution-phase $[Ru(dmesb)_3]^{2+}$ before and after any type of spectroscopy is performed on the sample.

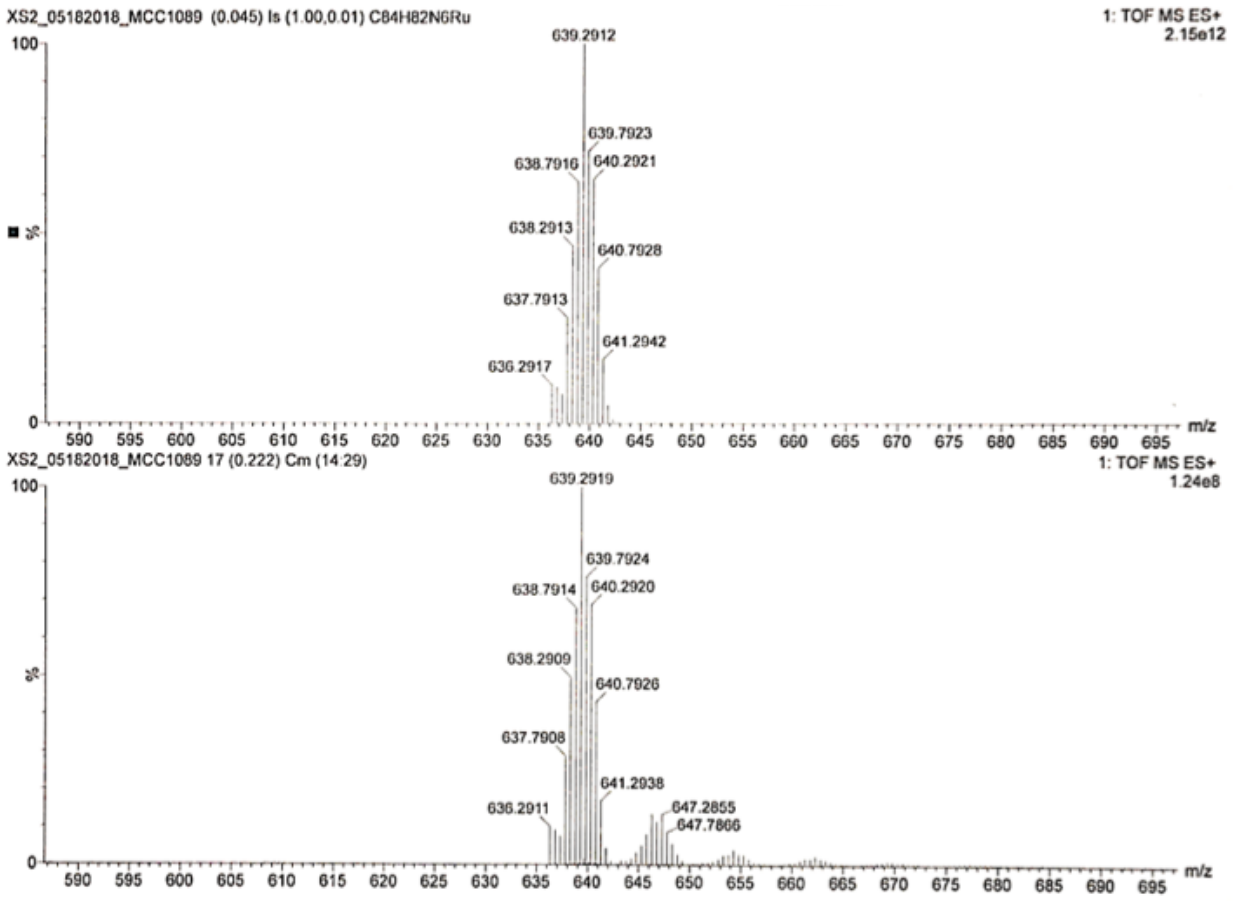

Figure 4.2. Electrospray ionization mass spectrum of $[Ru(dmesb)_3]^{2+}$ in positive mode. (Top) Calculated spectrum for the $[M]^{2+}$ ion. (Bottom) Experimental spectrum for the $[M]^{2+}$ ion. The repeating unit is attributed to the oxidation of the methyl substituents in the mesityl moiety to aldehydes.

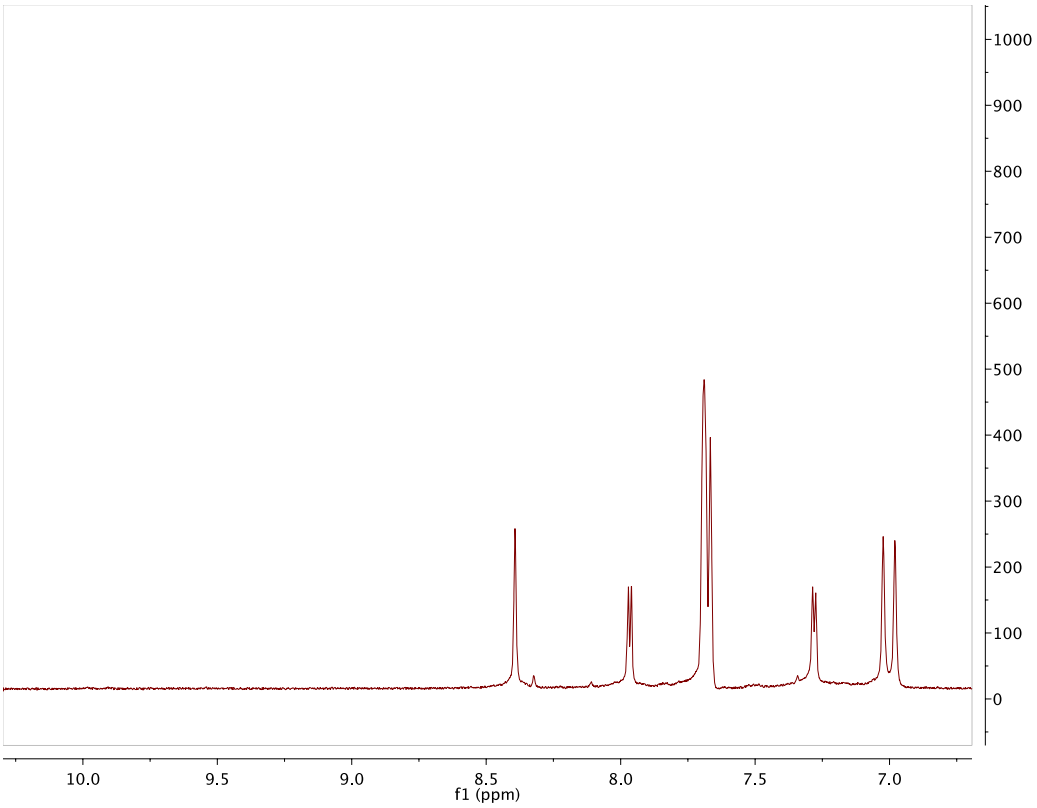

Figure 4.3. ^{1}H NMR spectrum of the [Ru(dmesb)$_3$](BAr^F)$_2$ sample used to collect the mass spectrometry data in Fig. 4.2. No evidence of an aryl-aldehyde is present, as indicated by the featureless area around 10 ppm.

3.2 X-Ray Crystallographic Data

Single crystals of [Ru(dpb)$_3$](PF$_6$)$_2$ were able to be grown by very slow Et$_2$O diffusion into MeCN solution. These crystals were obtained after approximately six months of growing, and were very fine, needle-like structures that ultimately did not diffract very well. Attempts were made to increase the thickness of the crystals through the addition of toluene, which should π-stack with the phenyl substituents and allow the crystals to grow outward. These were the crystals for which X-ray data were obtained. One system that appeared to show promise but was only explored briefly was through the slow diffusion of Et$_2$O into a solution of 1-OctOH. Surprisingly, the PF$_6^-$

salt of this complex is soluble in 1-OctOH, though only sparingly. The solubility must be improved to slow down the growth of crystals (thereby increasing their size and diffraction-ability) so a few drops of EtOH were added. This process did grow large crystals, but they unfortunately grew too quickly (i.e., within hours), meaning they did not produce data any better than was already acquired. We are noting this should others wish to attempt to improve the data reported here.

We report, for the first time, the single crystal X-ray data for $[Ru(dpb)_3](PF_6)_2$. These data can be found in Table 4.1, along with the same structural data of $[Ru(dmesb)_3](PF_6)_2$ and $[Ru(bpy)_3](PF_6)_2$ for comparison. The crystal structure itself is given in Fig. 4.4. Relative to the prototypical $[Ru(bpy)_3]^{2+}$ complex, the structural data of $[Ru(dpb)_3]^{2+}$ are largely unchanged. The Ru-N bond distances and *cis*-angles are consistent between the two complexes, indicating that the phenyl substituent does not greatly affect the ground state geometry relative to the bpy analogue. The only difference of note is the *trans* N-Ru-N angle, which is two degrees greater in $[Ru(dpb)_3]^{2+}$, implying a very slightly more octahedral geometry.

Table 4.1. X-ray crystallographic data of $[Ru(dpb)_3](PF_6)_2$ compared to the dmesb and bpy analogues.

	$[Ru(dpb)_3](PF_6)_2$	$[Ru(dmesb)_3](PF_6)_2$[a]	$[Ru(bpy)_3](PF_6)_2$[b]
Ru-N (Å)	2.050 ± 0.009	2.075 ± 0.013	2.0554 ± 0.0001
bpy N-Ru-N (°)	78.6 ± 0.2	78.04 ± 0.35	78.65
cis N-Ru-N (°)	93.8 ± 0.3	94.23 ± 0.60	93.91 ± 3.59
trans N-Ru-N (°)	175.4 ± 0.2	170.54 ± 0.35	173
bpy-bpy torsion (°)	0-15	9-15	5.94
bpy-Ph torsion (°)	31.9 ± 1.8	68.54 ± 9.53	N/A
bpy-Ph C-C (Å)	1.480 ± 0.017	1.4904 ± 0.0220	N/A

a Data taken from ref. 6.

b Data taken from ref. 35.

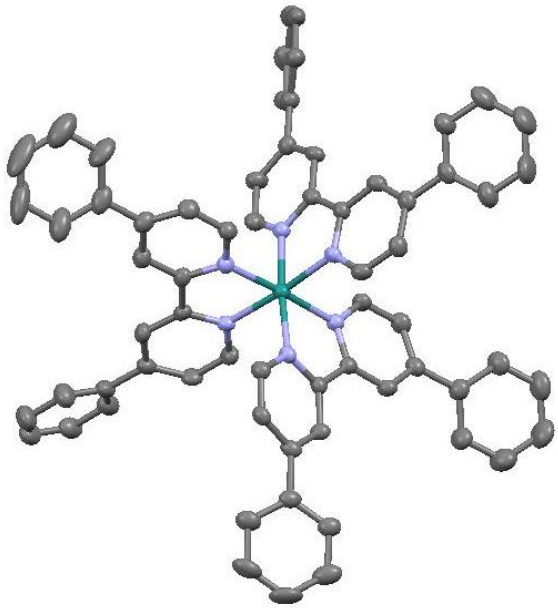

Figure 4.4. The X-ray crystal structure of $[Ru(dpb)_3](PF_6)_2$. The counteranions and solvent are omitted for clarity.

It is more informative to compare the structures of $[Ru(dpb)_3]^{2+}$ and $[Ru(dmesb)_3]^{2+}$, in order to better understand the effect of the methyl groups in the mesityl substituent. The most apparent difference between the complexes is the diplanar angle between the phenyl and bipyridine moieties: in the phenylated complex, it is an average of 32°, which is more than doubled to ~70° in $[Ru(dmesb)_3]^{2+}$. This diplanar angle in $[Ru(dpb)_3](PF_6)_2$ of 32º is an intermediate between the 9.60º angle of the free ligand[7] and the 44º calculated from 4-phenylpyridine, which was used in place of the actual Ru(dpb) moiety for computational work.[6,7] This would suggest that the complex is more driven to coplanarity than the 4-phenylpyridine (perhaps due to extended conjugation in dpb relative to 4-phenylpyridine) but that driving force does not extend to the complex, likely caused by steric strain around the metal center. It should also be noted that the Ru-N bond distance is lengthened in the mesityl complex by approximately 0.025 Å. This bond distance can often be an indicator of the electron donating or withdrawing effect of the substituent.[7] As compared to $[Ru(bpy)_3]^{2+}$, the bond distance is within error of that of $[Ru(dpb)_3]^{2+}$, implying that any electronic effects into the π system are extremely small, as is expected for a phenyl group. In the case of $[Ru(dmesb)_3]^{2+}$, the bond increase may be a result of the mesityl acting as a π-electron withdrawing substituent. However, the 70° angle between the mesityl and bpy backbone implies very little conjugation, which should effectively mitigate any electronic effects from the substituent. It therefore seems more likely that the increased Ru-N bond distance in $[Ru(dmesb)_3]^{2+}$ relative to that of $[Ru(dpb)_3]^{2+}$ is simply caused by the steric strain induced by the bulky mesityl groups (as evidenced by the increased bpy-phenyl C-C bond distance lengthening in Table 4.1), forcing the bipyridines into a geometry that decreases the M-L orbital overlap, weakening the Ru-N bonds. The effects of this can also be seen in the bpy torsion, or the degree of canting between the two pyridyl moieties in the bipyridine, which is much greater in $[Ru(dmesb)_3]^{2+}$ than either

$[Ru(dpb)_3]^{2+}$ or $[Ru(bpy)_3]^{2+}$. Likewise, the bpy, *cis*, and *trans* angles in the dpb and bpy analogues are consistently much closer to an octahedral geometry than in the mesitylated complex.

3.3 Role of Solvent on the Ground State Absorption Properties of $[Ru(dpb)_3]^{2+}$

The studies originally published by Damrauer and McCusker utilized a 532 nm probe upon excitation at 400 nm.[8] In Fig. 4.5. are shown the ground state absorption spectrum and the differential absorption spectrum of $[Ru(dpb)_3](BAr^F)_2$ in MeOH. These spectra are directly comparable to those reported previously,[8] indicating the identity of counteranion does not affect the photophysical properties being studied, as expected.[4] The steady state absorption spectrum displays a feature centered around λ_{max}=474 nm that is characteristic of an MLCT transition, here the ^{1}MLCT←^{1}A$_1$ absorption. The tail apparent at λ>520 nm is the ^{3}MLCT band, allowed by spin-orbit coupling due to the Ru(II) center.[36,37] The feature centered at ~350 nm has also been assigned as MLCT, likely due to the molar extinction coefficient which is on the order of 2.7×10^4 $M^{-1}cm^{-1}$. This value is approximately two times greater than that of $[Ru(bpy)_3]^{2+}$,[4,38] the increased oscillator strength owing to the extended conjugation in the dpb ligand. The exact nature of this band is an open question, and one that will be addressed further (vide infra). Finally, the feature farthest in the UV that is not entirely displayed in Fig. 4.5 is the dpb ligand π-π* absorption.

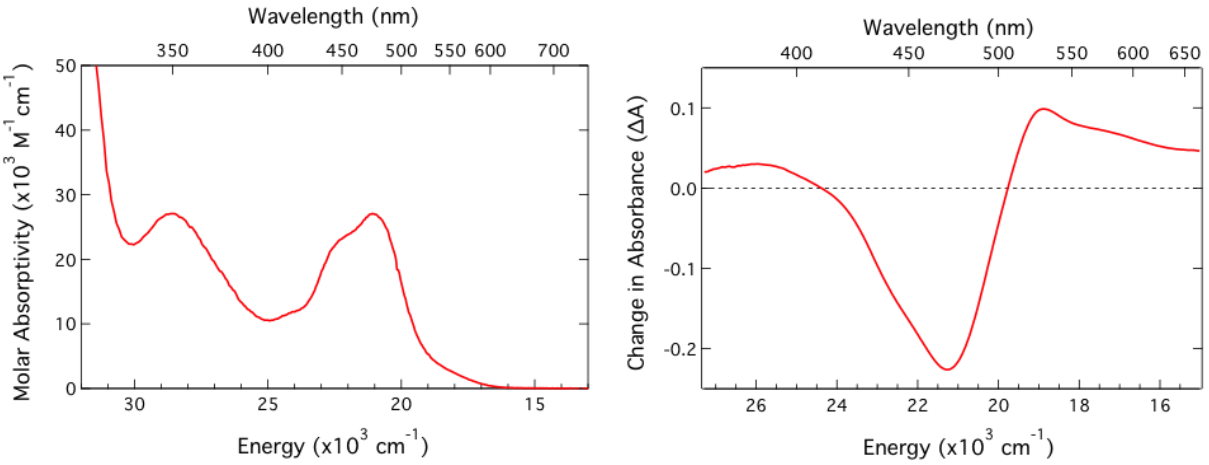

Figure 4.5. (Left) Ground state absorption spectrum of $[Ru(dpb)_3](BAr^F)_2$ in MeOH. (Right) Differential absorption spectrum of $[Ru(dpb)_3](BAr^F)_2$ in MeOH of the thermalized ^{3}MLCT excited state. See text for assignments.

As the pump wavelength assignments are made from the ground state absorption spectrum, so must the characteristics of the probe wavelengths be determined from the transient absorption spectrum (Fig. 4.5). The excited state absorption in the near-UV is assigned to the π-π* transition of the reduced dpb ligand. This transition is echoed in the feature with the greatest oscillator strength, at ~530 nm, which is the π*-π* absorption of the dpb radical. The ground state bleach at 474 nm is caused by the loss of the ground state upon absorption into the ^{1}MLCT excited state. The broad, featureless excited state absorption red of ~550 nm is attributed to ligand-to-metal charge transfer (LMCT) based on the spectroelectrochemistry.[8]

The purpose of this work is to study the effect of protic and aprotic polar solvents on the vibrational cooling dynamics of $[Ru(dpb)_3]^{2+}$ that occur concomitantly with the phenyl ring rotation in the ^{3}MLCT excited state. From the spectroelectrochemical and transient absorption data, the optimal probe wavelength to monitor such kinetics would be at the central wavelength of the π*-π* absorption of the dpb radical (i.e., 532 nm). The fact that this band is an excited state

absorbance is beneficial in that ligand-based dynamics can be measured directly without the interference of the loss of the ground state. Probing in the MLCT bleach, as was done when the probe wavelength (λ_{probe}) is 480 nm, was previously shown to decay within the IRF of the system with no additional dynamics.[8] Thus 532 nm is also taken as the probe wavelength for the ultrafast data reported herein.

The pump wavelength originally used (λ_{exc}) was the result of frequency doubling of the 800 nm regenerative amplifier output, and thus was experimentally limiting. Upon Gaussian deconvolution of the ground state absorption spectrum (Fig. 4.6), seven bands are found to describe the spectrum well. Gaussian deconvolution is highly arbitrary and should only be taken as a first approximation of the underlying transitions of any spectrum. From this analysis, it is apparent that excitation at 400 nm will populate multiple bands, particularly those centered at approximately 350 nm and at 430 nm. Gaussian deconvolution has been performed multiple times on this spectrum with various initial guesses; at every iteration, a minimum of two bands overlapped at 400 nm, bolstering this assertion. In an attempt to more thoroughly study the vibrational cooling kinetics of $[Ru(dpb)_3]^{2+}$, excitation at other wavelengths was desired. 480 and 550 nm were chosen as two additional pump wavelengths as these would (based on the Gaussian deconvolution) allow the molecule to be excited into only one band, thereby creating only one type of excited state initially. These wavelengths have the added benefit of forming two different excited states, in which λ_{exc} = 480 nm populates a ^{1}MLCT and λ_{exc} = 550 nm generates the ^{3}MLCT state.

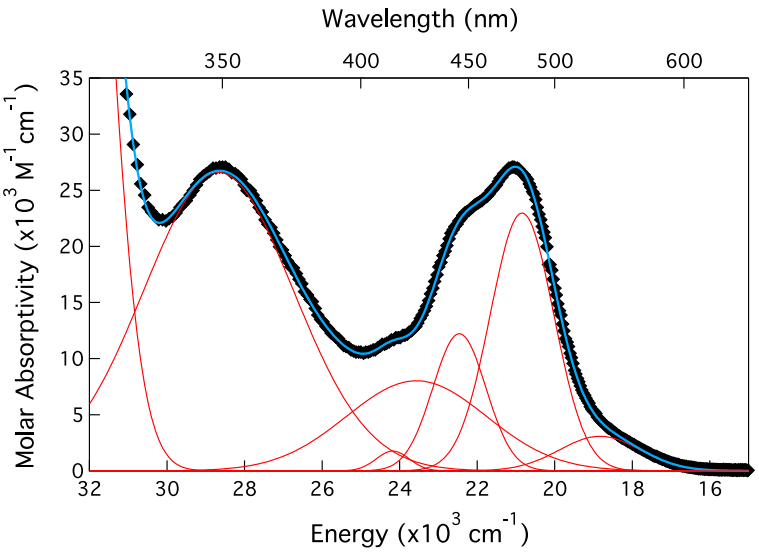

Figure 4.6. Steady state absorption spectrum (black diamonds) of $[Ru(dpb)_3](BAr^F)_2$ in MeOH. Gaussian deconvolution of this region revealed seven separate bands (red traces) were required to reconstruct the spectrum (blue trace).

The ground state absorption spectrum of $[Ru(dpb)_3]^{2+}$ was also collected and compared for all of the solvents used in the ultrafast transient absorption spectroscopy studies (Fig. 4.7). The alcohol series is comprised of MeOH, EtOH, 1-BuOH, 1-HexOH, and 1-OctOH. The general shape of the spectrum was consistent in all of the solvents, and only very minor solvatochromism was observed. In MeOH, the absorption maximum of the lowest energy MLCT transition is 474 nm, whereas it is red-shifted to 478 nm in 1-OctOH. This is a difference of only 177 cm^{-1} despite an eight-fold increase in alkyl chain length, indicating that only the polar -OH group is responsible for the spectral shifting. In the case of the nitrile series, MeCN, PrCN, BuCN, and HexCN are used. Again, these spectra show no major changes between these solvents, nor when compared to the spectra for the alcohol series. Minor solvatochromism is observable here too: λ_{max}(MeCN) = 474 nm and red-shifts in HexCN to 478 nm (Table 4.2). The same magnitude spectral shift occurs

in this case over a lengthening of the alkyl chain by a factor of six. As appears true for the alcohols, these data would indicate that only the polar nitrile functional plays a role in the stabilization of the ^{1}MLCT excited state. Interestingly, the band centered ~350 nm also displayed solvatochromism, where between the maximum red-shifted approximately 250 cm^{-1} in 1-OctOH relative to MeOH. These affects were significantly attenuated in the nitriles, for which the maximum in HexCN was only 80 cm^{-1} redder than in MeCN. As can be seen in Fig. 4.7 and Table 4.2, the relative intensities of the lowest and highest energy MLCT maximum of $[Ru(dpb)_3]^{2+}$ are variable depending on the specific solvent, as evidenced by the spectral maxima ca. 350 nm not overlapping well. These data may provide some insight into the nature of that transition.

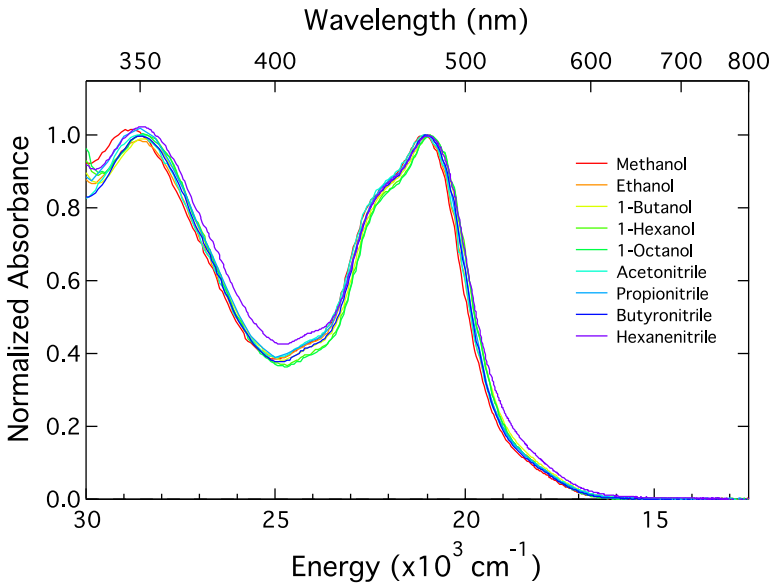

Figure 4.7. Ground state absorption spectra of $[Ru(dpb)_3](BAr^F)_2$ in the solvents used in the ultrafast transient absorption experiments. The spectra are normalized to the maximum of the lowest energy MLCT band. $[Ru(dpb)_3]^{2+}$ is modestly solvatochromic.

Table 4.2. Summary of the MLCT maxima of the ground state absorption spectra of $[Ru(dpb)_3](BAr^F)_2$ in the solvents used in the transient absorption spectroscopy measurements.

Solvent	E higher-energy ^{1}MLCT (nm)	E lower-energy ^{1}MLCT (nm)	ΔE (cm^{-1})	$\Delta\Delta E$ (cm^{-1})[a]	$\Delta\Delta E$ (%)[a]
MeOH	348	474	7639	-	-
EtOH	349	475	7601	-38	-0.5
1-BuOH	351	477	7526	-113	-1.5
1-HexOH	351	478	7570	-69	-1
1-OctOH	351	478	7570	-69	-1
MeCN	350	474	7474	-	-
PrCN	350	475	7519	44	0.5
BuCN	350	477	7607	133	2
HexCN	351	478	7570	95	1

a The alcohols are referenced to MeOH, whereas the nitriles are referenced to MeCN

A consistent trend can be observed throughout both the alcohols and the nitriles in which as the chain length increases, the lowest energy MLCT maximum red-shifts, indicating that the solvents with lower dielectric constants are better able to stabilize the ^{1}MLCT, which is a counterintuitive result. The MLCT excited states are species with large dipole moments and as such should be highly susceptible to polar solvation.[10,39] Alternatively, one might be tempted to postulate that the ^{1}MLCT excited state is likely stabilized equivalently in each solvent of a given family (this seems reasonable given that the polar moiety is the same for solvents within a series), and that the solvation effects on the ground state are driving the transition absorption energy.

However, the nonpolar $^1A_1$ ground state is more likely to be increasingly stabilized by the solvents with longer chain lengths, resulting in a net blue-shift of the spectrum in solvents with lower dielectric constants. At this time, all that might be said about these spectra is that the ground state absorption spectra are only somewhat affected by the solvents being studied.

3.4 Vibrational Cooling Dynamics in $[Ru(dpb)_3]^{2+}$

3.4.1 Ultrafast Kinetics Measured in Alcohol Solvents

In the alcohol series, five solvents of increasing alkyl chain length were used. The polar -OH group is maintained while the degree of nonpolarity is systematically increased via the chain. The major motion in the solute dynamics being studied is the aryl rotation, thus it might be expected that frictional forces would dominate the kinetics. If true, the vibrational cooling time constant (τ_{VC}) should increase as the alcohol chain length – and by extension, the viscosity – increased. On the other hand, vibrational cooling is occurring along the ^{3}MLCT potential energy surface, and this excited state has a very large dipole moment. This might alternatively elicit a dielectric response from the solvent, causing the τ_{VC} to track a bulk solvent property such as dielectric constant or solvent polarity.

Upon excitation at 480 and 550 nm, the vibrational cool dynamics are relatively consistent between the two pump wavelengths, as can be seen in Table 4.3. A trend is observed in which as the alkyl chain length is systematically increased, so too is τ_{VC} elongated. In MeOH, the time constant measured is ~ 1.8 ps, which then increases to ~18.5 ps in 1-OctOH. This can also be observed in the spectral comparison made in Fig. 4.8. These spectra are both normalized such that the final 30 data points collected average $\Delta A = 1$, allowing for a visual analysis of the lifetime of growth to the thermalized ^{3}MLCT excited state. It is evident that $[Ru(dpb)_3]^{2+}$ in MeOH grows in to $\Delta A = 1$ at a much faster rate than when the compound is in 1-OctOH. The stepwise growth in

τ_{VC} concomitant with the alkyl chain length tends to indicate that viscosity is playing a role in these vibrational cooling dynamics, such that it can be said a viscoelastic model represents these data well.

Table 4.3. Vibrational cooling time constants for $[Ru(dpb)_3](BAr^F)_2$ in the alcohol solvents of varying viscosities (η) as a function of excitation wavelength.

Solvent	η at 25 ºC (cP)[a]	τ_{VC} (ps)		
		λ_{exc} = 400 nm	λ_{exc} = 480 nm	λ_{exc} = 550 nm
MeOH	0.544	3.3 ± 1.8	1.6 ± 0.9	1.9 ± 0.7
EtOH	1.07	4.6 ± 1.7	5.0 ± 2.6	6.0 ± 1.6
1-BuOH	2.54	8.4 ± 4.9	5.9 ± 1.5	12.0 ± 3.9
1-HexOH	4.58	8.5 ± 3.4	14.4 ± 1.5	15.0 ± 4.5
1-OctOH	7.29	9.4 ± 5.0	17.1 ± 2.6	20.0 ± 3.6

a Taken from ref. 40.

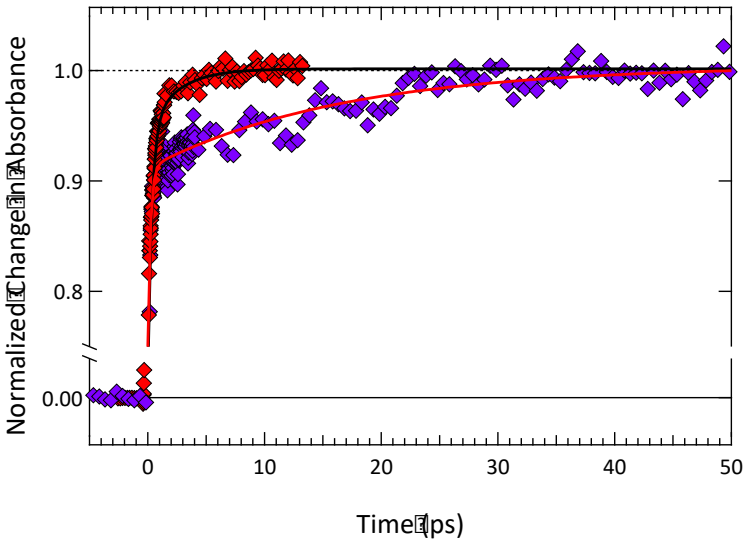

Figure 4.8. Overlay of the vibrational cooling dynamics of $[Ru(dpb)_3](BAr^F)_2$ in MeOH (red diamonds) and 1-OctOH (purple diamonds) upon excitation at 480 nm. The final 30 data points of each set are normalized so the average $\Delta A = 1$, such that when fit with a double exponential, the average τ_{VC} in MeOH (black trace) is 1.5 ± 0.3 ps, which is significantly lengthened in 1-OctOH (red trace) to 17.1 ± 2.6 ps.

The trends in τ_{VC} change drastically upon excitation at 400 nm. At this pump wavelength, the vibrational cooling lifetime of $[Ru(dpb)_3]^{2+}$ in MeOH and EtOH are consistent with the other excitation energies, that is 3.3 ± 1.8 and 4.6 ± 1.7 ps, respectively (Table 4.3). Upon solvation in longer chain alcohols, however, a saturation of the time constant is observed around ~9 ps. At no other excitation wavelength are the dynamics in 1-BuOH and 1-OctOH superimposable. It is apparent that the viscoelastic model that applied upon excitation at lower pump wavelengths is not the major solvation mechanism at work in these data. There is no observable bulk solvent property of which we are aware that is consistent between these longer alkyl length alcohols.

3.4.2 Ultrafast Kinetics Measured in Nitrile Solvents

With the vibrational cooling data for $[Ru(dpb)_3]^{2+}$ in the alcohol series in hand, the question of H-bonding became of concern. To rule out these strong solvent-solvent interactions, the polar aprotic nitriles were used. Unfortunately, the viscosity of the three shortest-chain solvents (i.e., MeCN, PrCN, and BuCN) is nearly unchanged, and are on the order of the viscosity of MeOH. It was necessary to include HexCN to the list, the viscosity for which is similar to that of EtOH. These will make for good direct comparisons to the alcohol series based solely on this bulk solvent property, as well as removing any effects inherent in H-bonding solvents.

The vibrational cooling kinetics of $[Ru(dpb)_3]^{2+}$ were monitored in the nitrile series as a function of excitation energy. The summary of these results can be found in Table 4.4 and Fig. 4.9. In these solvents, τ_{VC} is observed to display little to no pump wavelength dependence. The time constants for MeCN, PrCN, and BuCN average ~2.1 ps at each excitation energy, whereas τ_{VC} for HexCN is approximately 6.3 ps. While the size of the error bars (due to a very small $\Delta\Delta A$ for the vibrational cooling signal) make comparisons difficult, if the averages of τ_{VC} are observed, it does appear as if the time constant is lengthened slightly in BuCN relative to MeCN and PrCN. Taken separately, the average τ_{VC} in BuCN is 3.3 ps, whereas in MeCN and PrCN τ_{VC} = 1.6 ps. These comparisons are perhaps suggestive of an intermediate vibrational cooling lifetime in BuCN but should be viewed with skepticism without smaller error bars. Interestingly, the average values of τ_{VC} taken for MeCN, PrCN, and BuCN versus HexCN agree well with the data collected in the alcohol solvents of corresponding viscosities. In MeOH, the vibrational cooling time constant is 2.3 ps, which is increased to 5.2 ps for EtOH. These are also the only two alcohol solvents that appear to be pump wavelength independent, as is observed for all of the nitriles. Based on these results, it is immediately appealing to attribute the solvation dynamics in $[Ru(dpb)_3]^{2+}$ in polar

aprotic solvents to a viscoelastic model, as the vibrational cooling lifetime appears to track viscosity. The appropriateness of that assignment will be discussed further below.

Table 4.4. Vibrational cooling time constants for $[Ru(dpb)_3](BAr^F)_2$ in the nitrile solvents with varying viscosities (η) as a function of excitation wavelength.

Solvent	η at 25 °C (cP)[a]	τ_{VC} (ps)		
		λ_{exc} = 400 nm	λ_{exc} = 480 nm	λ_{exc} = 550 nm
MeCN	0.369	1.2 ± 0.4	1.5 ± 0.3	2.3 ± 1.6
PrCN	0.294	0.9 ± 0.4	1.7 ± 0.5	1.8 ± 0.7
BuCN	0.553	4.2 ± 2.5	2.3 ± 1.4	3.4 ± 1.5
HexCN	0.912	5.8 ± 1.0	5.8 ± 1.6	7.4 ± 4.0

a Taken from ref. 40.

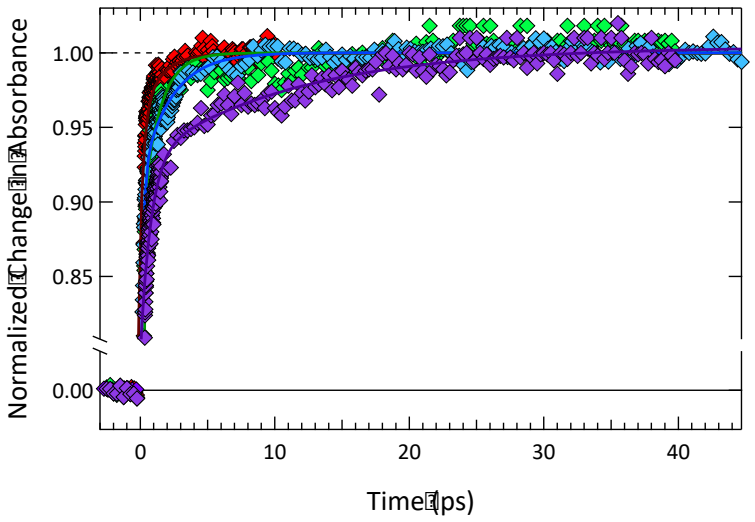

Figure 4.9. Vibrational cooling kinetics of $[Ru(dpb)_3](BAr^F)_2$ in the nitrile solvents (diamonds) with their fits (traces) upon excitation at 480 nm: MeCN (red) = 1.5 ± 0.3 ps, PrCN (green) = 1.7 ± 0.5 ps, BuCN (blue) = 2.3 ± 1.4 ps, and HexCN (purple) = 5.8 ± 1.6 ps.

4. Discussion

4.1 Dual Solvation Mechanism

The vibrational cooling dynamics of $[Ru(dpb)_3]^{2+}$ have an apparent dependence on both the nature of the polar solvent (protic vs. aprotic) and the excitation wavelength. The latter dictates the amount of excess vibrational energy put into the system, whereas the former determines the mechanism whereby that energy may be dissipated. In the nitriles at all excitation wavelengths, and in the alcohols at the lower pump wavelengths, one trend appears; in the alcohols at the highest pump energy, another. The former shows the vibrational cooling time constant to increase monotonically as the chain length of the alkyl part of the solvent increases. In the latter, τ_{VC} increases from MeOH to EtOH to 1-BuOH, and then remains constant from 1-BuOH to 1-OctOH. Maroncelli and coworkers have previously affirmed that solvation rates are dependent only the nature of the solvent, not the solvent.[10] Clearly in this instance, that assertion cannot be true.

To understand the intricacies of the dual solvation mechanism at work in these data, the vibrational cooling time constant must be correlated to different solvent parameters. It is evident that a better relationship will be found with respect to the λ_{exc} = 480 and 550 nm than the 400 nm data, and vice versa. In some instances, bulk constants are not known for the longer-chain solvents, specifically 1-HexOH, 1-OctOH, and HexCN. The solvent polarity, P(ϵ),[9,39,41] and polarizability, R(n),[41] are often found to be highly correlated to the rate of solvent relaxation. These parameters can be solved simply via eqns. (4.1) and (4.2):

$$P(\epsilon_0) = \frac{(\epsilon_0 - 1)}{(\epsilon_0 + 2)} \tag{4.1}$$

$$R(n) = \frac{(n^2 - 1)}{(n^2 + 2)} \tag{4.2}$$

in which the polarity is a function of the static dielectric constant (ϵ_0), and polarizability is a function of the index of refraction (n). The relationship between τ_{VC} and polarity and polarizability

of all of the solvents are displayed in Figs. 4.10 and 4.11, respectively. Modest correlations are observed for the vibrational cooling time constant versus polarity in Fig. 4.10 at the lower excitation wavelengths, as given by the coefficient of determination, R^2, being ~0.8 in both. The goodness of fit is worse in the data for which λ_{exc} = 400 nm, where R^2 = 0.57. This indicates that a polar solvation mechanism is at work as the phenyl rotates while in the ^{3}MLCT excited state. The dependence of τ_{VC} on polarizability (Fig. 4.11) is much weaker, with R^2 when the excitation wavelength is 400 and 480 nm both being approximately 0.38, and only moderately better with R^2 = 0.52 when λ_{exc} = 550 nm. This is likely a worse fit of the data due to the wavelength-dependence of *n*, where the values used to calculate R(*n*) being taken at 589 nm in most instances.[40]

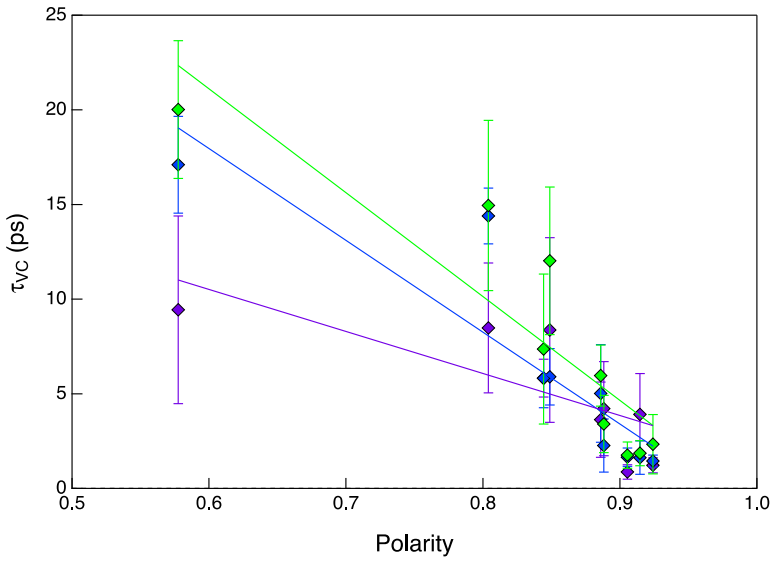

Figure 4.10. Correlation of the vibrational cooling time constant to the solvent polarity as a function of excitation wavelength: λ_{exc} = 400 nm (purple) fit with R^2 = 0.57, λ_{exc} = 480 nm (blue) fit with R^2 = 0.81, and λ_{exc} = 550 nm (green) fit with R^2 = 0.80.

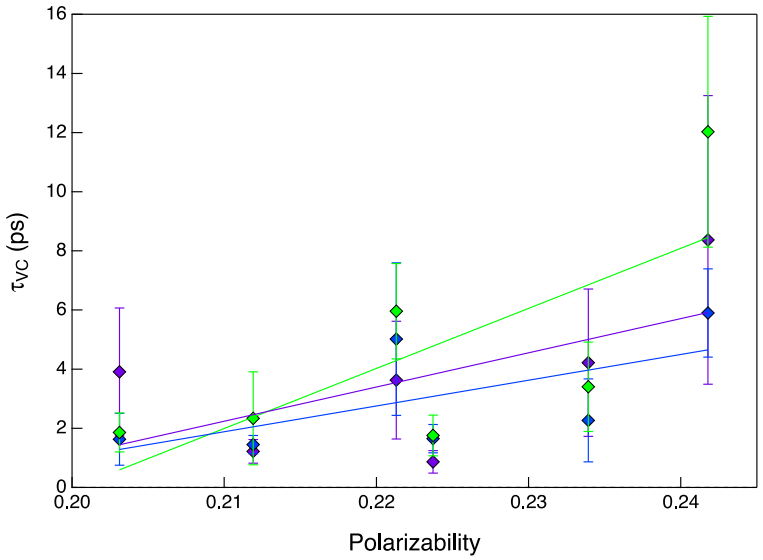

Figure 4.11. Correlation of the vibrational cooling time constant to the solvent polarizability as a function of excitation wavelength: λ_{exc} = 400 nm (purple) fit with R^2 = 0.37, λ_{exc} = 480 nm (blue) fit with R^2 = 0.39, and λ_{exc} = 550 nm (green) fit with R^2 = 0.52. No value of *n*, and therefore R(*n*), could be found for 1-HexOH, 1-OctOH, or HexCN.

A relationship can be made between the vibrational cooling time constant and the viscosity of the solvent (Fig. 4.12). In this case, solvation of the phenyl rotation follows a power law, as has been described previously.[9,16,41] This function is derived from Maroncelli and coworkers, who describe the solvation reorientation to a change in charge distribution in the solute as approximately equal to the reorganization dynamics of the solvent to a power given by the solvent dipole density.[9] The power law used to fit the data in Figs. 4.12 and 4.13 is defined as:

$$y = y_0 + Ax^{power} \tag{4.3}$$

for which y_0 is the y-offset, A is the amplitude, and x is taken to some power. This function may also be used to describe τ_{VC} vs. the average solvation time, a constant given for a specific probe molecule (here, Coumarin 153).[13] In both instances, a good correlation is found, as indicated by

the values of χ^2 in Table 4.5. The χ^2 test is a method for determining the appropriateness of a nonlinear curve to describe some data.[42] To evaluate the null hypothesis that the data follow the distribution of the curve, the probability is given by $\chi^2/d \leq s$, where d is the degrees of freedom (equal to the number of data points less the number of fit parameters) and s is the confidence interval according to the chi-squared probability distribution. The closer to 1, the higher the probability of the data fitting the model well. Take, for example, the curve fitting parameters for τ_{VC} vs. average solvation time at λ_{exc} = 400 nm. Here, χ^2 = 11.81, d = 3, so the probability that the vibrational cooling data will fit the power-law function with respect to average solvation time is 0.992, or a 99.2% chance that this model describes these data well. Viscosity (η) values could be found for all the solvents, so d = 6 here, whereas the average solvation time was only available for 6 of the solvents, making d = 3. Table 4.5 shows that the power law with respect to both viscosity and average solvation time describes the vibrational cooling data more accurately than it does the shorter time component. Interestingly, a strong correlation is found between the data for λ_{exc} = 480 and 550 nm and viscosity, whereas τ_{VC} is better described by the average solvation time when λ_{exc} = 400 nm. It is also notable that for the two lower excitation energies, the power that is found to describe the data is ~0.5 regardless of whether the fit is to the viscosity or the average solvation time; in the case of the higher excitation wavelength, the power is now closer to -0.3 for these fits. This parameter, as described by Maroncelli and coworkers,[9] is meant to indicate the solvent dipole density. Considering the same solvents are used between the three different excitation wavelengths, it seems more reasonable to assume that the power has changed as a response to the fact that the nature of the solvent reorientation is different between these two excitation regimes.

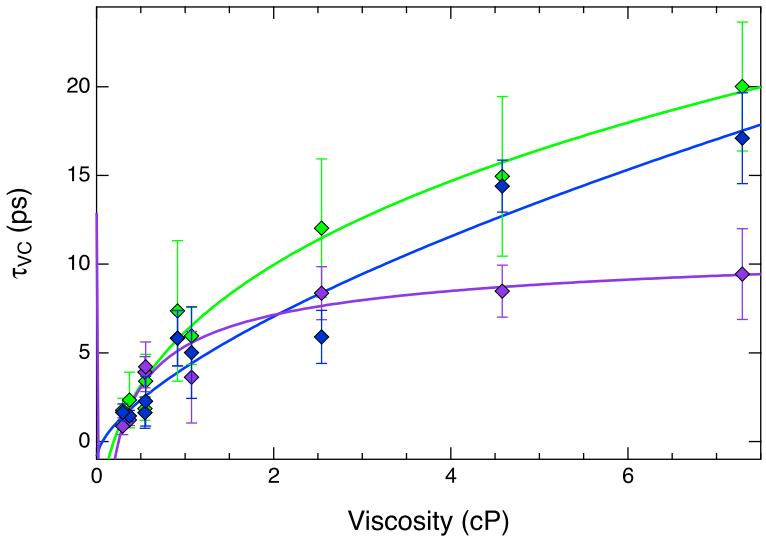

Figure 4.12. Correlation of vibrational cooling time constant of $[Ru(dpb)_3](BAr^F)_2$ with solvent viscosity as a function of excitation wavelength. The data for which λ_{exc} = 400 nm are shown in purple, λ_{exc} = 480 nm in blue, and λ_{exc} = 550 nm are in green.

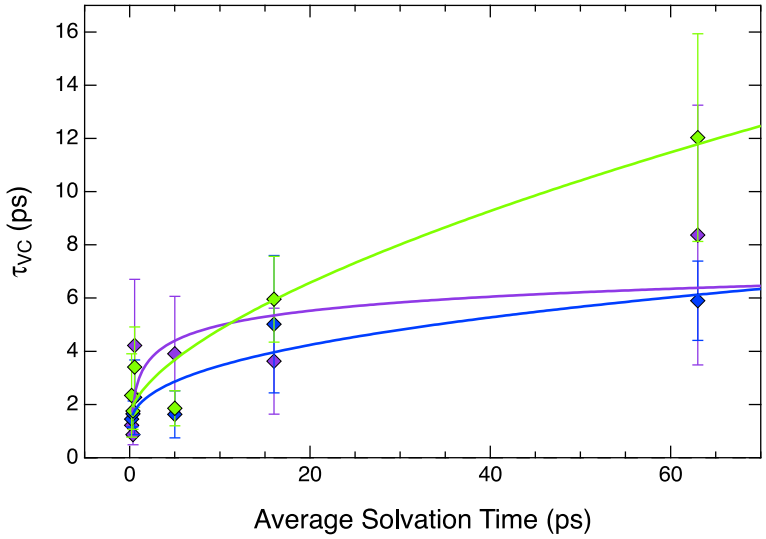

Figure 4.13. Vibrational cooling time constant of $[Ru(dpb)_3](BAr^F)_2$ versus the average solvation time (taken from refs. 13 and 43) as a function of excitation wavelength: λ_{exc} = 400 nm (purple), λ_{exc} = 480 nm (blue), and λ_{exc} = 550 nm (green).

Table 4.5. Fit parameters for τ_1 and τ_{VC} versus viscosity (η) and average solvation time, $\langle\tau\rangle$,[13] using eqn. (4.3).

λ_{exc}	Fit Parameter	τ_1 vs. η	τ_1 vs. $\langle\tau\rangle$	τ_{VC} vs. η	τ_{VC} vs. $\langle\tau\rangle$
400 nm	y_0	-0.1 ± 81.1	0.3 ± 0.2	12.9 ± 5.1	17.6 ± 138
	A	0.3 ± 81.2	-0.1 ± 0.2	-7.5 ± 5.4	-14.7 ± 139
	power	0.04 ± 8.81	-0.5 ± 1.1	-0.4 ± 0.3	-0.1 ± 0.7
	χ^2	0.110	0.044	6.14	11.81
480 nm	y_0	-0.3 ± 2.0	-0.8 ± 7.1	-0.8 ± 3.0	1.0 ± 1.7
	A	0.6 ± 2.0	1.0 ± 7.1	5.0 ± 3.3	1.0 ± 1.7
	power	0.20 ± 0.64	0.1 ± 0.3	0.7 ± 0.3	0.4 ± 0.4
	χ^2	0.068	0.014	14.4	2.94
550 nm	y_0	-0.3 ± 2.0	0.9 ± 12.3	-8.7 ± 7.9	1.5 ± 1.2
	A	0.5 ± 2.0	-0.7 ± 12.3	14.9 ± 8.3	0.8 ± 0.9
	power	0.13 ± 0.50	-0.04 ± 0.7	0.3 ± 0.1	0.6 ± 0.3
	χ^2	0.012	0.011	7.01	5.42

A general polar solvation model is given in Scheme 4.2. Here, the molecules are randomly oriented around the dication $[Ru(dpb)_3]^{2+}$ complex in its ground state, largely with their negative dipoles pointed toward the chromophore. Immediately upon excitation, a major charge redistribution occurs in the complex, but this instantaneous dipole moment is formed before the solvent can reorient, creating a Franck-Condon state in which the solvent molecules are still positioned as they were pre-excitation. The inertial solvent response likely occurs concomitantly

with the ^{1}MLCT→^{3}MLCT intersystem crossing. Vibrational cooling along this lowest energy excited state will also drive solvation relaxation such that the ^{3}MLCT is stabilized by the solvent. This relaxation mechanism of the solvent is what we are attempting to determine from the vibrational cooling data for $[Ru(dpb)_3]^{2+}$.

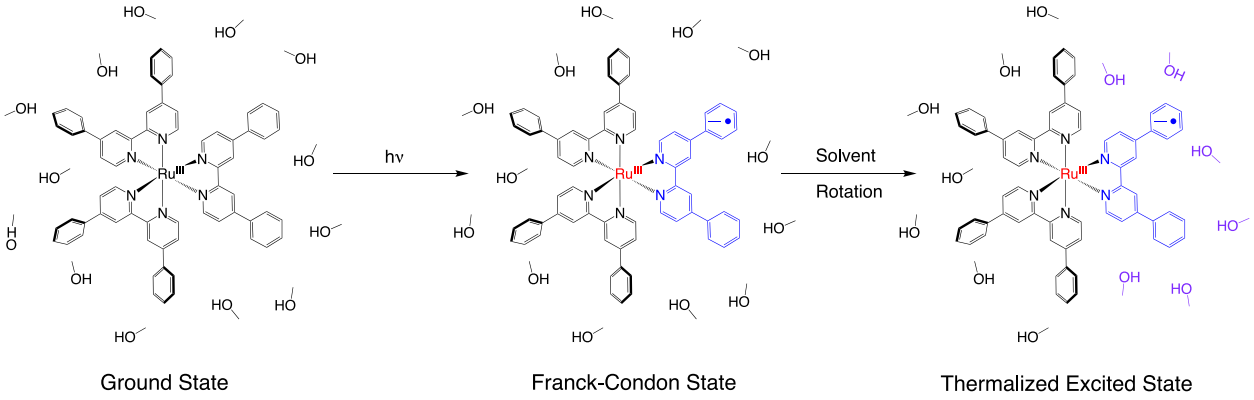

Scheme 4.2. The dielectric solvent mechanism present in $[Ru(dpb)_3](BAr^F)_2$ in alcoholic solvents at high excitation energy.

As outlined in the introduction, solvent can affect excited state dynamics in two ways: static solvation affects the energetics of the states, and dynamic solvation influences the kinetics of the reaction. The energetic stabilization afforded by the solvents, as described in Table 4.2, is less than 2% between MeOH and 1-OctOH; this cannot possibly be responsible for an increase of a factor of four in the vibrational cooling time constant at the highest energy excitation wavelength, let alone the order of magnitude difference observed when λ_{exc} = 550 nm. Static solvation is clearly not the primary factor in these data, leaving dynamic solvation models. Previously, the power-law dependence of an excited state process has been correlated to both the viscosity and average solvation time for peridinin in a variety of solvents.[41] This chromophore undergoes a torsional

event that facilitates excited state evolution. The relationship to viscosity suggested that solvent friction hindered the torsion of the molecule, whereas a stronger association to the average solvation time indicated that the twisting of this charge-redistributed state also produced solvent reorientation.

A similar analysis can be performed on the vibrational cooling dynamics observed in $[Ru(dpb)_3]^{2+}$. It is evident from Fig. 4.10 that a polar solvation model is appropriate to describe this excited state evolution, particularly for λ_{exc} = 480 and 550 nm. More specifically, the strong power dependence of τ_{VC} at these excitation energies on viscosity demonstrates that the twisting of the phenyl ring during the vibrational cooling process is increasingly encumbered due to friction from the longer alkyl chains of the solvent. It seems highly probable that the large-amplitude motion of the aryl rotation forces the solvent molecules to translate away from the chromophore. This viscoelastic diffusion process is almost nonpolar in nature.[16] However, the dynamics observed herein at λ_{exc} = 480 and 550 nm do not appear to follow a nonpolar mechanism as this type of response is directly proportional to the solvent viscosity. It is also relatively common for nonpolar solvation dynamics to become nonexponential in highly viscous solvents;[17] one would expect that in these data for 1-OctOH, but biexponential kinetics are clearly descriptive of the data. The data given by Table 4.5 also show a relationship between τ_{VC} and the average solvation time when λ_{exc} = 480 and 550 nm. In addition to the viscosity-induced dynamics in these data, it is apparent that the solvent must also reorient to the large instantaneous dipole moment in the MLCT excited state of $[Ru(dpb)_3]^{2+}$ (Scheme 4.2). This is not unexpected given that these dynamics are indicative of a polar solvation mechanism.

While the data for λ_{exc} = 400 nm do follow the power-law dependence to viscosity as is seen upon excitation at 480 or 550 nm, a stronger correlation is made instead to the average

solvation time, which implies that the solvent reorientation to the charge distribution of the MLCT is more prominent at this excitation wavelength than solvent translation. This is only observed in the alcohols, likely because the nitriles only span a limited viscosity range relative to the alcohol solvents. It can therefore be concluded that solvent reorientation (like by rotation) occurs as a response to the dipole moment of the MLCT excited state in $[Ru(dpb)_3]^{2+}$ at every excitation wavelength, in every solvent. The lower energy excitation wavelengths incur a greater viscoelastic response as the phenyl in the dpb ligand rotates. The leveling off of τ_{VC} in the alcohol series upon excitation at 400 nm is curious, however. To the best of our knowledge, this type of solvation response has not been previously reported. It would appear that for the longer-chain alcohols upon higher energy excitation exhibit a reorientation that is alkyl length-independent. A rotation about C-O bond to point the polar -OH head toward the charged chromophore seems to be the most likely response. This reorganization of the solvent becomes insensitive to the length of the alkane after a certain point – specifically after four carbons, $(CH_2)_3CH_3$. There are a few possibilities as to why these solvation dynamics appear for λ_{exc} = 400 nm only. The first is that the nature of the upper ^{1}MLCT excited state is substantially different from the lower excited states, inducing more specific solute-solvent interactions. The second is the possibility of an alternate relaxation pathway being accessed from $^1MLCT_1$ to the lowest energy excited state, driving the solvent reorientation. Finally, the amount of excess energy supplied to the ^{1}MLCT state relative to the ^{3}MLCT forces the solvent to reorganize in the most efficient method available, a process which is not necessary when exciting at 480 or 550 nm. The third seems the most probable, but a combination of all three could be possible and will be explored further.

4.1.1 Anomalous Trend in the Shorter Kinetic Component

Finally, the shorter time component in the ultrafast TA data must be discussed. This

component was found by Damrauer and McCusker to be 200 ± 50 fs in $[Ru(dpb)_3]^{2+}$ and <120 fs in the methylated version of the complex, $[Ru(dmb)_3]^{2+}$: an assignment was never made.[8] This feature, despite being <10% of the kinetic contribution, has an outsized amplitude, as shown in Table 4.6. It is also interesting that the amplitude of τ_1 follows separate trends for the different pump wavelengths depending on the solvent series.

Table 4.6. Comparison of percentage of amplitude (A) and kinetic (τ) components of the vibrational cooling transient absorption data for $[Ru(dpb)_3]^{2+}$ in alcohol and nitrile solvents.

Solvent Series	λ_{exc} (nm)	A_1 (%)	A_2 (%)	τ_1 (%)	τ_2 (%)
Alcohols	400	59	41	5	95
	480	54	46	8	92
	550	47	53	4	96
Nitriles	400	66	34	5	95
	480	49	51	8	92
	550	64	36	5	95

Despite using a laser system with shorter pulses, and therefore a shorter IRF, the order of magnitude of τ_1 did not change, and in some cases increased (Table 4.7). On average, this time constant was larger for the alcohol solvents with respect to the nitriles; this is however a somewhat dangerous statement as the error bars on the average data do not necessarily convey statistically significant values. While it may initially be appealing to assign this lifetime to ^{1}MLCT→^{3}MLCT intersystem crossing, the value of τ_1 does not decrease when λ_{exc} = 550 nm, for which excitation directly populates the ^{3}MLCT excited state such that there is no intersystem crossing process. It is likely that this kinetic component reflects a combination of processes: inertial solvent response

(60-90 fs in MeCN[44-46]) and ^{1}MLCT→^{3}MLCT intersystem crossing at the higher excitation energies (<100 fs[14,15]) are the two most likely processes. While 100s of fs is typical of IVR, $[Ru(dpb)_3]^{2+}$ is homoleptic, which reduces the chance that this relaxation process would be observed.[24] These time constants, while not being able to be assigned through the methods used here, have been definitively determined for this compound, paving the way for future studies to gain further insight into the photophysical processes of $[Ru(dpb)_3]^{2+}$.

Table 4.7. Short-time kinetic component (τ_1) of $[Ru(dpb)_3](BAr^F)_2$ as a function of solvent and excitation wavelength.

Solvent	τ_1 (ps)		
	λ_{exc} = 400 nm	λ_{exc} = 480 nm	λ_{exc} = 550 nm
MeOH	0.42 ± 0.15	0.33 ± 0.14	0.14 ± 0.08
EtOH	0.23 ± 0.13	0.45 ± 0.17	0.26 ± 0.11
1-BuOH	0.33 ± 0.10	0.41 ± 0.06	0.30 ± 0.13
1-HexOH	0.23 ± 0.22	0.61 ± 0.23	0.35 ± 0.26
1-OctOH	0.15 ± 0.09	0.50 ± 0.32	0.32 ± 0.29
MeCN	0.11 ± 0.02	0.20 ± 0.11	0.14 ± 0.07
PrCN	0.05 ± 0.03	0.14 ± 0.07	0.10 ± 0.06
BuCN	0.18 ± 0.05	0.15 ± 0.05	0.21 ± 0.15
HexCN	0.19 ± 0.11	0.18 ± 0.05	0.15 ± 0.02
Alcohols	0.27 ± 0.10	0.46 ± 0.10	0.27 ± 0.08
Nitriles	0.13 ± 0.07	0.17 ± 0.03	0.15 ± 0.05
All (Alcohols and Nitriles)	0.21 ± 0.11	0.33 ± 0.17	0.22 ± 0.09

4.2 $[Ru(dmesb)_3]^{2+}$: Determining the Nuclear Coordinate of Vibrational Cooling

One assumption prevalent throughout this discussion is that the vibrational cooling

dynamics occur along the phenyl-bipyridine dihedral angle nuclear coordinate. This mode was identified by Damrauer and McCusker as the most probable due to an increased rate of vibrational energy relaxation in $[Ru(dpb)_3]^{2+}$ relative to $[Ru(dmb)_3]^{2+}$.[8] From these data it was postulated that the aryl rotation actually facilitated vibrational cooling in this complex, and thus the process was less efficient in the methylated analogue. Based on the discussion of solvation dynamics above, the large-amplitude motion inherent in phenyl torsion is a prime candidate for redistributing energy into the bath. However, this hypothesis has not been directly verified. In its coplanar form in the thermalized ^{3}MLCT, the ligand likely exists in resonance with a form taking on a double-bond between the bipyridine and the phenyl. In this case, femtosecond stimulated Raman spectroscopy would be ideally suited to observe the growth of the C=C bond formation.[47] If the frequency for this stretch is seen on the same timescale as the vibrational cooling dynamics here, it seems very likely that the primary vibrational mode associated with this process is the phenyl twisting.

In the absence of this technique, the age-old inorganic chemistry trick is to prepare and study analogues. We have done just that with the mesityl version of the complex in question, $[Ru(dmesb)_3]^{2+}$. The methyl groups substituted in the *ortho*-positions of the peripheral phenyls inhibit rotation and ultimately reduce the delocalized nature of the excited state for this complex with respect to $[Ru(dpb)_3]^{2+}$.

When thinking about the nature of the mesityl group as a substituent, it is not immediately apparent how it should behave. Based on the ground state crystal structure, the ring is canted ~61° relative to the bipyridine backbone, which will greatly decrease any resonance effects that might have occurred from the extended conjugation. This is especially true with respect to $[Ru(dpb)_3](PF_6)_2$, for which the peripheral phenyl-bipyridine torsion is only approximately 32°. With the methyl groups, it might have been anticipated that the mesityl moiety could be slightly

more electron-donating than the simple phenyl group but being oriented closer to orthogonal to the bpy backbone, those effects are expected to be drastically reduced. In such a case, it might actually be more reasonable to approximate the mesityl simply as a bulky, greasy substituent with attenuated conjugation in comparison with the phenylated complex. This is confirmed by the ground state absorption spectrum of $[Ru(dmesb)_3]^{2+}$ (Fig. 4.14), which shows a lowest energy MLCT maximum much closer in energy to that of $[Ru(bpy)_3]^{2+}$ than $[Ru(dpb)_3]^{2+}$, implying that whatever conjugation is present in the excited state is greatly reduced relative to the phenyl complex.

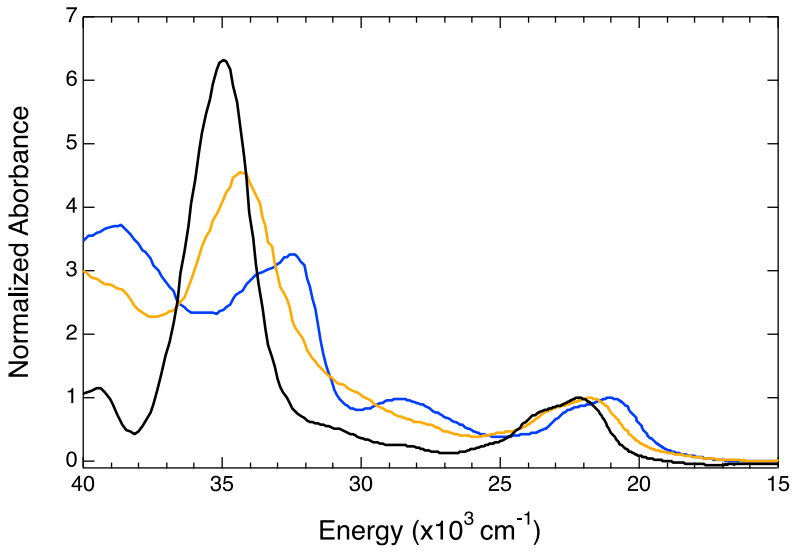

Figure 4.14. Ground state absorption spectra of $[Ru(bpy)_3]^{2+}$ (black), $[Ru(dpb)_3]^{2+}$ (blue), and $[Ru(dmesb)_3]^{2+}$ (yellow) in MeCN, normalized to the maximum of the lowest energy ^{1}MLCT transition. The two MLCT bands' maxima shift to the red as a function of delocalization in the excited state: 286 and 450 nm in $[Ru(bpy)_3]^{2+}$, 292 and 459 in $[Ru(dmesb)_3]^{2+}$, and 310 and 475 nm in $[Ru(dpb)_3]^{2+}$.

The vibrational cooling dynamics were studied for $[Ru(dmesb)_3](BAr^F)_2$ in MeOH, 1-

OctOH, and MeCN at the same excitation wavelengths used previously – namely, 400, 480, and 550 nm. As is evident from these data, the kinetics in 1-OctOH were highly non-biexponential and showed the same slow rise (Fig. 4.15, Table 4.8) that was observed in $[Ru(dpb)_3]^{2+}$. This may indicate a nonpolar solvation mechanism in this case, which would be unsurprising in the nonpolar nature of both the mesityl and 1-OctOH but would be startling in the fact that the nature of solvation has completely changed simply via ligand substitution in a transition metal complex.

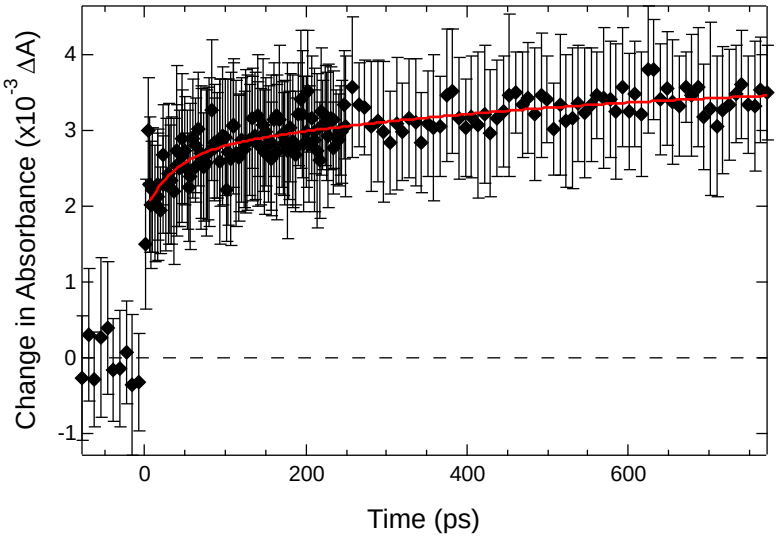

Figure 4.15. Vibrational cooling dynamics in $[Ru(dmesb)_3](BAr^F)_2$ in 1-OctOH at 532 nm upon excitation at 480 nm. The data (black diamonds) appear to rise slowly with a multiexponential fit (red trace) that was greater than the delay of the stage.

Table 4.8. Summary of the short-time kinetics observed upon probing at 530 nm in $[Ru(dmesb)_3]^{2+}$.

Solvent	λ_{exc} (nm)	τ_1 (ps)	τ_2 (ps)	τ_3 (ps)	τ_4 (ps)
MeOH	400	0.04 ± 0.05	2.0 ± 1.4		
	480	0.26 ± 0.23	31 ± 17		
	550[a]	<0.11	N/A		
1-OctOH	400[b]	N/A	N/A		
	480	<0.11	48 ± 21	335 ± 375	1520 ± 180
	550	0.05 ± 0.03	12 ± 7	145 ± 40	
MeCN	400[c]	0.09 ± 0.03	6.0 ± 0.7		
	480	0.10 ± 0.04	5.1 ± 1.3		
	550	0.10 ± 0.04	6.3 ± 4.3		

a The kinetics were within the IRF of the system. No longer-time component was observed.

b Unfortunately data could not be collected at this excitation wavelength due to laser stability. The kinetics observed at the lower energies were unusual (see text for details).

c From ref. 31.

The kinetics appeared well-behaved in both MeOH and MeCN, though. In each of these solvents, biexponential kinetics were observed. The difference here is the shape of the signal, in which the initial amplitude is large and decreases by only a small amount to the long-lived trace representing the thermalized ^{3}MLCT excited state (Fig. 4.16). This signal was also observed by Damrauer previously.[31] Disregarding the data in 1-OctOH, τ_1 is relatively unchanged in $[Ru(dmesb)_3]^{2+}$ relative to $[Ru(dpb)_3]^{2+}$. It is not unexpected for the inertial response of the solvent

and intersystem crossing of the complex to be unchanged with only the addition of methyl substituents on the peripheral phenyl moiety. The bigger differences are observed in τ_2, which is presumably τ_{VC}. At all excitation wavelengths in MeCN, this time constant is longer than was observed in $[Ru(dpb)_3]^{2+}$. The same trend is observed in MeOH upon excitation at 480 nm. The apparent lack of τ_{VC} when λ_{exc} = 550 nm is explained by the steady state absorption spectrum of $[Ru(dmesb)_3]^{2+}$ (Fig. 4.17). The excitation wavelengths were kept consistent with what was used to study $[Ru(dpb)_3]^{2+}$; the ground state absorption spectrum of $[Ru(dmesb)_3]^{2+}$ is somewhat blue-shifted relative to the phenyl complex. This will reduce the amount of excited state population produced, particularly at 550 nm. Furthermore, at this energy, the lowest vibrational modes of the ^{3}MLCT excited state are being formed, which means very little excess energy will exist to be dissipated to the solvent. It does appear that vibrational cooling dynamics were observed in MeCN, however, despite the spectrum in these two solvents being nearly superimposable in this region of the spectrum. The lowest-energy MLCT band is broadened toward the red in 1-OctOH, and also displays a greater oscillator strength at shorter wavelengths.

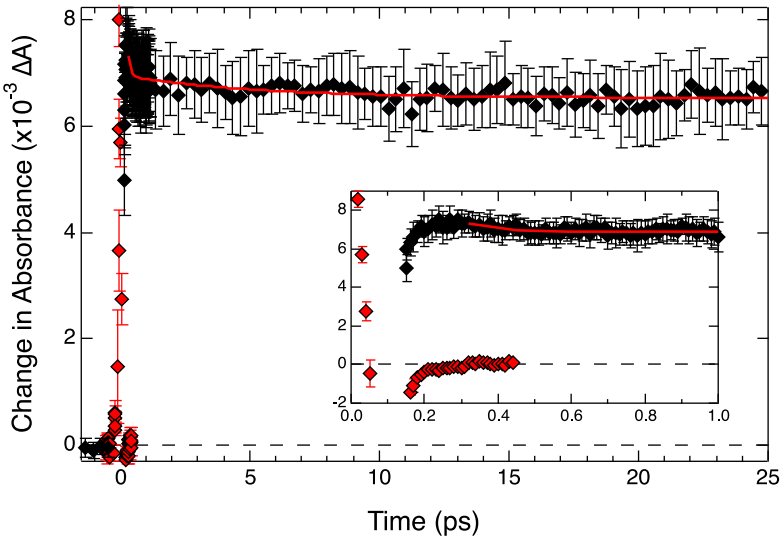

Figure 4.16. Vibrational cooling dynamics of $[Ru(dmesb)_3](BAr^F)_2$ in MeCN upon excitation at 480 nm with probing at 530 nm. Initially the amplitude of the signal is relatively high but decays with biexponential kinetics to a long-lived signal.

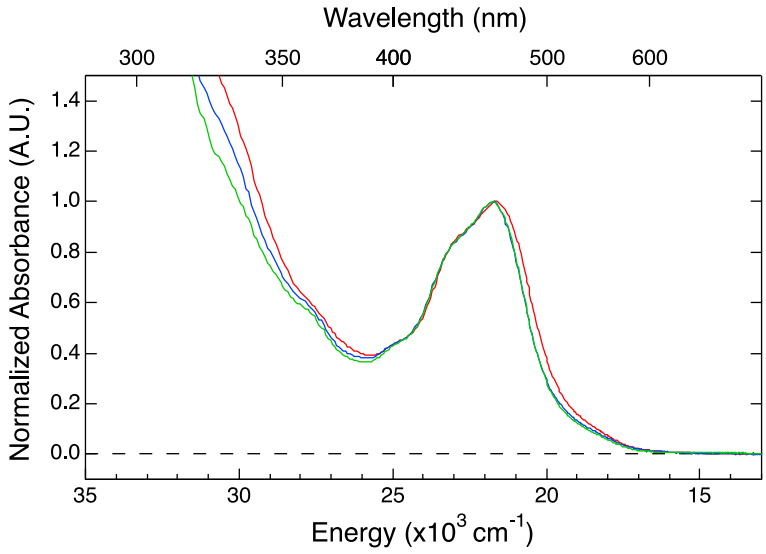

Figure 4.17. Ground state absorption spectra of $[Ru(dmesb)_3]^{2+}$ normalized to the maximum of the lowest-energy MLCT band. The data presented are of the complex in MeOH (blue), 1-OctOH (red), and MeCN (green).

$[Ru(dmesb)_3]^{2+}$ affords a complex that is similar in shape and size to $[Ru(dpb)_3]^{2+}$, but effectively reduces the degree of conjugation in the excited state. This should reduce the driving force toward ring rotation and slow the vibrational cooling kinetics. In fact, this does appear to be the case from the data presented here. In MeOH and MeCN, τ_{VC} is elongated relative to that of $[Ru(dpb)_3]^{2+}$. The vibrational cooling observed in 1-OctOH is greatly hindered to the point of perhaps achieving a nonpolar solvation mechanism. These data serve to verify the fact that the vibrational cooling process being observed is occurring along the phenyl-bipyridine dihedral angle coordinate.

The exception based on Table 4.8 is τ_{VC} in MeOH upon excitation at 400 nm. These data were the anomaly in $[Ru(dpb)_3]^{2+}$ as well, and lifetimes in 1-OctOH for $[Ru(dmesb)_3]^{2+}$ are still desired in order to better inform the assignment of solvation. However, based on this single (reproducible) data point, we are postulating that the vibrational dynamics observed are less due to any torsion of the mesityl as this should occur on a longer timescale, but are actually the reorientation of the solvent, as was seen at this excitation wavelength in the alcohol data for $[Ru(dpb)_3]^{2+}$. In this way, the two complexes maintain similar solvation dynamics.

4.3 Further Understanding of $[Ru(dpb)_3]^{2+}$

4.3.1 Ground State Recovery

With an understanding of how the solvation mechanism proceeds in $[Ru(dpb)_3]^{2+}$, the obvious next step was to determine why a dual response is observed based apparently on excitation wavelength. While the amount of excess energy provided to the chromophore via the excitation pulse is likely a contributing factor, it was necessary to determine if any other inherent differences were present. The two that immediately presented themselves are a significantly different excited state is populated or an alternate relaxation pathway is followed upon exciting at 400 nm, driving

local solute-solvent interactions.

TD-DFT was performed on both $[Ru(dpb)_3]^{2+}$ and $[Ru(dmesb)_3]^{2+}$ with help from S. Li. The ground state geometry was taken from the X-ray crystal structures, and the excited state geometry was optimized. No imaginary frequencies were found, meaning a global minimum was found for the geometry. Due to the soft potential in the geometry calculation from the aryl rotation, the excited state geometry for $[Ru(dmesb)_3]^{2+}$ is in the process of being determined. The ground state absorption spectrum was calculated from the TD-DFT transitions for $[Ru(dpb)_3]^{2+}$, as shown in Fig. 4.18, and was found to reproduce the experimentally-observed absorption spectrum well. No offset was applied though has been observed previously in calculations of Ru(II)-based chromophores.[25] The oscillator strength of the triplet transitions are defined as zero due to their spin-forbidden nature.

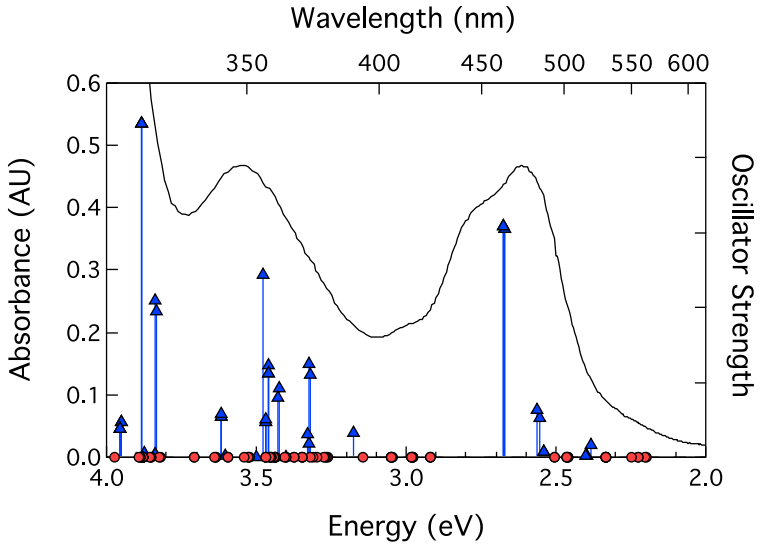

Figure 4.18. Overlay of the experimentally-determined ground state absorption spectrum of $[Ru(dpb)_3]^{2+}$ in MeCN (black trace) with the singlet (blue triangles) and triplet (red circles) transitions from time-dependent DFT calculations.

Orbital pictures corresponding to the transitions at the three excitation energies used in the ultrafast studies were calculated and are shown in Fig. 4.19. At 400 nm, one transition is found with a 49% probability. The ground state is predominantly d_{z^2} in nature, which then populates an excited state that is symmetrically distributed on the bpy backbone of all three dpb ligands. The excited state appears to be composed mainly of π character. Considering the MLCT excited state that is supposed to be achieved by excitation at 400 nm, it is expected that a metal-centered ground state is excited to populate a π* ligand-centered state. The results from TD-DFT appear to be consistent with what is expected upon excitation at 400 nm. Two 480 nm-based transitions were calculated, and each required two orbital pictures to be well-described, resulting in a total of four orbital pictures at 480 nm each with approximately 20% probability. In these transitions, two of four ground states are d_{z^2}, whereas the other two are another metal-centered state, the exact nature of which is unknown. As with the 400 nm excitation transition, the excited states in the 480 nm transitions are largely centered around the bpy backbone of the ligands. It is notable, however, that for the 480 nm calculated excited states, the orbital pictures are asymmetric about the bipyridines. The π character in three out of the four pictures are predominantly centered around only two bpy moieties, as opposed to the symmetric distribution observed in the 400 nm transitions. Despite this asymmetry, the general picture described by the TD-DFT calculations is consistent with the metal-centered orbital-to-ligand-centered π* transition predicted by the MLCT nature of the excited state. Finally, the 550 nm transition is well-described by one orbital picture with a 42% probability. Unlike the other two excitation energies, this transition is a triplet absorption, meaning the oscillator strength is defined as 0. The ground and excited states are very analogous to those in the 400 nm transition, in that a metal-centered d_{z^2} orbital ground state is excited into a π-based excited state in the bpy backbone of the dpb ligand.

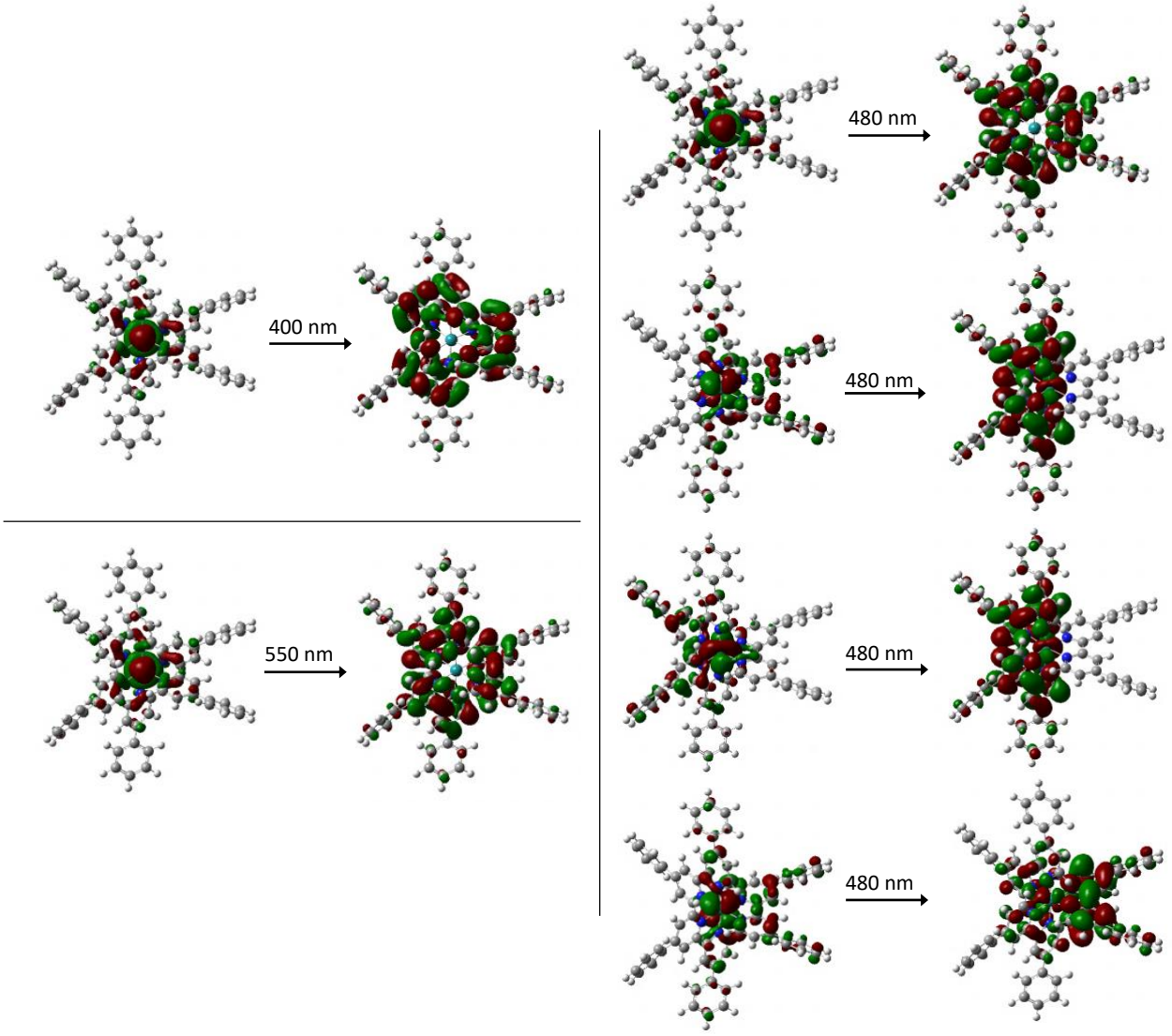

Figure 4.19. Orbital pictures of $[Ru(dpb)_3]^{2+}$ transitions as calculated from TD-DFT. The 400 nm absorption is a singlet transition found at 390.61 nm with f = 0.0327 (250α → 254α) with 49% probability. The 550 nm absorption is a triplet transition found at 551.71 nm with f = 0 (250α → 251α) with 42% probability. The top two 480 nm absorptions are singlet transitions found at 464.15 nm with f = 0.3043 (248α → 252α and 249α → 253α) with 21 and 22% probabilities, respectively. The bottom two 480 nm absorptions are singlet transitions found at 463.6 nm with f = 0.3088 (248α → 253α and 249α → 252α) with 21 and 23% probabilities, respectively.

With the successful application of TD-DFT calculations to understand the transitions in $[Ru(dpb)_3]^{2+}$, the method was applied to $[Ru(dmesb)_3]^{2+}$ in order to gauge the relative importance of the phenyl-bipyridine dihedral angle. Out of these calculations, the ground state absorption spectrum was calculated (Fig. 4.20) and reproduces the experimentally-obtained spectrum well. No offset was applied to the calculated spectrum.

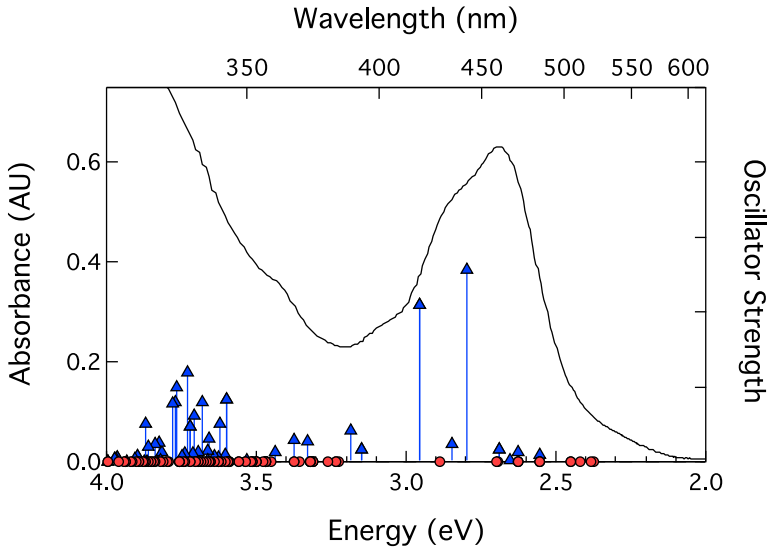

Figure 4.20. Overlay of the experimentally-determined ground state absorption spectrum of $[Ru(dmesb)_3]^{2+}$ in MeCN (black trace) with the singlet (blue triangles) and triplet (red circles) transitions from time-dependent DFT calculations.

From the ground state absorption spectrum, the orbital pictures corresponding to the three excitation energies may be calculated as well (Fig. 4.21). Unlike $[Ru(dpb)_3]^{2+}$, the processes in $[Ru(dmesb)_3]^{2+}$ only require one transition to describe each excitation energy. At 400 nm, an initially-formed metal-centered ground state (perhaps of the $d_{x^2-y^2}$ type) is excited to form a π-based excited state that resides solely on the bipyridine backbone of the dmesb ligands. This

description mimics the expected M(d)-L(π*) transition of an MLCT nature excited state in $[Ru(dmesb)_3]^{2+}$. The process occurring at 400 nm is believed to excite into a singlet state due to the oscillator strength of transition, which matches well with the calculated oscillator strength from TD-DFT, with f = 0.0271. The orbital pictures that describe the transitions at 480 and 550 nm excitation are very similar, and may be taken together, despite the fact that excitation at 480 nm is a singlet-singlet transition, whereas a 550 nm pump will prepare the ^{3}MLCT excited state. In both cases, a metal-centered ground state that is very analogous to that in the 400 nm transition (likely $d_{x^2-y^2}$) is initially present and upon excitation forms a ligand-centered excited state that is bpy π-based. What is of particular interest is the increasing asymmetry of the excited state upon decreasing excitation energy. In the 400 nm excited state, the orbital picture is highly symmetric with even distribution about all three bipyridine moieties. Moving to the 480 nm excited state picture, the wavefunction only resides on two bipyridines. Finally, at 550 nm excitation, two bipyridines are again required to describe the excited state, but one is more heavily favored than the other as evidenced by the size of the π-based orbitals. Furthermore, the excited states of the two lower energy excitation processes incorporate more metal character than excitation at 400 nm, which shows a void around the metal center. This would imply that the instantaneous dipole moment in at λ_{exc} = 480 and 550 nm is greatly reduced relative to that of λ_{exc} = 400 nm. While this phenomenon is expected in general for $[Ru(dmesb)_3]^{2+}$ relative to $[Ru(dpb)_3]^{2+}$ owing to the ability of the phenyl substituents to rotate and alter the degree of conjugation in the excited state, it is surprising to see any kind of dependence of that sort on the excitation energy. It is apparent from the orbital pictures for $[Ru(dpb)_3]^{2+}$ (Fig. 4.19) that the excited state wavefunction accesses the metal center for three out of four of the transitions used to describe the 480 nm excitation event, whereas at 400 and 550 nm, the metal only participates in the ground state.

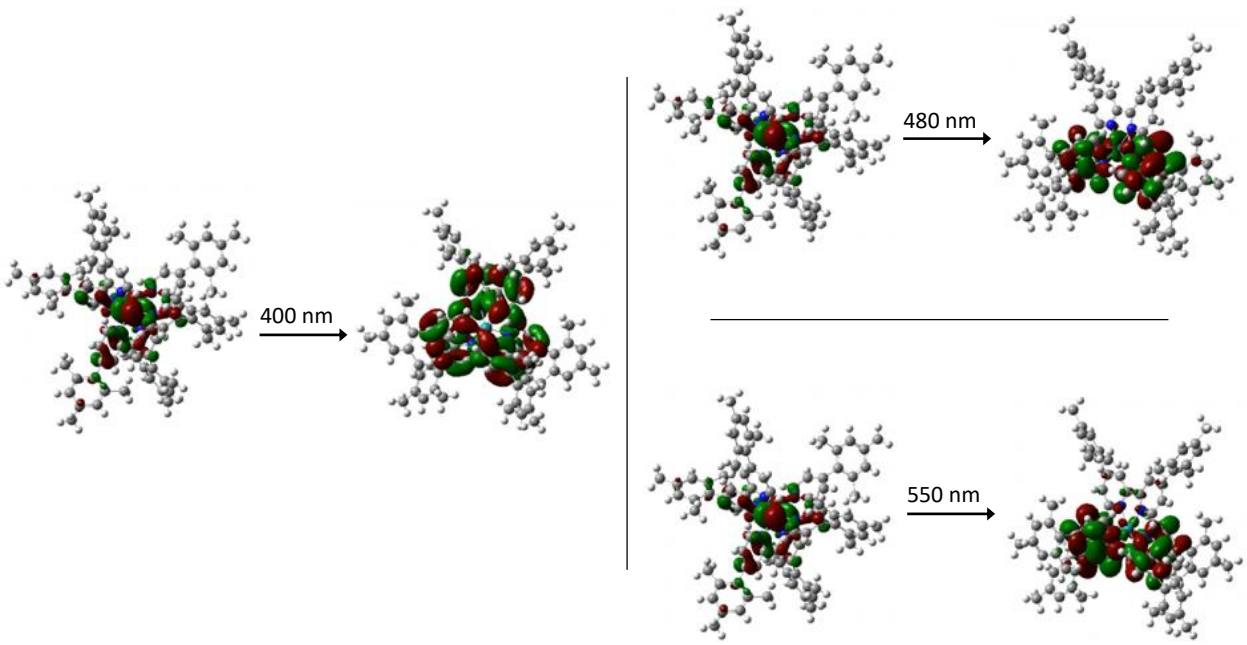

Figure 4.21. Orbital pictures of $[Ru(dmesb)_3]^{2+}$ transitions as calculated from TD-DFT. The 400 nm absorption is a singlet transition found at 372.60 nm with f = 0.0271 (322α → 326α) with 37% probability. The 480 nm absorption is a singlet transition found at 467.67 nm with f = 0.0014 (322α → 324α) with 35% probability. The 550 nm absorption is a triplet transition found at 522.64 nm with f = 0 (322α → 323α) with 26% probability.

From the TD-DFT results it is possible to conclude that the absorption processes for $[Ru(dpb)_3]^{2+}$ and $[Ru(dmesb)_3]^{2+}$ are dominated by ^{1}MLCT ← $^1A_1$ absorption for both the 400 and 480 nm excitation energies. At 550 nm excitation, however, the absorption process is ^{3}MLCT ← $^1A_1$ in nature, as evidenced by the weaker oscillator strength. The major result of note is the degree of asymmetry in the excited states. In the case of $[Ru(dpb)_3]^{2+}$, the wavefunctions of the excited states formed at λ_{exc} = 400 and 550 nm are evenly distributed among all three dpb ligands, whereas excitation at 480 nm biases the wavefunction towards only two of the three ligands. In $[Ru(dmesb)_3]^{2+}$, however, the degree of asymmetry increases as the excitation energy is reduced.

Surprisingly, the excited state wavefunction never delocalizes to the substituents in either $[Ru(dpb)_3]^{2+}$ or $[Ru(dmesb)_3]^{2+}$, despite the ability of the phenyl to rotate to coplanarity in the excited state of the dpb analogue. These results are unfortunately not conclusive, but do imply that nature of the excited state prepared at each of the excitation energies may be different enough to explain the differences observed in the ultrafast solvation dynamics previously described.

To better understand the relaxation pathway incurred with different excitation energies, emission spectra were collected for $[Ru(dpb)_3](BAr^F)_2$ in MeOH and 1-OctOH (Fig. 4.22). Excitation was performed at 340 nm to directly excite into the higher energy MLCT excited state. No change was observed with different pump wavelengths except differing intensities (which will be discussed thoroughly in Chapter 4 Section 4.3.2). The emission maximum is 10 nm blue-shifted in MeOH relative to 1-OctOH. No other differences are observed here, indicating that emission is occurring from the same excited state, here the ^{3}MLCT, regardless of which state is formed upon excitation. A spectral overlay of the steady state emission and absorption spectra of $[Ru(dpb)_3]^{2+}$ in 1-OctOH is shown in Fig. 4.23. Similar features are observed in the spectra for MeOH (not shown).

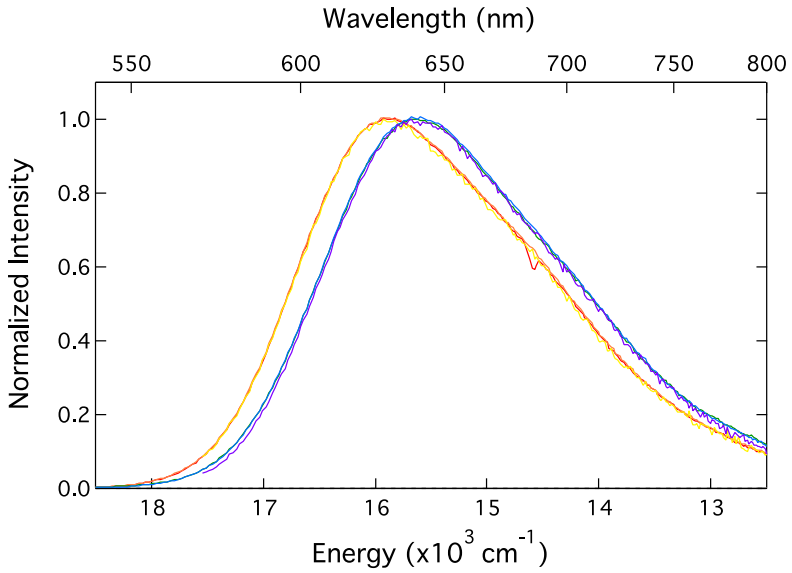

Figure 4.22. Steady state emission spectra of $[Ru(dpb)_3](BAr^F)_2$: in MeOH with λ_{exc} = 340 nm (red), 470 nm (orange), and 550 nm (yellow), and in 1-OctOH with λ_{exc} = 340 nm (green), 470 nm (blue), and 550 nm (purple). The emission spectra showed no dependence on excitation wavelength; the maximum in MeOH is 630 nm and is 640 nm in 1-OctOH.

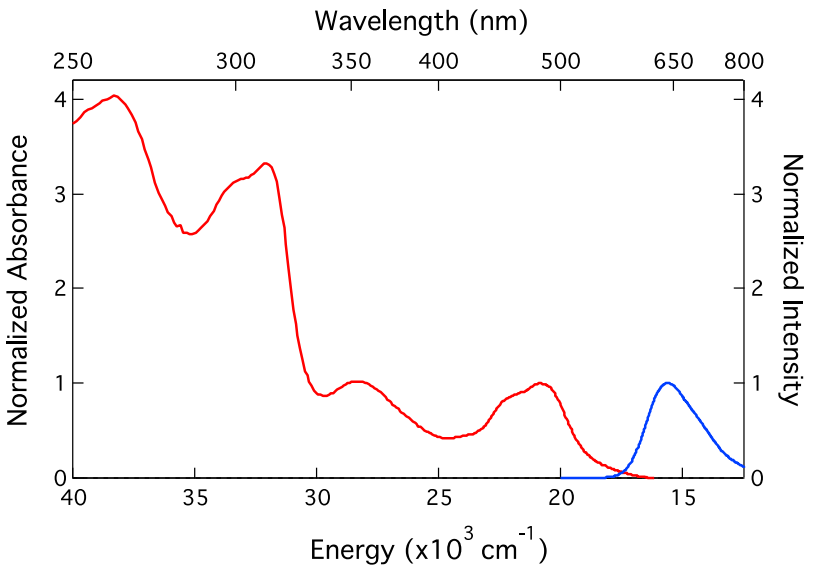

Figure 4.23. Overlay of the steady state absorption (red trace) and emission (blue trace) of $[Ru(dpb)_3](BAr^F)_2$ in 1-OctOH. The lowest energy MLCT transition and the emission maxima are normalized to each other.

To further clarify any pump wavelength dependence in the emission data, excitation spectra were collected in MeOH (Fig. 4.24) and 1-OctOH (not shown). In this experiment, the intensity at the emission maximum is reported as a function of excitation wavelength. The excitation spectrum should overlay nearly perfectly with the ground state absorption spectrum, as is observed in Fig. 4.24. Any deviation indicates either an impurity, or emission from the chromophore in a different form. The disparity occurring at higher excitation wavelengths may be caused by a $[Ru(dpb)_3]^{2+}$ conformer in which the phenyl-bipyridine dihedral angle is nearly 90º but is more likely explained by the fact that the absorbance at higher energy is outside the acceptable sensitivity range of the UV-Vis spectrophotometer. In either case, at the excitation wavelengths of interest, no impurity or second conformational species is present, thus the pathway to the emissive ^{3}MLCT excited state must be consistent between the different pump energies.

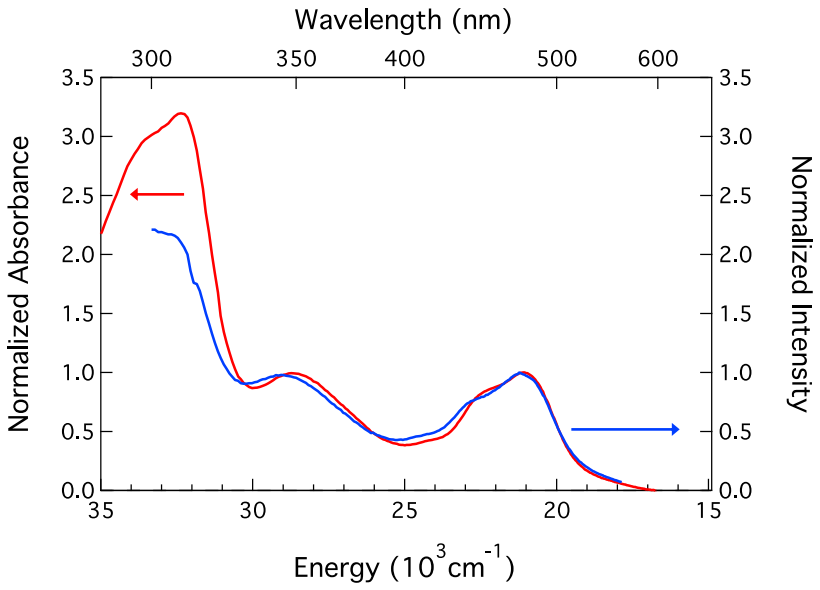

Figure 4.24. Overlay of the ground state absorption (red, left axis) and excitation emission (blue, right axis) spectra of $[Ru(dpb)_3](BAr^F)_2$ in MeOH. The spectra match moderately well for ~340-550 nm, indicating the phosphorescence process from the ^{3}MLCT is well-behaved (see text for more details).

4.3.2 ^{1}MLCT→^{3}MLCT Intersystem Crossing

The original motivation in studying the photophysical properties of $[Ru(dpb)_3]^{2+}$ was its anomalously high quantum yield (Φ). Here it is worth taking time to discuss the previously reported quantum yields in $[Ru(dpb)_3]^{2+}$. Cook and coworkers initially prepared this complex and found Φ = 0.306.[5] Alternatively, Damrauer et al. report a quantum yield for the same compound as being 0.20 ± 0.02.[6] This value is intrinsically dependent on such factors as solvent,[4-6,27] temperature,[4,27,48] excitation wavelength,[4,49-51] and the instrument detector.[27] The data presented by Cook et al. are collected in deaerated 4:1 (v/v) EtOH/MeOH at 293 K, whereas Damrauer and coworkers used deaerated MeCN at 298 K. A summary of these data can be found in Table 4.9. These values were collected as relative quantum yields, in which the emission intensity of the

compound of interest is compared to that of a known standard. Here, the quantum yield of $[Ru(bpy)_3]^{2+}$ (Φ_{std}) well-known and thus used as a reference to determine the quantum yield of the unknown complex (Φ_{unk}),[6,26] according to:

$$\Phi_{unk} = \Phi_{std}\left(\frac{I_{unk}}{A_{unk}}\right)\left(\frac{A_{std}}{I_{std}}\right)\left(\frac{n_{unk}}{n_{std}}\right)^2 \quad (4.4)$$

for which I is the integrated emission intensity, A is the absorbance of the sample at the excitation wavelength, and *n* is the index of refraction of the solvent; unk and std denote the unknown and standard, respectively. The choice of reference is critical and is meant to be nearly identical to the compound of interest. This minimizes uncertainty in the integrated intensities by calibrating the spectral sensitivity in the wavelengths that display emission. In the case of $[Ru(dpb)_3]^{2+}$, the phosphorescence of $[Ru(bpy)_3]^{2+}$ turns out to be a decent reference for quantum yield determination. As analogues of each other, they are emitting from the same state, and have similar emission profiles with λ_{max} of $[Ru(bpy)_3]^{2+} \cong 620$ nm[27] and 630 nm in $[Ru(dpb)_3]^{2+}$. As shown in Table 4.9, the quantum yields for $[Ru(bpy)_3]^{2+}$ and $[Ru(dpb)_3]^{2+}$ are given for the data from Cook and coworkers, and Damrauer and coworkers, as both of these sources calculated relative quantum yields.

Table 4.9. Quantum yield data and experimental setups for $[Ru(bpy)_3]^{2+}$ and $[Ru(dpb)_3]^{2+}$.

	Suzuki et al.[27]	Cook et al.[5]	Damrauer et al.[6]	This work
Temperature (K)	298	293	298	298
Solvent	MeCN	4:1 (v/v) EtOH/MeOH	MeCN	MeCN
λ_{exc} (nm)	350	not specified	450	480
$[O_2]$	air-free	air-free	air-free	air-free
Detector	BT-CCD	PMT	PMT	BT-CCD
$\Phi[Ru(bpy)_3]^{2+}$	0.095 ± 0.003	0.089	0.062 ± 0.006[48]	0.103 ± 0.002
$\Phi[Ru(dpb)_3]^{2+}$	N/A	0.306	0.20 ± 0.02	0.255 ± 0.006
Corrected $\Phi[Ru(dpb)_3]^{2+}$ *a*	N/A	0.354	0.33 ± 0.03	0.255 ± 0.006

a Calculated for using eqn. (4.5) from $\Phi[Ru(bpy)_3]^{2+}$ found in this work.

Since the time of these publications, however, new studies have made use of back-thinned CCD (BT-CCD) detectors within an integrating sphere setup for the purposes of measuring absolute quantum yields. Both of the quantum yields reported above were found using a setup that utilized a photomultiplier tube (PMT) in the detection scheme. While PMTs are good detectors for higher energy fluorescence signals, the emission from Ru(II) complexes comes from the ^{3}MLCT excited state. This phosphorescence is consequently lower energy (i.e., NIR), for which PMTs lose all spectral sensitivity. With these wavelengths, correction factors are critical to the integration of the spectra but may result in inaccurate quantum yields being reported. This is especially observable in the comparison of quantum yields for $[Ru(bpy)_3]^{2+}$ in Table 4.9. When using a PMT detector, Φ is lower than when using a BT-CCD. In the determination of Φ for $[Ru(dpb)_3]^{2+}$,

however, this can be corrected through the use of eqn. (4.5), in which the standard and sample under one set of conditions can be used, along with a standard, to find the quantum yield for a sample under a second set of conditions:

$$\frac{\Phi_{unk}^{Set\ 1}}{\Phi_{std}^{Set\ 1}} = \frac{\Phi_{unk}^{Set\ 2}}{\Phi_{std}^{Set\ 2}} \tag{4.5}$$

Using this relation, the corrected quantum yields for $[Ru(dpb)_3]^{2+}$ given the conditions used in this experiment were calculated and can be seen in Table 4.9.

This work utilized a BT-CCD detector in a setup with an integrating sphere. As such, the quantum yield in $Ru(bpy)_3]^{2+}$ was found to be 0.103, which is slightly higher but still in good agreement with that found by Suzuki et al. In the case of $[Ru(dpb)_3]^{2+}$, the quantum yield measured by the previous groups is a factor of three larger than that of the unsubstituted bpy complex. Although Damrauer and coworkers report a significantly smaller quantum yield, this can easily be attributed to both solvent and temperature. The quantum yield of $[Ru(bpy)_3]^{2+}$ has previously been shown to have a high temperature dependence,[27,48] which is likely to be true for the phenylated complex as well. This temperature dependence is caused by energetically nearby ligand field states that depopulate the ^{3}MLCT when the thermal barrier is low enough (i.e., warm temperatures). Ground state recovery from these ligand field states occurs via a nonradiative pathway, thereby decreasing the quantum yield of phosphorescence from the ^{3}MLCT excited state. The solvent dependence, on the other hand, is caused by the influence of polar solvents on the charge-separated MLCT excited state. One can imagine that solvents with increased dielectric constants might better stabilize this potential energy surface relative to the ground state, as might be true for MeCN. Alternatively, specific solute-solvent interactions such as H-bonding in alcohols could also affect the energetics of the MCLT state, thereby shifting the energetics of the potential energy surface.[48] And in fact, the quantum yield reported by Cook et al. for $[Ru(dpb)_3]^{2+}$ is 0.306 in an alcohol

mixture, whereas Damrauer et al. find $\Phi = 0.20$ in MeCN. This would tend to imply that the protic solvents are better able to stabilize the MLCT excited state such that there is little thermal deactivation through the ligand field states, whereas the polar aprotic solvent allows for greater mixing of these states to occur at warmer temperatures, thereby reducing the quantum yield.

The degree of energetic stabilization afforded by solvation is difficult to experimentally verify by ground state absorption measurements, as the ^{3}MLCT band is obscured by the higher energy ^{1}MLCT←^{1}A$_1$ transition. Lifetime measurements of $[Ru(dpb)_3]^{2+}$ in MeCN and MeOH, however, are a more compelling as these provide a measure of k_r and k_{nr}. The use of eqn. (4.6) to determine these kinetic parameters[6,26,48] requires quantum yield data:

$$\Phi = \frac{k_r}{k_r + k_{nr}} \tag{4.6}$$

These emission and transient absorption lifetimes are given in Table 4.10. The former are relatively constant for $[Ru(dpb)_3]^{2+}$ in MeOH, but vary in 1-OctOH, particularly upon excitation at 550 nm. As a consequence, k_r is found to be nearly constant in MeOH and less so in 1-OctOH. However, this may also be a result of the change in quantum yield with different pump wavelengths, which are also proven to be more variable in 1-OctOH than in MeOH. Originally, we had sought to perform quantum yield studies as a function of excitation energy and solvent in order to determine whether different conditions led to new relaxation pathways to the thermalized ^{3}MLCT. That was not found to be the case, but the studies performed herein did yield interesting results that help give new understanding to the excited state potential energy surfaces of $[Ru(dpb)_3]^{2+}$.

Table 4.10. Quantum yield (Φ), emission (τ_{em}) and transient absorption (τ_{abs}) lifetimes, and the radiative (k_r) and nonradiative (k_{nr}) rates of $[Ru(dpb)_3](BAr^F)_2$ in MeOH and 1-OctOH as a function of excitation wavelength.

Solvent	λ_{exc} (nm)	Φ	τ_{em} (μs)	τ_{abs} (μs)	$k_r \times 10^5$ (s^{-1})	$k_{nr} \times 10^5$ (s^{-1})
MeOH	400	0.244 ± 0.004	1.372 ± 0.008	-	1.78 ± 0.03	5.51 ± 0.18
	480	0.243 ± 0.003	1.352 ± 0.003	1.321 ± 0.001	1.82 ± 0.02	5.66 ± 0.13
	550	0.232 ± 0.006	1.380 ± 0.002	1.333 ± 0.002	1.71 ± 0.04	5.66 ± 0.27
1-OctOH	400	0.205 ± 0.007	1.292 ± 0.008	-	1.59 ± 0.06	6.15 ± 0.38
	480	0.239 ± 0.005	1.306 ± 0.006	-	1.83 ± 0.04	5.83 ± 0.23
	550	0.195 ± 0.019	1.543 ± 0.005	-	1.26 ± 0.01	5.22 ± 0.90

Excitation-wavelength dependent quantum yields were found for $[Ru(dpb)_3](BAr^F)_2$ in air-free conditions in both MeOH and 1-OctOH (Fig. 4.25), as these represent the extreme ends of the alcohol solvent series. It is immediately apparent that the excitation energy plays a role in the quantum yield of the phosphorescence, particularly when the compound is dissolved in 1-OctOH. At λ_{exc} = 350 nm, the quantum yield begins at ~0.32, which decreases steadily to a local minimum around λ_{exc} = 400 nm, for which Φ ~ 0.20. This increases to a plateau for which Φ = 0.24 for λ_{exc} = 440-500 nm, then decreases again for lower excitation energies. The error is much larger at these lower energies due to partial overlap with the emission band. Though greatly attenuated, a similar trend can be seen in the quantum yield data for $[Ru(dpb)_3]^{2+}$ in MeOH. Φ remains relatively constant for λ_{exc} = 400-500 nm but increases for bluer pump wavelengths and begins to decrease

at redder wavelengths before noise is introduced. No spectral shifting of the emission maximum was observed as a function of the excitation wavelength, which would affect the integrated area of the curve. Thus, the quantum yield dependence on the pump energy was found to be truly inherent in $[Ru(dpb)_3]^{2+}$. This phenomenon had not been previously reported for $[Ru(bpy)_3]^{2+}$, so the quantum yield for this compound was measured in MeCN as a function of excitation wavelength (Fig. 4.25). Indeed, no pump energy dependence is observed, indicating that this behavior is reserved for the phenyl-substituted complex.

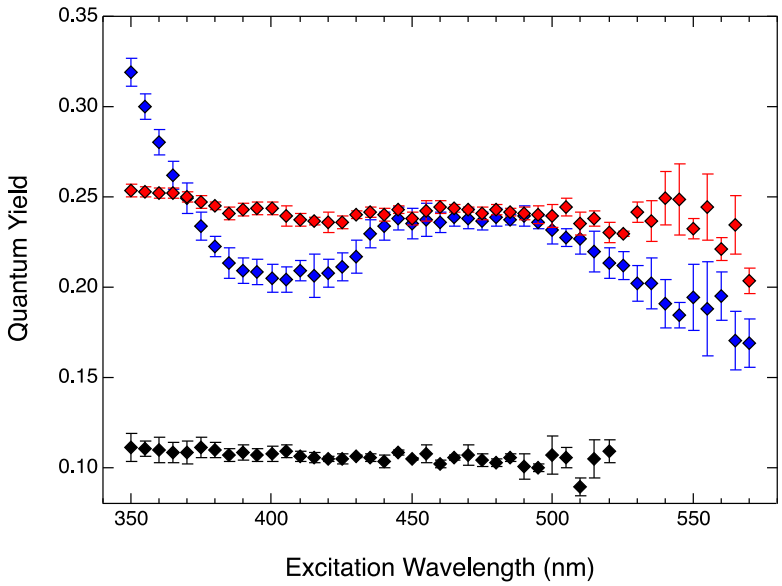

Figure 4.25. Quantum yields measured for deaerated $[Ru(dpb)_3](BAr^F)_2$ in MeOH (red diamonds) and 1-OctOH (blue diamonds) depicting the excitation wavelength dependence, particularly in 1-OctOH. These are shown in comparison to the quantum yield of air-free $[Ru(bpy)_3](PF_6)_2$ in MeCN which displays no excitation wavelength dependence.

To better understand the significance of the quantum yield dependence on excitation wavelength, Table 4.11 displays the values calculated for $[Ru(dpb)_3]^{2+}$ in MeOH and 1-OctOH,

MeCN and BuCN at the λ_{exc} used in the transient absorption experiments. Analogous data for $[Ru(bpy)_3]^{2+}$ in MeCN are given for comparison. The quantum yield for $[Ru(bpy)_3]^{2+}$ is unchanged with excitation at 400 or 480 nm. In each of the solvents, Φ upon excitation at 550 nm is the lowest value. This is the only consistency between the data for the four solvents. As was observed in Fig. 4.25, Φ in MeOH is relatively pump wavelength-independent, whereas excitation at 480 nm in 1-OctOH produces the highest quantum yield of the three wavelengths. The trend observed in 1-OctOH is amazingly also observed in MeCN (Fig. 4.26). In BuCN, however, the highest quantum yield is observed upon excitation at 400 nm. In this solvent, Φ for $[Ru(dpb)_3]^{2+}$ appears to simply decrease from ~0.37 at λ_{exc} = 350 nm with a slightly plateau around Φ ~0.28 for λ_{exc} = 480 nm, followed by a systematic decrease at lower excitation energies. These data would imply that, at least with respect to quantum yields, $[Ru(dpb)_3]^{2+}$ in MeCN behaves much more similarly to 1-OctOH than to either MeOH or BuCN, a very surprising result.

Table 4.11. Quantum yield of deaerated $[Ru(dpb)_3](BAr^F)_2$ as a function of solvent and excitation wavelength relative to air-free $[Ru(bpy)_3](PF_6)_2$ in MeCN.

Solvent	λ_{exc}		
	400 nm	480 nm	550 nm
MeOH	0.244 ± 0.004	0.243 ± 0.003	0.232 ± 0.006
1-OctOH	0.205 ± 0.007	0.239 ± 0.005	0.195 ± 0.019
MeCN	0.222 ± 0.010	0.255 ± 0.006	0.180 ± 0.009
BuCN	0.296 ± 0.017	0.267 ± 0.009	0.242 ± 0.030
$[Ru(bpy)_3]^{2+}$ in MeCN	0.108 ± 0.004	0.103 ± 0.002	N/A

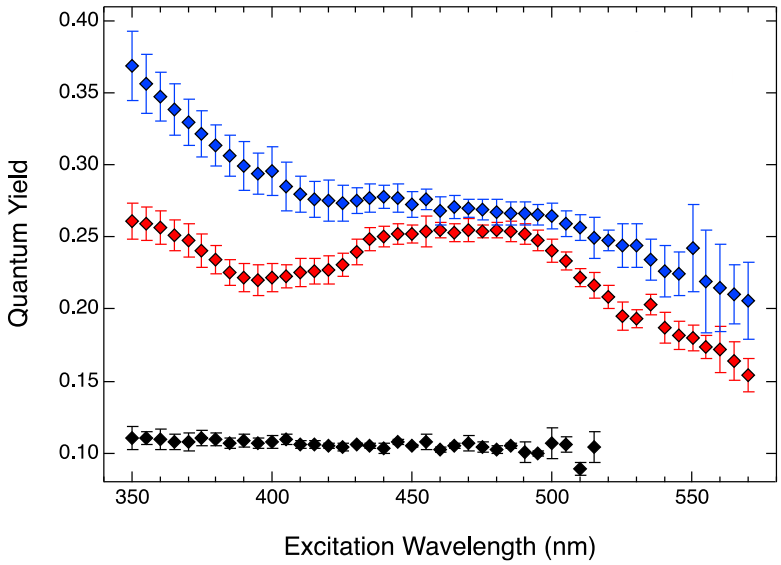

Figure 4.26. Excitation wavelength-dependent quantum yields of deaerated $[Ru(dpb)_3](BAr^F)_2$ in MeCN (red diamonds) and BuCN (blue-diamonds) as compared to the quantum yield of deaerated $[Ru(bpy)_3](PF_6)_2$ in MeCN (black diamonds) that is independent of the excitation wavelength.

The structure observed for in the excitation-dependent quantum yields for $[Ru(dpb)_3]^{2+}$ is reminiscent of the ground state absorption profile of the complex. Fig. 4.27 shows an overlay of the two spectra collected in 1-OctOH. The local maxima and minima appear to mimic each other: the quantum yield peaks for λ_{exc} = 350 nm, which is the central wavelength of the higher energy ^{1}MLCT band, and then falls to a minimum around λ_{exc} = 400 nm, which is a local minimum of the steady state absorption spectrum. The rise in quantum yield followed by subsequent plateau follows the rise of the lowest energy ^{1}MLCT peak. And finally, the ^{3}MLCT←$^1A_1$ transition coincides with the lowest quantum yields for $[Ru(dpb)_3]^{2+}$.

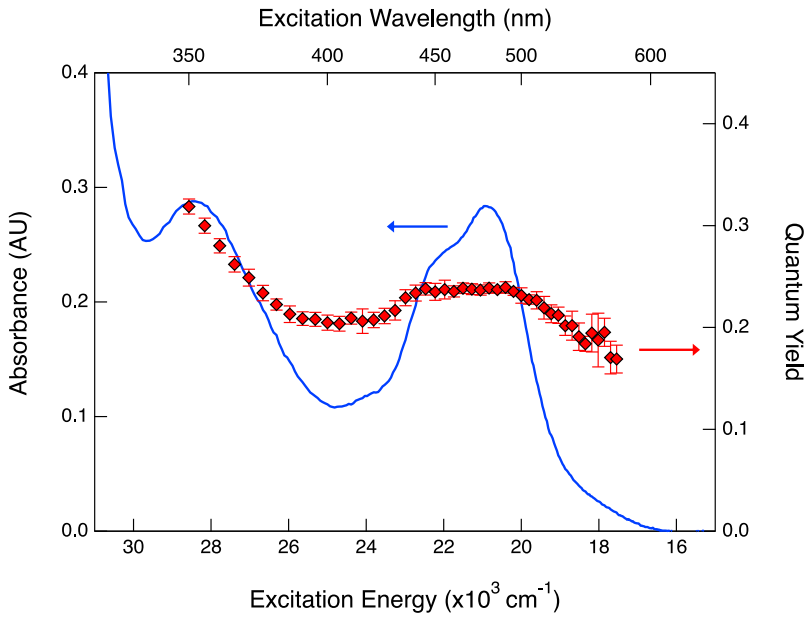

Figure 4.27. Overlay of the ground state absorption spectrum (blue trace, left axis) of $[Ru(dpb)_3](BAr^F)_2$ in 1-OctOH with the excitation wavelength-dependent deaerated quantum yield (red diamonds, right axis). There is a modest agreement between the trends of both.

It is highly unusual for chromophores to display excitation wavelength dependence. Kasha-Vavilov's Rule dictates that emission occurs from the lowest energy excited state and that the quantum yield is independent of excitation.[50] The assumption here is that regardless of the specific state that is formed upon pumping, the relaxation cascade always follows the same route to the same emissive excited state. Very few organic fluorophores have exhibited this type of behavior. One class of compounds that has recently been studied for excitation wavelength dependent quantum yields is the napthanediimide dyes. Yushchenko et al. prepared a series of compounds of this type with various substituents on the core of the molecule.[50] They found that heavier substituents like Br^- induced ultrafast (<200 fs) intersystem crossing from the initially populated S_2 excited state into the emissive S_1 state. This was due to the heavy atom effect caused by the bromide, in which the spin-orbit coupling is increased for the Br⁻substituted dye, which results in

spin mixing in the upper electronic states, allowing for faster intersystem crossing. In compounds with lighter substituents, that conversion rate was on the order of ~2 ps. The quantum yields were found to be excitation wavelength dependent in the case of the Br^- core-substituted napthanediimide dyes, which was not the case when light substituents were used. Ultimately this was believed to be a consequence of the altered photophysical pathways upon heavy atom substitution.

The heavy atom effect is not specific to organic chromophores; in fact it is often cited as the cause for increased spin-orbit coupling in second- and third-row transition metal complexes.[37] It is therefore unsurprising that excitation wavelength-dependent quantum yields have been observed previously in Ru(II) chromophores.[49,51] Yoshikawa and coworkers prepared a heteroleptic $[Ru^{II}(bpy)_2(biquinoline)]^{2+}$ complex which was observed to show decreased emission intensity (proportional to quantum yield if the excitation conditions are held constant[26]) with increasing excitation wavelength in the visible region.[49] When pumping in the UV part of the spectrum, dual emission was observed. The overall excitation wavelength dependence in this complex was attributed to emission from MLCT states associated with the two different types of ligands. Malouf and Ford studied a series of $[Ru(NH_3)(py\text{-}X)]^{2+}$ compounds in which the X substituent on a pyridyl ligand was varied to understand photosolvation reactions, which is the photoinitiated ligand dissociation and subsequent coordination by a solvent molecule.[51] The complexes for which the ^{3}LF was the lowest energy excited state were found to have quantum yields for photosolvation that were wholly independent of the excitation energy. For compounds with a lowest energy excited state that was MLCT in nature, the photolability of the ligand was drastically decreased and the photosolvation quantum yield was highly dependent on pump wavelength. This was found to be especially true at very high energy excitation, presumably

energies at which ligand-based π-σ* absorption occurred which would increase the likelihood of photodissociation of the complex. Particularly of interest for the studies presented here, when the ligand was 4-phenylpyridine (analogous to the dpb ligand), the quantum yield was observed to increase by an order of magnitude from excitation at 546 to 405 nm when the compound is dissolved in dimethyl sulfoxide. These quantum yields were also dependent on solvent, as when $[Ru(NH_3)_5(4\text{-phenylpyridine})]^{2+}$ was dissolved in N,N'-dimethylformamide, the quantum yield was relatively constant for λ_{exc} = 405-520 nm. Care should be taken when observing these values as the quantum yield of photosolvation in no way is equivalent to the quantum yield of emission. However, emission is occurring in these complexes, particularly in the 4-phenylpyridine derivative, from the MLCT excited state. When emission occurs with a high yield, then the photosolvation cannot be occurring as they require two separate lowest energy excited states. Thus, photodissociation of the pyridyl can only occur upon higher energy excitation in dimethyl sulfoxide, for which it is presumed the ^{3}LF states have been significantly stabilized relative to the MLCT manifold. These results echo what is observed in $[Ru(dpb)_3]^{2+}$ and may aid in the analysis of the emission quantum yields reported here.

This dependence of the quantum yield on pump wavelength is believed to give an indication of the seams and conical intersections between the MLCT excited states. A seam is where two potential energy surfaces meet, making it the site of population transfer from one state to the other; a conical intersection is a single point at which a transition can occur due to the meeting of the two states.[52] The potential energy surfaces for Ru(II) polypyridyl complexes are traditionally viewed along one nuclear coordinate, but can occur along as many dimensions as there are nuclear motions to describe the complex. And while the surfaces are almost certainly nested along the standard Ru-N bond distance coordinate (Scheme 4.3), other modes such as the

phenyl-bipyridine torsion angle or the C=C stretching in the rings could serve to bring the potential energy surfaces into contact with each other. Based on the ultrafast intersystem crossing observed in $[Ru(bpy)_3]^{2+}$,[1,15] it is expected for the electronic coupling between states in the MLCT manifold to be on the order of an adiabatic system. And considering the fact that this excitation wavelength dependence for the quantum yield has previously been observed in systems with extended conjugation,[51] it is probable then that phenyl rotation and subsequent delocalization are playing a critical role in the way in which the potential energy surfaces cross, thereby affecting the fundamental photophysical processes.

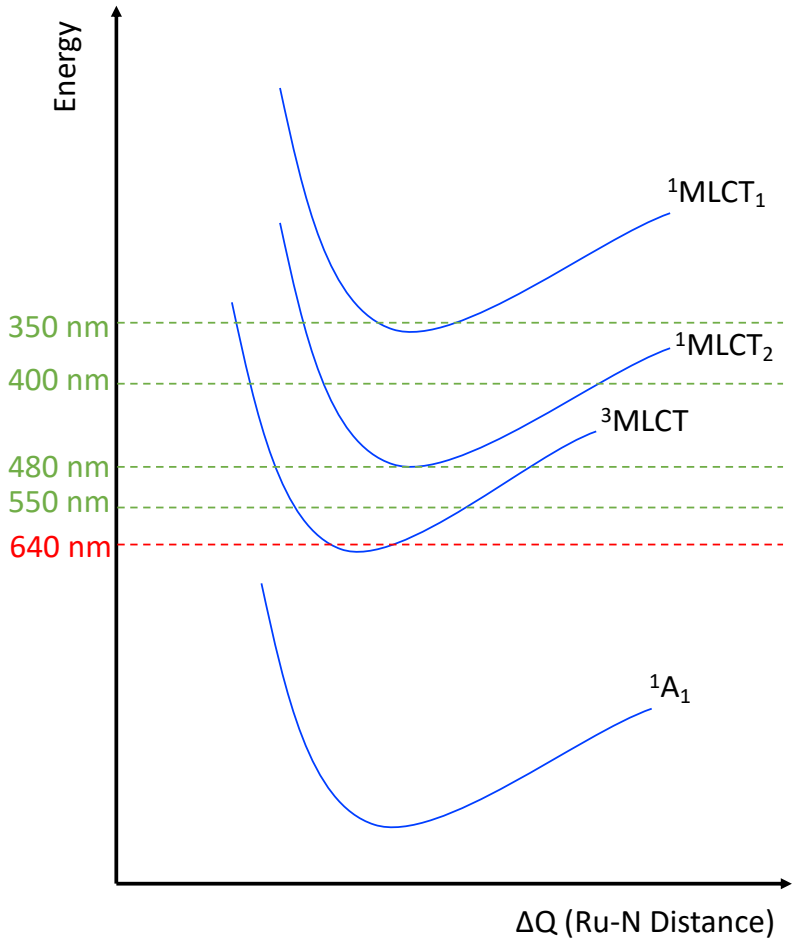

Scheme 4.3. Simplified potential energy surface diagram for $[Ru(dpb)_3]^{2+}$ from ground state absorption (green dashes) and steady state emission (red dash) spectroscopy. Although not known for certain in this specific complex, it is expected that the Ru-N bond distance will decrease in the ^{3}MLCT due to electrostatic interactions with the oxidized Ru(III) center, as has been shown to occur in $[Ru(bpy)_3]^{2+}$.[53]

The following is a discussion of the possible internal conversion and intersystem crossing pathways possible in $[Ru(dpb)_3]^{2+}$; it is largely based on the quantum yield data for the complex in 1-OctOH or MeCN, as these showed very similar excitation wavelength dependence. This type of analysis is generalizable for all of the solvents for which there is steady state absorption and

emission, transient absorption, and quantum yield data. From the latter, it would appear as though there is a seam or conical intersection at very high energies ($\lambda < 350$ nm), allowing for efficient population transfer from the upper MLCT excited state through the manifold or even directly into the ^{3}MLCT such that phosphorescence occurs with a high yield, but decreases with decreasing excitation energy. With ultrafast conversion of the upper ^{1}MLCT→^{3}MLCT, hot vibrational states would be created in the lowest energy excited state, providing an increased driving force for vibrational energy redistribution via vibrational cooling. This likely explains the predominantly dielectric solvation mechanism apparent in the alcohol series only upon excitation at 400 nm. Using Scheme 4.3 as a reference, the decreasing quantum yield for 350 nm > λ > 400 nm is reasonable as the upper ^{1}MLCT electronic state is only being partially populated, with the bulk of the excitation energy putting the complex into the lower ^{1}MLCT$_2$ state. At the 400 nm pump wavelength, most of the excess energy is being converted to thermal energy via vibrational cooling, as per the transient absorption spectroscopy data. This will necessarily increase k_{nr}, thereby reducing Φ. These data also therefore indicate that no seam exists in the ^{1}MLCT$_2$ state into lower-lying excited states near this energy. At lower excitation energies the quantum yield begins to increase again, plateauing at wavelengths for which the ^{1}A$_1$ to lowest energy ^{1}MLCT state oscillator strength is the greatest. Another seam or conical intersection is likely to occur here, increasing the efficiency of intersystem crossing into the phosphorescent ^{3}MLCT excited state. Finally, at the lowest excitation energies, the ^{3}MLCT state is being accessed directly. The only barrier to emission here is the nonradiative loss of excitation energy into the solvent. This analysis is based on the experimental data reported here but shows the need for rigorous calculation of the potential energy surfaces of $[Ru(dpb)_3]^{2+}$.

5. Future Works and Conclusions

The impetus for this work was to more thoroughly understand the photophysical process of $[Ru(dpb)_3]^{2+}$. As an analogue of the prototypical $[Ru(bpy)_3]^{2+}$, excitation in the visible region initially populates the MLCT manifold, whereupon intersystem crossing into the ^{3}MLCT excited state may precede vibrational cooling to the thermalized lowest energy excited state. This energetic redistribution process has been found to be facilitated by phenyl rotation in the dpb ligand, leading to coplanarity and therefore extended delocalization in the ^{3}MLCT excited state. The timescale of vibrational cooling and ring rotation has been found to be both solvent and excitation wavelength dependent. At higher excitation energy (i.e., 400 nm), the polar head of the solvent reorients to the large instantaneous dipole moment of the excited $[Ru(dpb)_3]^{2+}$ complex. This is a much more efficient solvation mechanism, allowing vibrational cooling to occur on the same timescale in 1-BuOH, 1-HexOH, and 1-OctOH, despite having varying alkyl chain lengths. Excitation at lower energies such as 480 and 550 nm induces a more viscoelastic solvent response, in which frictional forces dictate the timescale of ring rotation. Viscosity of the solvents, then, plays a critical role, with the vibrational cooling time constant increasing with a power dependence on viscosity. It was found that the viscoelastic mechanism also occurred in $[Ru(dpb)_3]^{2+}$ in nitrile solvents at all of the excitation wavelengths. This may be due to the more rigid C≡N moiety or could be caused by the lower viscosity of each of these solvents relative to the alcohol series. The latter is more likely to be true if both the dielectric and viscoelastic solvation models are acting simultaneously but one is being driven over the other by excess energy delivered to the system by the pump pulse.

The three excitation wavelengths chosen for this study each populated different excited states: λ_{exc} = 550 nm corresponds to the ^{3}MLCT, λ_{exc} = 480 nm is the ^{1}MLCT, and λ_{exc} = 400 nm excites into at least two separate ^{1}MLCT excited states. It was desirable to ensure that the unusual

solvation dynamics upon excitation at 400 nm were simply due to the driving force delivered by the excess energy from the pump, as opposed to a separate relaxation pathway being accessed or a new type of excited state being formed. To address these questions, time-dependent density functional calculations were performed in a comparison of the excited states formed upon excitation at different wavelengths. The results were not conclusive, but did indicate the probability of distinctly different excited states at each of the three excitation energies. This is not unexpected when pumping into three significantly different excited states. Additionally, nanosecond emission and transient absorption spectroscopy as well as quantum yield determinations were performed on $[Ru(dpb)_3]^{2+}$ in various solvents at the different pump wavelengths. Both the solvent and excitation wavelength played a role in the quantum yield of phosphorescence from the ^{3}MLCT state. This was believed to be indicative of points of intersection between the potential energy surfaces of the excited states, where population transfer might occur. These seams and/or conical intersections are likely found along non-traditional nuclear coordinates, potentially the phenyl-bipyridine dihedral angle. Analysis of the quantum yield data provided the explanation of the increased driving force producing the dielectric solvation model apparent when λ_{exc} = 400 nm in the alcohols series of solvents.

In an attempt to better define the nuclear coordinate associated with vibrational cooling, and possibly the population dynamics associated with the excitation wavelength-dependent quantum yields observed in $[Ru(dpb)_3]^{2+}$, an analogous complex was prepared in which the phenyl rotation was sterically hindered. The mesitylated $[Ru(dmesb)_3]^{2+}$ complex was studied as a function of both solvent and pump wavelength. The vibrational cooling time constants observed in this complex are consistently longer than in $[Ru(dpb)_3]^{2+}$ at each pump wavelength in MeOH, 1-OctOH, and MeCN, implying that the phenyl rotation is not only much more sterically restricted

due to the *ortho*-methyl groups on the phenyl substituent, but it is also a major vibrational mode in the energy redistribution process.

The use of shorter laser pulses did not increase the understanding of τ_1, the shorter time component observed concomitantly with the vibrational cooling response, showing the limitations of transient absorption spectroscopy. To parse out the photophysical process(es) occurring on this timescale, it is likely that other forms of ultrafast spectroscopies are required, such as time-resolved infrared spectroscopy[54,55] or time-resolved resonance Raman spectroscopy.[56-59] Additionally, two-dimensional spectroscopy (either in the visible or infrared regions) could be incredibly useful as this tool provides an understanding of the electronic communication between excited states.[46,60] To fully understand the surprisingly complex photophysics of $[Ru(dpb)_3]^{2+}$, more structural and vibrational data are required, as well as critical computational work on the potential energy surfaces of this compound. Extended delocalization in the excited state has already shown to both increase the extinction coefficient and extend the spectral range of absorption for this Ru(II) chromophore, both of which are highly desirable properties in molecular dyes for photovoltaic applications. Understanding the behavior of these conjugated systems is a first step towards designing higher efficiency solar energy conversion devices and advancing the redox properties of this class of compounds as a whole.

REFERENCES

REFERENCES

1. Pashaei, B.; Shahroosvand, H.; Grätzel, M.; Nazeeruddin, M. K. Influence of Ancillary Ligands in Dye-Sensitized Solar Cells. *Chem. Rev.* **2016**, *116*, 9485-9564; DOI: 10.1021/acs.chemrev.5b00621.

2. Nazeeruddin, M. K.; Splivallo, R.; Liska, P.; Comte, P.; Grätzel, M. A Swift Dye Uptake Procedure for Dye Sensitized Solar Cells. *Chem. Commun.* **2003**, *9*, 1456-1457; DOI: 10.1039/b302566g.

3. Tachibana, Y.; Moser, J. E.; Grätzel, M.; Klug, D. R.; Durrant, J. R. Subpicosecond Interfacial Charge Separation in Dye-Sensitized Nanocrystalline Titanium Dioxide Films. *J. Phys. Chem.* **1996**, *100*, 20056-20062; DOI: 10.1021/jp962227f.

4. Juris, A.; Balzani, V.; Barigelletti, F.; Campagna, S.; Belser, p.; von Zelewsky, A. Ru(II) Polypyridine Complexes: Photophysics, Photochemistry, Electrochemistry, and Chemiluminescence. *Coord. Chem. Rev.* **1988**, *84*, 85-277, and references therein; DOI: 10.1016/0010-8545(88)80032-8.

5. Cook, M. J.; Lewis, A. P.; McAuliffe, G. S. G.; Skarda, V.; Thomson, A. J. Luminescent Metal Complexes. Part 1. Tris-Chelates of Substituted 2,2'-Bipyridyls with Ruthenium(II) as Dyes for Luminescent Solar Collectors. *J. Chem. Soc. Perkin Trans. 2* **1984**, 1293-1301; DOI: 10.1039/p29840001293.

6. Damrauer, N. H.; Boussie, T. R.; Devenney, M.; McCusker, J. K. Effects of Intraligand Electron Delocalization, Steric Tuning, and Excited-State Vibronic Coupling on the Photophysics of Aryl-Substituted Bipyridyl Complexes of Ru(II). J. Am. Chem. Soc. 1997, 119, 8253-8268; DOI: 10.1021/ja971321m.

7. Damrauer, N. H.; Weldon, B. T.; McCusker, J. K. Theoretical Studies of Steric Effects on Intraligand Electron Delocalization: Implications for the Temporal Evolution of MLCT Excited State. *J. Phys. Chem. A* **1998**, *102*, 3382-3397; DOI: 10.1021/jp9805095.

8. Damrauer, N. H.; McCusker, J. K. Ultrafast Dynamics in the Metal-to-Ligand Charge Transfer Excited-State Evolution of $[Ru(4,4'\text{-diphenyl-}2,2'\text{-bipyridine})_3]^{2+}$. *J. Phys. Chem. A* **1999**, *103*, 8440-8446; DOI: 10.1021/jp9927754.

9. Maroncelli, M.; Kumar, V. P.; Papazyan, A. A Simple Interpretation of Polar Solvation Dynamics. *J. Phys. Chem.* **1993**, *97*, 13-17, and references therein; DOI: 10.1021/j100103a004.

10. Maroncelli, M.; MacInnis, J.; Fleming, G. R. Polar Solvent Dynamics and Electron-Transfer Reactions. *Science* **1989**, *243*, 1674-1681, and references therein; DOI: 10.1126/science.243.4899.1674.

11. Ladanyi, B. M.; Stratt, R. M. Short-Time Dynamics of Solvation: Relationship Between

Polar and Nonpolar Solvation. *J. Phys. Chem.* **1996**, *100*, 1266-1282; DOI: 10.1021/jp951326a.

12. Rondi, A.; Rodriguez, Y.; Feurer, T.; Cannizzo, A. Solvation-Driven Charge Transfer and Localization in Metal Complexes. *Acc. Chem. Res.* **2015**, *48*, 1432-1440; DOI: 10.1021/ar5003939.

13. Horng, M. L.; Gardecki, J. A.; Papazyan, A.; Maroncelli, M. Subpicosecond Measurements of Polar Solvation Dynamics: Coumarin 153 Revisited. *J. Phys. Chem.* **1995**, *99*, 17311-17337; DOI: 10.1021/j100048a004.

14. Bhasikuttan, A. C.; Suzuki, M.; Nakashima, S.; Okada, T. Ultrafast Fluorescence Detection in Tris(2,2'-bipyridine)ruthenium(II) Complex in Solution: Relaxation Dynamics Involving Higher Excited States. *J. Am. Chem. Soc.* **2002**, *124*, 8398-8405; DOI: 10.1021/ja026135h.

15. Yoon, S.; Kukura, P.; Stuart, C. M.; Mathies, R. A. Direct Observation of the Ultrafast Intersystem Crossing in Tris(2,2'-bipyridine)ruthenium(II) Using Femtosecond Stimulated Raman Spectroscopy. *Molec. Phys.* **2010**, *104*, 1275-1282; DOI: 10.1080/00268970500525846.

16. Bagchi, B.; Biswas, R. Polar and Nonpolar Solvation Dynamics, Ion Diffusion, and Vibrational Relaxation: Role of Biphasic Solvent Response in Chemical Dynamics. *Adv. Chem. Phys.* **1999**, *109*, 207-433; DOI: 10.1002/9780470141687.ch4.

17. Berg, M. Viscoelastic Continuum Model of Nonpolar Solvation. 1. Implications for Multiple Time Scales in Liquid Dynamics. *J. Phys. Chem. A* **1998**, *102*, 17-30; DOI: 10.1021/jp9722061.

18. Kahlow, M. A.; Kang, T. J.; Barbara, P. F. Electron-Transfer Times Are Not Equal to Longitudinal Relaxation Times in Polar Aprotic Solvents. *J. Phys. Chem.* **1987**, *91*, 6452-6455; DOI: 10.1021/j100310a005.

19. Kosower, E. M.; Hupper, D. Excited State Electron and Proton Transfers. *Annu. Rev. Phys. Chem.* **1986**, *37*, 127-156; DOI: 10.1146/annurev.pc.37.100186.001015.

20. Su, S.-G.; Simon, J. D. The Importance of Vibrational Motion and Solvent Diffusional Motion in Excited State Intramolecular Electron Transfer Reactions. *J. Chem. Phys.* **1988**, *89*, 908-919; DOI: 10.1063/1.455214.

21. Chang, S. M.; Fan, C. H.; Lai, C. C.; Chao, Y. C.; Hu, S. C. Red Electroluminescence From Ruthenium Complexes. *Surf. Coat. Technol.* **2006**, *200*, 3289-3296; DOI: 10.1016/j.surfcoat.2005.07.059.

22. Alston, J. R.; Kobayashi, S.; Younts, T. J.; Poler, J. C. Synthesis and Characterization of Rigid +2 and +3 Heteroleptic Dinuclear Ruthenium(II) Complexes. *Polyhedron* **2010**, *29*, 2696-2702; DOI: 10.1016/j.poly.2010.06.012

23. Gaussian 09, Revision D.01, M. J. Frisch, g. W. Trucks, H. B. Schlegel, G. E. Scuseria, M.

A. Robb, J. R. Cheeseman, G. Scalmani, V. Barone, B. Mennucci, G. A. Petersson, H. Nakatsuji, M. Caricato, X. Li, H. P. Hratchian, A. F. Izmaylov, J. Bloino, G. Zheng, J. L. Sonnenberg, M. Hada, M. Ehara, K. Toyota, R. Fukuda, J. Hasegawa, M. Ishida, T. Nakajima, Y. Honda, O. Kitao, H. Nakai, T. Vreven, J. A. Montgomery, Jr., J. E. Peralta, F. Ogliaro, M. Bearpark, J. J. Heyd, E. Brothers, K. N. Kuin, V. N. Staraoverov, T. Keith, R. Kobayashi, J. Normand, K. Raghavachari, A. Rendell, J. C. Burant, S. S. Iyengar, J. Tomasi, M. Cossi, N. Rega, J. M. Millam, M. Klene, J. E. Knox, J. B. Cross, V. Bakken. C. Adamo, J. Jaramillo, R. Gomperts, R. E. Stratmann, O. Yazyev, A. J. Austin, R. Cammi, C. Pomelli, J. W. Ochterski, R. L. Martin, K. Morokuma, V. G. Zakrzewski, G. A. Voth, P. Salvador, J. J. Dannenberg, S. Dapprich, A. D. Daniels, O. Farkas, J. B. Foresman, J. V. Ortiz, J. Cioslowski, and D. J. Fox, Gaussian, Inc., Wallingford CT, 2013.

24. Brown, A. M.; McCusker, C. E.; Carey, M. C.; Blanco-Rodriguez, A. M.; Towrie, M.; Clark, I. P.; Vlček, A.; McCusker, J. K. Vibrational Relaxation and Redistribution Dynamics in Ruthenium(II) Polypyridyl-Based Charge-Transfer Excited States: A Combined Ultrafast Electronic and Infrared Absorption Study. *J. Phys. Chem. A*; DOI: 10.1021/acs.jpca.8b06197.

25. Monat, J. E.; Rodriguez, J. H.; McCusker, J. K. Ground- and Excited-State Electronic Structures of the Solar Cell Sensitizer Bis(4,4'-dicarboxylato-2,2'-bipyridine)bis(isothiocyanato)ruthenium(II). *J. Phys. Chem. A* **2002**, *106*, 7399-7406; DOI: 10.1021/jp020927g.

26. Arias-Rotondo, D. M.; McCusker, J. K. The Photophysics of Photoredox Catalysis: A Roadmap for Catalyst Design. *Chem. Soc. Rev.* **2016**, *45*, 5803-5820; DOI: 10.1039/c6cs00526h.

27. Suzuki, K.; Kobayashi, A.; Kanehko, S.; Takehira, K.; Yoshihara, T.; Ishida, H.; Shiina, Y.; Oishi, S.; Tobita, S. Reevaluation of Absolute Luminescence Quantum Yields of Standard Solutions Using a Spectrometer With an Integrating Sphere and a Back-Thinned CCD Detector. *Phys. Chem. Chem. Phys.* **2009**, *11*, 9850-9860; DOI: 10.1039/b912178a.

28. Liard, D. J.; Busby, M.; Matousek, P.; Towrie, M.; Vlček, Jr., A. Picosecond Relaxation of ^{3}MLCT Excited states of $[Re(Etpy)(CO)_3(dmb)]^+$ and $[Re(Cl)(CO)_3(bpy)]$ as Revealed by Time-Resolved Resonance Raman, UV-Vis, and IR Absorption Spectroscopy; DOI: 10.1021/jp0366320.

29. Shaw, G. B.; Styers-Barnett, D. J.; Gannon, E. Z.; Granger, J. C.; Papanikolas, J. M. Interligand Electron Transfer Dynamics in $[Os(bpy)_3]^{2+}$: Exploring the Excited State Potential Surfaces with Femtosecond Spectroscopy. *J. Phys. Chem. A* **2004**, *108*, 4998-5006; DOI: 10.1021/jp0363850.

30. Juban, E. A.; McCusker, J. K. Ultrafast Dynamics of ^{2}E State Formation in $Cr(acac)_3$. *J. Am. Chem. Soc.* **2005**, *127*, 6857-6865; DOI: 10.1021/ja042153i.

31. Damrauer, N. H. Frank-Condon State Evolution in Metal-to-Ligand Charge Transfer Chromophores: Influence of Electronic Structure, Ligand Structure, and Solvent Environment on Photo-Induced Excited State Dynamics. Ph.D. Thesis, University of

California, Berkeley, 2001.

32. Pearson, P.; Bond, A. M.; Deacon, G. B.; Forsyth, C.; Spiccia, L. Synthesis and Characterisation of Bis(2,2'-bipyridine)-(4-carboxy-4'-(pyrid-2-ylmethylamido)2,2'-bipyridine)ruthenium(II) di(hexafluorophosphate): Comparison of Spectroelectrochemical Properties with Related Complexes. *Inorg. Chim. Acta* **2008**, *361*, 601-612; DOI: 10.1016/j.ica.2007.03.031.

33. Yakelis, N. A.; Bergman, R. G. Sodium Tetrakis[(3,5-trifluoromethyl)phenyl]borate ($NaBArF_{24}$): Safe Preparation, Standardized Purification, and Analysis of Hydration. *Organometallics* **2005**, *24*, 3579-3581; DOI: 10.1021/om0501428.

34. Feng, J.-B.; Wu, X.-F. Transition Metal-Catalyzed Oxidative Transformations of Methylarenes. *Appl. Organomet. Chem.* **2015**, *29*, 63-86; DOI: 10.1002/aoc.3244.

35. Rillema, D. P.; Jones, D. S. Structure of Tris(2,2'-bipyridyl)ruthenium(II) Hexafluorophosphate, $[Ru(bipy)_3][PF_6]_2$; X-ray Crystallographic Determination. *J. Chem. Soc. Chem. Commun.* **1979**, 849-851; DOI: 10.1039/C39790000849.

36. Crosby, G. A. Luminescence as a Probe of Excited State Properties. *Adv. Chem.* **1976**, *150*, 149-159; DOI: 10.1021/ba-1976-0150.ch013.

37. Kober, E. M.; Meyer, T. J. Concerning the Absorption Spectra of the Ions $M(bpy)_3^{2+}$ (M = Fe, Ru, Os; bpy = 2,2'-Bipyridine). *Inorg. Chem.* **1982**, *21*, 3967-3977; DOI: 10.1021/ic00141a021.

38. Juris, A.; Balzani, V.; Belser, P.; von Zelewsky, A. 211. Characterization of the Excited State Properties of Some New Photosensitizers of the Ruthenium (Polypyridine) Family. *Helv. Chim. Acta* **1981**, *64*, 2175-2182; DOI: 10.1002/hlca.19810640723.

39. Stsiapura, V. I.; Kurhuzenkau, S. A.; Kuzmitsky, V. A.; Bouganov, O. V.; Tikhomirov, S. A. Solvent Polarity Effect on Nonradiative Decay Rate of Thioflavin T. *J. Phys. Chem. A* **2016**, *120*, 5481-5496; DOI: 10.1021/acs.jpca.6b02577.

40. CRC Handbook of Chemistry and Physics, 98th ed., http://hbcponline.com/faces/documents/06_33/06_33_0001.xhtml, (accessed June 2018).

41. Ghosh, S.; Roscioli, J. D.; Bishop, M. M.; Gurchiek, J. K.; LaFountain, A. M.; Frank, H. A.; Beck, W. F. Torsional Dynamics and Intramolecular Charge Transfer in the $S_2(1\ ^1B_u^+)$ Excited State of Peridinin: A Mechanism for Enhanced Mid-Visible Light Harvesting. *J. Phys. Chem. Lett.* **2016**, *7*, 3621-3626; DOI: 10.1021/acs.jpclett.6b01642.

42. Hosmer, D. W.; Hosmer, T.; Le Cessie, S.; Lemeshow, S. A Comparison of Goodness-of-Fit Tests for the Logistic Regression Model. *Statistics in Medicine* **1997**, *16*, 965-980; DOI: 10.1002/(SICI)1097-0258(19970515)16.

43. Maroncelli, M. The Dynamics of Solvation in Polar Liquids. *J. Molec. Liq.* **1993**, *57*, 1-37; DOI: 10.1016/0167-7322(93)80045-W.

44. Yeh, A. T.; Shank, C. V.; McCusker, J. K. Ultrafast Electron Localization Dynamics Following Photo-Induced Charge Transfer. *Science*, **2000**, *290*, 307-313; DOI: 10.1126/science.289.5481.935.

45. Passino, S. A.; Nagasawa, Y.; Fleming, G. R. Three Pulse Stimulated Photon Echo Experiments as a Probe of Polar Solvation Dynamics: Utility of Harmonic Bath Models. *J. Chem. Phys.* **1997**, *107*, 6094; DOI: 10.1063/1.474277.

46. Jonas, D. M. Two-Dimensional Femtosecond Spectroscopy. *Annu. Rev. Phys. Chem.* **2003**, *54*, 425-463; DOI: 10.1146/annurev.physchem.54.011002.103907.

47. Delor, M.; Sazanovich, I. V.; Towrie, M.; Weinstein, J. A. Probing and Exploiting the Interplay Between Nuclear and Electronic Motion in Charge Transfer Processes. *Acc. Chem. Res.* **2015**, *48*, 1131-1139; DOI: 10.1021/ar500420c.

48. Caspar, J. V.; Meyer, T. J. Photochemistry of $Ru(bpy)_3^{2+}$. Solvent Effects. *J. Am. Chem. Soc.* **1983**, *105*, 5583-5590; DOI: 10.1021/ja00355a009.

49. Yoshikawa, N.; Kimura, H.; Yamabe, S.; Kanehisa, N.; Inoue, T.; Takashima, H. Emission Property and DFT Calculation for the ^{3}MLCT Luminescence of $Ru(bpy)_2(L)^{2+}$ Complex. *J. Molec. Struct.* **2016**, *1117*, 49-56; DOI: 10.1016/j.molstruc.2016.03.069.

50. Yushchenko, O.; Licari, G.; Mosquera-Vazquez, S.; Sakai, N.; Matile, S.; Vauthey, E. Ultrafast Intersystem-Crossing Dynamics and Breakdown of the Kasha-Vavilov's Rule of Naphthalenediimides. *J. Phys. Chem. Lett.* **2015**, *6*, 2096-2100; DOI: 10.1021/acs.jpclett.5b00882.

51. Malouf, G.; Ford, P. C. Photochemistry of the Ruthenium(II) Ammine Complexes, $Ru(NH_3)_5(py\text{-}X)^{2+}$. Variation of Systemic Parameters to Modify Photochemical Reactivities. *J. Am. Chem. Soc.* **1977**, *99*, 7213-7221; DOI: 10.1021/ja00464a020.

52. Levine, B. G.; Martínez, T. J. Isomerization Through Conical Intersections. *Annu. Rev. Phys. Chem.* **2007**, *58*, 613-634; DOI: 10.1146/annurev.physchem.57.032905.104612.

53. Sato, T.; Nozawa, S.; Tomita, A.; Hoshino, M.; Koshihara, S.-Y.; Fujii, H.; Adachi, S.-I. Coordination and Electronic Structure of Ruthenium(II)-*tris*-2,2'-bipyridine in the Triplet Metal-to-Ligand Charge-Transfer Excited State Observed by Picosecond Time-Resolved Ru *K*-Edge XAFS. *J. Phys. Chem. C* **2012**, *116*, 14232-14236; DOI: 10.1021/jp3038285.

54. Sun, Q.; Dereka, B.; Vauthey, E.; Lawson Daku, L. M.; Hauser, A. Ultrafast Transient IR Spectroscopy and DFT Calculations of Ruthenium(II) Polypyridyl Complexes. *Chem. Sci.* **2016**, *8*, 223-230; DOI: 10.1039/c6sc01220e.

55. Maçôas, E. M. S.; Kananavicius, R.; Myllyperkiö, P.; Pettersson, M.; Kunttu, H. Ultrafast Electronic and Vibrational Energy Relaxation in $Fe(acetylacetonate)_3$ in Solution. *J. Phys. Chem. A* **2007**, *111*, 2054-2061; DOI: 10.1021/jp066271z.

56. Henry, W.; Coates, C. G.; Brady, C.; Ronayne, K. L.; Matousek, P.; Towrie, M.; Botchway,

S. W.; Parker, A. W.; Vos, J. G.; Browne, W. R.; McGarvey, J. J. The Early Picosecond Photophysics of Ru(II) Polypyridyl Complexes: A Tale of Two Timescales. *J. Phys. Chem. A* **2008**, *112*, 4537-4544; DOI: 10.1021/jp711873s.

57. Browne, W. R.; McGarvey, J. J. The Raman Effect and Its Application to Electronic Spectroscopies in Metal-Centered Species: Techniques and Investigations in Ground and Excited States. *Coord. Chem. Rev.* **2007**, *251*, 454-473; DOI: 10.1016/j.ccr.2006.04.019.

58. Nibbering, E. T. J.; Fidder, H.; Pines, E. Ultrafast Chemistry: Using Time-Resolved Vibrational Spectroscopy for Interrogation of Structural Dynamics. *Annu. Rev. Phys. Chem.* **2005**, *56*, 337-367; DOI: 10.1146/annurev.physchem.56.092503.141314.

59. Mabrouk, P. A.; Wrighton, M. S. Resonance Raman Spectroscopy of the Lowest Excited State of Derivatives of Tris(2,2'-bipyridine)ruthenium(II): Substituent Effects on Electron Localization in Mixed-Ligand Complexes. *Inorg. Chem.* **1986**, *25*, 526-531; DOI: 10.1021/ic00224a027.

60. Henry, W.; Coates, C. G.; Brady, C.; Ronayne, K. L.; Matousek, P.; Towrie, M.; Botchway, S. W.; Parker, A. W.; Vos, J. G.; Browne, W. R.; McGarvey, J. J. The Early Picosecond Photophysics of Ru(II) Polypyridyl Complexes: A Tale of Two Timescales. *J. Phys. Chem. A* **2008**, *112*, 4537-4544; DOI: 10.1021/jp711873s.

CHAPTER 5. INCREASED CHARGE SEPARATION DISTANCE VIA EXTENDED LIGAND DELOCALIZATION AS A STRATEGY TO LENGTHEN THE MLCT LIFETIME IN FE(II) POLYPYRIDYL COMPLEXES

1. Introduction

Very recently, increased attention has been paid to highly conjugated systems in inorganic materials for photovoltaic applications. In work that appears to have begun by Reynal et al., the goal was to systematically increase the linkage between a cobalt-based dye and the titanium dioxide (TiO_2) it was bound to in order to force an electron to travel a linear path to the semiconductor, thereby reducing recombination.[1] The half-lives of these chromophores were found to increase as the distance between the cobalt center and the TiO_2 interface increased: by adding 2 Å in linkages between the two entities, the half-life of recombination was slowed by an order of magnitude. Analogous work has been done on organic photovoltaics[2] and Zn porphyrins,[3] all showing that through delocalization, an excited state can be extended spatially from the point of origin; if the electron and hole are separated by a great enough distance, then the lifetime of that charge-separated state will be drastically lengthened.

The Schmehl group has explored the concept of this very research extensively.[4,5] They have prepared complexes of Fe(II),[6] Ru(II),[4-7] Os(II),[7] and Zn(II)[8] in which the ligand structure is modified by the addition of aromatics and fused rings so as to understand the effect on the photophysics of these complexes. In one study, a series of 4'-substituted terpyridine ligands were prepared in which an extended chain of phenylene and vinylene linkers were added.[6] The photophysical properties of Rutvt were compared to those of Rutvpvt; here, t is a terpyridine, p is a phenylene, and v is a vinylene group. The emission lifetime of Rutvt was found to be less than

10 ns in aerated solution, which is comparable to the parent complex, $[Ru(terpy)_2]^{2+}$ considering the temporal resolution of their spectrometer. Upon addition of a phenylene-vinylene linker to form Rutvpvpt, the emission lifetime increased to 320 ns. This lifetime is four orders of magnitude longer than that of $[Ru(terpy)_2]^{2+}$. They then prepared a Ru_2Fe trimer, which follows their naming convention to be RutvtFetvtRu (with capping terpyridine ligands on both ruthenium atoms). This complex was found to behave very analogously to a typical Fe(II) compound, with a very short-lived excited state absorption feature, here indicative of the metal-to-ligand charge transfer (MLCT) state. Again, by extending the distance between the Ru and Fe centers such that RutvpvtFetvpvtRu was prepared, the MLCT lifetime of this complex was found to be 275 ± 10 ns.

These results would seem to indicate that if excited electron is removed a far enough distance from the Fe(II) center, then the complex will exhibit a very long-lived MLCT, particularly for an iron-based system. The rationale behind this is the delocalization of the excited state wavefunction, spreading further away from the metal center, which is the physical origin of the lower-lying ligand field excited states. With enough distance between the metal and the electron, it can be imagined that the electron would lose all memory of the metal center to which it would otherwise normally return. It is quite probable that there would be limitations on the length of conjugated ligand the electron would travel before recombining with the metal center (i.e., a Goldilocks problem).

Care should be taken, though, when discussing this strategy for Fe(II) chromophores when nearly all the work thus far has been performed on second- or third-row transition metal-containing complexes. With the heavier atoms in place, the ligand field strength will be high enough that the lowest-energy excited states are most likely MLCT in nature. This is a point of some contention considering that the tridentate terpyridine Ru(II) complex is believed to actually relax to the ground

state from a triplet ligand field state, thus its very short lifetime.[9] With the complexes studied here, it is observed that the ligand modification to extend delocalization decreases the energy of the MCLT excited state. In order for the charge-separated state to exist for hundreds of nanoseconds, the decrease in MLCT energy must be sufficient to reaffirm its status as lowest-lying excited state, bypassing any ligand field states. When moving to Fe(II) systems, though, the relative energetics of the MLCT and ligand field manifolds will not be quite so degenerate. The lengthening of the charge-separated lifetime in Ru(II) complexes works because that is a system that already has MLCT states as the lowest-energy excited state, or at least energetically nearby. This is not true for iron chromophores. Any MLCT lifetime lengthening we observe here will have to be explained in terms of the nuclear coordinate, not the energetic coordinate. But in the quest to decrease the deactivation rate out of the MLCT for Fe(II) complexes, many strategies must be attempted, and here we take our inspiration from Ru(II) photophysics.

2. Experimental

2.1 Materials and Synthesis

2.1.1 General

The complexes studied herein are: tris(4,4'-diphenyl-2,2'-bipyridine) iron(II) hexafluorophosphate, $[Fe(dpb)_3](PF_6)_2$; bis(8'-diquinolinyl-2,6-pyridine) iron(II) hexafluorophosphate, $[Fe(dqp)_2](PF_6)_2$; bis(8'-quinolinyl-2-phenanthroline) iron(II) hexafluorophosphate, $[Fe(qphen)_2](PF_6)_2$; tris[4,4'-(di-2,5-dimethylisoxazolyl)-2,2'-bipyridine] iron(II) hexafluorophosphate, $[Fe(dmib)_3](PF_6)_2$; tris(4,4'-cyanoacrylic acid-2,2'-bipyridine) iron(II) hexafluorophosphate, $[Fe(caab)_3](PF_6)_2$; bis(phenyl-*trans*-vinyl-phenyl-*trans*-vinyl-phenyl-4'-terpyridine) iron(II) hexafluorophosphate, $[Fe(tpvpvp)_2](PF_6)_2$. $[Fe(dqp_2](PF_6)_2$ and

$[Fe(qphen)_2](PF_6)_2$ were synthesized and characterized by L. Wickramasinghe of the Thummel group from the University of Houston. $[Fe(dmib)_3](PF_6)_2$ and $[Fe(caab)_3](PF_6)_2$ were synthesized and characterized by C. R. Tichnell. $[Fe(tpvpvp)_2](PF_6)_2$ was provided by R. Schmehl of Tulane University.

$[Fe(dpb)_3](PF_6)_2$ was synthesized by a route commonly employed to prepare iron(II) polypyridyl complexes.[10] Ferrous ammonium sulfate hexahydrate (Jade Scientific, ACS grade), ammonium hexafluorophosphate (Sigma-Aldrich, $\geq$ 95%), and methanol (Fisher Scientific, ACS grade) were all used as received. The dpb ligand was prepared by C. R. Tichnell.[11] On a Schlenk line, the dpb ligand (0.081 mmol, 25.0 mg) was added to hot methanol (15 mL) and bubble-degassed for 15 min. This solution was heated until no white solid of the ligand was visible, indicating complete solvation. A solution of $(NH_4)Fe(SO_4)_2{\cdot}6H_2O$ (0.028 mmol, 11.0 mg) was prepared in minimal water (3 mL) under N_2 and was bubble-degassed for 15 min. The dpb solution was allowed to come to room temperature, at which time the iron solution was cannula-transferred into the ligand by positive N_2 pressure. Immediately, the solution turned a deep purple color. The complex was allowed to stir under N_2 for 3.5 h, while the reaction was monitored by ^{1}H NMR spectroscopy. When the reaction was complete, a solution of NH_4PF_6 (0.280 mmol, 45.6 mg) in water (10 mL) was added, causing the sample to appear to be a lighter pink color, and a precipitate to form and coat the surface of the flask. Addition water (~300 mL) was added to further induce precipitation of the product. The product was dried on a medium frit attached to a vacuum filter flask and washed with excess water. It was allowed to dry on the frit for ~ 21 h. Yield: 96% (33 mg).

^{1}H NMR spectra were collected on a Bruker 500 MHz NMR spectrometer. Electrospray-ionization mass-spectrometry (ESI-MS) was performed on a Waters Xevo G2-XS Quadrupole

Time-of-Flight spectrometer in positive mode. HPLC grade acetonitrile and methanol were purchased from Sigma-Aldrich and used as received for spectroscopic measurements. Ground state absorption spectra were collected with a Varian (now Agilent) Cary 50 UV-Vis spectrophotometer.

$[Fe(dpb)_3](PF_6)_2$ was recrystallized by evaporation of acetonitrile solution doped with ethanol. The single crystal was mounted in paratone oil and transferred to the cold nitrogen gas stream of the diffractometer for data collection. Single crystal X-ray diffraction was collected on suitable crystals mounted on a Bruker APEX-II CCD diffractometer with CuK_α radiation at the Center for Crystallographic Research at Michigan State University. The crystal structure was solved by S. Li and R. J. Staples.

2.1.2 Characterization of Free Ligands and Complexes

4,4'-diphenyl-2,2'-bipyridine (dpb) ^1H NMR (500 MHz, [d_3-chloroform], δ) [8.75 (m, 2 H), 7.79 (m, 2 H), 7.57 (dd, 1 H, J = 1.84, 5.08 Hz), 7.52 (m, 2 H), 7.47 (m, 1 H).

Tris(4,4'-diphenyl-2,2'-bipyridine) iron(II) hexafluorophosphate $[Fe(dpb)_3](PF_6)_2$ ^1H NMR (500 MHz, [d_6-acetone], δ) [9.48 (s, 1 H), 8.01 (m, 3 H), 7.62 (m, 4 H). ESI-MS (m/z): $[C_{66}H_{46}N_6Fe]^{2+}$ calcd. 490.1646; found 490.1701, $[C_{44}H_{30}N_4Fe]^{2+}$ calcd. 336.0988; found 336.1005, $[C_{44}H_{31}N_4FeF]^+$ calcd. 691.1961; found 691.1951, $[C_{44}H_{31}N_4FeCl]^+$ calcd. 707.1666; found 707.1656. CHN analysis for $FeC_{66}H_{48}N_6P_2F_{12}\cdot 2H_2O$ calcd: C 60.65, H 4.01, N 6.43, found: C 61.25, H 4.52, N 5.77.

2.1.3 Crystal Structure Determination

$[Fe(dpb)_3](PF_6)_2$ crystal data: $C_{66}H_{48}F_{12}FeN_6P_2$, M_r = 1270.89, monoclinic, a = 34.8978(9) Å, b = 17.7797(3) Å, c = 23.7698(7) Å, T= 173 K, space group C2/c, Z = 8, 46917 reflections measured, 12616 unique (Rint = 0.1954), which were used in all calculations. The final wR(F2) was 0.1986 (all data). CCDC 1810752. Solvent molecules in the structure were heavily disordered

and the program BYPASS implemented in Olex2 showed the following void and electrons: 1230.4, 72.4. Possible solvents include Et_2O, EtOH, and MeCN.

2.2 Ultrafast Transient Absorption Spectroscopy

Ultrafast transient absorption (TA) spectroscopy was used to carry out ground state recovery and MLCT lifetime measurements as previously described in Chapters 2 and 3 of this work. Variable-temperature studies of these lifetimes were collected using the variable-temperature setup also described in Chapter 2. Various pump-probe combinations were used and are specified for each measurement. The instrument response function (IRF) was measured as the cross- and self-phase modulation of the pulses in a cuvette of MeOH and was found to be dependent on the specific pump and probe wavelengths, but overall it was approximately 150 fs. Pulse durations were measured by optical Kerr effect in MeOH and were consistently ~130 fs.

3. Results and Discussion

3.1 $[Fe(dpb)_3](PF_6)_2$

3.1.1 Synthesis

When substituted in the 4,4'-positions, the phenyl rings of dpb proved to be quite problematic for the complexation and stability of $[Fe(dpb)_3]^{2+}$. Initially, it was presumed that the synthetic route used to acquire $[Ru(dpb)_3]^{2+}$ (as described in Chapter 4) would be able to be implemented with an iron(II) starting material to achieve the iron analogue. This was attempted with $FeCl_2 \cdot 2H_2O$ and the addition of tetrakis[(3,5-trifluoromethyl)phenyl]borate salt (BAr^{F-}) as the counteranion. It was immediately apparent that the BAr^{F-} salt was complicating the purification of the $[Fe(dpb)_3]^{2+}$ product. This route was attempted again but no BAr^{F-} counterion was added, thereby presumably generating $[Fe(dpb)_3]Cl_2$. The ^1H NMR of the crude reaction mixture showed

free ligand was still present. Solubility studies on this product showed that the product was soluble in solvents such as 1-octanol and dichloromethane, which are two solvents that are not typically very good at solvating a doubly charged product, particularly not chloride salts of iron(II) complexes. This was the first indication that the product formed was perhaps not the tris-ligated species. The next sign came from the recrystallization attempts. In this instance, recrystallization by vapor diffusion was attempted, in which diethyl ether was allowed to diffuse into a solution of $[Fe(dpb)_3]Cl_2$ in acetonitrile. Over the course of ~24 h, the solution of iron complex was observed to change from the pink color to colorless (Fig. 5.1). From the loss of the MLCT absorption, it is apparent that the ligand has dissociated from the iron(II). Furthermore, a comparison of the absorption spectrum of the free dpb ligand and the colorless recrystallization product shows that the ligand itself also decomposes, which is very unexpected. Based on what was observed with $[Ru(dmesb)_3]Cl_2$ (Chapter 4) and previously reported with $[Ru(bpy)_3]Cl_2$,[12] it was expected that the Cl^- was preferentially binding to the iron center over the dpb ligand. Metathesis to the BF_4^- salt produced no better results, indicating that the counteranion may have in fact coordinated to the metal center. Attempts to purify the complex by column chromatography were made; similar conditions to those used for $[Ru(dpb)_3](BAr^F)_2$ showed promise by thin-layer chromatography. This involved the use of a silica gel stationary phase with pure dichloromethane as the mobile phase. Under these conditions, the free ligand should remain at the top of the column while the complex runs with the mobile phase. However, the product appeared to dissociate on the column as indicated by the presence of free ligand by ^1H NMR spectroscopy.

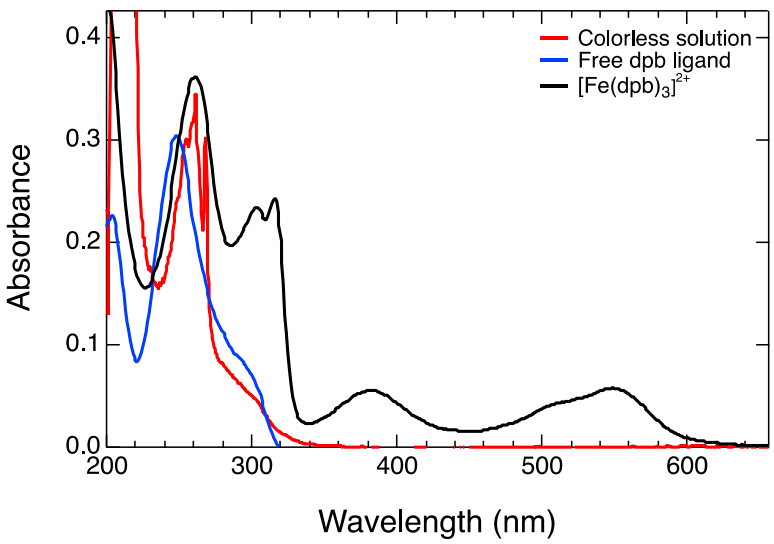

Figure 5.1. Steady state absorption spectrum of $[Fe(dpb)_3](PF_6)_2$ in acetonitrile (black) prior to recrystallization. After ~24 h, the solution was observed to go colorless (red). This indicated ligand dissociation from the metal center, but also suggests decomposition of the ligand itself, as the spectrum does not match that of the free dpb ligand (blue).

The route that was ultimately used attempted to deal with the issues outlined above. To decrease the risk of oxidation of the metal center, the free dpb ligand was recrystallized out of hot ethanol before the complexation. Each of the reactants were kept under nitrogen throughout the reaction, and every solvent was carefully sparged. To reduce the amount of free ligand in the final product, an excess of the iron(II) starting material was used. The dpb was fully dissolved in the reaction solvent first to improve the likelihood of coordination. No chloride was used at any point, and the counterion PF_6^- was chosen as it is slightly larger than BF_4^-. A better choice might even be tetraphenylborate BPh_4^- in the future since it both larger in size than either BF_4^- or PF_6^- and there is no chance of coordination to the metal center due to its lack of fluorides. The product was kept out of solution as much as possible, and the solvents of choice were intentionally non-coordinating.

The complex was recrystallized, and it was the single crystals that grew out of CD_3CN/EtOH that were used for further characterization. Despite being able to get a crystal structure of the product with no indication of free ligand, when the crystals were redissolved in $(CD_3)_2CO$ for ^1H NMR, the spectrum indicated ~40% free ligand impurity, as well as <5% heteroleptic complex impurity (Fig. 5.2). This may imply that product is inherently unstable in solution. Additionally, the CHN analysis indicated the presence of EtOH, despite the product being pumped on while in a desiccator for multiple days. The mass spectrum, it should be noted, does show the presence of a bis-ligated species that has abstracted a fluorine presumably from the PF_6^- at m/z 691.1961. It also shows the same species but instead with a Cl atom at m/z 707.1656, despite the fact that care was taken to never introduce Cl^-. The bis-nature of the complex may imply that the tris-product was not formed, or it may simply be caused by fragmentation in the instrument. In any event, the product seems relatively unstable in solution, so any solution-phase characterization presented here are subject to a relatively high degree of uncertainty.

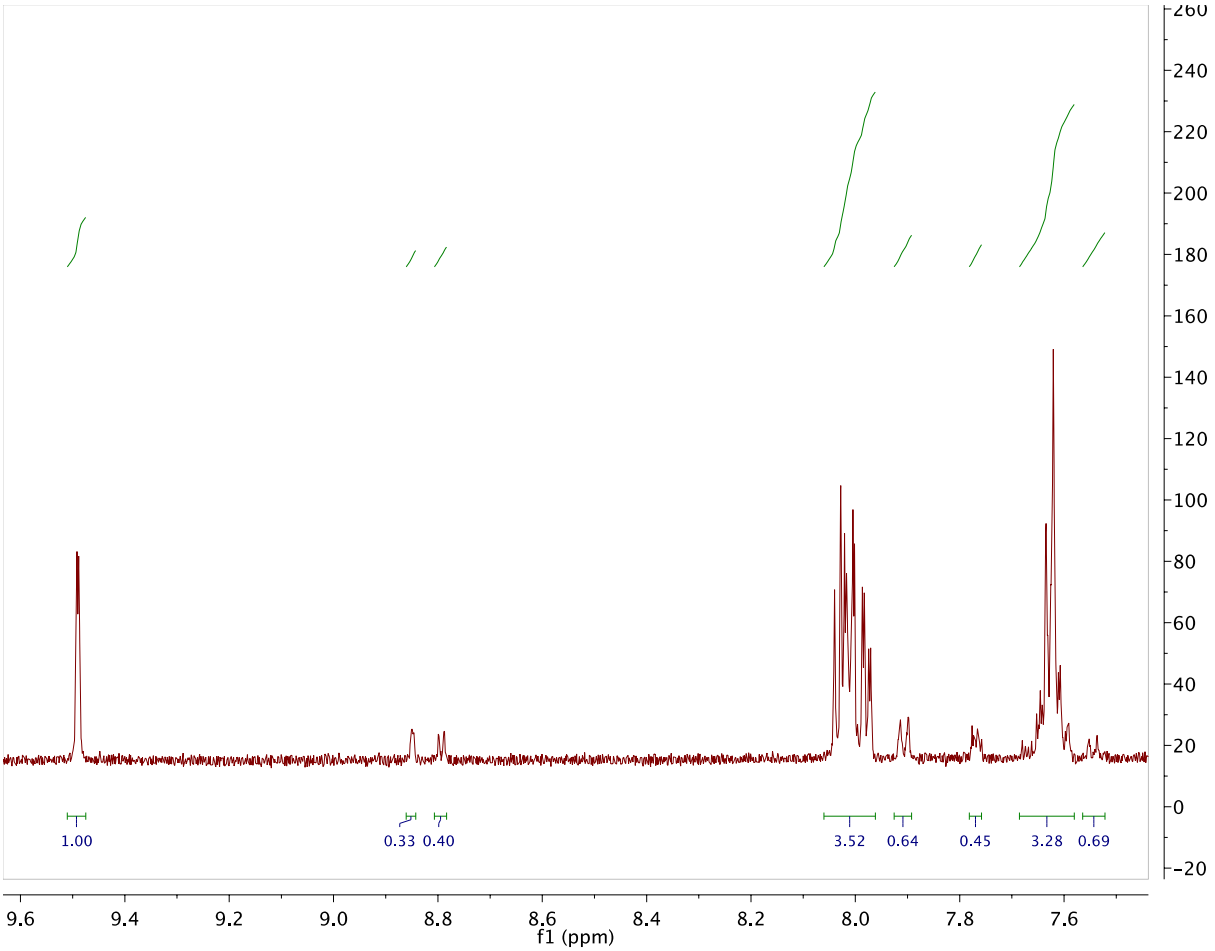

Figure 5.2. ^{1}H NMR spectrum of $[Fe(dpb)_3](PF_6)_2$ in $(CD_3)_2CO$. This product was first recrystallized and used for single crystal X-ray diffraction studies, and then redissolved for this spectrum. The main product, as well as the free ligand and bis-ligated complex are present.

In the literature, reports of the synthesis of $[Fe(dpb)_3]^{2+}$ have been published.[13-16] In a number of these studies, it is found that free ligand is a common byproduct, indicating that dissociation is often occurring in this complex.[13,14] An analogous complex, [Fe(4,7-diphenyl-phenanthroline)$_x$(phenanthroline)$_{3-x}$]$I_2 \cdot 2H_2O$ (x = 1, 2), likewise showed a proclivity towards dissociation, particularly with the iodide salt.[17] When they metathesized to the perchlorate salt, though, this appeared to be less of a problem. It is possible, due to the highly polarizable nature of

iodide, that this halide anion was able to coordinate or disrupt the coordination of the diphenyl-phenanthroline ligand. But this would seem to require that the ligand itself is easily displaced from the metal center. That the dpb ligand should have trouble binding to Fe(II) but no such problems are observed for Ru(II) is perplexing. $[Fe(bpy')_3]^{2+}$-based complexes are known to have very high formation constants,[18] indicating that the phenyl substituent on the ligand is the cause of the problems. To a first order approximation, this is highly unexpected because the ring should be only slightly withdrawing, and much more electron-withdrawing groups have been substituted on a homoleptic iron(II) complex previously: the carboxylic acid, in fact, should be more electron-withdrawing than phenyl, and also displays resonance.[19] In this work, Ferrere reports no complex dissociation. The next most obvious cause is the size of the phenyl ring, that it may be so sterically encumbering that it cannot be supported in a tris-ligated complex. Work done by Bergman et al. studied the tris(eilatin) iron(II) complex and found that for this ligand (that is even bulkier than dpb), free ligand was always observed when the complex was in solution.[20] It is not obvious that a phenyl ring would be so bulky as to reduce binding ability of the bipyridine to the iron(II), especially when in solution and able to rotate freely. However, as was shown in the case of $[Ru(dpb)_3]^{2+}$ from Chapter 4, the dihedral angle between the phenyls and the bipyridine backbone is approximately 30º, which is more coplanar than orthogonal, indicating that the ring bulk is not as out of the way as it could be. Furthermore, the size of the metal cation here may play a large role. The ionic radius of Ru(II) is ~0.94 Å, highly analogous to the radius of the high-spin Fe(II) radius of 0.95 Å.[21] However, in the case of low-spin Fe(II), as is being studied here, the radius is much closer to 0.75 Å;[21] a smaller ionic radius of the metal may in fact bring the ligands even closer to each other, as well as increase the distortion in the ligands. The torsion between the two moieties also implies that there is a degree of electronic communication. We therefore propose

that it is the dual effects of slight electron-withdrawing ability and sterics that decreases the binding strength of dpb to the Fe(II) center, particularly in a tris-ligated homoleptic complex. With a reduced coordinating ability, the molecule will be especially susceptible to coordination from nearby anions (e.g., Cl^-, F^-), solvent (e.g., MeCN), and will ultimately result in a heteroleptic complex and free ligand in solution.

3.1.2 Crystal Structure Data

To the best of our knowledge, the crystal structure of $[Fe(dpb)_3](PF_6)_2$ has not be reported. X-ray crystallographic data were collected on single crystals of $[Fe(dpb)_3](PF_6)_2$ that was grown out of evaporation of an MeCN solution with a drop of EtOH. We believe that higher quality crystals can be grown by ether diffusion into a solution of 1-OctOH and EtOH. The complex is sparingly soluble in 1-OctOH, so the addition of EtOH increases solubility in order to slow the growth of the crystals. The structure can be found in Fig. 5.3, and the relevant angles and distances are in Table 5.1 along with those of $[Ru(dpb)_3](PF_6)_2$ for comparison. The Fe-N bond distances are indicative of a low-spin Fe(II) complex but are shorter than those of $[Fe(bpy)_3](PF_6)_2$, which were found to be 1.967 Å.[22] These data would tend to support the phenyl group being slightly electron-donating into the bipyridine ring. Interestingly, in terms of Fe-N distance and *cis* N-Fe-N angles, $[Fe(dpb)_3](PF_6)_2$ most nearly resembles $[Fe(dtbb)_3](PF_6)_2$.[23] When comparing the *trans* N-Fe-N angles, however, $[Fe(dpb)_3](PF_6)_2$ is closer to 180º than any other Fe(II) complex studied in this work.[24] With the relatively shorter Fe-N distances in $[Fe(dpb)_3]^{2+}$, it is reasonable that the bulkier phenyl substituents also force the bipyridines further from each other.

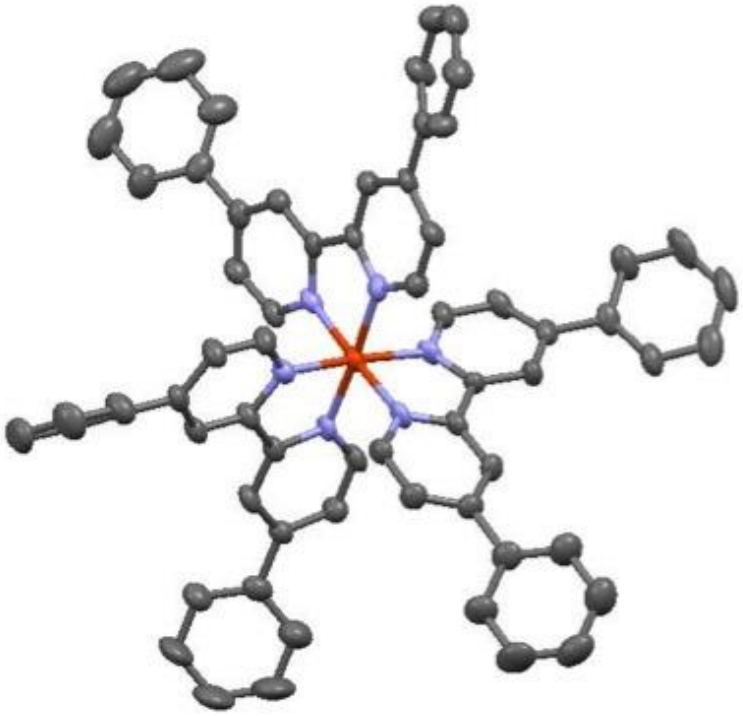

Figure 5.3. Single crystal X-ray structure of $[Fe(dpb)_3](PF_6)_2$. The protons, counterions, and solvent are omitted for clarity.

Table 5.1. Single crystal X-ray data of $[Fe(dpb)_3](PF_6)_2$ and $[Ru(dpb)_3](PF_6)_2$.

	$[Fe(dpb)_3](PF_6)_2$	$[Ru(dpb)_3](PF_6)_2$
M-N (Å)	1.958 ± 0.012	2.050 ± 0.010
cis N-M-N (º)	80.9 – 97.2	78.1 – 99.2
trans N-M-N (º)	176.4 ± 1.1	175.4 ± 0.9
bpy torsion (º)	1 – 17	0 – 15
Ph-bpy torsion (º)	33.2 ± 4.1	31.9 ± 3.5

In its ground state, the torsion between the phenyl groups and the bipyridine backbone is 33º, which is the same as that in the Ru(II) analogue, 32º. The M-N distance is 0.1 Å longer in $[Ru(dpb)_3](PF_6)_2$ relative to $[Fe(dpb)_3](PF_6)_2$. A minor, but important, difference between the two complexes is the bpy dihedral torsion, measuring the angle between the planes of the individual pyridyl moieties. This angle was measured in all three bpy groups of both complexes and was found across the board to be larger in the Fe(II) complex. The most readily apparent explanation for this is the smaller ionic radius of Fe(II) compared to Ru(II), and the inability of that Fe(II) size to support the sterically bulky dpb ligand, thus forcing the torsion of the ligand backbones.

3.1.3 Extinction Coefficient

The molar extinction coefficient was measured for $[Fe(dpb)_3](PF_6)_2$ in MeCN. The data can be seen in Figs. 5.4 and 5.5. The extinction coefficient is 15980 $M^{-1}cm^{-1}$ at the maximum of the lowest energy MLCT band, λ_{max} = 18263 cm^{-1} (548 nm). It has the typical structure of a 4,4'-disubstituted 2,2'-bipyridine iron(II) complex and is similar to $[Ru(dpb)_3]^{2+}$ in that it has another MLCT band of nearly equal intensity in the bluer part of the visible spectrum. This band displays a molar absorptivity of 15860 $M^{-1}cm^{-1}$ at λ_{max} = 26285 cm^{-1} (380 nm). Relative to $[Fe(bpy)_3]^{2+}$ (Fig. 5.5), the extinction coefficient of $[Fe(dpb)_3]^{2+}$ has nearly doubled (8800 $M^{-1}cm^{-1}$) and is red-shifted (λ_{max} = 19196 cm^{-1}, 521 nm), with the parentheticals indicating the values of $[Fe(bpy)_3]^{2+}$. The lowest-energy MLCT band is also much sharper than that of $[Fe(bpy)_3]^{2+}$. This is exactly as expected based on the analogous Ru(II) complexes.[25] Interestingly, more fine structure is observed in $[Fe(bpy)_3]^{2+}$, particularly in the higher energy part of the spectrum. These features are likely due to ligand field transitions lying underneath the MLCT band centered at ~360 nm, whereas in $[Fe(dpb)_3]^{2+}$, the Gaussian at 380 nm appears to be of such a high intensity that it swamps out any lower-strength transitions.

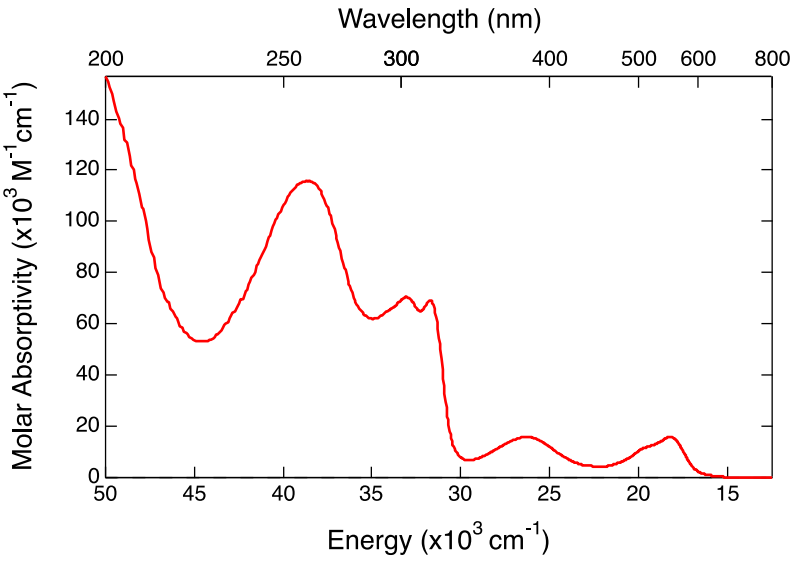

Figure 5.4. Ground state absorption spectrum of $[Fe(dpb)_3](PF_6)_2$ in MeCN, with molar extinction coefficients.

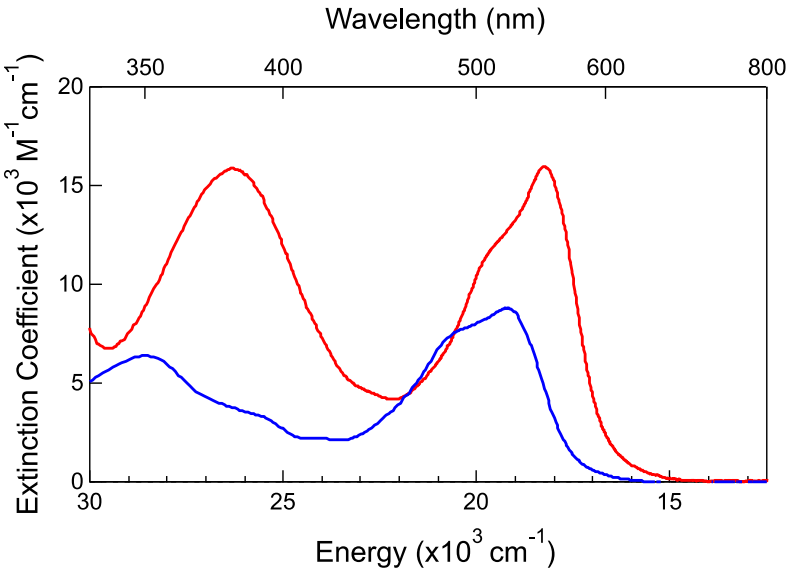

Figure 5.5. Comparison of the steady-state absorption spectra of $[Fe(dpb)_3]^{2+}$ (red) and $[Fe(bpy)_3]^{2+}$ (blue).

To further analyze the spectral features of $[Fe(dpb)_3]^{2+}$, Fig. 5.6 shows the overlay of the absorption spectra of the Fe(II), Ru(II), and Zn(II) complexes, as well as the free ligand. In the case of the free ligand, the π-π* absorption is the main feature, with the maximum occurring at 40330 cm^{-1} (248 nm). This band is red-shifted upon complexation to Zn(II), which is expected due to the stabilization afforded by coordination. In this complex, the maximum is found at approximately 39530 cm^{-1} (253 nm), a net stabilization of 810 cm^{-1} of the ligand's π* orbitals. Zn(II) is d^{10}, and therefore no MLCT transition will occur, as evidenced by the spectroscopically silent visible region of the spectrum. When dpb is coordinated to Ru(II), though, MLCT bands appear centered at 28650 and 21100 cm^{-1} (349 and 474 nm, respectively). The π-π* absorption further red-shifts, in this case to 38930 cm^{-1} (257 nm), which corresponds to a stabilization of 1410 cm^{-1} relative to the free ligand. An additional feature is observed to grow in on the red shoulder of the ligand-based π-π* absorption, at λ_{max} = 32470 cm^{-1} (308 nm). Spectroelectrochemistry on this complex has previously been performed, however, this band was much further into the UV than was measured.[25] The oscillator strength of this transition is on par with that of the π-π* feature; this band is also very blue-shifted, both pieces of information making an MLCT assignment very unlikely. From the intensity, a ligand-based transition would make sense. However, the appearance of the band with the presence of a non-d^{10} metal center is curious. The transition may be an MLCT feature intensity stealing from the π-π* absorption with which it overlaps. This seems to be the most likely explanation, as a ligand-field state would most probably be swamped out by the ligand-based feature or appear only as a shoulder. In the spectrum for $[Fe(dpb)_3]^{2+}$, the π-π* band is the most red-shifted of all the complexes, centered at 38170 cm^{-1} (262 nm), a stabilization of 2170 cm^{-1} relative to the free ligand. Again, as with the spectrum of $[Ru(dpb)_3]^{2+}$, the shoulder of the π-π* absorption in $[Fe(dpb)_3]^{2+}$ has a large oscillator strength, though in this case, it is not quite as

intense as was observed for $[Ru(dpb)_3]^{2+}$. It also appears to have more fine structure, possibly indicating the existence of ligand field transitions overlaying with other bands. At this time, it is difficult to make an exact assignment of these features. When comparing the MLCT bands in $[Ru(dpb)_3]^{2+}$ and $[Fe(dpb)_3]^{2+}$, it is apparent that the transitions in the latter are lower in energy. This is likely due to the greater extension of the d orbitals in Ru(II) relative to Fe(II), allowing for greater M-L overlap and therefore higher energy transitions. Increased spin-orbit coupling in Ru(II) (owing to it being a second-row transition metal) perpetuates mixing of the triplet and singlet excited states, thereby increasing the oscillator strength of the nominally spin-forbidden $^3MLCT \leftarrow {}^1A_1$ transition (red shoulder of lowest energy MLCT band) in $[Ru(dpb)_3]^{2+}$, a phenomenon that is not observed in the $[Fe(dpb)_3]^{2+}$ analogue.

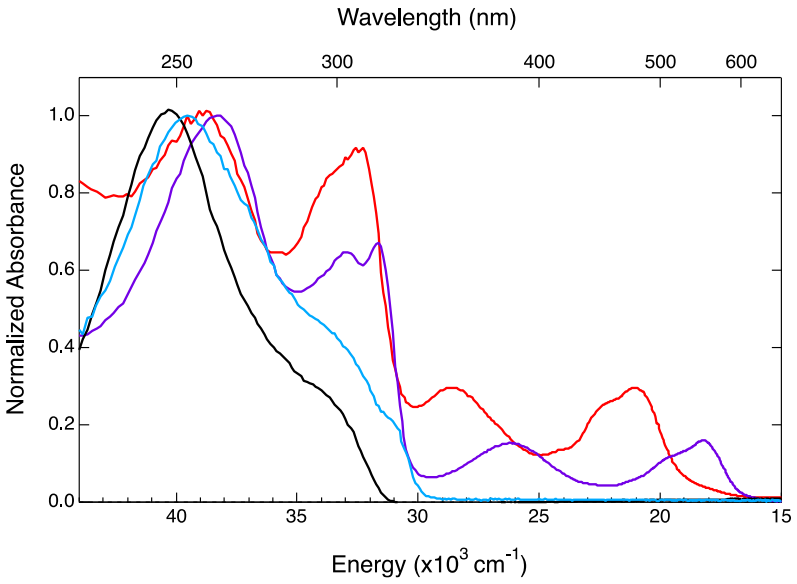

Figure 5.6. Overlay of the ground state absorption spectra of $[Fe(dpb)_3]^{2+}$ (purple), $[Ru(dpb)_3]^{2+}$ (red), $[Zn(dpb)_3]^{2+}$ (blue), and the free dpb ligand (black). The spectra are normalized to the maximum of the dpb-based π-π* absorption.

3.1.4 Ultrafast Spectroscopy Results

The ultrafast kinetics of $[Fe(dpb)_3](PF_6)_2$ were measured in MeOH. By exciting at 490 nm and probing at 540 nm, the ground state recovery lifetime was found to be 760 ± 10 ps (Fig. 5.7). When in MeCN, the lifetime is 800 ± 15 ps. This complex shows a ~20% decrease in lifetime as compared to $[Fe(bpy)_3]^{2+}$ in the same solvents. In the Ru(II) analogues of these compounds, the addition of the phenyl substituents increases the lifetime by over 50%. However, that is ground state recovery from a ^{3}MLCT state, as opposed to the $^5T_2$ ligand field state in the Fe(II) complexes. It was therefore desirable to measure the MLCT lifetime in $[Fe(dpb)_3]^{2+}$. While this process could be measured from the deactivation into the lower-lying ligand field states using the pump-probe combination used for ground state recovery, these kinetics are so fast that they are likely to be complicated by the solvent-related dynamics on the same timescale. It is much better, then, to find a probe wavelength capable of measuring the MLCT lifetime directly. In Fe(II) complexes, this is signified by a low energy, low intensity excited state absorption. These may be found on the red side of the lowest energy MLCT bands where the ground state does not absorb. In this case, the pump produces the $^5T_2$, and then the probe absorbs into the ^{5}MLCT, the lifetime of which is then measured. More definitive identification of the MLCT process may be found by spectroelectrochemical methods;[26] however, no electrochemistry was done in-house on this complex due to its proclivity to dissociate. In this complex, excited state absorption was observed upon excitation at 490 nm and probing at 690 nm (Fig. 5.8). The data were found to fit well to a single exponential with a time constant of 160 ± 20 fs. This is a 20% increase in MLCT lifetime relative to $[Fe(bpy)_3]^{2+}$.[27,28] A summary of the kinetics measured in this complex and all complexes discussed in this chapter can be found in Table 5.2.

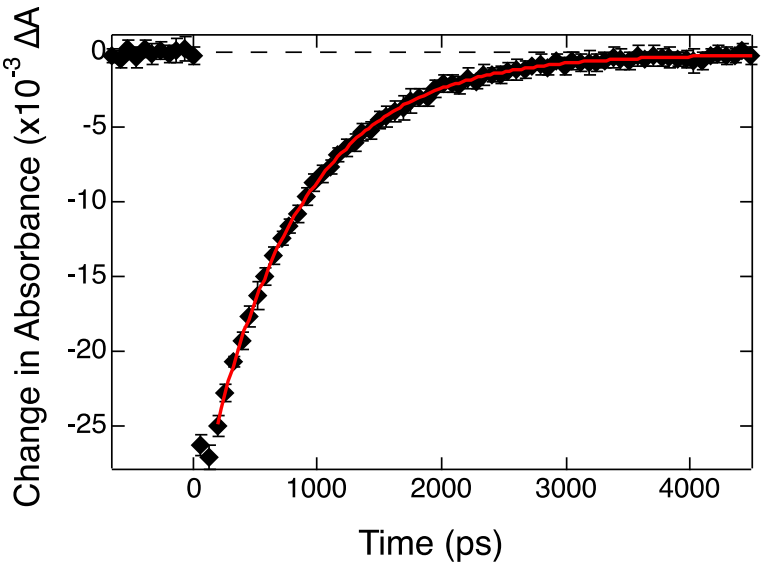

Figure 5.7. Ground state recovery dynamics of $[Fe(dpb)_3](PF_6)_2$ in MeOH (black diamonds) measured by probing at 540 nm after exciting at 490 nm. The fit (red trace) gives a lifetime of 760 ± 10 ps.

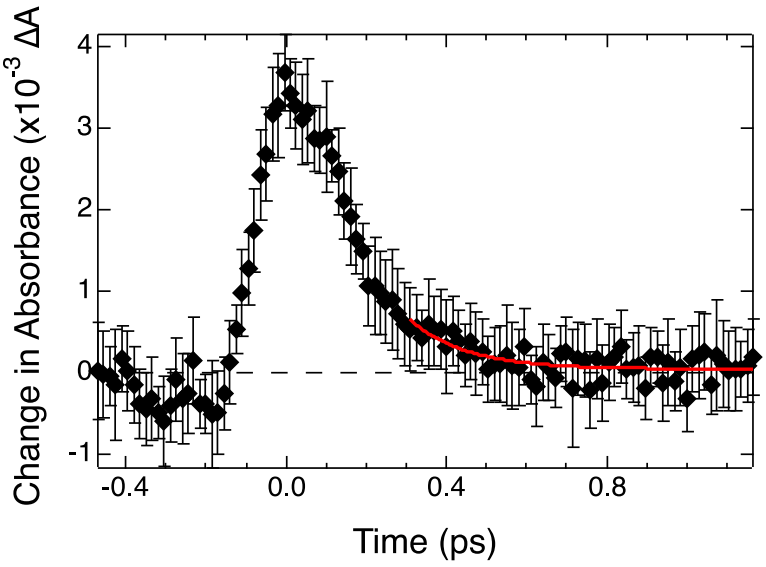

Figure 5.8. Presumed MLCT decay of $[Fe(dpb)_3](PF_6)_2$ in MeOH upon excitation at 490 nm and probing at 690 nm. The data (black diamonds) show a positive feature that in Fe(II) complexes is indicative of MLCT absorption. The lifetime (red trace) was found to be 160 ± 20 fs.

Table 5.2. Kinetic parameters of the Fe(II) complexes studied to determine the effect of extended delocalization on the rate of MLCT deactivation.

Complex	Ground State Recovery (ns)	MLCT Lifetime (fs)
$[Fe(dpb)_3](PF_6)_2$	0.76 ± 0.01	160 ± 20
$[Fe(dqp)_2](PF_6)_2$	4.29 ± 0.03	145 ± 10
$[Fe(qphen)_2](PF_6)_2$	3.16 ± 0.03	170 ± 40
$[Fe(dmib)_3](PF_6)_2$	0.94 ± 0.01	900 ± 400
$[Fe(caab)_3](PF_6)_2$	0.79 ± 0.01	≪ 150

Prior to the ultrafast measurements made here, it was hoped that a similar set of solvent- and excitation wavelength-dependent kinetics would be able to be collected on $[Fe(dpb)_3]^{2+}$ in analogy to those of $[Ru(dpb)_3]^{2+}$ expanded on in Chapter 4. In the case of the Ru(II) complex, the vibrational cooling (VC) associated with solvation dynamics occurs on the ^{3}MLCT surface, which is the lowest energy excited state. If such kinetics were to be measured in Fe(II), it is obvious that they would not appear in the MLCT due to its lifetime. Vibrational cooling is typically thought of as a 1-10 ps process;[29-31] by the time this could occur, the MLCT state would already be depopulated. On the other hand, if VC is occurring along the lowest energy excited state in $[Fe(dpb)_3]^{2+}$, that would be on the $^5T_2$ surface. These dynamics have previously observed in $[Fe(bpy)_3]^{2+}$,[32] and other Fe(II) complexes.[31] However, it is difficult to cleanly monitor these kinetics as VC is a subtle modulation overlaid on the electronic state population dynamics. When those dynamics happen to present as a ground state bleach, it is all the more difficult to observe

the VC, simply due to its small ΔΔA on top of a much larger signal. These studies are still worth pursuing, however, though it may be fruitful to initially attempt to view the VC dynamics as the band sharpening and blue-shifting in the full spectral data – spectral tags for the vibrational cooling process. Singular value decomposition and global analysis (Appendix E) may be of use in this endeavor.

To further characterize $[Fe(dpb)_3]^{2+}$, VT measurements were performed with the complex in MeOH. The same pump-probe combination of 490-540 nm (respectively) was used. The data can be seen in Fig. 5.9, and the Arrhenius plot is given in Fig. 5.10. From these data an activation energy of 260 ± 10 cm^{-1} was determined. This is significantly less than any of the $[Fe(bpy')_3]^{2+}$ complexes found in Chapter 2. The frequency factor, however, is the same as those measured for the $[Fe(bpy')_3]^{2+}$ family, at 205 ± 10 ps^{-1}. The Marcus values were determined for this complex using the same method outlined in Chapters 2 and 3. Electrochemical data was not collected in-house but work by Leidner et al. did determine oxidation potentials for both $[Fe(bpy)_3](PF_6)_2$ and $[Fe(dpb)_3](PF_6)_2$ under identical conditions, making the relative difference between the two usable to determine ΔG^o.[14] In this data, the Fe(II/III) couples were 1.02 V for $[Fe(bpy)_3]^{2+}$ and 0.96 V for $[Fe(dpb)_3]^{2+}$ (both referenced to SSCE). Based on these values, ΔG^o for $[Fe(dpb)_3]^{2+}$ would be -6650 ± 670 cm^{-1}. From this approximation, λ = 9900 ± 900 cm^{-1} and H_{ab} = 4.6 ± 0.2 cm^{-1}. Both the reorganization energy and H_{ab} are the same as that of the bpy' series of complexes. This is not wholly unexpected considering the electron-donating ability of the methyl and ^{t}butyl groups discussed in Chapter 2 affected ΔG^o significantly, but neither λ or H_{ab} were drastically altered relative to the parent complex. In fact, what is most interesting about these results, is the fact that ΔG^o for $[Fe(dpb)_3]^{2+}$ trends in the direction expected of an electron-donating group, which is in agreement with the crystallographic data. This may imply more complicated effects caused by the

phenyl group than previously believed. That being said, the H_{ab}^4/λ ratio was calculated to be 1/(23 ± 2). This is rather unexpected as the ratio is calculated solely from A, the preexponential factor, and seeing as that value was in keeping with the bpy' series of complexes, it is unusual that the ratio for $[Fe(dpb)_3]^{2+}$ would actually be right between that of $[Fe(bpy')_3]^{2+}$ and $[Fe(terpy)_2]^{2+}$ or $[Fe(dcpp)_2]^{2+}$. Interestingly, the ratio for the dpb complex is actually within error of all of the compounds measured in Chapters 2 and 3.

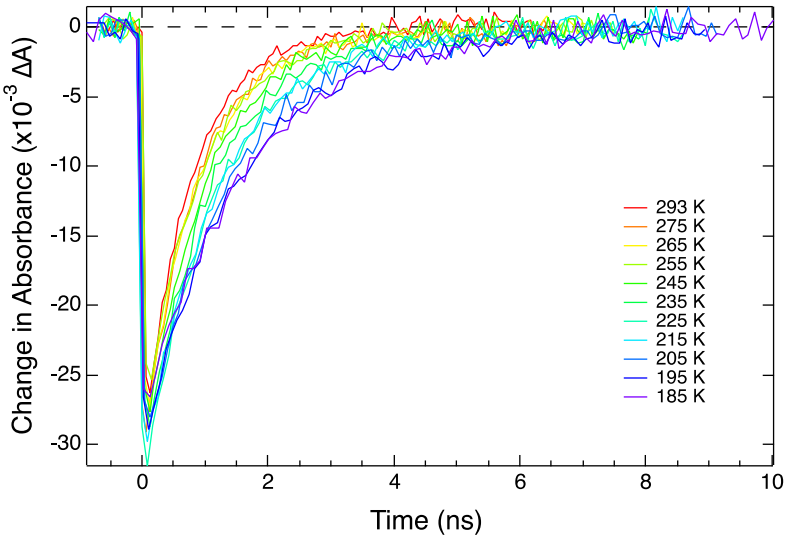

Figure 5.9. Ground state recovery lifetime of $[Fe(dpb)_3](PF_6)_2$ in MeOH as a function of temperature. Excitation occurred at 490 nm with probing at 540 nm.

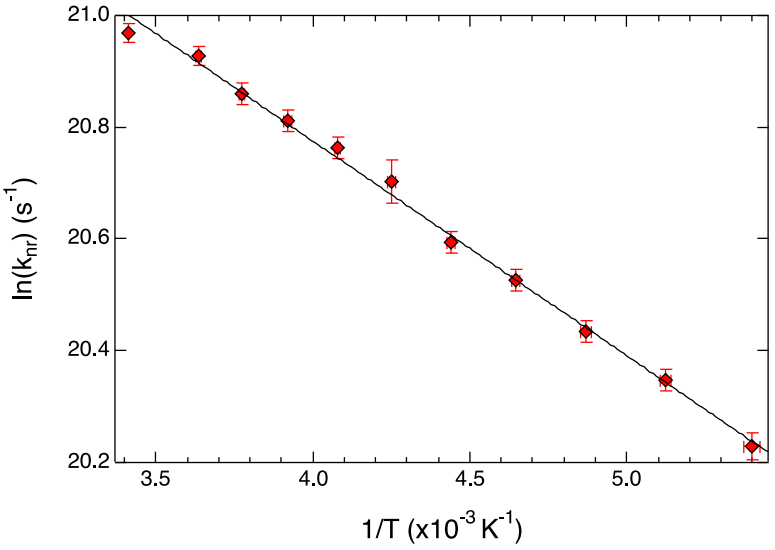

Figure 5.10. Arrhenius plot of the variable-temperature lifetimes of $[Fe(dpb)_3](PF_6)_2$ in MeOH, as shown in Fig. 5.9. From these data an activation energy of 260 ± 10 cm^{-1} is found, as well as a barrierless rate of 205 ± 10 ps^{-1}. The data fit well to a single mode, with $R^2 = 0.996$.

The increased rate of ground state recovery relative to $[Fe(bpy)_3]^{2+}$ is clearly due to the reduction in activation energy. The magnitude of this barrier, however, may either be caused by greater ligand field strength in $[Fe(dpb)_3]^{2+}$ or by this transition occurring via an alternate nuclear coordinate. It is possible that the former is playing a role: increased ligand field strength caused by the phenyl substituent withdrawing electron density out of the bipyridine backbone, decreasing the strength of the Fe-N bonds. This is expected based on the slight electron withdrawing nature of phenyls, but there is no real indication of this, at least in the ground state from the crystal structure for which the Fe-N distances are 0.01 Å shorter in $[Fe(dpb)_3]^{2+}$ than in $[Fe(bpy)_3]^{2+}$.[22,33] This is not a true representation of the ligand field strength, only an approximation. As for the second hypothesis, an alternate nuclear coordinate seems much more likely given the unusual effects the phenyl substituents have already displayed (particularly in the synthesis of the complex). The substituent itself may not even be playing a role in ground state recovery, it is

possible that its mere presence increases the steric bulk of the ligand such that the vibrational modes accessed in $[Fe(bpy')_3]^{2+}$ for the $^5T_2 \rightarrow {}^1A_1$ transition become blocked or energetically disfavored.

The MLCT lifetime lengthening in $[Fe(dpb)_3]^{2+}$ is of much greater interest, due to the goal of this work. Increasing the extent of delocalization in the MLCT excited state, as was observed in $[Ru(dpb)_3]^{2+}$, increased the oscillator strength in the MLCT bands of the ground state absorption profile of $[Fe(dpb)_3]^{2+}$. For this to be true, the ^{1}MLCT states must be shifted along one nuclear coordinate relative to the $^1A_1$ ground state such that Franck-Condon overlap is much greater than in the unsubstituted bipyridine complex. This means more nested potentials in the case of $[Fe(dpb)_3]^{2+}$. A longer-lived MLCT lifetime, then, requires that the electronic communication between the MLCT and ligand field manifolds be weaker, and/or the barrier between these states be larger. With a more delocalized wavefunction in the excited state, the coupling to the lower-lying electronic states should be weakened, thereby reducing the rate of deactivation from the MLCT manifold. As discussed in the introduction, the work described here is intended to study the effect of increased delocalization in the MLCT as a possible path to increase the lifetime of that state. While this is only a first step toward that route, the results are promising. Clearly, though, further characterization of the excited states in this (and other) Fe(II) complex(es) is necessary, and that work is currently ongoing.

3.2 Extending Delocalization By Synthetic Modification of the Ligand

3.2.1 Increased Conjugation Around the Metal Center

When considering extending the delocalization in a ligand system, there are two alternatives possible: increasing the conjugated moieties encircling the metal center or expanding the delocalized state away from the metal center. Obviously both can be utilized simultaneously,

but our hypothesis is that the latter mechanism will push the wavefunction away from the metal such that the electron "forgets" where it originated, thereby lengthening the time the electron survives away from the metal (i.e., the MLCT lifetime). This mechanism is likely to make a greater impact in decreasing the rate of MLCT deactivation. The role of delocalization in the excited state must be thoroughly examined, though. Is increased delocalization in any arbitrary direction sufficient to improve the MLCT lifetime? That is the question being addressed through the use of the two quinoline-substituted complexes shown in Scheme 5.1. These compounds were prepared by L. Wickramasinghe of the Thummel group and use quinoline moieties to extend conjugation around the iron center.

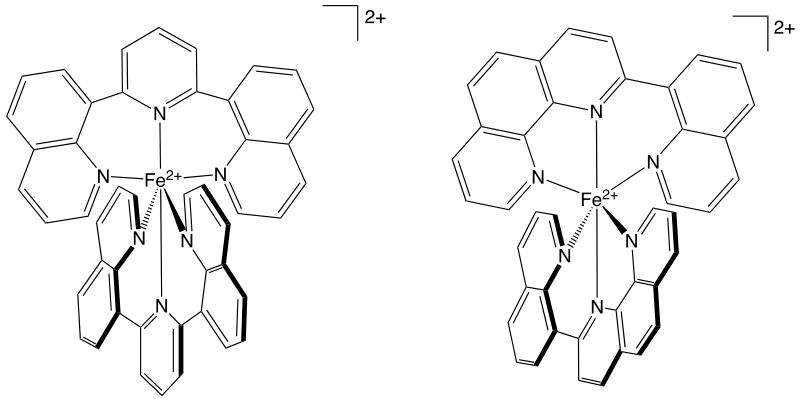

Scheme 5.1. Complexes intended to extend delocalization around the iron(II) center: (left) bis(8'-diquinolinyl-2,6-pyridine) iron(II), $[Fe(dqp)_2](PF_6)_2$; (right) bis(8'-quinolinyl-2-phenanthroline) iron(II), $[Fe(qphen)_2](PF_6)_2$.

These compounds display very unusual ground state absorption spectra (Fig. 5.11). Both are very broad, with MLCT features expanding over 400-700 nm. When both are taken in MeCN, $[Fe(dqp)_2]^{2+}$ displays a MLCT maximum at 17392 cm^{-1} (575 nm), while $[Fe(qphen)_2]^{2+}$ is slightly

more blue-shifted with λ_{max} = 17761 cm^{-1} (563 nm). However, the lowest energy MLCT band in $[Fe(qphen)_2]^{2+}$ actually has a shoulder that extends farther into the red than $[Fe(dqp)_2]^{2+}$. Both complexes display interesting structure in their steady state absorption spectra, perhaps owing to the highly asymmetric nature of the ligands. Additionally, it can be expected that the complex is vastly distorted from octahedral symmetry due to the rigid quinoline ligand.

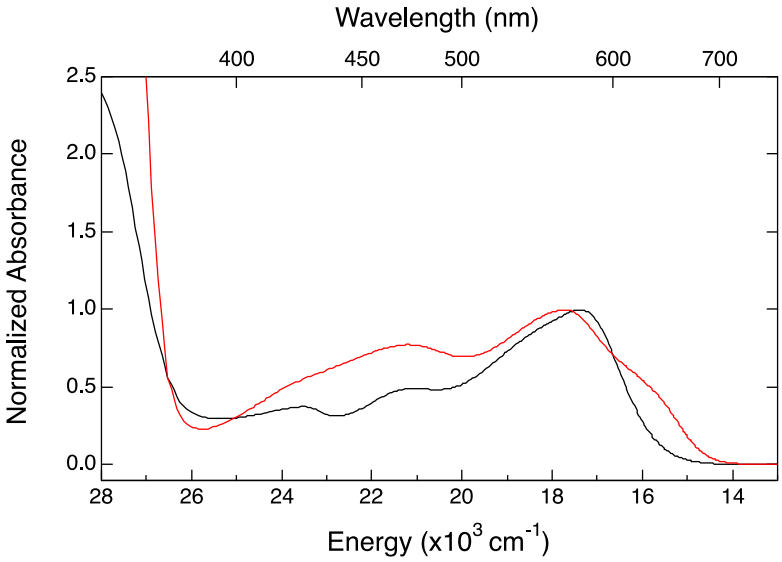

Figure 5.11. Overlay ground state absorption spectra of $[Fe(dqp)_2](PF_6)_2$ (black) and $[Fe(qphen)_2](PF_6)_2$ (red).

The dqp ligand might be likened to an extended terpyridine in that it contains three separate N-donating moieties, with the quinoline increasing the distance between the central pyridine and the peripheral ends of the ligand. With that in mind, the ground state recovery dynamics of $[Fe(dqp)_2](PF_6)_2$ (Fig. 5.12, Table 5.2) are unsurprising, with a lifetime of 4.29 ± 0.03 ns in MeCN that is very close to that of $[Fe(terpy)_2]^{2+}$, which is 5.2 ± 0.1 ns. The shortening of the lifetime of $[Fe(dqp)_2]^{2+}$ relative to $[Fe(terpy)_2]^{2+}$ in fact mimics the relationship between $[Fe(terpy)_2]^{2+}$ and

$[Fe(dcpp)_2]^{2+}$, though to a much lesser extent. Analogously to dcpp, dqp has an extended ligand distance that likely improves the overlap of the N-donor atoms with the d orbitals on the Fe(II) center. While $[Fe(dqp)_2]^{2+}$ is probably not as perfectly octahedral as $[Fe(dcpp)_2]^{2+}$, it is certainly more symmetric than $[Fe(terpy)_2]^{2+}$, thus making it slightly more barrierless than the terpy complex. This is what decreases the ground state recovery rate in $[Fe(dqp)_2]^{2+}$. What is unexpected, though, is the drastic increase in MLCT lifetime, as evidenced by Fig. 5.13. This lifetime was previously measured by A. M. Brown in $[Fe(terpy)_2]^{2+}$ in MeCN and found to be 60 ± 15 fs (λ_{exc} = 560 nm, λ_{probe} = 410 nm).[34] In $[Fe(dqp)_2]^{2+}$ in MeCN, though, the MLCT lifetime is 145 ± 10 fs, an increase of more than a factor of two.

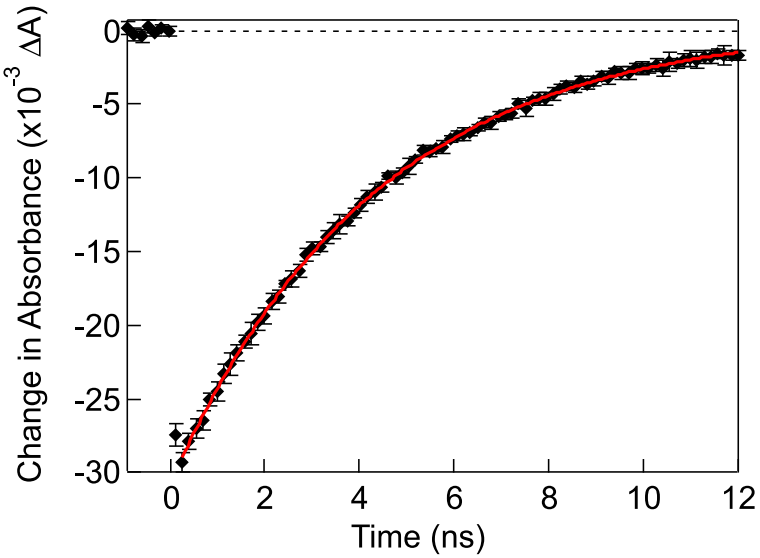

Figure 5.12. Ground state recovery of $[Fe(dqp)_2](PF_6)_2$ in MeCN, upon excitation at 570 nm and probing at 480 nm. The data (black diamonds) fit well to a lifetime of 4.29 ± 0.03 ns (red trace).

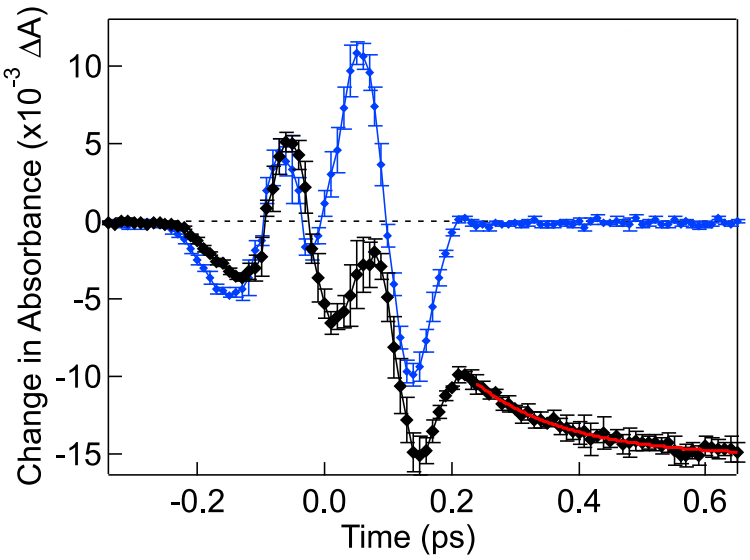

Figure 5.13. The MLCT deactivation of $[Fe(dqp)_2](PF_6)_2$ in MeCN (black diamonds) fit to single exponential kinetics (red trace) with a 145 ± 10 fs lifetime. The solvent data (blue diamonds) are shown for comparison.

The ligand structure of $[Fe(qphen)_2]^{2+}$ is not quite as simple to compare to any one prototypical Fe(II) polypyridyl complex. Obviously $[Fe(phen)_3]^{2+}$ is a well-known and commonly studied compound, but its bond to the quinoline makes the structure not exactly terpy-like, but not a true phen-based system. The ground state recovery lifetime (Fig. 5.14, Table 5.2) shows kinetics that are essentially right between $[Fe(phen)_3]^{2+}$ and $[Fe(terpy)_2]^{2+}$, being 3.16 ± 0.03 ns in MeCN when pumped at 570 nm and probed at 480 nm. This may imply that the ligand field strength in $[Fe(qphen)_2]^{2+}$ is weaker than that of $[Fe(phen)_3]^{2+}$ (not unexpected for tridentate vs. bidentate ligand), but more likely indicates an alternate relaxation pathway for the process. No variable-temperature studies were performed on either $[Fe(dqp)_2]^{2+}$ or $[Fe(qphen)_2]^{2+}$ but considering that the quinoline will contain vibrational modes that are not present in a simple phen or terpy ligand

system, it seems reasonable to expect that those modes will play a role in the photophysical processes of the iron(II) complexes at hand.

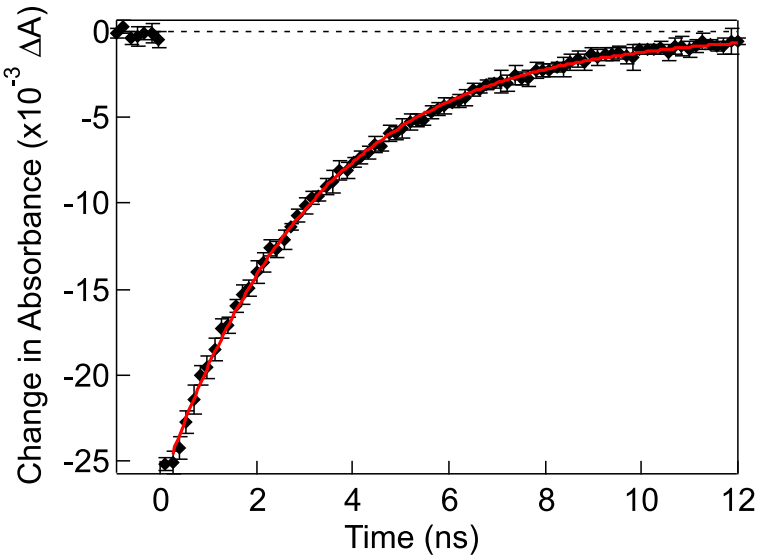

Figure 5.14. Ground state recovery lifetime of $[Fe(qphen)_2](PF_6)_2$ in MeCN (black diamonds). Excitation occurred at 570 nm and probing at 480 nm. The data fit well to a single exponential (red trace) with a lifetime of 3.16 ± 0.03 ns.

The MLCT deactivation was likewise measured in $[Fe(qphen)_2](PF_6)_2$ in MeCN and showed a lifetime of 170 ± 40 fs (Fig. 5.15, Table 5.2). While the average is slightly longer than that of $[Fe(dqp)_2]^{2+}$, the two are within error of each other. Unfortunately, no excited state absorption was observed for either of these complexes, meaning the MLCT lifetime had to be measured as the deactivation into the ground state bleach. In addition to the problem of solvent dynamics obscuring this decay feature that was mentioned previously, the error associated with these kinetics will also be larger due to the fact that less than $3\tau_{MLCT}$ occurs before the ground state recovery process begins, further complicating the fitting of these data. Regardless, both of the

quinoline-substituted complexes displayed MLCT lifetimes that were longer than those previously measured in standard Fe(II) compounds, such as $[Fe(bpy)_3]^{2+}$ and $[Fe(terpy)_2]^{2+}$.[27,28,34] These data in combination with the those measured in $[Fe(dpb)_3]^{2+}$ support the proposal that increased delocalization across the ligand is able to lengthen the lifetime of the MLCT state in Fe(II) polypyridyl chromophores.

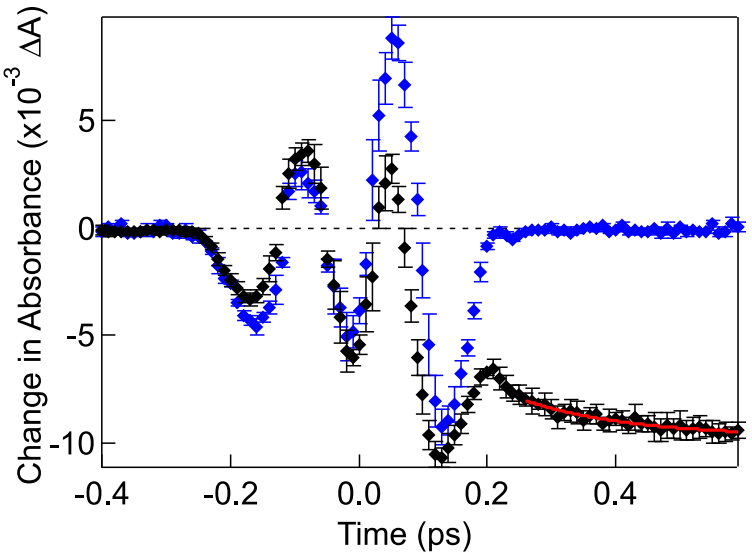

Figure 5.15. MLCT deactivation of $[Fe(qphen)_2](PF_6)_2$ in MeCN (black diamonds) fit to a lifetime of 170 ± 40 fs (red trace). The data were collected at 660 nm upon 570 nm excitation. The solvent trace (blue diamonds) is given for reference.

3.2.2 Extending Delocalization Away from the Fe(II) Center

The next series of complexes that will be studied to understand the role delocalization plays in the MLCT lifetime is shown in Scheme 5.2. These two compounds (prepared by C. R. Tichnell) are more analogous to $[Fe(dpb)_3]^{2+}$ than either $[Fe(dqp)_2]^{2+}$ or $[Fe(qphen)_2]^{2+}$ were. In part, this is caused by the bidentate nature of these complexes versus the tridentate quinoline-based systems.

More importantly, the molecules being studied here are 4,4'-disubstituted bipyridine analogues, making for a better comparison between the two. In the first complex, $[Fe(dmib)_3]^{2+}$, a 2,5-dimethylisoxazole is the substituent in question. The aromatic nature of the group will extend delocalization away from the metal center, though it may be slightly mediated by the methyl groups, which may serve to sterically hinder full coplanarity of the isoxazole relative to the bpy backbone. The whole of the isoxazole group, though, is taken to be electron-withdrawing, which is a great comparison to the second complex, $[Fe(caab)_3]^{2+}$, in which the 4,4'-substituent is a cyanoacrylic acid moiety. The cyano- and carboxylic acid groups both serve to pull electron density away from the metal center, and the whole appendage is conjugated via the vinyl moiety into the carboxylic acid group. Both the dmib and caab ligands have electron-withdrawing functional groups; they also have steric bulk in their own unique ways. The main difference, and therefore the point of comparison, between these two is the way in which the conjugation is extended. In $[Fe(dmib)_3]^{2+}$, the MLCT excited state would be delocalized across an aromatic ring (as was true with $[Fe(dpb)_3]^{2+}$), whereas the conjugation in $[Fe(caab)_3]^{2+}$ extends in a linear fashion. The comparison of these two complexes will help determine if the mode of delocalization matters for MLCT lifetime elongation.

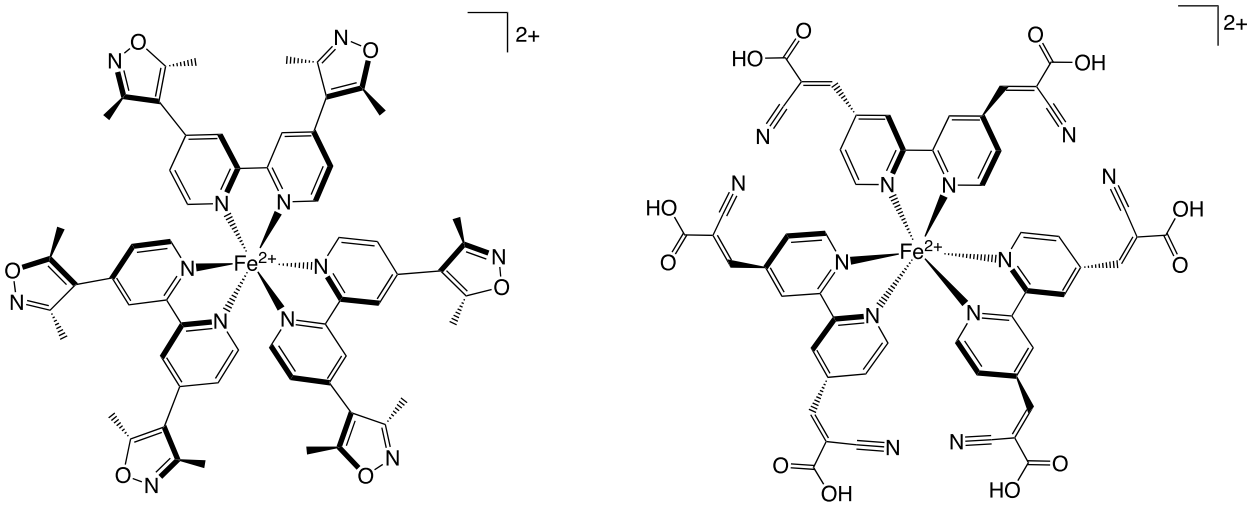

Scheme 5.2. Two complexes that extend delocalization away from the metal center via two different mechanisms. (Left) The tris[4,4'-(di-2,5-dimethylisoxazolyl)-2,2'-bipyridine] iron(II) complex, $[Fe(dmib)_3]^{2+}$, which has an aromatic isoxazole moiety. (Right) The tris(4,4'-cyanoacrylic acid-2,2'-bipyridine) iron(II) complex, $[Fe(caab)_3]^{2+}$, which extends delocalization across a linear chain.

As with $[Fe(dqp)_2]^{2+}$ and $[Fe(qphen)_2]^{2+}$, it is worthwhile to compare the absorption spectra of the 4,4'-disubstituted Fe(II) bipyridine-based complexes (Fig. 5.16). The spectra for these two compounds are very similar, not only to each other but also relative to $[Fe(dpb)_3]^{2+}$ and $[Fe(bpy)_3]^{2+}$ from Fig. 5.5. The lowest energy MLCT band in $[Fe(dmib)_3]^{2+}$ is at 542 nm, whereas the maximum occurs at 543 in $[Fe(caab)_3]^{2+}$. Comparing this to $[Fe(dpb)_3]^{2+}$ (λ_{max} = 548 nm) and $[Fe(bpy)_3]^{2+}$ (λ_{max} = 521 nm). As expected, delocalization in the ^{1}MLCT lowers the energy of that state, thus causing the red-shift observed for all three of the disubstituted complexes relative to the parent compound. Interestingly, it would appear that the degree of delocalization is the greatest in $[Fe(dpb)_3]^{2+}$ as its MLCT absorption maximum is the farthest to the red. This may be a consequence of the larger size of the phenyl ring relative to the other two conjugated substituents,

increasing its instantaneous dipole moment and thus the delocalization in its excited state wavefunction. Based on this reasoning, one could argue that the extent of delocalization in both $[Fe(dmib)_3]^{2+}$ and $[Fe(caab)_3]^{2+}$ is very similar, making them great candidates in this study.

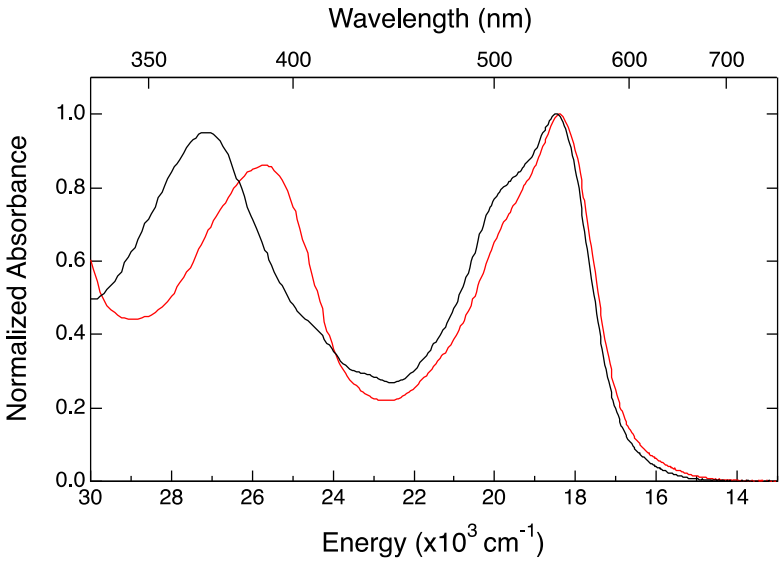

Figure 5.16. Comparison of the ground state absorption spectra of $[Fe(dmib)_3](PF_6)_2$ (black) and $[Fe(caab)_3](PF_6)_2$ (red).

One other point of interest in the comparison of steady state spectra of the four $[Fe(bpy')_3]^{2+}$ complexes: the shape of the spectra. All members of this family have the same band shape for the lowest energy ^{1}MLCT absorption: the asymmetric double Gaussian with the redder feature having a slightly greater oscillator strength. In the three disubstituted complexes, there is another band toward the blue edge of the spectrum. The central wavelength of this feature shifts pretty substantially depending on the complex (λ_{max} = 368 nm in $[Fe(dmib)_3]^{2+}$, λ_{max} = 380 nm in $[Fe(dpb)_3]^{2+}$, and λ_{max} = 391 nm in $[Fe(caab)_3]^{2+}$), but more importantly, it is altogether absent from the spectrum of $[Fe(bpy)_3]^{2+}$. This band has long been assigned as being MLCT in nature; if true, it seems most likely that the wavefunction of this excited state must be weighted more on the

substituents, whereas the lower energy bands must be a largely bpy-based wavefunction. It is unreasonable to believe that a MLCT excited state would ever lie fully on one the substituent with 0% probability of the wavefunction existing on the bipyridine, or vice versa. The two communicate electronically with one another, it is simply a question of whether the excitation energy biases the excited electron to more fully occupy one moiety over the other. This is a very interesting fundamental physical organic chemistry question, and one that is being studied currently by S. L. Adelman with other $[Fe(bpy')_3]^{2+}$ analogues and showing exciting results.[35]

The ground state recovery dynamics of $[Fe(dmib)_3]^{2+}$ are shown in Fig. 5.17 and Table 5.2. They were measured in MeCN at 510 nm upon excitation at 570 nm. The lifetime of this complex is 0.94 ± 0.01 ns, which is very similar to that of $[Fe(bpy)_3]^{2+}$. Moreover, the MLCT lifetime was measured (Fig. 5.18, Table 5.2) at 650 nm where excited state absorption was observed to occur. These data were best fit with a double exponential, though the error bars on the fit are quite large as the time delay was not long enough to observe the full relaxation of the molecule. The first time constant is 45 ± 10 fs, which is too short to be believed with the IRF of this system (here, 150 fs). However, the longer kinetic component was found to be 900 ± 400 fs, which is nearly a factor of seven longer than the lifetime of $[Fe(bpy)_3]^{2+}$. This is fascinating considering that the isoxazole would not extend delocalization any farther than a phenyl group, and yet the MLCT lifetime of $[Fe(dmib)_3]^{2+}$ is possibly a factor of five longer than that of $[Fe(dpb)_3]^{2+}$. This may in fact be caused by the methyl groups on the isoxazole. These functional groups would sterically hinder the ring from rotating into coplanarity with the bipyridine; coplanarity here would actually be expected to allow for delocalization back onto the bpy, thereby decreasing the charge-separated distance and possibly decreasing the MLCT lifetime. If borne out, this method of blocking the electron from returning to the metal center may need to be employed in more conjugated systems.

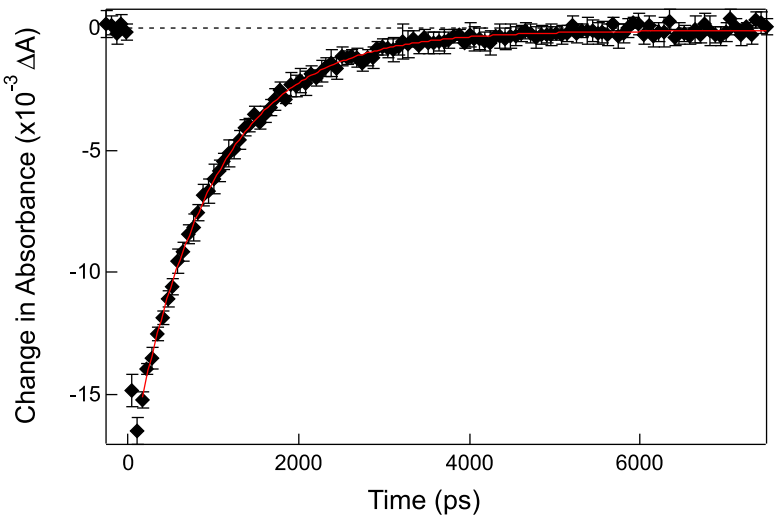

Figure 5.17. Ground state recovery dynamics (black diamonds) of $[Fe(dmib)_3](PF_6)_2$ in MeCN. The complex was excited at 570 nm and probed at 510 nm. The data were fit with a single exponential (red trace) with a lifetime of 0.94 ± 0.01 ns.

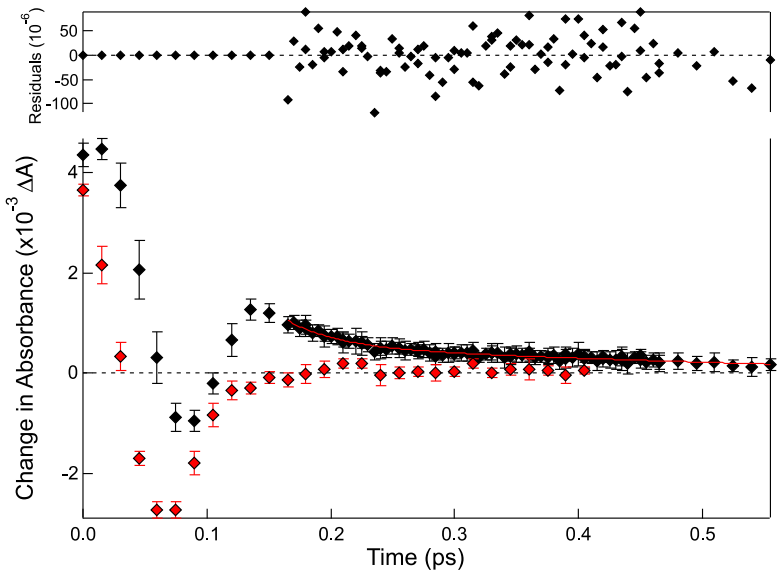

Figure 5.18. MLCT kinetics (black diamonds, lower) measured for $[Fe(dmib)_3](PF_6)_2$ in MeCN upon excitation at 570 nm and probing at 650 nm. The data required a double exponential (red trace) for an adequate fit, with two lifetimes of 45 ± 10 fs and 900 ± 400 fs. Because the data did not fit the second exponential very well, the residuals are plotted (black diamonds, upper) along with the solvent trace (red diamonds) for reference.

The photophysical kinetics of $[Fe(caab)_3]^{2+}$ were then studied for comparison to $[Fe(dmib)_3]^{2+}$. The ground state recovery dynamics are shown in Fig. 5.19, along with the MLCT lifetime in Table 5.2. First, the ground state recovery of the complex is observed to have a time constant of 0.79 ± 0.01 ns associated with it when in MeCN and probed at 550 nm upon excitation at 605 nm. This lifetime is very comparable to that of $[Fe(dpb)_3]^{2+}$, perhaps indicating greater ligand field strength than $[Fe(bpy)_3]^{2+}$, as induced by the electron-withdrawing nature of the cyanoacrylic acid substituents. However, when the MLCT deactivation was attempted to be measured, it was found to be much shorter than the IRF of the system, essentially making it unmeasurable.

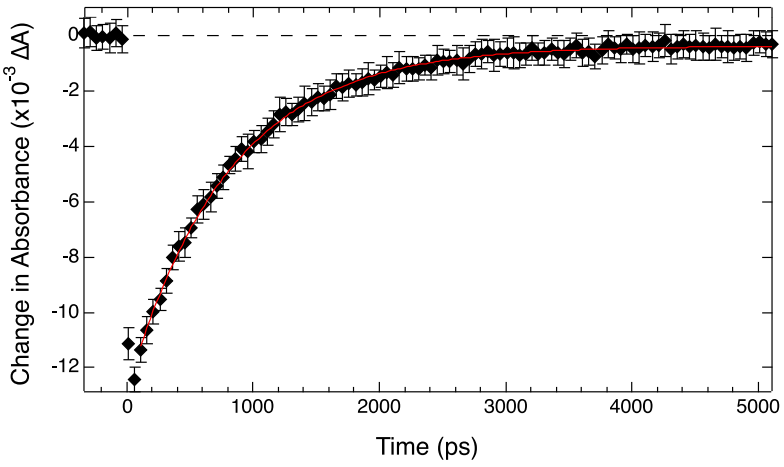

Figure 5.19. Ground state recovery measurement of $[Fe(caab)_3](PF_6)_2$ in MeCN (black diamonds). These data were collected at 550 nm with 605 nm excitation. The lifetime (red trace) was found to be 0.79 ± 0.01 ns.

The huge disparity in MLCT lifetimes between $[Fe(dmib)_3]^{2+}$ and $[Fe(caab)_2]^{2+}$ yields some interesting conclusions for this research. It should first be acknowledged that an isoxazole and cyanoacrylic acid are in no way perfect analogues of each other. However, both are electron withdrawing, both are conjugated, and both will adopt a twisted conformation such that the π system of the substituent will likely not be coplanar with the bipyridine. The latter point is based on the bulkiness of the two groups. The most important structural difference between these two functionals is that the isoxazole is aromatic, while the cyanoacrylic acid is a conjugated chain. Based on these results, it would appear as though aromaticity is a requirement for a longer-lived charge-separated excited state. At first glance, one might argue that the reason for the lengthened MLCT lifetime in $[Fe(dmib)_3]^{2+}$ is that the methyl groups are better able to hinder delocalization back into the bipyridine backbone once the electron is on the isoxazole. However, in the case of $[Fe(dpb)_3]^{2+}$, there are no steric barriers to deter ring rotation into coplanarity with the bpy. In that complex, the MLCT lifetime is outside of the IRF of the laser system, a fact which invalidates the

sterics argument. One way in which this hypothesis could be tested is through the MLCT lifetime measurement of a tris(4,4'-diisoxazole-2,2'-bipyridine) iron(II) complex in which there are no methyl groups present. If the theory put forward here is correct, this complex will display MLCT-based kinetics more similar to those of $[Fe(dpb)_3]^{2+}$. Alternatively, an $[Fe(dmesb)_3]^{2+}$-type complex (in which dmesb is the 4,4'-dimesityl-2,2'-bipyridine ligand) might also be telling and would be expected to have a longer-lived MLCT state than the unsubstituted $[Fe(dpb)_3]^{2+}$.

4. Future Works and Conclusions

4.1 Results from Extended Delocalization Studies

The dpb, dmib, and caab ligands were useful in the determination of the role of delocalization in the lifetime of a MLCT excited state. As 4,4'-disubstituted bipyridine complexes, they separated the excited electron from the oxidized metal center to varying degrees of distance and via different mechanisms (i.e., aromaticity, chain). In comparison, the dqp and qphen ligands extended the conjugation not away from the metal center, but around it. When comparing these two different types of complexes, it appears as though delocalization in general improves the MLCT lifetime. This conclusion has one caveat: conjugation via a chain-type substituent such a vinyl group appears to have no effect on the MLCT lifetime or may in fact shorten it relative to the parent compound, $[Fe(bpy)_3]^{2+}$. These studies have not only generated a complex with a nearly 1 ps MLCT lifetime in $[Fe(dmib)_3]^{2+}$, but they have also provided invaluable insight into the mechanisms by which delocalization may lengthen a charge-separated state.

To further understand the excited state wavefunctions, time-dependent density functional theory may be of use. This method provides snapshots of the orbital contributions to different transitions from the ground state. While theoretical, this may yield insights into extent of

delocalization in the excited states, or the amount of participation of the substituents. In terms of future experimental work, a full variable-temperature study of these complexes should be performed so that the barriers associated with ground state recovery may be known. These data will also be crucial in determining (to a first-order approximation) if the $^5T_2 \rightarrow {}^1A_1$ transition occurs via the same nuclear coordinate, particularly amongst the $[Fe(bpy')_3]^{2+}$ series of compounds. In that vein, VT-TA should be attempted on the MLCT kinetics of these Fe(II) polypyridyls. This will be a technically challenging experiment to set up owing in large part to the fact that very short pulses would be desired to get the most accurate measure of the MLCT lifetimes. These pulses will be readily broadened by the glass introduced by the cryostat, but that chirp can be compensated for with the folded Brewster prism pair used in the laser system outlined in Chapters 3 and 4. Not only for these compounds, but for all future Fe(II) complexes prepared, a full MLCT kinetic work-up should be done in order to gain the most information from these photophysical processes as possible.

For the chromophores discussed in this chapter, electrochemical data was collected only on $[Fe(dqp)_3]^{2+}$ and was measured by L. Wickramasinghe of the Thummel group. These data should be recollected along with the electrochemical properties of the other complexes. The oxidation and reduction potentials garnered from this experiment will provide more insight into the energetics of these molecules and may help inform the synthetic modifications of future ligands. To the best of our knowledge, spectroelectrochemical measurements have not been performed on any of the complexes here, and these data should likewise be collected so as to ascertain if there are spectrally selective signatures for the MLCT states. This will allow for ultrafast measurements to be unencumbered by extraneous, complicating photophysical processes and thus yield the most accurate MLCT lifetimes.

4.2 Proposed Future Complexes

There is a series of Fe(II) polypyridyls that was hinted at in the introduction of this chapter that have an incredibly high potential for a long-lived MLCT lifetime as caused by extended delocalization in the excited state. These are homoleptic complexes with a terpy-based ligand with a chain of conjugated linkers built off the 4'-position. The linkers include phenyl rings and vinylene moieties, as shown in Scheme 5.3. In the mid-2000s, a graduate student from this research group, A. L. Smeigh, studied a variety of complexes of this type that were prepared by the Schmehl group. Notably, the ligands that contained the highest number of linkers (i.e., the longest conjugated chains) had very long-lived excited state absorption features. It was never confirmed that this positive signal was caused by the MLCT. Upon excitation into the MLCT, electron delocalization into the conjugated chain is likely; the farther the electron travels down the chain, the more spread out the wavefunction and less probable the return of the electron to the metal center. These ligands, then, are very attractive options to study the hypothesis set forward at the beginning of this chapter. That is further bolstered by the promising results obtained by Smeigh on these Fe(II) complexes.

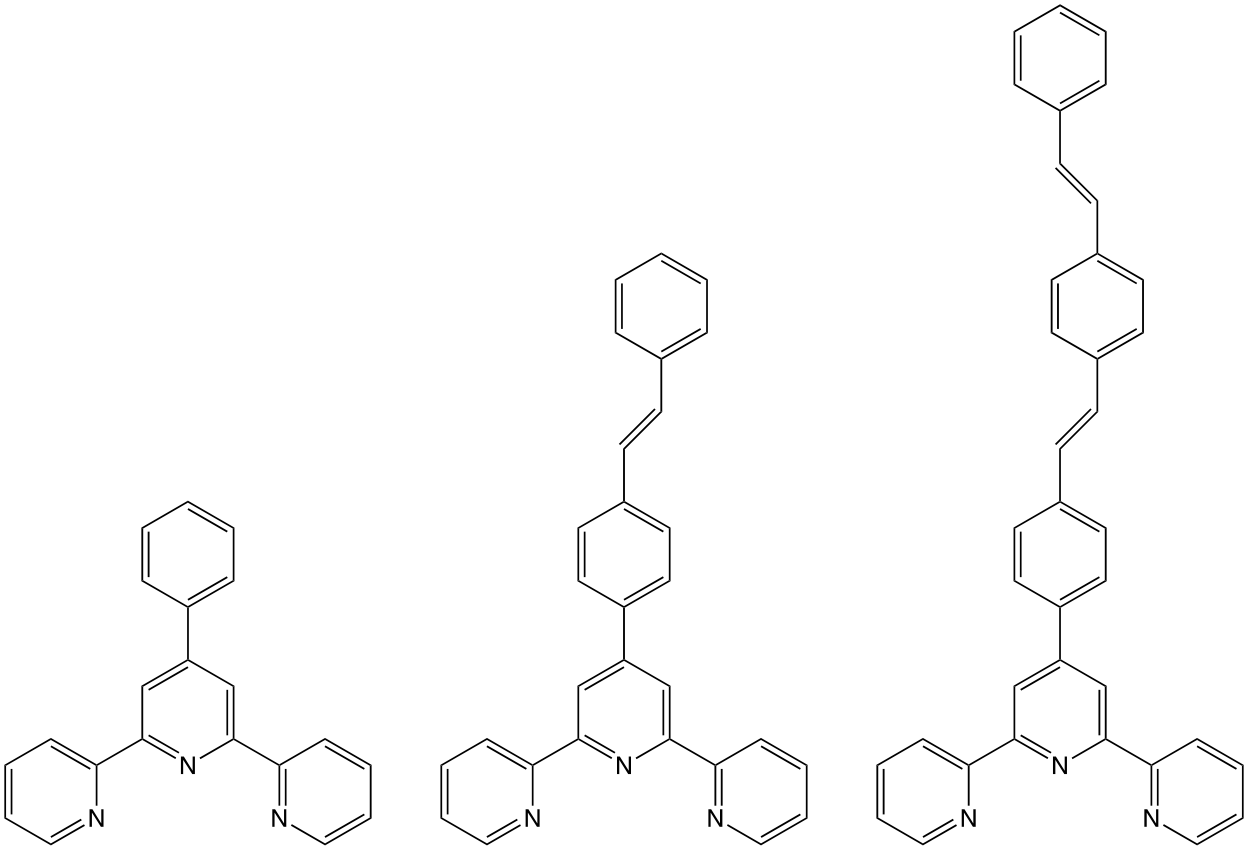

Scheme 5.3. Terpy (t)-based ligands with extended conjugation with phenyl (p) and vinyl (v) linkers. From left to right: tp, tpvp, and tpvpvp. These ligands and the naming scheme are based on those originally prepared by the R. Schmehl group.

What we propose here is a systematic study of the tp-type ligands as bound to Fe(II). The exact ligands proposed can be found in Scheme 5.3. This set of compounds would increase the chain length by one vinylene and one phenylene linkage at a time, allowing for a more thorough study of the distance dependence of MLCT lifetime. To determine whether it is in fact the conjugation that allows for an extended MLCT lifetime, or a secondary feature of these ligands, the compounds $[Fe(tpvp)_2]^{2+}$ and $[Fe(tpmp)_2]^{2+}$ should be studied, in which m stands for a methylene linker (Scheme 5.4). This would require a simple reduction of the vinylene moiety, but

that would essentially cut out communication between the two phenyl rings. If conjugation is the method by which the MLCT lifetime is lengthened, then $[Fe(tpmp)_2]^{2+}$ should behave more analogously to $[Fe(tp)_2]^{2+}$ than $[Fe(tpvp)_2]^{2+}$. For any and all of the complexes proposed here, full electrochemical and spectroelectrochemical analyses should be performed to know with certainty that the MLCT is the excited state being probed.

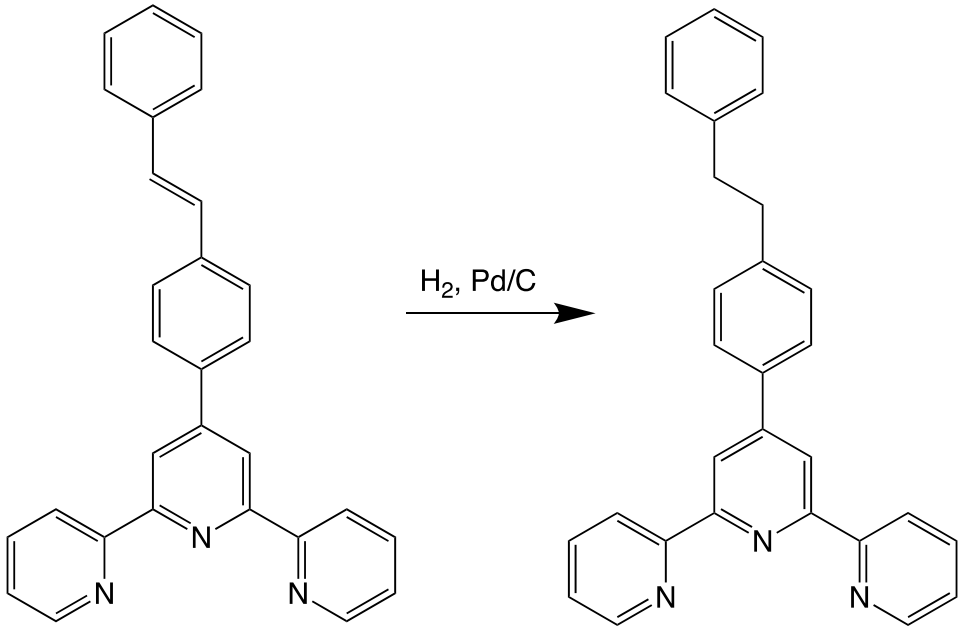

Scheme 5.4. Proposed hydrogenation reaction of the tpvp ligand into tpmp. The homoleptic iron(II) complexes of these ligands are expected to have very different MLCT lifetimes if conjugation in the excited state is the main determinant of the kinetics.

There are a few potential issues with the ligands outlined in Schemes 5.3 and 5.4. As was shown extensively in Chapter 4 of this work, phenyl rings rotate in solution;[30,36] alkenes, additionally, are known to undergo *cis-trans* isomerizations upon photoexcitation.[37,38] These processes will not only require energy (thereby reducing the driving force of the electron to

perform photochemistry), but they may also change the nature of the ligand such that the MLCT lifetime is shortened. One way this may occur is by the phenyl rotation that produces a substituent with a π system that is coplanar with the π system of the bipyridine, which may serve to drive the excited electron back to the metal center. A few proposed substituents to extend the MLCT lifetime but that may not have the inherent issues of the {tp...} ligands are shown in Scheme 5.5. The first is a pyrene extender, which has the benefits of delocalization across four fused aromatic rings as well as a large size that will require much greater reorganization energy to cant into a coplanar position to the bpy backbone. The second is very similar to tpvp, but replaces the vinylene linker with an acetylene group, thereby eliminating the *cis-trans* isomerization reorganization energy. The triple bond also serves to maintain rigidity in the extender such that the π system beyond the terpyridine is coplanar, increasing delocalization. With these two linkers, though, there is still the possibility of energy being used to reorient the substituent to be coplanar with the bipyridine. And because these are designed to be rigid, they will use a much greater amount of energy during the rotation. To avoid this altogether, inspiration is taken from the dmib ligand and appends methyl groups in the *ortho-* positions on the phenyl directly bound to terpy, thus sterically hindering coplanarity and reducing the inner-sphere reorganization energy.

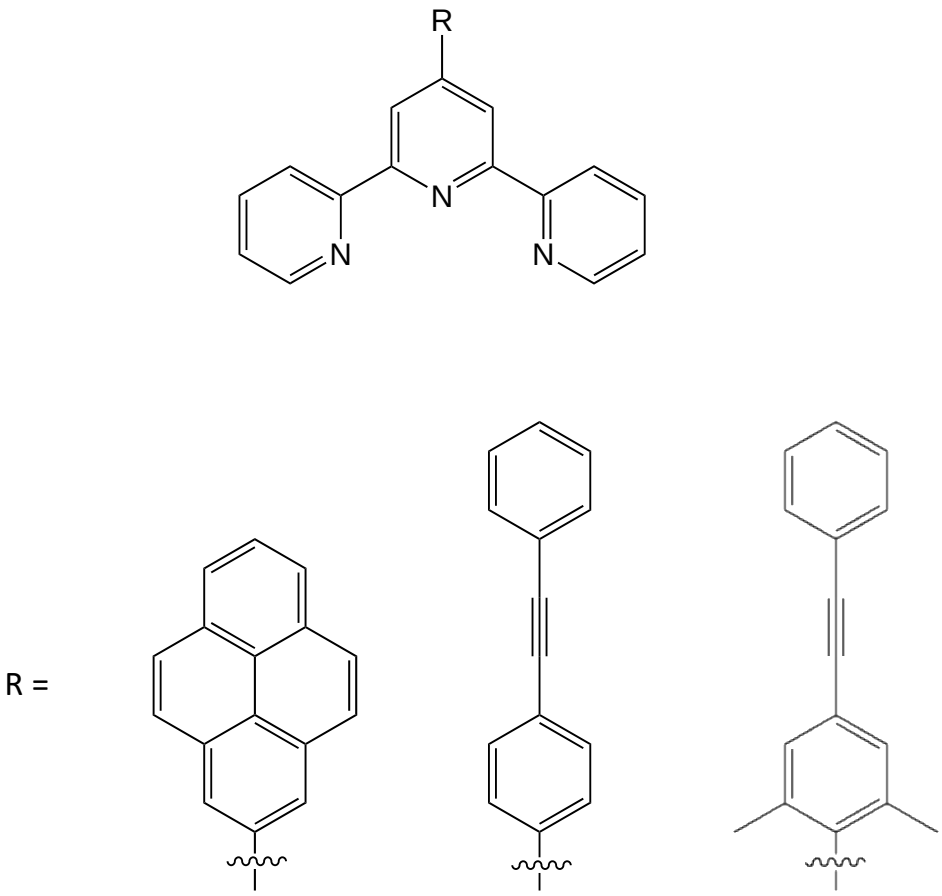

Scheme 5.5. A proposed series of extenders to be added to terpyridine in the 4'-position (top): pyrene (bottom left), phenyl-acetylene-phenyl (bottom middle), and 2,6-dimethylphenyl-acetylene-phenyl (bottom right).

One latent question that may come up when looking at these complexes is the concern that the extenders may drastically alter the ligand field strength of the complexes, thereby preemptively changing the energetics of the excited states and potentially increase electronic coupling that leads to a faster MLCT deactivation. The determination of ΔG^{o} between ligand field states is a concept that has come up repeatedly in this work, and efforts are ongoing to experimentally and/or theoretically derive that value in Fe(II) complexes. For the time being, though, approximations and guesswork must be made. An interesting observation was made when comparing the ground

state absorption spectra of $[Fe(terpy)_2]^{2+}$ and $[Fe(tpvpvp)_2]^{2+}$ (Fig. 5.20). In both complexes, two very small bumps appear to sit on top of larger features. In $[Fe(terpy)_2]^{2+}$, these are present at 36759 and 35706 cm^{-1} (272 and 280 nm, respectively). For the extended complex, these peaks are centered at 36506 and 35213 cm^{-1} (274 and 284 nm, respectively). As has been discussed previously, these may be underlying ligand field states that borrow intensity from the ligand-based π-π* transition that lies energetically very close. Considering the coordination environment around the Fe(II) center will not have changed considerably between $[Fe(terpy)_2]^{2+}$ and $[Fe(tpvpvp)_2]^{2+}$ and knowing that the phenyl ring is only slightly affecting the electron density on the N atoms in the terpyridine, it seems reasonable to believe that if these features are in fact ligand field transitions, then they must be the same ligand field transitions in both complexes. In the case of the higher energy transition, a red-shift of 253 cm^{-1} occurs when the extender is added. For the lower energy bands, the red-shift corresponds to a 493 cm^{-1} energetic stabilization. The exact transition occurring in these two bands is unknown but can be narrowed down based on the fact that the lower energy absorption changes at twice the rate of the higher energy feature. This limits the high and low energy transitions to either the $^3T_1 \leftarrow {}^1A_1$ and $^5T_2 \leftarrow {}^1A_1$, respectively, or to the $^1T_2 \leftarrow {}^1A_1$ and $^5E \leftarrow {}^1A_1$. The high energy of the transitions make the latter choice much more likely. Of course, neither of these terpy-based complexes is actually octahedral in symmetry, so the T and E term states cannot be supported and will split into A and B states. This exercise is simply to show that the application of group theory here may help in determining the Racah B and C parameters, which are largely unknown in Fe(II) polypyridyls.[39] Moreover, the energy of the transitions is affected by less than $3k_BT$, and the same general low-energy MLCT features are observed, implying that the ligand field strength was not so drastically affected by the addition of conjugated linkers.

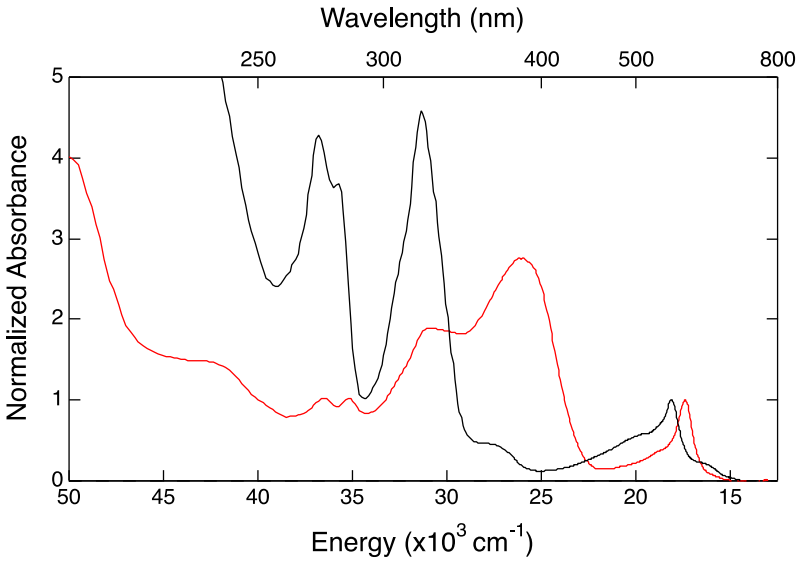

Figure 5.20. Overlay of the steady-state absorption spectra of $[Fe(terpy)_2]^{2+}$ (black) and $[Fe(tpvpvp)_2]^{2+}$ (red).

4.3 The Future of the Quest for Long-Lived MLCT Lifetime in Fe(II) Complexes

Charge-separated species are capable of being utilized in many important photovoltaic applications. These states are highly desirable in the fields of photoredox catalysis and solar energy conversion, to name two. The metal-to-ligand charge transfer excited states that dominate the photophysics in Ru(II) complexes are present in Fe(II) analogues but are quickly deactivated into lower-lying ligand field states. Not only are they energetically below the MLCT (therefore providing less driving force for the reaction of interest), but these states are also metal-centered, meaning the charge separation that was present in the MLCT is now gone. For photovoltaic applications, these ligand field excited states are essentially useless. From the outset of this work, three methods have been outlined that could extend the MLCT lifetime in Fe(II) complexes. As a graduate student, I have worked on research that addresses all three strategies. Below are the ways in which I have impacted this field, and the directions I see as the future of these endeavors.

4.3.1 Altering the Nuclear Coordinate

The development and implementation of the ultrafast variable-temperature transient absorption spectroscopy experiment is without doubt the most important work I have done in my time here. This setup has enabled us to measure barriers and estimate reorganization energies of large number of iron(II) complexes, for which these values were only ever estimated. This is a major contribution to the fundamental understanding of these chromophores. More importantly, the experiment is able to be used for any ultrafast process. It has been previously suggested that Cu(I) systems could be studied, in which they undergo massive reorganizations in the excited state.[40] Being able to broadly apply this work to the inorganic chemistry community at large is incredibly valuable and may help shape future complexes and/or experiments.

One potentially very exciting result that came from this work is the H_{ab}^4/λ ratio, which we currently believe to be indicative of the major relaxation pathway accessed by the molecule to undergo the transition being studied. Further work must be done to verify or reject this hypothesis, but at the very least, relative ratios of these Marcus parameters can instruct computational chemists in the determination of the nuclear modes relevant to the photophysical processes. This pertains to the ultimate question of which vibrational modes are facilitating the ultrafast MLCT deactivation. With this information in hand, one can imagine designing a ligand system to purposefully hinder or remove altogether the relaxation pathway. Analogous work has already been done in this group on $[Cr(acac)_3]$, in which sterically bulky ^{t}butyl groups were installed on the ligand backbone and served to slow down the intersystem crossing in this complex.[41,42] Additionally, studies on $[Fe(terpy)_2]^{2+}$ (prior to the ultrafast X-ray[43] or theoretical[44] work that were published more recently) sought to slow down the MLCT deactivation process by appending large substituents on the periphery of the ligand.[10] Ultrafast transient absorption results showed that these synthetic

modifications were not hindering the terpy-rocking mode, and therefore did not hinder this process. Moreover, in some cases, the MLCT lifetime was made even shorter relative to the parent complex.[34] While these data did not display the desired result, they clearly depict the power of substituents to affect the kinetics of the excited state processes. Current work is being done in which a ligand scaffolding was designed to impede the vibrational modes in the $^5T_2 \rightarrow {}^1A_1$ relaxation in an Fe(II) chromophore and shows promise in the goal of lengthening the MLCT lifetime.[45]

The key to this work will be the use of vibrational techniques, such as vibrational coherence and ultrafast infrared transient absorption spectroscopy, to more directly determine the modes involved in ground state recovery in these Fe(II) complexes. Simultaneous work with theoretical chemists may help in the identification of the importance of certain modes. It may also aid in the understanding of the coupling between excited electronic states, which will play a role in the photophysics of the chromophores. Ashley and Jakubikova have recently published results on what they have found to be important nuclear modes in the relaxation of $[Fe(bpy)_3]^{2+}$.[46] With these data, synthetic chemists will be better armed to intelligently design ligands that slow down the deactivation of the MLCT state or stop it entirely.

4.3.2 Inverting the MLCT and LF Manifolds

Perhaps the most obvious strategy towards increasing the MLCT lifetime is through the increase of ligand field strength of the complex, such that the ligand field manifold now lies energetically above the MLCT manifold. This excited state ordering is analogous to what is observed for most Ru(II) compounds. The way in which this might be achieved is open to debate. Work in our group has largely focused on the increased octahedral symmetry of the complex, thereby improving metal-ligand orbital overlap. A higher symmetry molecule is better able to

support E and T states that are higher in energy than their split counterparts. $[Fe(dcpp)_2]^{2+}$ has been prepared and studied to that end, including in Chapter 4 of this work.[47,48] Complexes with a similar ligand scaffolding but with modified extenders are in the process of being synthesized so as to better understand whether this phenomenon is more broadly applicable. Early results indicate that this method is not viable, though (Appendix A). The dcpp ligand was modified such that the carbonyl was replaced with a vinyl group, resulting in $[Fe(dvpp)_2]^{2+}$. Though the two complexes are nearly identical, the ground state recovery of $[Fe(dvpp)_2]^{2+}$ is greatly elongated to ~1 ns, more in line with $[Fe(bpy)_3]^{2+}$. True, this says nothing about the MLCT lifetime, which should be measured for this complex. But the variable-temperature data imply that $[Fe(dvpp)_2]^{2+}$ is more similar to $[Fe(bpy)_3]^{2+}$ than it is to $[Fe(dcpp)_2]^{2+}$, implying that the higher symmetry around the metal center is not the only requirement to increasing the ligand field strength.

Another method that is currently being hotly pursued by other research groups in this field is through the use of *N*-heterocyclic carbenes and other ligands with C-donor atoms.[49-52] The simple switch from nitrogen to the strong σ-donor carbon as the atom on the ligand bonding to iron will greatly increase the ligand field strength, much more than any simple substituent on a pyridine-based ligand as calculations show.[53] This work is showing tremendous results, with MLCT lifetimes on the order of 100s of picoseconds.[51] One complex with a 16 ps lifetime has even been used in a DSSC device[49,52] and shown improved efficiency relative to the Ferrere cell, the first improvement on this device reported since Ferrere and Gregg first published their findings.[54] The single greatest downside to this work is that synthetic modifications to the ligand to fine-tune the energetic or kinetic properties of the complex are nearly impossible. Still, as a general strategy, switching away from pyridine groups may serve to open up an entirely new and promising realm of Fe(II) chromophores.

4.3.3 Increasing Charge-Separated Distance via Delocalization

The strategy of MLCT lifetime lengthening by extended delocalization in the excited state only developed very recently in our group. Limited work has been done in this realm, but the rationale has been examined and we believe it to be promising. The synthesis of $[Fe(dpb)_3]^{2+}$ to begin to understand the effects of increased delocalization on the MLCT lifetime was a positive first step. The extended conjugation of the ligand allowed for a more delocalized wavefunction in the excited state, removing the electron physically farther from the metal center than in the traditional $[Fe(bpy)_3]^{2+}$. The proposition is that the greater the distance of the charge-separated state, the less memory of the ground state the electron will have, thereby decreasing the rate of MLCT deactivation. This was observed in $[Fe(dpb)_3]^{2+}$, as well as in two complexes with ligands that had increased conjugation around the metal center relative to either bpy or terpy. Both of these Fe(II) compounds exhibited a longer-lived MLCT state. Even more promising was the isoxazole-substituted complex, which displayed an extremely (~900 fs) long-lived MLCT. From these data, it was also observed that the use of an aromatic system to increase conjugation performs better than a chain linker (such as a vinylene) when attempting to decrease the rate of deactivation. This was evident from the data collected on the 4,4'-dicyanoacrylic acid-substituted iron(II) complex.

A series of complexes have been proposed to increase the delocalization even farther from the iron center, using a chain of phenyl and vinylene linkers. Data collected by a past group member shows a multi-hundreds of picosecond lifetime for a positive feature in compounds of that type.[55] The key to MLCT identification will be spectroelectrochemistry, and possibly Zn(II) analogues to eliminate any LMCT or ILCT (interligand charge transfer) features. Of the three avenues being pursued, this route currently appears to have the most promise.

That being said, it should be evident that no single strategy will be the silver bullet to

increasing the MLCT lifetime. Each and every piece of information that is known about these chromophores must be put to use to build high efficiency iron dyes for photovoltaic applications. In fact, a combination of the methods may yield the best photosensitizers. An "ideal" iron system is proposed in Scheme 5.6. This complex uses information garnered from many experiments on these Fe(II) compounds. First, an *N*-heterocyclic carbene ligand scaffolding is used to drive the ligand field strength up. The ligand is tridentate to increase conjugation around the metal center. To further increase that delocalization, a phenyl-acetylene-phenyl linker is attached at the *para*-position of the central pyridine ring. Taking inspiration from the work on hindering vibrational modes, methyl groups are substituted in the *ortho*-positions of the phenyl directly bound to the pyridine moiety. The goal is to direct the excited electron to delocalize down the chain of linkers, so a cyano group is placed in the *para*-position of the furthest phenyl group, acting to draw electron density down the π system away from the metal center. Furthermore, a homoleptic complex would pull the electron density evenly across both ligands, which would be counterproductive to the goal. Thus, a heteroleptic system must be devised in which the alternate ligand is incredibly electron donating. While this complex is clearly a synthetic nightmare, and may not even ultimately perform very well, it draws inspiration from all the work being performed on Fe(II) systems, and even work not on Fe(II) systems. Only in this way can we move the bar forward toward making Fe(II) have long-lived charge-separated excited states.

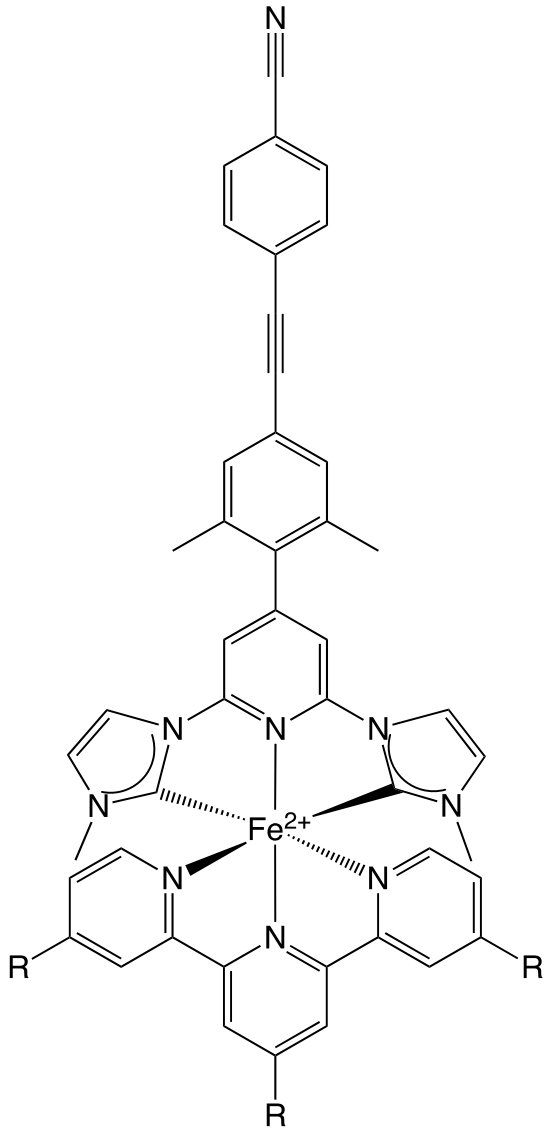

Scheme 5.6. Proposed Fe(II) complex that incorporates all of the strategies used in this work to lengthen the MLCT lifetime. R substituents here refer to electron-donating groups, such as methyl, methoxy, amine, or dimethylamine moieties.

4.4 Fe(II) and Ru(II) Complexes as Analogues

One of the major themes of this research project in general is the idea that methodologies can be developed on the photophysically more simple Ru(II) complexes, and then used to study

the true molecules of interest, the Fe(II) analogues. In $[Ru(dpb)_3]^{2+}$ and $[Fe(dpb)_3]^{2+}$, we have a perfect case study of how this technique works. The energetics of the excited states in $[Ru(dpb)_3]^{2+}$ were relatively straightforward to determine and assign with the use of electrochemistry and emission spectroscopy.[25,56] The role of delocalization in the excited state was expanded on through the use of stimulated Raman scattering and ultrafast transient absorption spectroscopy.[25,30,36] Once the more fundamental characteristics of the chromophore were understood, more nuanced studies of the influence of solvent and excitation wavelength could be used to give insight into solvation dynamics and conical intersections (Chapter 4).[36] In moving to iron, though, there were more differences between the two complexes than was originally presumed. It is likely that the smaller ionic radius of the low-spin iron(II) center in conjunction with the bulky, slightly electron-withdrawing phenyl substituents on the ligand caused complex dissociation to be a favorable mechanism when in solution or in the presence of anions or solvents capable of coordinating. This led to purity issues that were not observed for the Ru(II) complex. Additionally, no excited state absorption was observed in the ultrafast transient absorption spectroscopy that was performed on $[Fe(dpb)_3]^{2+}$. In $[Ru(dpb)_3]^{2+}$, this broad positive feature red of ~510 nm is assigned to ligand-based π^*-π^* on the ^{3}MLCT surface, convolved with a ligand-to-metal charge transfer (LMCT) feature further to the red. The 532 nm probe wavelength was chosen for its ability to measure ligand-based dynamics in the long-lived (μs) ^{3}MLCT excited state. In the $[Fe(dpb)_3]^{2+}$ analogue, though, it was expected that switch from a second- to a first-row transition metal would drastically decrease the ligand field strength, thus reducing the ligand field manifold energy to such that those states were energetically below the MLCT manifold. As with the other Fe(II) polypyridyls, this decreased the MLCT lifetime drastically, in this case to 160 ± 20 fs. Upon population of the lowest-energy excited state, the $^5T_2$, no vibrational cooling was observed at the pump-probe combination

used. Exciting with a greater amount of energy will increase the driving force for excess energy to be dispersed via vibrational mechanisms. This may allow for vibrational cooling to be observed in the ground state bleach of $[Fe(dpb)_3]^{2+}$.

The side-by-side comparison of Fe(II) and Ru(II) analogues does not appear to be appropriate, not just from this study but from other results. The inherent differences in the two types of complexes allow for different techniques to be used to study one relative to the other. For example, Ru(II) chromophores are often analyzed by various emission spectroscopies. This would be an incredibly useful experiment to help determine the energetics of excited states in Fe(II) compounds, but due to the excited state structure, they do not emit. Even something as simple as electrochemistry performed on a Ru(II) dye can give information on the excited states, clearly not the case with Fe(II) complexes. Instead of comparing the photophysics of polypyridyl complexes of two metals with nothing more in common than a valence electron count, it would be more useful to begin considering alternative experiments to study the Fe(II) complexes, at least until they truly do begin to photophysically resemble their Ru(II) congeners. In many cases, theoretical work will be the first and best choice to understand the excited state dynamics. But experimental techniques that have not yet been explored on Fe(II) compounds should be considered. These methods might include 2D spectroscopy, to understand the coupling of the excited states; ultrafast vibrational spectroscopies, to more directly probe vibrational modes and solute-solvent interactions; simultaneous ultrafast X-ray absorption and emission spectroscopies have already proven incredibly powerful on a small number of Fe(II) complexes; and thermodynamic measurements to truly begin to understand the ΔG^{o} of these complexes.

The latter point may be the most crucial piece of information needed for non-spin-crossover Fe(II) compounds. Without it, only approximations can be made, possibly leaving open more

questions than answers. In the work done throughout this dissertation, it became more and more apparent that fundamental questions with respect to Fe(II) photophysics were still largely unknown. To that end, an old inorganic chemistry trick has been to use large series of complexes to compare to each other and determine the effects of the changes made. That tactic is being used currently to address questions of ligand field strength, electron-donating and -withdrawing ability of substituents, and other various aspects of Fe(II) chromophores that have largely been taken for granted until now. With these data, a more complete understanding of the thermodynamic and kinetic factors that affect these iron-based complexes can be harnessed and used to design molecules with long-lived MLCT states, such that a more earth-abundant material can be used in photovoltaic applications. While this will improve the viability of photoredox catalysis and other applications, it is much more important on a global level that solar energy conversion become more cost-effective but also more environmentally efficient. While high-performing iron photovoltaic devices are not what will ultimately save this planet, they are a step in the right direction, and may go a long way in improving the sustainability of electricity generation for an ever-expanding global population.

REFERENCES

REFERENCES

1. Reynal, A.; Willkomm, J.; Muresan, N. M.; Lakadamyali, F.; Planells, M.; Reisner, E.; Durrant, J. R. Distance Dependent Charge Separation and Recombination in Semiconductor/Molecular Catalyst Systems for Water Splitting. *Chem. Commun.* **2014**, *50*, 12768-12771; DOI: 10.1039/c4cc05143b.

2. Feier, H. M.; Reid, O. G.; Pace, N. A.; Park, J.; Bergkamp, J. J.; Sellinger, A.; Gust, D.; Rumbles, G. Local Intermolecular Order Controls Photoinduced Charge Separation at Donor/Acceptor Interfaces in Organic Semiconductors. *Adv. Energy Mater.* **2016**, *6*, 1502176; DOI: 10.1002/aenm.201502176.

3. Hartnett, P. E.; Mauck, C. M.; Harris, M. A.; Young, R. M.; Wu, Y.-L.; Marks, T. J.; Wasielewski, M. R. Influence of Anion Delocalization on Electron Transfer in a Covalent Porphyrin Donor-Perylenediimide Dimer Acceptor System. *J. Am. Chem. Soc.* **2017**, *139*, 749-756; 10.1021/jacs.6b10140.

4. Gu, J.; Yan, Y.; Helbig, B. J.; Huang, Z.; Lian, T.; Schmehl, R. H. The Influence of Ligand Localized Excited States on the Photophysics of Second Row and Third Row Transition Metal Terpyridyl Complexes: Recent Examples and a Case Study. *Coord. Chem. Rev.* **2015**, *282-283*, 100-109; DOI: 10.1016/j.ccr.2014.06.028.

5. Wang, X.-Y.; Del Guerzo, A.; Schmehl, R. H. Photophysical Behavior of Transition Metal Complexes Having Interacting Ligand Localized and Metal-to-Ligand Charge Transfer States. *J. Photochem. Photobiol. C Photochem. Rev.* **2004**, *5*, 55-77; DOI: 10.1016/j.jphotochemrev.2004.01.002.

6. Baitalik, S.; Wang, X.-Y.; Schmehl, R. H. A Trimetallic Mixed Ru(II)/Fe(II) Terpyridyl Complex with a Long-Lived Excited State in Solution at Room Temperature. *J. Am. Chem. Soc.* **2004**, *126*, 16304-16305; 10.1021/ja044561s.

7. Wang, X.-Y.; Del Guerzo, A.; Tunuguntla, H.; Schmehl, R. H. Photophysical Behavior of Ru(II) and Os(II) Terpyridyl Phenylene Vinylene Complexes: Perturbation of MLCT State by Intra-Ligand Charge-Transfer State. *Res. Chem. Intermed.* **2007**, *33*, 63-77; DOI: 10.1163/156856707779160834.

8. Wang, X.-Y.; Del Guerzo, A.; Schmehl, R. H. Preferential Solvation of an ILCT Excited State in Bis(terpyridine-phenylene-vinylene) Zn(II) Complexes. *Chem. Commun.* **2002**, 2344-2345; DOI: 10.1039/b205042k.

9. Sun, Q.; Mosquera-Vazquez, S.; Suffren, Y.; Hankache, J.; Amstutz, N.; Lawson Daku, L. M.; Vauthey, E.; Hauser, A. On the Role of Ligand-Field States for the Photophysical Properties of Ruthenium(II) Polypyridyl Complexes. *Coord. Chem. Rev.* **2015**, *282-283*, 87-99; DOI: 10.1016/j.ccr.2014.07.004.

10. Jamula, L. L. Design and Synthesis of Iron(II) Terpyridyl Complexes for Application in Dye-Sensitized Solar Cells. Master's Thesis, Michigan State University, East Lansing, MI, 2010.

11. Robo, M. T.; Prinsell, M. R.; Weix, D. J. 4,4',4"-Trimethyl-2,2':6',2"-terpyridine by Oxidative Coupling of 4-Picoline. *J. Org. Chem.* **2014**, *79*, 10624-10628; DOI: 10.1021/jo501925s.

12. Pearson, P.; Bond, A. M.; Deacon, G. B.; Forsyth, C.; Spiccia, L. Synthesis and Characterisation of Bis(2,2'-bipyridine)(4-carboxy-4'-(pyrid-2-ylmethylamido)-2,2'-bipyridine)ruthenium(II) di(hexafluorophosphate): Comparison of Spectroelectrochemical Properties with Related Complexes. *Inorg Chim Acta*, **2008**, *361*, 601-612; DOI: 10.1016/j.ica.2007.03.031.

13. Rao, J. M.; Hughes, M. C.; Macero, D. J. Further Studies on the Stabilization of High and Low Oxidation States in Aromatic Imine Ligand Complexes of First Row Transition Metals. I. Substituted Bipyridine Complexes of Cobalt and Iron. *Inorg. Chim. Acta* **1979**, *35*, L369-L373; DOI: 10.1016/S0020-1693(00)93402-9.

14. Leidner, C. R.; Murray, R. W. Electron-Transfer Reactions of Iron, Ruthenium, and Osmium Bipyridine and Phenanthroline Complexes at Polymer/Solution Interfaces. *J. Am. Chem. Soc.* **1984**, *106*, 1606-1614; DOI: 10.1021/ja00318a010.

15. Braga, T. G.; Wahl, A. C. Rates of Electron Transfer from Osmium(II) to Iron(III) Complex Ions Containing 2,2'-Bipyridine or Its Derivatives as Ligands. Effects of Electrolytes at Low Concentrations and Reactant-Separation Distance. *J. Phys. Chem.* **1985**, *89*, 5822-5828; DOI: 10.1021/j100272a049.

16. Donohoe, R. J.; Tait, C. D.; DeArmond, M. K.; Wertz, D. W. Spectroscopic Study of the Parent and Reduction Products of Some Substituted Bipyridine Complexes of Iron(II) and Osmium(II). 2. Substitution at the 4,4' Positions. *J. Phys. Chem.* **1986**, *90*, 3927-3930; DOI: 10.1021/j100408a020.

17. Taylor, P. J.; Schilt, A. A. Synthesis, Isolation and Characterization of Some Iron(II) Complexes with Mixed α,α'-Diimine Ligands. *Inorg. Chim. Acta* **1971**, *5*, 691-697; DOI: 10.1016/S0020-1693(00)96011-0.

18. Josceanu, A. M.; Moore, P. Comparison of the Rates and Mechanisms of Formation and Solvolysis of $[Fe(bipy)_3]^{2+}$ (bipy = 2,2'-bipyridine) and $[FeL]^{2+}$ [L = 1,4,7-tris(2,2'-bipyridyl-5-ylmethyl)-1,4,7-triazacyclononane] and Their Stabilities in Dimethylformamide Solution. *J. Chem. Soc., Dalton Trans.* **1998**, 369-374; DOI: 10.1039/a705824a.

19. Ferrere, S. New Photosensitizers Based Upon $[Fe(L)_2(CN)_2]$ and $[Fe(L)_3]$ (L = Substituted 2,2'-Bipyridine): Yields for the Photosensitization of TiO_2 and Effects on the Band Selectivity. *Chem. Mater.* **2000**, *12*, 1083-1089; DOI: 10.1021.cm990713k.

20. Bergman, S. D.; Frantz, R.; Gut, D.; Kol, M.; Lacour, J. Effective Chiral Recognition Among Ions in Polar Media. *Chem. Commum.* **2006**, 850-852; DOI: 10.1039/b516255f.

21. WebElements, https://www.webelements.com, (accessed December 2017).

22. Dick, S. Crystal Structure of Tris(2,2'-bipyridine)iron(II) Bis(hexafluorophosphate), $(C_{10}H_8N_2)_3Fe(PF_6)_2$. *Z. Kristallogr. - New Cryst. Struct.* **1998**, *213*, 356; DOI: 10.1524/ncrs.1998.213.14.355.

23. England, J.; Scarborough, C. C.; Weyhermüller, T.; Sproules, S.; Wieghardt, K. Electronic Structures of the Electron Transfer Series $[M(bpy)_3]^n$, $[M(tpy)_2]^n$, and $[Fe(^tbpy)_3]^n$ (M = Fe, Ru; *n* = 3+, 2+, 1+, 0, 1-): A Mössbauer Spectroscopic and DFT Study. *Eur. J. Inorg. Chem.* **2012**, 4605-4621; DOI: 10.1002/ejic.201200232.

24. Carey, M. C.; Adelman, S. L.; McCusker, J. K. Insights Into the Excited State Dynamics of Fe(II) Polypyridyl Complexes from Variable-Temperature Ultrafast Spectroscopy. *Submitted.*

25. Damrauer, N. H.; Boussie, T. R.; Devenney, M.; McCusker, J. K. Effects of Intraligand Electron Delocalization, Steric Tuning, and Excited-State Vibronic Coupling on the Photophysics of Aryl-Substituted Bipyridyl Complexes of Ru(II). *J. Am. Chem. Soc.* **1997**, *119*, 8253-8268; DOI: 10.1021/ja971321m.

26. Brown, A. M.; McCusker, C. E.; McCusker, J. K. Spectroelectrochemical Identification of Charge-Transfer Excited States in Transition Metal-Based Polypyridyl Complexes. *J. Chem. Soc., Dalton Trans.* **2014**, *43*, 17635-17646; DOI: 10.1039/c4dt02849j.

27. Zhang, W.; Alonso-Mori, R.; Bergmann, U.; Bressler, Ch.; Chollet, M.; Galler, A.; Gawelda, W.; Hadt, R. G.; Hartsock, R. W.; Kroll, T.; Kjær, K. S.; Kubiček, K.; Lemke, H. T.; Liang, H. W.; Meyer, D. A.; Nielsen, M. M.; Purser, C.; Robinson, J. S.; Solomon, E. I.; Sun, Z.; Sokaras, D.; van Driel, T. B.; Vankó, G.; Weng, T.-C.; Zhu, D.; Gaffney, K. J. Tracking Excited-State Charge and Spin Dynamics in Iron Coordination Complexes. *Nature* **2014**, *509*, 345-348; DOI: 10.1038/nature13252.

28. Cannizzo, A.; Milne, C. J.; Consani, C.; Gawelda, W.; Bressler, Ch.; van Mourik, F.; Chergui, M. Light-Induced Spin Crossover in Fe(II)-Based Complexes: The Full Photocycle Unraveled by Ultrafast Optical and X-ray Spectroscopies. *Coord. Chem. Rev.* **2010**, *254*, 2677-2686; DOI: 10.106/j.ccr.2009.12.007.

29. Shaw, G. B.; Styers-Barnett, D. J.; Gannon, E. Z.; Granger, J. C.; Papanikolas, J. M. Interligand Electron Transfer Dynamics in $[Os(bpy)_3]^{2+}$: Exploring the Excited State Potential Surfaces with Femtosecond Spectroscopy. *J. Phys. Chem. A* **2004**, *108*, 4998-5006; DOI: 10.1021/jp0363850.

30. Damrauer, N. H.; McCusker, J. K. Ultrafast Dynamics in the Metal-to-Ligand Charge Transfer Excited-State Evolution of $[Ru(4,4'\text{-diphenyl-}2,2'\text{-bipyridine})_3]^{2+}$. *J. Phys. Chem. A* **1999**, *103*, 8440-8446; DOI: 10.1021/jp9927754.

31. Monat, J. E.; McCusker, J. K. Femtosecond Excited-State Dynamics of an Iron(II) Polypyridyl Solar Cell Sensitizer Model. *J. Am. Chem. Soc.* **2000**, *122*, 4092-4097; 10.1021/acs.jpca.7b12522.

32. Consani, C.; Prémont-Schwarz, M.; ElNahhas, A.; Bressler, Ch.; van Mourik, F.; Cannizzo, A.; Chergui, M. Vibrational Coherences and Relaxation in the High-Spin State of Aqueous $[Fe^{II}(bpy)_3]^{2+}$. *Angew. Chem. Int. Ed.* **2009**, *48*, 7184-7187; DOI: 10.1002/anie.200902728.

33. Khalil, M.; Marcus, M. A.; Smeigh, A. L.; McCusker, J. K.; Chong H. H. W.; Schoenlein, R. W. Picosecond X-ray Absorption Spectroscopy of a Photoinduced Iron(II) Spin Crossover Reaction in Solution. *J. Phys. Chem. A* **2006**, *110*, 38-44; DOI: 10.1021/jp055002q.

34. Brown, A. M. Excited-State Dynamics of Iron(II)-Based Charge-Transfer Chromophores. Ph.D. Thesis, Michigan State University, East Lansing, MI, 2011.

35. Adelman, S. L. Unpublished results.

36. Carey, M. C.; Li, S.; Damrauer, N. H.; McCusker, J. K. Excitation Energy-Induced Dual Solvation Mechanism in Ru(II) Polypyridyl Revealed by Ultrafast Spectroscopy. *Manuscript in preparation.*

37. Nibbering, E. T. J.; Fidder, H.; Pines, E. Ultrafast Chemistry: Using Time-Resolved Vibrational Spectroscopy for Interrogation of Structural Dynamics. *Annu. Rev. Phys. Chem.* **2005**, *56*, 337-367; DOI: 10.1146/annurev.physchem.56.092503.141314.

38. Yutaka, T.; Mori, I.; Kurihara, M.; Mizutani, J.; Kubo, K.; Furusho, S.; Matsumura, K.; Tamai, N.; Nishihara, H. Synthesis, Characterization, and Photochemical Properties of Azobenzene-Conjugated Ru(II) and Rh(III) Bis(Terpyridine) Complexes. *Inorg. Chem.* **2001**, *40*, 4986-4995; DOI: 10.1021/ic010351u.

39. Hahn, A. W.; van Kuiken, B. E.; al Samarai, M.; Atanasov, M.; Weyhermüller, T.; Cui Y.-T.; Miyawaki, J.; Harada, Y.; Nicolaou, A.; DeBeer, S. Measurement of the Ligand Field Spectra of Ferrous and Ferric Iron Chlorides Using 2p3d RIXS. *Inorg. Chem.* **2017**, *56*, 8203-8211; Bolvin, H. d→d Spectrum and High-Spin/Low-Spin Competition in d^6 Octahedral Coordination Compounds: ab Initio Study of Potential Energy Curves. *J. Phys. Chem. A* **1998**, *102*, 7525-7534; DOI: 10.1021/jp982759r.

40. Chen, L. X.; Shaw, G. B.; Novozhilova, I.; Liu, T.; Jennings, G.; Attenkofer, K.; Meyer, G. J.; Coppens, P. MLCT State Structure and Dynamics of a Copper(I) Diimine Complex Characterized by Pump-Probe X-ray and Laser Spectroscopies and DFT Calculations. *J. Am. Chem. Soc.* **2003**, *125*, 7022-7034; DOI: 10.1021/ja0294663.

41. Schrauben, J. N.; Dillman, K. L.; Beck, W. F.; McCusker, J. K. Vibrational Coherence in the Excited State Dynamics of $Cr(acac)_3$: Probing the Reaction Coordinate for Ultrafast Intersystem Crossing. *Chem. Sci.* **2010**, *1*, 405-410; DOI: 10.1039/c0sc00262c.

42. Paulus, B. C.; Foszcz, E. D.; Proshlyakov, D. A.; McCusker, J. K. Probing Excited State Deactivation Mechanisms of Transition Metal Complexes Through Observation of Vibrational Coherence. *Manuscript in preparation.*

43. Vankó, G.; Bordage, A.; Pápai, M.; Haldrup, K.; Glatzel, P.; March, A. M.; Doumy, G.; Britz, A.; Galler, A.; Assefa, T.; Cabaret, D.; Juhin, A.; van Driel, T. B.; Kjær, K. S.; Dohn,

A.; Møller, K. B.; Lemke, H. T.; Gallo, E.; Rovezzi, M.; Németh, Z.; Rozsályi, E.; Rozgonyi, T.; Uhlig, J.; Sundström, V.; Nielsen, M. M.; Young, L.; Southworth, S. H.; Bressler, Ch.; Gawełda, W. Detailed Characterization of a Nanosecond-Lived Excited State: X-ray and Theoretical Investigation of the Quintet State in Photoexcited $[Fe(terpy)_2]^{2+}$. *J. Phys. Chem. C* **2015**, *119*, 5888-5902; DOI: 10.1021/acs.jpcc.5b00557.

44. Nance, J.; Bowman, D. N.; Mukherjee, S.; Kelley, C. T.; Jakubikova, E. Insights into the Spin-State Transitions in $[Fe(tpy)_2]^{2+}$: Importance of the Terpyridine Rocking Motion. *Inorg. Chem.* **2015**, *54*, 11259-11268; DOI: 10.1021/acs.inorgchem.5b01747.

45. Adelman, S. L.; Paulus, B. C.; Jakubikova, E.; McCusker, J. K. Disrupting the Nuclear Coordinate in a Low-Spin Iron(II) Polypyridyl Complex to Extend its MLCT Excited-State Lifetime. *Manuscript in preparation.*

46. Ashley D. C.; Jakubikova, E. Ray-Dutt and Bailar Twists in Fe(II)-tris(2,2'-bipyridine): Spin States, Sterics, and Fe−N Bond Strengths. *Inorg. Chem.* **2018**, *57*, 5585-5596; DOI: 10.1021/acs.inorgchem.8b00560.

47. Jamula, L. L.; Brown, A. M.; Guo, D.; McCusker, J. K. Synthesis and Characterization of a High-Symmetry Ferrous Polypyridyl Complex: Approaching the $^5T_2/^3T_1$ Crossing Point for Fe^{II}. *Inorg. Chem.* **2014**, *53*, 15-17; DOI: 10.1021/ic402407k.

48. Carey, M. C.; McCusker, J. K. Tuning the Barrierless Nature of an Octahedral Fe(II) Complex Using Spin-Crossover-Inspired Strategies. *Manuscript in preparation.*

49. Duchanois, T.; Etienne, T.; Cebrián, C.; Liu, L.; Monari, A.; Beley, M.; Assfeld, X.; Haacke, S.; Gros, P. C. An Iron-Based Photosensitizer with Extended Excited-State Lifetime Photophysical and Photovoltaic Properties. *Eur. J. Inorg. Chem.* **2015**, 2469-2477; DOI: 10.1002/ejic.201500142.

50. Harlang, T. C.; Liu, Y.; Gordivska, O.; Fredin, L. A.; Ponseca, C. S., Jr.; Huang, P.; Chábera, P.; Kjær, K. S.; Mateos, H.; Uhlig, J.; Lomoth, R.; Wallenberg, R.; Styring, S.; Persson, P.; Sundström, V.; Wärnmark, K. Iron Sensitizer Converts Light to Electrons with 92% Yield. *Nat. Chem.* **2015**, *7*, 883-889; DOI: 10.1038/nchem.2365.

51. Chabera, P.; Kjær, K. S.; Prakash, O.; Honarfar, A.; Liu, Y.; Fredin, L. A.; Harlang, T. B.; Lidin, S.; Uhlig, J.; Sundström, V.; Lomoth, R.; Persson, P.; Wärnmark, K. A Fe Hexa *N*-Heterocyclic Carbene Complex with a 528 ps Metal-to-Ligand Charge-Transfer Excited-State Lifetime. *J. Phys. Chem. Lett.* **2018**, *9*, 459-463; DOI: 10.1021/acs.jpclett.7b02962.

52. Liu, Y.; Harlang, T.; Canton, S. E.; Chábera, P.; Suárez-Alcántara, K.; Fleckhaus, A.; Vithanage, D. A.; Göransson, E.; Corani, A.; Lomoth, R.; Sundström, V.; Wärnmark, K. Towards Longer-Lived Metal-To-Ligand Charge Transfer States of Iron(II) Complexes: An *N*-Heterocyclic Carbene Approach. *Chem. Commun.* **2013**, *49*, 6412-6414; DOI: 10.1039/c3cc43833c.

53. Mukherjee, S.; Torres, D. E.; Jakubikova, E. HOMO Inversion as a Strategy for Improving the Light-Absorption Properties of Fe(II) Chromophores. *Chem. Sci.* **2017**, *8*, 8115-8126; DOI: 10.1039/c7sc02926h.

54. Ferrere, S.; Gregg, B. A. Photosensitization of TiO_2 by Band Selective Injection from Ultra-Short-Lived Excited States. *J. Am. Chem. Soc.* **1998**, *120*, 843-844; DOI: 10.1021/ja973504e.

55. Smeigh, A. L. Unpublished results.

56. Damrauer, N. H.; McCusker, J. K. Variable-Temperature Emission Studies of Solvation Dynamics: Evidence for Coupling of Solvation to Chromophore Structural Dynamics in the Evolution of Charge-Transfer Excited States. *Inorg. Chem.* **1999**, *38*, 4268-4277; DOI: 10.1021/ic990703l.

APPENDICES

APPENDIX A. ADDITIONAL VARIABLE-TEMPERATURE RESULTS

1. $[Fe(bpy)_3]Cl_2$

Initially, the question of outer-sphere reorganization energy in Fe(II) complexes was going to be studied in $[Fe(bpy)_3]^{2+}$ (bpy = 2,2'-bipyridine) as it is the prototypical Fe(II) compound. It was soon determined that the magnitude of change in reorganization energy as imposed by the solvent and counteranion was much smaller than the activation energy in the $[Fe(bpy')_3]^{2+}$ family of complexes. This in part led to the use of the $[Fe(dcpp)_2]^{2+}$ (dcpp = 2,6-bis(2-carboxypyridyl)pyridine) and its barrierless kinetics to study outer-sphere components. The work presented in this section is the initial results of the study of solvent and counteranion and their effects on the ground state recovery process in $[Fe(bpy)_3]^{2+}$. The results of the solvent series of the Cl^- salt will be analyzed on their own, and then compared to the results of $[Fe(bpy)_3](PF_6)_2$ in acetonitrile.

1.1 Four Different Solvents

1.1.1 Acetonitrile

Variable-temperature transient absorption (VT-TA) spectroscopy was performed to study the ground state recovery dynamics of $[Fe(bpy)_3]Cl_2$ in acetonitrile (MeCN) as outlined in Chapter 2. The results of these experiments are shown in Figs. A.1 and A.2. When excited at 490 nm and probed at 530 nm, the room temperature lifetime is 1.03 ± 0.01 ns, as has been previously observed for other $[Fe(bpy)_3]^{2+}$ salts in MeCN.[1,2] For everything reported herein, room temperature is approximately 293 K. The lowest temperature accessible in solution phase is 235 K. Over this temperature range, an activation energy of 320 ± 25 cm^{-1} is obtained. The barrierless rate from the Arrhenius fit is found to be 220 ± 25 ps^{-1}. Both of these values are within error of those found for

the PF_6^- salt of this complex, also in MeCN.

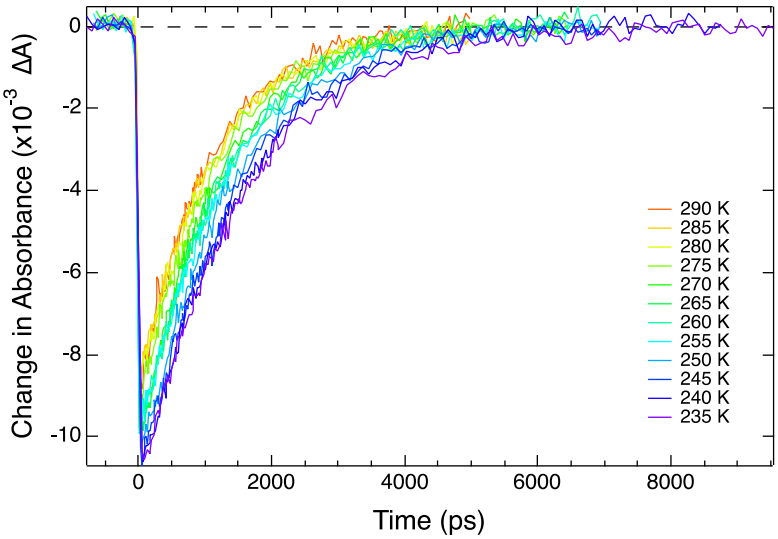

Figure A.1. Representative ground state recovery data as a function of temperature of $[Fe(bpy)_3]Cl_2$ in MeCN. Excitation occurred at 490 nm and probing at 530 nm.

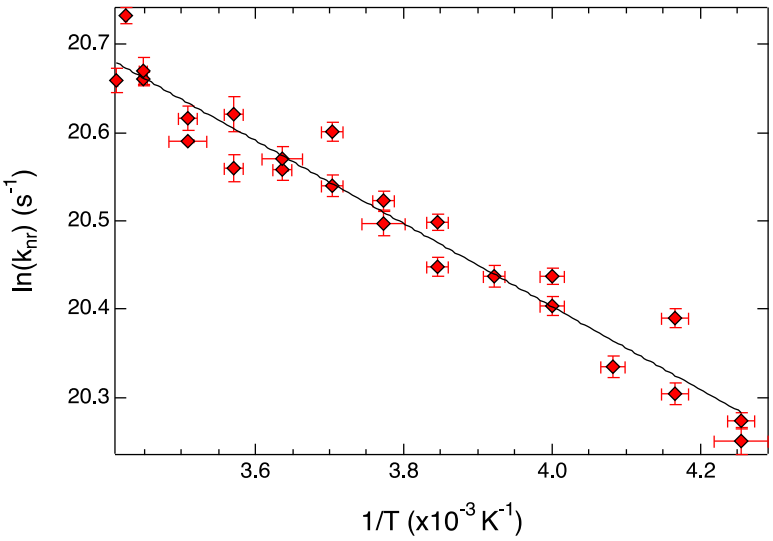

Figure A.2. Arrhenius plot of VT-TA data of $[Fe(bpy)_3]Cl_2$ in MeCN. The fit (black trace) of these data (red diamonds) gave an activation energy of 320 ± 25 cm^{-1} and a preexponential factor of 220 ± 25 ps^{-1}. The data fit well to a single-mode with $R^2 = 0.947$.

As was outlined in Chapter 2, the electrochemical data of the Fe(II/III) oxidation potential can be used in eqn. (A.1) to estimate the driving force for this reaction, according to:

$$\Delta G^{\circ}_{complex} = \Delta G^{\circ}_{[Fe(bpy)_3]^{2+}} + \left(E^{ox}_{complex} - E^{ox}_{[Fe(bpy)_3]^{2+}}\right) \quad \text{(A.1)}$$

In this equation, E^{ox} is the (II/III) oxidation potential for the iron complex specified. To use this equation, an initial assumption of $\Delta G^{\circ}_{[Fe(bpy)_3]^{2+}}$ must be made, and here it is -7300 ± 730 cm^{-1}, as discussed in Chapter 2.[3] Because we have not performed electrochemical experiments in-house on $[Fe(bpy)_3]^{2+}$ as a function of counteranion or solvent, we must assume the same driving force for the studies herein. Considering the relatively large error bars, we believe that the actual change in ΔGº is encompassed in the error propagation performed.

Marcus parameters were calculated for $[Fe(bpy)_3]Cl_2$ in MeCN from the Arrhenius values. The reorganization energy was found to be 11100 ± 1000 cm^{-1}, and the electronic coupling constant is 4.6 ± 0.2 cm^{-1}. From these, the H_{ab}^4/λ is calculated to be 1/(25 ± 5). These values are completely within error of the same parameters of $[Fe(bpy)_3](PF_6)_2$ in MeCN.

1.1.2 Methanol

VT-TA was performed on $[Fe(bpy)_3]Cl_2$ in methanol (MeOH) to study the ground state recovery dynamics as a function of temperature. Those data are shown in Fig. A.3. From these results, an Arrhenius plot can be made (Fig. A.4). Based on the curve fitting, E_a = 290 ± 20 cm^{-1}, which is within error of the MeCN data. The frequency factor is likewise unchanged from the data in MeCN, at A = 250 ± 25 ps^{-1}. Using eqn. (A.1) and ΔGº = -7300 ± 730 cm^{-1}, λ is found to be 10800 ± 1000 cm^{-1}. H_{ab}, again, is within error of the MeCN data, 4.3 ± 0.1 cm^{-1}, such that H_{ab}^4/λ = 1/(32 ± 4).

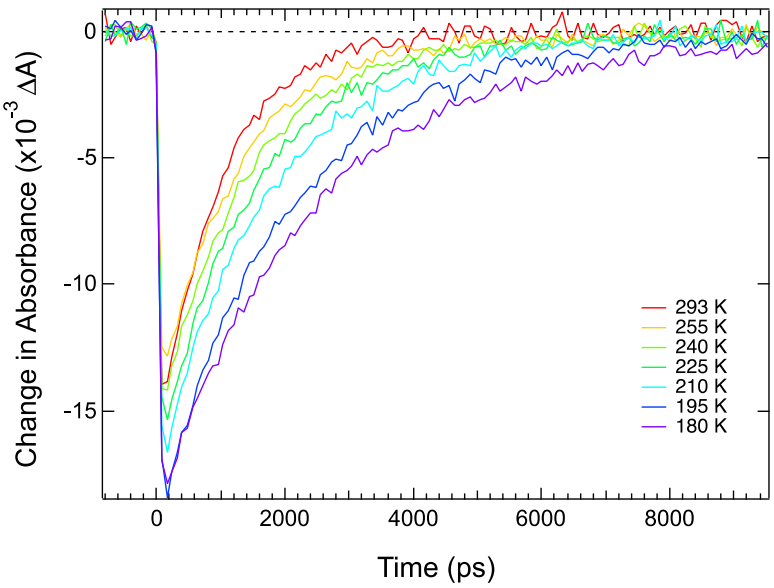

Figure A.3. Representative ground state recovery data as a function of temperature of $[Fe(bpy)_3]Cl_2$ in MeOH. Excitation occurred at 490 nm and probing at 530 nm.

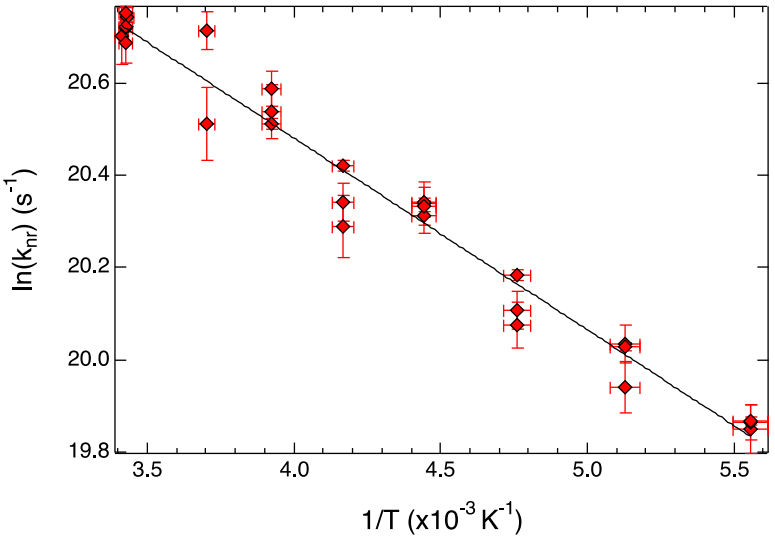

Figure A.4. Arrhenius plot of VT-TA data of $[Fe(bpy)_3]Cl_2$ in MeCN. The fit (black trace) of these data (red diamonds) gave an activation energy of 250 ± 25 cm^{-1} and a preexponential factor of 250 ± 25 ps^{-1}. The data fit well to a single-mode with $R^2 = 0.968$.

1.1.3 Acetone

The ground state recovery dynamics of $[Fe(bpy)_3]Cl_2$ were studied in acetone, probed at 530 nm upon excitation at 490 nm. It should be noted that these data were only collected once and need to be recollected for reproducibility. The VT-TA data are shown in Fig. A.5. At room temperature, the lifetime is 1.13 ± 0.05 ns. The lowest temperature that could be accessed while keeping the sample in solution was 185 K. At this temperature, the lifetime of the complex is 2.47 ± 0.06 ns. From the VT data, an Arrhenius plot can be made (Fig. A.6), from which E_a = 295 ± 10 cm^{-1} and A = 255 ± 20 ps^{-1}. With these values, the reorganization energy is found to be 10900 ± 1000 cm^{-1} and H_{ab} is 4.2 ± 0.2 cm^{-1}. The ratio of H_{ab}^4/λ is calculated, then, to be 1/(36 ± 5).

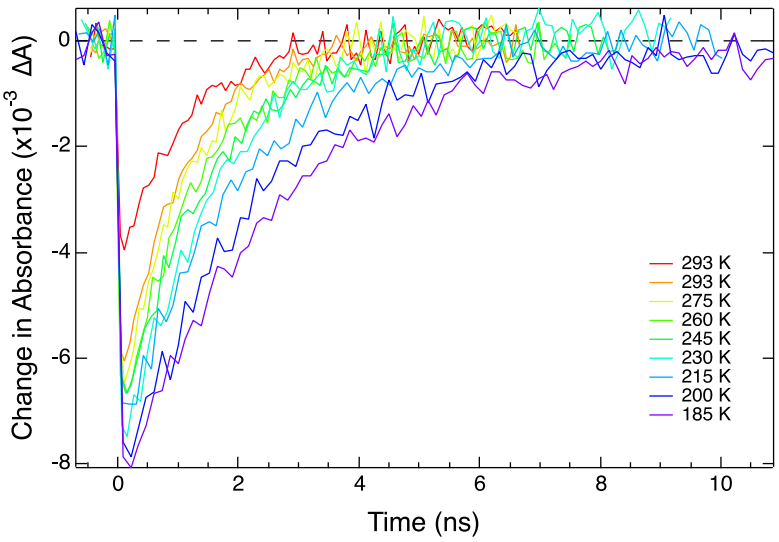

Figure A.5. Ground state recovery data as a function of temperature of $[Fe(bpy)_3]Cl_2$ in acetone. Excitation occurred at 490 nm and probing at 530 nm.

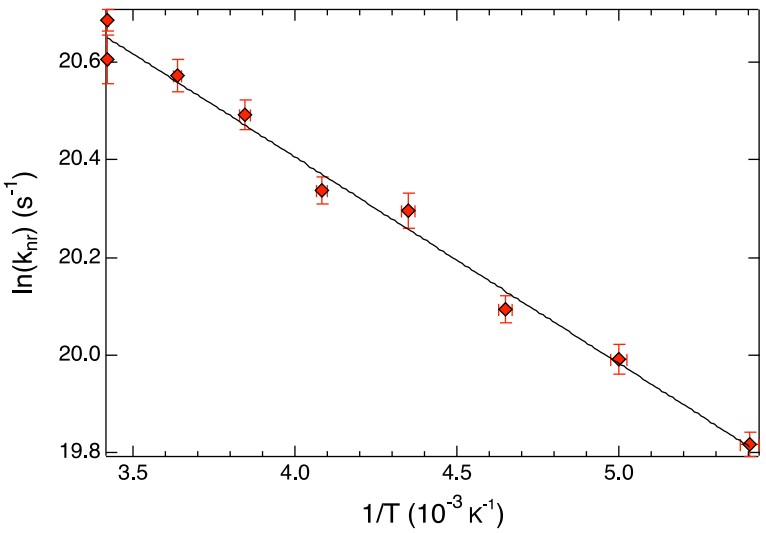

Figure A.6. Arrhenius plot of VT-TA data of $[Fe(bpy)_3]Cl_2$ in acetone, collected once. The fit (black trace) of these data (red diamonds) gave an E_a of 295 ± 10 cm^{-1} and A = 255 ± 20 ps^{-1}. The data fit well to a single-mode with R^2 = 0.989.

1.1.4 Water

As with the other three solvents, the ground state dynamics of $[Fe(bpy)_3]Cl_2$ are determined as a function of solvent (Fig. A.7). One of the major issues with water, however, is the very high freezing point. This limits the temperature range accessible in the fluid solution to 275 K to room temperature. As has been previously observed,[1] the lifetime of $[Fe(bpy)_3]Cl_2$ in H_2O at room temperature is 0.68 ± 0.01 ns. This is a more than 30% reduction in the lifetime relative to any of the other solvents studied here. Additionally, from the VT-TA data and Arrhenius fitting (Fig. A.8), the barrier associated with this process is 175 ± 30 cm^{-1}, which is significantly different from the other solvents. The barrierless rate, likewise, is also outside of error with A = 295 ± 40 ps^{-1}.

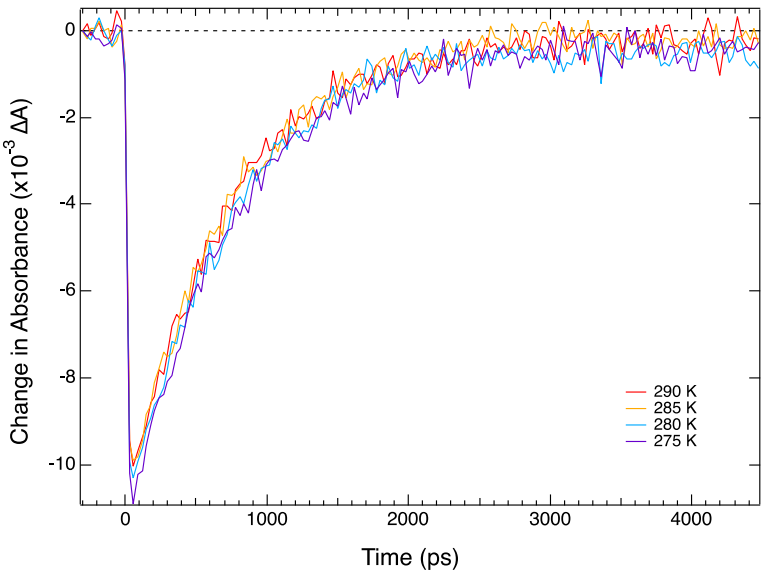

Figure A.7. Representative ground state recovery data as a function of temperature of $[Fe(bpy)_3]Cl_2$ in acetone. Excitation occurred at 490 nm and probing at 520 nm. The kinetics were not significantly different when probed at 530 nm.

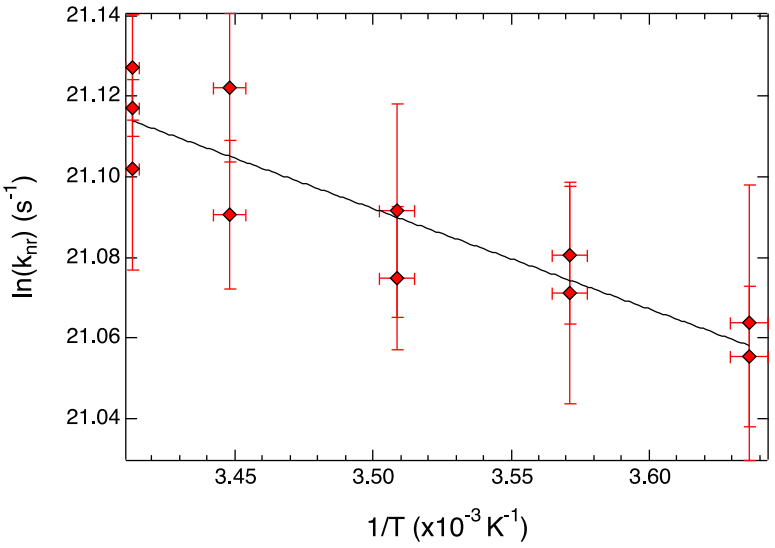

Figure A.8. Arrhenius plot of VT-TA data of $[Fe(bpy)_3]Cl_2$ in acetone. These data were only collected once. The fit (black trace) of these data (red diamonds) gave an activation energy of 175 ± 30 cm^{-1} and a preexponential factor of 295 ± 40 ps^{-1}. The data fit modestly to a single-mode with $R^2 = 0.804$.

The Arrhenius values obtained from Fig. A.8 can be used with eqn. (A.1) to find the Marcus parameters associated with the $^5T_2 \rightarrow {}^1A_1$ transition in $[Fe(bpy)_3]Cl_2$ in H_2O. With an initial assumption of $\Delta G^o = -7300 \pm 730$ cm^{-1}, it is calculated that $\lambda = 9900 \pm 1000$ cm^{-1}. Surprisingly, the reorganization energy in H_2O is not significantly different from those found in MeCN, MeOH, or acetone. H_{ab}, however, is only within error of the value calculated in acetone; the electronic coupling constant in water is found to be 3.8 ± 0.3 cm^{-1}, such that $H_{ab}^4/\lambda = 1/(49 \pm 14)$.

1.2 Analysis of Results

A summary of the data discussed above can be found in Tables A.1 and A.2. From these results, it is clear that no significant difference in observed in the data collected in MeCN, MeOH, or acetone. Even with the slightly longer lifetime in acetone at room temperature, all of the Arrhenius and Marcus parameters for those three solvents are calculated to be within error of each

other. Furthermore, they are all within error of the same parameters found for $[Fe(bpy)_3](PF_6)_2$ in MeCN. This verifies that for these dynamics, in these complexes, the counteranion does not affect the kinetics or energetics.

Table A.1. Summary of lifetimes and Arrhenius parameters of the ground state recovery dynamics in $[Fe(bpy)_3]Cl_2$ in various solvents.

Solvent	Lifetime at RT (ns)	E_a (cm^{-1})	A (ps^{-1})
MeCN	1.03 ± 0.01	320 ± 25	220 ± 25
MeOH	1.00 ± 0.03	290 ± 20	250 ± 25
Acetone[a]	1.13 ± 0.05	295 ± 10	255 ± 20
Water	0.68 ± 0.01	175 ± 30	295 ± 40

a Data only collected once.

Table A.2. Marcus parameters for ground state recovery of $[Fe(bpy)_3]Cl_2$ in various solvents.

Solvent	$-\Delta G^o$ (cm^{-1})	λ (cm^{-1})	H_{ab} (cm^{-1})	H_{ab}^4/λ
MeCN	7300 ± 730	11100 ± 1000	4.6 ± 0.2	1/(25 ± 5)
MeOH	7300 ± 730	10800 ± 1000	4.3 ± 0.1	1/(32 ± 4)
Acetone[a]	7300 ± 730	10900 ± 1000	4.2 ± 0.2	1/(36 ± 5)
Water	7300 ± 730	9900 ± 1000	3.8 ± 0.3	1/(49 ± 14)

a Data only collected once.

The biggest (and only) difference is observed when water is used as the solvent. In this case, the activation energy is nearly half of what is found in the other three solvents. Interestingly,

though, the barrierless rate in water is within error of those in MeOH and acetone. This could, however, be an artifact of the larger error bars on the data collected in water. These error bars are likely so large simply because only five temperature points are being considered. It does make sense that the data in H_2O would be substantially different in some way to the other solvents measured. The work done by Miller and McCusker expands on the idea that as a solvent, H_2O fundamentally changes the dynamics of ground state recovery in $[Fe(bpy)_3]^{2+}$ compared to other solvents like alcohols, nitriles, and diols.[1] The only true indicators of what may be occurring come from the activation energy and H_{ab}^4/λ ratio. Increasing the temperature range while performing VT-TA on $[Fe(bpy)_3]^{2+}$ in H_2O through the use of cryostat heaters may help improve error bars on the measurements, thereby ensuring which parameters are within error of each other.

2. $[Fe(dcpp)_2]^{2+}$

These results are a continuation of those presented in Chapter 3 of this work. The data showed in that chapter are for the three counteranions (i.e., BF_4^-, PF_6^-, BAr^{F-}) of $[Fe(dcpp)_2]^{2+}$ in acetonitrile, whereas here those three salts are still of interest, but in acetone. This was to address the question of whether or not counteranion interaction and therefore the outer-sphere reorganization energy was influenced by the specific solvent. Although previous work on $[Fe(bpy)_3]^{2+}$ has shown that the counteranion plays no real role in the ground state recovery dynamics,[1] it is also known that the nature of the solvent can influence the relationship between a cation and anion.[4,5] These results will be analyzed on their own but also in comparison to the analogous data collected in acetonitrile.

2.1 Different Counteranions in Acetone

2.1.1 BF_4^-

The ground state recovery lifetime of $[Fe(dcpp)_2](BF_4)_2$ was measured as a function of temperature when in acetone; representative data are shown in Fig. A.9. The excitation wavelength was 490 nm, and the dynamics were probed at 540 nm. When the Arrhenius plot (Fig. A.10) was made, an activation energy of 50 ± 10 cm^{-1} was found. Additionally, the preexponential rate was 190 ± 10 ps^{-1}. Because electrochemical data was not collected for $[Fe(dcpp)_2]^{2+}$ in different supporting electrolytes, the oxidation potential for the Fe(II/III) couple is only observed in the PF_6^- salt. Based on past work on different complexes,[6] we do not believe that the counteranion will drastically change this potential. That being said, ΔG^o for $[Fe(dcpp)_2]^{2+}$ is calculated from the same Fe(II/III) oxidation potential regardless of counteranion or solvent. From eqn. (A.1), ΔG^o is estimated to be -12220 ± 1220 cm^{-1}, with λ = 13900 ± 1500 cm^{-1} and H_{ab} = 5.2 ± 0.3 cm^{-1}. Finally, the H_{ab}^4/λ ratio was found to be 1/(20 ± 2). Comparison of these values with those of other salts and solvents will be reserved until Appendix A Section 2.2.

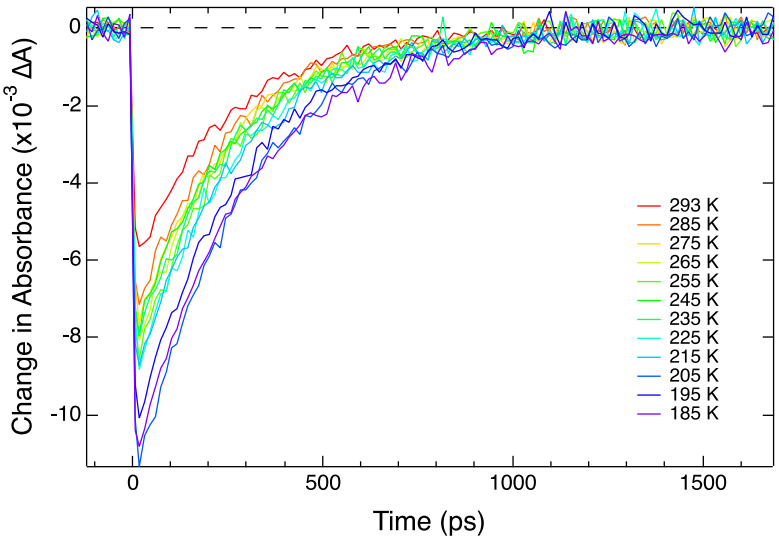

Figure A.9. Representative VT-TA data of the ground state recovery of $[Fe(dcpp)_2](BF_4)_2$ in acetone, in which λ_{exc} = 490 nm and λ_{probe} = 540 nm.

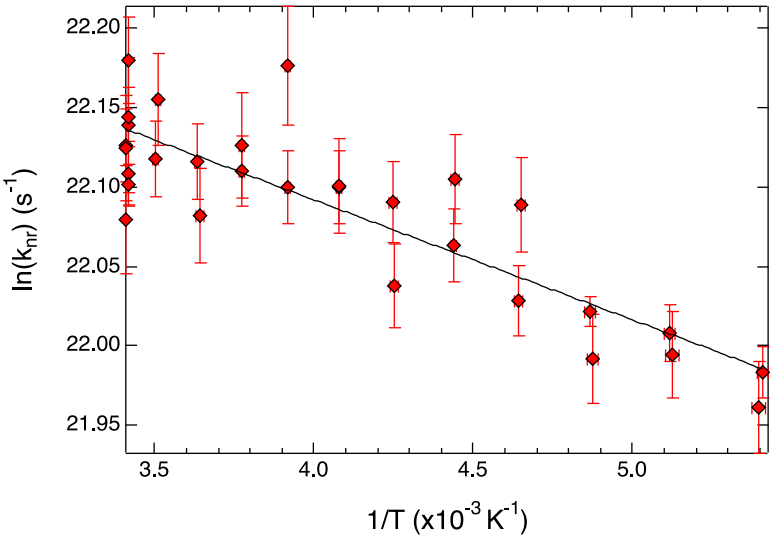

Figure A.10. Arrhenius plot of all the VT-TA data collected of $[Fe(dcpp)_2](BF_4)_2$ in acetone. From this plot, E_a = 50 ± 10 cm^{-1} and A = 190 ± 10 ps^{-1}. The data were found to fit modestly to a single mode with R^2 = 0.747.

2.1.2 PF_6^-

The VT-TA data for the $^5T_2 \rightarrow {}^1A_1$ transition in $[Fe(dcpp)_2](PF_6)_2$ in acetone are shown in Fig. A.11. They were measured at 540 nm upon excitation at 490 nm. The dynamics were also collected when pumped at 610 nm, and all values were within error between the two excitation energies; the only difference being the average R^2 value of the Arrhenius plot, with $R^2 = 0.900$ for $\lambda_{exc} = 610$ nm and $R^2 = 0.819$ for $\lambda_{exc} = 490$ nm. The Arrhenius plot (Fig. A.12) yielded $E_a = 50 \pm 10$ cm^{-1} and $A = 190 \pm 10$ ps^{-1}. As with the BF_4^- salt, $\Delta G^o = -12220 \pm 1220$ cm^{-1} such that $\lambda = 13900 \pm 1500$ cm^{-1} with $H_{ab} = 5.2 \pm 0.3$ cm^{-1}. The ratio, $H_{ab}^4/\lambda = 1/(20 \pm 2)$.

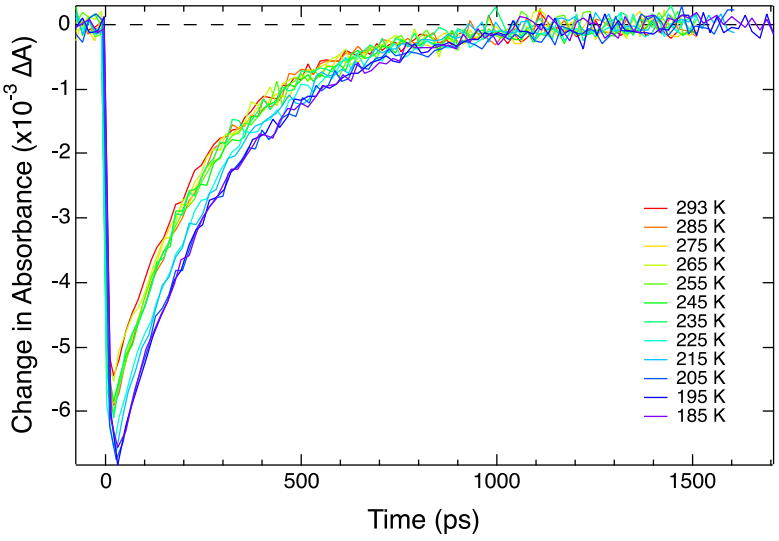

Figure A.11. Representative VT-TA data of $[Fe(dcpp)_2](PF_6)_2$ in acetone at 540 nm when excited at 490 nm.

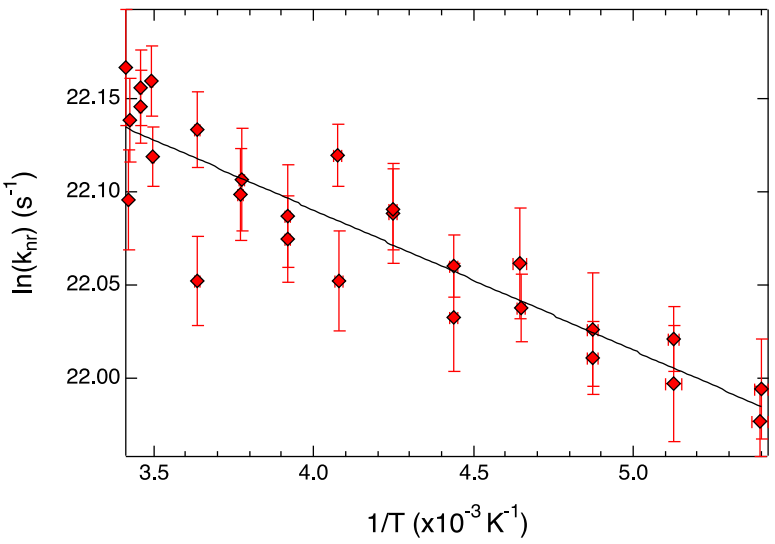

Figure A.12. Arrhenius plot of all the data collected by VT-TA of $[Fe(dcpp)_2](PF_6)_2$ in acetone. From this fit, the activation energy was found to be 50 ± 10 cm^{-1} and the frequency factor is 190 ± 10 ps^{-1}. The data fit modestly to a single mode with $R^2 = 0.816$.

2.2 Analysis of Results

The data for the BF_4^- and PF_6^- salts of $[Fe(dcpp)_2]^{2+}$ in acetone are shown above whereas the BAr^{F-} salt data can be found in Chapter 3. Table A.3 gives a comparison of the Arrhenius values of the three salts, and Table A.4 does the same with the Marcus parameters. From these data, it is apparent that even without the perhaps overly generous 10% error bars, all of the Arrhenius and Marcus values are identical in acetone. In fact, in most cases the parameters measured for $[Fe(dcpp)_2]^{2+}$ in acetone were within error of those measured in acetonitrile. The only exception to this, obviously, is the activation energy, which is twice as large in acetonitrile than in acetone. Based on these results, it does not appear as though the solvent significantly affects how the counteranion interacts with and therefore stabilizes the Fe(II) cation. Because the mechanism of solvation is yet unknown for this complex (and in Fe(II) polypyridyls in general), it is unlikely that these results are applicable to all solvents. That being said, as was true with

acetonitrile, the counteranion does not appear to significantly affect the energetics or kinetics of ground state recovery in $[Fe(dcpp)_2]^{2+}$.

Table A.3. Summary of lifetimes and Arrhenius values of $[Fe(dcpp)_2]^{2+}$ in acetone.

Anion	Lifetime at RT (ps)	Lifetime at 245 K (ps)	E_a (cm^{-1})	A (ps^{-1})
BAr^{F-}	240 ± 5	255 ± 5	55 ± 15	185 ± 15
PF_6^-	240 ± 5	255 ± 5	50 ± 10	190 ± 10
BF_4^-	245 ± 5	250 ± 5	50 ± 10	190 ± 10

Table A.4. Marcus parameters for $[Fe(dcpp)_2]^{2+}$ in acetone.

Anion	$-\Delta G^o$ (cm^{-1})	λ (cm^{-1})	H_{ab} (cm^{-1})	H_{ab}^4/λ
BAr^{F-}	12220 ± 1220	14000 ± 1500	5.2 ± 0.3	1/(19 ± 4)
PF_6^-	12220 ± 1220	13900 ± 1500	5.2 ± 0.3	1/(20 ± 2)
BF_4^-	12220 ± 1220	13900 ± 1500	5.2 ± 0.3	1/(20 ± 2)

3. $[Fe(dvpp)_2](PF_6)_2$

In this complex, dvpp is the vinyl analogue of dcpp as seen in Scheme A.1, such that dvpp = 2,6-bis(2-divinylpyridyl)pyridine. By replacing the carbonyl moiety in dcpp with a $=CH_2$ group, it was expected that only specific carbonyl-solvent effects would be mitigated, and that the overall dynamics of $[Fe(dvpp)_2]^{2+}$ would be overall very similar to those of $[Fe(dcpp)_2]^{2+}$. This premise was furthered by the fact that the X-ray crystal structures of the two analogues overlay nearly

perfectly on top of each other.[7] However, the room temperature ground state recovery lifetime of $[Fe(dvpp)_2]^{2+}$ immediately told a different story (Fig. A.13). This process was found to occur with a 1.06 ± 0.03 ns lifetime at room temperature, which is within error of the lifetime of $[Fe(bpy)_3]^{2+}$. Electrochemical data helped, in part, to explain this disparity: while the Fe(II/III) oxidation couple in $[Fe(dcpp)_2]^{2+}$ occurred at 1.29 V vs. Fc/Fc^+,[8] in $[Fe(dvpp)_2]^{2+}$, that same one-electron process occurred at 0.64 V vs. Fc/Fc^+.[9] Relative to the 0.665 V vs. Fc/Fc^+ oxidation potential of $[Fe(bpy)_3]^{2+}$, it is apparent that the electronics of $[Fe(dvpp)_2]^{2+}$ have been drastically altered relative to $[Fe(dcpp)_2]^{2+}$. As has previously been discussed, electrochemistry is only a measure of the t_{2g} orbitals in these Fe(II) complexes and does not truly describe the electronic states.[2] We will continue to use it as a first-approximation of the ligand field strength difference, and therefore the driving force difference between iron chromophores. Based on eqn. (A.1), ΔG^o for $[Fe(dvpp)_2](PF_6)_2$ is found to be -7100 ± 710 (with 10% error bars by convention[2]). This is within error of $[Fe(bpy)_3]^{2+}$. From all of these data, it was highly desirable to perform variable-temperature studies in order to determine further kinetic and energetic parameters of $[Fe(dvpp)_2]^{2+}$ so as to be compared to the carboxy-analogue, $[Fe(dcpp)_2]^{2+}$.

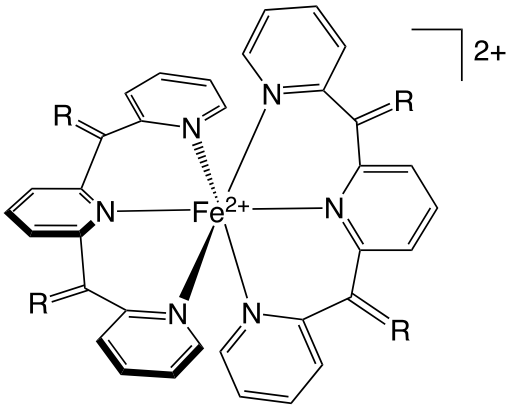

Scheme A.1. General structure for both $[Fe(dcpp)_2]^{2+}$ and $[Fe(dvpp)_2]^{2+}$.

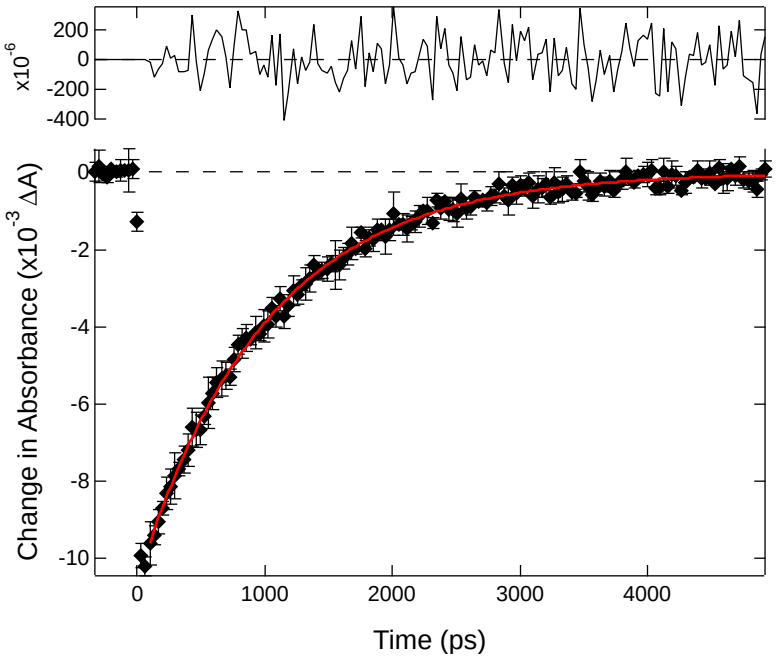

Figure A.13. Room temperature ground state recovery dynamics of $[Fe(dvpp)_2](PF_6)_2$ in MeCN. The data (black diamonds) fit well to a single exponential (red trace), as determined by the residuals (black trace, above) centered around 0. These data have been collected multiple times and the error propagated to determine a lifetime of 1.06 ± 0.03 ns.

3.1 Acetonitrile

The VT-TA data of the ground state recovery in $[Fe(dvpp)_2](PF_6)_2$ in acetonitrile are shown in Fig. A.14. For these data, excitation occurred at 480 nm and probes of 530 and 510 nm were used. Without further experiments being performed, it cannot be said that the results of these two probes yielded significantly different Arrhenius and Marcus values. The lifetime at 240 K was found to be 1.44 ± 0.05 ns, which is an approximately 35% increase from the room temperature kinetics. This corresponds to a barrier of 310 ± 40 cm^{-1} (Fig. A.15), which is the same as that of $[Fe(bpy)_3]^{2+}$. Similarly, the barrierless rate was found to be 265 ± 40 ps^{-1}. The error bars on these measurements were very large, possibly because the sample was too concentrated for the pump and probe wavelengths used here.

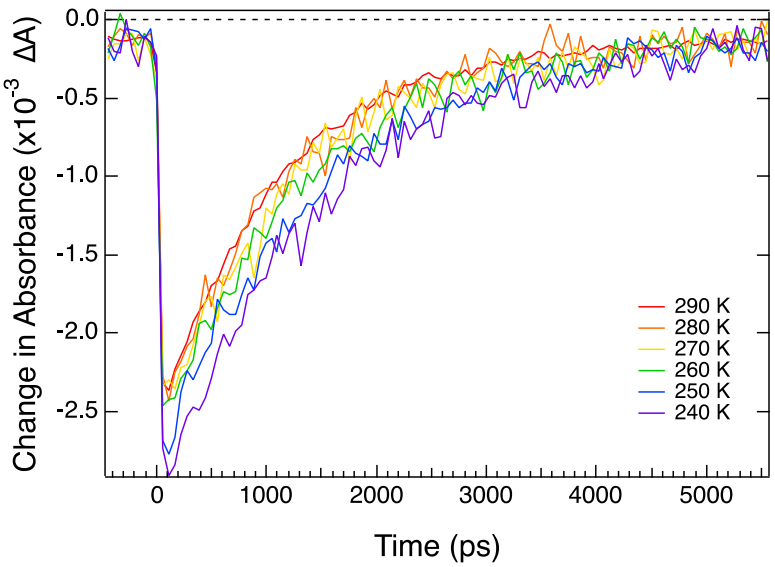

Figure A.14. Representative VT-TA data of $[Fe(dvpp)_2](PF_6)_2$ in MeCN upon excitation at 480 nm and probing at 530 nm.

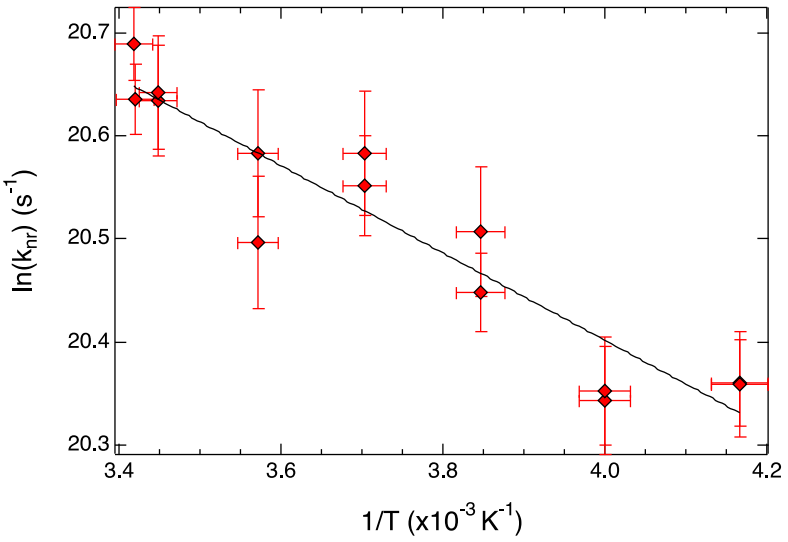

Figure A.15. Arrhenius plot for $[Fe(dvpp)_2](PF_6)_2$ in MeCN. Fitting these data yielded E_a = 310 ± 40 cm^{-1} and A = 265 ± 40 ps^{-1}. The data fit modestly to a single mode with R^2 = 0.885.

From the electrochemical data and the Arrhenius plot, the Marcus values for $[Fe(dvpp)_2](PF_6)_2$ in acetonitrile can be found. With ΔG^o = -7100 ± 710 cm^{-1}, the reorganization energy is determined to be 10700 ± 1000 cm^{-1}. The electronic coupling constant was then determined to be 4.1 ± 0.5 cm^{-1}, from which H_{ab}^4/λ = 41 ± 16. Considering the very large error bars, particularly on H_{ab} and $H_{ab}^{4/}\lambda$, all of the values calculated for this complex are within error of those of $[Fe(bpy)_3](PF_6)_2$, as were shown in Chapter 2. It is apparent that major electronic changes have been imparted on this Fe(II) complex by the change of the carbonyl to a vinyl group. By this seemingly simple substitution, a bis-tridentate complex's photophysics greatly resemble those of a tris-bidentate. Clearly these data will need to be recollected under various conditions (e.g., solvent, pump and probe wavelengths). It would also be beneficial to have further characterization of $[Fe(dvpp)_2]^{2+}$ by simultaneous ultrafast X-ray absorption and emission spectroscopies as were performed for the carboxy-version.[10]

4. $[Fe(dtbb)_3]Br_2$

These data were originally collected in order to better understand the dynamics at work in the studies by Miller and McCusker.[1] $[Fe(dtbb)_3]^{2+}$ (dtbb = 4,4'-di-^{t}butyl-2,2'-bipyridine) had been shown via theoretical work to display a larger difference in solvation energy than $[Fe(bpy)_3]^{2+}$. This corresponds to the energetic de-/stabilization (ΔE) afforded to the $^5T_2$ and $^1A_1$ potential energy surfaces by the solvent. Their work showed that the magnitude of ΔE may not be the same for both of these states, and thus with larger differences (i.e., $\Delta\Delta E$) observed in $[Fe(dtbb)_3]^{2+}$, it was believed that the best experimental verification of these results would be obtained by the variable-temperature study of ground state recovery of this complex in two solvents of the same family with variable chain length (i.e., MeOH and 1-BuOH). Those results are presented here.

4.1 Two Different Solvents

4.1.1 Methanol

The ground state recovery dynamics of $[Fe(dtbb)_3]Br_2$ were measured in MeOH upon excitation at 550 nm and probing at 490 nm. Representative data are shown in Fig. A.16. The room temperature lifetime of this complex in MeOH is 1.08 ± 0.05 ns. The lowest temperature achieved in MeOH was 180 K to maintain fluid solution, at which temperature the lifetime was 2.87 ± 0.14 ns. From the Arrhenius plot (Fig. A.17), an activation energy of 325 ± 20 cm^{-1} is determined and a barrierless rate of 225 ± 30 ps^{-1}. These values are within error those collected for the $[Fe(bpy')_3]^{2+}$ family. Applying these parameters to Marcus theory and using the driving force found in Chapter 2 (ΔG^o = -6100 ± 600 cm^{-1}), the reorganization energy is found to be 9600 ± 900 cm^{-1} with H_{ab} = 4.3 ± 0.3 cm^{-1}, which are unchanged from the data collected in MeCN in Chapter 2. The H_{ab}^4/λ ratio was determined to be 1/(28 ± 7), which is completely in keeping with the ratio found for all of the $[Fe(bpy')_3]^{2+}$ compounds. It is unsurprising that the ground state recovery process in

$[Fe(dtbb)_3]^{2+}$ should occur with the same kinetics and energetics when in MeCN and MeOH. The more telling results will be in the comparison to the data collected in 1-BuOH.

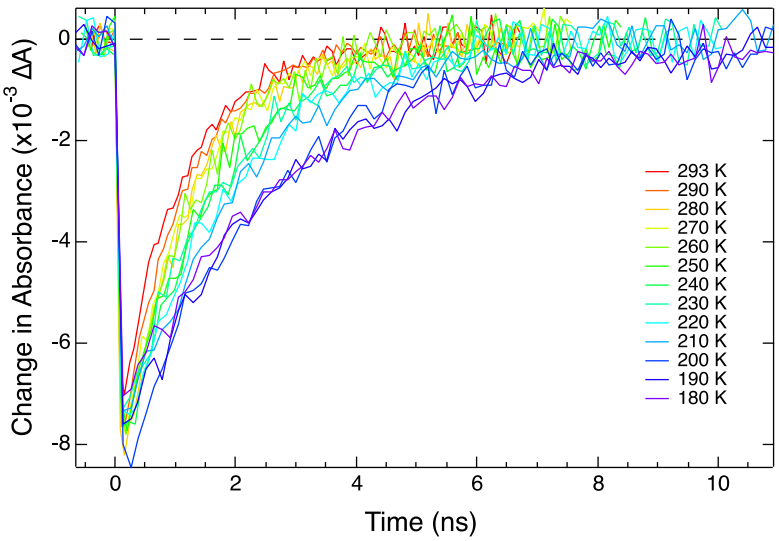

Figure A.16. Representative variable-temperature data of $[Fe(dtbb)_3]Br_2$ in MeOH. Excitation occurred at 550 nm, with probing at 490 nm.

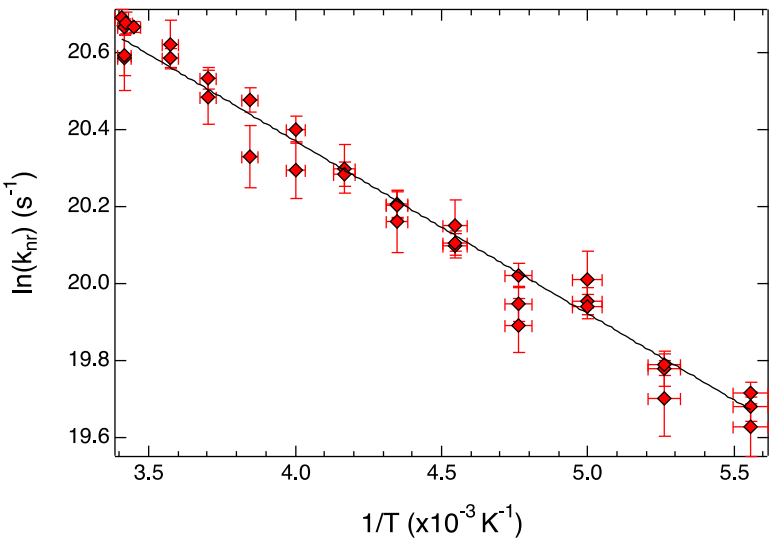

Figure A.17. Arrhenius plot of all the data of $[Fe(dtbb)_3]Br_2$ in MeOH. This fit gives an activation energy of 325 ± 20 cm^{-1} and a barrierless rate of 225 ± 30 ps^{-1}. These data fit well to a single Arrhenius mode with $R^2 = 0.971$.

4.1.2 1-Butanol

When studied at room temperature, the ground state recovery lifetime of $[Fe(dtbb)_3]Br_2$ in 1-BuOH is lengthened relative to the dynamics in MeOH, at 1.28 ± 0.04 ns. From the variable-temperature transient absorption studies (Fig. A.18), the coldest temperature lifetime is 2.15 ± 0.08 ns at 220 K. The Arrhenius plot of all the combined data are shown in Fig. A.19. An initial fit of these data yielded a barrier of 250 ± 10 cm^{-1}. However, it can be seen that the Arrhenius line does not fit the data well as determined by the residuals, despite the fact that the $R^2 = 0.938$. If the lowest three temperatures are excluded (Fig. A.20), though, the fit is greatly improved, with $R^2 = 0.961$. this fit yields an E_a of 330 ± 15 cm^{-1} and A = 255 ± 20 ps^{-1}.

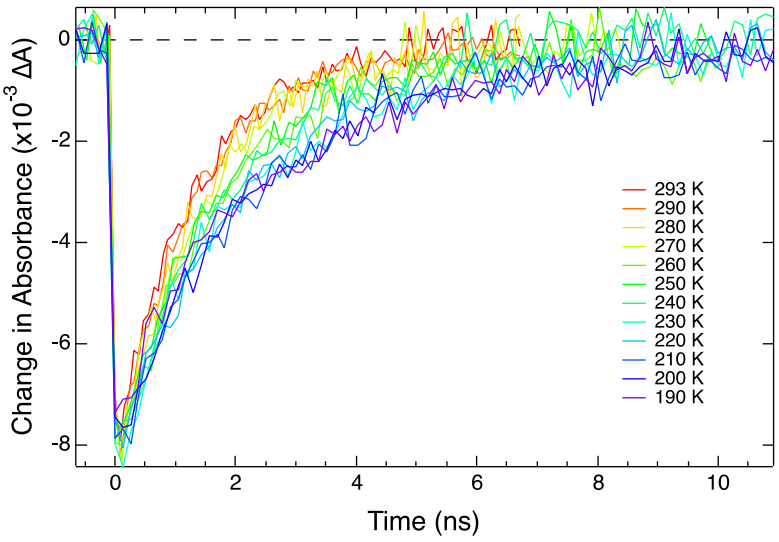

Figure A.18. Representative data of the variable-temperature ground state recovery dynamics of $[Fe(dtbb)_3]Br_2$ in 1-BuOH upon excitation at 550 nm and probing at 500 nm. The dynamics did not change significantly when probed at 490 nm, as is expected of ground state recovery.

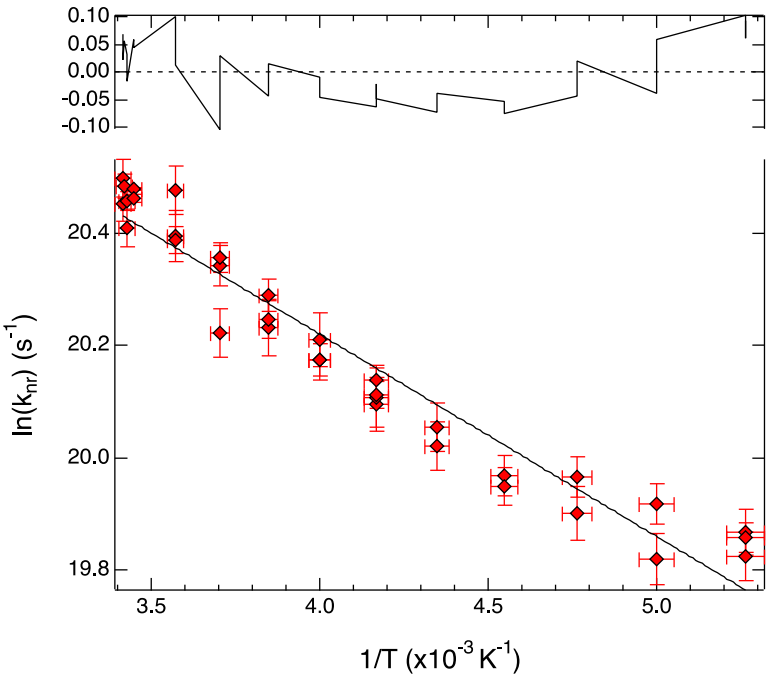

Figure A.19. Arrhenius plot of the ground state recovery lifetimes of $[Fe(dtbb)_3]Br_2$ in 1-BuOH. The data (red diamonds) are not represented well by the fit (black trace, lower) as determined by the residuals (black trace, upper). This is likely due to the water content of 1-BuOH (see text for details).

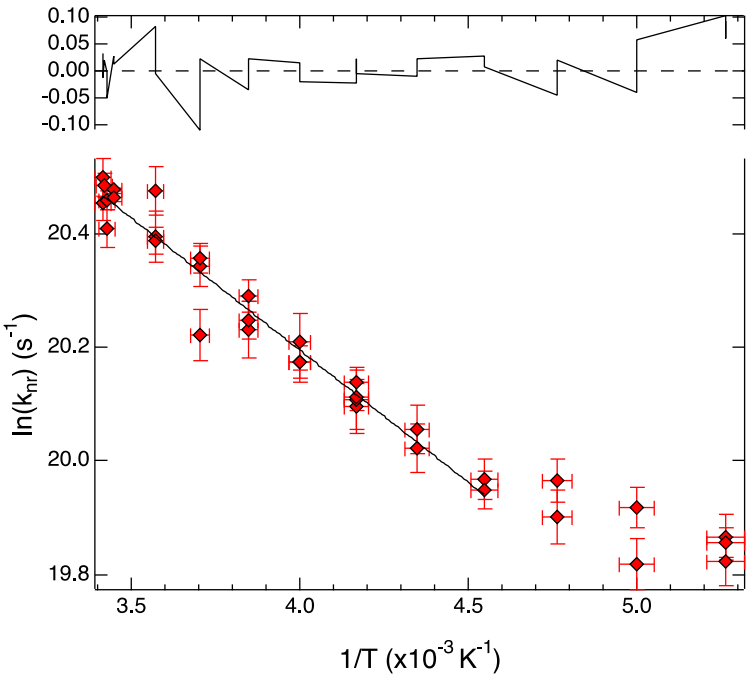

Figure A.20. Arrhenius fit of the temperature-dependent lifetimes of $[Fe(dtbb)_3]Br_2$ in 1-BuOH. The data (red diamonds) are fit (black trace, lower) best when excluding the lowest three temperatures, as indicated by the residuals (black trace, upper). This fit yields an E_a = 330 ± 15 cm^{-1} and A = 255 ± 20 ps^{-1}.

The most likely explanation for the need to exclude the lowest three temperatures is the greater water content of 1-BuOH relative to MeOH. Water has a much higher freezing point (272 K) than 1-BuOH (183 K), serving to raise the freezing point and perhaps inducing the fluid-to-glass transition at a higher temperature than would normally occur. This transition is known to cause the kinetics measured to behave in a non-Arrhenius fashion.[11] Considering the bi-modal Arrhenius behavior, only the warmer temperatures (T > 220 K) were considered in the fitting. From the E_a and A obtained from these data, and a ΔG^o = -6100 ± 600 cm^{-1}, it was found that the reorganization energy is 9700 ± 900 cm^{-1}. The electronic coupling constant is 4.1 ± 0.2 cm^{-1}, and the H_{ab}^4/λ is 1/(34 ± 5). The 1-BuOH used here was ACS reagent grade, indicating that it likely

has a higher water content than either spectrophotometric or HPLC grade would. In that case, these data should simply be recollected in fresher solvent with higher purity. If the Arrhenius plot is linear, then water was most likely the culprit. If however, the Arrhenius plot remains bimodal, pump scatter could be an issue, or there truly are two separate barriers associated with ground state recovery kinetics of $[Fe(dtbb)_3]^{2+}$ that are only observable when the compound is in 1-BuOH. This would clearly be a phenomenon of considerable interest, if it is real.

4.2 Analysis of Results

A summary of the data of $[Fe(dtbb)_3]^{2+}$ complex in various solvents, can be found in Tables A.5 and A.6. Despite the difference in room temperature lifetimes in $[Fe(dtbb)_3]^{2+}$ in MeOH versus 1-BuOH, the Arrhenius and Marcus parameters show no substantial change with the different solvents. From these results, it cannot be said that the increase in chain length in the solvent affects the solvation energy of the $^5T_2$ and $^1A_1$ electronic states any differently than with a short-chain alcohol, or even with the short-chain nitrile. The data should not be extrapolated to other systems, though. It is probable that the specific alcohol-solute interaction is not changing with the chain length (as is expected). What would be more telling, likely, is a comparison of the effect of chain length with different polar heads; for example, a comparison of the results in 1-BuOH to 1-BuCN. In general, it should be apparent that VT-TA is a strong tool that should be used regularly to give greater insight into the photophysical processes of various chromophores.

Table A.5. Summary of lifetimes and Arrhenius values of $[Fe(dtbb)_3]^{2+}$ in three different solvents.

Anion/Solvent	Lifetime at RT (ns)	Lifetime at 240 K (ns)	E_a (cm^{-1})	A (ps^{-1})
PF_6^- in MeCN	1.07 ± 0.01	1.48 ± 0.02	315 ± 15	230 ± 15
Br^- in MeOH	1.08 ± 0.05	1.54 ± 0.07	325 ± 20	225 ± 30
Br^- in 1-BuOH	1.28 ± 0.04	1.86 ± 0.09	330 ± 15	255 ± 20

Table A.6. Marcus parameters of $[Fe(dtbb)_3]^{2+}$ in various solvents.

Anion/Solvent	$-\Delta G^o$ (cm^{-1})	λ (cm^{-1})	H_{ab} (cm^{-1})	H_{ab}^{4}/λ
PF_6^- in MeCN	6100 ± 600	9500 ± 900	4.3 ± 0.2	1/(29 ± 4)
Br^- in MeOH	6100 ± 600	9600 ± 900	4.3 ± 0.3	1/(28 ± 7)
Br^- in 1-BuOH	6100 ± 600	9700 ± 900	4.1 ± 0.2	1/(34 ± 5)

REFERENCES

REFERENCES

1. Miller, J. N.; McCusker, J. K. Outer-Sphere Effects on the Excited State Dynamics of Ligand Field States in Fe(II) Polypyridyl Complexes. *Manuscript in preparation.*

2. Carey, M. C.; Adelman, S. L.; McCusker, J. K. Insights Into the Excited State Dynamics of Fe(II) Polypyridyl Complexes from Variable-Temperature Ultrafast Spectroscopy. *Submitted.*

3. Sutin, N. Nuclear, Electronic, and Frequency Factors in Electron-Transfer Reactions. *Acc. Chem. Res.* **1982**, *15*, 275-282; DOI: 10.1021/ar00081a002.

4. Marcus, R. A.; Sutin, N. Electron Transfers in Chemistry and Biology. *Biochim. Biophys. Acta* **1985**, *811*, 265-322; DOI: 10.1016/0304-4173(85)90014-X.

5. Barbara, P. F.; Meyer, T. J.; Ratner, M. A. Contemporary Issues in Electron Transfer Research. *J. Phys. Chem.* **1996**, *100*, 13148-13168; DOI: 10.1021/jp9605663.

6. Shinkle, A. A. Non-Aqueous Single-Metal Redox Flow Batteries. Ph.D. Thesis, University of Michigan, Ann Arbor, MI, 2013.

7. Yarranton, J. T.; Staples, R. J. Unpublished results.

8. Jamula, L. L. Design and Synthesis of Iron(II) Terpyridyl Complexes for Application in Dye-Sensitized Solar Cells. Master's Thesis, Michigan State University, East Lansing, MI, 2010.

9. Jamula, L. L. Exploring Design Strategies to Tune the Electronic Structure and Ultrafast Dynamics of Iron(II) Polypyridyl Chromophores. Ph.D. Thesis, Michigan State University, 2013.

10. Britz, A.; Assefa, T.; Galler, A.; Gawełda, W.; Khakhulin, D.; Doumy, G.; March, A. M.; Németh, Z.; Pápai, M.; Roszályi, E.; Cho, H.; Kim, T. K.; Yarranton, J. T.; Mukherjee, S.; Schoenlein, R. W.; Jakubikova, E.; Huse, N.; McCusker, J. K.; Southworth, S. H.; Young, L.; Vankó, G.; Bressler, Ch. $[Fe(dcpp)_2]^{2+}$ Ligand-Field Excited State Geometry and Spin Characterized with Combined Ultrafast X-ray Spectroscopies. *Submitted.*

11. Lumpkin, R. S.; Meyer, T. J. Effect of the Glass-to-Fluid Transition on Excited-State Decay: Application of the Energy Gap Law. *J. Phys. Chem.* **1986**, *90*, 5307-5312; DOI: 10.1021/j100412a080.

APPENDIX B. ULTRAFAST PULSE DURATION DETERMINATION

1. Ultrafast Pulses

The advent of ultrafast laser systems brought about an entirely new set of challenges to spectroscopists, evoked by the ultrashort nature of the laser pulses. Many applications for laser spectroscopy require that pulses be as short as possible, a restriction that brings about many unwanted side-effects in the generation and characterization of these pulses. From the Heisenberg Uncertainty Principle the time-bandwidth product can be derived:

$$\Delta t \Delta \nu \geq 0.441 \tag{B.1}$$

Here, the temporal bandwidth or time duration of the pulse (Δt) and the spectral bandwidth (Δν) are inversely related, their product yielding a value no less than 0.441 for pulses with a Gaussian shape.[1] A pulse is said to be transform-limited if the temporal duration is as short as possible given the amount of available spectral bandwidth. The more spectral bandwidth provided, the shorter the pulses may be in the time domain. The generation of ultrashort pulses, therefore, requires large amounts of bandwidth in the frequency domain, which explains the appeal of broadband lasers.[2]

One laser system in our laboratory is shown in Scheme B.1. It is described in more detail in Chapter 4 of this work, and elsewhere.[3-5] The optical parametric amplifier (OPA) uses the output from the regenerative amplifier (regen) to generate a single wavelength beam with some approximately Gaussian distribution of frequencies. There are three main methods by which data may be collected: 1) one-color, 2) two-color, and 3) full spectra. These differ in their origin of the pump and probe beams and may be further differentiated in the detection scheme used to collect data. In (1), a one-color experiment refers to the use of the output from only a single OPA. This generates the pump beam, which is then separated by the use of beam splitter to allow for both a

pump and probe line of the same color. The two-color experiment (2), then, refers to the use of two OPAs to generate the pump and probe individually (Scheme B.1). This increases the number of pump-probe wavelength combinations that are available to the spectroscopist. Finally, (3) full spectral data collection uses one OPA to generate the pump, while the probe uses the regen output directly and propagates through some white light generating medium such that spectra can be collected over the entire visible region.

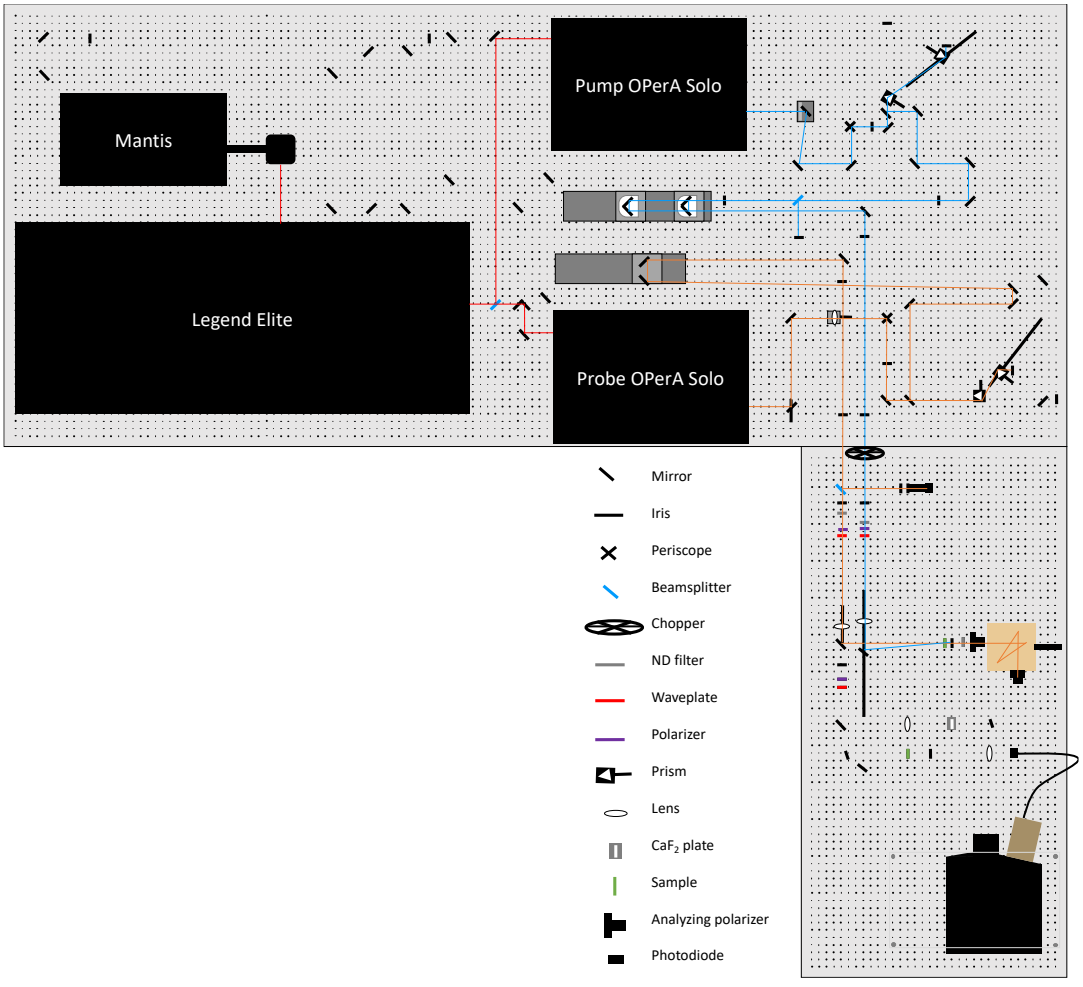

Scheme B.1. Schematic of the ultrafast laser setup that produces nominally 35 fs pulses out of the OPAs. A two-color experiment is shown in this layout, in which both OPAs are used to produce single wavelength pump and probe beams. For a more complete description, please see Chapter 4.

These experimental setups may be further altered in the choice of detection setup. If single-wavelength kinetics are desired, it is typical to use some type of wavelength separator, like a bandpass filter or monochromator (MC) with a single-channel photodiode. This setup is shown in Scheme B.2, but can be used in combination with any of the experiments mentioned. In this scheme, both the pump and probe are focused by a lens and turned by steering mirrors (black lines) such that the probe is focused directly into the sample and the focal point of the pump is slightly behind the sample (on the side of the detector). A beam block is used to keep the pump from entering the detector. A Glan-Taylor polarizing beam splitter (analyzing polarizer, AP) may be used after the sample in order to correct for polarization effects, or for use in pulse characterization.

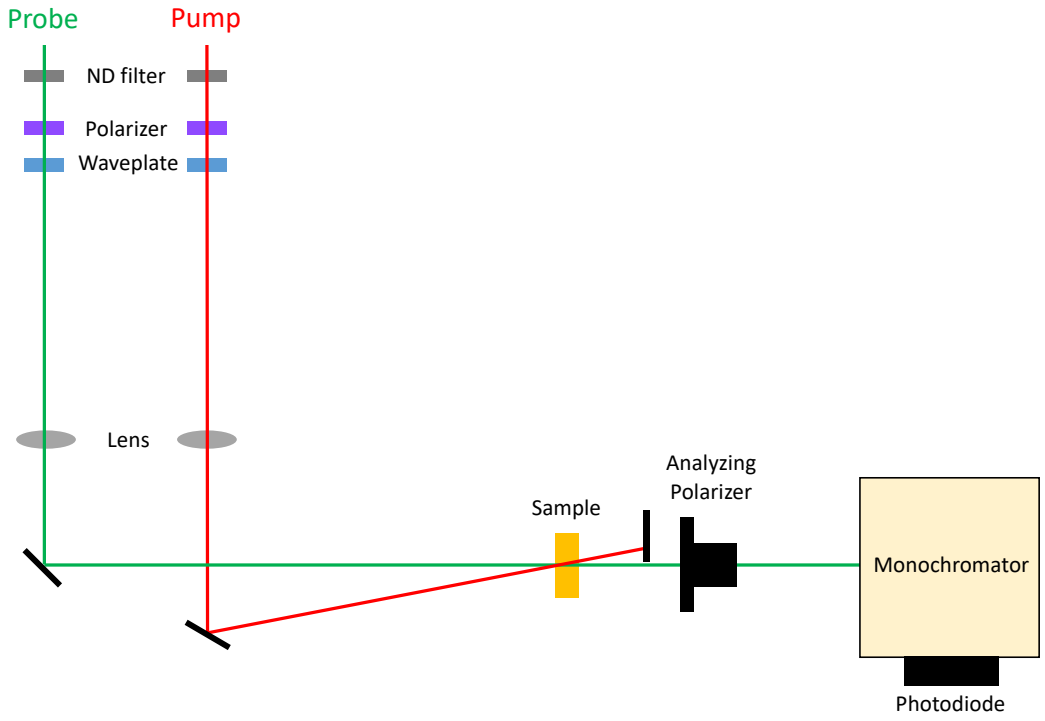

Scheme B.2. Enhanced view of the two-color setup near the sample and detection unit, from Scheme B.1. This layout and detection scheme may be used for other experiments, not just a two-color setup.

Alternatively, full spectral data collection may be desired. This can be used in conjunction with any of the three setups outlined above. In this case, no wavelength selector is used, and instead the probe beam after the sample is focused onto the face of a liquid light guide (as seen in Scheme B.1) or a fiber optic cable. This directs the beam into a spectrometer equipped with a grating to disperse the transmitted light that is then recorded by a multichannel photodiode array or charge-coupled device detector. This allows for all the probe wavelengths to be detected individually, as opposed to being treated as identical, which occurs with the single-channel photodiode. Ultimately, full spectral detection increases the spectral resolution of the data.

The pulses that emerge from the regen and the OPAs are nominally 35 fs in duration. Due to dispersion, however, these ultrashort pulses that have large spectral bandwidth are high in susceptibility to smearing temporally when they propagate through media. See Chapter 2 or Appendix F for further explanation. The laser system as shown in Scheme B.1 requires that the pump and probe propagate through – at a minimum – an ND filter (neutral density), a waveplate, a polarizer, a lens, and the sample in its cuvette. To preemptively compensate for the positive chirp introduced by these materials, a Brewster prism pair is used on the respective pump and probe lines to present negative or anomalous chirp.[6] This pair is implemented in a folded fashion, such that two prisms may do the work of four. When the pulse propagates through the first prism, spectral smearing occurs; passage through the second prism essentially acts to collimate beam such that no further spectral expansion happens. The beam is then reflected by a mirror back into the second prism, slightly above the position where it originally propagated through. In this step, the additional spectral bandwidth introduced allows the beam to be temporally compressed. The reverse passage through the prism also spectrally compresses the pulse. Finally, the beam traverses back through the first prism to recombine the pulse temporally, producing an ultrashort pulse. As

this pulse propagates through the optics on the laser table, it will be spread temporally; the precompensation of chirp afforded by the Brewster prism pair means that by the time the pulses reach the detector, they should be approximately 35 fs in duration again, provided the prism compensation is ideal.

Many applications require pulses that are as temporally short as possible. In conjunction with the highly susceptible nature of these pulses to dispersion, it is critical to thoroughly characterize ultrafast pulses. Unfortunately, there is no real consensus in the literature as to the best method for this. The methods outlined below are simply the techniques that we have chosen to use in our lab. Others exist, such as two-photon absorption,[7,8] frequency-resolved optical gating,[9] or spectral phase interferometry for direct electric-field reconstruction,[10] but will not be expanded on here. Ultimately, the methods utilized herein provide two critical pieces of information: the pulse duration (referred to as τ_{pulse} generally, or τ_{exc} or τ_{probe} for the pulse durations of the pump and probe respectively) and the instrument response function, or IRF. The latter refers to the dead time in a spectral measurement at early time that is due to the system itself. Any kinetics that are occurring during this time will be obscured by the response of the system. The IRF is then measured so that only true kinetics specific to the sample may be reported. Pulse durations may be found through the use of the optical Kerr effect or autocorrelation, whereas a cross-correlation measurement is used to determine the IRF of the system. In each of these collection methods, it is important to use the solvent that the sample of interest will eventually be dissolved in. Some solvents have drastically different responses to ultrafast laser pulses than others.[5] Furthermore, a sample cuvette should be used when characterizing the pulses that is similar if not identical to the cuvette that will hold the sample. In this way, a "blank" may be taken for the system, allowing the spectroscopist to differentiate between laser-related phenomena and true features originating from

the sample molecule.

Our laboratory also houses a second laser system, which is limited to (3). This discussion generally applies to that system, but due to its longer pulses and intended use (i.e., measuring nanosecond ground state recovery lifetimes in Fe(II) chromophores), chirp compensation and pulse characterization are not as critical. There is no prism pair on this laser system, and pulse characterization by the methods outlined below is performed only when short-time kinetics are collected.

2. Characterization Techniques

2.1 Cross-Correlation

Cross-correlation allows for the measurement of the time associated with the ultrashort pump and probe pulses interacting with each other and with the surrounding medium.[11] This interaction is known as cross-phase modulation and is used to describe two different pulses. These pulses may have been generated by two different means (e.g., two different OPAs, output from the regen and an OPA), and thus they must be mathematically treated as two separate entities.

Cross-phase modulation occurs because of the very high peak powers present in ultrafast pulses. While the energy of the pulse (E_{pulse}) may be relatively low (ca. 5 μJ), the peak power accounts for the ultrashort time duration of the pulse. when the average power (P_{ave}) of the laser beam is 3 mW, for example, the energy per pulse may be found by

$$E_{pulse} = \frac{P_{ave}}{f} \tag{B.2}$$

in which f is the repetition rate of the laser, 1 kHz for the systems used herein. In this example, the energy per pulse is 3 μJ. For a 50 fs pulse (τ_{pulse}), P_{peak} may be calculated using eqn. (B.3):

$$P_{peak} = \frac{P_{ave}}{f\tau_{pulse}} \tag{B.3}$$

Under these conditions, P_{peak} = 60 MW. Not only could such a power be extremely damaging, but it clearly will induce many power-related phenomena within the sample.

This incredibly high peak power may be utilized to measure the IRF of the system through the use of cross-phase modulation in a cross-correlation spectrum. The pump and probe are polarized at magic angle with respect to one another. When they meet temporally and spatially in the solvent, a huge amount of energy is transferred between the two pulses and into the solvent itself, inducing a large transient signal, despite the solvent not absorbing visible light. This can be seen in Fig. B.1. To determine the IRF, the signal is centered about $\Delta t = 0$. The IRF is taken as one-half the difference between when the signal starts to appear at negative time and when the signal returns to baseline at positive time. In a nanosecond system, the pulse powers are much weaker and thus a Gaussian is observed for this process, which is why the IRF for these systems is frequently reported in terms of a FWHM. With higher peak powers, the measured signal is often some derivative of a Gaussian, such as is seen in Fig. B.1.

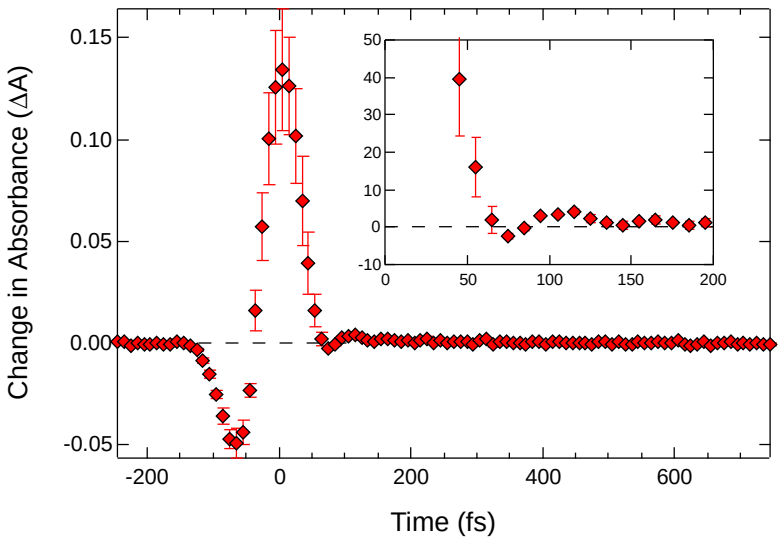

Figure B.1. Single-wavelength kinetics of acetonitrile upon excitation at 550 nm and probing at 530 nm. The resultant cross-correlation can be used to identify the IRF of the system, or one-half the time from when signal begins to appear until it returns to baseline. From the inset, the IRF for this experiment is 135 fs.

2.2 Optical Kerr Effect

The optical Kerr effect is a lensing process in which the high intensity of the pump beam induces a thermal change within the solvent. This effect may be used to characterize pulses through the use of the AP. The pump and probe enter the solvent at magic angle relative to each other, and the AP is set behind the solvent 90º to the polarization of the probe. This orientation means that when the pump and probe are not present at the same time within the sample, no light is transmitted to the detector, such that $\Delta A = 0$. The intensity of the pump introduces a third-order nonlinear distortion in the sample, causing a change in the polarization of the sample. As the probe propagates through this sample, it too is repolarized; the birefringence induced by the pump is then transmitted by the probe and allowed to pass through the AP to the detector. The 90º repolarization can only occur with both the pump and probe in the same at the same time. OKE, then, provides a

convolved Gaussian made up of the two pulses meeting in the sample (Fig. B.2), as expressed by

$$\tau_{conv}^2 = \tau_{exc}^2 + \tau_{probe}^2 \tag{B.4}$$

for which τ_{conv} is the convolution of the two Gaussians from the duration of the pump (τ_{pump}) and the duration of the probe (τ_{probe}).

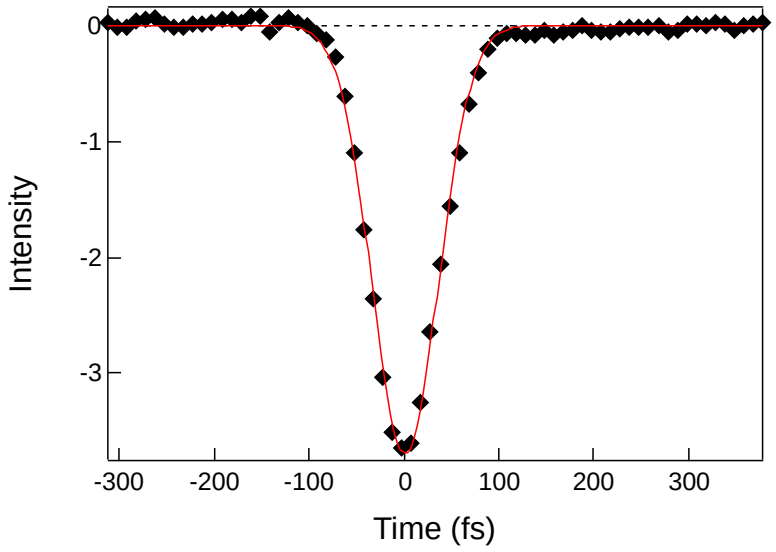

Figure B.2. OKE spectrum of methanol (black diamonds) upon excitation at 550 nm and probing at 530 nm. The data can be fit with a Gaussian curve (red trace) to yield pulse durations of the pump or probe pulses.

The Igor Pro curve fitting software can be used to determine the fit parameters for the Gaussian, according to eqn. (B.5).

$$y = y_0 + Ae^{\left(-\left(\frac{x-x_0}{width}\right)^2\right)} \tag{B.5}$$

It should be noted that the "width" parameter is neither the pulse duration nor the full-width at half maximum (FWHM), another common measure of ultrafast pulses. Instead, width in Igor corresponds to twice the deviation (c), which can then be related to the FWHM by

$$FWHM = 2\sqrt{2ln2}c \tag{B.6a}$$

$$FWHM \cong 2\sqrt{2ln2}\left(\frac{width}{2}\right) \tag{B.6b}$$

The FWHM is another measure of τ_{conv}, and the two can be used interchangeably. When implementing a one-color experiment, it is assumed that the pump and probe pulse durations are the same. This may or may not be a fair assumption, but it is used to simplify the math. Combining eqns. (B.5) and (B.6b) allows for the pump pulse duration to be found, according to:

$$\tau_{exc} = (width)(1.177) \tag{B.7}$$

If a two-color experiment is the final desired setup, a one-color experiment must be performed first in order to separately identify the pulse duration of the pump. Moving directly to a two-color setup without performing an OKE to solve for τ_{exc} will not allow τ_{probe} to be found. Once the OKE has found τ_{exc}, τ_{probe} may be determined by eqn. (B.8), in which the factor of 1.665 is derived from the fact that the two pulses interacting in the sample are distinct from one another.

$$\tau_{probe} = \sqrt{[(width)(1.665)]^2 - \tau_{exc}^2} \tag{B.8}$$

As was mentioned previously, different solvents produce different signals. Methanol and acetonitrile are typically used for OKE measurements, but acetonitrile often exhibits a long exponential decay on the positive side of the Gaussian, as shown in Fig. B.3.[12] Where the Gaussian function is induced by electronic reorientation caused by the change in instantaneous dipole moment, the exponential tail is the nuclear motion of the solvent reorganizing to accommodate that new electronic redistribution. Additionally, wings may be visible near the baseline of the Gaussian function; these may be seen on either the positive or negative side but are typically large on the positive end. The cause of these wings is third-order dispersion, often introduced by the Brewster prism pair. They may also be induced by the huge energy transfer of the pump pulse into the solvent, making the average pump power an important variable.

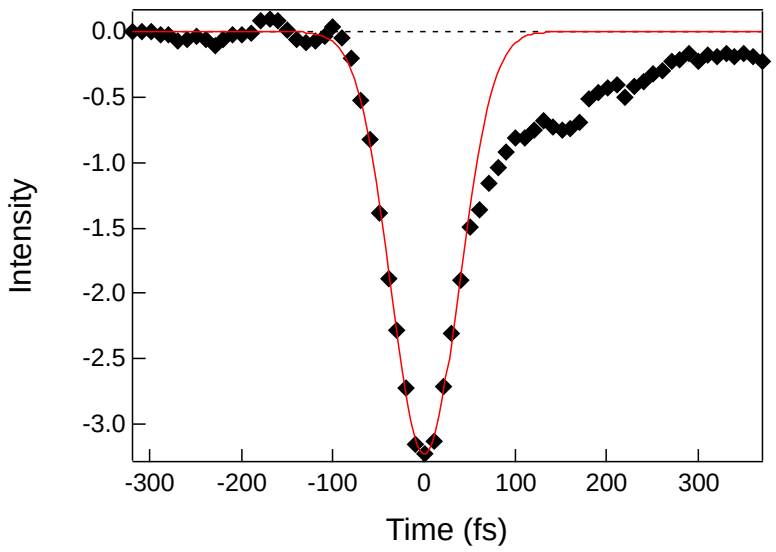

Figure B.3. OKE spectrum of acetonitrile (black diamonds) upon excitation at 550 nm and probing at 530 nm. Although the main signal is fit well with a Gaussian (red trace), there is an exponential decay at positive times.

2.3 Autocorrelation

It should be noted that a more commonly employed method for the determination of pulse durations is through the use of an autocorrelator.[13] This may be done in different ways, but the general theory is that a copy of a single pulse is made when it passes through a beam splitter. The two pulses are then directed to meet within a material, such that some nonlinear process occurs. One beam oscillates in time relative to the other so that a time-resolved pattern may be generated for the two pulses interacting with each other. An autocorrelator exists in our lab in which one beam is temporally shifted through the use of a mirror mounted on a speaker. The two pulses centered at λ = 800 nm from the regen output meet inside of a BBO crystal (β-barium borate). when the pulses meet spatially and temporally inside BBO, frequency doubling occurs, allowing for the generation of 400 nm light. This light is collected as a function of the distance the mirror

on the speaker is moved, providing a time-resolved autocorrelation spectrum.

3. Results as a Function of Experimental Setups

The cross-correlation and OKE spectra are highly dependent on the experimental conditions. This is not limited to the type of experiment being used (e.g., one- versus two-color), but is very specific to the exact pump and probe wavelengths, the pulse duration, peak powers of the respective pulses, the solvent being used, and other factors. Below is an accounting of some of these variables and their observed effects.

3.1 Pump/Probe Power Ratios

Because of the high prevalence of energy transfer in the cross-phase modulation and OKE phenomena, the powers of the pump and probe beams are of great importance. Moreover, the ratio of the powers between these two pulses is also of interest. A 10:1 power ratio of the pump/probe is often cited in the literature. This ensures that the pump is generating the excited state whereas the probe is monitoring the kinetics; if the probe power is too high, nonlinear effects may be observed. On the other hand, the pump power is meant to be greater than that of the probe, but if it is too high, similar nonlinear effects will be generated. This is why it is critical to ensure that the kinetics being monitored occur within the linear region. (To perform this check, look at the maximum of the signal when the pump and probe overlap. Then place a 0.3 ND filter in front of the pump, which should block 50% of the photons. If the signal now is equal to or less than 50% of what it was without the ND filter, then the system is in the linear regime. If the signal is greater than 50%, nonlinearity is occurring, and the pump power should be reduced until the linear regime is obtained.)

The effects of the pump and probe powers and the power ratio were measured in 1-octanol

(1-OctOH) and are displayed in Table B.1. To draw the most fair comparison, care was taken to ensure that regardless of probe power, I_0 at the sample was consistent. This was done by rotating the AP to be parallel with the probe polarization and attenuating the signal using the ND filter. The AP was turned back to 90º for the measurement. The pump pulse duration had been measured independently in a one-color experiment such that only τ_{probe} is under investigation here.

Table B.1. Summary of signal-to-noise ratios and probe pulse durations (τ_{probe}) from OKE data in 1-OctOH for λ_{exc} = 480 nm and λ_{probe} = 530 nm, as a function of the pump/probe power ratio.

Average Power (mW)		Pump/Probe Power Ratio	Signal/Noise Ratio	τ_{probe} (fs)
Pump	Probe			
4.0	0.4	10:1	1875	141
3.0	1.6	2:1	225	138
3.0	0.3	10:1	125	138
3.0	0.2	15:1	25	109
2.0	0.4	5:1	25	76
2.0	0.2	10:1	5	132

From these data, it can be seen that a reduction in either pump or probe power necessarily correlates with a reduction in S/N. Decreasing the pump power by 1 mW reduces the S/N ratio by an order of magnitude. Reducing probe power also decreases S/N, but to a lesser extent. At the 10:1 power ratio, the measured τ_{probe} is nearly constant at ~135 fs. Upon changing the ratio to 15:1 and 5:1, a decrease in τ_{probe} is observed, yielding 109 and 76 fs pulses, respectively. It is unusual that both an increase and decrease in the power ratio results in a decrease in pulse duration. Alternatively, when the power ratio is 2:1, the same ~135 fs probe pulse is observed. This is an effect of this combination being in the nonlinear regime. While these results may be generally

observed, the exact powers and power ratio must be determined for the sample and wavelengths being used, with reiterative checking of the linearity of the signal.

3.2 One- vs. Two-Color Experiments

One- and two-color experimental setups utilize laser beams that are generated from different sources, and therefore will inherently produce slightly different data when the pulses are being characterized. As discussed previously, a one-color OKE assumes that the two pulses meeting in the sample are nearly identical. This assumption is carried through to the cross-correlation performed. When a pulse is introduced from a different source, such as a second OPA or the regen, that pulse is more likely than not to be fundamentally different from the first pulse. Even if the wavelengths were the same between the pump and probe of a two-color experiment (remember, "two-color" refers to two separate sources of pulses, not necessarily two distinct wavelengths for the pump and probe beams), the spectral bandwidths of the pulses are likely to be different, which then propagates to the pulse duration. A comparison of cross-correlation spectra are shown in Fig. B.4. In this case, the amplitude of the observed signal greatly reduced for the two-color data relative to those collected in the one-color setup. That being said, the measured IRF was approximately constant between these two experiments at ~145 fs, indicating that the pump and probe pulses are likely similar.

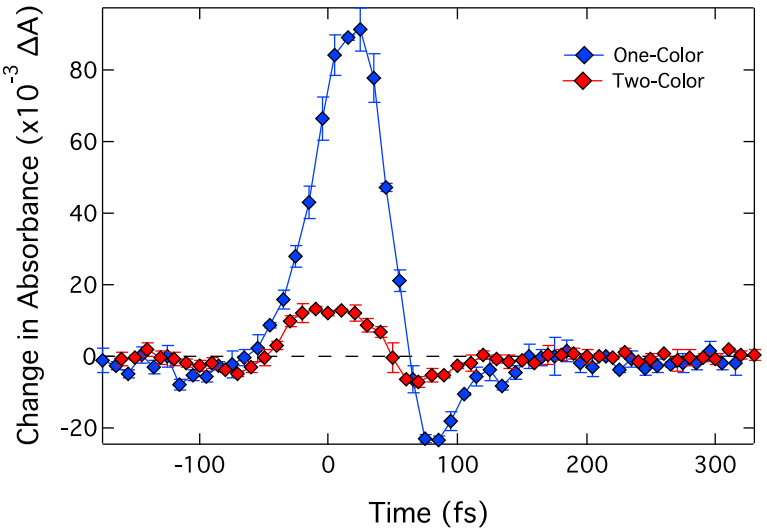

Figure B.4. Cross-correlation spectra of ethanol in a one- (blue) and two-color (red) experiment. In each the pump was 490 nm, and the probe for the two-color experiment was 530 nm. Both yielded an IRF of 145 fs.

3.3 Solvent

The nature of the solvent may play a role in the observed spectra used for pulse characterization. This is why it is critical to perform cross-correlations and OKE measurements in the solvent that will be used for the real experiment. These effects may appear benign or small in magnitude. Take, for example, the OKE spectra for a two-color experiment collected in methanol (MeOH) and ethanol (EtOH), shown in Fig. B.5. These spectra appear very similar and indeed yield pump and probe durations that are within 5 fs of each other. These differences, however, are more noticeable upon the collection of cross-correlation data (Fig. B.6). Relative to methanol, the IRF in ethanol has been increased by 20 fs, from 125 to 145 fs. When short-time kinetics are desired, this can be a major loss of observable temporal signal.

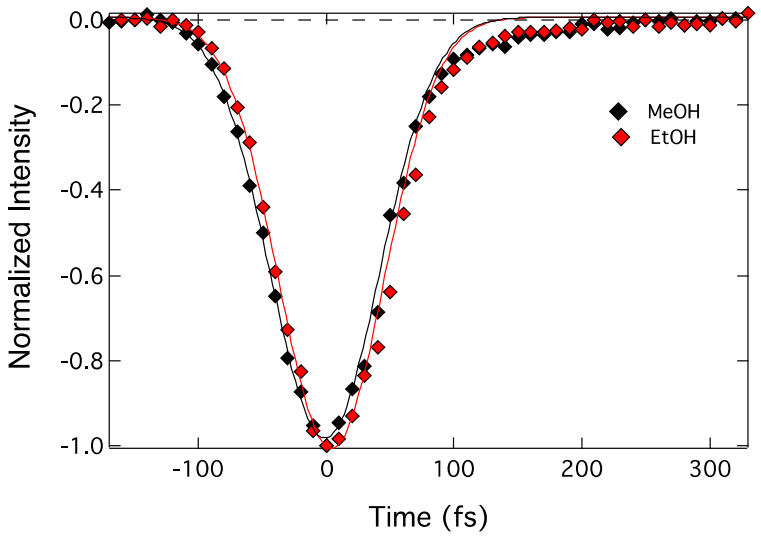

Figure B.5. OKE spectra collected for λ_{exc} = 490 nm and λ_{probe} = 530 nm in both methanol (black diamonds) and ethanol (red diamonds). When fit with a Gaussian, the pulse durations in methanol (black trace) and ethanol (red trace) may be found.

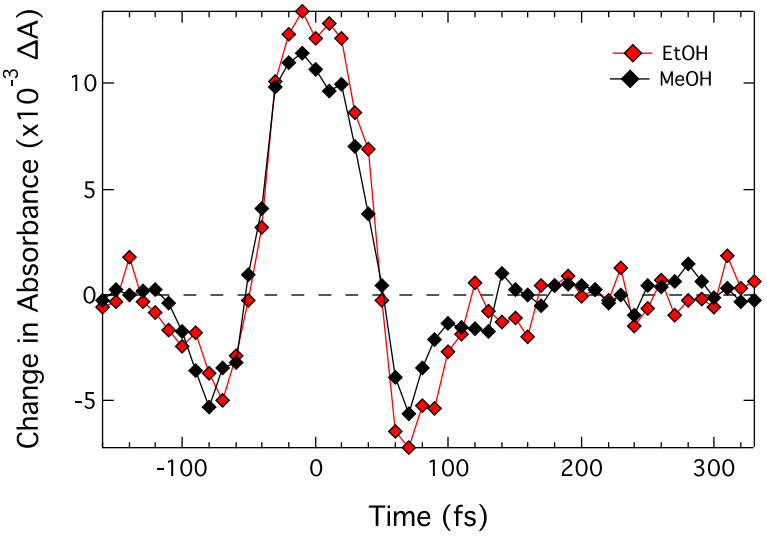

Figure B.6. Cross-correlations found in methanol (black) and ethanol (red) in a two-color setup utilizing a 490 nm pump and 530 nm probe. The IRF was found in each solvent, being 125 fs in methanol, and 145 fs in ethanol.

These cross-correlation spectra are changed more dramatically in moving to longer-chain alcohols (Fig. B.7), or when moving out of the alcohol family of solvents altogether. The shape of the signal changes noticeably from MeOH to 1-OctOH. It should also be pointed out that there are more third-order dispersion effects present in some of the spectra in comparison to others, as evidenced by the wings at both the negative and positive time ends of the signal. These wings will elongate the measured IRF for the system. From these data, it is clear that simply collecting a solvent spectrum in one solvent of a family is not sufficient when comparing data in many solvents. Some effects may be observable in a data set of one solvent that cannot be explained by a solvent trace collected in another.

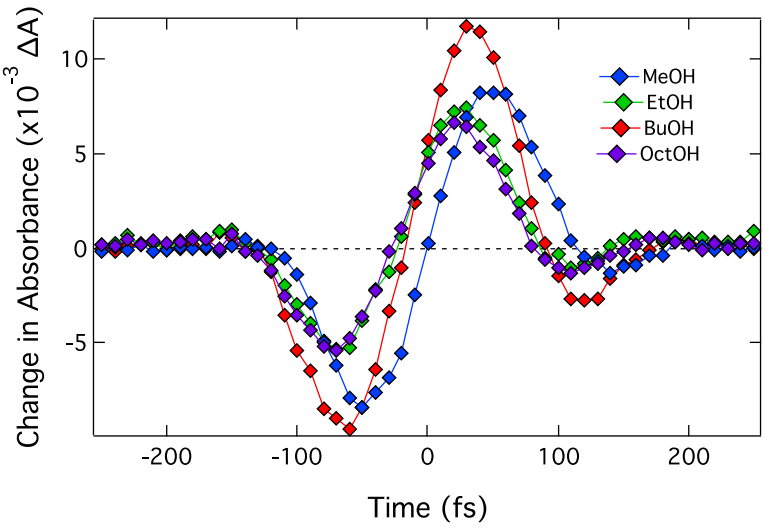

Figure B.7. Cross-correlation spectra in a series of 1-alcohols: methanol (blue), ethanol (green), 1-butanol (orange), and 1-octanol (purple). The pump and probe wavelengths used for this two-color experiment were 490 and 530 nm, respectively.

3.4 Detection Scheme

3.4.1 Monochromator and Single-Channel Photodiode

The first commonly employed detection setup is with a monochromator, or some other probe wavelength separator, and a single-channel photodiode. The input beam has a large spectral bandwidth owing to its ultrafast nature. It is therefore possible to probe at any wavelength within the probe bandwidth, as was done by tuning the MC for Fig. B.8. Here, a one-color experiment was being performed in which the pump and probe were nominally 600 nm. With this red wavelength, a very large bandwidth is achieved, and thus the effective probe wavelength was scanned from one end to the other, allowing for the time-zero kinetics of λ_{probe} = 579-617 nm to be measured. I_0 through the sample was kept constant through the use of the ND filter, a necessary precaution as the intensity of the signal at the red- and blue-most edges of the spectrum was very low. An interesting inversion of the Gaussian derivative signal was observed.

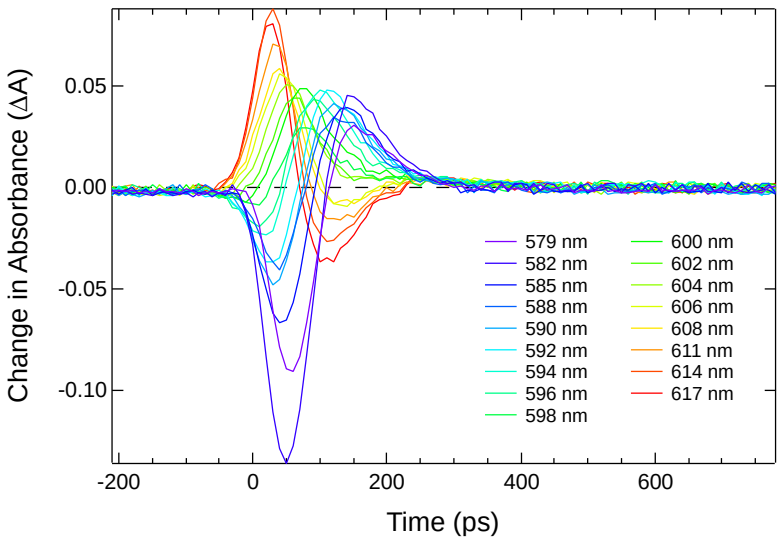

Figure B.8. One-color cross-correlation spectra collected in acetonitrile for λ_{exc} and λ_{probe} = 600 nm with the analyzing polarizer in place. The effective probe wavelength measured was scanned over the bandwidth of the probe (579-617 nm) through the use of a monochromator. Care was taken to ensure I_0 was the same for every probe wavelength.

In the data collected above, the AP was in place after the sample. To test its effect, the AP was removed and the same experiment was performed (Fig. B.9). In this case, the same sign swapping was observed, but the spectra collected show the inverted signal to begin with. Take λ_{probe} = 579 nm, for instance: in Fig. B.8 (with the AP in place), the first peak is a minimum, followed by a positive signal; in Fig. B.9 (without the AP), the first peak is positive and then decays into a negative signal. It is evident from these data that the AP is playing some role in the observed processes.

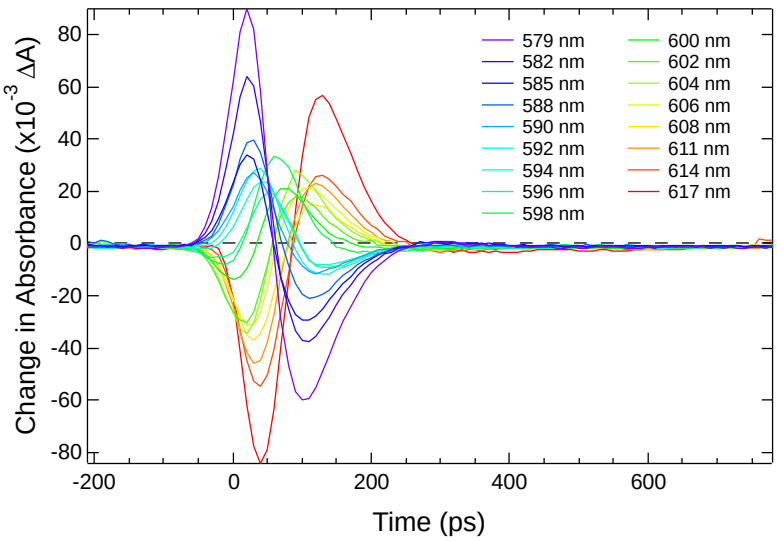

Figure B.9. One-color cross-correlation spectra collected in acetonitrile for λ_{exc} and λ_{probe} = 600 nm without the analyzing polarizer in place. The effective probe wavelength measured was scanned over the bandwidth of the probe (579-617 nm) through the use of a monochromator. Care was taken to ensure I_0 was the same for every probe wavelength.

OKEs were collected using this same technique of scanning the MC across the probe bandwidth to determine τ_{probe} and are compiled with a summary of the measured IRFs taken from Figs. B.8 and B.9. As the probe energy decreases, both the IRF measured with the AP and τ_{probe} decrease. This likely indicates that with bluer probes there is a greater degree of energy transfer, inducing third-order dispersions that affect the pulse duration and consequent IRF. A trend is not so evident in the IRFs measured without the AP. It can be said, however, that these values are consistently greater than those measured with the AP, evidence of the fact that pre-compensation with the prism pair was performed with the AP in place. The system must have been optimized in this setup, so removing the AP would actually result in longer observed pulses.

Table B.2. Summary of the cross-correlation results with and without the analyzing polarizer (AP) from Figs. B.8 and B.9 and the pulse durations (τ_{probe}).

λ_{probe} (nm)	IRF (fs)		τ_{probe} (fs)
	With AP	Without AP	
579	185	245	80
582	195	225	92
585	170	240	70
588	165	220	79
590	180	200	73
592	215	190	89
594	180	185	72
596	190	215	94
598	160	250	86
600	170	190	74
602	180	170	74
604	175	225	71
606	150	255	76
608	145	265	67
611	150	170	79
614	155	230	64
617	155	>375	57

Monochromators traditionally have both entrance and exit slits that serve to reduce the amount of ambient light entering the housing, as well as to limit the spectral bandwidth of the diffracted light exiting the housing and hitting the photodiode. In order to understand the effects of these slits, as well as the MC itself, on the measured IRFs and pulse durations, cross-correlation spectra were collected in acetonitrile with and without the AP in place (Figs. B.10 and B.11, respectively). There are huge temporal shifts in the removal of any one set of slits. The shape of

the spectra are also substantively different depending on which set of slits is in place or removed. Again, the AP appears to play a definitive role in the IRFs measured based on the inversion of the cross-correlation signal between Fig. B.10 (without the AP) and Fig. B.11 (with the AP in place).

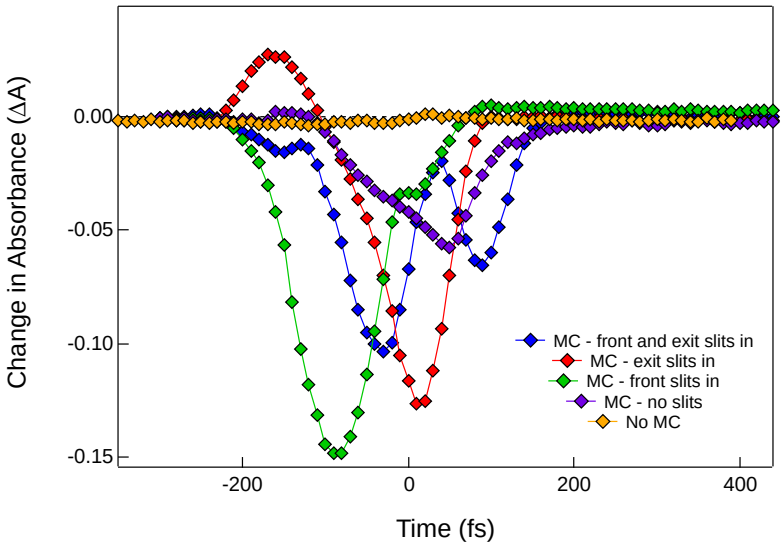

Figure B.10. Cross-correlation spectra in acetonitrile adjusting the use of entrance and exit slits with the monochromator: both slits in (blue), only exit slits in (red), only entrance slits in (green), no slits (purple), and the removal of the monochromator entirely (orange). Excitation occurred at 600 nm with probing at 480 nm. No analyzing polarizer was used to collect these data.

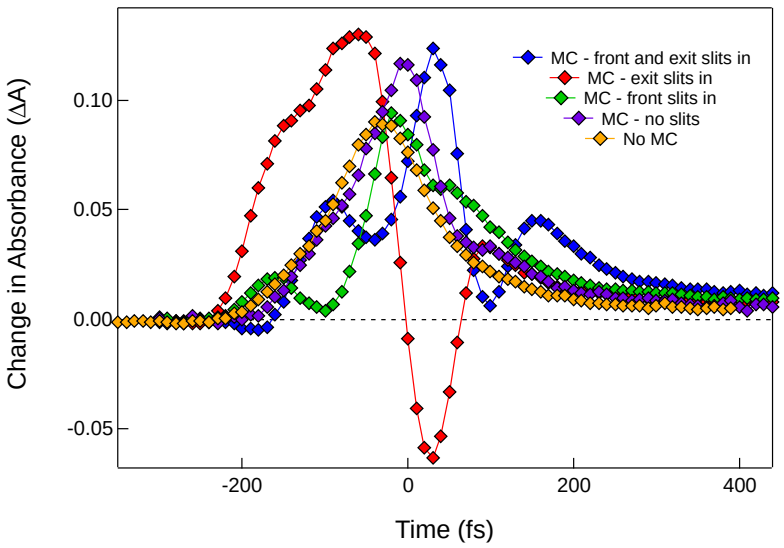

Figure B.11. Cross-correlation spectra in acetonitrile adjusting the use of entrance and exit slits with the monochromator: both slits in (blue), only exit slits in (red), only entrance slits in (green), no slits (purple), and the removal of the monochromator entirely (orange). Excitation occurred at 600 nm with probing at 480 nm. The analyzing polarizer was used to collect these data.

OKE spectra were then collected in acetonitrile while adjusting the placement of the slits in the MC, and also by removing the MC entirely. Temporal shifts are again observed. A significant attenuation in the magnitude of the signal is observed both when the exit slits are removed (but the entrance slits remain in place), and when the MC is removed. Interestingly, a double-Gaussian feature is observed when both sets of slits are in place. In this case, it appears as if two distinct pulses are propagating through the MC to reach the detector. The cross-correlation spectra appear to confirm this, as the shape of those have many features, a characteristic of multiple pulse phenomena. This double peak is not observed in any of the other spectra, implying that the use of both sets of slits in some way perpetuated the unusual behavior.

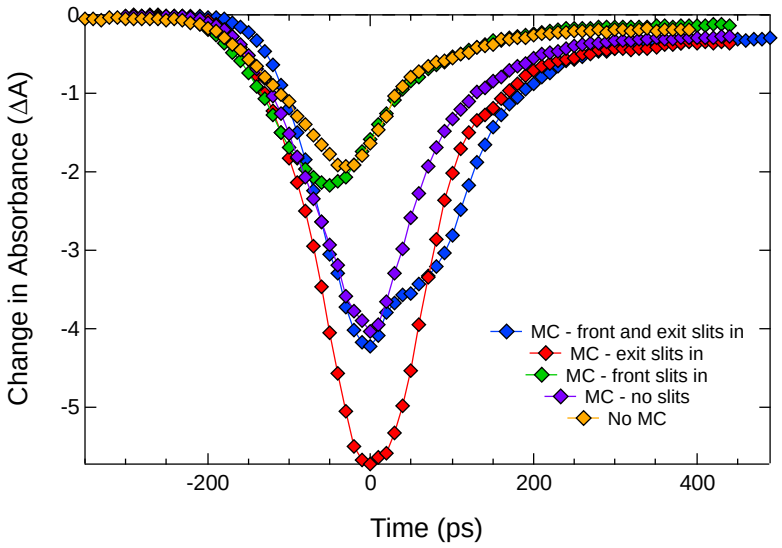

Figure B.12. OKE spectra in acetonitrile adjusting the use of entrance and exit slits with the monochromator: both slits in (blue), only exit slits in (red), only entrance slits in (green), no slits (purple), and the removal of the monochromator entirely (orange). Excitation occurred at 600 nm with probing at 480 nm. No analyzing polarizer was used to collect these data.

A comparison of the results given by Figs. B.10-12 are shown in Table B.3. Despite being measured at different pump/probe combinations with different amounts of excitation bandwidth (as evidenced by the respective τ_{probe}), the results are very similar between the two data sets. For these data, when the MC was in place, it was tuned to the central wavelength of the probe pulse. Primarily, the longest measured IRF is found when the AP is in place, and both sets of slits are in the MC. In this case, the chirp compensation was performed without the AP, meaning that its nearly 1" of glass introduces a great amount of chirp that effectively elongates the measured pulse duration. The IRF is consistently shorter by an average of nearly 50% without the AP in place. It is further shortened either by the removal of both sets of slits, or by removing the MC entirely. From the spectra above, however, it is known that without the slits or the MC, the magnitude of the signal is drastically reduced. The observed pulse durations as measured by OKE is relatively

constant regardless of the detection scheme. Removing the entrance slits should have the effect of increasing I_0 and thus allowing for a greater signal to be observed. The exit slits, however, reduce the effective bandwidth that is measured. There are indications that this will result in a longer observed pulse duration, in which case full spectral detection of the pump and probe is desirable.

Table B.3. Summary of one-color studies for acetonitrile, including the cross-correlations with and without the analyzing polarizer, OKE-determined pulse durations.

$\lambda_{exc}/\lambda_{probe}$ (nm)	Slits	IRF				τ_{probe} (fs)	% Change[b]
		With AP (fs)	% Change[a]	Without AP (fs)	% Change[a]		
600	Front and Exit	260	-	115	-56	68	-
	None	210	-19	1600	-39	65	-4
	No MC	185	-29	100	-62	73	+7
590	Front and Exit	260	-	105	-60	36	-
	None	215	-17	125	-52	37	+3
	No MC	200	-23	60	-43	35	-3

a Percent change for cross-correlations calculated relative to the value found with the AP both slits in place.

b Percent change for OKE pulse durations calculated relative to the value found with both slits in place.

3.4.2 Full Spectral Detection

Full spectral detection allows for each of the probe wavelengths to be measured

individually. This experiment is incredibly useful when a white light probe is used but can also give meaningful information for one- and two-color experiments in which the probe pulse has less spectral bandwidth. Cross-correlation spectra were collected in acetonitrile in a one-color setup ($\lambda_{exc} = \lambda_{probe} = 600$ nm) both with and without the AP in place, as shown in Figs. B.13 and B.14. For these data, no MC was used. An inversion of the sign of the signal occurs as the probe wavelength shifts from bluer to redder wavelengths. The point of inversion appears to be around $\lambda = 600$ nm. Interesting, spectral features are observed from ca. 530-670 nm, which is much greater than the spectral bandwidth of the 600 nm light, for which $\Delta\nu$ is approximately 25 nm. This is another indication of energy transfer between the two pulses, otherwise these frequencies would be inaccessible given the spectral bandwidth of the pump and probe.

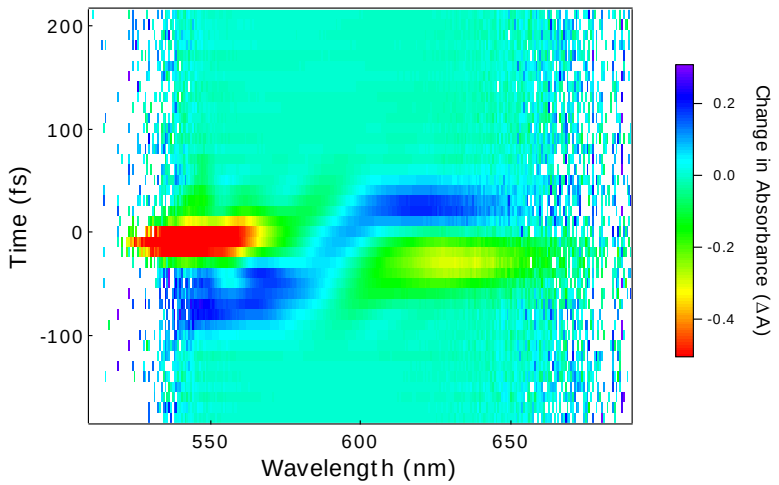

Figure B.13. Full spectral cross-correlation data collected in acetonitrile. The pump and probe wavelengths were 600 nm in this one-color setup. No analyzing polarizer or monochromator was used to collect these data.

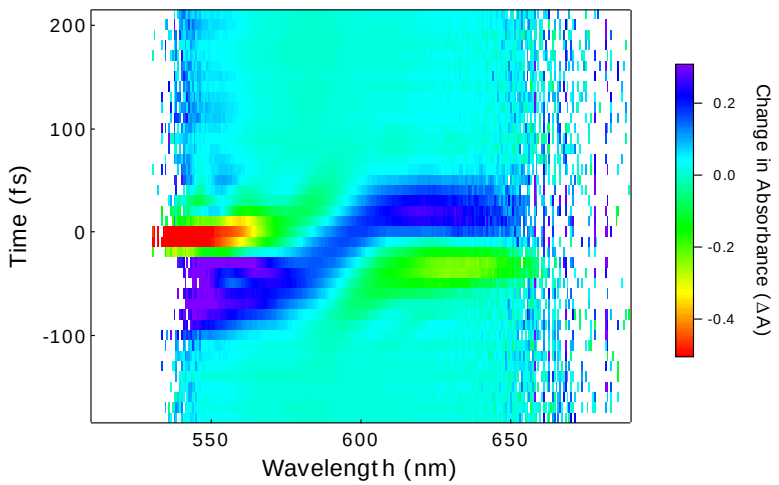

Figure B.14. Full spectral cross-correlation data collected in acetonitrile. The pump and probe wavelengths were 600 nm in this one-color setup. No monochromator was used to collect these data, but the analyzing polarizer was in place after the sample.

The AP does not appear to play much of a role in these spectra, and the relative signs of the observed signals are the same with or without it in place, which was not true when the MC was used. It is likely, then that the unusual effects observed previously (Figs. B.8 and B.9) were due to the combined use of the MC and AP.

An OKE may also be collected by full spectral detection, as is shown in Fig. B.15. The same one-color experiment with $\lambda_{exc} = \lambda_{probe} = 600$ nm in acetonitrile was used without the MC in place. The spectrum is very unusually in that two Gaussian forms appear for any given Δt, but at any select probe wavelength (Fig. B.16), only one Gaussian would be visible (Fig. B.17). Additionally, neither of these peaks is centered around 600 nm, which is the central wavelength of both the pump and probe beams. Based on Fig. B.16, for which the spectrum is shown at $\Delta t = 0$, the two features are centered around 560 and 615 nm. This is likely another manifestation of energy transfer between the pulses in the solvent medium.

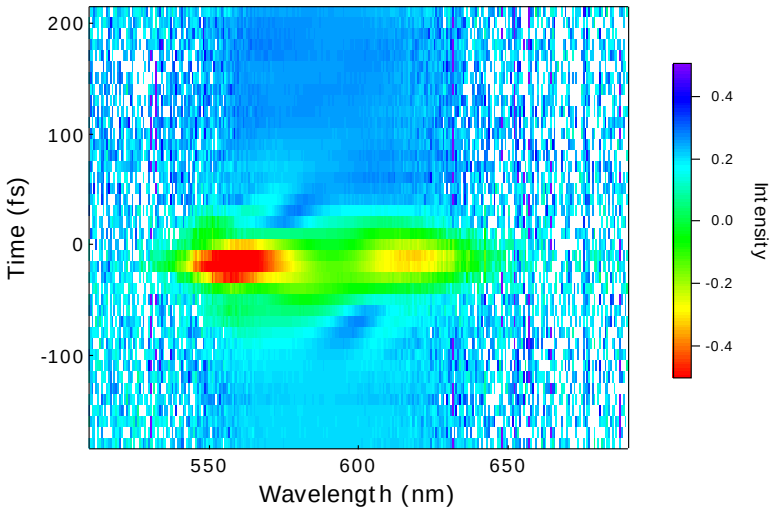

Figure B.15. Full spectral OKE data collected in acetonitrile. The pump and probe wavelengths were 600 nm in this one-color setup. No monochromator was used to collect these data.

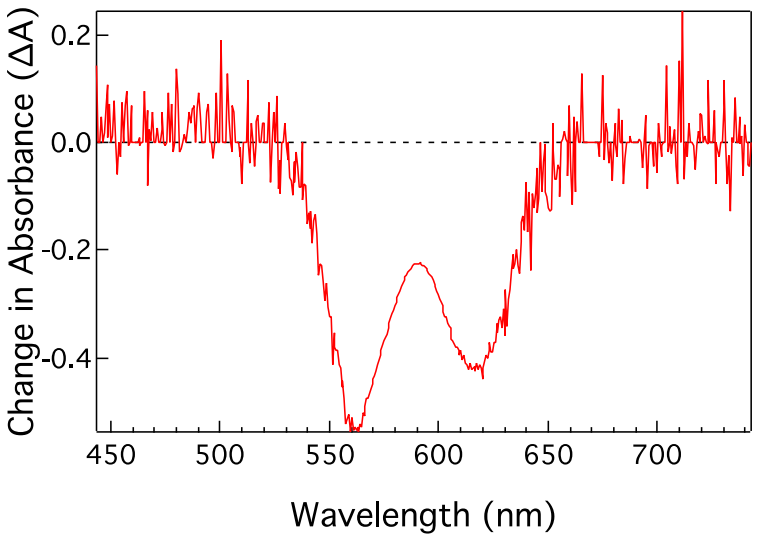

Figure B.16. A full spectral snapshot taken from Fig. B.15 when $\Delta t = 0$. This is the full spectral trace of the pump and probe within the acetonitrile solvent during the OKE event. The setup was a one-color experiment, with the pump and probe being 600 nm.

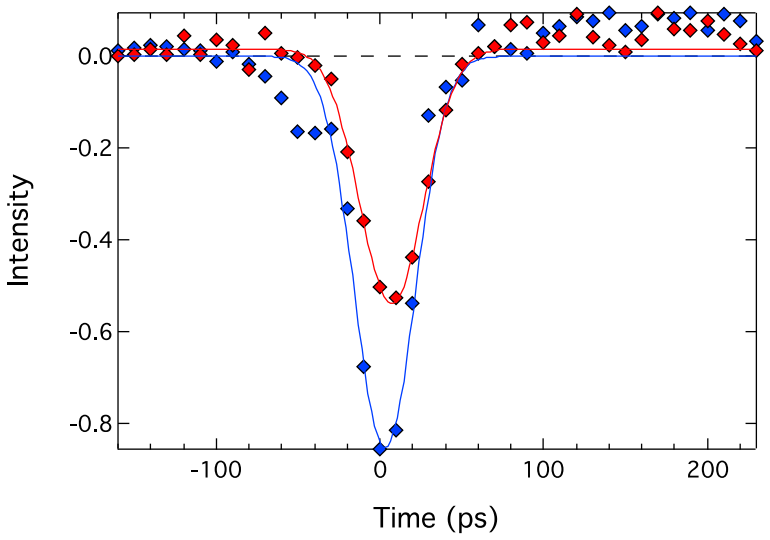

Figure B.17. Taken from Fig. B.15, these are the kinetic traces of the pump and probe within the acetonitrile sample during the OKE event for the probe wavelengths of 560 (blue) and 620 (red) nm. The setup was a one-color experiment, with the pump and probe being 600 nm.

Fig. B.17 shows the spectrum from Fig. B.15 versus the time access for λ_{probe} = 560 and 620 nm, approximately the center of the two Gaussians observed in the full spectrum. The observed pulse duration for the bluer peak is slightly longer by ~10 fs than that seen for the redder Gaussian. These data show how critical the choice of central wavelength is when performing single-wavelength experiments, particularly when the detection scheme utilizes a single-channel photodiode that is not capable of differentiating between different wavelengths of the probe spectra. The results displayed in Fig. B.15 are unusual and may be caused by the very large spectral bandwidth observed for 600 nm beams. It is also possible that this spectrum indicates that the pump and/or probe pulses are not chirped well.[5,9]

To further understand these effects, full spectral OKEs were performed in 1-OctOH for $\lambda_{exc} = \lambda_{probe}$ = 550 nm, as shown in Fig. B.18. In this case, the observed spectrum is perfectly round, indicating that the pump line is well chirp-corrected.[5] Upon the introduction of a 530 nm probe,

however, the OKE became more oblong and distorted (Fig. B.19). In neither case, however, was there a double-Gaussian present as was observed for the 600 nm one-color experiment from above. Performing the one- and two-color experiments with full spectral detection allows the spectroscopist to observe that while the pump beam is compensated well for chirp through the prism compressor, the probe line is not nearly as well corrected for dispersion. At some probe wavelengths, particularly on the blue- and red-most edges, a very short OKE may be measured, which would not be representative of the true pump-probe interaction in the sample.

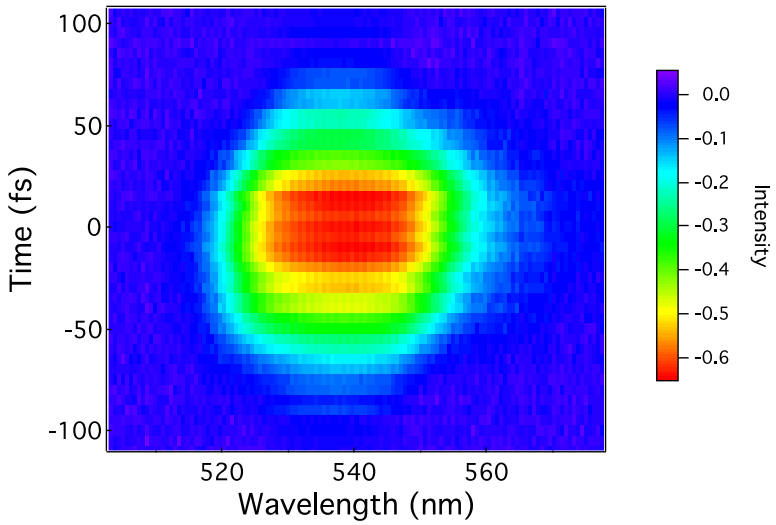

Figure B.18. Full spectrum of a one-color OKE experiment in 1-OctOH, for which the pump and probe wavelengths are 550 nm.

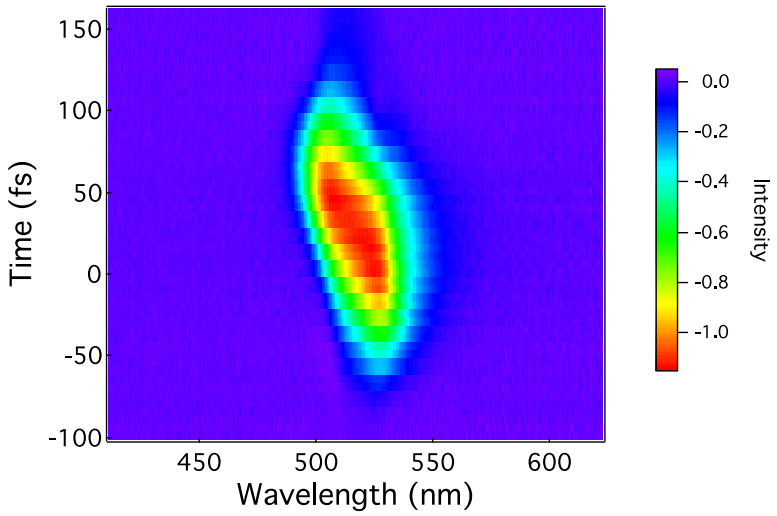

Figure B.19. Full spectrum of a two-color OKE experiment in 1-OctOH, for which the pump wavelength is 550 nm, and the probe is 530 nm.

Under the same set of conditions, a two-color cross-correlation was measured in 1-OctOH with full spectral detection (Fig. B.20). The same sign-switching is observed here as was found in the cross-correlation in acetonitrile for the 600 nm one-color experiment. The IRF also appears to become shorter as the probe wavelength energy is decreased. The kinetic traces for the two main features, specifically when λ_{probe} = 495 and 535 nm, are shown in Fig. B.21, as taken from the full spectral data. The sign inversion of the signal is the most dominant feature. It should also be noted that the relative magnitudes of the negative signals are vastly different between these two probe wavelengths. A small amount of temporal shifting is observed to occur (as is expected considering the wavelength-dependence of dispersion), but the overall IRF measured between these two probe wavelengths is largely unchanged.

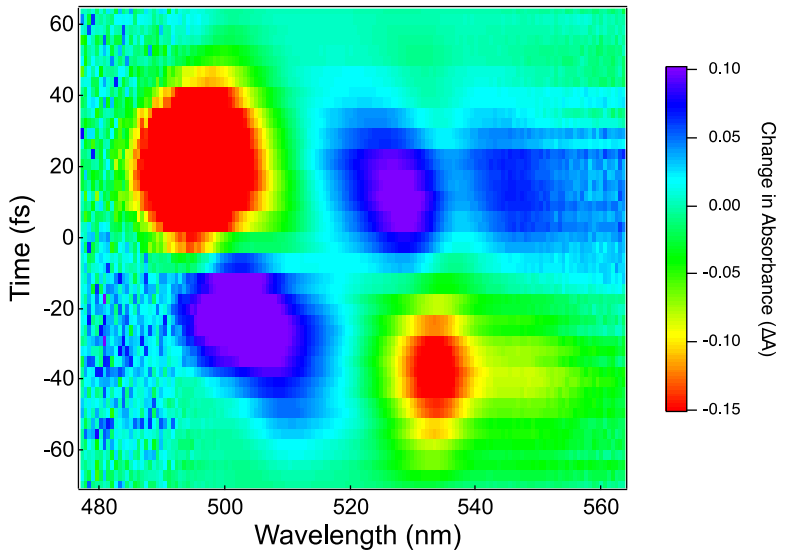

Figure B.20. Full spectrum of a two-color cross-correlation in 1-OctOH. Here, λ_{exc} = 550 nm and λ_{probe} = 530.

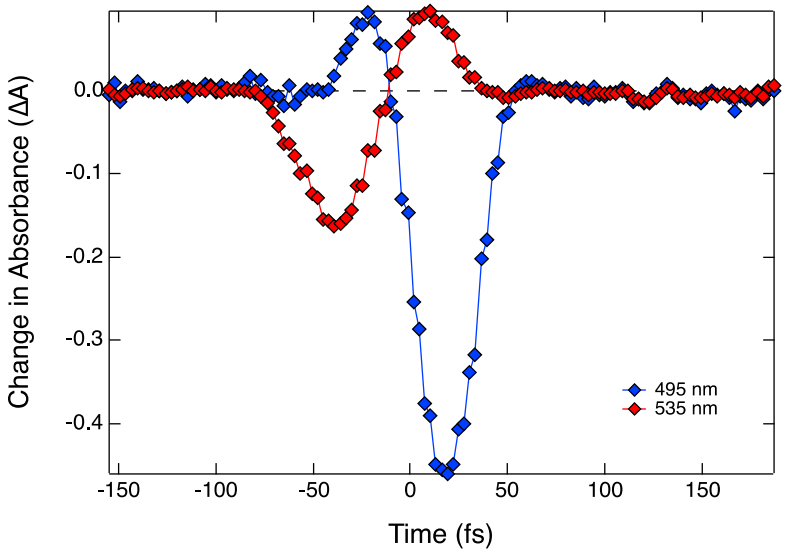

Figure B.21. Single-wavelength kinetics abstracted from the full spectrum in Fig. B.20. When probing at two different wavelengths, 495 nm (blue) and 535 nm (red), in the same spectrum, a similar IRF is observed despite having opposite signals.

The cross-correlation data taken from Fig. B.20 may also be plotted against the wavelength axis, as is done in Fig. B.22. While not as meaningful as the single-wavelength cross-correlation plot in Fig. B.21, these spectra serve to illustrate the extent of energy transfer within the sample through which the high-intensity pump and probe beams propagate. The pump and probe wavelengths used in this one-color experiment were 550 and 530 nm. It is not unusual in full spectral data to observe a high-intensity signal in the region of the pump pulse. Often, it appears as a distinct Gaussian sitting on top of other signals with smaller magnitudes. In this spectrum, however, no such feature is observed. This is highly unusual given the fact that 1-OctOH does not absorb in the visible region, in which the pump and probe lie. Many fluctuations are observed centered right around time-zero, as one would expect for a cross-correlation spectrum. However, huge amplitude swings are also observed at positive times in the blue part of the spectrum (λ_{max} = 490 nm), which is likely an effect of chirp in addition to energy transfer.

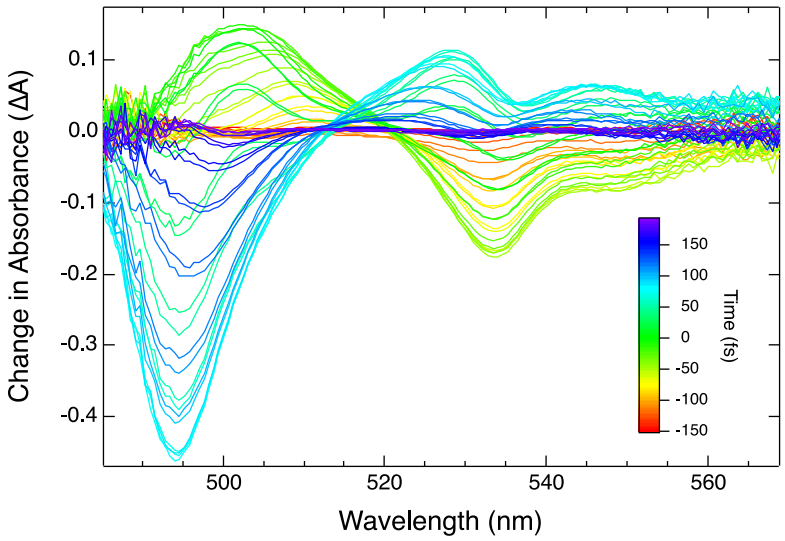

Figure B.22. Full spectral data from Fig. B.20 represented in a two-dimensional fashion. Here, a two-color cross-correlation is collected in 1-OctOH, for which λ_{exc} = 550 nm and λ_{probe} = 530.

4. Future Studies and Comments

Prior to ca. 2014, it was a long-held belief in this research group that only optics or processes that occur before or during the moment that the pump and probe pulses meet in the sample will have any effect on the respective pump and probe pulse durations. This has been repeatedly proven to be incorrect, and if taken for granted, may drastically alter data analysis. The effect of specific optics and changes were tested during the collection of two-color data, in which a 490 nm pump was used with a white light generated probe. A monochromator was placed after the sample and tuned to allow 530 nm light to pass into the photodiode. For the baseline setup, after the sample, the probe beam would traverse through an ND filter wheel, the monochromator, and a lens that was being used to focus onto the face of the photodiode. OKEs were taken in EtOH, as shown in Fig. B.23, upon the change in optic placement after the sample. Further results are summarized in Table B.4. They depict a clear trend of decrease in pulse duration as optics are removed. Additionally, the angling of optics so that they are more perpendicular to the beam also reduces the pulse duration as the pulse propagates through less optic material.

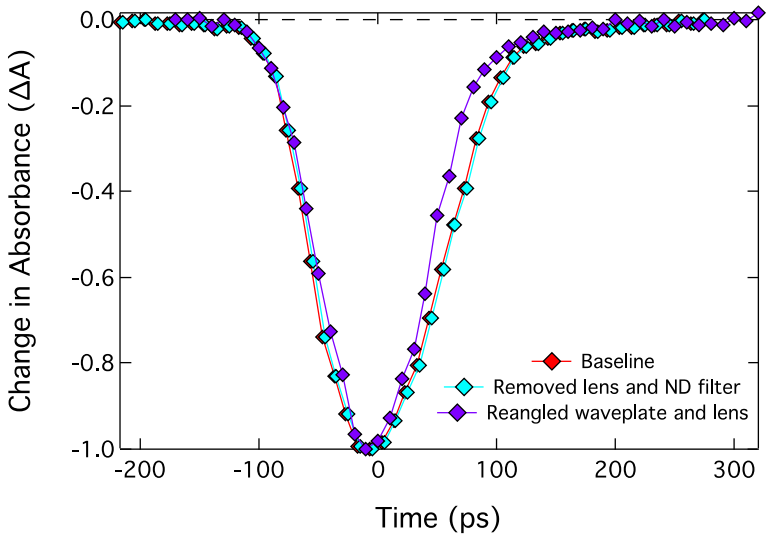

Figure B.23. OKE traces that were collected in ethanol in a two-color setup, in which a pump of 490 nm and a probe of 530 nm were used. The pump pulse duration was known from the one-color experiment, allowing for the probe pulse duration to be found. The baseline τ_{pulse} = 138 fs, removing a lens and ND filter yields τ_{pulse} = 97 fs, and further reangling other optics produces τ_{pulse} = 86 fs.

Table B.4. Summary of pulse durations by OKE as optics are removed and reangled after the sample for the data shown in Fig. B.23.

Change After the Sample	τ_{probe} (fs)
Baseline	138
Removed ND filter, reangled CaF_2	113
Removed lens focusing into photodiode	97
Reangled waveplate after CaF_2	91
Reangled lens focusing into CaF_2	86

Despite some of these changes being made after the sample position, including the removal of the ND filter and lens, the probe pulse duration is clearly affected. The lens after the monochromator alone appears to have accounted for 16 fs. This is not a perfect correlation as the OKE performed on the pump in the one-color experiment kept the optics and positions that were used for the baseline measurement in the two-color experiment, meaning that for a true understanding of the effect of these optics on the pump and probe, the one-color OKE should be repeated. Furthermore, chirp is wavelength dependent, as discussed in Appendix F. The result of this is an unequal effect of the optic medium on pump and probe beams of different wavelengths. A white light probe will see the greatest amount of dispersion due to its broad bandwidth.

To fully understand dispersion as it is affecting the experiment being performed, these tests should be undergone in the setup desired. Particularly, the choice of pump and probe wavelengths on the pulse duration is an undetermined quantity. The data reported herein largely displayed a one-color setup, or a two-color setup with specifically a ~480 nm pump and a 530 nm probe. The pulse duration should be tested as a function of pump-probe cross-sections, and the wavelengths observed should be expanded to include redder pumps and both redder and bluer probes. It would be interesting, as well, to determine if a 530 nm pump with a 480 nm probe behaves similarly as when these are reversed, as was reported here. There is an indication that the energy transferred from the pump into the sample is bandwidth-dependent, and redder wavelengths are capable of achieving greater bandwidths on this laser system. This may result in shorter measured two-color OKEs and IRFs.

Ultimately, to produce the shortest ultrafast pulses possible, the pulses must be allowed to propagate to the sample and again to the detector along a pathway that uses as few optics as possible. The Brewster prism pair can correct for an amount of chirp produced by these optics, but

(especially for the probe line) this system is as yet imperfect. It is therefore useful to remove unnecessary optics or select those that are specified for use with ultrafast pulses. These optics tend to be made of thinner materials, allowing for a reduction of dispersion relative to thicker optics. However, this may be a game of give-and-take, in that the removal of a lens after the monochromator will undoubtedly reduce the measured pulse duration, but it may have the unfortunate side-effect of also reducing the quality of the data. Polarization optics, especially, should be moved with care, and the polarization of the beams at the sample position should be checked before and after doing this in order to ensure that no unwanted polarization effects are observed.

REFERENCES

REFERENCES

1. Berera, R.; van Grondelle, R.; Kennis, J. T. M. Ultrafast Transient Absorption Spectroscopy: Principles and Application to Photosynthetic Systems. *Photosynth. Res.* **2009**, *101*, 105-118; DOI: 10.1007/s11120-009-9454-y.

2. Megerle, U.; Pugliesi, I.; Schriever, C.; Sailer, C. F.; Riedle, E. Sub-50 fs Broadband Absorption Spectroscopy with Tunable Excitation: Putting the Analysis of Ultrafast Molecular Dynamics on Solid Ground. *Appl. Phys. B* **2009**, *96*, 215-231; DOI: 10.1007/s00340-009-3610-0.

3. Brown, A. M.; McCusker, C. E.; Carey, M. C.; Blanco-Rodriguez, A. M.; Towrie, M.; Clark, I. P.; Vlček, A.; McCusker, J. K. Vibrational Relaxation and Redistribution Dynamics in Ruthenium(II) Polypyridyl-Based Charge-Transfer Excited States: A Combined Ultrafast Electronic and Infrared Absorption Study. *J. Phys. Chem. A*; DOI: 10.1021/acs.jpca.8b06197.

4. Miller, J. N. Ultrafast Dynamics of Iron(II)-Based Complexes in Solution and Semiconductor-Chromophore Assemblies. Ph.D. Thesis, Michigan State University, East Lansing, MI, 2018.

5. Foszcz, E. D. Understanding the Interplay Between Geometry and Ultrafast Dynamics in Ligand Field Excited States of Inorganic Chromophores. Ph.D. Thesis, Michigan State University, East Lansing, MI, 2015.

6. Fork, R. L.; Martinez, O. E.; Gordon, J. P. Negative Dispersion Using Pairs of Prisms. *Optics Lett.* **1984**, *9*, 150-152; DOI: 10.1364/OL.9.000150.

7. Damrauer, N. H.; McCusker, J. K. Ultrafast Dynamics in the Metal-to-Ligand Charge Transfer Excited-State Evolution of $[Ru(4,4'\text{-diphenyl-}2,2'\text{-bipyridine})_3]^{2+}$. *J. Phys. Chem. A* **1999**, *103*, 8440-8446; DOI: 10.1021/jp9927754.

8. Rasmusson, M.; Tarnovsky, A. N.; Åkesson, E.; Sundström, V. On the Use of Two-Photon Absorption for Determination of Femtosecond Pump-Probe Cross-Correlation Functions. *Chem. Phys. Lett.* **2001**, *335*, 201-208; DOI: 10.1016/S0009-2614(01)00057-4.

9. Radzewicz, C.; Wasylczyk, P.; Krasinski, J. S. A Poor Man's FROG. *Optics Commun.* **2000**, *186*, 329-333, and references therein; DOI: 10.1016/S0030-4018(00)01077-4.

10. Iaconis, C.; Walmsley, I. A. Spectral Phase Interferometry for Direct Electric-Field Reconstruction of Ultrashort Optical Pulses. *Optics Lett.* **1998**, *23*, 792-794; DOI: 10.1364/OL.23.000792.

11. Nicholson, J. W.; Jasapara, J.; Rudolph, W.; Omenetto, F. G.; Taylor, A. J. Full-Field Characterization of Femtosecond Pulses by Spectrum and Cross-Correlation Measurements. *Optics Lett.* **1999**, *24*, 1774-1776; DOI: https://doi.org/10.1364/OL.24.001774.

12. Nikiforov, V. G.; Shmelev, A. G.; Safiullin, G. M.; Lobkov, V. S. Coherent Control of Vibrational and Rotational Molecular Motions Using Double-Pulse Optical Kerr Effect. *Chem. Phys. Lett.* **2013**, *592*, 196-199; DOI: 10.1016/j.cplett.2013.12.023.

13. Steinmeyer, G. A Review of Ultrafast Optics and Optoelectronics. *J. Opt. A: Pure Appl. Opt.* **2003**, *5*, R1-R15; DOI: 10.1088/1464-4258/5/1/201.

APPENDIX C. MARCUS ANALYSIS

1. Initial Assumption of Driving Force

In Chapter 2 of this work, the variable-temperature methodology was developed and described in detail. An integral component of that research is the analysis of the ground state recovery lifetimes of the various Fe(II) polypyridyl complexes as a function of temperature. For reasons outlined in Chapter 1, Arrhenius theory, eqn. (C.1), is well-suited to described the high

$$k_{nr} = Ae^{\left(\frac{-E_a}{k_B T}\right)} \tag{C.1}$$

temperature (i.e., 235-293 K) data. Here, k_{nr} is the nonradiative rate of ground state recovery, A is the frequency factor (rate in the absence of a barrier), E_a is the activation energy (energy required to overcome the barrier from reactants to products), k_B is Boltzmann's constant, and T is the temperature. Arrhenius theory can be modified to achieve semi-classical Marcus theory, eqn. (C.2):[1]

$$k_{nr} = \frac{2\pi}{\hbar}|H_{ab}|^2 \frac{1}{\sqrt{4\pi\lambda k_B T}} e^{\left(\frac{-(\lambda+\Delta G^o)^2}{4\lambda k_B T}\right)} \tag{C.2}$$

Here, H_{ab} is the electronic coupling constant, λ is the reorganization energy, and ΔG^o is the driving force for the reaction. The pictorial representation of these and the Arrhenius constants can be seen in Scheme C.1. H_{ab} is essentially a measure of the degree of communication between the two electronic states. Two states of the same spin would be expected to be highly coupled ($H_{ab} \gg \hbar\omega$, adiabatic), whereas two states of different spins are likely uncoupled ($H_{ab} \ll \hbar\omega$, diabatic).[1,2] Diabaticity, though, is an idealized state in which H_{ab} = 0 cm^{-1} and does not exist. What is used instead is the term non-adiabatic, which describes a system under the same $H_{ab} \ll \hbar\omega$ conditions but is not constrained to 0 cm^{-1}. The driving force, ΔG^o, is a measure of the energetic difference

between the two electronic states of interest. It is slightly different from the zero-point energy difference, which is specifically between the lowest vibrational states in each potential energy surface and would be true at very cold temperatures, whereas ΔG^{o} incorporates any thermal energy in the system. Finally, the reorganization energy is the energy required to transform the reactants into products without completing the electron transfer or surface crossing. Ultimately, while this parameter is described as being an energetic value, it also encapsulates all vibrational and nuclear motion of the complex prior to reaction, and thus gives an idea as to the nuclear coordinate. It should be noted that the potential energy surfaces in question are multi-dimensional and incorporate an array of nuclear coordinates made up of vibrational modes. However, implicit in each of the Marcus parameters (and Marcus theory in general) is that only one "active" nuclear coordinate is accessed and therefore H_{ab}, ΔG^{o}, and λ are defined according to a single-mode picture.

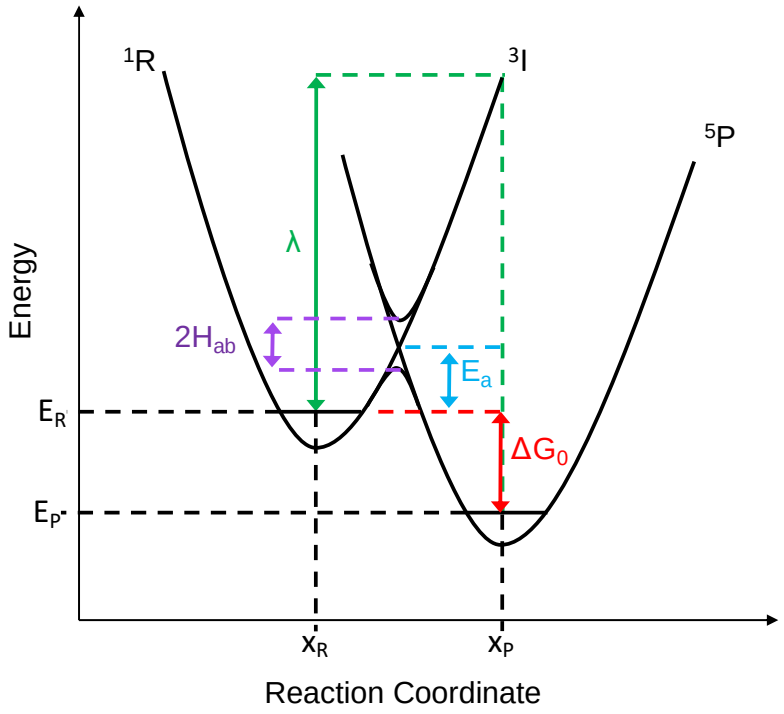

Scheme C.1. Generalized schematic for an exothermic reaction as defined with both Arrhenius and Marcus theory. Two potential energy surfaces (PESs) representative of the reactants with a singlet spin state (^{1}R) and quintet products (^{5}P) are shown in black lines. ΔG^o (red double-headed arrow) shows the energetic difference between these two surfaces (E_R and E_P), and reorganization energy (λ) is the given by a vertical green double-headed arrow but in fact represents motion from the reactants equilibrium position (x_R) along the side of the reactant PES to the equilibrium position of the product curve (x_P). The activation energy (E_a, blue double-headed arrow) is the energy required for the reactants to overcome the barrier to cross into the product curve. The magnitude of H_{ab} as given by the purple double-headed arrow determines the type of crossing: the gray lines that cross imply no electronic coupling and represent a diabatic reaction, whereas in an adiabatic scenario, the coupling is large enough such that an upper surface is accessed to act as an intermediate (^{3}I).

While this formulation is apt to describe the data collected herein, application of Marcus theory is made more complicated by the need to determine three unknown variables (H_{ab}, λ, and ΔG^{o}) with only two inputs (k_{nr} and T). The most that can be done with the information we have available to us, either through experimentally-determined or literature values, is to define the relative ratio of the three Marcus parameters to each other. This will be the most accurate representation of the data collected. However, we are also able to make educated approximations as to an appropriate range of values. For example, it is possible to calculate a range of values of H_{ab} and ΔG^{o} given λ = 0-50000 cm^{-1}, with the upper limit being taken arbitrarily: this would yield an unreasonable range of both the coupling constant and the driving force. There is no literature precedence for Fe(II) polypyridyl complexes having a reorganization energy even approaching 2 eV (17700 cm^{-1}). To be fair, obtaining literature values for λ in Fe(II) complexes is rather difficult. This would require both variable-temperature magnetic and transient absorption data to be collected. Sutin approximates this energy in $[Fe(bpy)_3]^{2+}$ (bpy = 2,2'-bipyridine) specifically to be on the order of 0.5 eV.[3] However, this value reflects the ground state recovery of the complex being in the inverted region, so when corrected for the Marcus normal behavior of $[Fe(bpy)_3]^{2+}$, a value closer to 1.3 eV is found. For spin-crossover complexes, this value is expected to be much lower, closer to 0.5 eV, due to the fact that the low- and high-spin states are structurally much more similar than in non-spin-crossover chromophores, thus reducing their reorganization energy.[4] λ would obviously be increased if the complex is in its solid state, at which point the matrix is much more restrictive, and thus the reorganization energy is increased; still the relative order of magnitude is less than ~1.5 eV.[5] Alternatively, SCO complexes are not always the best analogues for the Fe(II) polypyridyls being invested here, and in general are expected to have lower reorganization energies than chromophores such as $[Fe(bpy)_3]^{2+}$. To a first approximation, the

coordination environment around the Fe(II) center is generally more distorted in SCOs; this weakened metal-ligand orbital overlap is one cause for the SCO behavior.[6,7] The driving force for the $^5T_2 \leftrightharpoons {}^1A_1$ interconversion in these complexes is also drastically smaller relative to that of Fe(II) polypyridyls (~200 vs. ~7000 cm^{-1}, respectively). With ground state recovery occurring in the Marcus normal region, the reorganization energy of SCO complexes must therefore also be greatly reduced relative to other Fe(II) compounds. Thus, while initially appealing, a comparison to Fe(II) SCO compounds may in fact be misleading. Unfortunately, the only other remotely comparable studies in which Marcus parameters are found are performed on Fe(II) porphyrins,[8] Fe(II) centers in proteins such as heme,[9] and Co(III/II) polypyridyls,[10] each a worse analogue than the last. We will therefore base our analysis on SCO complexes where appropriate but will largely work within ranges that seem scientifically reasonable.

All that being said, the easiest path is to assume an initial value of one of the Marcus constants and calculate the other two. While this may potentially be more misleading than just reporting simple ratios of unknown quantities, this method still provides information for a more constrained set of conditions. Previously, H_{ab} for Fe(II) has been determined by Buhks and coworkers to be 170 cm^{-1}.[11] This value was later cited by Hauser in fitting low-temperature data of the lifetime of $[Fe(bpy)_3]^{2+}$ as doped into a $[Zn(bpy)_3](PF_6)_2$ matrix.[12] From these data, Hauser determined that the free energy difference between the $^5T_2$ and $^1A_1$ states was on the order of 3000 cm^{-1} when H_{ab} ~ 150 cm^{-1}. This is less than half of the driving force predicted by Sutin, who calculated ΔG^o = -7300 cm^{-1} in $[Fe(bpy)_3]^{2+}$.[3] Even more interestingly, Sutin predicted this driving force from an estimate of H_{ab} that covered two orders of magnitude, specifically 20-200 cm^{-1}, which clearly encompasses the values calculated and used by Jortner and Hauser, respectively.

It should be pointed out, though, that the assumptions Jortner based his calculations on

were inherently faulty. For example, the Fe(II) free ion was used as the basis, which has almost zero covalent character – a far cry from the highly covalent $\{Fe(N)_6\}^{2+}$ complexes studied by Hauser, Sutin, and others. The degree of covalency is propagated through the calculation by a spin-orbit coupling parameter (ξ): the greater the degree of covalency, the smaller the spin-orbit coupling value, as evidenced by eqn. (C.3).

$$H_{ab} = -3\sqrt{2}\xi^2\left(\frac{1}{\Delta E_1} + \frac{1}{\Delta E_2}\right) \tag{C.3}$$

ΔE_n here denotes the free energy between the excited states. Typically, this would involve only the two states that make up the interconversion. However, the $^5T_2 \rightarrow {}^1A_1$ transition is a $\Delta S = 2$ doubly spin-forbidden interconversion that must therefore occur via a triplet intermediate, here the ^3T ligand-field excited state, eqn. (C.4). The assumption explicit in these calculations is the near degeneracy of the $^1A_1$ and $^5T_2$ electronic states, as would exist in a spin-crossover complex.

$$\left\langle {}^1A_{1g}\middle|H_{SO}\middle|{}^3T_{1g}\right\rangle = -\sqrt{6}\xi \tag{C.4a}$$

$$\left\langle {}^5T_{2g}\middle|H_{SO}\middle|{}^3T_{1g}\right\rangle = \sqrt{3}\xi \tag{C.4b}$$

Furthermore, the Racah B and C parameters used by Jortner were found for a compound with octahedral symmetry, which $[Fe(bpy)_3]^{2+}$ does not have. This was an assumption made for simplicity, and many frequently make this assumption (including us), but it will result in inaccurate energies being found for states with degeneracies that could not possibly be supported by the actual geometry of the complex at hand. It should therefore be obvious that Jortner's H_{ab} estimate is likely much larger than reality. If the ξ value used was for the free Fe(II) ion, then it must be much greater than would be true for $[Fe(bpy)_3]^{2+}$; H_{ab} is proportional to ξ^2, and thus is likely to be drastically smaller than 170 cm^{-1}. We also know that this electronic coupling is used to calculate ΔG^o by Hauser, as given by eqn. (C.5):[12]

$$k_{nr}(T \rightarrow 0) = \frac{2\pi}{\hbar^2\omega}H_{ab}^2(FC)^2 \tag{C.5a}$$

$$p = \frac{\Delta G^0}{\hbar\omega} \tag{C.5b}$$

Here, ω is the frequency of the active vibrational mode, (FC) denotes the Franck-Condon factor, and p is the reduced energy gap that is deemed appropriate for spin-crossover conditions. The vibrational frequency of the active mode here is ~250 cm^{-1}. Again, we know H_{ab} must be an overestimated value; Hauser also explicitly states that p in this work is being used based on a SCO system, which means ΔG° is likely smaller form this calculation than in reality. Thus, it is apparent that H_{ab} must be $\ll 150$ cm^{-1}, as is appropriate for a highly non-adiabatic transition such as is undergone in the $^5T_2 \rightarrow {}^1A_1$ process, though the exact value cannot be narrowed down much more than that.

Contrary to what has been done by Jortner and Hauser, we are choosing to begin with an initial assumption of ΔG° rather than H_{ab}. We believe the driving force is a slightly more known quantity. To a certain extent, we can experimentally limit the range of values to being between k_BT and 19200 cm^{-1}. $[Fe(bpy)_3]^{2+}$ is not a spin-crossover complex and must therefore have a driving force greater than 200 cm^{-1}. The upper estimate comes from the fact that this energy is the maximum of the $^1MLCT \leftarrow {}^1A_1$ transition from ground-state absorption spectroscopy. This remains a rather large range of values available. Fortunately, there is a bit more consensus among the literature, for which ΔG° is typically described as being approximately 3000-9000 cm^{-1}, generally ~1 eV. We take our exact value from Sutin, who estimated ΔG° as being -7300 cm^{-1}.[3] There is a danger, though, that in reporting an exact driving force as opposed to Marcus parameter ratios we will be misleading in our confidence of any of the values calculated here. We attempt to mitigate any seeming dishonesty by applying rather large error bars such that the degree of uncertainty is represented. If the error bars were much larger, though, they would cause all the values to be statistically equal, thus the uncertainty was restricted to 10%.

Finally, the data that is analyzed and discussed in this appendix will be specific to $[Fe(bpy)_3]^{2+}$. This data set is representative of the other $[Fe(bpy')_3]^{2+}$ series of complexes, and in many ways, of all Fe(II) polypyridyls. Except where specified, the conclusions drawn here can be more broadly applied to all $\{Fe(N)_6\}^{2+}$ complexes. Even when spin-crossover and high-spin Fe(II) compounds are studied, the methods used herein are appropriate.[13] The major complication to this assessment is the lack of an exact ΔG^o value. With current methods, this value remains unknown to researchers for all the reasons outlined in Chapter 2. The ratios of parameters herein are accurate, but any "exact" values should be viewed critically.

1.1 Averages and Error Reported Within the Chapters

In this first section, a detailed description of the method of working up and analyzing variable-temperature ultrafast transient absorption measurements of the ground state recovery lifetimes that were used in Chapter 2 will be given, along with the error analysis. Other methods will then be explicated and compared. Data were collected for $[Fe(bpy)_3]^{2+}$ at each temperature at least twice (Fig. C.1). The Arrhenius parameters were checked in three different ways to determine self-consistency and the appropriate size of error. In the first method (Fig. C.2), each complete data set was worked up to determine the Arrhenius parameters for those data. All Arrhenius values for a given complex were averaged. Secondly, all the data were plotted as k_{nr} versus inverse temperature and A and E_a were calculated from the fit of the accumulated data (Fig. C.3). Finally, the average of all the data were plotted in an Arrhenius plot, and parameters were determined from the fit (Fig. C.4). In the case of $[Fe(bpy)_3]^{2+}$, the averages of E_a were within 10 cm^{-1} of each other. The same procedure was performed on A, and similar results were seen. These methods verify the robustness of the data collected.

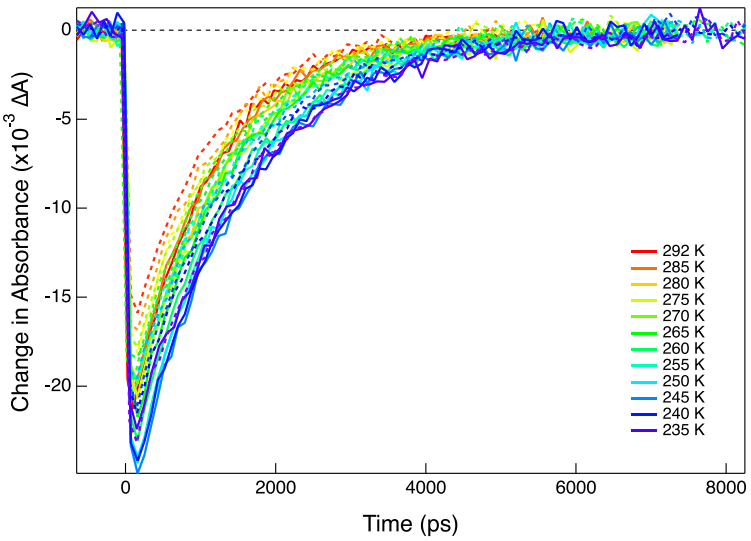

Figure C.1. Two sets of variable-temperature transient absorption data collected on the ground state recovery process of $[Fe(bpy)_3](PF_6)_2$ in MeCN. Excitation occurred at 490 nm with probing at 530 nm. One set is represented with a solid line, and the other with a dashed line. Even without normalization, both sets overlay well indicating good reproducibility.

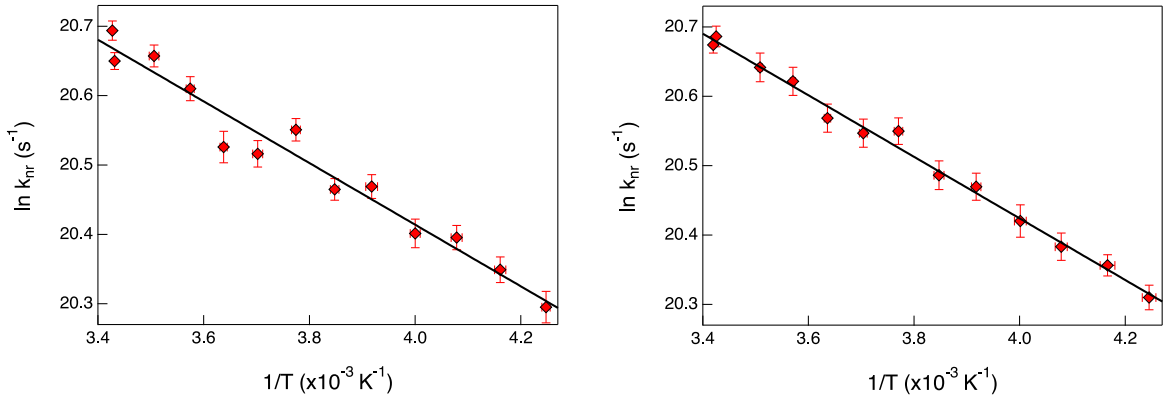

Figure C.2. Arrhenius plots for the data (red diamonds) shown in Fig. C.1 with the fits being the black trace. (Left) Data set 1 with $R^2 = 0.961$, $E_a = 309 \pm 19$ cm^{-1}, and $A = 233 \pm 24$ ps^{-1}. (Right) Data set 2 with $R^2 = 0.993$, $E_a = 309 \pm 8$ cm^{-1}, and $A = 229 \pm 10$ ps^{-1}. Both data sets are in good agreement with each other.

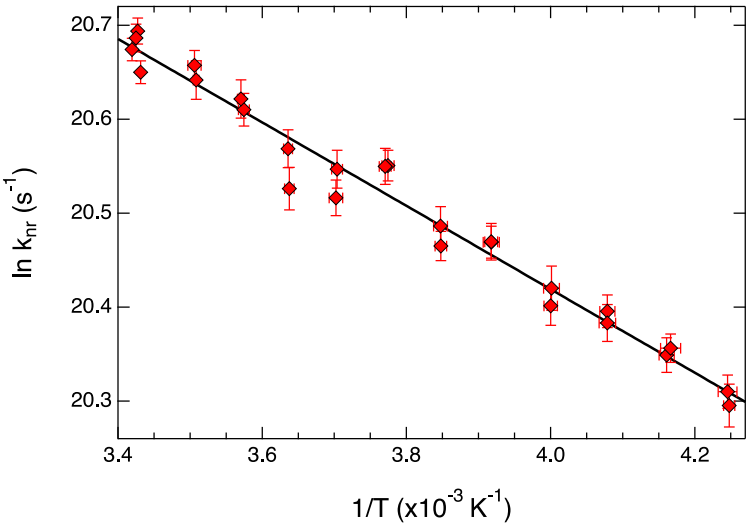

Figure C.3. Arrhenius plot fitting the combined total data from Fig. C.1 with the data in red diamonds and the fit being the black trace. This fit gives $R^2 = 0.975$, $E_a = 309 \pm 10$ cm^{-1}, and $A = 230 \pm 13$ ps^{-1}.

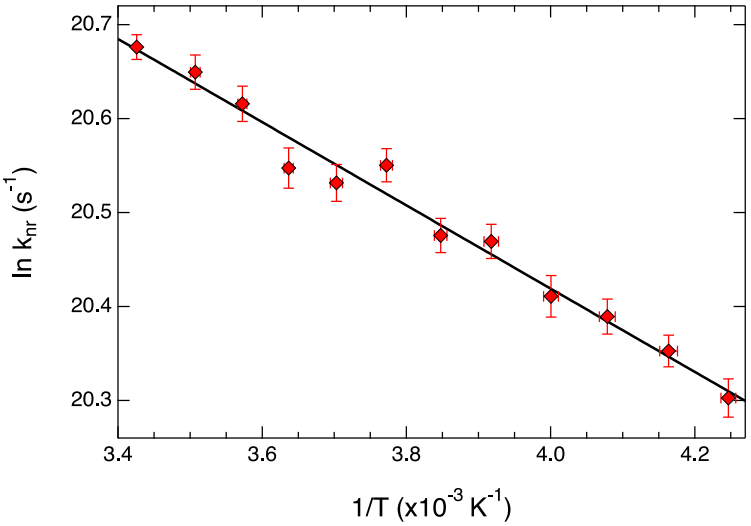

Figure C.4. Arrhenius plot fitting the data from Fig. C.1 when averaged at each temperature point, with the data in red diamonds and fit being the black trace. This fit gives $R^2 = 0.980$, $E_a = 308 \pm 14$ cm^{-1}, and $A = 232 \pm 18$ ps^{-1}.

In order to solve for Marcus parameters, relationships to the Arrhenius equation must be utilized. With an initial value of ΔG^o = -7300 ± 730 cm^{-1} assumed from Sutin[3] and the value of A found from the Arrhenius plots, eqn. (C.6) is used to find the two values possible for λ due to the parabolic nature of the Marcus activation energy:

$$E_a = \frac{(\lambda+\Delta G^0)^2}{4\lambda} \quad \text{(C.6)}$$

For example, for $[Fe(bpy)_3]^{2+}$, ΔG^o = -7300 ± 730 cm^{-1} and E_a = 310 ± 15 cm^{-1}. From these, λ = 4850 or 10980 cm^{-1}. $[Fe(bpy)_3]^{2+}$ is believed to be barrierless, and in this region, $-\Delta G^o < \lambda$, therefore λ = 11000 cm^{-1}. To determine the size of the error bars on this value, the uncertainty of ΔG^o and E_a are propagated. For this, the "extreme ends" of each parameter are used in every combination to calculate λ, according to Table C.1. Ultimately, it is found that λ = 11000 ± 1000 cm^{-1}.

Table C.1. Propagating uncertainties in ΔG^o and E_a to calculate λ.

	ΔG^o (cm^{-1})	E_a (cm^{-1})	λ (cm^{-1})
Upper ΔG^o, Upper E_a	-6570	325	10200
Upper ΔG^o, Lower E_a	-6570	295	12000
Lower ΔG^o, Upper E_a	-8030	325	10000
Lower ΔG^o, Lower E_a	-8030	295	11700
Average	-7300 ± 730	310 ± 15	11000 ± 1000

While this method is not the analytical method of propagating error, it has the added benefit of returning realistic error bars. Eqn. (C.7)[14] may be used with the values from Table C.1 in

conjunction

For $M = A \pm B$ $$\delta M = \sqrt{(\delta A)^2 + (\delta B)^2} \quad \text{(C.7a)}$$

For $M = \frac{AB}{C}$ $$\delta M = |M|\sqrt{\left(\frac{\delta A}{A}\right)^2 + \left(\frac{\delta B}{B}\right)^2 + \left(\frac{\delta C}{C}\right)^2} \quad \text{(C.7b)}$$

For $M = A^B$ $$\delta M = \frac{|MB|\delta B}{|A|} \quad \text{(C.7c)}$$

with eqn. (C.8) which is derived from eqn. (C.6) to determine the statistical uncertainty of the reorganization energy.

$$E_a\lambda = \lambda^2 + (\lambda)(\Delta G^0) + (\Delta G^0)^2 \quad \text{(C.8a)}$$

$$\lambda = -\Delta G^0 + E_a \pm \sqrt{E_a^2 - E_a\Delta G^0} \quad \text{(C.8b)}$$

$$\delta\lambda = \sqrt{(\delta E_a)^2 + (\delta\Delta G^0)^2 + \frac{\sqrt{(2E_a\delta E_a)^2 + \left(E_a\Delta G^0\sqrt{\left(\frac{\delta E_a}{E_a}\right)^2 + \left(\frac{\delta\Delta G^0}{\Delta G^0}\right)^2}\right)^2}}{2\sqrt{E_a^2 - E_a\Delta G^0}}} \quad \text{(C.8c)}$$

Lowercase delta refers to the error associated with that value. Any constants in eqn. (C.6) are removed as they are considered exact numbers with zero uncertainty. With this method, $\lambda = 11000 \pm 4600$ cm^{-1} which is rather large and does not reflect the uncertainty associated with the measurements or even with the assumption of ΔG°. It also has the unfortunate side effect of masking any trends that might be observed when comparing across different complexes by causing all calculated values to be within error of each other. Therefore, the method outlined in Table C.1 is predominantly used when propagating error through the Marcus values within this work.

Once a value of λ has been determined, eqn. (C.9) can be used to solve for H_{ab} analytically.

$$A = \frac{2\pi}{\hbar}|H_{ab}|^2\frac{1}{\sqrt{4\pi\lambda k_B T}} \quad \text{(C.9)}$$

This is also how H_{ab}^4/λ is calculated. To verify the values of H_{ab} that were found using this method, A is used to calculate the H_{ab}^4/λ ratio for a variety of H_{ab} and λ values. Based on the error associated

with A, a range of ratios is therefore known. This range is explored within the given range of λ values as determined above to find the appropriate H_{ab} average and its uncertainty. For example: the preexponential factor for $[Fe(bpy)_3]^{2+}$ is 230 ± 20 ps^{-1}. In solving for H_{ab}^4/λ, the range found using eqn. (C.9) is 0.0286-0.0412. Using this ratio and the reorganization energy gives H_{ab} = 4.4 ± 0.2 cm^{-1}. From Table C.1, λ is known to fall within 10000-12000 cm^{-1}. A table is made for H_{ab} = 0-10 cm^{-1} in steps of 0.1 cm^{-1} for λ = 10000-12000 cm^{-1}. The only values of H_{ab} that give a ratio within the window found from the experimentally determined value of A for $[Fe(bpy)_3]^{2+}$ are 4.1-4.7 cm^{-1}, or H_{ab} = 4.4 ± 0.3 cm^{-1}. This range is in excellent agreement with the values found analytically.

The error associated with the H_{ab}^4/λ ratio is calculated in a similar fashion to how A in ps^{-1} is determined. These are both inverse functions of the true values that are found. In $[Fe(bpy)_3](PF_6)_2$ in MeCN, for example, A = (4.36 ± 0.40)×10^9 s^{-1}. We have chosen to show this in inverse picoseconds to describe the time constant of the barrierless process, which is more convenient and informative. Simply inverting the time constant and its error would yield A = 229 ± 2525 ps^{-1}. Instead, the inverse of (4.36 + 0.40)×10^9 and (4.36 - 0.40)×10^9 are taken, giving 210 and 252 ps^{-1}, respectively. The average, therefore, is 231 ps^{-1}, and the difference between the average and the sum/difference is 21 ps^{-1}, thus A = 230 ± 20 ps^{-1}. In all likelihood, this is an overestimate of the error bars. The process is repeated with H_{ab}^4/λ so that the ratio can be reported in a more easily digested fashion (i.e., 1/(30 ± 5) vs. 0.035 ± 0.006).

1.2 Relative Ratios of Marcus Parameters

The three Marcus parameters can be found either as discrete numbers as outlined above provided there is an initial estimate of one of those constants, or as ratios relative to each other. These are simply rough ratios and will vary with the complex being studied. From the exponential

in the Marcus equation, the driving force and reorganization energy are related by $(\Delta G^0)^2/\lambda$. In $[Fe(bpy)_3]^{2+}$ (which is in the Marcus normal region), this ratio is 4900 ± 1200. It was found that this ratio remains constant across the entire $[Fe(bpy')_3]^{2+}$ series of complexes and is within error at 4200 ± 1000 in $[Fe(terpy)_2](PF_6)_2$ (terpy = 2,2':6',2"-terpyridine) in MeCN, but is doubled to 10200 ± 2600 for $[Fe(dcpp)_2](PF_6)_2$ (dcpp = 2,6-bis(2-carboxypyridyl)pyridine) in MeCN. While the numbers themselves are meaningless, the trend seems to indicate that from $[Fe(terpy)_2]^{2+}$ to $[Fe(bpy)_3]^{2+}$ to $[Fe(dcpp)_2]^{2+}$, the increase observed could be explained by an increase in ΔG^o while λ is held constant: in other words, the complexes increase in ligand field strength in the normal region toward the barrierless region. This analysis is consistent with what is observed directly from the activation energy and in the comparison between k_{nr} and A. One would expect that upon reaching the Marcus inverted region, where ΔG^o continues to increase while λ decreases, the $(\Delta G^0)^2/\lambda$ would continue to grow at an exponentially faster rate.

The second ratio comparing the electronic coupling constant and driving force is a more difficult ratio to pin down analytically. This is due to the fact that ΔG^o is in the exponential as part of the activation energy, whereas H_{ab} is a function of the preexponential factor. If the exponential form were removed, what would be left is the $\Delta G^o/H_{ab}$ ratio. On the surface, this may be a decent approximation of the inverse proportionality between these parameters for these Fe(II) complexes. It is expected that as ΔG^o increases (i.e., the separation between the electronic states increases), H_{ab} would decrease. To be fair, the rate of change is likely not 1:1 as implied by this ratio. In low-spin Fe(II) polypyridyls, specifically, an increase in the electronic coupling increases the degree of coupling to the $^3T_1$ intermediate state (Scheme C.1). From the Tanabe-Sugano diagram, it is observed that as ligand field strength increases, the energy of the $^5T_2$ state increases with essentially a slope of 2 whereas in the $^3T_1$ state, the slope is closer to 1.[15] It is apparent then that the inverse

relationship between ΔG^o and H_{ab} is only a rough approximation and will change in magnitude with various ligand field strengths.

Some values of $\Delta G^o/H_{ab}$ were calculated, with $[Fe(bpy)_3]^{2+}$ = -1660 ± 210, $[Fe(terpy)_2]^{2+}$ = -1270 ± 320, and the other $[Fe(bpy')_3]^{2+}$ complexes being within error of both of these compounds. The only compound that showed any difference was $[Fe(dcpp)_2]^{2+}$, for which $\Delta G^o/H_{ab}$ = -2190 ± 290, which is very slightly outside of error of the others. It is unsurprising that the $[Fe(bpy')_3]^{2+}$ family yielded the same results as they have been shown to be nearly identical by most metrics. Interestingly, the ratio for $[Fe(terpy)_2]^{2+}$ was the same as the bpy-based series, just as was true with respect to the $(\Delta G^o)^2/\lambda$ ratio. Based on the electrochemical data and a series of Co(III) analogues,[16] the ligand field strength of terpy appears to be greater than that of bpy, but only slightly greater. Based on the longer lifetime and increased reorganization energy in $[Fe(terpy)_2]^{2+}$, however, we have postulated that ground state recovery in this complex is occurring along a nuclear coordinate for which the Huang-Rhys factor (i.e., nuclear displacement) is greater between the $^5T_2$ and $^1A_1$ states than is observed in any of the $[Fe(bpy)_3]^{2+}$-type analogues.[12] ΔG^o and H_{ab} are parameters that strictly measure the energetics of the electronic states, whereas λ also gives insight into the nuclear coordinate. If $\Delta\Delta G^o$ between $[Fe(bpy)_3]^{2+}$ and $[Fe(terpy)_2]^{2+}$ is not substantial, it is reasonable that the $\Delta G^o/H_{ab}$ ratio would be nearly constant between the two compounds as well. The $(\Delta G^o)^2/\lambda$ ratio is likewise easily explained by a slight increase in the driving force accompanied by a drastic increase in reorganization energy. These two modifications would offset each other to yield a nearly constant $(\Delta G^o)^2/\lambda$ ratio in $[Fe(terpy)_2]^{2+}$ relative to that of $[Fe(bpy)_3]^{2+}$. In the case of $[Fe(dcpp)_2]^{2+}$, it is apparent from the $\Delta G^o/H_{ab}$ data that the energetic difference between the $^5T_2$ and $^1A_1$ is increased more than the electronic coupling. This likely indicates that this compound exists at a different point on the Tanabe-Sugano diagram than any of the other complexes discussed

thus far.

1.3 The H_{ab}^4/λ Ratio

1.3.1 Calculation Methods

The final ratio of Marcus parameter is the H_{ab}^4/λ ratio, and it has been defined in Chapter 2. There are two ways in which this can be calculated: (1) Directly from the preexponential factor, A, or (2) as a ratio taken from the independently-determined H_{ab} and λ values. It should be apparent that the former is greatly preferred as it can be taken from the experimental Arrhenius parameters, whereas the latter requires the use of an initial estimate of one of the Marcus constants. When calculating the ratio from A, eqn. (C.9) is rearranged to solve for H_{ab}^4/λ and the error is propagated using the method outlined in Appendix C Section 1.1 using Table C.1. The ratio is found to be $1/(30 \pm 5)$ for $[Fe(bpy)_3](PF_6)_2$ in MeCN.

Alternatively, H_{ab}^4/λ can be found using H_{ab} and λ. These values can be calculated as described previously, provided an initial assumption of ΔG^o is made. In the case of $[Fe(bpy)_3]^{2+}$, then, λ is found to be 11000 ± 1000 cm^{-1} and $H_{ab} = 4.4 \pm 0.2$ cm^{-1}, as is shown in Table C.2. Using these values and their errors, the H_{ab}^4/λ ratio is found to be $1/(28 \pm 3)$, which is in good agreement with that found using the Arrhenius frequency factor. When calculated using this method, the ratio is consistently underestimated relative to when taken from A; the error bars are also smaller when finding H_{ab}^4/λ from its individual components. The first point would seem to imply that the reorganization energy used to determine H_{ab}^4/λ is smaller than A might suggest. This is an interesting point considering that λ in these data is found from the activation energy and eqn. (C.6) but is then being used to calculate a ratio in the preexponential term. It is unclear what the significance of this is. On the other hand, the reduced uncertainty when calculation the ratio from H_{ab} and λ may arise from the fact that the error is not determined on an inverse function, as was

described above. The uncertainty is propagated, but the ratio is found explicitly from its individual functions, not through a slightly more circuitous route in which error inherently increases. Ultimately, this analysis serves to reinforce the ratio reported in Chapter 2 and our confidence in the data workup and error propagation methods.

Table C.2. H_{ab}^4/λ ratio values when calculated directly from A or from H_{ab} and λ.

Complex[a]	A (ps^{-1})	λ (cm^{-1})	H_{ab} (cm^{-1})	H_{ab}^4/λ from A	H_{ab}^4/λ from H_{ab} and λ
$[Fe(bpy)_3]^{2+}$	230 ± 20	11000 ± 1000	4.4 ± 0.2	1/(30 ± 5)	1/(28 ± 3)
$[Fe(dmb)_3]^{2+}$	240 ± 20	9700 ± 900	4.2 ± 0.2	1/(33 ± 4)	1/(32 ± 2)
$[Fe(dtbb)_3]^{2+}$	230 ± 15	9500 ± 900	4.3 ± 0.2	1/(29 ± 4)	1/(28 ± 2)
$[Fe(terpy)_2]^{2+}$	150 ± 55	14100 ± 1200	6.2 ± 1.2	1/(14 ± 9)	1/(7 ± 3)

a Data collected for PF_6^- salts of complexes in MeCN. dmb = 4,4'-dimethyl-2,2'-bipyridine. dtbb = 4,4'-di-*tert*-butyl-2,2'-bipyridine.

1.3.2 The Physical Meaning of the H_{ab}^4/λ Ratio

The Arrhenius frequency factor, A, is a measure of the rate of the reaction should it be barrierless. Marcus's preexponential term is a way to account for nuclear motion where the exponential is a measure of the electronic movement. The two major unknown entities in the Marcus preexponential are H_{ab} and λ, which denote the coupling between electronic states and the energy of transformation from reactants into products, respectively. The former is strictly energetic, whereas the latter incorporates both an energetic and a nuclear displacement quantity. Taken as a ratio derived from A, H_{ab}^4/λ initially appears to represent specific energetics between the excited and ground states as inner-sphere reorganization occurs. In these Fe(II) polypyridyls, this would be the electronic coupling between the $^5T_2$ and $^3T_1$ states, as well as between the $^3T_1$

and $^1A_1$ states. The fact that this value was so similar between all three bpy-based complexes and distinctly unique for $[Fe(terpy)_2]^{2+}$ led to the postulation that this parameter could in fact be a numerical representation of the vibrational mode(s) associated with the photophysical process, or in this case the nuclear coordinate linked to ground state recovery.

Upon comparing this ratio to a wider array of complexes – including $[Fe(bpy)_3]^{2+}$ in various solvents (see Appendix A), terpy-based complexes with bulky substituents,[17] $[Fe(phen)_3]^{2+}$ and its spin-crossover analogue $[Fe(mono\text{-}2\text{-}OMe\text{-}phen)_3]^{2+}$,[13] an Fe(II) chromophore in a sterically-hindered Lehn cage motif[18] – it was determined that the above analysis is still open for debate. For example, H_{ab}^4/λ for $[Fe(bpy)_3]Cl_2$ in MeOH = 1/(32 ± 4), but in H_2O it is 1/(49 ± 14).[19] These two ratios are just within error of each other, but the average values differ drastically despite being for the exact same complex. If this ratio represented the major mode of ground state recovery, the only way this should be significantly different in different solvents is if there is a massive reorganization energy for one (both are ~10500 cm^{-1}) or if the solvent were somehow coordinating to the complex itself (which has never been suggested and X-ray evidence does not support[20,21]).

It is absolutely probable that this ratio does not suggest any inherent property of the compounds themselves and is simply a mathematical by-product, as it were. However, in performing dimensional analysis, the units for the H_{ab}^4/λ ratio are cm^{-3}, inverse volume. As Miller and McCusker note, solvation dynamics of the ground state recovery of $[Fe(bpy)_3]^{2+}$ appears to be related to the volume of expansion from the $^1A_1$ to the $^5T_2$ state.[22]

Furthermore, H_2O is often noted to be a special case for solvation of these polypyridyl chromophores, a factor that may lead to H_2O being better able to intercalate into the more elongated $^5T_2$ excited state than any other solvent molecule might.[21-23] Interestingly though is the fact that the Fe-N bond distance in $[Fe(dmb)_3]^{2+}$ has been observed by ultrafast X-ray spectroscopy

to lengthen less when the complex is dissolved in water than when it is dissolved in MeCN (specifically, ΔFe-N = 0.181 ± 0.003 Å in H_2O and 0.199 ± 0.003 Å in MeCN).[21] If H_{ab}^4/λ is in fact a measure of the volume change the complex undergoes during the ground state recovery process, then this ratio would be its smallest (inverse of the largest number) for the complex that has the smallest degree of volume change, i.e., $[Fe(bpy)_3]^{2+}$ in H_2O. This is purely speculation, as is the proposal that the ratio may represent the active nuclear coordinate of ground state recovery. There are other complexes that would seem to support this volume expansion hypothesis, such as $[Fe(paniterpy)_2]^{2+}$ (paniterpy = 5,5”-bis-(4-methoxy-2,6-di-*iso*-propylphenyl)-2,2’:6’,2”-terpyridine), a highly sterically encumbered terpy derivative, for which $H_{ab}^4/\lambda \sim ½$.[24] Further work must be performed in order to determine the true nature of this ratio, and whether any physical origin can be ascribed to it.

2. The Influence of Holding Different Variables Constant

As was discussed in Chapter 2, the Marcus parameters calculated from the variable-temperature ultrafast transient absorption spectroscopy are found upon assuming a value for ΔG^o = -7300 ± 730 cm^{-1} for $[Fe(bpy)_3]^{2+}$.[3] The driving forces of the other complexes are found from the electrochemical oxidation potential of the Fe(II/III) couple for the specific compounds as referenced to that of $[Fe(bpy)_3]^{2+}$. This is clearly an imperfect system with many potential pitfalls. However, without using other methods either not currently available to us or that would require a database of complexes and techniques, this appeared to be the best system for acquiring a crucial element for all future Marcus analysis. The question arose, however, as to how much the individual Marcus parameters might change in magnitude or uncertainty if a different constant was assumed, such as H_{ab} or λ. Obviously electrochemistry is a guide as to the direction of the t_{2g} set of orbitals

that play a role in the ligand field strength of the Fe(II) complexes. With no measure to base initial values of H_{ab} or λ, they were assumed to be constant across all complexes. These numbers are not meant to be taken as true estimates of either parameter but are instead to give a sense of how much the calculations depend on the initial assumption of ΔGº. In Table C.3 can be found the original Marcus parameters as given in Chapter 2.

Table C.3. Marcus parameters calculated for four Fe(II) polypyridyl complexes using an assumed value of ΔGº from electrochemical data.

Complex[a]	-ΔGº (cm^{-1})	λ (cm^{-1})	H_{ab} (cm^{-1})
$[Fe(bpy)_3]^{2+}$	7300 ± 730	11000 ± 1000	4.4 ± 0.2
$[Fe(dmb)_3]^{2+}$	6000 ± 600	9700 ± 900	4.2 ± 0.2
$[Fe(dtbb)_3]^{2+}$	6100 ± 610	9500 ± 900	4.3 ± 0.2
$[Fe(terpy)_2]^{2+}$	7600 ± 760	14100 ± 1200	6.2 ± 1.2

a Data collected for PF_6^- salts of complexes in MeCN.

As a point of comparison, ΔGº may be held constant at a fixed value for all four complexes so as to better discern the relationship between variables. These data are given in Table C.4, for which the free energy is defined as -6800 ± 680 cm^{-1}. With this as a starting point, all reorganization energies for the $[Fe(bpy')_3]^{2+}$ series are the same, as are the H_{ab} values for those compounds. This is consistent with what is observed when ΔGº is held constant but calculated based on electrochemical potentials. ΔGº = -6800 ± 680 cm^{-1} was chosen as it is the mean free energy of the bpy-based family. Despite it not being the average driving force for any of the complexes, there is a high degree of similarity between the values in Tables C.3 and C.4. Even more interesting is the agreement in λ and H_{ab} for even $[Fe(terpy)_2]^{2+}$. These parameters are outside of error of those of the $[Fe(bpy')_3]^{2+}$ complexes but remain consistent with those calculated for

$[Fe(terpy)_2]^{2+}$ in Table C.3. This would tend to support the trends observed in λ and H_{ab} for all four complexes as outlined in Chapter 2.

Table C.4. Marcus parameters calculated for four Fe(II) polypyridyl complexes using an assumed value of ΔG° from electrochemical data.

Complex[a]	-ΔG° (cm^{-1})	λ (cm^{-1})	H_{ab} (cm^{-1})
$[Fe(bpy)_3]^{2+}$	6800 ± 680	10400 ± 1000	4.4 ± 0.3
$[Fe(dmb)_3]^{2+}$	6800 ± 680	10600 ± 1000	4.3 ± 0.2
$[Fe(dtbb)_3]^{2+}$	6800 ± 680	10400 ± 1000	4.4 ± 0.2
$[Fe(terpy)_2]^{2+}$	6800 ± 680	13100 ± 1100	6.1 ± 1.4

a Data collected for PF_6^- salts of complexes in MeCN.

The reorganization energy is taken to be constant at 10000 ± 1000 cm^{-1} across all four complexes; this might conceivably be true in the case of the $[Fe(bpy')_3]^{2+}$ family but is highly unlikely to be consistent with $[Fe(terpy)_2]^{2+}$. $[Fe(terpy)_2]^{2+}$ is known to relax by multiple nuclear coordinates, which is not the case for $[Fe(bpy)_3]^{2+}$.[25] The specific value was chosen due to it being the mean value of the bpy-based series. If the expectation is that all $\{Fe(N)_6\}^{2+}$ complexes will have similar Marcus parameters, then the values found for $[Fe(terpy)_2]^{2+}$ should be within those of $[Fe(bpy')_3]^{2+}$ assuming a constant reorganization energy. Taking the first three complexes in Table C.5, all parameters are very similar and within error of each other. This is to be expected with complexes that have the same ligand skeleton. H_{ab} is essentially unchanged from Table C.4 to Table C.5 in this series of compounds, again showing the restricted range possible for H_{ab} due to its magnitude. The greatest difference is seen in $[Fe(terpy)_2]^{2+}$, which has a driving force outside of error of the other complexes. ΔG° for $[Fe(terpy)_2]^{2+}$ is 4500 ± 500 cm^{-1}, whereas that same parameter is more on the order of 6500 ± 600 cm^{-1} for the $[Fe(bpy')_3]^{2+}$ compounds. Furthermore,

while the H_{ab} values for all four complexes are within error of each other, the average value for $[Fe(terpy)_2]^{2+}$ is increased from 4.3 to 5.7 cm^{-1}. This is a relatively large change of 28% (despite being small in overall magnitude, ~1 cm^{-1}) and is indicative of the greater electronic coupling between the $^5T_2$ and $^1A_1$ states in $[Fe(terpy)_2]^{2+}$, as is observed in both Tables C.4 and C.5.

Table C.5. Marcus parameters calculated for four Fe(II) polypyridyl complexes using an assumed value of λ.

Complex[a]	$-\Delta G^o$ (cm^{-1})	λ (cm^{-1})	H_{ab} (cm^{-1})
$[Fe(bpy)_3]^{2+}$	6500 ± 600	10000 ± 1000	4.3 ± 0.3
$[Fe(dmb)_3]^{2+}$	6300 ± 600	10000 ± 1000	4.2 ± 0.2
$[Fe(dtbb)_3]^{2+}$	6500 ± 600	10000 ± 1000	4.3 ± 0.2
$[Fe(terpy)_2]^{2+}$	4500 ± 500	10000 ± 1000	5.7 ± 1.3

a Data collected for PF_6^- salts of complexes in MeCN.

Finally, λ and ΔG^o are calculated while H_{ab} is held at 4.3 ± 0.3 cm^{-1}, again being chosen due to it being the average H_{ab} value for the $[Fe(bpy')_3]^{2+}$ series of complexes. With the values found in Table C.6, it is immediately apparent that restricting the electronic coupling parameter greatly increases the relative uncertainty of each of the other Marcus constants. In Tables C.3-C.5, the error associated with the parameters not being held constant was ~10% (with the exception of H_{ab} for $[Fe(terpy)_2]^{2+}$). When H_{ab} is limited to 4.3 ± 0.3 cm^{-1}, however, the size of the uncertainty increases to 20-40% for the $[Fe(bpy)_3]^{2+}$-based complexes, and even further to 45-85% in $[Fe(terpy)_2]^{2+}$. While ΔG^o and λ are within error of those values calculated in Tables C.3-C.5 for the bpy' series, the changes in $[Fe(terpy)_2]^{2+}$ are significant. Here, the driving force has been reduced from -7600 cm^{-1} in Table C.3 to 1100 cm^{-1}. Reorganization energy also demonstrated a sizeable decrease from 14100 cm^{-1} to 4900 cm^{-1}. The data in this table serve to illustrate the point

that H_{ab} is a highly-constrained parameter due to its magnitude. Substantial changes to the electronic coupling will greatly alter both ΔG^o and λ, which is why all values for $[Fe(bpy')_3]^{2+}$ are identical to those calculated above, whereas the parameters of $[Fe(terpy)_2]^{2+}$ are drastically attenuated. Table C.6 also appears to reinforce the approximate magnitude of H_{ab} for $[Fe(terpy)_2]^{2+}$ being closer to 6 cm^{-1} than 4 cm^{-1}; when H_{ab} = 4.3 ± 0.3 cm^{-1}, ΔG^o and λ for this complex are on the order of a spin-crossover complex's driving force and reorganization energy, which $[Fe(terpy)_2]^{2+}$ clearly is not spin-crossover.

Table C.6. Marcus parameters calculated for four Fe(II) polypyridyl complexes using an assumed value of H_{ab}.

Complex[a]	$-\Delta G^o$ (cm^{-1})	λ (cm^{-1})	H_{ab} (cm^{-1})
$[Fe(bpy)_3]^{2+}$	6800 ± 1500	10400 ± 4000	4.3 ± 0.3
$[Fe(dmb)_3]^{2+}$	7500 ± 1400	11400 ± 4000	4.3 ± 0.3
$[Fe(dtbb)_3]^{2+}$	6700 ± 1400	10300 ± 3700	4.3 ± 0.3
$[Fe(terpy)_2]^{2+}$	1100 ± 500	4900 ± 4200	4.3 ± 0.3

a Data collected for PF_6^- salts of complexes in MeCN.

3. Conclusions

This appendix was not intended to be a tutorial on the determination of Marcus parameters from Arrhenius data, nor is it meant to define error propagation methods. The data shown herein are the Marcus values calculated for the four Fe(II) complexes outlined in Chapter 2, and this appendix shows how they were obtained as well as a full accounting of how the magnitude of the uncertainty was determined. This is a new field of work being done, not just on these types of chromophores, but on complexes without well-defined excited state energetics in general. Trial and error is the path forward, and we are simply attempting to be transparent in the methods

employed.

True analytical error propagation was shown to grossly overestimate the uncertainty of the Marcus parameters calculated. Instead, a method was introduced that accounted for the error associated with the constants but was not so incredibly large as to put all values calculated within error of each other. Then, the ratios of Marcus constants were examined, with H_{ab}^4/λ being determined to be the most readily digestible. The exact nature of this ratio is yet unknown, but work is ongoing to further define it. Finally, the role a fixed value of ΔG^o plays on the calculation of other parameters was tested by holding each of the other Marcus values constant. $[Fe(terpy)_2]^{2+}$ was consistently found to lie outside of error of the three $[Fe(bpy')_3]^{2+}$ complexes. It was also determined that even small (~1 cm^{-1}) perturbations on H_{ab} can cause drastic shifts in ΔG^o and λ, as well as grossly overestimated error bars for those parameters. Ultimately, this analysis helped bolster confidence in the values reported, but serve to remind us that this research is yet in its infancy.

REFERENCES

REFERENCES

1. Marcus, R. A.; Sutin, N. Electron Transfers in Chemistry and Biology. *Biochim. Biophys. Acta* **1985**, *811*, 265-322; DOI: 10.1016/0304-4173(85)90014-X.

2. Barbara, P. F.; Meyer, T. J.; Ratner, M. A. Contemporary Issues in Electron Transfer Research. *J. Phys. Chem.* **1996**, *100*, 13148-13168; DOI: 10.1021/jp9605663.

3. Sutin, N. Nuclear, Electronic, and Frequency Factors in Electron-Transfer Reactions. *Acc. Chem. Res.* **1982**, *15*, 275-282; DOI: 10.1021/ar00081a002.

4. Besora, M.; Careon-Macedo, J. L.; Cimas, A.; Harvey, J. N. Spin-State Changes and Reactivity in Transition Metal Chemistry: Reactivity of Iron Tetracarbonyl. *Adv. Inorg. Chem.* **2009**, *61*, 573-623; DOI: 10.1016/S0898-8838(09)00210-4.

5. Xie, C.-L.; Hendrickson, D. N. Mechanism of Spin-State Interconversion in Ferrous Spin-Crossover Complexes: Direct Evidence for Quantum Mechanical Tunneling. *J. Am. Chem. Soc.* **1987**, *109*, 6981-6988; DOI: 10.1021/ja00257a013.

6. Berdiell, I. C.; Kulmaczewski, R.; Halcrow, M. A. Iron(II) Complexes of 2,4-Dipyrazolyl-1,3,5-triazine Derivatives – The Influence of Ligand Geometry on Metal Ion Spin State. *Inorg. Chem.* **2017**, *56*, 8817-8828; DOI: 10.1021/acs.inorgchem.7b00699.

7. Smeigh, A. L.; Creelman, M.; Mathies, R. A.; McCusker, J. K. Femtosecond Time-Resolved Optical and Raman Spectroscopy of Photoinduced Spin Crossover: Temporal Resolution of Low-to-High Spin Optical Switching. *J. Am. Chem. Soc.* **2008**, *130*, 14105-14107; DOI: 10.1021/ja805949s.

8. Sigfridsson, E.; Olsson, M. H.; Ryde, U. A Comparison of the Inner-Sphere Reorganization Energies of Cytochromes, Iron-Sulfur Clusters, and Blue Copper Proteins. *J. Phys. Chem. B* **2001**, *105*, 5546-5552; DOI: 10.1021/jp0037403.

9. Matyushov, D. V. Nanosecond Stokes Shift Dynamics, Dynamical Transition, and Gigantic Reorganization Energy of Hydrated Heme Proteins. *J. Phys. Chem. B* **2011**, *115*, 10715-10724; DOI: 10.1021/jp200409z.

10. Feldt, S. M.; Lohse, P. W.; Kessler, F.; Nazeeruddin, M. K.; Grätzel, M.; Boschloo, G.; Hagfeldt, A. Regeneration and Recombination Kinetics in Cobalt Polypyridine Based Dye-Sensitized Solar Cells, Explained Using Marcus Theory. *Phys. Chem. Chem. Phys.* **2013**, *15*, 7087-7097; DOI: 10.1039/c3cp50997d.

11. Buhks, E.; Navon, G.; Bixon, M.; Jortner, J. Spin Conversion Processes in Solution. *J. Am. Chem. Soc.* **1980**, *102*, 2918-2923; DOI: 10.1021/ja00529a009.

12. Hauser, A. Excited-State Lifetimes of $[Fe(bipy)_3]^{2+}$ and $[Fe(phen)_3]^{2+}$. *Chem. Phys. Lett.* **1990**, *173*, 507-512; DOI: 10.1016/0009-2614(90)87244-L.

13. Adelman, S. L. Unpublished results.

14. Farrance, I.; Frenkel, R. Uncertainty of Measurement: A Review of the Rules for Calculating Uncertainty Components through Functional Relationships. *Clin. Biochem. Rev.* **2012**, *33*, 49-75; PubMed ID: 22896744.

15. Tanabe, Y.; Sugano, S. On the Absorption Spectra of Complex Ions II. *J. Phys. Soc. Jpn.* **1954**, *9*, 766-779; DOI: 10.1143/JPSJ.9.766.

16. Yarranton, J. T. Unpublished results.

17. Brown, A. M. Excited-State Dynamics of Iron(II)-Based Charge-Transfer Chromophores. Ph.D. Thesis, Michigan State University, East Lansing, MI, 2011.

18. Adelman, S. L.; Paulus, B. C.; Jakubikova, E.; McCusker, J. K. Disrupting the Nuclear Coordinate in a Low-Spin Iron(II) Polypyridyl Complex to Extend its MLCT Excited-State Lifetime. *Manuscript in preparation.*

19. Appendix A of this work.

20. Zhang, W.; Alonso-Mori, R.; Bergmann, U.; Bressler, Ch.; Chollet, M.; Galler, A.; Gawelda, W.; Hadt, R. G.; Hartsock, R. W.; Kroll, T.; Kjær, K. S.; Kubiček, K.; Lemke, H. T.; Liang, H. W.; Meyer, D. A.; Nielsen, M. M.; Purser, C.; Robinson, J. S.; Solomon, E. I.; Sun, Z.; Sokaras, D.; van Driel, T. B.; Vankó, G.; Weng, T.-C.; Zhu, D.; Gaffney, K. J. Tracking Excited-State Charge and Spin Dynamics in Iron Coordination Complexes. *Nature* **2014**, *509*, 345-348; DOI: 10.1038/nature13252.

21. Liu, C.; Zhang, J.; Daku, L. M. L.; Gosztola, D.; Canton, S. E.; Zhang, X. Probing the Impact of Solvation on Photoexcited Spin Crossover Complexes with High-Precision X-ray Transient Absorption Spectroscopy. *J. Am. Chem. Soc.* **2017**, *139*, 17518-17524; DOI: 10.1021/jacs.7b09297.

22. Miller, J. N.; McCusker, J. K. Outer-Sphere Effects on the Excited State Dynamics of Ligand Field States in Fe(II) Polypyridyl Complexes. *Manuscript in preparation.*

23. Caspar, J. V.; Meyer, T. J. Photochemistry of $Ru(bpy)_3^{2+}$. Solvent Effects. *J. Am. Chem. Soc.* **1983**, *105*, 5583-5590; DOI: 10.1021/ja00355a009.

24. This value was obtained by performing Marcus analysis on data in ref. 18.

25. Vankó, G.; Bordage, A.; Pápai, M.; Haldrup, K.; Glatzel, P.; March, A. M.; Doumy, G.; Britz, A.; Galler, A.; Assefa, T.; Cabaret, D.; Juhin, A.; van Driel, T. B.; Kjær, K. S.; Dohn, A.; Møller, K. B.; Lemke, H. T.; Gallo, E.; Rovezzi, M.; Németh, Z.; Rozsályi, E.; Rozgonyi, T.; Uhlig, J.; Sundström, V.; Nielsen, M. M.; Young, L.; Southworth, S. H.; Bressler, Ch.; Gawełda, W. Detailed Characterization of a Nanosecond-Lived Excited State: X-ray and Theoretical Investigation of the Quintet State in Photoexcited [Fe(terpy)2]2+. *J. Phys. Chem. C* **2015**, *119*, 5888-5902; DOI: 10.1021/acs.jpcc.5b00557.

APPENDIX D. CARTESIAN COORDINATES USED IN TIME-DEPENDENT DENSITY FUNCTIONAL THEORY CALCULATIONS

1. $[Ru(dpb)_3](PF_6)_2$ Ground State

Atom	X	Y	Z
Ru	10.485	0.963	5.563
N	11.377	1.475	7.338
N	9.314	-0.039	6.918
N	11.588	2.24	4.309
N	9.333	2.731	5.588
N	9.61	0.083	3.915
N	11.725	-0.659	5.241
C	12.492	2.21	7.499
C	13.13	2.382	8.682
C	12.612	1.808	9.844
C	11.408	1.098	9.712
C	10.827	0.933	8.475
C	13.364	1.946	11.141
C	13.641	3.24	11.645
C	14.469	3.352	12.756
C	15.039	2.261	13.363
C	14.711	1.002	12.896
C	13.843	0.826	11.814

C	8.198	-0.761	6.634
C	7.403	-1.325	7.616
C	7.691	-1.167	8.955
C	8.836	-0.404	9.253
C	9.612	0.127	8.236
C	6.783	-1.718	10.004
C	5.603	-1.039	10.317
C	4.688	-1.647	11.16
C	4.874	-2.899	11.712
C	6.084	-3.524	11.422
C	7.039	-2.956	10.585
C	12.673	1.852	3.61
C	13.22	2.662	2.623
C	12.627	3.881	2.309
C	11.556	4.273	3.105
C	11.062	3.415	4.081
C	13.066	4.681	1.129
C	14.374	5.168	1.029
C	14.737	5.901	-0.132
C	13.833	6.133	-1.155
C	12.563	5.606	-1.052
C	12.13	4.887	0.053
C	8.246	2.908	6.333

C	7.619	4.146	6.453
C	8.186	5.248	5.846
C	9.33	5.03	5.03
C	9.856	3.756	4.936
C	7.689	6.632	6.069
C	8.455	7.536	6.829
C	7.968	8.849	7.003
C	6.787	9.272	6.412
C	6.039	8.354	5.714
C	6.432	7.042	5.537
C	8.448	0.473	3.344
C	7.825	-0.291	2.351
C	8.412	-1.469	1.886
C	9.622	-1.834	2.453
C	10.203	-1.055	3.454
C	7.696	-2.283	0.875
C	7.234	-3.56	1.196
C	6.433	-4.225	0.266
C	6.107	-3.661	-0.954
C	6.651	-2.454	-1.283
C	7.444	-1.738	-0.392
C	12.884	-0.923	5.909
C	13.735	-1.905	5.541

C	13.446	-2.725	4.443
C	12.281	-2.437	3.744
C	11.437	-1.425	4.158
C	14.32	-3.855	4.047
C	14.007	-5.131	4.459
C	14.828	-6.212	4.067
C	15.902	-6.019	3.224
C	16.22	-4.74	2.881
C	15.451	-3.634	3.237
H	12.857	2.636	6.733
H	13.931	2.892	8.721
H	10.992	0.728	10.481
H	14.642	4.216	13.111
H	15.087	0.239	13.318
H	7.955	-0.884	5.722
H	6.64	-1.833	7.365
H	9.077	-0.254	10.159
H	3.889	-1.176	11.369
H	6.265	-4.372	11.811
H	13.069	1.008	3.797
H	14.004	2.382	2.16
H	11.169	5.133	2.981
H	15.621	6.239	-0.209

H	11.954	5.741	-1.769
H	7.884	2.163	6.802
H	6.809	4.231	6.946
H	9.72	5.754	4.554
H	8.461	9.457	7.541
H	5.216	8.633	5.336
H	8.043	1.284	3.626
H	6.995	-0.003	1.99
H	10.059	-2.623	2.156
H	6.104	-5.092	0.477
H	6.484	-2.092	-2.146
H	13.103	-0.396	6.668
H	14.537	-2.04	6.031
H	12.061	-2.944	2.971
H	14.639	-7.083	4.394
H	17.01	-4.596	2.374
H	4.13108	-3.36219	12.32716
H	7.95968	-3.46526	10.39031
H	5.40979	-0.06726	9.91291
H	6.46557	10.28901	6.49731
H	9.38472	7.23464	7.26455
H	5.80731	6.34938	5.01265
H	14.115	6.71095	-2.01019

H	11.13433	4.49852	0.10435
H	15.08452	4.99215	1.80947
H	15.72114	2.38212	14.17843
H	13.55095	-0.15669	11.50754
H	13.22346	4.10975	11.18229
H	7.48688	-4.01714	2.12979
H	5.44157	-4.16123	-1.62621
H	7.85395	-0.7891	-0.66846
H	16.46736	-6.84749	2.85134
H	13.14723	-5.30288	5.07231
H	15.71078	-2.65011	2.9063

2. $[Ru(dpb)_3](PF_6)_2$ Excited State

Atom	X	Y	Z
Ru	0.002601642542	-0.000059459906	-0.000686979186
N	-0.142622971292	-1.806554489876	-1.046069711160
N	-1.499540409950	-0.988432978459	1.067631973168
N	1.632221937520	0.772399494614	-1.061847605894
N	1.618798976616	-0.800238094655	1.060480571828
N	-0.111302900637	1.808333070349	1.045053087658
N	-1.482632404369	1.014202029938	-1.068403016112
C	0.610677891318	-2.163950245931	-2.122033309597
C	0.469802866431	-3.395756034871	-2.763638227316

C	-0.481070620859	-4.335796688956	-2.296918423503
C	-1.251450614375	-3.955814014481	-1.175375850155
C	-1.074483891959	-2.702793998092	-0.570204735622
C	-0.662509581792	-5.656614476552	-2.954643655943
C	0.421547323783	-6.293299379757	-3.608444949421
C	0.251491907599	-7.542236598187	-4.230397559139
C	-1.006680252178	-8.177587181060	-4.214750799809
C	-2.093137979713	-7.552595718304	-3.569782622257
C	-1.922380506244	-6.305297520443	-2.944827640978
C	-2.160627325276	-0.491716065534	2.148634613948
C	-3.168039625328	-1.200438619397	2.805356457607
C	-3.540116662188	-2.490168838812	2.353678357196
C	-2.847359416988	-2.993715063548	1.230064467834
C	-1.843464018080	-2.239340593517	0.604757324414
C	-4.605407904642	-3.277174698613	3.028990688328
C	-4.851399644879	-3.116895526552	4.415313385786
C	-5.855588864140	-3.861665832422	5.057412946608
C	-6.636367662890	-4.778950432468	4.325390943035
C	-6.402739947044	-4.944874104975	2.945182639508
C	-5.396371369659	-4.202552545470	2.303618484311
C	1.555453596607	1.596019337148	-2.142606264230
C	2.686827901484	2.103697271694	-2.783529665205
C	3.980324095172	1.766305842902	-2.315673040579

C	4.046380185431	0.907019906309	-1.196294992517
C	2.878022002953	0.426341405233	-0.586663348041
C	5.208746960053	2.291244130380	-2.968167366895
C	5.216171565002	2.598777179686	-4.351390287144
C	6.376141383831	3.095300185677	-4.970560334929
C	7.550778894194	3.297971632791	-4.218208872324
C	7.554687608728	2.998102519410	-2.840847563346
C	6.395718929676	2.498480805147	-2.222238707991
C	1.527977816336	-1.622159701691	2.141452684374
C	2.650505490101	-2.148835225028	2.782616908605
C	3.949547148720	-1.833515412474	2.314722924068
C	4.030298389518	-0.975895733200	1.195046996864
C	2.870305884862	-0.475530506967	0.585249196036
C	5.168874796204	-2.378795589356	2.967505847758
C	6.351550730619	-2.608120226646	2.221263021637
C	7.501916205367	-3.126983718523	2.840118066105
C	7.493508267453	-3.424370736790	4.218007832610
C	6.323044959829	-3.199795120982	4.970649421912
C	5.171613441719	-2.684030289751	4.351243731516
C	0.648551654482	2.152464745666	2.120727109743
C	0.528941496657	3.386221055338	2.762879757623
C	-0.406104009277	4.342425390217	2.297037811173
C	-1.183208932284	3.976142399283	1.175550208753

C	-1.027858691372	2.720520677856	0.569837809437
C	-0.564761343682	5.665753102356	2.955537663794
C	-1.813496157121	6.335670440096	2.947153364226
C	-1.962565307988	7.585284740764	3.573033987570
C	-0.865153215352	8.191357853724	4.217527048657
C	0.382062671112	7.534728102774	4.231828867069
C	0.530413281881	6.283487640544	3.608949795061
C	-2.152459030552	0.529132849252	-2.149285464872
C	-3.148084077620	1.255000520302	-2.805251627602
C	-3.498098414878	2.550686523364	-2.353019483945
C	-2.796333213602	3.042107493757	-1.229596352384
C	-1.805077069443	2.270624147769	-0.604983727591
C	-4.550001997840	3.355825735614	-3.028059590446
C	-5.324715166337	4.294939758073	-2.302758275007
C	-6.318375288470	5.054245080167	-2.944238338655
C	-6.555342588761	4.891826751575	-4.324293196666
C	-5.790770212449	3.960928401075	-5.056227494409
C	-4.799312816906	3.199235690713	-4.414208506109
H	1.327626393232	-1.435587862595	-2.477223428588
H	1.084877927189	-3.601220796798	-3.632140478218
H	-1.973783499678	-4.648938016529	-0.763126240837
H	1.096697243021	-8.019753040541	-4.718720112307
H	-3.069075110447	-8.030328964561	-3.560136690139

H	-1.869845793265	0.494940737033	2.483895083163
H	-3.667035270036	-0.733079156758	3.646432236971
H	-3.078640565295	-3.983899369854	0.858548078352
H	-6.023490389382	-3.732250910469	6.123185893784
H	-7.005521736520	-5.643099502316	2.370802002488
H	0.562581403463	1.849803021278	-2.489495159183
H	2.549469727999	2.773872805577	-3.624297712146
H	5.011588687477	0.599169705227	-0.814702412804
H	6.365693414861	3.316852236376	-6.034345507297
H	8.452746576356	3.159530154183	-2.250755348081
H	0.530920413567	-1.858883538133	2.488384924232
H	2.501802434610	-2.816347928614	3.623577549591
H	5.000651293090	-0.684567799263	0.813516447303
H	8.396650670100	-3.305216613829	2.249812100290
H	6.309324347329	-3.419297747729	6.034822613468
H	1.353243327431	1.411899953950	2.475240257623
H	1.147900270971	3.580932925803	3.631101317058
H	-1.893729899652	4.681647676899	0.763789543301
H	-2.930271462958	8.079495348189	3.564501386089
H	1.235608509279	7.997480977268	4.719861018369
H	-1.878242210992	-0.462031959979	-2.485188482221
H	-3.655169497737	0.796506326396	-3.646370619576
H	-3.010451494002	4.036034527582	-0.857801848527

H	-6.908845505599	5.762954753327	-2.369908417979
H	-5.961317359144	3.833970835201	-6.121876391863
H	-7.413545199064	-5.354133291553	4.821571581955
H	-5.249716595098	-4.327007468280	1.234096687036
H	-4.244217741622	-2.432790767930	5.001843942099
H	8.383284394659	-3.824648590197	4.696663376532
H	6.370961426890	-2.410610490444	1.152843235900
H	4.286710629138	-2.496270029772	4.953192019262
H	8.447203180508	3.683354470720	-4.696685930065
H	6.412370019721	2.298774893570	-1.154188732454
H	4.327799064466	2.427747635047	-4.953179615348
H	-1.138301440916	-9.142483876020	-4.697128285169
H	-2.778976391664	-5.828617178078	-2.475890611120
H	1.404997292357	-5.831214538571	-3.611323038423
H	-2.678478982704	5.873841350254	2.478755126727
H	-0.980012832427	9.158038405054	4.700618267069
H	1.505838915216	5.804659791231	3.610859934281
H	-7.322686054444	5.480103343963	-4.820429151863
H	-5.175658451135	4.417245612862	-1.233338344346
H	-4.204293395609	2.504457237289	-5.000672714183

3. $[Ru(dmesb)_3](PF_6)_2$ Ground State

Atom	X	Y	Z
Ru	10.4621845479	0.9083771661	5.5159985485
N	11.471886981	1.5233678181	7.2677345918
N	9.4524422457	-0.1667029052	6.9988092902
N	11.464732617	2.1146379866	4.1315185454
N	9.4087365629	2.7337911444	5.6769988282
N	9.4289581285	0.129512613	3.9070936713
N	11.5503645293	-0.8111989846	5.1775362343
C	12.4906269437	2.421964272	7.3136704796
C	13.1007428137	2.7947098614	8.512131617
C	12.6536254606	2.2446903033	9.7385407602
C	11.5848509349	1.3205601003	9.6720204078
C	11.0140961769	0.9709336677	8.4415052051
C	13.2750957518	2.6197622284	11.0341797248
C	13.8646322449	3.896793118	11.2078374207
C	14.4507361958	4.254982786	12.4335198766
C	14.4638694266	3.3416322469	13.5071127931
C	13.8837069892	2.0672200248	13.3447532837
C	13.2928792148	1.7101861563	12.1209410976
C	8.4374224938	-1.0404124018	6.7611298137
C	7.8148978921	-1.7491887758	7.7884756291
C	8.2375957902	-1.5778656609	9.1298005518

C	9.2997528407	-0.6710657531	9.3546472434
C	9.893327113	0.0179491228	8.28995467
C	7.5999410491	-2.3166589988	10.2485417636
C	6.2443223129	-2.7218749268	10.1652201081
C	5.638174053	-3.4177499186	11.2246298138
C	6.3767769138	-3.7270415021	12.3847448097
C	7.727027188	-3.3326851212	12.4770171439
C	8.3323442977	-2.6321312264	11.4203261828
C	12.4946459369	1.6945480949	3.3488380558
C	13.1166915883	2.5376230383	2.4280511958
C	12.6766193903	3.876019256	2.2784583438
C	11.5975467487	4.290099749	3.0938493252
C	11.0049596518	3.4059600993	4.0037445051
C	13.3142374548	4.8018138002	1.3087028444
C	14.6814354109	4.6549513249	0.965672267
C	15.2882952992	5.531050869	0.0501630362
C	14.5386281293	6.5663294449	-0.5441782824
C	13.1769389169	6.719676169	-0.2131341335
C	12.5706617883	5.8475916863	0.7066372643
C	8.3637522229	2.9652675137	6.514583108
C	7.7291218934	4.2058323762	6.5871809959
C	8.1708515398	5.2789399774	5.7749523194
C	9.2623307764	5.0206778878	4.9132034613

C	9.8646442667	3.7564956469	4.8778402162
C	7.5184081711	6.6121861113	5.8240859889
C	8.2491220197	7.7902014938	5.5291383121
C	7.6284438798	9.0497829908	5.5786290722
C	6.2647145401	9.1556273896	5.9194347156
C	5.5276699046	7.9905561876	6.213297808
C	6.148964269	6.7311663817	6.1689690435
C	8.3756254687	0.7180946031	3.2565382432
C	7.7606531322	0.1511126713	2.154820706
C	8.2393772276	-1.1087578147	1.6324688528
C	9.3296128799	-1.693739025	2.2794579846
C	9.9408514937	-1.090156839	3.4136968859
C	7.5993120613	-1.7378471784	0.4490293937
C	7.6489214626	-3.1419410822	0.2447183015
C	7.0482613744	-3.7314363678	-0.8802016501
C	6.3780805875	-2.9328190267	-1.8304431875
C	6.315661799	-1.5380006831	-1.638644813
C	6.9162767056	-0.9484635856	-0.5123423218
C	12.6101120345	-1.259944397	5.9226521638
C	13.2717042409	-2.4437785801	5.6513718754
C	12.8342790701	-3.2771828356	4.5541131842
C	11.7393373127	-2.8311752472	3.8116734475
C	11.0801858599	-1.6060802243	4.1095960865

C	13.5298700472	-4.5509738945	4.2393450081
C	12.8534157458	-5.6212789828	3.5969848243
C	13.5195806511	-6.8207473826	3.2950172581
C	14.8800870304	-6.9839944305	3.6301561793
C	15.5637710208	-5.9322814393	4.2725780903
C	14.8965842145	-4.7324005704	4.5756855665
H	12.8304540144	2.8295501311	6.3703921802
H	13.9295217051	3.4916571805	8.4756777988
H	11.1873415856	0.8941481349	10.5839022459
H	14.8887672954	5.2421018367	12.5525826816
H	13.897831765	1.3538324999	14.1640597681
H	8.1312351241	-1.1625895255	5.730831835
H	7.025690893	-2.4454591188	7.5312440988
H	9.64649907	-0.4912216332	10.3638298585
H	4.5949335029	-3.711504649	11.148588789
H	8.3062500592	-3.5753356604	13.3635737683
H	12.8128772416	0.6682630129	3.4737025962
H	13.9196228641	2.1377587167	1.8202409955
H	11.2390149876	5.3091444189	3.0303657672
H	16.3402202419	5.4110461956	-0.1937374878
H	12.5898298964	7.509310293	-0.6737463852
H	8.0345310916	2.1384324105	7.1302334834
H	6.9129619332	4.3295107882	7.2889079917

H	9.6222356194	5.8016419447	4.2560329894
H	8.2062019113	9.9434705019	5.3596651677
H	4.4742373912	8.062384571	6.4693971287
H	8.0173918723	1.6546665483	3.6666123118
H	6.9043352031	0.6520223368	1.7197093261
H	9.7483772874	-2.6182111525	1.8993865467
H	7.0934272124	-4.8096467696	-1.0107221287
H	5.8059309252	-0.910900048	-2.3656875741
H	12.9235205742	-0.628096156	6.7449346424
H	14.0959121047	-2.74004422	6.2888950922
H	11.3859480005	-3.4149133361	2.9698324504
H	12.9781596068	-7.6288933416	2.8098571847
H	16.6134906713	-6.0437655138	4.5320371318
H	5.9080868581	-4.2668593093	13.2031630087
H	9.381199024	-2.3604340002	11.5013654499
H	5.6508043709	-2.4718595917	9.2903027125
H	5.7845447589	10.1297869106	5.9559260038
H	9.307473475	7.7336824436	5.2898472851
H	5.5576750423	5.8434279207	6.3752737725
H	15.0077300278	7.2424209604	-1.253914183
H	11.5135381823	5.9668199323	0.9279362552
H	15.2816905743	3.8784017719	1.4315342477
H	14.9189264949	3.6181818413	14.4543919266

H	12.874748957	0.7135765585	12.0091735996
H	13.8433615726	4.6236258193	10.4006853052
H	8.1343519219	-3.7810471754	0.9774068461
H	5.9117835891	-3.3891395846	-2.6996833208
H	6.8732304997	0.13104946	-0.3989168895
H	15.3946579086	-7.9128213994	3.3983197283
H	11.7977654314	-5.5307749031	3.3552505838
H	15.4510138817	-3.928340199	5.0513912665

APPENDIX E. DATA PROCESSING AND ANALYSIS

1. Curve Fitting

Nearly all of the ultrafast data collected on the systems described in this dissertation require curve fitting. The only exception to that would be stage molecules, which are meant to show little-to-no decay over the delay of the translation stage and are used to determine the goodness of alignment of the laser system. Oddly enough, though, two of the three stage molecules also require population analysis when used on the longer-pulse system because their lifetimes actually cause a slight decay over the course of the 13 ns measured. These are $[Fe(tren(py)_3)]^{2+}$ ($\tau \sim 60$ ns in MeCN)[1] and $[Os(bpy)_3]^{2+}$ ($\tau \sim 60$ ns in MeCN),[2] for which $tren(py)_3$ = tris((N-(2-pyridylmethyl)-2-iminoethyl)amine) and bpy = 2,2'-bipyridine. But for the vast majority of complexes, even if the lifetimes are too long for the ultrafast systems to measure, there are other kinetic processes to be monitored, and these require exponential curve fitting. The Igor (WaveMetrics, Inc.) software is typically used for this, and the data presented in this work use IgorPro v. 6.37 or IgorPro v. 8.00. To access these capabilities in Igor, go to "Analysis" in the top bar and choose "Curve Fitting..." This will open a dialogue box with four tabs across the top. The first is "Function and Data," then "Data Options," followed by "Coefficients," and finally "Output Options."

The most common function used to fit data is a monoexponential (or the "exp_XOffset" function in the software), which models one lifetime from the ΔA vs. time (y vs. x) data:

$$y = y_0 + Ae^{\left(\frac{-(x-x_0)}{\tau}\right)} \tag{E.1}$$

in which y_0 and x_0 are the offsets of the y- and x-axes, respectively, A is the amplitude, and τ represents the lifetime. If multiexponential kinetics are observable, then this equation may be modified, as shown in eqn. (E.2):

$$y = y_0 + A_1 e^{\left(\frac{-(x-x_0)}{\tau_1}\right)} + A_2 e^{\left(\frac{-(x-x_0)}{\tau_2}\right)} + \cdots \quad \text{(E.2)}$$

The second most common function used to fit data is the Gaussian (or the "gauss" function). This follows the form:

$$y = y_0 + A e^{\left(-\left(\frac{x-x_0}{width}\right)^2\right)} \quad \text{(E.3)}$$

Width here is equal to twice the standard deviation of the Gaussian function. This type of curve is used for a variety of purposes in the ultrafast laser lab, including in the calculation of the pulse duration, Gaussian deconvolution, finding the beam width, and many others.

When fitting the kinetics of a complex with IgorPro, in the dialogue box under the "Function and Data" tab, choose the desired function. If the kinetics are unknown, it is often useful to begin with a monoexponential function and increase the number of exponentials in the fit only as needed. Choose the y and x data from the drop-down menus; selecting "From Target" is useful if the last window that was open was the one with the data being fit. Next, choose the "Data Options" tab. If no values are supplied for the "Range," then all the data will be fit, including any negative-time points. It is best if the cursors are placed around the data that displays the kinetics (Fig. E.1). The cursors are accessed by pressing ctrl+i on Windows or command+i on iOS when the graph is selected. Both cursors can be placed on the graph, or just one. If using the cursors, in the "Curve fitting" window under "Data Options," press "Cursors" if using both, or type "pcsr(A)" for the ⊕ (or "pcsr(B)" for the ⊠) into the Start or End window if only using one.

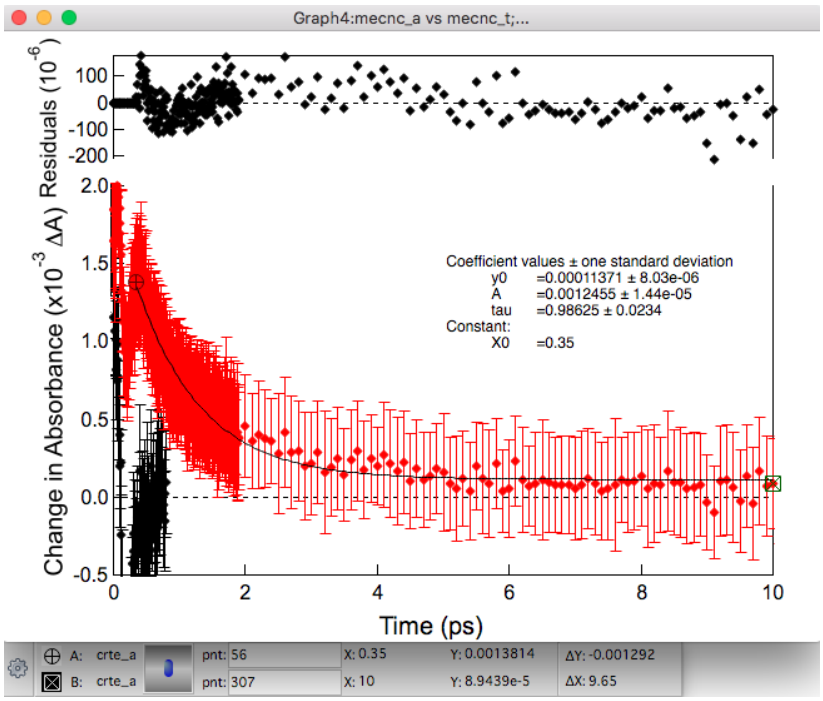

Figure E.1. Example of data (red diamonds) fit in Igor Pro 8 with a monoexponential function with an x-offset (black trace). The constants are provided in a box on the graph, and residuals are displayed as black diamonds above. The solvent scan (black diamonds, below) is provided for reference. The cursors can be seen in the gray box below the graph. In the residuals an oscillation is visible, particular before ~6 ps. This indicates that another exponential may be required to fit the data well. (Data shown are of the complex CRT-S3-174 in MeCN, λ_{exc} = 430 nm, λ_{probe} = 620 nm.)

Once the data to be fit has been selected, initial guesses for the coefficients can be made in the "Coefficients" tab, though this is only required when performing a user-defined fitting function for the first time. Finally, in the "Output Options" tab, the Destination should read "_auto_". Residuals can be added (as in Fig. E.1) by selecting "_auto trace_" from Residuals, as can the fit coefficients be added to the graph by checking the "Add Textbox to Graph" box. When finished making adjustments, select "Do It." This should result in a graph similar to that shown in Fig. E.1.

The residuals are a measure of the goodness of fit of the model to the data. Ultimately, they should be evenly centered around ΔΔA = 0, and there should be no visible oscillations in the residuals. In Fig. E.1, there is a well-defined oscillation for Δt < 6 ps in the residuals: initially they begin above 0, decrease to less than 0, and increase again to >0, at which point they eventually level out to ΔΔA = 0. This typically implies that a second exponential must be added to the fitting function. When this is done (Fig. E.2), in fact, the residuals are more evenly dispersed around 0, and no well-defined oscillations are observable any longer. Furthermore, the error bars on both the amplitudes and lifetimes are reasonable; often if a biexponential is fit to data that is well-described by one exponential, the error bars are many orders of magnitude greater than the average value.

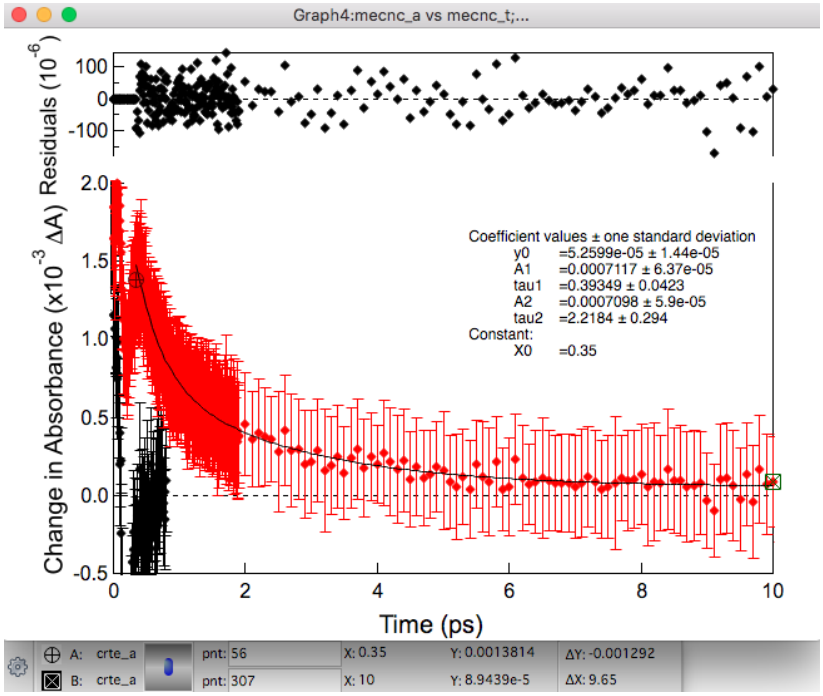

Figure E.2. Data of CRT-S3-173 in MeCN (red diamonds) fit in IgorPro with a double exponential function with an x-offset (black trace). The residuals (black diamonds, above) are more evenly distributed around ΔΔA = 0, confirming goodness of fit. The black diamonds below represent the solvent trace, for reference.

1.1 Writing and Saving Procedures

For the data presented in Chapters 2, 3, and 5, an Arrhenius model was used to calculate values of activation energy (E_a) and frequency factor (A) from variable-temperature transient absorption spectra. The Arrhenius equation, eqn. (E.4),

$$k_{nr} = Ae^{\left(\frac{-E_a}{k_B T}\right)} \tag{E.4}$$

for which k_{nr} represents the ground state recovery rate, k_B is Boltzmann's constant, and T is temperature, can be linearized, such that

$$\ln k_{nr} = lnA - \frac{E_a}{k_B}\left(\frac{1}{T}\right) \tag{E.5}$$

for which the y-intercept is ln(A) and the slope is given by E_a/k_B. While a simple linear fit is easily done in Igor, the Arrhenius function is not one that comes pre-loaded to the software. For this, and other functions that may need to be called on semi-regularly or more, Igor allows users to write functions and to save them for use at a later time.

In order to demonstrate writing a user-defined function in Igor, the linearized Arrhenius equation will be used as an example. In the "Function and Data" tab of the Curve Fitting window, click the button labeled "New Fit Function..." This will open a new dialogue box named "New Fit Function." The first step is to name the function. Then, under "Fit Coefficients," type any variables that are not to be held constant. For instance, if eqn. (E.5) is the desired function, "A" and "Ea" would be entered as the fit coefficients so that Igor can do all the calculating. Because the x-data for this fit is 1/T, under "Independent Variables" would be typed "InverseT". Once all the coefficients are described, move to the "Fit Expression" box, where it will begin formulating the function as "f(InverseT) =". From here, the rest of the expression is typed in, and it ultimately will appear as:

$$\text{f(InverseT)} = \ln(A) - ((Ea/0.69503)*\text{InverseT}) \tag{E.6}$$

This is the Igor representation of eqn. (E.5), where 0.69503 ≅ k_B in cm^{-1}. When the function is properly formatted, press "Save Fit Function Now." This will close the New Fit Function window and bring the user back to the "Function and Data" tab of the Curve Fitting window, with the newly-written function selected. Ensure that the correct waves are chosen for the x and y data, then go to the "Coefficients" tab. At this point, there is no option to do the curve fitting with this function. The bottom of the window has an error message that explains, "You have selected a user-defined fit function so you must enter an initial guess for every fit coefficient." Therefore, initial guesses as to the variables' values must be made, mostly so that the curve fitting can begin with the correct order of magnitude for each. Type the estimated value under "Initial Guess" for each variable; if the curve returned is wildly inaccurate, it is likely that the guesses were not close to the right order of magnitude. With the guesses in place, press "Do It." This should return a curve on the graph, as well as a box with the values of the variables. Once the function has been run once on a set of data, it is not necessary to make initial guesses as to the coefficients any longer. This is only needed if fitting a new set of data, or if the curve fit poorly the first time.

If there is a user-defined function that would be convenient to have readily available for use in Igor in the future, Igor allows for curves to be saved for exactly that purpose. Write the function as outlined above, then from the "Windows" menu in the top bar, go to "New" then choose "Procedure..." This will open a dialogue box. Name the Procedure then press "OK." A window will open that is similar to the Command Window. Now choose Windows → Procedure Windows → Procedure Windows, which will appear very similar to the new procedure window but will have text in it. This text should resemble Scheme E.1 below. Select all of the text, then copy and paste it into the blank procedure window. Choose File → Save Procedure As... To open the procedure in a new experiment, select File → Open File → Procedure... This will open the procedure dialog

box with the text that defines the curve fitting function. The function should now appear in the Curve Fitting options.

```
Function arrhenius(w,InverseT) : FitFunc
    Wave w
    Variable InverseT

    //CurveFitDialog/ These comments were created by the Curve Fitting dialog. Altering them
        will
    //CurveFitDialog/ make the function less convenient to work with in the Curve Fitting dialog.
    //CurveFitDialog/ Equation:
    //CurveFitDialog/ f(InverseT) = ln(A)-((Ea/0.69503)*InverseT)
    //CurveFitDialog/ End of Equation
    //CurveFitDialog/ Independent Variables 1
    //CurveFitDialog/ InverseT
    //CurveFitDialog/ Coefficients 2
    //CurveFitDialog/ w[0] = A
    //CurveFitDialog/ w[1] = Ea

    return ln(w[0])-((w[1]/0.69503)*InverseT)
End
```

Scheme E.1. Text held within the "Procedure" window in Igor upon creation of a user-defined function. This code can be saved for use at a later date.

2. Gaussian Deconvolution

To better understand the electronics of the excited states of a complex, spectroscopists will on occasion use a method known as Gaussian deconvolution of ground state absorption spectra. This is the process of taking a simple UV-Vis and using a summation of Gaussians to recreate the original spectrum. This technique was used throughout this dissertation in an attempt to better define pump and probe wavelengths. It has been noted previously, and should be noted again, that Gaussian deconvolution only provides one possible set of Gaussians that might describe the spectrum. Deconvolution is arbitrary and simply a mathematical function, so it should only be used as a first approximation.

Igor currently has two programs for multipeak fitting: 1.4 (old version) and 2. These can be accessed by selecting Analysis → Packages → Multipeak Fitting. We will begin by using the old version, and then the method for the new version will be described after. First, the data should be plotted versus energy units, not wavelength. This allows the Gaussians to be accurately determined. From the Multipeak Fitting menu in Igor, choose Multipeak Fitting 1.4 (old version). This will bring up a dialog box, as seen in Fig. E.3. It is often useful to change the x-axis on the graph so that it reads from high energy (left) to low energy (right), as a typical UV-Vis spectrum would. To do this, double-click on the x-axis on the graph, then select the last tab at the top labeled "Axis Range" and check "Reverse Axis" under Autoscale Settings.

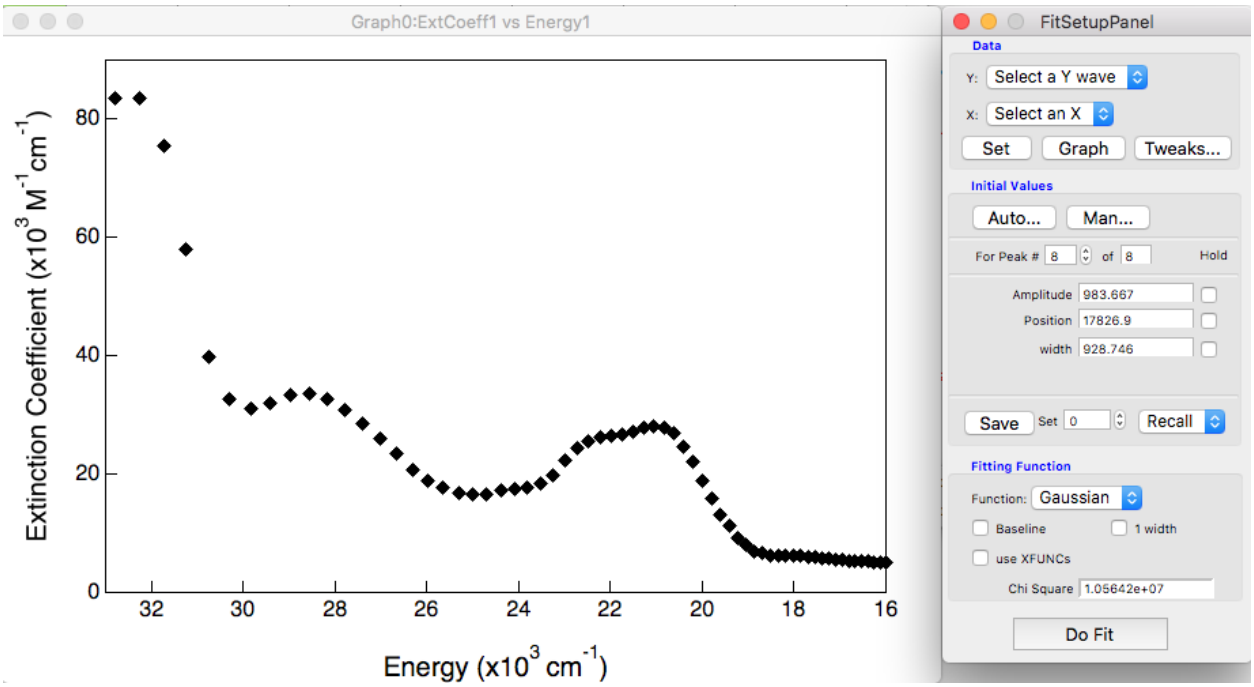

Figure E.3. (Left) The absorption spectrum of $[Ru(dpb)_3](PF_6)_2$ in MeCN plotted against energy. (Right) The multipeak fitting panel for version 1.4 in Igor.

When fitting an absorption spectrum for the first time, it is often useful to limit the range of the x-axis, which will also limit the number of peaks Igor attempts to find. Additionally, in moving to higher energies, there is a much greater density of states which will inherently increase the degree of overlap between absorption peaks. Obviously this will make it harder to fit the spectra in these areas. For example, in Fig. E.3, the band centered at ~28000 cm^{-1} significantly overlaps with the high-intensity feature at ~32000 cm^{-1}. The identity of the lower energy transition was desired for the analysis of $[Ru(dpb)_3]^{2+}$, so the higher energy band was included in the analysis for accuracy. However, the exact parameters of the feature at ~32000 cm^{-1} will be viewed with skepticism as any higher-energy bands are discounted from this analysis.

In the peak fitting panel, choose the x- and y-waves from the spectrum that should be fit. Choose "Set," and an initial guess of peaks will be added to the figure in red. These peaks will be

offset by some amount, so the y-axis may need to be expanded. This is also necessary as Igor may calculate a Gaussian with a negative amplitude (which is physically impossible but demonstrates the point that this process is a mathematical construct). It is often very useful to generate the Gaussian curves in a table in Igor and sum them in a separate wave, so that the summation can be added to the plot. This will allow for better visual confirmation of the goodness of fit, as opposed to the χ^2 value supplied by Igor (Fig. E.4). For example, the spectrum provided may appear as if only four Gaussians are needed to describe the data, as shown in Fig. E.4. But the summation of these bands clearly demonstrate that this is a poor fit clearly missing features, particularly low-amplitude, high-bandwidth features that underlie nearly the entire spectrum.

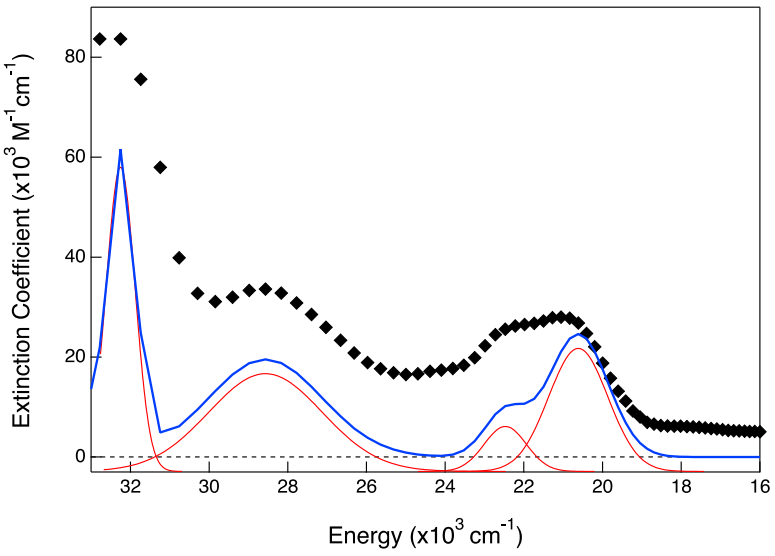

Figure E.4. Ground state absorption spectrum (black diamonds) of $[Ru(dpb)_3](PF_6)_2$ in MeCN. Igor initially finds four main Gaussians (red traces) but when summed together (blue trace), the spectrum is clearly not well-represented.

It is evident from Fig. E.4 that more than four Gaussians are required to reconstruct the

ground state absorption spectrum. Therefore, the number should be increased in the Multipeak Fitting dialog box by one. Under "Initial Values," go to the second box in the "For Peak #" line and type in the number of Gaussians desired. The initial guess for the added Gaussian is likely to be wildly off. It is then useful to hold the first iteration of peak values (check the "Hold" box next to each) while doing the initial fitting, and then slowly relaxing the fit parameters individually to allow Igor to find the best estimate. This should be done reiteratively while increasing the number of Gaussians until the best representation of the data is achieved (Fig. E.5).

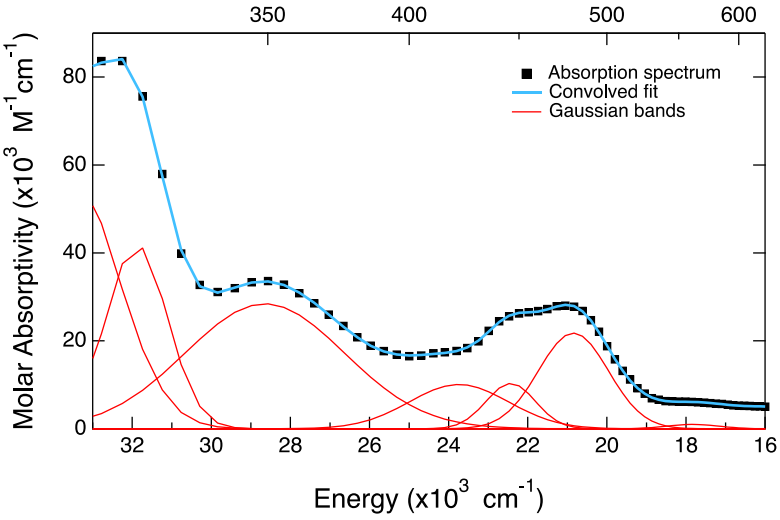

Figure E.5. Steady state absorption spectrum (black diamonds) of $[Ru(dpb)_3](PF_6)_2$ in MeCN reconstructed (blue trace) by Gaussian deconvolution. Seven bands were required to fit these data.

Alternatively, the newer version of Multipeak Fitting in Igor (version 2) may be used. This will initiate a dialog box (Fig. E.6) that requires the x- and y-waves to be selected, as well as the target for the new waves. When "Continue" is pressed, a second dialog box appears (Fig. E.7) that allows the user to "Auto-locate Peaks Now," which should be pressed. This will result in an initial guess as to the number and shape of the peaks, as well as the summation spectrum in overlaid on

the original spectrum, and the calculated residuals. Under "Set Peak Type for All Peaks," choose "Gauss." By clicking the arrow next to any peak, the parameters can be viewed and held, as above.

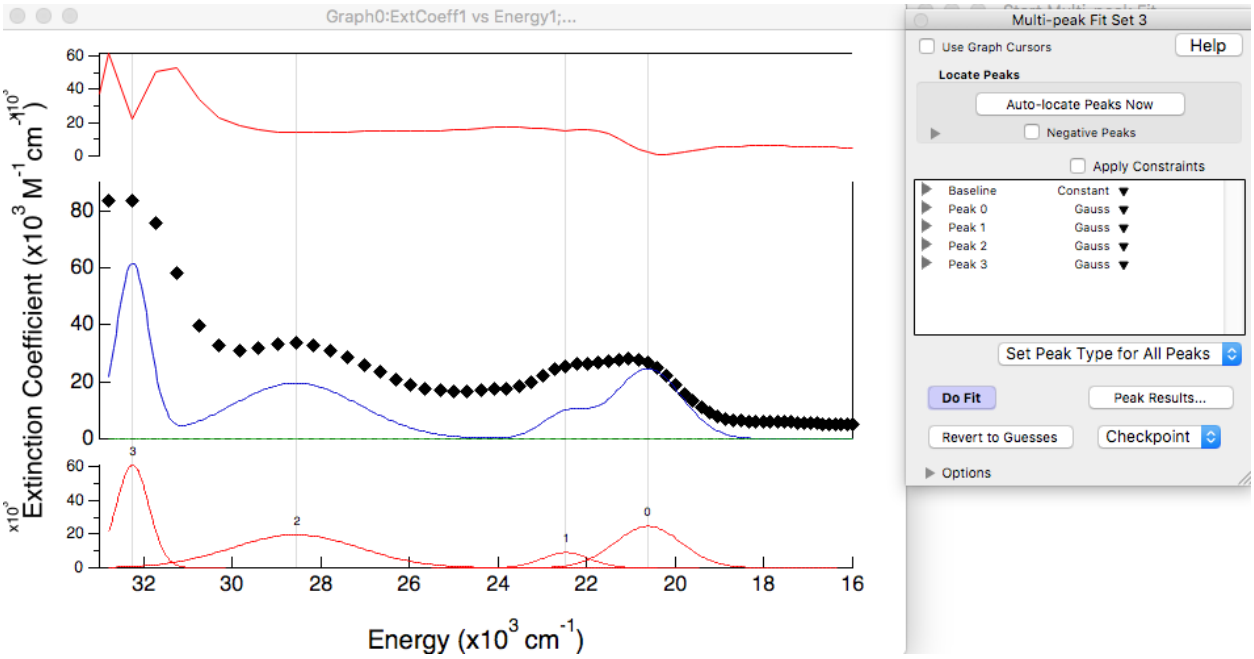

Figure E.6. (Left) Ground state absorption data of $[Ru(dpb)_3](PF_6)_2$ in MeCN. (Right) Multipeak fitting dialog box for version 2 in Igor.

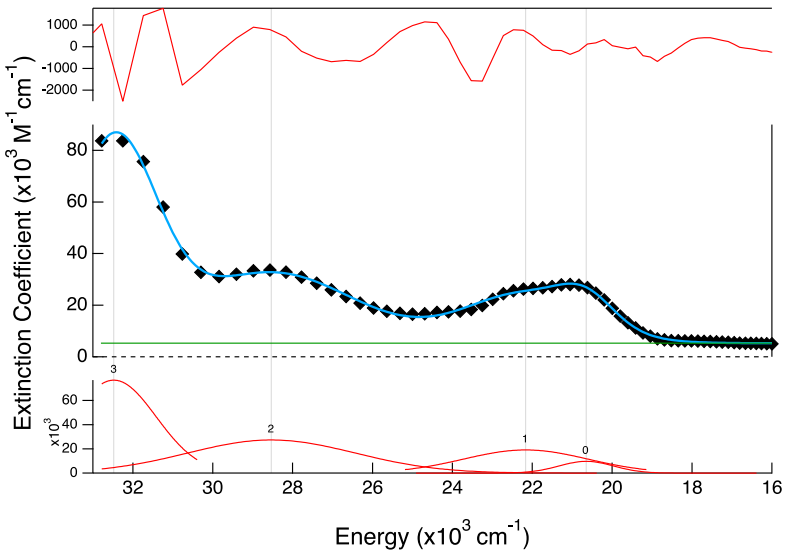

Figure E.7. Multipeak Gaussian fitting of the absorption spectrum of $[Ru(dpb)_3](PF_6)_2$ in MeCN using version 2 of the software. The original data are held in the middle panel (black diamonds) along with the summation of Gaussians (blue trace) that is composed of the individual Gaussians calculated in the bottom panel. Above is shown the residuals.

After pressing "Do Fit" three times without changing any parameters, a new spectrum that modestly represented the data was achieved with only four peaks and a baseline (Fig. E.7). It is evident, however, that this convolved spectrum does not fully represent the ground state absorption spectrum in its entirety. While it may be subtle, the red feature ~18000 cm^{-1} is underestimated, there is poor fitting of the blue shoulder of the low-energy MLCT transition (~23000 cm^{-1}), as is true of the blue shoulder of the higher energy MLCT band at ~29000 cm^{-1}. This would appear to imply at least three bands are missing from the analysis. To do this using the version 2 software, drag a box around the area that appears to be missing a peak. Right click in the box and select "Add or Edit Peaks." This will bring up an expanded view of the spectrum (likely with an inverted x-axis). Click and hold on the spectrum and drag the cursor down, creating a positive Gaussian.

Press “Done,” which will close the dialog box and return to the original spectrum that now has an addition peak. To optimize the shape of this new Gaussian, in the Multipeak Fitting box, press “Do Fit.” Do this reiteratively until the convolved spectrum matches the original as well as it can without adding further Gaussians (Fig. E.8).

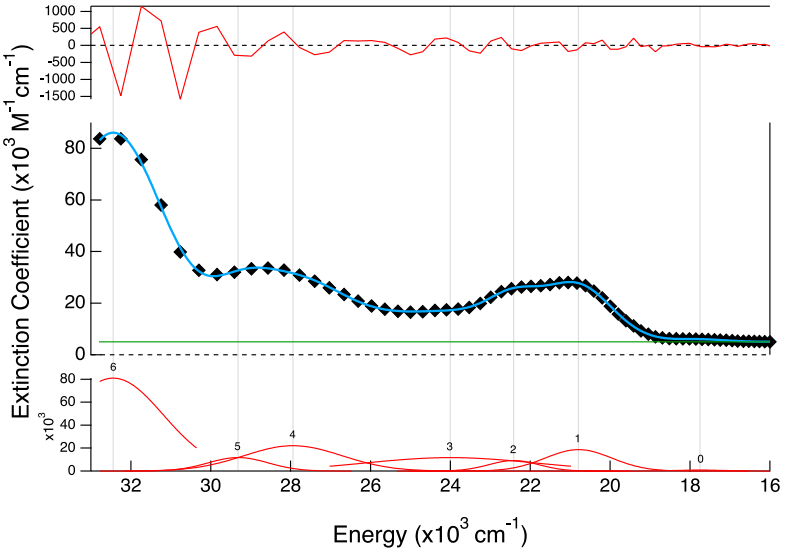

Figure E.8. Ground state absorption spectrum of $[Ru(dpb)_3](PF_6)_2$ in MeCN (black diamonds) overlaid with the convolved Gaussian fit (blue trace) in the center panel made up of the sum of the individual curves in the lower panel. The residuals (upper panel) are evenly dispersed around $\Delta A = 0$. The greatest amplitude features are near the highest energy portion of the spectrum, which is to be expected (see text for details). Seven Gaussians were required to reconstruct these data.

Ultimately, both versions of the software provided seven Gaussians for the best fit. Additional curves may always be added, but they likely become extraneous. The summary of the curves are given in Table E.1 for comparison between the two methods. Version 2 of the software tends to be more user-friendly in that it generates the residuals and the summation curve

automatically. But either can be used for this technique with comparable results. In fact, the central energy of each of the bands are very similar, particularly for the four lowest-energy peaks ($\Delta x_0 <$ 100 cm^{-1}). The greatest differences are in the higher energy bands, and in peak 4. The higher energy transitions are explained using the density of states logic outlined above. Peak 4 is defined by the v.2 software to have a width of 3000 cm^{-1}, which consequently causes the amplitude of the four bands nearest in energy to it to have drastically smaller amplitudes relative to those calculated by the v. 1.4 software. This serves to illustrate the fact that Gaussian deconvolution, even when performed by the same curve fitting software (Igor Pro), can result in two different sets of peaks, proving the point that these data should only be viewed as a first approximation of the excited states.

Table E.1. Fit parameters for Gaussian deconvolution in Igor by both version 1.4 and 2.

Software Version	Fit Parameters	Peak 1	Peak 2	Peak 3	Peak 4	Peak 5	Peak 6	Peak 7
v. 1.4	A (M^{-1} cm^{-1})	57900	41900	28400	10100	10300	21800	1000
	x_0 (cm^{-1})	33600	31900	28700	23700	22400	20800	17800
	width (cm^{-1})	1700	1100	2800	1800	900	1300	900
v. 2	A (M^{-1} cm^{-1})	81000	11800	22100	11700	9200	18700	900
	x_0 (cm^{-1})	32400	29300	27900	24000	22400	20800	17700
	width (cm^{-1})	1800	1100	1700	3000	900	1200	900

3. Full Spectral Data

Single-wavelength experiments are a powerful method for very accurately determining

lifetimes associated with photophysical processes. However, if a sample is entirely new, it is often necessary to begin by collecting full spectral data. This allows for a full picture understanding of the time-dependence of the spectra, not just the kinetics at one specific probe wavelength. Full spectra are essential if photochemistry is believed to be occurring in the sample under irradiation, such that new chemical species are being formed. The set-up of this experiment has in essence already been described in Chapter 2, which utilizes a pump and a white light probe; the difference comes down to detection. Instead of using a photodiode which treats all colors as one signal, a polychromator must be used which is capable of detecting signal from many different probe wavelengths at the same time. This can be in the form of a photodiode array (PDA) or a charge-coupled device (CCD). PDAs are often cited as having a sensitivity range better suited for transient absorption signals whereas CCD detectors are more frequently used in emission experiments, however some have shown that both are capable of producing equally high-quality data.[3] The detector must be well-calibrated prior to use, and this is typically done with the use of a Hg/Ar lamp which has well-defined emission peaks. This procedure has previously been described by J. N. Miller.[4]

When collecting full spectral data, if a window of ~1 ns or less is collected, a solvent scan should also be included so that the wavelength-dependent dispersion, or chirp, can be accounted for (see Appendix F for a more thorough description of chirp). This requires running the solvent under the same conditions as the sample (i.e., density of points). The number of points and number of scans can be different between the two, however. Additionally, because of the nature of the chirp-correcting procedure, the time points must be evenly spaced, and it is important to collect an extraneous number of points in the negative time, and again with points after the signal being measured. Chirp-correction applies a polynomial function to the solvent response, then linearizes

the data based on that polynomial. Therefore, any pixels on the edges are smeared greatly, so these should not be points that are used in the calculation of the kinetics. It is also imperative to collect full spectral data under unchanging conditions, meaning any ambient light or stray laser scatter must stay constant during the collection period.

3.1 Data Work Up Procedure

This work-up procedure (known as ChirpCorr_v6-4.ipf) was previously written by A. L. Smeigh[5] with modifications from A. M. Brown.[6] For ease of discussion, line numbers are added to the beginning of each line and should not be included when input into the Igor Command Window. The procedure must be called on before any of the code in Scheme E.2 can be applied. The code to be entered in the Command Window is given in black. Actions that must be taken by the user are given in red.

---

1 Load ChirpCorr_v6-4.ipf

2 In Excel, or wherever the averaged full spectra data can be opened in a table, an array of the ΔA data should be starting in the second row of the second column. The top row should contain the time points, and the first column shows the wavelengths. Correct the time points so that Δt = 0 is near the center of the solvent scan. The exact placement of time-zero is not critical, but it must remain constant between the solvent and sample data sets. Ensure the wavelengths are correct given the number of pixels and the calibration of the spectrometer. These should be the only data outside of the ΔA array, so delete any extraneous columns

---

Scheme E.2. Code for IgorPro for full spectral transient absorption data work up. The code is provided in black, where the comments are presented in red. Italicization indicates that the value given is a placeholder and should only be taken as an example.

Scheme E.2. (cont'd)

---

or rows. Save this as a worked up file; it will be called on by Igor for processing.

3 loadSpectrum("*FolderName*","*FileName*", "solvent")

4 The quotation marks are required when name the folder and file names that are titled whatever they are in the computer being used. This will open a dialog box and allow the user to choose the correct file. Here, the final averaged solvent scan that was worked up as outlined above is chosen. The third input in this command is the name that the window with the spectra will be given.

5 SetScale/I x 315.065,611.959,"Wavelength (nm)", solvent; SetScale/I y -0.134,1.5,"Time (ps)", solvent

6 This redefines the x- and y-axes of the solvent window. The values given should be the bluest and reddest wavelengths from the worked up solvent file for the x-axis, just as the most negative and most positive time points are given for the y-axis. The names given in quotations are the axis titles. The spectrum displayed should have time in the y-axis and wavelength in the x-axis.

7 DTSpectrum(solvent, "solvent_trans")

8 The copies the spectrum in solvent and pastes it into a new window transposed. See Fig. E.9.

9 ShowInfo

10 edit

11 Lines 10 and 11 should bring up the cursors and open a new table, respectively. Use the cursors to follow the center of the solvent trace. In the table, type the wavelength in the first wave, and the time in the second wave. Do this for as much of the solvent trace as possible. It is likely that the shape will change as redder wavelengths are reached. For tricks on finding

Scheme E.2. (cont'd)

---

the center of the solvent trace, see Appendix E Section 4.2 below.

12 Display wave1 vs wave0

13 This will display a plot that should be time versus wavelength. The general shape should arc from the bottom left toward the top right.

14 CurveFit dblexp_XOffset, wave1 /X=wave0 /D

15 This fits the time versus wavelength data with a double-exponential function. If this function does not describe the data well, a polynomial of the 4th or 5th order can be used. The fit coefficients it returns are, in order: y_0, A_1, τ_1, A_2, τ_2, and x_0. See Fig. E.10.

16 DupSpectrum(solvent_trans, "solvent_cc")

17 This duplicates the spectrum so the chirp-correction will not alter the original data.

18 solvent_cc=solvent_trans(x+Chirp(y_0, A_1, τ_1, A_2, τ_2, x_0, y))(y)

19 The coefficients obtained from the exponential fit of the solvent trace are used here. The rest of the code should be copied exactly. This should then correct the solvent_copy data so that $\Delta t = 0$ for each wavelength is one unified $\Delta t = 0$ (Fig. E.11), not spread over 1-1.5 ps as was the case before.

20 loadSpectrum("*FolderName*","*FileName*", "sample")

21 SetScale/I x 315.065,611.959,"Wavelength (nm)", sample; SetScale/I y -0.134,1.5,"Time (ps)", sample

22 DTSpectrum(sample, "sample_trans")

23 Lines 20-22 are the same for the sample as they were for the solvent. After transposing the sample data, a table should be made with the sample_trans data. Select all of the TA data by clicking on the first wave name, then pressing control+a on PC or command+a for Macs.

Scheme E.2. (cont'd)

Copy the data into the clipboard by pressing control+c (PC) or command+c (Mac).

24 LoadWave/J/D/A=sample_SW/E=1/K=0 "Clipboard"

25 This will paste what was previously copied into a new table.

26 Instead of using the code above, it is possible to do this manually. Choose Data → Load Waves → Load Waves... or press control+l for PC or command+l for Mac. Uncheck "Read Wave Names" and check "Make Table," "Load From Clipboard," and "AutoName & Go." If basing this on the command in line 24, use the basename "sample_SW" in the autonaming. Pressing "Do It" will cause a new table to appear with the copied data.

27 From the sample_SW matrix, select the time points and copy them.

28 LoadWave/J/D/A=time_sample/K=0 "Clipboard"

29 BaselineAdj("sample_SW", 0, *4*, *495*)

30 This corrects for any baseline offset that is present in the data. The name of the sample waves to be corrected are named, followed by the first point collected (always = 0), followed by the number of negative time points that can safely be counted as background meaning no signal has begun by this time point at any wavelength. The last number is the total number of points in the wavelength vector.

31 DupSpectrum(sample_trans ,"sample_copy")

32 Copy the data from sample_SW and paste it into the sample_copy matrix.

33 DupSpectrum(sample_copy,"sample_cc")

34 sample_cc=sample_copy(x+Chirp((*y*$_0$, *A*$_1$, *τ*$_1$, *A*$_2$, *τ*$_2$, *x*$_0$, y))(y)

35 These should be the exact coefficients used in line18 above. The spectrum of the sample data should now also be chirp-corrected.

Scheme E.2. (cont'd)

36 DTSpectrum(sample_cc,"sample_final")

37 Copy the wavelengths from the sample_final table.

38 LoadWave/J/D/A=wavelength_sample/K=0 "Clipboard"

39 Copy all of the TA data from sample_final.

40 LoadWave/J/D/A=sample_FS/K=0 "Clipboard"

41 plotSpectra("sample_FS",wavelength_sample0,*140*)

42 This plots the final, chirp-corrected spectral data against the wavelength vector. The final input number is the number of time points. The chirp-correction can often leave the spectra looking very jagged, particularly around time-zero (Fig. E.12). It is useful, then to apply a smoothing function. From the sample_FS vs. wavelength_sample0 plot, choose Analysis → Smooth... From the source, select the sample_FS waves that will be plotted. This is easier if the "From target" box is checked. From the algorithm, select boxcar and set the smoothing number to 30. This number should never be greater than 30 or else it implies there are fundamental issues with the data collected. Hit "Do It." From here, the smoothed waves (_smth will be appended to the names) can be plotted against the wavelength vector.

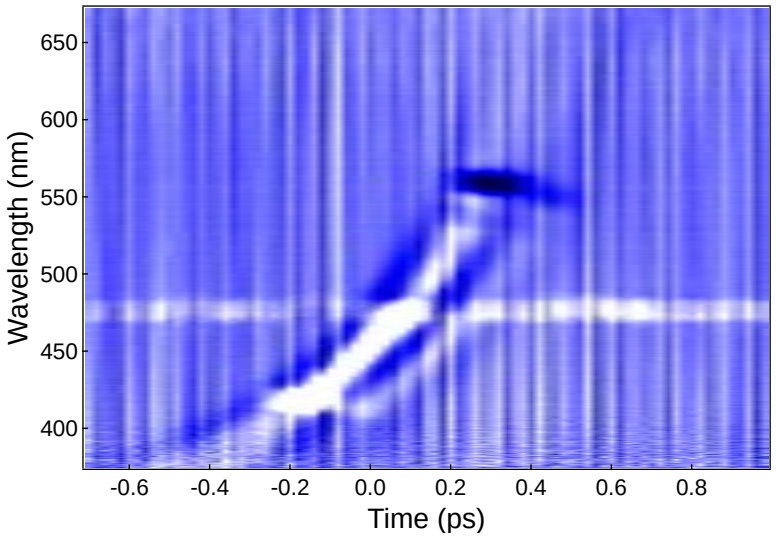

Figure E.9. Full spectral data of a solvent scan. Pale blue indicates $\Delta A = 0$, whereas white is a positive feature and dark blue is a negative feature. The center of the signal is taken to be time zero at that wavelength. From these data, it is clear that "time-zero" actually spreads from -0.4 ps at the bluest wavelengths to nearly 0.3 ps at ~550 nm.

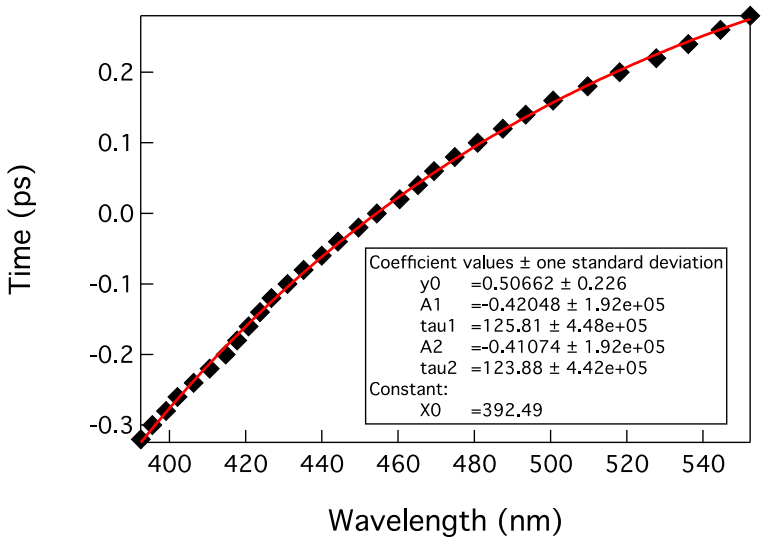

Figure E.10. Plot of the time and wavelength points (black diamonds) from the full spectral solvent scan fitted with a double exponential (red trace) that is used for the chirp correction.

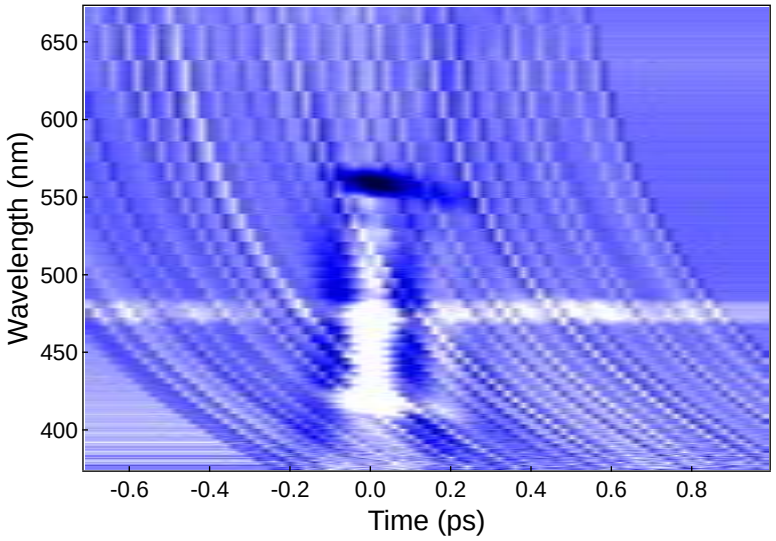

Figure E.11. Full spectral solvent trace after the chirp correction has been applied. Here, the center of the solvent traces are all lined up at $\Delta t = 0$. In the lower left and upper right corners, the chirp-correction is evident in the smearing of the pixels, which is why it is important to collect extra time points before and after the signal.

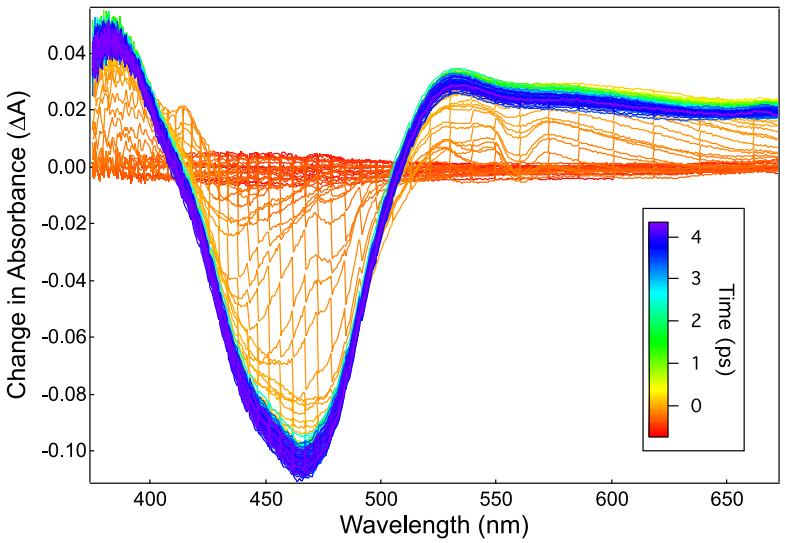

Figure E.12. Full spectral data of $[Ru(dpb)_3](PF_6)_2$ in EtOH. These data have been chirp-corrected but not smoothed, which is why there are jagged features in the spectra that are near $\Delta t = 0$.

3.2 Solvent Fitting

One of the more challenging procedures in the full spectral data work up is the determination of the center of the solvent trace for any given wavelength. Fig. E.13 will be taken as an example; these are the same data shown in Fig. E.9, but in different colors. The first step is to choose a color scheme with a high degree of separation between the different signs. To do this, go to Graph → Packages → Color Table Control. The color table chosen for Fig. E.13 is "YellowHot." Additionally, the color scale was changed to increase the contrast, allowing for better understanding of the spectra. The best contrast with this color table is when the most positive and most negative values are roughly equal. Next, identify the shape of the solvent response. For approximately 400-530 nm, the shape of the signal appears to be roughly the same. Going from negative to positive time, the signal dips, goes very positive, dips below negative again, and then has a very small positive feature. Looking specifically at 450 nm, the negative signal begins at -0.14 ps (where it begins to go darkest), and the signal appears to be complete by 0.18 ps. The center of this signal must then be 0.04 ps. This happens to be where the brightest yellow turns into red (positive goes to negative), which may not intuitively be where one would call the center of the signal.

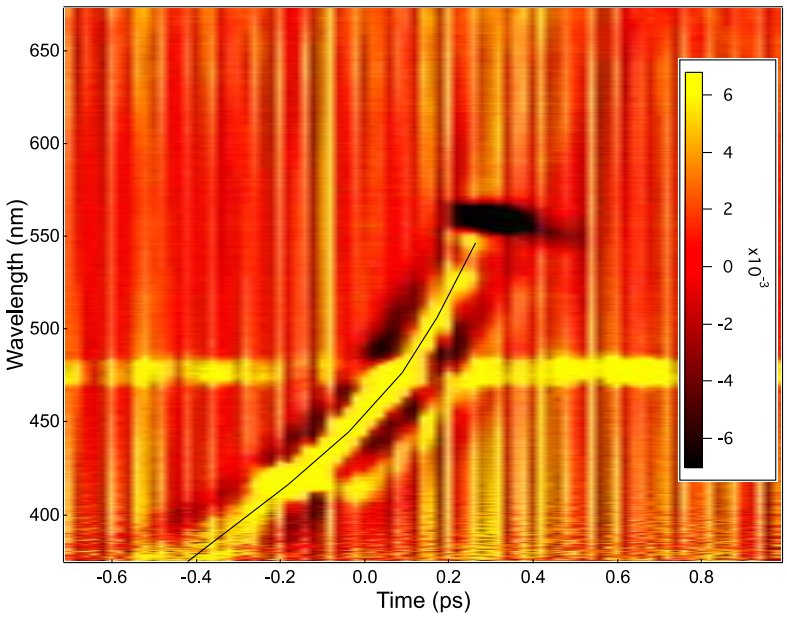

Figure E.13. The data plotted in Fig. E.9 but recast in a different color scheme and modulated so the positive and negative color scales were roughly equal. This helps increase the contrast. The black line in the center of the yellow signal helps guide the eye and is user-drawn.

Another method can be combined with the procedure above or may be used on its own. It involves drawing a line at the approximate center of the most distinguishable feature (here, the yellow stripe), and using that as a guide for the eye. To do this, type ctrl+t or command+t from the solvent window. This will open a Toolbar on the side of the window. If the topmost option is selected, click on the tab below it, which shows grayed geometric shapes. Then click the tab with the line. Go to the center of the most identifiable feature, at the bottommost wavelength. Click once and drag the cursor away. A black line should be following the cursor. Use this to place a series of small black lines to draw a curve through the center of the feature. This line can be seen in Fig. E.13. Then, use the cursors to follow this line in order to determine the wavelength-time correlations for the chirp-correction.

4. Singular Value Decomposition

As is true for all spectroscopic techniques, pump-probe spectroscopy has inherent artifacts that require thorough understanding and potential correction.[7] Many of these signals come from the fact that peak powers of ultrafast pulses are on the order of 10^9 W. It should come as no surprise then that the majority of the high-intensity artifacts are observed at time zero, the point at which the pump and probe pulses meet both spatially and temporally within the sample. During negative time (when the probe pulse propagates through the sample prior to the pump pulse) and positive time (vice versa), these signals are less likely to occur. Unfortunately, low signal/noise ratios and wavelength-dependent noise are two time-independent problems that also occur. In all of these situations, little to no knowledge *a priori* of the molecular dynamics makes it nearly impossible to discern real signal from spectral artifacts.

Since 1982, singular value decomposition (SVD) has been a mathematical approach for analyzing spectral data in order to separate real signals from instrumental artifacts.[8] To implement this tool in our lab, the underlying mathematical principles of SVD were used to write MATLAB scripts. SVD was built on the principles of linear algebra, and begins by assuming that every matrix A (λ, t) can be decomposed according to eqn. (E.7):

$$A = USV^T \tag{E.7}$$

in which U (λ, n) is an array of the left orthonormal eigenvectors of AA^T, S (n, n) is a diagonal matrix of decreasing eigenvalues of AA^T, and V (t, n) is an array of the right orthonormal eigenvectors of A^TA.[9] In layman's terms, S determines the significance of the n^{th} columns of U and V. Columns of U and V in turn are the spectral and kinetic traces of A, respectively.

For ultrafast TA spectroscopy, SVD is a powerful tool that can allow the spectroscopist to determine the origin of spectral and kinetic features in full spectra data. The first way in which this

is done is by determining which values of S are significantly greater than the noise. Although components in the noise do correlate to real spectral and/or kinetic features they are typically insignificant to the point that assignment is unnecessary.[9] The number of vectors of U and V that are significant directly correlate to the components of S that are separate from the noise. U and V are then plotted against wavelength and time to give the respective spectral and kinetic traces of the data.

4.1 Using the MATLAB Code

MATLAB is a powerful calculating tool which has the added benefit of already coming equipped with the SVD coding. MATLAB (MathWorks) R2012a was used for the results presented herein. While the MATLAB-based code was used, some additional modifications were made in order to make the data more understandable to the user, thus resulting in the code provided in Scheme E.3. For ease of reading, line numbers are given to the left of the code, but these should not be included in the actual script. Any font in green is a comment meant to explain what function the line(s) of code is performing. Both scripts given below are functions such that only the input variables need be known ahead of time. The format of the function is: brackets denote what outputs will be given once the function is performed (these can be changed from the Command Line and do not require the script to be rewritten), the name in blue denotes the name of the function being used, and parentheses indicate the inputs required to perform the function. Inputs can be placed directly into the command line when calling on the function, or they can be defined as variables previously, in which case the variable needs only be called on. For the inputs, startw is the first wavelength from the full spectral data, endw is the final wavelength, and wint is the interval between each wavelength. Similarly, startt is the first time point collected, endt is the final time point, and tint is the interval between each time point. A is the two-dimensional array of full

spectral data. This data can be baseline-corrected and/or chirp-corrected; the effect of these corrections should be viewed on a case-by-case basis as different data sets will require different handling prior to SVD analysis.

```
1   function [U,S,V,time,wavelength] = mccSVD(startw,endw,wint,startt,endt,tint,A)
2
3   %% The SVD function
4
5   %The purpose of this function is to perform SVD on the full spectral data,
6   %A, input by the user. This function does not plot the significant
7   %singulars, it only gives the user the information about which components
8   %are significant. For the plotting of those vectors, please use
9   %mccSVDsings.m.
10
11  wavelength = [startw:wint:endw]'; %build the wavelength vector based on the
12  %starting and ending points, as well as the interval distance
13  time = [startt:tint:endt]'; %build the time vector based on the starting
14  %and ending points, and the time interval
15
16  %% Displaying the SVD results
17
```

Scheme E.3. Code for MATLAB function mccSVD which performs SVD on a two-dimensional array of full spectral data.

Scheme E.3. (cont'd)

```
%This panel has two subplots and a table. The topmost plot is the raw
%data. Then SVD is performed and the middle plot displays the reconstructed
%full spectral data. The table on the bottom shows in various ways the
%significance of the components. This will be discussed further below.
A(A==inf) = 0; %search data for points at infinity and set them to zero
A(isnan(A)) = 0; %search data for non-numerals and set them to zero
fspanel=figure('Name','Full Spectra','NumberTitle','off',...
'Units','normalized','Position',[0 1 0.4 1]); %build a pane for figures
subplot('Position',[0.09 0.71 0.87 0.24]); %uppermost plot will contain
%raw 3D data
surf(time,wavelength,A,'EdgeColor','none');
title('Raw Data','FontSize',12);
xlabel('Time','FontSize',10);
ylabel('Wavelength (nm)','FontSize',10);
zlabel('Change in Absorbance','FontSize',10);
[U S V] = svd(A); %performing SVD
A_svd = U*S*V'; %recombining the decomposed vectors
subplot('Position',[0.09 0.37 0.87 0.26]); %middle plot will contain 3D
%data recombined from SVD vectors
surf(time,wavelength,A_svd,'EdgeColor','none');
title('SVD of Raw Data','FontSize',12);
xlabel('Time','FontSize',10);
```

Scheme E.3. (cont'd)

```
40      ylabel('Wavelength','FontSize',10);
41      zlabel('Change in Absorbance','FontSize',10);
42
43      %Columns 1 and 2 of Significance table contain autocorrelation values for
44      %singular vectors of U and V. The equations for the autocorrelation come
45      %from Henry and Hofrichter, Methods Enzymol. 210, 129-192.
46
47      ncol = length(U);
48      nrow = ncol;
49      u = zeros(1,ncol);
50      for icol = 1:ncol;
51              u(icol)=0;
52              for irow=1:nrow-1;
53                      u(1,icol) = u(icol)+(U(irow,icol)*U(irow+1,icol));
54              end
55      end
56      Significance = zeros(10,4); %building array that will be used in the table
57      Significance(:,1) = u(1,1:10)';
58      ncol = length(V);
59      nrow = ncol;
60      v = zeros(1,ncol);
61      for icol = 1:ncol;
```

Scheme E.3. (cont'd)

```
62              v(icol)=0;
63              for irow=1:nrow-1;
64                      v(1,icol) = v(icol)+(V(irow,icol)*V(irow+1,icol));
65              end
66      end
67      Significance(:,2) = v(1,1:10)';
68
69      %Column 3 of Significance table contains F-ratios from F-test. This is
70      %essentially comparing the standard deviation of reduced data set and the
71      %raw data set, with the standard deviation of just one data set. For more
72      %information on F-tests please see F_test.m.
73
74      p = length(A);
75      fb = 2*length(time)-1; %for the Between groups ratio
76      fw = 2*(p-1); %for the Within groups ratio
77      for q = 1:10;
78              z1 = U(:,q)*S(q,q)*V(:,q)'; %recompose data using q singulars
79              mean_c = mean(z1); %find the mean of each of the columns of z
80              z_m = mean(mean(z1)); %find the overall mean of z
81              Sb = sum(p*(mean_c-z_m).^2);
82              between_groups = Sb/fb; %Between groups value
83              z_b = z1(:,q)-mean_c(1,q); %difference of z column value and average column
```

Scheme E.3. (cont'd)

```
                value
84              Sw = sum(sum(z_b.^2));
85              within_group = Sw/fw; %Within groups value
86              Significance(q,3) = between_groups/within_group; %F-test ratio
87      end
88
89
90      %Column 4 of Significance table is value of S corresponding to rank.
91      for n = 1:10;
92              Significance(n,4) = S(n,n); %building a vector of the diagonal values of S
93      end
94
95      %The following commands insert the Significance array as a table into the
96      %third subplot area of the panel.
97      uitable('Data',Significance,'ColumnName',{'U','V','F-ratio',...
98          'Value of S'},'RowName',{'1','2','3','4','5','6','7','8','9','10'},...
99          'Units','normalized','Position',[0.4 0.04 0.59 0.24],'FontSize',12);
100     annotation('textbox',...
101         [0.0253055555555555 0.0421052631578947 0.363583333333333
            0.23625730994152],...
102         'String',{'','The number of significant singular','values is given by the number
            of','singular values in columns U or V','and >0.99, in column F-ratio >10.'},...
```

Scheme E.3. (cont'd)

```
103         'FontSize',12,...
104         'FitBoxToText','off');
105
106     end
```

The first line of code in the mccSVD script is calling on the function to be performed. There are lines of comments (which will be ignored for the present discussion), followed by the wavelength and time vectors being built in lines 11 and 13, respectively. Then non-numbers such as "NaN" and "inf" (not a number and infinity, respectively) are set as equal to zero. This returns a data set that can be handled by the SVD function. Ultimately, setting these values to zero does not change the analysis as these pixels were dark in the raw data. The "figure" function is in lines 24-25 used to create a panel which will display the results desired. The upper third of this panel will show the surface plot of the raw full spectral data, A vs. wavelength and vs. time, the axis titles of which are defined in the next lines (29-32). After the labels are given, SVD is performed in line 33, with the recombined A_svd value being calculated in the next line and plotted as the middle third in the previously-built figure panel.

The next section of code (lines 47-end) describes the statistical analysis performed on the weighting factors. First, autocorrelation is performed on both the U and V eigenvectors, which provides a measure of S/N for the specific elements of U and V.[9] The size of the autocorrelation matrix is defined in lines 47-48 for U and 58-59 for V; defining the array size first reduces the amount of processing time required to perform the calculation. Two for-loops are used with eqn. (E.8) to determine the autocorrelation values for U and V, $C(U_i)$ and $C(V_i)$, respectively:

$$C(U_i) = \sum_{j=1}^{m-1} U_{j,i} U_{j+1,i} \quad \text{(E.8a)}$$

$$C(V_i) = \sum_{j=1}^{n-1} V_{j,i} V_{j+1,i} \quad \text{(E.8b)}$$

Here, the j notation calls on the element of the i^{th} column of the array being selected. These values for each of the first 10 elements of U and V are placed into the first and second columns of the Significance table in the bottom third of the figure panel. From lines 74-87, the F-ratios are calculated and placed in the third column, which are a measure of the statistical comparability of the SVD data set and the raw data set. The F-test, eqn. (E.9)[10] to be more precise determines exactly

$$F = \frac{f_{Between\ Groups}}{f_{Within\ Groups}} \quad \text{(E.9a)}$$

$$f_{Between\ Groups} = \sum_{i=1}^{K} \frac{n_i(\bar{Y}_i - \bar{Y})^2}{K-1} \quad \text{(E.9b)}$$

$$f_{Within\ Groups} = \sum_{i=1}^{K} \sum_{j=1}^{n_i} \frac{(Y_{ij} - \bar{Y}_i)^2}{N-K} \quad \text{(E.9c)}$$

how many singulars of U and V are statistically required to describe the data set well. It is therefore presumed that all others will only contribute to minor changes or will increase the noise. In eqn. (E.9a) a ratio is taken of the variance between groups to the variance within groups. This is essentially looking at the error from one data set as a reference ($f_{Within\ Groups}$) and comparing it to a second data set and its error ($f_{Between\ Groups}$). In eqns. (E.9b and E.9c), K is the number of data sets being evaluated, Y_{ij} would represent the j^{th} element of the i^{th} group in the sample (with $\bar{Y}$ therefore being the mean of the sample), with N being the overall sample size and n being the number of elements in the group. The F-test and autocorrelations are performed to be independent measures of the statistical significance of the component being observed. They are compared, then, to S which is the weighting factor built into SVD. Lines 90-93 take the first ten S values and place them into the fourth column of the Significance table. The final ~10 lines of the code are used to generate the table itself.

Once SVD has been performed, it is often useful to compare the raw spectra with the SVD-analyzed spectra to ensure that the procedure is being done properly. From there, the Significance Table is an incredibly useful way of estimating the number of singulars that are required to describe the data well. This can be somewhat arbitrary as the autocorrelation values may agree with the S values that there are two significant components, for example, but the F-test may determine only one singular is necessary. It is often best to overestimate the number of needed parameters and add one (to account for noise). Once that value has been determined, it will become r in the next code that is used (Scheme E.4), the function mccSVDsings. This code takes the SVD results from mccSVD above and uses it to plot U vs. wavelength and V vs. time so as to best allow the user to decide visually the number of singulars needed to describe the data. It should be noted that the only way mccSVDsings can input U, S, V, time, and wavelength are if these are outputs from the mccSVD function.

```
1   function [singpanel] = mccSVDsings(r,U,S,V,time,wavelength)
2
3   %Build a panel which will contain surface plot of the reduced data set, as
4   %well as plots of the significant singular vectors of U versus wavelength,
5   %and V versus time.
6
7   %r is the previously-determined number of significant components (from
8   %mccSVD.m).
```

Scheme E.4. Code for the MATLAB function mccSVDsings which takes the SVD results from mccSVD and plots the user-determined most important singulars.

Scheme E.4. (cont'd)

```
9   s = U(:,1:r)*S(1:r,1:r)*V(:,1:r)'; %reconstruction of data set from significant vectors
10
11  singpanel=figure('Name','Reduced Plots','NumberTitle','off',...
12      'Units','normalized','Position',[0.6 1 0.4 1]);
13  subplot('Position',[0.09 0.71 0.87 0.26]);
14  surf(time,wavelength,s,'EdgeColor','none');
15  title('Reduced SVD Data','FontSize',12);
16  xlabel('Time','FontSize',10);
17  ylabel('Wavelength','FontSize',10);
18  zlabel('Change in Absorbance','FontSize',10);
19
20  subplot('Position',[0.09 0.37 0.87 0.26]);
21  plot(wavelength,U(:,1:r));
22  title('Left Singular Values','FontSize',12);
23  xlabel('Wavelength (nm)','FontSize',10);
24  ylabel('Change in Absorbance','FontSize',10);
25  legend('show');
26
27  subplot('Position',[0.09 0.05 0.87 0.26]);
28  title('Right Singular Values','FontSize',12);
29  plot(time,V(:,1:r));
30  xlabel('Time (ps)','FontSize',10);
```

Scheme E.4. (cont'd)

```
31      ylabel('Change in Absorbance','FontSize',10);
32      legend('show');
33
34      end
```

Line 9 is the first line of code that is not either the command or comments. Here, the data set is being reconstructed with r number of singulars, as is defined by the user. In line 11 a panel is built that will house three spectra. The top third is the surface plot of the reconstructed data ("Reduced SVD Data") vs. wavelength and vs. time. The middle third is U vs. wavelength, showing r number of U vectors. Similarly, the bottom third is V vs. time and displays r number of V components. With these spectra in hand, it much more simple to visually determine the number of relevant singulars. A case study for following this method is outlined below.

4.2 Analyzing SVD Results

The current procedure for SVD involves often frequent examination of the raw data and comparison with the mathematical constructs produced. Seemingly extraneous vectors of U and V are intentionally plotted in order to determine the origin of these less significant traces. This also provides a method to determine the traces that are meaningful, and those that are not. The full spectrum, A, is then reconstructed using first one vector each of U and V, then two, and so on until the spectrum is unchanged (not shown). A spectrum that remains essentially unchanged confirms that the components being factored into A are part of the noise and are thus insignificant.

To determine the validity of the MATLAB scripts, SVD has been carried out on full spectral data for $[Ru(dpb)_3](PF_6)_2$ (in which dpb = 4,4'-diphenyl-2,2'-bipyridine) in ethanol

(EtOH), the raw data for which are presented in Fig. E.14. The assignments for these features are based off of those given by Damrauer and McCusker.[11] Overall, the main trace grows in quickly (~ps) to a long-lived state with a lifetime of ~1 μs. A ground state bleach (GSB) is centered at ca. 470 nm that is due to loss of the ground state upon population of the MLCT excited state. The positive signal on the blue edge of the ground state bleach is assigned to the π-π^* absorption of the reduced dpb ligand. Similarly, excited state absorption (ESA) in the redder wavelengths ($\lambda > 520$ nm) are of two origins: a band centered around 540 nm that is due to the π^*-π^* absorption of the reduced dpb ligand, and the broad, featureless band at even lower energy is assigned as a ligand-to-metal charge transfer (LMCT) transition. A spectral trace in orange in Fig. E.14 is observed to oscillate about the breadth of the spectrum; this is the trace for $\Delta t = 0$, when the peak powers of the pump and probe pulses overlap maximally and induce energy transfer events in the solvent, and as such can be disregarded as artifact.

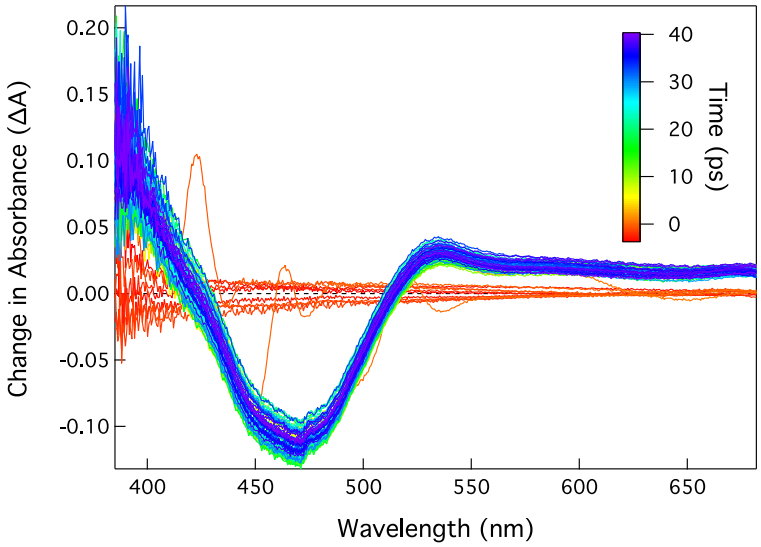

Figure E.14. Raw full spectra data of $[Ru(dpb)_3]^{2+}$ in EtOH when pumped at 480 nm. Before time-zero (red and orange traces), no real signal is observed due to the probe hitting the sample before the pump can excite it. After time-zero, the long-lived transient grows in resulting in the final purple trace that decays over the course of ~1 μs (not shown).

Upon performing SVD on this data set, the weighting factors of the first three values of S (hereon denoted S_1, S_2, S_3) are found to be 16.5, 2.6, and 2.0, respectively. From this, one might be inclined to assume that only one component is needed to accurately describe the data. The spectral component, U_1 (Fig. E.15) displays ESA $\lambda < 410$ nm and $\lambda > 520$ nm, and GSB in the region 410-520 nm. V_1, the kinetic trace, in Fig. E.16 shows a rise (indicative of an absorptive feature) that never returns to baseline. This trace is clearly the long-lived transient that is predominant in Fig. E.14. When A_1 is reconstructed from U_1, S_1, and V_1 in Fig. E.17, the resultant spectrum obviously does not replicate the original data. In this way, we have determined that one component is not sufficient to exactly describe the original data.

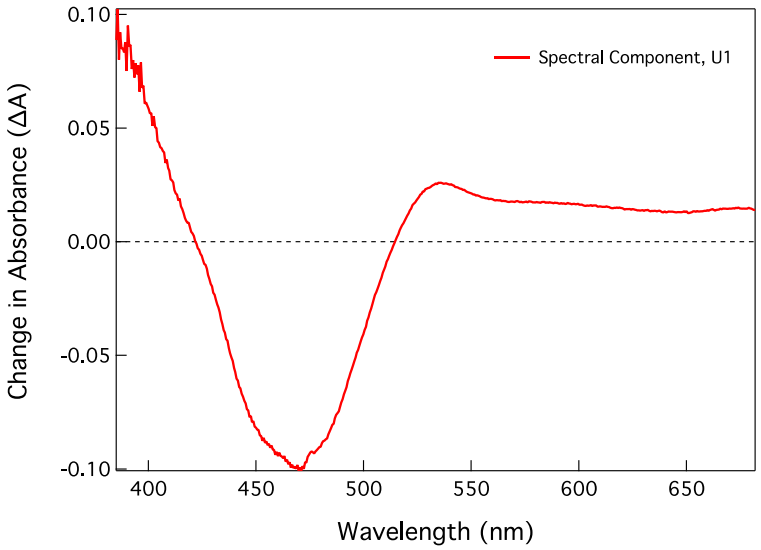

Figure E.15. The first spectral component, U_1, of $[Ru(dpb)_3]^{2+}$ in EtOH (S_1 = 16.5). This trace represents the long-lived transient for this complex.

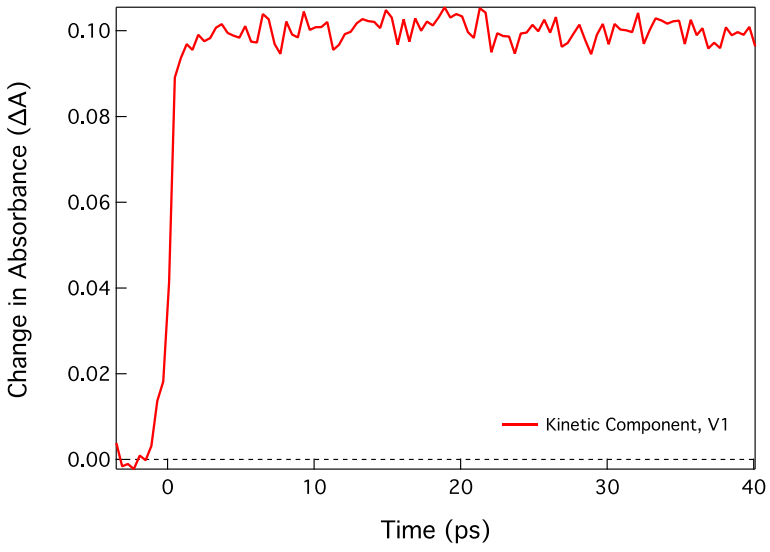

Figure E.16. The first kinetic component, V_1, of $[Ru(dpb)_3]^{2+}$ in EtOH (S_1 = 16.5). This trace represents the temporal behavior of U_1, and shows a single picosecond grow-in followed by a long (>40 ps) static signal.

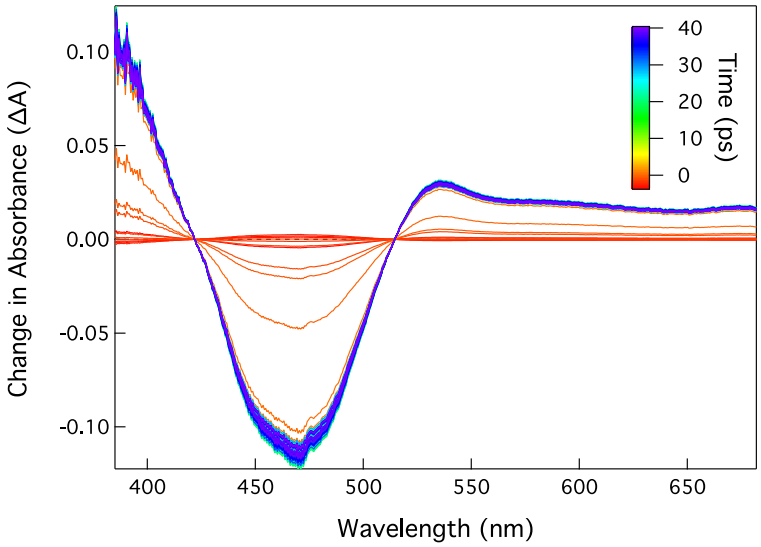

Figure E.17. The recombined spectra for the first spectral and kinetic components, A_1. While these data do generally describe the full data set, there are obviously more features that must be included.

The same analysis is performed on U_2 (Fig. E.18), which displays only ESA. The largest signal seems to be a remnant of the noise from the near ultraviolet (UV) region in U_2. This is likely the spectral trace for the π-π^* absorption that occurs in the dpb radical ligand. Interestingly, V_2 (Fig. E.19) only shows one real signal centered at time-zero, whereas the rest of the kinetics are dominated by essentially large-amplitude noise that is shorter than the instrument response function (IRF) of the system, which is on the order of 250 fs. It is possible that V_2 is showing the immediate depopulation of the π-π^* absorption as it deactivates into the MLCT manifold. When A_2 is reconstructed using U_1, U_2, S_1, S_2, V_1, and V_2, a spectrum that is much more reminiscent of the original data is produced (Fig. E.20). However, the spectral features toward the red edge of the spectrum are clearly not well reproduced by A_2, implying the need for at least three elements each of U, S, and V.

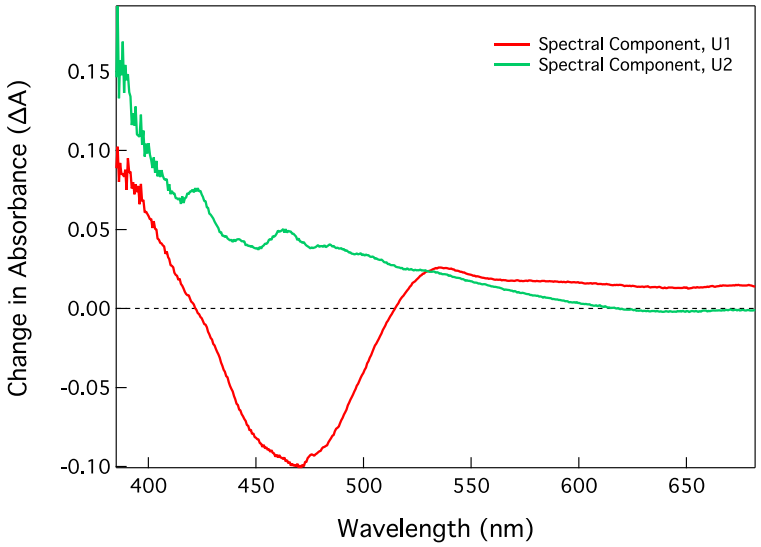

Figure E.18. The second spectral component, U_2, of $[Ru(dpb)_3]^{2+}$ in EtOH (S_2 = 2.6) is shown in green compared to the first (in red). This trace is predominantly ESA at higher energy and is assigned to represent the π-π^* absorption of the reduced dpb ligand.

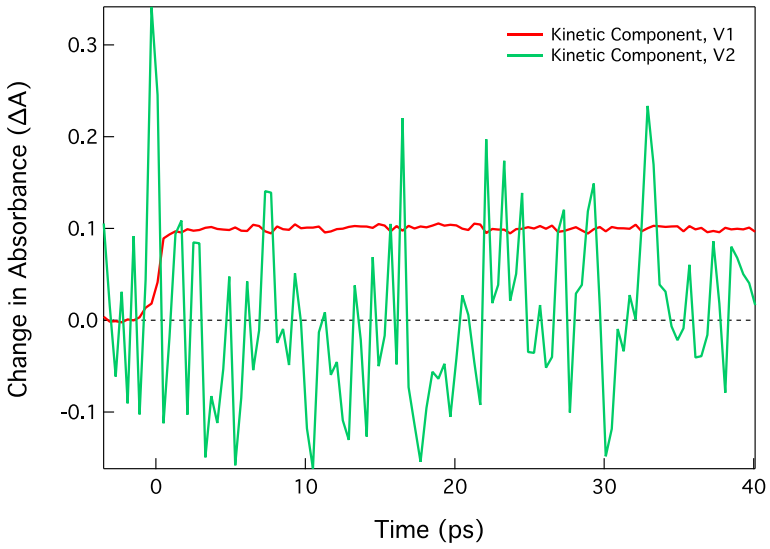

Figure E.19. The second kinetic component, V_2, of $[Ru(dpb)_3]^{2+}$ in EtOH (S_2 = 2.6) is shown in green compared to the first (in red). This trace shows only a large spike centered around time-zero, implying the spectral features associated with it (U_2) are very short-lived (i.e., <IRF).

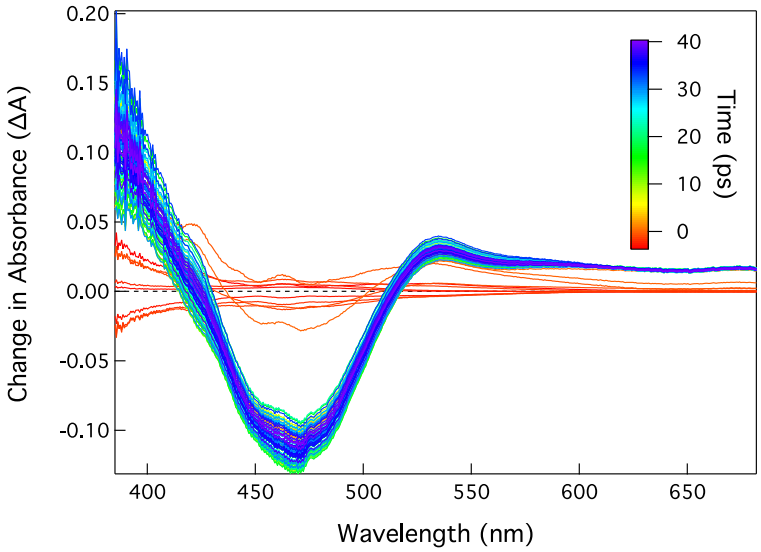

Figure E.20. The recombined spectrum of $[Ru(dpb)_3]^{2+}$ in EtOH using the first and second spectral and kinetic components, A_2. This is a closer approximation of the raw full spectral data.

The process is repeated a third time. Here, U_3 can be seen in Fig. E.21. This trace shows the distinctive features red of 520 nm that are due to the π^*-π^* absorption of the radical dpb ligand (centered around 540 nm), and the LMCT transition that is broad and absorbs 550-700 nm. The corresponding kinetic component, V_3 (Fig. E.22) mimics V_2 in that the only real feature is centered at $\Delta t = 0$. Where V_2 had a positive amplitude, however, V_3 is negative. The full-width at half-maximum (FWHM) of V_3 does appear to be approximately twice as long as that of V_2. Considering both features are due to similar processes, it would appear to be reasonable that the processes also occur on similar timescales. Reconstructing A_3 using three components of each eigenvector and eigenvalue is also shown in Fig. E.23. Improvement is made to the red side of the spectrum in the calculation of the dynamics of the LMCT transition, as well as in the time-zero trace. When A_4 was calculated, no discernible change in the spectrum was observed, indicating that three elements

are required to accurately represent the full spectral data of $[Ru(dpb)_3]^{2+}$ in EtOH.

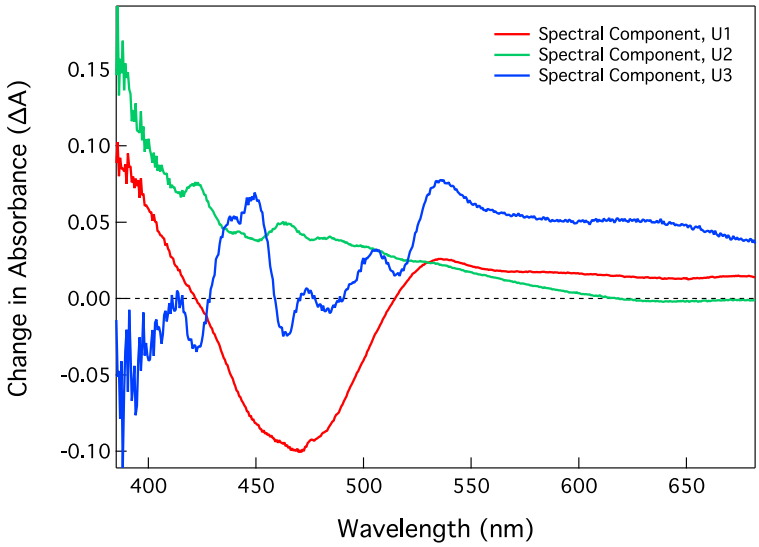

Figure E.21. The first (red, U_1), second (green, U_2), and third (blue, U_3) spectral components of $[Ru(dpb)_3]^{2+}$ in EtOH are shown. U_3 has a significance of $S_3 = 2.0$. The third trace is dominated by ESA at lower energies which is like due to the π^*-π^* transition of the reduced dpb ligand (λ_{max} ~ 540 nm) and LMCT transitions at redder wavelengths. Also observable is a noisy pattern overlaying with the MLCT bleach feature.

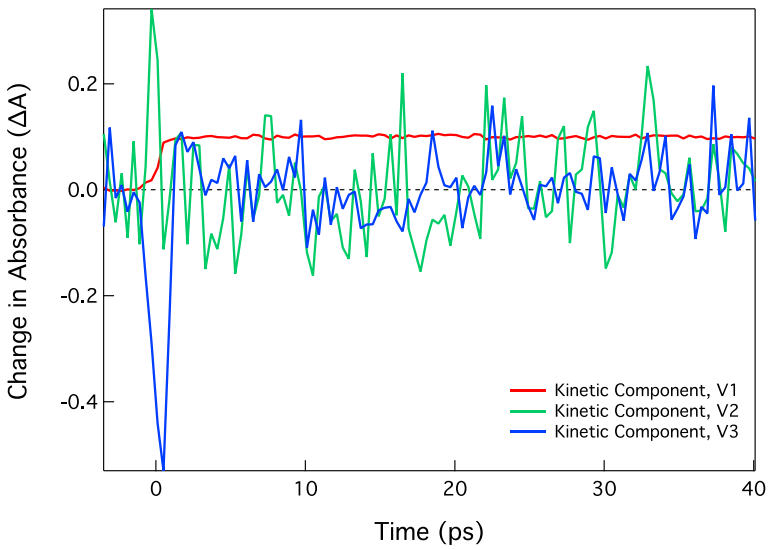

Figure E.22. The first (red, V_1), second (green, V_2), and third (blue, V_3) kinetic components of $[Ru(dpb)_3]^{2+}$ in EtOH. V_3 has a significance of $S_3 = 2.0$. As with V_2, the third feature has a trace that is predominantly centered around time-zero, though with a moderately larger FWHM.

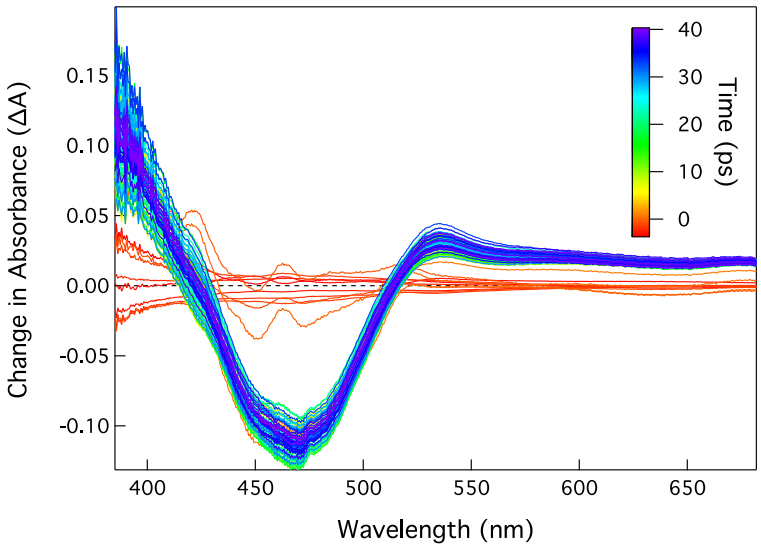

Figure E.23. The recombined spectra of the first three kinetic and spectral components of $[Ru(dpb)_3]^{2+}$ in EtOH, A_3. This spectrum reproduces the original full spectral data very well.

As demonstrated, this type of analysis is extremely informative, but lends itself readily to misinterpretation. Not shown are results on the simpler $[Fe(bpy)_3]^{2+}$, which exhibits only monophasic kinetics corresponding to ground state recovery. In this case, the SVD described the system perfectly, and was even able to extract pump scatter as a unique spectral component with the corresponding kinetic component demonstrating the expected noise-dominated behavior. In $[Ru(dpb)_3]^{2+}$, the signal at 532 nm is biphasic, as has been described previously.[11] However, fitting of V_1 does not yield biphasic kinetics, but rather the best fit being monoexponential in which $\tau = 0.47 \pm 0.09$ ps. This time constant does not correspond to either of the time constants measured via single wavelength studies. It is probable, then, that the kinetic components do not correlate to one specific feature, but actually a combination of processes. This is an ongoing challenge with SVD and may simply require the combination of SVD analysis on full spectral data being used in combination with kinetics measured from single-wavelength experiments.

5. Global Analysis-Type Procedure

In very recent years, global analysis (GA) methods have become more commonly employed in the analysis of ultrafast spectroscopic data.[12-14] The underlying principle of GA is that for two-dimensional data (e.g., ΔA vs. λ vs. time or I_{em} vs. time vs. temperature) can be analyzed across both dimensions simultaneously. That is, if full spectral transient absorption data were collected, for example, the kinetic lifetimes corresponding to distinct spectral features could be determined at the same time. This is a useful tool in understanding complex spectra with multiple timescales occurring out of different states. A great advantage is that timescales of drastically different orders of magnitude are easily separated from each other, such that a sequential kinetic scheme can be identified. One of the disadvantages is that in many cases, the kinetics are not

verified independently by single-wavelength kinetics, meaning that the deconvolved spectra that result from GA are simply a mathematical product that result out of some arbitrary initial guess. Many spectroscopists cite these lifetimes as absolutes, when in reality they should be observed simply as estimates.

5.1 Combined with SVD

We have taken advantage of this type of methodology and developed a global analysis-type technique (Scheme E.5) for use with the SVD analysis described above. Here, steady-state features are removed initially and SVD is performed on the residuals. These should ultimately be the shorter-lived and smaller-amplitude features that may be hidden by the long lifetime components, and GA is a tool we can use to better understand some of these processes. Specifically, the script below is designed to remove the steady-state absorption spectrum from the transient absorption full spectral data. The UV-Vis is forced to decay with the lifetime of the molecule, thus removing the long-lived components from the ultrafast spectra. This should result in only ultrafast features remaining observable.

```
1  %% This script is meant to be a catchall for the functions used in the home-built "Global
       Analysis" method.
2
3  %The first script is the actual performance of the "Global Analysis."
4  [res A_res A_ga wavelength time] =
```

Scheme E.5. Code for the MATLAB script GlobalAnalysis which plots the user-defined most important singulars that results from global analysis-type application to the SVD results from mccSVD.

Scheme E.5. (cont'd)

```
        GA(startw,endw,wint,startt,endt,tint,A,SSAbs,SSAw,ti,tf,amp,tau,offset);
5       %startw = starting wavelength in nm
6       %endw = ending wavelength in nm
7       %wint = wavelength step size in nm
8       %startt = starting time in ps
9       %endt = ending time in ps
10      %tint = time step size in ps
11      %A = 2D data to be analyzed
12      %SSAbs = steady state or long-time transient absorption spectrum
13      %SSAw = wavelength vector for SSAbs
14      %ti = integer value of starting time (e.g. first point of positive time...
15          %is 13th time point in time vector, so ti = 13)
16      %tf = integer value of ending time
17      %amp, tau, offset correlate to the lifetime decay values of the molecule
18
19
20      %The use of the SVD function here is to perform SVD on the residuals of the
21      %"globally analyzed" model data.
22      [U S V time_res] = mccSVDGA(A_res, ti, tf, time, wavelength);
23      r = input('What is value of r? '); %this is the number of significant singulars
24
25      %This function then plots the significant singular vectors such that it can
```

Scheme E.5. (cont'd)

```
26      %be determined if they are relevant to the kinetics of the molecule, as
27      %opposed to their simply being wavelength- or time-dependent noise.
28      mccSVDsingsGA(r, U, S, V, time_res, wavelength);
29
30      %% Displaying the data
31
32      %This is to show the S-values (importance) of each of the components
33      figure
34      l = [1:length(time_res)]';
35      s = l;
36      for n = 1:length(time_res);
37              s(n,1) = S(n,n); %build a vector of the diagonal elements of S
38      end
39      plot(l,s,'ro')
40      xlabel('Component Number')
41      ylabel('Significance')
42      title('Values of S')
43
44      A1 = U(:,1)*S(1,1)*V(:,1)';
45      A2 = U(:,1:2)*S(1:2,1:2)*V(:,1:2)';
46      A3 = U(:,1:3)*S(1:3,1:3)*V(:,1:3)';
47      A4 = U(:,1:4)*S(1:4,1:4)*V(:,1:4)';
```

This script contains within it multiple functions that have been previously coded and compiled for ease of use. Because it calls on functions within the script, all inputs to the functions must be defined before running the script. In the GA function (Scheme E.6), the input variables are startw, endw, wint, startt, endt, tint, and A (which are defined for the function mccSVD above), as well as SSAbs and SSAw (the ground state absorbance spectrum and its wavelength vector, respectively), and the lifetime fitting parameters ti (time point at which to start fitting), tf (time point at which to stop fitting), amp(litude), tau (lifetime), and offset. These last five variables should be independently measured via a nanosecond technique or something similar and can be determined with curve fitting software. Once MATLAB has these parameters, the code given in line 4 can be executed, leaving the outputs of res (sum of the squares of the residuals), A_res (the residuals of A after the steady-state data have been removed), A_ga (the steady-state data), and the wavelength and time vectors. The GA function is meant to be a different, less linear algebra-based version of Global Analysis. Here, the data that are already available in steady-state (or long-time differential) absorption spectra and time-resolved spectroscopy are used to model what the short-time differential absorption spectrum should look like. The first step is to use the ground state absorption profile and interpolate for the wavelengths that are present in the full spectral TA data that are not collected by a standard UV-Vis. This allows for good comparison between these two types of data. The grounds state recovery rate of the molecule is then applied to the total spectrum, producing the "globally analyzed" model. The user should input known or reasonable values for the amplitude, time of recovery, and offset for the exponential fit. The "globally analyzed" model is normalized to the same amplitude of the long-time full spectral data for calculation of the residuals. A panel will appear with three subplots. In the uppermost plot is the raw data, the middle plot contains the modeled data, and the bottom plot displays the residuals.

```
1   function [ res A_res A_ga wavelength time] = GA( startw, endw, wint, startt, endt, tint, A,
2       SSAbs, SSAw, ti, tf, amp, tau, offset )
3   %Meant to be a different, less linear algebra-based version of Global
4   %Analysis. Here, use the data that are already available in steady-state
5   %(or long-time differential) absorption spectrum and time-resolved
6   %spectroscopy to model what the differential absorption spectrum should do.
7
8   %% Building vectors and arrays to be filled upon calculations
9
10  time = [startt:tint:endt]'; %build the time vector
11  wavelength = [startw:wint:endw]'; %build the wavelength vector
12
13  A_ga = zeros(length(wavelength),tf-ti+1); %build array for modeled data
14  yi = zeros(length(wavelength),1); %build vector for interpolated
15
16  %% Performing "Global Analysis"
17
18  %The first for loop is meant to be used should the steady-state absorption
19  %profile be used. (This is appropriate for spectra that display only ground
20  %state bleach for the region being analyzed.) The for loop is used to take
```

Scheme E.6. Code for the MATLAB function GA which performs a global analysis-type method to full spectral transient absorption data. This code is built into the GlobalAnalysis script.

Scheme E.6. (cont'd)

```
%the wavelengths from SSA and interpolate to build a vector, yi, of
%wavelengths appropriate for comparison with the full spectral data.
for n = 1:length(wavelength);
        yi(n,1) = interp1(SSAw,SSAbs,wavelength(n,1));
end

%Within these for loops, the recovery rate of the molecule is applied to
%the total spectrum. The user should input known or reasonable values for
%the amplitude, time of recovery, and offset for the exponential fit.
for p = ti:tf;
        for n = 1:length(wavelength);
                A_ga(n,p-ti+1) = (((amp*exp(-(1/tau)*time(p,1)-offset))))*(yi(n,1));
        end
end

%Here the "globally analyzed" model is normalized to the same amplitude of
%the long-time full spectral data for the calculation of the residuals.
normval = min(min(A_ga))/min(min(A));
A_norm_ga = A_ga/normval;
A_res = A(:,ti:tf)-A_norm_ga;

res = sum(sum(A_res .^2));
```

Scheme E.6. (cont'd)

```
43
44      %% Displaying the Data
45
46      %One panel will appear with three subplots. In the uppermost plot is the
47      %raw data. The middle plot contains the modeled data. The bottom plot
48      %displays the residuals.
49      singpanel=figure('Name','Reduced Plots','NumberTitle','off',...
50          'Units','normalized','Position',[0.6 1 0.4 1]);
51      subplot('Position',[0.09 0.71 0.87 0.26]);
52      surf(time,wavelength,A,'EdgeColor','none');
53      title('Raw Data','FontSize',12);
54      xlabel('Time','FontSize',10);
55      ylabel('Wavelength','FontSize',10);
56      zlabel('Change in Absorbance','FontSize',10);
57
58      subplot('Position',[0.09 0.39 0.87 0.26]);
59      surf(time(ti:tf),wavelength,A_norm_ga,'edgecolor','none');
60      title('Reconstructed from Steady State Data','FontSize',12);
61      xlabel('Time','FontSize',10);
62      ylabel('Wavelength','FontSize',10);
63      zlabel('Change in Absorbance','FontSize',10);
64
```

Scheme E.6. (cont'd)

```
65      subplot('Position',[0.09 0.03 0.87 0.26]);
66      title('Residuals','FontSize',12);
67      surf(time(ti:tf),wavelength,A_res,'edgecolor','none');
68      xlabel('Time','FontSize',10);
69      ylabel('Wavelength','FontSize',10);
70      zlabel('Change in Absorbance','FontSize',10);
71
72      end
```

The next important line of code in Scheme E.5 is line 22, which then uses the outputs from the GA function to perform SVD on the residuals using the function mccSVDGA (which is provided in Scheme E.7). As described above, the user also determines the number of significant singulars that should be plotted which is then defined as r in line 23. A panel will be created: the top third is a plot of the raw data, the middle third shows the reconstructed data after SVD has been performed, and the lower third is a table with the Significance table. Apart from the GA aspect of the code, this function is very similar to mccSVD in its function and the data it displays.

```
1       function [U,S,V,time_res] = mccSVDGA(A_res,ti,tf,time,wavelength)
2
```

Scheme E.7. Code for the MATLAB function mccSVDGA, which takes the globally analyzed data from the GA function and performs SVD on the residuals. This code is built into the GlobalAnalysis script.

Scheme E.7. (cont'd)

```
3   %% The SVD function for use with "Global Analysis"
4
5   %The purpose of this function is to perform SVD on the full spectral
6   %residual data, upon completion of the global analysis function, GA.m.
7   %This function does not plot the significant singulars, it only gives the
8   %user the information about which components are significant.
9
10  time_res = time(ti:tf,:); %the time vector corresponding to positive time after the IRF is
        complete
11
12  %% Displaying the SVD results
13
14  %This panel has two subplots and a table. The topmost plot is the raw
15  %data. Then SVD is performed and the middle plot displays the reconstructed
16  %full spectral data. The table on the bottom shows in various ways the
17  %significance of the components. This will be discussed further below.
18  A_res(A_res==inf) = 0;
19  fspanel=figure('Name','Full Spectra','NumberTitle','off',...
20          'Units','normalized','Position',[0 1 0.4 1]);
21  subplot('Position',[0.09 0.71 0.87 0.24]);
22  surf(time_res,wavelength,A_res,'EdgeColor','none');
23  title('Raw Data','FontSize',12);
```

Scheme E.7. (cont'd)

```
24      xlabel('Time','FontSize',10);
25      ylabel('Wavelength (nm)','FontSize',10);
26      zlabel('Change in Absorbance','FontSize',10);
27      [U S V] = svd(A_res); %performing SVD on the residuals
28      A_svd = U*S*V'; %recombining the decomposed vectors
29      subplot('Position',[0.09 0.37 0.87 0.26]);
30      surf(time_res,wavelength,A_svd,'EdgeColor','none');
31      title('SVD of Raw Data','FontSize',12);
32      xlabel('Time','FontSize',10);
33      ylabel('Wavelength','FontSize',10);
34      zlabel('Change in Absorbance','FontSize',10);
35
36      %Columns 1 and 2 of Significance table contain autocorrelation values for
37      %singular vectors of U and V. The equations for the autocorrelation come
38      %from Henry and Hofrichter, Methods Enzymol. 210, 129-192.
39
40      ncol = length(U);
41      nrow = ncol;
42      u = zeros(1,ncol);
43      for icol = 1:ncol;
44              u(icol)=0;
45              for irow=1:nrow-1;
```

Scheme E.7. (cont'd)

```
46                      u(1,icol) = u(icol)+(U(irow,icol)*U(irow+1,icol));
47              end
48      end
49      Significance = zeros(10,4); %building the array that will be used to complete the table
50      Significance(:,1) = u(1,1:10)';
51      ncol = length(V);
52      nrow = ncol;
53      v = zeros(1,ncol);
54      for icol = 1:ncol;
55              v(icol)=0;
56              for irow=1:nrow-1;
57                      v(1,icol) = v(icol)+(V(irow,icol)*V(irow+1,icol));
58              end
59      end
60      Significance(:,2) = v(1,1:10)';
61
62      %Column 3 of Significance table contains F-ratios from F-test. This is
63      %essentially comparing the standard deviation of reduced data set and the
64      %raw data set, with the standard deviation of just one data set. For more
65      %information on F-tests please see F_test.m.
66
67      p = length(A_res);
```

Scheme E.7. (cont'd)

```
68      fb = 2*length(time_res)-1; %for the Between groups ratio
69      fw = 2*(p-1); %for the Within groups ratio
70      for q = 1:10;
71              z1 = U(:,q)*S(q,q)*V(:,q)'; %recompose data using q singulars
72              mean_c = mean(z1); %find the mean of each of the columns of z
73              z_m = mean(mean(z1)); %find the overall mean of z
74              Sb = sum(p*(mean_c-z_m).^2);
75              between_groups = Sb/fb; %Between groups value
76              z_b = z1(:,q)-mean_c(1,q); %difference of z column value and average column
                    value
77              Sw = sum(sum(z_b.^2));
78              within_group = Sw/fw; %Within groups value
79              Significance(q,3) = between_groups/within_group; %F-test ratio
80      end
81
82      %Column 4 of Significance table is value of S corresponding to rank.
83      for n = 1:10;
84              Significance(n,4) = S(n,n); %building a vector of the diagonal values of S
85      end
86
87      %The following commands insert the Significance array as a table into the
88      %third subplot area of the panel.
```

Scheme E.7. (cont'd)

```
89      uitable('Data',Significance,'ColumnName',{'U','V','F-ratio',...
90              'Value of S'},'RowName',{'1','2','3','4','5','6','7','8','9','10'},...
91              'Units','normalized','Position',[0.4 0.04 0.59 0.24],'FontSize',12);
92      annotation('textbox',...
93              [0.0253055555555555 0.0421052631578947 0.363583333333333
                    0.23625730994152],...
94              'String',{'','The number of significant singular','values is given by the number
                    of','singular values in columns U or V','and >0.99, in column F-ratio >10.'},...
95      'FontSize',12,...
96              'FitBoxToText','off');
97
98      end
```

The final job that the Global Analysis script (Scheme E.5) performs is to display the data in a user-friendly way. The S values are plotted in lines 33-42. Then in 44-47, the reconstructed A data using the first four singulars of U and V are calculated by default. Based on the user's prior knowledge as to the number of significant components, the user will be able to plot and analyze these spectra as has been described previously. A case study for the usefulness of this application is given below.

5.2 Analyzing Results

In a recently published article, Brown and coworkers used ultrafast transient absorption spectroscopy to identify intramolecular vibrational energy redistribution (IVR) in a series of

heteroleptic Ru(II) complexes.[15] IVR is the dissipation of excess vibrational energy from high energy modes in the chromophore into lower energy modes. This is separate from vibrational cooling, which dissipates energy from the complex into the solvent bath and is known instead as intermolecular vibrational relaxation.[16] Full spectral data were collected on $[Ru(CN\text{-}Me\text{-}bpy)_x(bpy)_{3-x}]^{2+}$ (in which CN-Me-bpy = 4,4'-dicyano-5,5'-dimethyl-2,2'-bipyridine, and x = 1-3 for compounds **1**-**3**, respectively). The raw data are shown in Fig. E.24, as it was collected by A. M. Brown. The complex that displayed the greatest amplitude for the IVR signal was **1**, so that will be the focus of this discussion, although these methods were also applied successfully to **2** and **3**, though the exact number of significant components varies.

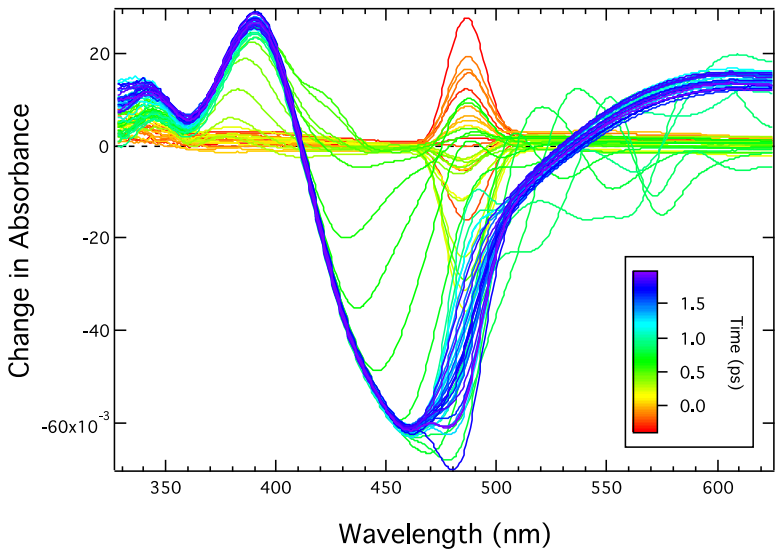

Figure E.24. Raw full spectral data of $[Ru(CN\text{-}Me\text{-}bpy)(bpy)_2]^{2+}$ as collected by A. M. Brown.

The kinetics of interest were at very short timescales (<200 fs) which was on the cusp of the IRF of the system. Full spectral data, being high quality in spectral resolution, necessarily lose out in temporal quality; this is especially true around time-zero, where the wavelength-dependence

of chirp greatly affects the early-time spectra, as is discussed more fully above. The question attempting to be answered was were there short-time kinetics being masked by chirp, and how can we separate out these processes?

To address these questions, the spectra were analyzed by the same method after two different work-up procedures. SVD and GA were performed on both the raw spectra, and the same spectra but post-chirp correction. The GA/SVD combinatorial approach was applied (Fig. E.25), yielding three significant singulars required to successfully reproduce the raw data (Fig. E.26).

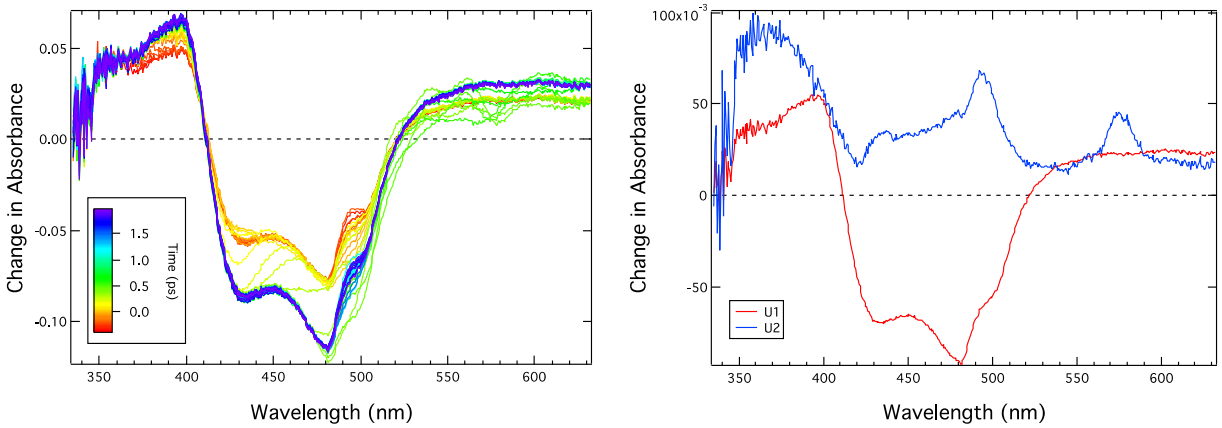

Figure E.25. (Left) Spectra of the residuals after performing GA on the raw full spectral data for compound **1**. (Right) The two most significant spectral contributions as determined by SVD of the residuals.

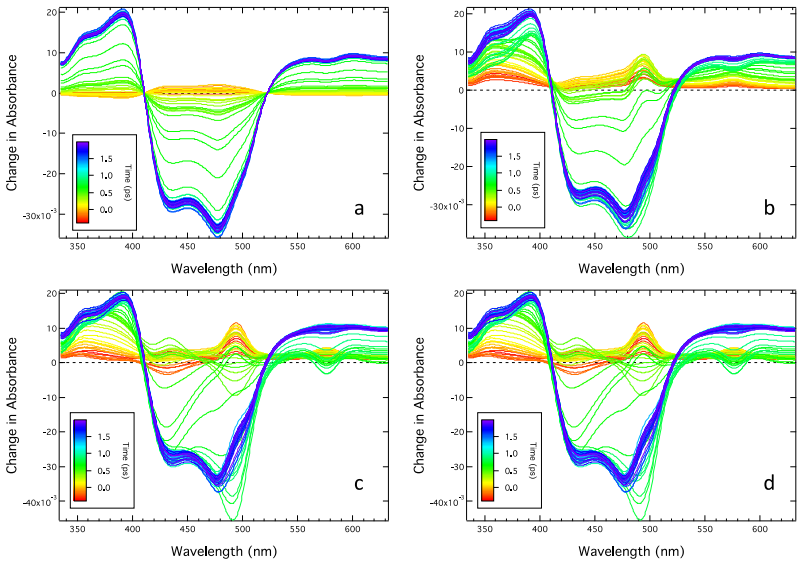

Figure E.26. The reconstructed spectra from SVD analysis of the raw full spectral data of compound **1** using 1 (a), 2 (b), 3 (c), and 4 (d) singulars. It is evident that there is no significant difference between (c) and (d), thus only three singulars are required. Additionally, the differences between (b) and (c) are minimal due to the third component likely only contributing noise.

The data for complex **1** were then chirp-corrected and are shown in Fig. E.27. The differences between the raw and the chirp-corrected data primarily consist of the traces centered around $\Delta A = 0$, and those that grow into the higher amplitude, longer-lived signal. In the raw data, spectra collected as late as 500 fs were still associated with the solvent and chirp of the laser pulses. There was also a slower growth into the long-lived signal as fluctuations in after 1.5 ps could still be observed. After chirp-correction, however, the solvent-related traces are reduced to less than 200 fs after time-zero, as would be expected even with a single-wavelength experiment. Additionally, blue of ~400 nm, the spectra are superimposable after 1.5 ps, indicating the thermally relaxed ^{3}MLCT excited state has been reached.

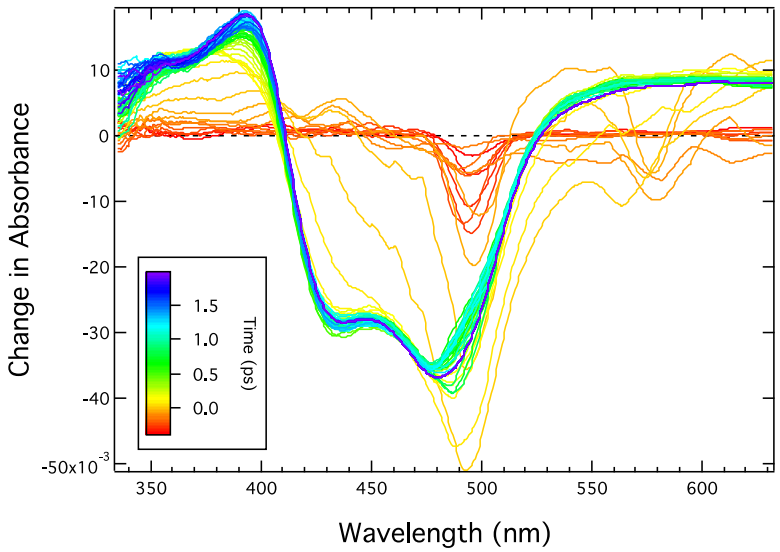

Figure E.27. Chirp-corrected full spectral data of compound **1**. These data were collected by A. M. Brown and worked up by M. C. Carey.

Upon chirp correction, the full spectral data was analyzed by GA (Fig. E.28). Only two singulars were required to describe the data well. The first is clearly the long-lived transient, while the second contains the pump scatter centered around 490 nm, as well as a sharp excited state decay feature at ca. 400 nm. The fact that these data only required two singulars indicates that the third component needed to reproduce the raw data is associated with the solvent response; it points toward the need to chirp-correct the data prior to performing SVD and/or GA. Likewise, SVD was performed on the data sets (Fig. E.29), and from these spectra it is apparent that a third component only introduces noise, specifically on the red side of the spectrum near ~580 nm which is assigned as Stokes shifting from the MeCN solvent and unrelated to the dynamics of the Ru(II) chromophore.

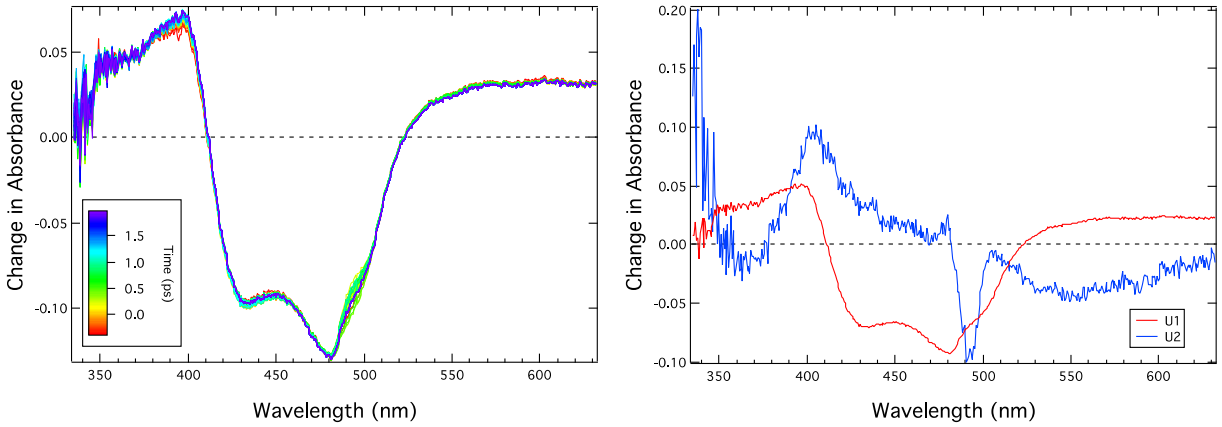

Figure E.28. (Left) Spectra of the residuals after performing GA on the chirp-corrected full spectral data for compound **1**. (Right) The two most significant spectral contributions as determined by SVD of the residuals.

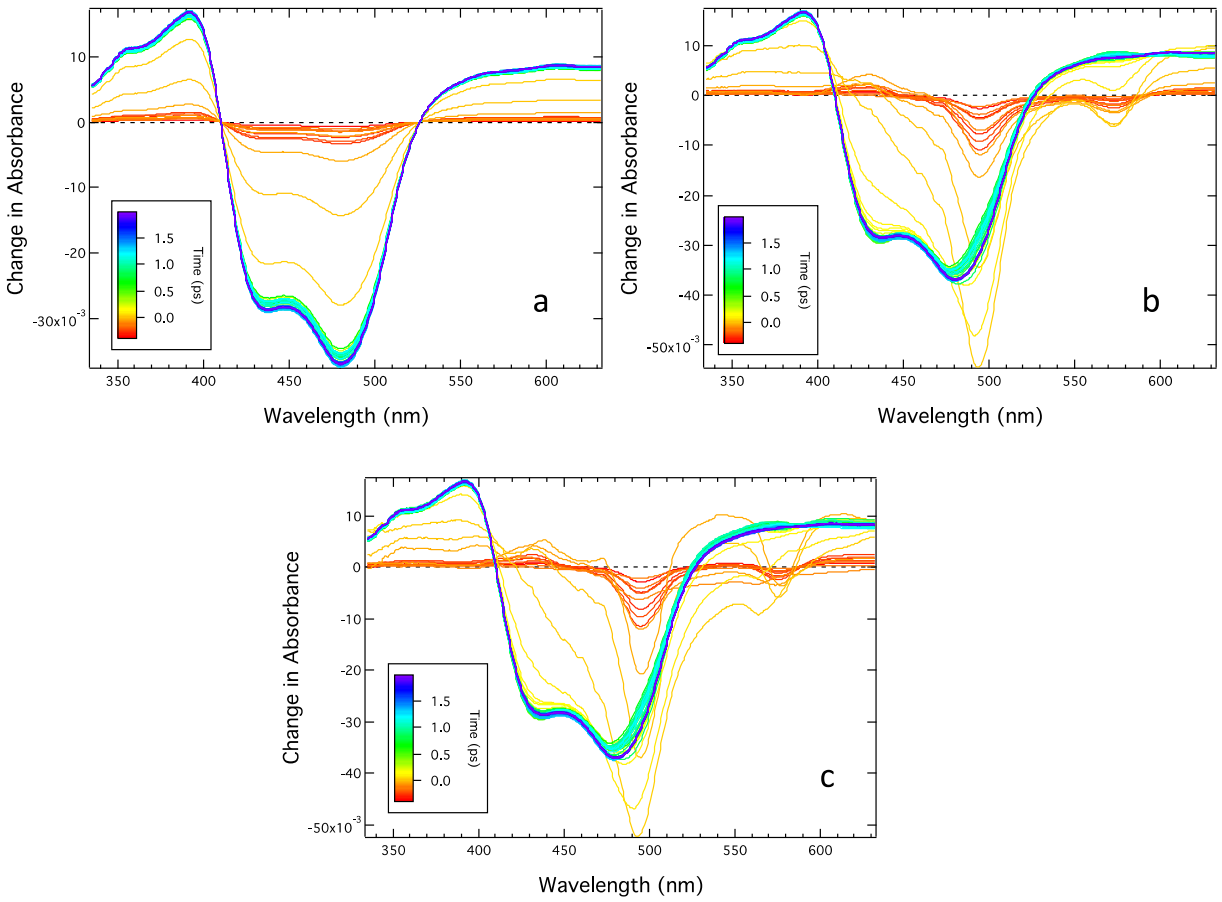

Figure E.29. The reconstructed spectra from SVD analysis of the raw full spectral data of compound **1** using 1 (a), 2 (b), and 3 (c) singulars. There are only slight differences between (b) and (c), thus only two singulars are required.

The most compelling data to indicate IVR actually come from the band centered at ~390 nm (Fig. E.30). This feature grows in very quickly (170 ± 50 fs),[15] which is consistent with the lifetime of IVR.[16] Furthermore, this signal was apparent in the heteroleptic compound **1**, but had disappeared in the homoleptic compound **3**. The asymmetry of **1** is conducive to the IVR process, and SVD and particularly the GA analysis of the raw and chirp-corrected spectra helped identify a spectral tag for this process, as well as to separate it from the temporally similar solvent response.

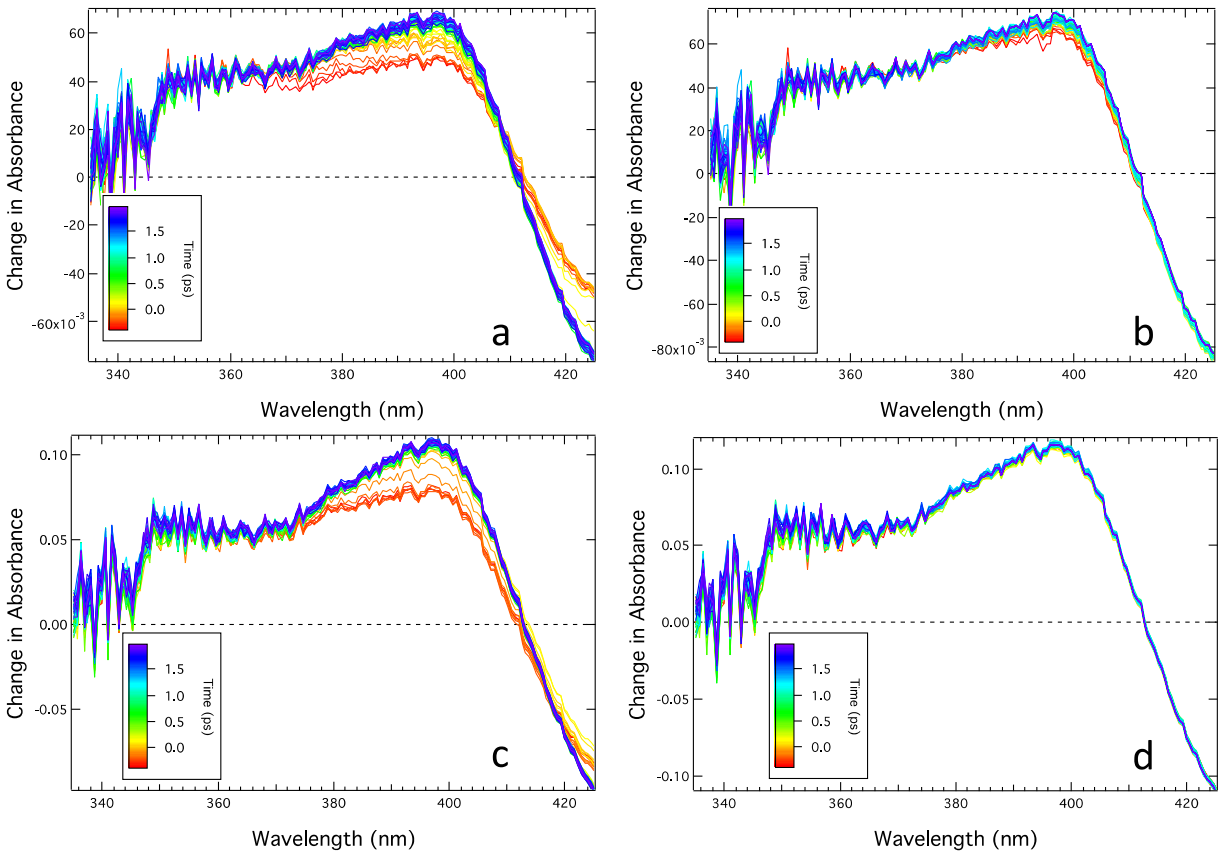

Figure E.30. Enlargement of the near-UV features the residuals from GA of compounds **1** and **3**. (a) Raw full spectral data of **1**, (b) chirp-corrected full spectral data of **1**, (c) raw full spectral data of **3**, and (d) chirp-corrected full spectral data of **3**. The residuals of the uncorrected data (a) and (c) are nearly identical. After chirp-correction and GA, (b) shows signal growing in on a very fast timescale that is not observed in (d).

REFERENCES

REFERENCES

1. Monat, J. E.; McCusker, J. K. Femtosecond Excited-State Dynamics of an Iron(II) Polypyridyl Solar Cell Sensitizer Model. *J. Am. Chem. Soc.* **2000**, *122*, 4092-4097, and references therein; DOI: 10.1021/ja992436o.

2. Johnson, S. R.; Westmoreland, T. D.; Caspar, J. V.; Barqawi, K. R.; Meyer, T. J. Influence of Variations in the Chromophoric Ligand on the Properties of Metal-to-Ligand Charge-Transfer Excited States. *Inorg. Chem.* **1988**, *27*, 3195-3200; DOI: 10.1021/ic00291a031.

3. Megerle, U.; Pugliesi, I.; Schriever, C.; Sailer, C. F.; Riedle, E. Sub-50 fs Broadband Absorption Spectroscopy with Tunable Excitation: Putting the Analysis of Ultrafast Molecular Dynamics on Solid Ground. *Appl. Phys. B* **2009**, *96*, 215-231; DOI: 10.1007/s00340-009-3610-0.

4. Miller, J. N. Ultrafast Dynamics of Iron(II)-Based Complexes in Solution and Semiconductor-Chromophore Assemblies. Ph.D. Thesis, Michigan State University, East Lansing, MI, 2018.

5. Smeigh, A. L. Ultrafast Dynamics Associated with Transition Metal-Based Sensitizers for the Titanium Dioxide Based Solar Cells. Ph.D. Thesis, Michigan State University, East Lansing, MI, 2007.

6. Brown, A. M. Excited-State Dynamics of Iron(II)-Based Charge-Transfer Chromophores. Ph.D. Thesis, Michigan State University, East Lansing, MI, 2011.

7. Ruckebusch, C.; Sliwa, M.; Pernot, P.; de Juan, A.; Tauler, R. Comprehensive Data Analysis of Femtosecond Transient Absorption Spectra: A Review. *J. Photochem. Photobiol. C Photochem. Rev.* **2012**, *13*, 1-27, and references therein; DOI: 10.1016/j.jphotochemrev.2011.10.002.

8. Shrager, R. I.; Hendler, R. W. Deconvolutions Based on Singular Value Decomposition and the Pseudoinverse: A Guide for Beginners. *J. Biochem. Biophys. Methods* **1994**, *28*, 1-33; DOI: 10.1016/0165-022X(94)90061-2.

9. Henry, E. R.; Hofrichter, J. Singular Value Decomposition: Application to Analysis of Experimental Data. *Methods Enzymol.***1992**, *210*, 129-192; DOI: 10.1016/0076-6879(92)10010-B.

10. Dioumaev, A. K. Evaluation of Intrinsic Chemical Kinetics and Transient Product Spectra from Time-Resolved Spectroscopic Data. *Biophys. Chem.* **1997**, *67*, 1-25, and references therein; DOI: 10.1016/S0301-4622(96)02268-5.

11. Damrauer, N. H.; McCusker, J. K. Ultrafast Dynamics in the Metal-to-Ligand Charge Transfer Excited-State Evolution of $[Ru(4,4'\text{-diphenyl-}2,2'\text{-bipyridine})_3]^{2+}$. *J. Phys. Chem. A* **1999**, *103*, 8440-8446; DOI: 10.1021/jp9927754.

12. Slavov, C.; Hartmann, H.; Wachtveitl, J. Implementation and Evaluation of Data Analysis Strategies for Time-Resolved Optical Spectroscopy. *Anal. Chem.* **2015**, *87*, 2328-2336; DOI: 10.1021/ac504348h.

13. Borgwardt, M.; Wilke, M.; Kiyan, I. Y.; Aziz, E. F. Ultrafast Excited States Dynamics of $[Ru(bpy)_3]^{2+}$ Dissolved in Ionic Liquids. *Phys. Chem. Chem. Phys.* **2016**, *18*, 28893-28900; DOI: 10.1039/c6cp05655e.

14. Zhang, Y.; Dood, J.; Beckstead, A. A.; Li, X.-B.; Nguyen, K. V.; Burrows, C. J.; Improta, R.; Kohler, B. Efficient UV-Induced Charge Separation and Recombination in an 8-Oxoguanine-Containing Dinucleotide. *Proc. Natl. Acad. Sci.* **2014**, *111*, 11612-11617; DOI: 10.1073/pnas.1404411111.

15. Brown, A. M.; McCusker, C. E.; Carey, M. C.; Blanco-Rodriguez, A. M.; Towrie, M.; Clark, I. P.; Vlček, A.; McCusker, J. K. Vibrational Relaxation and Redistribution Dynamics in Ruthenium(II) Polypyridyl-Based Charge-Transfer Excited States: A Combined Ultrafast Electronic and Infrared Absorption Study. *J. Phys. Chem. A*; DOI: 10.1021/acs.jpca.8b06197.

16. Nibbering, E. T. J.; Fidder, H.; Pines, E. Ultrafast Chemistry: Using Time-Resolved Vibrational Spectroscopy for Interrogation of Structural Dynamics. *Annu. Rev. Phys. Chem.* **2005**, *56*, 337-367; DOI: 10.1146/annurev.physchem.56.092503.141314.

APPENDIX F. VARIABLE-TEMPERATURE SET-UP

1. Description of the Set-Up

Below is a complete description of each of the components required to perform variable-temperature ultrafast transient absorption (VT-TA) spectroscopy within the laser system available to us. The cryostat is placed on the laser table and secured using a base specially made by Glenn Wesley of the MSU Machine Shop. A securing rod was also made for the transfer line arm to minimize any movement of the cryostat during data collection. The liquid nitrogen storage Dewar is placed near to the laser table so that the transfer line can remain attached throughout laser operation. Because the transfer line is very flexible and relatively heavy, care is taken to avoid touching it during the experiment. On the other side of the cryostat is placed the turbomolecular pump on its own transportable cart; the cart allows the pump to be moved away from the laser table during times when the cryostat is not in operation. While the cryostat is being pumped down to vacuum, the pump itself is vibrating quite noticeably, such that the cart is moved as far as is possible away from the table so as to not have any vibrations perturbing the laser experiment. The temperature control unit is housed in the scaffolding above the cryostat and positioned so the temperature monitors can be viewed when standing next to the storage Dewar and house nitrogen line. This allows for optimal ease of control of the temperature either by heating with the temperature control unit, or cooling with the house nitrogen and liquid nitrogen Dewar.

1.1 Optical Dewar/Cryostat

The complete set-up can be seen in Figure F.1. This is a Janis SVT-300 Optical Cryostat.[1] The sample sits at the bottom of the cryostat. It is mounted to the sample rod, which is inserted at the top of the cryostat. There are two sets of windows on all four sides at the base of the cryostat

(Figure F.2), allowing for both collinear and scatter-based spectroscopies to be performed. Two 12-pin ports sit at the top of the cryostat for connection to an external temperature control unit. The long arm extended 90° from the cryostat is the cryogenic fluid transfer arm.

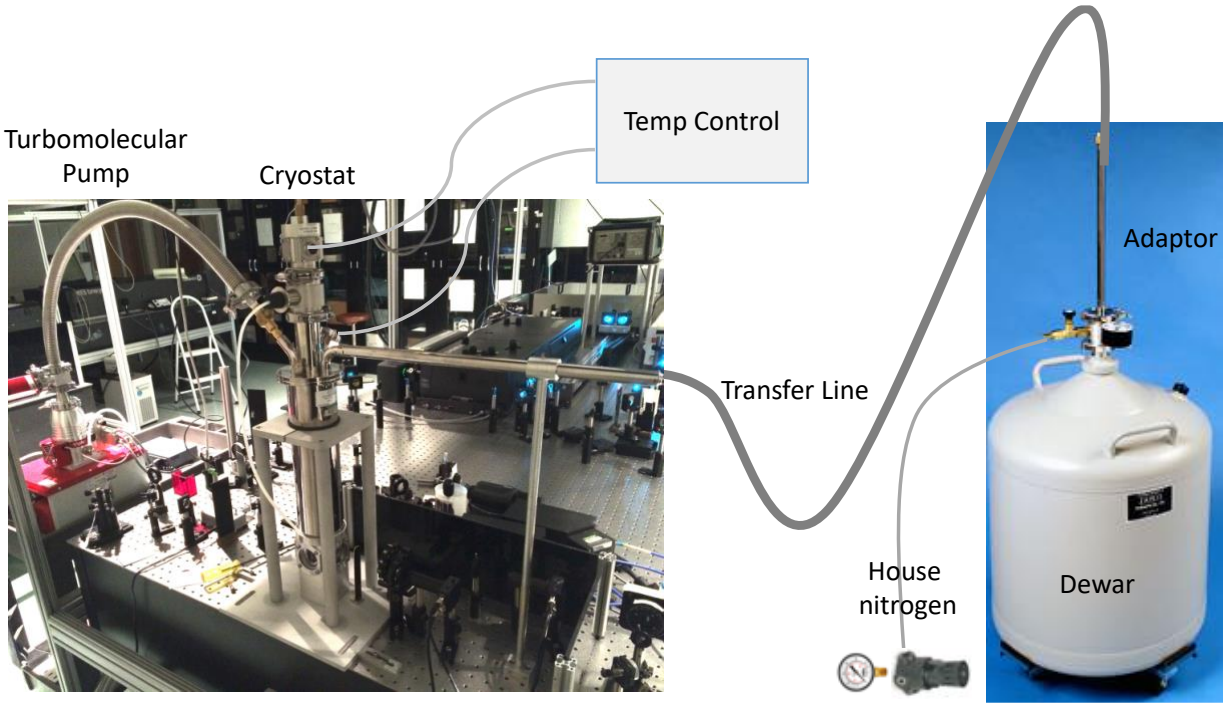

Figure F.1. On the left is a photograph of the variable-temperature set-up with each of its components labeled. The right shows the N_2 gauge adapted from ref. 2 and storage Dewar from ref. 1.

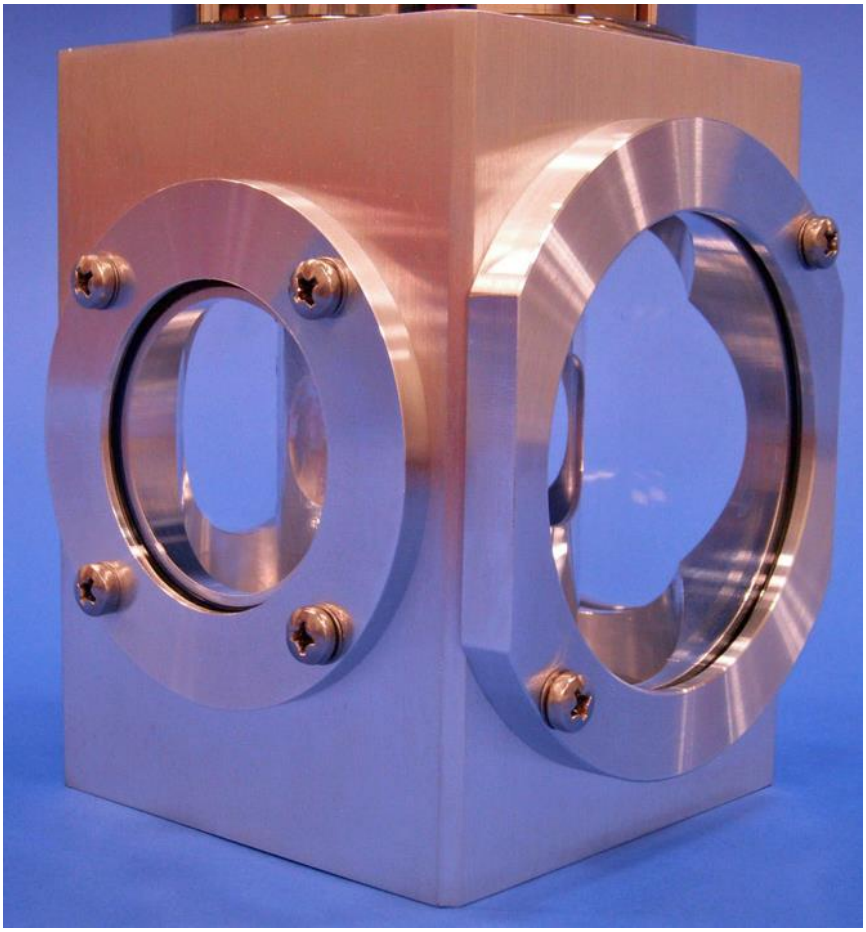

Figure F.2. Blow-up of the bottom-most portion of the optical Dewar from Janis Research. Each of the outer- and inner-jacket have four optical windows, allowing for collinear of 90º experiments to be performed in this one cryostat. Image reproduced from ref. 1.

1.2 Turbomolecular Pump

The Pfeiffer Vacuum HiCube 80 Eco pumping station is equipped with a backing and a turbomolecular pump (Figure F.3).[3] The backing pump is capable of reaching pressures down to 3.5 mbar. The turbomolecular pump can reach $<1x10^{-7}$ mbar. An aluminum hose is used to connect the pump to the cryostat. Between this hose and the pump, extended 90° from the pump is a Pirani cold cathode pressure gauge.

Figure F.3. Pfeiffer Vacuum HiCube 80 Eco pumping station. The bottom houses the control unit and rough pump, and the silver cylinder on top is the turbomolecular pump. A hose is attached at the top of the turbopump and connected directly to the cryostat. Image reproduced from ref. 3.

1.3 Liquid Nitrogen Storage Dewar and Cryogenic Transfer Line

An International Cryogenics 35 L Dewar intended for liquid nitrogen storage[4] comes with this set-up, although other appropriate Dewars may be used in its place. This Dewar is fitted with a DN 40 ISO-KF flange for attaching both a pressure gauge[2] and an adaptor for the transfer line, as seen in Figure F.4.

Figure F.4. (Left) International Cryogenics, Inc. 35 L liquid nitrogen storage Dewar utilized in these experiments. Image reproduced from ref. 4. (Right) Attachments for the storage Dewar, including flanges, pressure gauge, and transfer line inlet port. The liquid nitrogen capacitive level sensor shown above is not included in our set-up. Image reproduced from ref. 1.

1.4 Temperature Control Unit

The LakeShore Model 335 Temperature Controller connects to the cryostat, providing both real time monitoring of the temperature within the cryostat, as well as sample heating capabilities (Figure F.5).[5] Port A connects to the lower portion of the cryostat, and thus is more susceptible to rapid thermal fluctuations. Port B, however, monitors the temperature at the top of the cryostat.

Figure F.5. The LakeShore Cryotronics Model 335 temperature control unit that is connected directly to the optical cryostat. It has two thermocouples within the cryostat that allow for an average temperature to be monitored and controlled externally with this unit. Image reproduced from ref. 5.

1.5 Cuvette and Sample Holder

Two different types of cuvettes have been specially-made for use in this set-up, both by FireFlySci.[6] They are both a maximum of 30 mm tall with the cap on, so that they can fit within the sample holder within the bottom chamber of the cryostat. Because the cuvettes are being used in an ultrafast transient absorption experiment, they are made from UV quartz with high optical quality in the region 190-2500 nm. The quartz is sealed for use with a cryogenic fluid, and we have one set of two cuvettes with a PTFE stopper and one set of two cuvettes with a ground glass cap. Neither top has been shown to guard against capillary action, which decreases the amount of sample in the cuvette, and increases the concentration of the sample by allowing for evaporation of the solvent. The cuvettes with the PTFE stoppers have an optical pathlength of 10 mm, whereas those with the ground glass cap have a pathlength of 2 mm.

The sample holder was specially designed by Glenn Wesley. This aluminum piece conducts heat and is affixed to the bottom of the sample rod that is inserted into the cryostat. Its thermal conductivity is critical, as it means that sample it is holding is more likely be of the same temperature as the holder itself, which the bottom thermocouple reads. If this piece were non-conducting, there would likely be a large mismatch between the sample temperature and the temperature on the LakeShore temperature control unit.

2. Effects Introduced by the Cryostat

2.1 Dispersion

In Chapter 2, the effects that dispersion (also known as chirp) can have on an ultrafast pulse were outlined. Briefly, a temporally short, spectrally broad pulse propagates is highly susceptible to temporal broadening when it propagates through a medium, such as quartz.[7,8] This is due to the

refractive index of the optic being wavelength-dependent, such that the group velocity of bluer wavelengths is slowed relative to that of the red wavelengths for normal dispersion, but vice versa for anomalous dispersion. By Heisenberg's time-energy uncertainty principle, eqn. (F.1), the

$$\Delta E \Delta t \geq \frac{\hbar}{2} \tag{F.1}$$

spectral and temporal characteristics of a pulse are inversely related and an ultrashort laser pulse must therefore have a large spectral bandwidth. A pulse that is as short as it temporally can be with the given spectral bandwidth is known as transform-limited. Thus, the effect of dispersion becomes more and more significant as the pulse becomes shorter and shorter temporally. The pulses on Wile E, the longer pulse system in our lab, are >150 fs, depending on the solvent and pump/probe combination. At this pulse duration, even 20 mm of fused silica only introduce <10 fs of broadening. But this is only what the theory says, not what is necessarily true in the system.

The best way to measure the effects of dispersion is through the use of the optical Kerr effect (OKE) and cross-correlations in a solvent blank. The former provides information about the pulse duration (τ_{pulse}), whereas the latter gives the overall instrument response function (IRF). The typical pathlength used in our ultrafast measurements is a 1 mm cuvette. In this sample holder with acetonitrile (MeCN), τ_{pulse} was found to be an average of 225 fs. In moving to a 10 mm pathlength cuvette with MeCN, τ_{pulse} ~250 fs, an increase of 25 fs (10%) by the addition of 9 mm of solvent. Placing the 10 mm pathlength cuvette into the cryostat further broadens the pulse to 277 fs, which is another 10% increase. This trend shows that both solvent pathlength and additional glass introduced by the cryostat elongate the ultrafast laser pulses. The pulse duration was also found to be surprisingly dependent on the orientation of the cuvette. The cuvette can be angled to nearly 45° relative to the probe input angle, meaning that in the case of the 10 mm pathlength sample cell, the probe may actually propagate through nearly 14 mm of solvent. Likewise, the cryostat itself is

canted slightly, increasing the amount of fused silica through which the laser pulse traverses. It is quite probable that we are simply underestimating the amount of solvent and glass in the laser path. One benefit, however, to studying Fe(II) complexes is that their ground state recovery lifetimes are typically on the order of hundreds of picoseconds or longer. For these data, a broadened pulse lifetime is of no concern.

2.2 Multiple Pulses

As discussed above, neither sample holder nor the cryostat are perfectly square to the probe beam. It was found that when these components were oriented 90º to the input beam, it caused a false pump-probe signal in which the probe was interacting with a pump back-reflection, and not the true pump. It appeared as if the size of the signal greatly decreased despite having a normal amount of I_0 for the sample (i.e., amount of light not being absorbed by the compound). Thus, when held within the cryostat, the cuvette is angled so that back-reflections bounce away from the detector and/or do not re-propagate through the sample. One concern might be consistency of the angle of the sample within the cryostat over the course of data collection, as any change in orientation runs the risk of changing the overlap of the pump and probe pulses. This is especially important when removing the sample rod in order to swap out the stage molecule and sample of interest. To ensure proper orientation, a beam block is placed near the pump directing mirror into the cryostat. The angle of the cuvette is adjusted until the back-reflections from the sample are at the same spot on the block as they were when the stage molecule was in place. It is ideal, then, for the solvent to be the same between the long-lived compound and the sample of interest, so as to minimize effects from different refractive indices.

2.3 Scatter

By far the greatest concern with these measurements is the scatter induced by the pump reflecting on defects on glass surfaces. This extraneous light is now diffuse and is ultimately focused with the probe beam into the detector, overlaying across the pump-probe signal as a negative offset. The negative sign of the scatter is simply due to an increase of transmitted light being seen by the detector. At the least, it decreases the S/N ratio. And with the laser systems in our lab, the pump is translated relative to the stationary probe, meaning that the intensity of the scatter is easily changed with stage position (i.e., time delay). In that scenario, one might expect to see normal kinetics around time zero, and then an offset growing in at later positive times. This has the potential to drastically alter observable kinetics. Scatter is likely to increase with a greater number of surfaces from which light can be reflected. As can be imagined, this makes cryostats prime targets for adverse scatter effects. Again, reorientation of the cuvette and cryostat may help with minimizing the unwanted signal. Additionally, as was mentioned in Chapter 2, probing spectrally far from the pump wavelength should also mitigate these effects. Ideally, a monochromator could be used to completely isolate the true signal from the scatter offset.

3. Temperature-Dependent Artifacts

Molecular lifetimes, solvation dynamics, index of refraction, and most other bulk solvent properties display a temperature dependence. Thus, a VT experiment of any kind but particularly one that utilizes ultrafast pulses will be fraught with artifacts caused by a change in temperature of the sample and surrounding environment. Many of these effects were outlined extensively in Chapter 2 of this work. Two of the more problematic issues will be discussed here: (1) temperature-dependent scatter, and (2) a change in pump-probe overlap with temperature.

Scatter, as defined above, is perhaps the greatest nuisance to VT spectroscopists. It is particularly problematic at colder temperatures, when the viscosity has increased, thus making the medium better able to diffract light. Care should be taken to minimize or completely eliminate if possible the scatter at room temperature. However, it has often happened that upon reaching the coldest temperature, the scatter has greatly increased. Combine this effect with any stage-dependence of the scatter (Fig. F.6), and the result is colder-temperature ground state recovery having a shorter apparent lifetime; when the scatter is reduced at warmer temperatures and the lifetimes being measured are accurate, the Arrhenius plot will consequently appear to have two phases. Especially when working on complexes which have not been previously characterized by VT-TA, care must be taken to reduce scatter so as to not report misleading lifetimes or Arrhenius parameters.

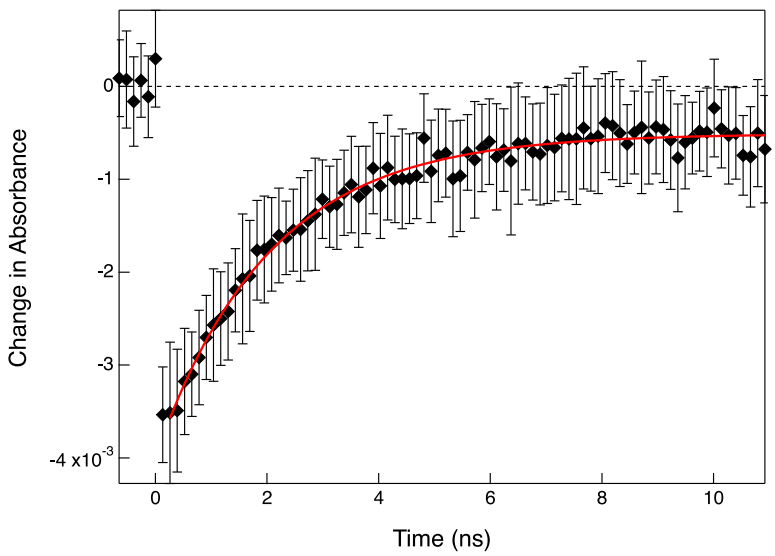

Figure F.6. Ground state recovery VT-TA data of $[Fe(dtbb)_3]Br_2$ in MeOH at 190 K. An apparent offset at positive times is evident and causes the lifetime measured to be 2.03 ± 0.07 ns. This offset is due to scatter overlaying a signal that is increasingly negative at longer time delays. When scatter is minimized, the lifetime at this temperature is 2.57 ± 0.12 ns.

The second critical artifact that temperature can produce is a change in the overlap of the pump and probe beams within the sample. This is a consequence of the index of refraction having a temperature dependence, such that when the sample is colder, the refractive index increases and results in displacing the beams a greater distance than at warmer temperatures. An interesting effect of this that upon going from room temperature to the first (coldest) point, a significant change in I_0 is observed, with $I_0(RT) \geq 2I_0(180\text{-}235\ K)$. This is rather unexpected as a decrease in sample I_0 is typically correlated with the sample absorbing more of the probe light, whereas at colder temperatures, if any change is to occur in the sample then the solubility should have decreased considerably thereby decreasing the effective concentration which would increase the amount of transmitted light through the sample. The attenuation of I_0 must then be attributed to

the change in refractive index shifting the probe such that less light is observed by the detector.

It should be apparent that a shift in the probe position must also mean that the pump beam has also been shifted relative to where it was positioned at warmer temperatures. This will inherently change the amount of signal produced as a function of temperature, which is observed in Fig. F.7. These spectra display the cross-correlation for the longer-pulse system in MeCN as a function of temperature. At warmer temperatures (275-290 K), the amplitude of the positive feature is ~3 mOD. At around 270 K this changes significantly such that the spectra for 235-270 K display positive feature amplitude of ~6 mOD. Based on these results, it would appear that the pump and probe have a better overlap at the colder temperatures. It is unclear why the change in signal magnitude is so abrupt and discontiguous, but this phenomenon has been observed on multiple occasions. Interestingly, the IRF calculated from these cross-correlations is unchanged as a function of temperature (Table F.1).

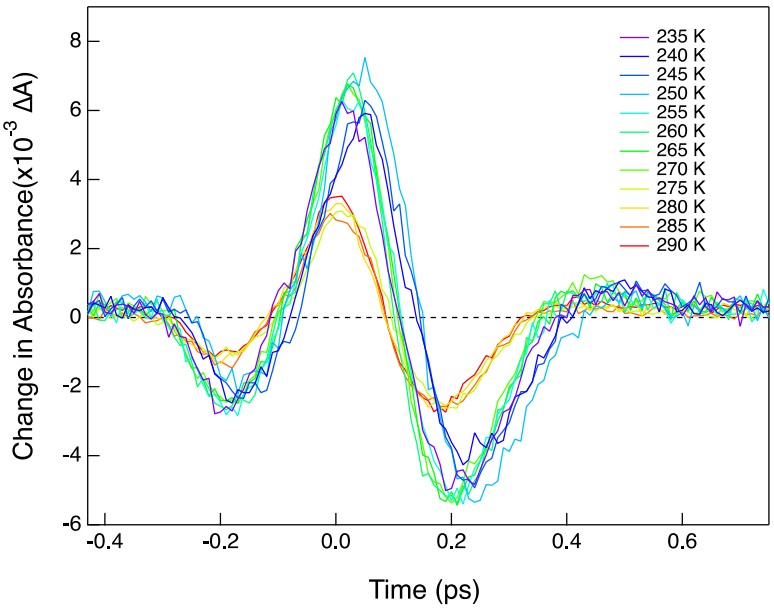

Figure F.7. Cross-correlation in MeCN within the cryostat as a function of temperature. An apparent amplitude increase occurs that separates the warmer temperature data (275-290 K) from the colder temperature data (235-270 K). The IRF remains constant across the profiles.

Table F.1. Summary of pulse characterization data as a function of temperature.

Temperature (K)	τ_{pulse} (fs)	OKE amplitude	IRF (fs)
235	246	8	450
240	223	7	450
245	215	8	455
250	230	7	415
255	224	5	440
260	233	5	440
265	220	4	430
270	219	3	400
275	254	2	435
280	157	1	410
285	120	1	455
290	181	-1	415

Pulse durations were measured by the optical Kerr effect (OKE) in MeCN in conjunction with the IRFs above. The spectra for the temperature-dependent traces are shown in Fig. F.8, and the data summarized in Table F.1. MeCN has been previously observed to have an exponential tail on the positive edge.[8] Unlike the cross-correlation spectra, the OKE traces are fairly smooth and systematic in their changes. In the intermediate temperatures (245-280 K), a steady decrease in signal amplitude is observed in which the intensity begins at ~8 and ends at ~1. The maximum of the Gaussian for the coldest two temperatures is shifted forward in time by nearly 100 fs relative to the intermediate temperatures. At 285-290 K, the spectra now take on a Gaussian derivate-type shape displaying both a positive and negative feature.

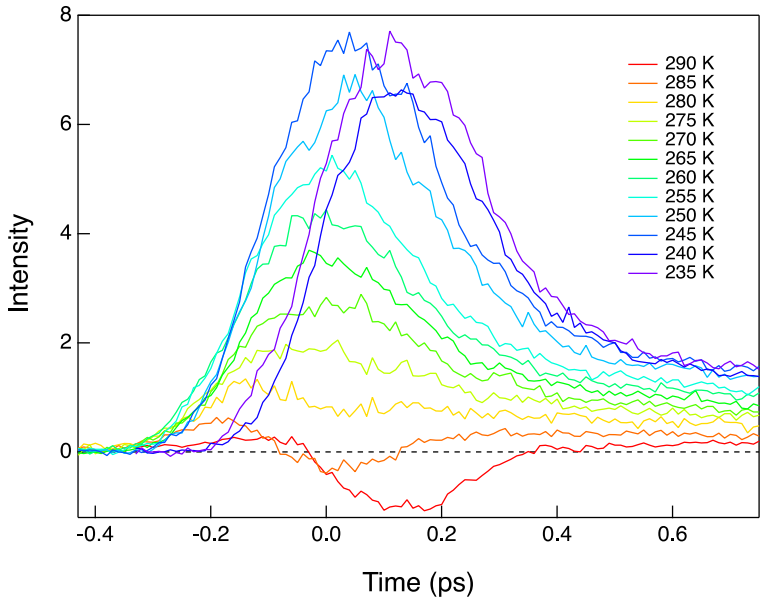

Figure F.8. OKE profiles in MeCN inside the cryostat as a function of temperature. The coldest two temperatures are clearly shifted more positively in time relative to the other traces. Subsequently, a systematic decrease in amplitude occurs until 285 K, at which point the traces are observed to behave less Gaussian and more as a Gaussian derivative.

An overlay of the pulse duration with the OKE amplitude as a function of temperature was made (Fig. F.9). This plot shows the systematic decrease in OKE amplitude in moving from colder to warmer temperatures, which potentially indicates optimal overlap decreasing significantly over the same temperature range. Alternatively, the pulse duration is ~230 fs over the course of 40 K until 275 K, at which point the apparent τ_{pulse} decreases to ~150 fs. This is not the true pulse duration, only a result of the poor signal to noise in the OKE spectrum.

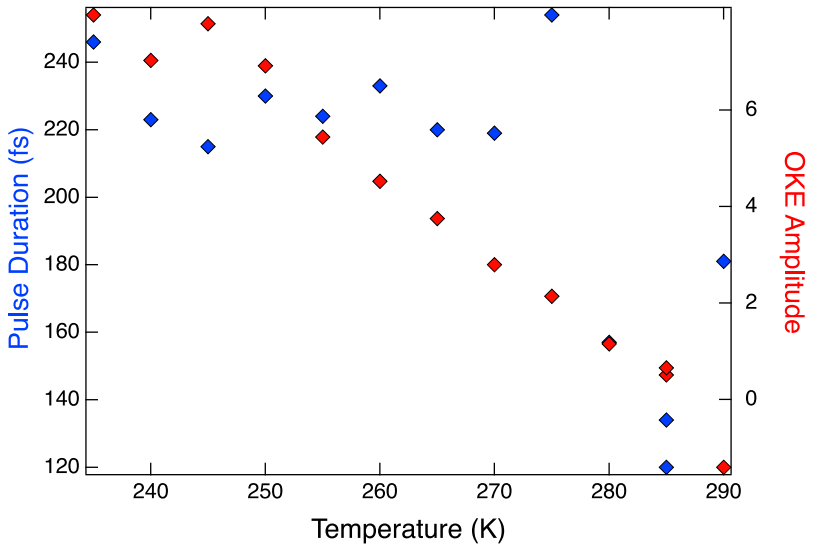

Figure F.9. Comparison of the OKE amplitude (red diamonds, right axis) and pulse duration (blue diamonds, left axis) changes as a function of temperatures. The pulse duration remains relatively constant at 230 fs from 235-275 K, but then is observed to drop to ~150 fs for 280-290 K. The OKE amplitude is observed to decrease systematically from colder to warmer temperatures.

It is clear that as temperature changes, the degree of overlap between the pump and probe beams can also be altered significantly. The S/N will decrease with worsening overlap, time-zero will shift temporally, and other deleterious effects may be seen. That being said, a surprisingly simple method for controlling the overlap during VT data collection is by re-optimizing overlap at each temperature point. One might be concerned about the flatness of the stage being affected by such a process in a molecule that is not long-lived enough to be a stage molecule. However, VT-TA was performed on $[Ru(dpb)_3]^{2+}$ which has a lifetime of approximately 1 μs and therefore does not decay over the temporal delay of this laser set-up. At each temperature, overlap was re-found and the traces were not observed to change significantly in their degree of "flatness." Further tests should be done to verify the robustness of this method, but it is an appealing solution in its simplicity.

4. User Manual for the VT Set-Up

4.1 Assembly

Begin by placing the cryostat in the sample position of the instrument being used. Be sure the base is well-stabilized as torque will be applied from two different sides to the top of the cryostat. It may be helpful to find a way to secure the transfer arm to the base of the instrument being used.

Attach the turbopump to the cryostat via the aluminum hose. Be sure that the port is open between the two (toggle that rotates 90° on the cryostat where the hose attaches should be pointed toward the hose). All flange clamps should be finger tight. Flanges should be connected with an O-ring and aluminum centering ring. Make sure to never have the pump pulling vacuum and then open the cryostat if it is at atmospheric pressure. Pulling that pressure into the turbopump could cause the motor to fail.

Attach the two cables from the temperature control unit to the cryostat such that A monitors the lower gauge, and B monitors the upper. Prepare the cryogenic liquid. If using liquid nitrogen, it is recommended that more than half of the 35 L Dewar is filled. This will ensure that enough liquid is present for the duration of the experiment, as well as reducing the need for external pressure.

4.2 Operation

Mount the sample. Glenn Wesley has made a sample holder than screws into the bottom of the cryostat's sample rod. Be sure that a good connection is formed between the holder and the rod, as this will provide the heating pathway to the sample.

Insert the sample rod into the cryostat. The beam of the spectrometer should go through two windows of glass, into the cuvette and sample, and exit through two panes of glass. If the

height of the sample is not correct, the top of the sample rod can be used to make adjustments. Unscrew the rough gold ring and raise or lower the rod. This same procedure can be used to rotate the sample itself. Care must be taken, however, to not rotate the sample rod more than 180° in either direction, or the heating coils mounted to the rod could become entangled and burn each other.

It may be desirable at this time to collect a room temperature data set of the sample mounted in the cryostat.

When ready to begin the variable-temperature measurements, turn on the temperature controller, and make sure both heaters are turned off. Close the connection between the cryostat and the pump via the toggle. Once that port is closed, turn off the turbopump.

Insert the transfer line into the adaptor in the cryogenic liquid Dewar. Wait for the liquid to begin to escape from the other end of the transfer line. It should be only a small, steady stream of gaseous fluid, with minimal amounts of liquid. If only liquid is pouring out, there is the possibility of flooding the cryostat, which may result in the cuvette breaking. To relieve the pressure and slow the stream of liquid, lift the transfer line so that less of it is in the Dewar. You can also open the outlet port and relieve pressure in that way.

Set the temperature on the control unit by pressing the desired monitor (e.g. “A” or “B”), then “SET POINT,” then key in the temperature and press “ENTER.” Do this for both monitors.

When only gas or a very small amount of liquid cryogen is flowing, insert the transfer line into the side arm of the cryostat. Secure the O-ring using the rough gold ring. Make sure the transfer line is fully seated within the cryostat.

Turn on the heaters by choosing “A” or “B,” then “Heater Range” and press the up arrow for the desired heater setting. The highest setting should not be used due to the ease with which

the wiring burns. Typically, only the lowest setting, or no heater, is required. The heaters should never be left on when the transfer line is not attached to the cryostat.

Monitoring the temperature control unit, allow the sample to reach the desired temperature. It is common to see monitor A drop very quickly, and B much less so. It may be necessary to open the release valve on the Dewar to relieve pressure and thus slow the flow of cryogenic liquid into the cryostat. On the other hand, if the temperature is not dropping, then it is likely that no cryogenic liquid is being transferred. In this case, external pressure must be applied in the form. For example, when liquid nitrogen is being used, a line of house nitrogen is connected to the release valve on the Dewar. The valve is opened and nitrogen is applied to force the liquid nitrogen through the transfer line.

When the average of the two monitors is the approximately equal to the set point, data collection may begin. However, if that collection process takes less than 30 minutes, it may be necessary to allow the system to sit at the set temperature for 30 minutes, to allow the sample to equilibrate.

4.3 Disassembly

When data collection is complete, turn both heaters off using the "ALL OFF" function on the temperature controller. Turn off external gas and remove any tubing to the cryogenic Dewar. Remove the transfer line from the side arm of the cryostat. Close the release valve on the Dewar. Remove the transfer line from the Dewar and hang to air out. Fully close the Dewar.

Slowly open the valve on the cryostat between it and the turbopump. You will hear air rushing into the cryostat. Allow both the cryostat and the turbopump to return to atmospheric pressures. The pumping station should be kept on for >1 h after the pump itself has been turned off prior to data collection. This allows for the venting function to turn on and operate, clearing

out any leftover condensate in the pump.

The cryostat should be allowed to come back to room temperature on its own before the sample is removed. Opening the cryostat before it is fully warmed will cause water vapor to freeze within the sample chamber of the cryostat and may cause issues for future data collection. Turn off the pumping station. Turn off the temperature controller. Remove the cryostat from the instrument.

4.4 Notes

If the pump displays error E006, it is most likely due to condensation build-up in the backing pump. Open the gas ballast valve (located below the red housing, in the back right corner) and allow the pump to run for 15 min to 1 h. It may be necessary to clear the error message and restart the pump. If the error is still present after this, turn the pumping station on, and with the gas ballast valve open, turn off the backing pump. There is a toggle on the backing pump, underneath the red housing, facing the back of the station. It should light up when it is turned on. Flip it to off and allow the pumping station to run in this state for 15 min. Turn the backing pump on with the toggle and run the pumping station normally.

For the sake of time and not wasting the cryogenic liquid, it is best to initially drop to the lowest temperature point, and then rise back to room temperature, as opposed to starting at room temperature and moving to colder temperatures.

It has happened that when the heater is set to, for example, 270 K and low, and the real temperature is more than a degree below that (i.e. the heater is working at maximum voltage), the monitor for the temperature will switch off and read “OVER”. This can mean one of three things:[9] (1) The plug for the monitor may not be fully seated into the port on the cryostat. (2) The port on the cryostat may have faulty connections. Allow the cryostat to fully come to room temperature

(>12 h). Remove the face of the port and pull very slightly away from the cryostat to inspect the wiring at pins G and H. (3) The wires have been fried and must be replaced. Remove the vacuum shroud and radiation shield to expose the sample tube and vaporizer, where the cartridge heater is installed. There is Teflon tubing insulating the solder joints where the wiring joins the leads from the heater. Slide the tubing back to expose the leads and measure the resistance of the heater at the leads. If it measures 50 Ω or more, then the problem is with the wiring. Trace back along the feedthrough to find the damaged area. For both the second and third options, when the burnt section of wiring is found, clip the bad section and splice the wiring back together. Use Teflon tubing or Kapton tape to insulate the solder joint.

REFERENCES

REFERENCES

1. Janis. SVT-300 Optical Cryostat. https://www.janis.com/Products/productsoverview/SuperVariTempReservoirCryostatSystems/SVT-300OpticalReservoirCryostat.aspx (accessed Jul 30, 2018).

2. Grainger. Dial Pressure and Vacuum Gauges. https://www.grainger.com/category/dial-pressure-and-vacuum-gauges/pressure-and-vacuum-gauges/pressure-and-vacuum-measuring/test-instruments/ecatalog/N-1dm5 (accessed Oct 6, 2015)

3. Pfeiffer Vacuum. HiCube 80 Eco, DN 40 ISO-KF MVP 015-2, 100-240 V. https://www.pfeiffer-vacuum.com/en/products/vacuum-generation/pumping-stations/turbo-pumping-stations/hicube-eco/ (accessed Jul 30, 2018).

4. International Cryogenics, Inc. LN2 Storage Dewars. https://www.internationalcryogenics.com/products/ln2_storage_dewars/index.html (accessed Oct 6, 2015).

5. LakeShore Cryotronics. Model 335 Cryogenic Temperature Controller. https://www.lakeshore.com/products/Cryogenic-Temperature-Controllers/Model-335/Pages/Overview.aspx (accessed Jul 30, 2018).

6. FireFlySci Cuvette Shop. Cryogenic Cuvettes. https://www.fireflysci.com/cryogenic-spectrophotometer-cuvettes/ (accessed Jul 30, 2018).

7. Megerle, U.; Pugliesi, I.; Schriever, C.; Sailer, C. F.; Riedle, E. Sub-50 fs Broadband Absorption Spectroscopy with Tunable Excitation: Putting the Analysis of Ultrafast Molecular Dynamics on Solid Ground. *Appl. Phys. B* **2009**, *96*, 215-231; DOI: 10.1007/s00340-009-3610-0.

8. Rasmusson, M.; Tarnovsky, A. N.; Åkesson, E.; Sundström, V. On the Use of Two-Photon Absorption for Determination of Femtosecond Pump-Probe Cross-Correlation Functions. *Chem. Phys. Lett.* **2001**, *335*, 201-208; DOI: 10.106/S0009-2614(01)00057-4.

9. Gonzalez, S. Janis Research Company, Woburn, MA. Personal communication, May 2016.